ABSTRACT

Title of Dissertation:	THE GEOCHEMICAL BEHAVIOR OF SCANDIUM DURING FRACTIONAL CRYSTALLIZATION AND IMPLICATIONS FOR ORE FORMATION
	Austin Michael Gion, Doctor of Philosophy, 2020
Dissertation directed by:	Dr. Philip M. Piccoli, Research Scientist, Department of Geology Dr. Philip A. Candela, Professor Emeritus, Department of Geology

Demand for scandium is increasing due to the use of scandium-aluminum alloys in the aerospace and sporting goods industries, and in solid-oxide fuel cells. Scandium deposits are associated with mafic intrusions and laterites, carbonatites, and granitic pegmatites and the element is recovered as a byproduct of uranium, titanium, apatite, and rare earth element mining. Understanding the processes that form scandium-rich deposits is vital in order to inform exploration for such deposits. The deposits and mafic intrusions at Kiviniemi, Finland and Nyngan, Australia, as well as the granitic pegmatites of Evje-Iveland, Norway are of particular interest. Experiments and thermodynamic modeling of magmatic-hydrothermal systems have been performed in order to constrain the petrogenesis of these deposits.

Cold-seal pressure vessel experiments have been performed on systems with basaltic to rhyolitic compositions in order to evaluate the behavior of scandium in upper crustal magmas. Partition coefficients for scandium between olivine, pyroxene, plagioclase, biotite, spinel, cordierite, aluminosilicates, ilmenite, rutile, apatite and silicate melts, were determined and found to vary as a function of mineral and melt compositions. These partition coefficients were combined with MELTS modeling (MELTS is a software package that is used for performing thermodynamically constrained phase equilibria calculations) to evaluate the behavior of scandium during fractional crystallization of a mafic melt and formation of a cumulate, the subsequent partial melting of that cumulate, then the isothermal decompression and final cooling of that melt. Fractional crystallization can produce scandium-rich cumulates, such as those found at Kiviniemi and Nyngan. However, felsic melts produced by partial melting of a scandium-rich cumulate have, at most, scandium concentrations consistent with the upper continental crust.

Amphibolite partial melting experiments were performed in a piston-cylinder to constrain the petrogenesis of the Evje-Iveland pegmatites. These experiments are inconsistent with the long-held hypothesis that the pegmatites formed by partial melting of their host amphibolite. Instead, magmatic differentiation is the preferred petrogenic model. This model requires that few ferromagnesian phases occur during crystallization of a felsic melt or the presence of scandium complexes that reduce scandium partition coefficients.

THE GEOCHEMICAL BEHAVIOR OF SCANDIUM DURING FRACTIONAL CRYSTALLIZATION AND IMPLICATIONS FOR ORE FORMATION

by

Austin Michael Gion

Dissertation submitted to the Faculty of the Graduate School of the
University of Maryland, College Park, in partial fulfillment
of the requirements for the degree of
Doctor of Philosophy
2020

Advisory Committee:
Dr. Richard J. Walker, Professor, Chair
Dr. Philip M. Piccoli, Research Scientist, Co-Chair
Dr. Philip A. Candela, Professor Emeritus
Dr. Sarah C. Penniston-Dorland, Professor
Dr. Efrain Rodriguez, Dean's Representative, Associate Professor

Foreword

This dissertation contains two chapters that are presented as manuscripts that have been or will be submitted, in their current format to be published. These chapters are Chapters 4 and 5. The author of the dissertation is the primary author for these chapters and was responsible for the design of the project, performing experiments, data collection, data interpretation, and writing of results. The author of this dissertation received technical assistance for the experiments and data collection presented in Chapter 4 and those who provided assistance are listed in the acknowledgements for that chapter, as well as below. Those listed as co-authors at the beginning of each chapter acted as advisors to the author of this dissertation. Additionally, the references in the main body of the dissertation for all chapters has been combined into a single list at the end of this document. Chapter 4 builds on the primary study conducted as part of this dissertation (Chapters 1 through 3) and further discusses the formation of scandium-bearing pegmatites. Chapter 5 is a separate work outside of the primary project of this dissertation that aims at further classifying granites based on the composition of ferromagnesian silicates.

Dedication

To my family, thank you for the support.

Acknowledgements

I would like to thank my advisors Philip Candela and Philip Piccoli for their mentorship and assistance during my time at the University of Maryland and for introducing me to experimental petrology and rigorous science. I would also like to thank John Nance who initially trained me in the experimental lab. This work would not be possible without the assistance of numerous other individuals. Yingwei Fei of the Carnegie Institution for Science Earth and Planets Laboratory (formerly Geophysical Laboratory) is thanked for allowing me to work in this laboratory and advising me in the operation of a piston-cylinder apparatus. Axel Müller, University of Oslo, is thanked for providing samples of the Evje-Iveland amphibolite. Amanda Lindoo and Jing Yang, of the Earth and Planets Laboratory are thanked for technical assistance while the piston-cylinder experiments where being performed. Emma Bullock, Earth and Planets Laboratory, and Richard Ash, University of Maryland, are thanked for assistance in performing electron microprobe analyses and analysis by LA-ICP-MS, respectively. A. Jay Kaufman, Richard J. Walker, Sarah C. Penniston-Dorland, and Andrew Houston are also thanked for providing use of lab equipment and assistance, at the University of Maryland, in preparing materials for use in piston-cylinder experiments. Paula Antoshechkina is thanked for providing guidance when performing MELTS modeling. I would also like to thank Phil Blevin, Colleen Bryant, Penelope King, David Lescinsky, Joseph Whalen, and Lesley Wyborn for assisting me and providing me with data on granites located in Australia and Canada. Additionally, I would like to acknowledge financial support from the National Science Foundation [grant EAR 1348010], the Department of Geology, University of

Maryland, ESSIC, and the Graduate School. Finally, I would like to thank my parents Betty and Paul, my sister Amanda, brother-in-law Abe, and niece Tatum for support during my time at the University of Maryland.

Table of Contents

List of Tables

List of Figures

1. Chapter 1: Introduction

1.1. Scandium in Society

Scandium is a lithophile (Goldschmidt, 1937), first-row, d-block metallic chemical element that is present in the continental crust at a concentration of ~22 ppm (31, 19, and 14 ppm in the lower, middle, and upper crust, respectively) (Rudnick and Gao, 2003) and 16 ppm in the bulk silicate Earth (McDonough and Sun, 1995). Additionally, the average MORB has a scandium concentration of ~40 ppm (Gale et al., 2013). The electron configuration of scandium is [Ar] $3d^1$ $4s^2$ leading to a common oxidation state of 3^+. According to the recommendations of the International Union of Pure and Applied Chemistry (Connelly et al., 2005), scandium is grouped with the rare earth elements (REEs). However, Goldschmidt (1954) noted that due to its ionic radius, the geochemistry of scandium is more similar to magnesium and iron than the REEs.

Scandium is used in the production, often during additive manufacturing (i.e. 3D printing), of scandium-aluminum alloys used in airplane bodies, sporting equipment (baseball bats and bicycle frames), and the frames of firearms (Riva et al., 2016; Røyset and Ryum, 2005). The addition of scandium to aluminum alloys increases strength and decreases weight (Riva et al., 2016); it also the increases the weldability of the alloy, which reduces the need for rivets in the construction of large objects, such as aircraft (Lenczowski, 2002; Madhusudhan Reddy et al., 2005). Scandium has also been incorporated into electrolytes for use in solid oxide fuels cells (SOFCs). SOFCs are high-efficiency (up to 65%), high-temperature, electrochemical cells (Yamamoto, 2000) that are capable of generating power in large

facilities, portable generators, and potentially used to power space craft (Goldsby et al., 2019; Stambouli and Traversa, 2002). The addition of scandium to SOFCs reduces operating temperatures and increases ionic conductivity (Spirin et al., 2012; Sun and Stimming, 2007; Yamamoto et al., 1995).

The global supply of scandium has remained low; however, exploration for scandium continues to grow as the demand is expected to increase (U.S. Geological Survey, 2020). Worldwide, scandium is predominantly produced as a byproduct of titanium, uranium, REE mining, iron, and phosphorus in countries such as China, Kazakhstan, Russian, and Ukraine (U.S. Geological Survey, 2020). Deng et al. (2017) have also reported the recovery of scandium from bauxite ore. The price of scandium oxide (for 99.99% purity Sc_2O_3) was ~$3,900 per kilogram and the price of scandium-aluminum alloy (2% Sc – 98% Al) was $300 per kilogram in 2019 (U.S. Geological Survey, 2020). These prices are significantly higher than other elements with similar uses and abundances in the crust, such as titanium (0.7 wt% TiO_2 in the crust; ~$10 per kg of sponge metal), aluminum (15.9 wt% Al_2O_3 in the crust; ~$2 per kg of ingot metal), lanthanum (20 ppm in the crust; $2 per kg of La_2O_3 at 99.5% purity), and neodymium (20 ppm in the crust; $45 per kg of Nd_2O_3 at 99.5% purity) (U.S. Geological Survey, 2020).

1.2. Economic Geology of Scandium

Minerals with scandium as an essential constituent are rare (Table 1.1). Scandium can substitute for magnesium, iron, and aluminum and is often associated with minerals that contain high-field strength elements (Nb, Ta, Sn, W, and Ti), such as columbite, tantalite, ilmenite, etc. (Williams-Jones and Vasyukova, 2018).

Scandium-bearing deposits have been identified in Australia, China, Ukraine, Russia, Finland, Canada, Germany, Norway, United States, Madagascar, Italy, the Czech Republic, and Japan; although not all are currently being mined (U.S. Geological Survey, 2020). These deposits span a wide variety of types and are discussed in detail below.

Table 1.1: Scandium Minerals

Mineral Name	Mineral Formula	Type Locality	Reference
Allendeite	$Sc_4Zr_3O_{12}$	Allende meteorite, New Mexico	Ma et al. (2014a)
Bazzite	$Be_3Sc_2Si_6O_{18}$	Baveno, Italy	Artini (1915)
Bonacinaite	$Sc(AsO_4)\cdot 2H_20$	Varenche mine, Italy	Cámara et al. (2018)
Cascandite	$CaScSi_3O_8(OH)$	Baveno, Italy	Mellini et al. (1982)
Davisite	$CaScAlSiO_6$	Allende meteorite, New Mexico	Ma and Rossman (2009)
Eringaite	$Ca_3Sc_2Si_3O_{12}$	Wiluy River, Russia	Galuskina et al. (2018)
Heftetjernite	$ScTaO_4$	Tørdal, Norway	Kolitsch et al. (2010)
Jervisite	$NaScSi_2O_6$	Baveno, Italy	Mellini et al. (1982)
Juonniite	$CaMgSc(PO_4)_2(OH)\cdot 4H_20$	Kovdor, Russia	Liferovich et al. (1997)
Kampelite	$Ba_3Mg_{1.5}Sc_4(PO_4)_6(OH)_3\cdot 4H_2O$	Tørdal, Norway	Yakovenchuk et al. (2018)
Kangite	Sc_2O_3	Allende meteorite, New Mexico	Ma et al. (2013)
Kolbeckite	$Sc(PO_4)\cdot 2H_2O$	Schmiedeberg, Germany	Edelmann (1926)
Kristiansenite	$Ca_2ScSnSi_4O_{13}(OH)$	Tørdal, Norway	Raade et al. (2002)
Oftedalite	$(Sc,Ca,Mn^{2+})_2K(Be,Al)_3Si_{12}O_{12}$	Tørdal, Norway	Cooper et al. (2006)
Pretulite	$ScPO_4$	Fischbacher Alpen, Styria, Austria	Bernhard et al. (1998)
Scandiobabingtonite	$Ca_2(Fe^{2+},Mn)ScSi_5O_{14}(OH)$	Baveno, Italy	Orlandi et al. (1998)
Thortveitite	$Sc_2Si_2O_7$	Iveland, Norway	Schetelig (1911)
Warkite	$Ca_2Sc_6Al_6O_{20}$	Murchison meteorite, Australia and Vigarano meteorite, Italy	Ma et al. (2014b)

1.2.1. Nyngan and Syerston-Flemington, Australia

Laterite deposits with elevated scandium have been located in highly weathered ultramafic complexes. The Nyngan deposit, located ~450 km northwest of Sydney, NSW, Australia, is associated with the Alaskan-type Nyngan Igneous Complex (also known as the Gilgai Complex) and is spatially related to the intrusions

of the Fifield Platinum district (Johan et al., 1989; Rangott et al., 2016; Suppel et al., 1986). Rangott et al. (2016) completed a feasibility study of the Nyngan deposit and the following is a general description of the complex and its scandium reserves from that study. The Nyngan complex is concentrically zoned with an ultramafic core and a mafic rim comprising pyroxenite, olivine pyroxenite, hornblende pyroxenite, hornblendite, magnetite pyroxenite, dunite, and monzonite. These rocks are overlain by a lateritic profile which consists, from top to bottom, of a hematitic clay, limonitic clay, saprolitic clay, weathered bedrock, and fresh bedrock. The limonitic and saprolitic layers host the scandium and the grade is highest when the clay is sourced from the pyroxene-bearing rocks. The reserves at Nyngan are 1.4 Mt with a grade of 409 ppm scandium and a cut-off grade of 155 ppm. The Syerston-Flemington deposit, which overlays the Tout Complex, in eastern Australia has also been identified as a scandium-bearing laterite deposit (Chassé et al., 2017; Johan et al., 1989). It bears similar characteristics (rock types and laterite profiles) to the Nyngan deposit with estimated resources of 3.1 Mt with a 434 ppm scandium (Chassé et al., 2017; Pursell, 2016).

1.2.2. Bayan Obo, China

The Bayan Obo deposit is a large, complex REE-Nb-Fe deposit located in China that contains elevated scandium. The ore is hosted in dolomite with mineral assemblages comprising magnetite, hematite, apatite, biotite (phlogopite), aegirine, amphibole (riebeckite-arfvedsonite), fluorite, calcite, barite, and various REE- and niobium-bearing minerals including perrierite-[Ce] ($Ce_4MgFe_2^{3+}Ti_2O_8(Si_2O_7)_2$), bastnaesite-[Ce] ($Ce(CO_3)F$), monazite-[Ce], fergusonite, and columbite

($(Fe,Mn)Nb_2O_6$) (Fan et al., 2016; Smith, 2007; Song et al., 2018). The mineralization and alteration at Bayan Obo occurred in multiple stages and is interpreted to be the result of interactions of the host dolomite with aqueous-carbonic fluids derived from carbonatitic magma (Smith, 2007; Smith and Henderson, 2000). Fan et al. (2016) simplified the REE mineralization into three stages: disseminated, banded/massive (main stage), and aegirine vein-forming alteration. Scandium occurs in aegirine (primary host; average 1.19 wt% Sc_2O_3), perrierite-[Ce] (average 3.26 wt% Sc_2O_3), and columbite-[Fe] ($FeNb_2O_6$; average 0.22 to 0.67 wt% Sc_2O_3) (Shimazaki et al., 2008). Aegirine formation was the result of alteration from oxidized, sodium-rich aqueous-carbonic fluids with 5-15 wt% NaCl equivalent at 430 to 460 °C (Smith, 2007; Smith and Henderson, 2000). Additionally, aegirine is also associated with the main stage of REE mineralization, which includes the formation of fluorite, amphibole, and magnetite, as well as the third vein-forming alteration (Fan et al., 2016). Estimates of scandium production from Bayan Obo are difficult to obtain; however, scandium concentrations in the ores range from 40-169 ppm, reaching 250 ppm Sc in tailings (Duyvesteyn and Putnam, 2014)

1.2.3. Zhovti Vody, Ukraine

The Zhovti Vody, located in Ukraine, is a scandium-vanadium-uranium-REE deposit that formed by the metasomatism of quartz-biotite schists and a magnetite-bearing amphibolite (Tarkhanov et al., 1992). The metasomatism of the magnetite amphibolite resulted in the formation of aegirine and riebeckite (Tarkhanov et al., 1992). Aegirine is the primary scandium-bearing mineral and riebeckite contains minor scandium (Tarkhanov et al., 1992).

1.2.4. Kovdor, Russia

Kovdor, Russia is a baddeleyite-apatite-magnetite deposit hosted in a phoscorite-carbonatite (Kalashnikov et al., 2016). The host rock is concentrically zoned with a margin of forsterite and apatite-forsterite phoscorites; an intermediate zone of low-calcite and magnetite-rich phoscorite; and an inner zone of calcite-rich phoscorites and phoscorite related carbonatites (Kalashnikov et al., 2016). The inner zone contains the scandium-bearing minerals baddeleyite (ZrO_2; 0.078 wt% Sc_2O_3; totaling 420 t), pyrochlore group minerals (0.017 wt% Sc_2O_3), zirconolite ($CaZrTi_2O_7$; 0.032 wt% Sc_2O_3), ilmenite ($FeTiO_3$; 0.043 wt% Sc_2O_3), geikelite ($MgTiO_3$; 0.016 wt% Sc_2O_3), pyrophanite ($MnTiO_3$; 0.226 wt% Sc_2O_3), and juonniite ($CaMgSc[PO_4]_2 \cdot 4H_2O$) (Kalashnikov et al., 2016).

1.2.5. Kumir, Russia

The Kumir scandium-uranium-REE deposit, located in Russia, is the result of greisen-like alteration at the contact between alkaline granitoids (described by Gusev et al. (2009) as A-type granitoids) and a volcanogenic-sedimentary sequence (Egorov et al., 1993; Gusev et al., 2009). The deposit contains two ore types, referred to as "white" and "black" ore (Gusev et al., 2009). The white ore is light in color, exhibits albitization and contains minerals such as tourmaline, fluorite, and sulfides (pyrite, minor pyrrhotite, chalcopyrite, sphalerite, and arsenopyrite) (Gusev et al., 2009). The black ore is dark in color and exhibits fluorite-biotite metasomatism (Gusev et al., 2009). The interior of the deposit (endozone) comprises the white ore and the contact (exozone) with the granitoids comprises the black ore (Gusev et al., 2009). Scandium is primarily found in the form of thortveitite or hosted in tourmaline, which are

disseminated amongst uranium, thorium, and beryllium mineralization (Gusev et al., 2009). Fluorapatite and topaz also occur within the deposit (Gusev et al., 2009). Scandium resources at Kumir have been estimated to be 3.6 t with grades of scandium ranging from 50 to 2400 g/t and an average grade of 205 g/t (Gusev et al., 2009; Williams-Jones and Vasyukova, 2018).

1.2.6. Kiviniemi, Finland

Elevated scandium also occurs at the Kiviniemi Intrusion northwest of Helsinki, Finland (Hokka and Halkoaho, 2015). The Kiviniemi Intrusion comprises a ferrogabbro (ferrodiorite), a leucogabbro (leucoferrodiorite), a garnet-bearing fayalite gabbro (ferrodiorite), and a diorite surrounded by a porphyritic granite (Ahven, 2012; Halkoaho et al., 2013; Hokka and Halkoaho, 2015). The scandium has been magmatically concentrated and the highest grade of scandium is ~300 ppm and occurs in the fayalite ferrogabbro (Halkoaho et al., 2020). Within the intrusion, amphibole, clinopyroxene, and apatite are the major scandium-bearing phases and have concentrations of Sc_2O_3 that range from 103-2088 ppm, 610-1740 ppm, and 940-1133 ppm, respectively (Ahven, 2016; Halkoaho et al., 2020). Resources at Kiviniemi are estimated to be 11.1 Mt grading 175.3 ppm scandium with a cut-off grade of 150 ppm; with no cut-off grade resources are 14.3 Mt with a grade of 154.3 ppm scandium (Hokka and Halkoaho, 2015).

1.2.7. Misery Lake

Exploration for scandium in Canada has begun at Misery Lake (also referred to as the Crater Lake Project; Daigle, 2017) . The deposit is a REE-Nb deposit with

elevated scandium hosted within the Misery Syenite Intrusion (Daigle, 2017; Petrella et al., 2014). The intrusion is ring shaped and its core is obscured by Misery Lake; however, along the margins of the lake those rocks that are exposed comprise a ferrosyenite, felsic syenite, and quartz-fayalite dikes (Petrella et al., 2014). The ferrosyenite is up to 50 modal % mafic minerals including fayalite, hedenbergite, ferropargasite, ilmenite, and annite (Petrella et al., 2014). The felsic syenite is primarily feldspar with ~5% ferromagnesian minerals (Petrella et al., 2014). Surrounding the intrusion are the Mistastin granitoids (rapakivi granite and monzonite) (Petrella et al., 2014). The composition of both the Misery Syenites and Mistastin granitoids are indicative of A-type magmatism and the Nd and Sr isotopic signatures suggest a lower crustal origin (Petrella et al., 2014). Petrella et al. (2014) speculated that the lower crustal material, which may have been partially melted and then fractionally crystallized forming the ferrosyenite, followed by the felsic syenite, and finally quartz-fayalite dikes was enriched in REEs, Zr, Nb, and F due to metasomatism. Magmatic processes concentrated REEs, Zr, and Nb, which are hosted in apatite, britholite-[Ce] $(Ce,Ca)_5(SiO_4)_3OH$), fergusonite-[Y] ($YNbO_4$), and zircon (Petrella et al., 2014). Additionally, aqueous fluids in equilibrium with the Mistastin granitoids further concentrated REEs in fluorocarbonates and britholite-[Ce] (Petrella et al., 2014). Williams-Jones and Vasyukova (2018) stated that scandium is hosted primarily in hedenbergite. Although no total resource estimates for scandium have been made to date; Daigle (2017) noted that drill core contain ~230 to 350 ppm Sc_2O_3.

1.2.8. Deposits Associated with Fluorine-rich Granites

Scandium has also been noted in elevated concentrations in deposits associated with fluorine-rich, topaz-bearing granites and rhyolites at the Climax, Colorado, USA molybdenum deposit; the Sn-W deposits of the Erzgebirge region in Germany; and in the Thomas Range, Utah, USA. At Climax, elevated concentrations of scandium have been found in ilmenorutile ($(Nb, Ti, Fe^{3+})O_2$) (Desborough and Sharp, 1978). At the Erzgebirge deposits, scandium has been reported to reach up to 1 wt% in cassiterite (SnO_2) and zircon ($ZrSiO_4$) and scandium has been interpreted to have been carried by a fluorine-rich fluid (Kempe and Wolf, 2006). In the Thomas Range the concentration of scandium in minerals including pseuodbrookite ($Fe_2^{3+}TiO_5$), bixbyite ($Mn_2^{3+}O_3$), spessartine ($Mn_3Al_2Si_3O_{12}$), hematite (Fe_2O_3), and beryl ($Be_3Al_2Si_6O_{18}$) ranges from 0.1 to 0.7 wt% (Frondel, 1970).

1.2.9. Granitic Pegmatite Deposits

The mineral thortveitite has been found in granitic pegmatites at Crystal Mountain, Montana, USA (Foord et al., 1993); Baveno, Italy (Guastoni et al., 2012); Iveland and Tørdal, Norway (Bergstøl and Juve, 1988; Bjørlykke, 1935); Befanamo pegmatite, Madagascar (Lacroix, 1922); Kyoto, Japan (Sakurai et al., 1962); and Bližná, Bohemia, Czech Republic (Novák, 2007). At Crystal Mountain, thortveitite is found as inclusions within fluorite and actinolite, which are associated with granitic pegmatites and a melagabbro, respectively (Foord et al., 1993). Foord et al. (1993) have suggested that the scandium is sourced from the magma that formed the melagabbro and that the thortveitite exsolved from the actinolite during cooling. Additionally, Foord et al. (1993) stated that the fluorite is hydrothermal in origin, but

does not state whether the thortveitite inclusions are hydrothermal or magmatic. At Baveno, thortveitite occurs as a late stage mineral that crystallized from a hydrothermal fluid and is found in miarolitic cavities within pegmatites (Guastoni et al., 2012; Pezzotta et al., 2005). Pezzotta et al. (2005) and Guastoni et al. (2012) suggested that the scandium is complexed with fluorine and carbon dioxide and that scandium minerals form by one of two methods: 1. Scandium is removed from a melt by a fluorine-rich fluid followed by the crystallization of scandium minerals or 2. Scandium is incorporated into gadolinite-[Y] ($Y_2Fe^{2+}Be_2Si_2O_{10}$) or siderophyllite ($KFe_2Al_2Si_2O_{10}(OH)_2$), which are altered by a fluorine-rich fluid to form scandium minerals. Notably, Baveno is also the type locality of the scandium end-member beryl, bazzite (Gramaccioli et al., 2004).

At Tørdal, the pegmatites are hosted within the Tørdal granite, which are thought to have crystallized from differentiated magmatic fluids (Bergstøl and Juve, 1988). Although the pegmatites are genetically related to the Tørdal granite, Bergstøl and Juve (1988) suggested that the elevated scandium was the result of contamination from the country rock, which includes amphibolites, rhyolitic tuff, hornblende-biotite gneisses, porphyritic gneiss and gabbros. Additionally, the scandium mineral bazzite, as well as ixiolite ($(Ta,Mn,Nb)O_2$) and pyrochlore ($(Na,Ca)_2Nb_2O_6(OH,F)$), which contain weight percent levels of Sc_2O_3 have been found at Tørdal (Bergstøl and Juve, 1988). Further, it is important to note that the Tørdal pegmatites are classified as a mixture of NYF (niobium-yttrium-fluorine) and LCT (lithium-cesium-tantalum) types (Černý and Ercit, 2005).

Perhaps the most well studied occurrence of thortveitite is from the Evje-Iveland pegmatite field in Norway. Thortveitite was first discovered in an Iveland pegmatite by Schetelig (1911) and is the type locality for the mineral. Hypotheses for the origin of the scandium can be traced to Goldschmidt (1934), who suggested that the scandium was sourced from the country rock (amphibolite or gabbro). Bjørlykke (1935) agreed with Goldschmidt (1934) and stated that thortveitite formed as an early- to middle-stage mineral. Neumann (1961) argued against the hypothesis of Goldschmidt (1934), but an alternative hypothesis was not put forth. In recent years, the Evje-Iveland pegmatites have been classified as NYF types (Černý and Ercit, 2005), although they are poor in fluorine (Müller et al., 2015; Müller et al., 2017b). NYF pegmatites are thought to originate from A-type melts (Černý and Ercit, 2005; London, 2008; London and Kontak, 2012). However, Müller et al. (2015) and Müller et al. (2017b) noted that there are no granites that are temporally (the Høvringsvatnet granite is too old; ~ 70 Ma year age difference) or spatially (the Herefoss granite is too distant; 18 km away) related to the pegmatites. Thus, the pegmatites have been interpreted to be the result of anatexis (15 to 30% partial melting; Snook, 2014) of the host amphibolite (Müller et al., 2015; Müller et al., 2017b), which is associated of the Vånne banded gneiss (an amphibolite gneiss) or the Iveland-Gautestad gabbro (Müller et al., 2015; Pedersen et al., 2009). It has been suggested that the pegmatites were emplaced at 400 to 500 MPa and 550 to 600 °C, which was constrained by estimated pressures and temperatures generated during emplacement of the nearby and temporally related Rogaland anorthosite-mangerite-charnockite complex; titanium-in-quartz geothermometry constrains the crystallization temperature of

quartz in the pegmatites to 613 ± 70 °C (Müller et al., 2015; Müller et al., 2017b). An origin resulting from anatexis has been supported by a low initial $^{87}Sr/^{86}Sr$ (0.7063; Stockmarr, 1994), which would indicate a primitive or mantle source (Müller et al., 2015). Additionally, oxygen isotopes of mineral separates from the Evje-Iveland pegmatites range from $\delta^{18}O_{SMOW}$ 0 to ~+11‰ and hydrogen isotopes for biotite and muscovite of δD_{SMOW} -37 to -93 ‰ (Taylor and Friedrichsen, 1983a). These values are similar to both the Høvringsvatnet granite and the host amphibolites and gneisses, although the data from the host rocks are minimal (Taylor and Friedrichsen, 1983a). These observations show that the origin of the pegmatites may be anatexis of the amphibolite.

1.3. Synthesis of Scandium Economic Geology

A notable theme among several of the deposits is that scandium appears to be closely associated with fluorine-rich hydrothermal fluids (Gramaccioli et al., 2004; Guastoni et al., 2012; Kempe and Wolf, 2006; Pezzotta et al., 2005); fluorine-rich fluids may contain on the order of hundreds of ppm fluorine (Candela, 1989a, b). This is consistent with the observations of Gramaccioli et al. (2000) and Wood and Samson (2006), who stated that hydroxyl and fluorine complexes are important in the transport of scandium in low-temperature hydrothermal systems (<300° C). Additionally, the association of scandium-bearing deposits with A-type magmatism is suggested in many of the deposits listed above such as Misery Lake, Canada; Kumir, Russia; Climax, USA; Erzgebirge, Germany; and the Thomas Range, Utah. A-type granites are rocks within the genetic classification scheme for granites (S-I-A(-M)) that are often fluorine- and iron-rich granites formed by partial melting of lower

crustal material (Anderson and Bender, 1989; Clemens et al., 1986; Collins et al., 1982; Eby, 1990; Frost and Frost, 2011; Loiselle and Wones, 1979; Whalen et al., 1987). Because the Tørdal, Norway pegmatites are NYF pegmatites and NYF pegmatites can be associated with A-type melts (Černý and Ercit, 2005; London, 2008; London and Kontak, 2012) this locality may also be associated with A-type magmatism. Although the Evje-Iveland pegmatites are thought to be the result of anatexis (Goldschmidt, 1934; Müller et al., 2015; Müller et al., 2017b), because the source of scandium is unconstrained, A-type magmatism cannot be ruled out. Further, London (2008) noted that the partial melting of an orthopyroxene-, clinopyroxene-, garnet-, and quartz- (or silica-rich phase such as anorthite; Kogiso et al., 2004) bearing mafic rocks may be a potential source for NYF pegmatite-forming, A-type melts. This mineralogy is similar to that of the Kiviniemi, Finland deposit (Ahven, 2012). Thus, the rocks at Kiviniemi (and perhaps at Nyngan) may represent early fractionates of A-type systems, which may evolve and form high-silica A-type granites (e.g. topaz granites) and NYF pegmatites. These rocks may also act as the source material that, when partially melted and further differentiational, could produce scandium-rich felsic rocks. Overall, it is often unclear what causes scandium enrichment in felsic rocks or if there is a connection between the mafic and felsic scandium-rich rocks.

1.4. Research Outline

In order to constrain the processes that resulted in the enrichment of scandium in the types of ore deposits described above, the following chapters address the behavior of scandium in magmatic-hydrothermal systems that may be related to ore

formation. Particular attention is paid to scandium enrichment during the formation of mafic cumulates, such as those at Kiviniemi, as well as the granitic pegmatites at Evje-Iveland and if there is a connection between mafic and felsic scandium-rich rocks. The first step in this research was to evaluate the behavior of scandium by conducting cold-seal pressure vessel experiments in basaltic to rhyolitic systems in order to determine mineral/melt partition coefficients. These experiments are described in detail in Chapter 2. In Chapter 3, these partition coefficients are used, in conjunction with thermodynamic modeling, to evaluate if scandium can be enriched in melt and rocks formed by igneous processes such as fractional crystallization and partial melting. Chapter 4 deals explicitly with the petrogenesis of the Evje-Iveland pegmatite field. Constraints on this petrogenesis were determined by performing piston-cylinder experiments and testing the hypothesis that the pegmatites were formed by partial melting of their host amphibolite. The final chapter deals with evaluating the variations in the composition of biotite and amphibole in S-, I-, and A-type granites. Although this chapter is not directly applied to the formation of scandium-rich ore deposits, the results of this chapter can be used by geologists exploring for deposits that are commonly associated with in S-, I-, or A-type granites.

2. Chapter 2: Experimental Constraints on the Behavior of Scandium During Fractional Crystallization

2.1. Introduction

As noted in Chapter 1 there is a lack of understanding of how scandium-rich felsic rocks form and what their connection to scandium-rich mafic rocks is. In order to place constraints on the formation of mafic and felsic scandium-rich ore deposits, it is necessary to understand the behavior of scandium in magmatic-hydrothermal systems. This chapter details cold-seal pressure vessel experiments performed in basaltic to rhyolitic systems and reports the resulting mineral/melt partition coefficients acquired from the experiments. The starting point for these experiments is based on the hypothesis that the mafic intrusions at Kiviniemi represent a part of a system that, through magmatic differentiation, forms felsic scandium-rich rocks. Thus, the composition of the Kiviniemi ferrogabbro is the starting composition for these experiments. This hypothesis will be further elaborated on in Chapter 3 after the behavior of scandium is constrained by using the results of the cold-seal pressure vessel experiments.

2.2. Previous Work

Several prior experimental studies reported data on scandium partitioning; however, the results of these studies are not necessarily applicable to the formation of ore deposits. Most such studies did not incorporate an aqueous volatile phase and do not extensively study felsic melts, both of which are features commonly associated with scandium-bearing ore deposits. Published experimental partitioning studies have two common themes: pressures of 0.1 MPa or close to 1 GPa (with rare exception;

see Table 2.1). The majority of experiments excluded pressures at shallow to middle crustal levels. One study has been performed at a pressure of 0.7 GPa (Nandedkar et al., 2016), but studies between pressures of 100 to 400 MPa, the pressures where most ore-related magmatic systems crystallize, have not previously been conducted. Additionally, the vast majority of studies are concerned with temperatures >1000 °C. Melt compositions in previous studies range from mafic to intermediate and include komatiite, basalt, andesite, nepheline basanite, among others, with few studies including felsic (granitic) melts. Generally, the mineral/melt partition coefficients that were reported are for olivine and pyroxene and several partition coefficients are reported for amphibole, garnet, and mica (Table 2.1). Many studies also did not include an aqueous volatile phase, which scandium may partition into or affect the properties of a system (solidus temperature, melt composition, phase equilibria, etc.), which in turn could affect the partition coefficients, as well as the occurrence of phases that scandium may strongly partition into. Additionally, the presence of an aqueous volatile phase, which may be a brine or vapor depending on temperature, pressure, and composition, may serve as the transport medium for metals that are ultimately found in ore deposits. Thus, volatile/melt partition coefficients for scandium are needed to assess the formation of scandium-bearing ores.

Experimental studies are not the only source of scandium partition coefficients in the literature. Bédard (2005, 2007, 2014) compiled and analyzed trends in scandium partition coefficients for olivine, orthopyroxene, and clinopyroxene obtained from studies of natural samples and experimental systems. The consensus from published experimental and natural studies is that the partitioning of scandium

depends on mineral and melt compositions, as well as pressure and temperature. Bédard (2005, 2007, 2014) suggested that a major control on scandium partition coefficients is the MgO content of the melt, observing that as MgO decreases, partition coefficients increase.

The most relevant experimental data on the formation of scandium-bearing ores are from Nandedkar et al. (2016) who provided a comprehensive study of trace element partitioning between amphibole and a series of fractionated melts from basaltic-andesite to rhyolite (Table 2.1). However, Nandedkar et al. (2016) did not consider other phases such as biotite, feldspars, apatite, pyroxene, olivine, or spinel at the conditions of their experiments, yet these phases may be significant sinks for scandium, and are the focus of the research described here.

Table 2.1: Mineral/melt partition coefficients from previous experimental studies

Study	Crystal	Melt	Pressure	Temperature	Partition Coefficient
Beattie (1994)					
	Olivine	Basalt to Komatiite	0.1 MPa	1190 to 1500 °C	0.12 to 0.38
Colson et al. (1988)					
	Olivine	Basaltic	0.1 MPa	1180 to 1420 °C	0.13 to 0.3
	Low Ca-Pyroxene	Basaltic	0.1 MPa	1180 to 1420 °C	0.21 to 1.5
Evans et al. (2008)					
	Olivine	Synthetic CMAS	0.1 MPa	1400 °C	Function of Melt Composition
Gallahan and Nielsen (1992)					
	High Ca-Pyroxene	Basaltic	0.1 MPa	1050 to 1180 °C	1.9 to 4
Grant and Wood (2010)					
	Olivine	Synthetic Diopside-Forsterite and Albite-Forsterite	0.1 MPa	1390 °C	0.05 to 0.87
McKay and Weill (1977)					
	Olivine	LKFM	0.1 MPa	1240 °C	0.265
	Low-Ca Pyroxene	LKFM	0.1 MPa	1190 °C	1.4
Nielsen et al. (1992)					
	Olivine	Basalt to Andesite	0.1 MPa	1050 to 1120 °C	0.18 to 0.29
	Low-Ca Pyroxene	Basalt to Andesite	0.1 MPa	1050 to 1120 °C	0.6 to 2.3
Ray et al. (1983)					
	Pyroxene	Synthetic Diopside-Albite-Anorthite	0.1 MPa	1250 to 1345 °C	0.35 to 2.6
Adam and Green (2006)					
	Clinopyroxene	Nepheline Basanite	1 to 2.5 GPa	1050 to 1180 °C	1.3 to 3.6
	Orthopyroxene	Nepheline Basanite	2.7 GPa	1160 °C	0.64
	Garnet	Nepheline Basanite	3.5 GPa	1180 to 1190 °C	4 to 5.8
	Mica	Nepheline Basanite	2 to 2.7 GPa	1050 to 1160 °C	0.16 to 0.25
	Olivine	Nepheline Basanite	1 to 2 GPa	1100 to 1175 °C	0.22 to 0.32
	Amphibole	Nepheline Basanite	1 to 2 GPa	1025 to 1050 °C	1.6 to 2.9
Hart and Dunn (1993)					
	Clinopyroxene	Alkali Basalt	3 GPa	1380 °C	1.31
Hauri et al. (1994)					
	Garnet	Basalt	2.5 GPa	1430 °C	2.62
	Clinopyroxene	Basalt	1.7 GPa	1405 °C	1.66
Hill et al. (2011)					
	Clinopyroxene	Intermediate to Basaltic	1 to 3 GPa	1235 to 1538 °C	0.77 to 7.4
Jenner et al. (1994)					
	Clinopyroxene	Basalt	2.5 GPa	1000 °C	1.4
	Garnet	Basalt	2.5 GPa	1000 °C	3.3. to 4.7
Irving and Frey (1976) (aq)					
	Garnet	Dacite	3 GPa	950 °C	27.6
Adam et al. (2007) (aq)					
	Amphibole	Olivine Basalt	1 to 2 GPa	1050 °C	1.8-2.4
	Amphibole	Nepheline Basanite	2 GPa	1050 °C	1.8
Nandedkar et al. (2016) (aq)					
	Paragasite	Basaltic Andesite	0.7 GPa	1010 °C	4.8
	Magnesiotaramite	Andesite	0.7 GPa	1010 °C	6.6
	Paragasite	Andesite	0.7 GPa	950 °C	7.7
	Paragasite	Dacite	0.7 GPa	920 °C	14.0
	Paragasitichornblende	Dacite	0.7 GPa	890°C	16.3
	Magnesiohornblende	Dacite	0.7 GPa	860°C	17.0
	Magnesiohornblende	Rhyolite	0.7 GPa	830°C	15.9
	Cummingtonite	Rhyolite	0.7 GPa	780°C	35.1

All studies are experimental and exclude partition coefficients calculated using a phenocryst/matrix technique.
(aq) = aqueous volatile phase added to experimental charge

2.3. Hypotheses

Primary (1) Working Hypothesis: At magmatic temperatures (800-1000 °C) and pressures (~100 MPa), scandium will behave as a compatible element in crystalline phases (olivine, pyroxene, biotite, plagioclase, and spinel) relative to a silicate melt.

Null: Scandium will behave as an incompatible ($D \leq 1$) or neither a compatible nor incompatible ($D = 1$) element in the crystalline phases relative to a silicate melt.

Secondary (2) Working Hypothesis: The magnitude of scandium compatibility or incompatibly is dependent on the composition of crystalline phases and/or the composition of the melt (glass).

Null: The magnitude of scandium compatibility or incompatibly is not dependent on the composition of crystalline phases and/or the melt.

Table 2.2: Composition of the Kiviniemi Ferrogabbro and Starting Materials

wt%	**Ferrogabbro**	**KSM1C (N =18)**	**KSM2A (N=10)**	**KSM2C (N=26)**	**KSM3A (N-15)**
SiO_2	47.9	49.7 ± 0.2	63.58 ± 0.46	64.82 ± 0.08	72.24 ± 0.26
Al_2O_3	15.4	17.39 ± 0.08	19.80 ± 0.05	17.65 ± 0.05	14.95 ± 0.13
TiO_2	3.54	3.02 ± 0.09	1.99 ± 0.26	0.69 ± 0.02	0.36 ± 0.02
FeO	13.4	11.1 ± 0.1	3.22 ± 0.15	6.56 ± 0.03	3.47 ± 0.05
MgO	2.98	3.47 ± 0.06	1.97 ± 0.02	1.51 ± 0.01	1.04 ± 0.02
MnO	0.18	0.28 ± 0.01	0.19 ± 0.01	0.21 ± 0.01	0.20 ± 0.02
CaO	7.43	6.76 ± 0.06	2.94 ± 0.03	2.84 ± 0.02	1.59 ± 0.03
Na_2O	2.96	2.87 ± 0.03	1.77 ± 0.02	2.43 ± 0.01	1.68 ± 0.02
K_2O	2.37	3.28 ± 0.04	3.15 ± 0.03	3.25 ± 0.01	2.82 ± 0.02
P_2O_5	1.83	2.15 ± 0.02	0.66 ± 0.01	0.50 ± 0.05	0.59 ± 0.02
Total	98.0	100.0 ± 0.3	99.3 ± 0.6	100.5 ± 0.1	98.9 ± 0.3
Sc (ppm)	~200	172 ± 8	358 ± 14	396 ± 7	432 ± 11

Analysis of ferrogabbro from Ahven (2012). Scandium concentrations are approximated from ferrogabbro analyses with the highest concentrations.

2.4. Experimental Methods

Starting materials for all experiments were synthetic glasses. These glasses were generated by homogenizing a mixture of fired oxide and hydroxide powders and synthetic gels in a platinum crucible at 1300 °C in a box furnace, after the method of Nandedkar et al. (2014). The initial melt (KSM1C; most mafic) was generated so that the composition approximated the whole rock composition of the Kiviniemi Intrusion ferrogabbro (Ahven, 2012). All starting melt compositions are given in Table 2.2. In order to evaluate the effect of fractionation on the budget of scandium, glasses with varying compositions were generated. Those starting glasses (synthetic melts KSM2A, KSM2C, and KSM3A; Table 2.2) are approximations of the average, anhydrous glass composition produced by partially crystallizing a previous starting glass. For example, the KSM1C starting material was partially crystallized and the average composition of the residual glass was determined. Then a new synthetic glass (KSM2A/KSM2C) with this average composition was generated by mixing oxide and hydroxide powders as described above. This process was repeated in order to generate KSM3A, i.e. KSM2A/KSM2C was partially crystallized and the average composition of that residual melt was the composition of the synthetic KSM3A melt. See Figure 2.1 for generalized schematic of this process. This process of generating successively more felsic melts and using those melts in subsequent experiments approximates the effects of fractional crystallization. The numbering scheme used to identify experiments is KSM (Kiviniemi Synthetic Melt) followed by a number denoting the set of experiments (1, 2, or 3), a letter denoting the attempts needed to generate the melt (A to C), and the experiment number ("-1" to "-12"). The Al_2O_3

content and ASI (aluminum saturation index) of KSM2A was deemed too high after completing two experiments and a new mixture (KSM2C) was generated. Additionally, KSM2C was generated by the remelting of KSM2B with additional scandium added. KSM2B is not used or reported here but has the same bulk composition as KSM2C. This procedure was utilized successfully by Nandedkar et al. (2014) to study the evolution of arc magmas and was modified in this study. Modifications include, the homogenization of powders prior to the experiments and a starting initial melt that is lower in CaO and MgO and higher in FeO, K_2O, TiO_2, and P_2O_5 to approximate the Kiviniemi ferrogabbro. KSM2A is aluminosilicate-saturated and KSM1C and KSM2C are spinel-saturated.

Experimental charges were constructed in a multistep process. First, gold tubing (0.127 mm x 5 mm diameter x 20 mm length) was cut to the appropriate length and cleaned with distilled water and acetone. One end of the capsule was tri-crimped and welded. Next, the powdered starting glass was added and distilled water or an aqueous chloride solution (0.05 M NaCl, 0.05 M KCl, 0.01 M HCl) was pipetted into the capsule. Additionally, in a select number of experiments, a synthetic fluorphlogopite was added to the charge in order to introduce fluorine into the system. The open end was then tri-crimped and welded shut. Finally, the capsule was weighed and placed into a drying oven for ~12 hours. Once removed from the oven the capsule was weighed again to check for leaks. Capsules with weight changes of greater than 1 mg were rejected.

The sealed capsules were loaded into René 41 or Molybdenum-Hafnium-Carbide (MHC) cold-seal pressure vessels then pressurized with an argon or water

pressure medium and heated to run conditions. Experiments performed at temperatures above 800° C were performed in MHC vessels, and those at 800° C were performed in René 41 vessels. Temperatures were measured using type-K thermocouple placed next to the pressure vessel (reffered to as the external thermocouple). These type-K thermocouples have an accuracy of ±1 °C. The internal temperature of the MHC vessels was determined by placing a thermocouple into the vessel and calibrating the external thermocouple to the internal thermocouple prior to performing each set of experiments. The René 41 vessels have a small thermocouple well that allows the temperature to be measured within a few millimeters of the capsule. The first set of experiments performed in MHC cold-seal vessels utilized the KSM1C glass and distilled water as the starting materials. These polythermal experiments were initially heated to, and held at temperatures of 937 to 965 °C for one hour, then the temperature was decreased to, and held at 880 to 907 °C for up to 48 hours to induce crystallization, and rapidly quenched from run temperature to room temperature in several seconds. After several experiments, it was determined that crystallization occurred at a higher temperature and later isothermal experiments were heated to, and held at 965 °C for up to 24 hours then rapidly quenched. This change was made to increase the amount of melt present, which in turn increased the cross-sectional area of crystal-poor zones that are needed to obtain reproducible analyses of the glass phase. The second set of experiments performed in MHC cold-seal vessels utilized KSM2A/KSM2C glasses and distilled water as the starting materials. These experiments were heated to, and held at a temperature of 900 °C for up to 40 hours and then rapidly quenched. The third set of

experiments performed in René 41 cold-seal utilized KSM3A glasses and distilled water as the starting materials. In select KSM3A experiments distilled water was replaced by an aqueous chloride solution ± fluorphlogopite. All KSM3A experiments were heated to, and held at a temperature of 800 °C for up to 163 hours and then rapidly quenched. All experimental conditions are summarized in Table 2.3.

Oxygen fugacity (f_{O_2}) control was required because, although the oxidation state of scandium does not change, the f_{O_2} will affect the phases present in the mineral assemblage, as well as the composition of iron-bearing phases (e.g. olivine). The f_{O_2} imposed on the experimental charges ranged from quartz-fayalite-magnetite (QFM) to nickel-nickel oxide (NNO) + 1.4 and was set by changing the partial pressure of H_2 (f_{H_2}) in the pressure medium (when using the MHC cold-seal vessels), which at a known total pressure and water fugacity (f_{H_2O}), fixes the oxygen fugacity (f_{O_2}). It should be noted that experiments performed in MHC cold-seal vessels are limited to ~48 hour run times due to the loss of H_2 to the vessel wall or hydrogen consuming reactions, which reduces the ability to control f_{O_2}. The intrinsic f_{O_2} of the René 41 cold-seal vessels in the Laboratory for Mineral Deposits Research at the time these experiments were performed was NNO + 0.8 to +2 (average +1.44) (Gion et al., 2018). For experiments performed in MHC cold-seal vessels f_{O_2} was determined at the completion of the experiment by analyzing CoPd sensors that were placed next to the experimental charge (after the calibration of Taylor et al. (1992)). The CoPd sensors comprise a pellet of cobalt and palladium metal powders (mix of $X_{Co} = 0.37$) and distilled water placed inside a sealed platinum capsule (0.127 mm x 2-3 mm diameter x <10 mm length). Prior to placing the CoPd pellet in the platinum capsule,

the capsule was lined with yttrium-stabilized zirconium oxide paper to prevent alloying. At the elevated temperatures of these experiments, gold and platinum act as hydrogen-permeable membranes and permit the control and monitoring of f_{O_2} (Chou, 1986).

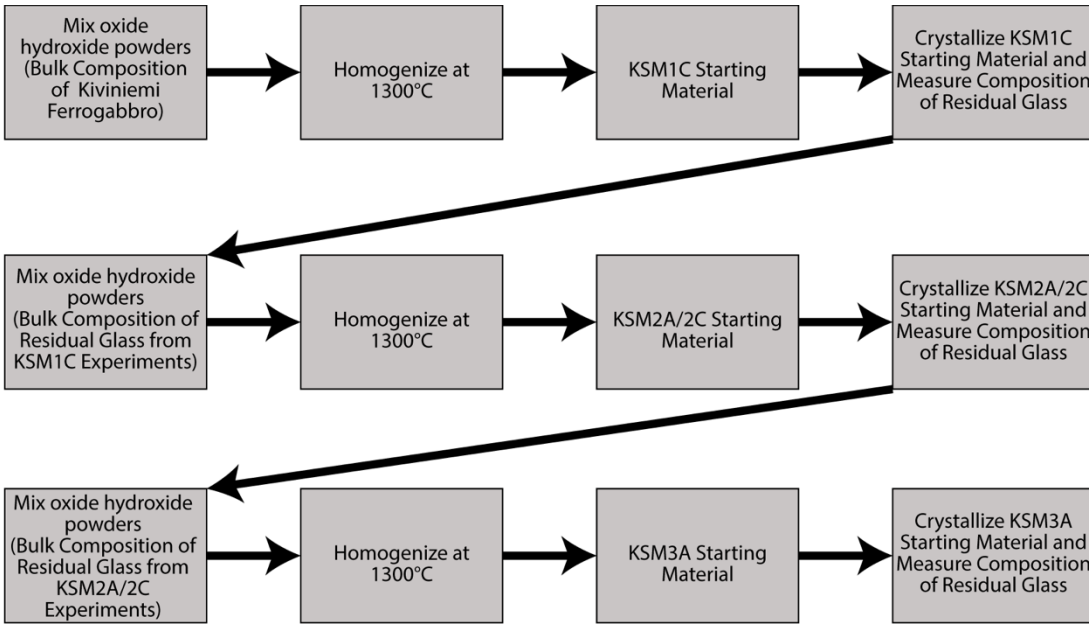

Figure 2.1: Generalized schematic of the process used to generate starting materials used in cold-seal pressure vessel experiments.

Table 2.3: Experimental conditions and masses of starting materials

	Starting Glass (mg)	Water (ml)	Starting Temperature (°C)	Final Temperature (°C)	Pressure (MPa)	ΔNNO f_{O_2}	Duration (hours)
KSM1C-1	14.94	9.38	937	880	93	+ 0.11 ± 0.02	1 + 6.5
KSM1C-2	15.22	9.9	937	880	103	+ 0.54 ± 0.06	1 + 20.5
KSM1C-3	14.87	5.04	965	907	100	+ 0.65 ± 0.08	2 + 24
KSM1C-4	14.85	9.73	952	894	103	+ 0.51 ± 0.03	1 + 24
KSM1C-5	15.36	9.9	965	907	97	+ 1.16 ± 0.03	1 + 48
KSM1C-6	14.87	15	965	965	98	+ 0.37 ± 0.04	24
KSM1C-7	15.2	15.03	965	965	98	+ 0.64 ± 0.03	16
KSM1C-8	14.94	9.93	965	965	99*	+ 0.91 ± 0.02	24
KSM1C-9	14.89	11.94	965	965	100	- 0.377 ± 0.004	22.25
KSM1C-10	15.78	9.82	965	965	100	- 0.23 ± 0.03	22
KSM1C-11	15.46	9.67	965	965	99	0.003 ± 0.01	23.33
KSM1C-12	14.78	9.6	965	965	102	-0.006 ± 0.009	26.2
KSM2A-1	14.95	9.4	900	900	105	+ 1.0 ± 0.1	21.25
KSM2A-2	15.53	9.16	900	900	100	+ 0.69 ± 0.04	23.5
KSM2C-1	15.86	9.99	900	900	101	+ 1.3 ± 0.2	40
KSM2C-2	15.7	10.04	900	900	100	+ 0.9 ± 0.1	33.33
KSM2C-3	15.42	9.82	900	900	101	+ 0.94 ± 0.05	24
KSM2C-4	15.12	9.97	900	900	100	+ 1.12 ± 0.04	22.5
KSM2C-5	14.82	9.73	900	900	100	- 0.19 ± 0.02	25
KSM2C-6	14.81	10.03	900	900	102	- 0.34 ± 0.02	26.5
KSM2C-7	15.15	9.28	900	900	102	- 0.09 ± 0.03	24
KSM2C-8	15.06	-	900	900	102	- 0.14 ± 0.02	22.5
KSM2C-9	15.16	9.68	900	900	103	- 0.13 ± 0.02	25.5
KSM3A-1	14.83	10.1	800	800	100	+ 1.44[c]	162.5
KSM3A-2	15.13	9.64	800	800	100	+ 1.44[c]	163
KSM3A-3	14.97	9.68	800	800	100	+ 1.44[c]	160.25
KSM3A-4	14.76	9.87	800	800	100	+ 1.44[c]	163.5
KSM3A-5	15.43	10.62[a]	800	800	100	+ 1.44[c]	166
KSM3A-6	14.93	10.39[a]	800	800	100	+ 1.44[c]	165.33
KSM3A-7	15.49	10.44[a] (0.49)[b]	800	800	100	+ 1.44[c]	164
KSM3A-8	14.95	10.37[a] (0.46)[b]	800	800	100	+ 1.44[c]	165.5

See text of further details on the starting and final temperatures. Duration is the duration at the starting temperature plus the duration at the final temperature (e.g. 1 + 6.5 means the temperature was held at the starting temperature for 1 hour and then decreased to the final temperature for 6.5 hours). *Pressure dropped ~12 MPa during the duration of the experiment. a = aqueous chloride solution of (0.5 NaCl, 0.5 KCl, 0.01 HCl instead of water used). b = amount in mg of flurophlogopite added. c = average oxygen fugacity of the René 41 vessels determined by Gion et al. (2018). Uncertainty in the oxygen fugacity is 1 σ_m.

2.5. Analytical Techniques

Crystalline and glass run products were extracted from the capsules after quench, mounted in Struers EpoFix® epoxy, and polished. These run products were analyzed by using a JEOL 8900R electron probe microanalyzer at the Advanced Imaging and Microscopy Laboratory at the University of Maryland to determine major, minor, and trace element concentrations. Depending on the exposed area of the run products, the diameter of the electron beam for EPMA was 1 to 5 μm, with an electron beam current of 5 to 20 nA, and an accelerating voltage of 15 kV. Major, minor, and trace elements in the majority of experiments were measured with a beam current of 20 nA. In experiments KSM1C-6, KSM1C-7, KSM2C-1, and KSM2C-2 major and minor elements were measured with a beam current of 10 nA followed by trace (scandium) analyses at 20 or 200 nA. In experiments KSM2C-3 and KSM2C-4 major and minor elements were measured with a beam current of 5 nA followed by trace (scandium) analyses at 20 or 200 nA. This dual current approach was performed to limit "burn in" of aluminum and silicon and minimize diffusion of alkali and alkaline metals, and destruction of hydrous phases. In some cases, one method did not appear to be more advantageous over the other; however, during analyses of more siliceous and more hydrous experiments a small beam diameter and a higher current of 20 nA resulted in the diffusion of sodium away from the electron beam. Standards used for analyses were microcline, Clear Lake plagioclase, rhodonite, Indian Ocean basalt, Mount St. Helens andesite, Yellowstone Rhyolite, Kakanui hornblende, magnetite, spinel, ilmenite, forsterite, fayalite, augite, hypersthene, topaz, scapolite, $ScPO_4$, cobalt metal, and palladium metal. The detection limit for

scandium was ~ 50 ppm. Uncertainties are reported as standard deviations of the mean (σ_m), determined by the equation $\sigma_m = \left(\sqrt{\frac{1}{N-1}\sum_{i=1}^{N}(x-\bar{x})^2}\right)/\sqrt{N}$.

The presence of small crystals sometimes resulted in analyses that are a mixture of glass and crystalline phases. This was particularly problematic with pyroxene analyses. In such cases, the mixed analyses were identified by comparing the compositions and mineral formulas to end-member phases, as well as run-product glass compositions. Analyses determined to be mixtures were excluded from the data presented in this study. Although every attempt to remove these mixed analyses made, it is possible that due to the small grain size mixed analyses were still present. These analyses may cause low or high analytical totals or an unusually high concentration of an element in a mineral. In this study this may be refected in high iron in plagioclase, high aluminum in pyroxene, and high calcium in biotite (see section 2.6).

The abundance or mass fraction of each phase (both crystalline and melt phases) present in the run product assemblage was determined by a constrained linear least-squares method. Linear least-squares equations were solved in MATLAB by using the function *lsqlin* and were constrained such that the mass fraction of each phase present was greater than zero and the sum of all mass fractions was equal to one. For all least-squares calculations, iron was assumed to be present as FeO.

Inherent in the application of the least-squares method was the assumption that there was no exchange of mass with the capsule walls. Given this assumption, the bulk composition of the run products is equivalent to the bulk composition of the starting material. Thus, the sum of the mass fraction of each run product phase

multiplied by the composition of that phase (determined by using WDS), for each major element, should equal the bulk composition of the starting material. In order for this calculation to be performed, identification of all phases and the composition of those phases, as well as the bulk composition of the starting material was required.

In cases where a phase was observed by using EPMA, but analytical results were poor (due to small grain size), an end-member composition was used (as in the case of apatite) or a composition from experiments with better analytical results were used as a proxy (as in the case of spinel). For KSM2A, KSM2C, and KSM3A all calculations were performed assuming ilmenite and rutile were present, as they occur in trace quantities in several experiments. Additionally, because the starting materials contain minor residual phases (e.g. spinel) the glass composition is not necessarily the bulk composition of the starting material (i.e. the bulk composition would be the glass plus any residual crystals), and thus two calculations were performed wherein the bulk composition of the starting material was set equal to 1) the measured composition of the starting material as listed in Table 2.2 (glass alone) and 2) the target composition of starting material (i.e. the sum of the measured glass composition and residual, crystalline solids,). For calculation 2, the bulk composition can be best represented by the mixture of oxide, hydroxide, and synthetic gels that were used to create the synthetic glass (Appendix 2.A). This is thus the idealized bulk starting composition, assuming no mass was lost during synthesis of the starting material and takes into account any unmelted crystals if present.

2.6. Results

2.6.1. Mineralogy and Petrology

2.6.1.1. Mineral Assemblages

The first of three sets of experiments (KSM1C) has two run-product mineral assemblages present. The first assemblage comprises pyroxene, plagioclase, a spinel phase, biotite, and apatite and occurs in three experiments that had an initial (starting) temperature of ~950 °C or lower, prior to a decrease in the temperature. The second assemblage comprises olivine, plagioclase, a spinel phase, and apatite ± minor biotite and pyroxene and occurs in nine experiments that had an initial (starting) temperature of 965°C prior to a decrease in the temperature, as olivine is only stable at a temperature at or above 965°C. Additionally, KSM1C experiments have two mineralogical domains. The cores of each experiment have a higher density of spinel crystals compared to the rims (Figures 2.2 and 2.3). In isothermal experiments, these spinel-poor rims are also crystal-poor and glass-rich. The second set of experiments (KSM2A and KSM2C) has different run-product mineral assemblages for each subset of experiments depending on the starting material used. The run-product mineral assemblage of the KSM2A experiments comprises plagioclase, coexisting aluminum-rich and aluminum-poor spinel, aluminosilicates, cordierite, and trace rutile, and a phase that resembles corundum. The run-product mineral assemblage of KSM2C experiments comprises plagioclase, pyroxene, spinel, ilmenite, and trace rutile (Figure 2.4). In the third set of experiments (KSM3A) the run-product mineral assemblage comprises plagioclase and cordierite, minor quartz and an

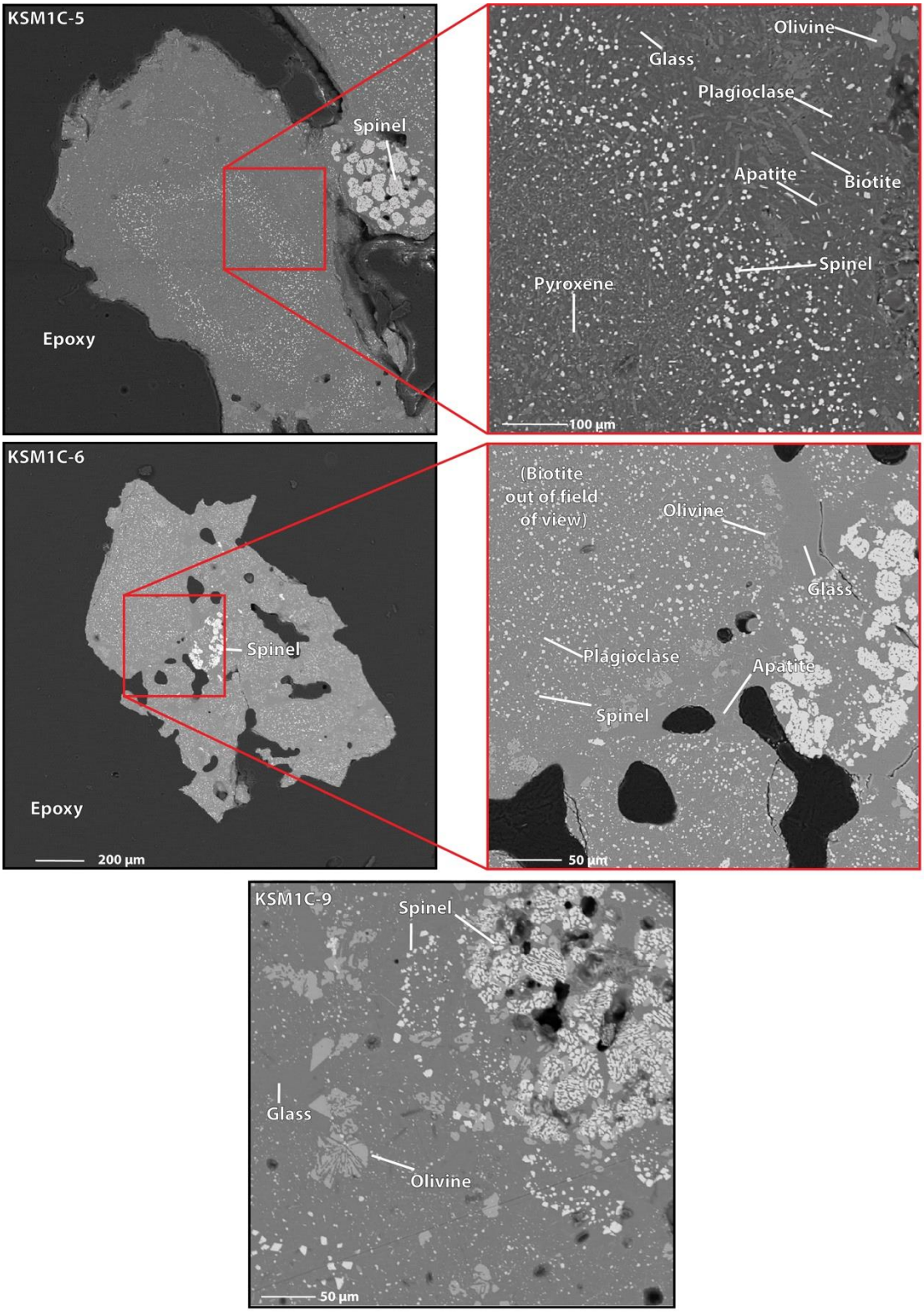

Figure 2.2: Backscatter electron images of run products from KSM1C-5, KSM1C-6, and KSM1C-9 illustrating the mineralogy and primary textures, including glass-rich and spinel-poor rims and spinel-rich cores, skeletal olivine, and acicular apatite.

aluminosilicate mineral, as well as minor biotite in fluorine-bearing experiments (Figure 2.5 and 5). Additionally, in all experiments a glass and volatile phase (i.e. water) is present after quench (with exception of one anhydrous experiment). The volatile phase was visually identified as free water upon opening of the gold capsule after quench.

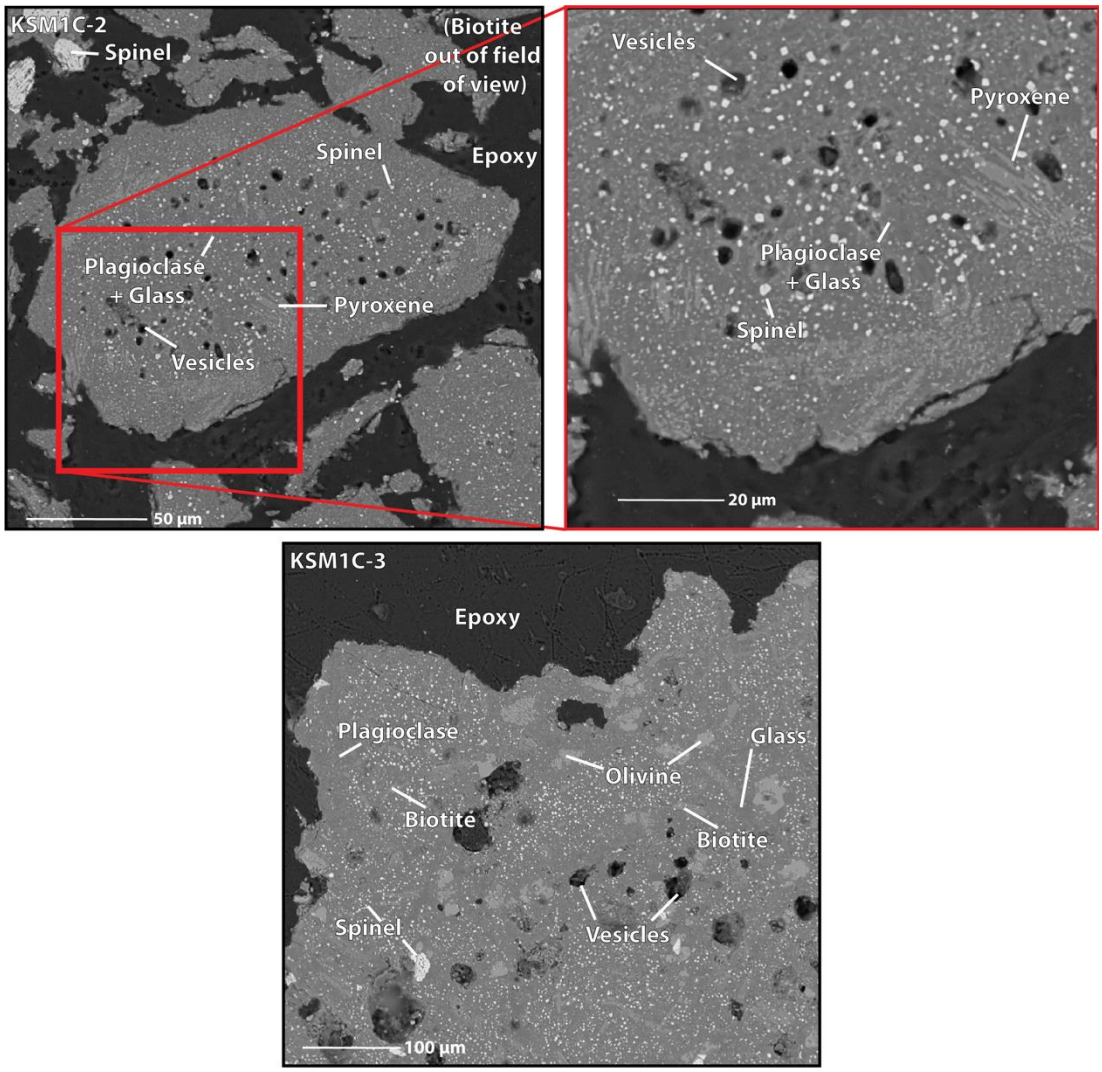

Figure 2.3: Backscatter electron images of KSM1C-2 and KSM1C-3, illustrating vesicular cores of run-product fragments and skeletal pyroxene.

The mass fractions of each run-product phase (crystalline and glass phases) determined by both least squares calculations (i.e. measured and target starting material compositions) are given in Table 2.4. Again the measured composition is the composition of the glass in the starting material only and the target composition is the idealized bulk composition (i.e. glass plus residual crystalline phase). There are some discrepancies between the observed and calculated mineralogies. For example, the mass fraction of olivine calculated for experiment KSM1C-5 is << 1% (0.0% when rounded to one place past the decimal), even though significantly more olivine was observed by using EPMA. The same is true for pyroxene in experiments KSM1C-11 and KSM1C-12. Additionally, experiments KSM1C-3, KSM1C-4, and KSM1C-5 have higher mass fractions of biotite than other experiments. In the case of the mass fraction of biotite, the differences in the amount of biotite is due to a

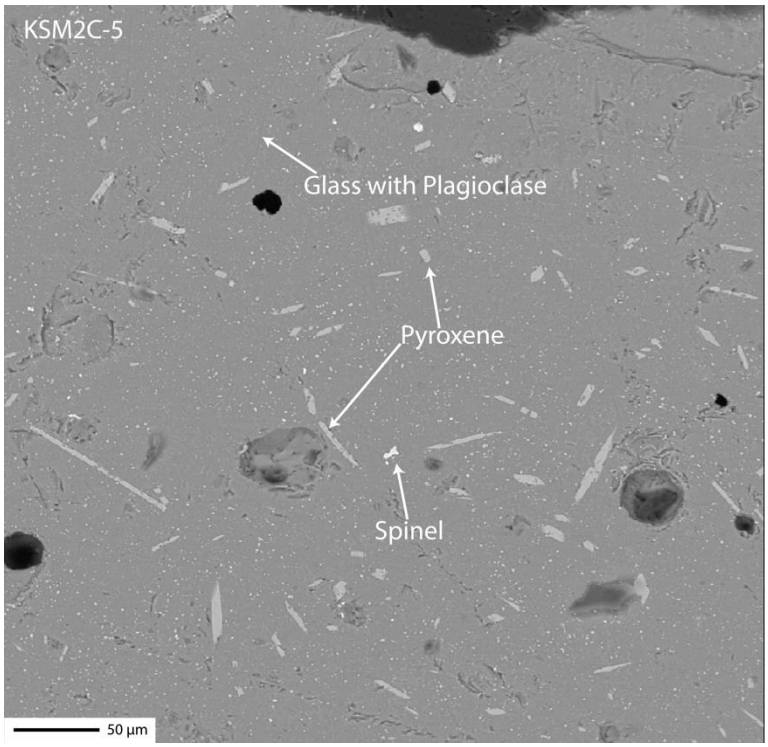

Figure 2.4: Backscatter electron images of KSM2C-5.

multistage crystallization sequence. The first stage of crystallization included olivine, plagioclase, a spinel phase, apatite, and minor biotite ± pyroxene, which occurred at a higher run temperature of 965 °C. After the run temperature was decreased, biotite nucleated and grew, becoming a more prominent phase. There are slight differences in the results of the two least-squares calculations (measured and target starting material compositions). In the calculations performed wherein the target composition of the starting material was used, higher percentages of olivine, spinel, and pyroxene, as well as a lower percentage of biotite in KSM1C experiments were calculated as compared to the calculation performed by using the measured composition of the starting material. In KSM2A, KSM2C, and KSM3A experiments, the least-squares calculations performed by using the target composition of the starting material calculated greater amounts of plagioclase and total solids and lower amounts of pyroxene and spinel as compared to the calculations performed by using the measured composition of the starting material. In some cases, the least-squares calculation performed by using the measured composition of the starting material for KSM3A experiments did not include plagioclase or cordierite, even though these are the most abundant phases. Additionally, for fluorine-bearing experiments, biotite was observed, partly due to the introduction of fluorphlogopite; however, analyses were poor and proxies were not available and thus biotite was not included in the mass balance for those experiments. In some cases, the least-squares calculation performed by using the target composition of the starting material fit the mineral assemblages better. Generally, the calculations performed by using the measured composition of

the starting material have lower residual sum of squares. As a result, the two calculations are interpreted to represent a range of mineral abundances (Table 2.4).

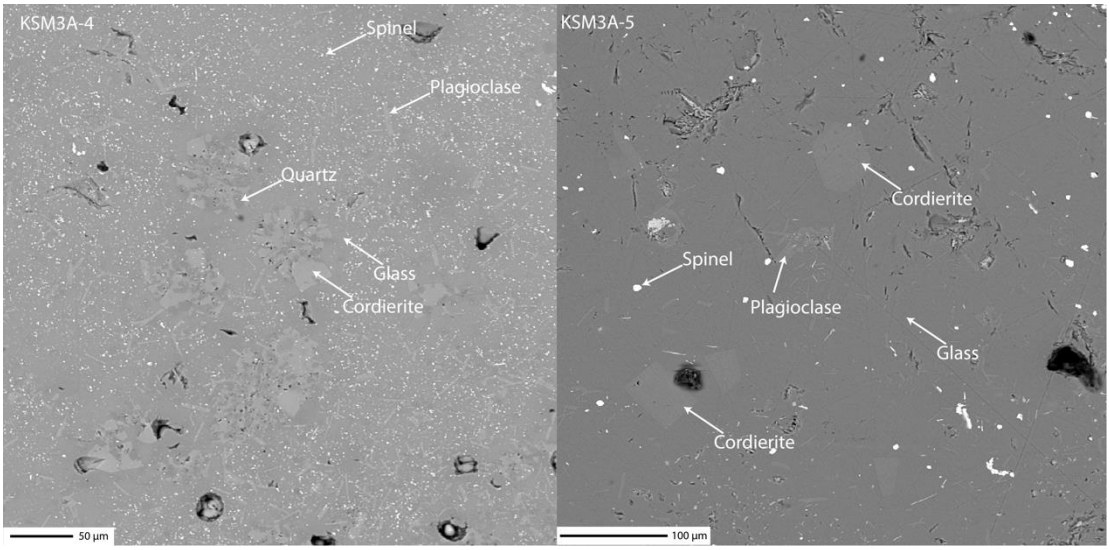

Figure 2.5: Backscatter electron images of KSM3A-4 and KSM3A-5.

Table 2.4: Mass fraction of run products in experiments calculated by linear-least squares

	Olivine	Plagioclase	Pyroxene	Biotite	Spinel Group	Ilmenite + Rutile	Apatite	Aluminosilicates	Cordierite	Corundum	Glass	Solids	SSQ
Target Glass													
KSM1C-1	0.0%	0.0%	5.8%	0.0%	9.9%	0.0%	0.0%	0.0%	0.0%	0.0%	84.3%	15.7%	13.2
KSM1C-2	0.0%	0.0%	6.9%	0.0%	9.9%	0.0%	0.3%	0.0%	0.0%	0.0%	82.8%	17.2%	5.2
KSM1C-3	3.8%	22.6%	0.0%	8.0%	15.0%	0.0%	3.7%	0.0%	0.0%	0.0%	47.0%	53.0%	5.3
KSM1C-4	0.0%	25.8%	3.1%	17.3%	13.9%	0.0%	4.4%	0.0%	0.0%	0.0%	35.5%	64.5%	6.8
KSM1C-5	0.0%	26.7%	2.6%	9.3%	15.2%	0.0%	4.0%	0.0%	0.0%	0.0%	42.2%	57.8%	6.6
KSM1C-6	2.5%	13.8%	0.0%	1.3%	14.7%	0.0%	5.2%	0.0%	0.0%	0.0%	62.6%	37.4%	5.8
KSM1C-7	2.8%	10.6%	0.0%	0.0%	14.3%	0.0%	4.9%	0.0%	0.0%	0.0%	67.4%	32.6%	5.1
KSM1C-8	5.7%	42.9%	0.0%	0.0%	15.2%	0.0%	2.6%	0.0%	0.0%	0.0%	33.6%	66.4%	16.6
KSM1C-9	5.8%	24.3%	0.0%	0.0%	10.1%	0.0%	5.0%	0.0%	0.0%	0.0%	54.8%	45.2%	5.9
KSM1C-10	4.1%	10.4%	0.0%	11.2%	11.9%	0.0%	5.6%	0.0%	0.0%	0.0%	56.9%	43.1%	6.6
KSM1C-11	5.8%	23.4%	0.0%	0.0%	12.3%	0.0%	5.3%	0.0%	0.0%	0.0%	53.1%	46.9%	5.2
KSM1C-12	6.7%	28.3%	0.0%	0.0%	11.5%	0.0%	5.0%	0.0%	0.0%	0.0%	48.5%	51.5%	4.9
KSM2A-1	0.0%	7.4%	0.0%	0.0%	2.4%	0.3%	0.0%	0.1%	6.0%	0.0%	89.7%	16.2%	1.9
KSM2A-2	0.0%	10.3%	0.0%	0.0%	3.1%	0.3%	0.0%	0.4%	0.0%	0.0%	85.9%	14.1%	1.2
KSM2C-1	0.0%	12.2%	0.0%	0.0%	1.7%	0.0%	0.0%	0.0%	0.0%	0.0%	86.2%	13.8%	8.3
KSM2C-2	0.0%	17.7%	1.6%	0.0%	0.8%	0.0%	0.0%	0.0%	0.0%	0.0%	79.8%	20.2%	3.1
KSM2C-3	0.0%	18.8%	0.7%	0.0%	0.6%	0.0%	0.0%	0.0%	0.0%	0.0%	79.9%	20.1%	3.7
KSM2C-4	0.0%	10.3%	0.0%	0.0%	0.0%	0.0%	0.0%	0.0%	0.0%	0.0%	89.7%	10.3%	8.5
KSM2C-5	0.0%	21.2%	2.2%	0.0%	0.0%	0.3%	0.0%	0.0%	0.0%	0.0%	76.3%	23.7%	2.3
KSM2C-6	0.0%	17.2%	0.2%	0.0%	0.0%	0.0%	0.0%	0.0%	0.0%	0.0%	82.7%	17.3%	4.0
KSM2C-7	0.0%	18.9%	1.3%	0.0%	0.0%	0.2%	0.0%	0.0%	0.0%	0.0%	79.5%	20.5%	3.0
KSM2C-8	0.0%	15.3%	0.0%	0.0%	0.0%	0.4%	0.0%	0.0%	0.0%	0.0%	84.3%	15.7%	9.0
KSM2C-9	0.0%	22.2%	2.1%	0.0%	0.0%	0.0%	0.0%	0.0%	0.0%	0.0%	75.7%	24.3%	2.8
KSM3A-1	0.0%	6.7%	0.0%	0.0%	0.3%	0.0%	0.0%	0.0%	0.2%	0.0%	92.8%	7.2%	6.0
KSM3A-2	0.0%	2.6%	0.0%	0.0%	0.8%	0.0%	0.0%	0.0%	3.9%	0.0%	92.7%	7.3%	5.6
KSM3A-3	0.0%	9.8%	0.0%	0.0%	2.5%	0.0%	0.0%	0.0%	0.0%	0.0%	87.7%	12.3%	5.1
KSM3A-4	0.0%	3.8%	0.0%	0.0%	0.5%	0.0%	0.0%	0.0%	5.5%	0.0%	90.3%	9.7%	5.5
KSM3A-5	0.0%	3.2%	0.0%	0.0%	2.4%	0.0%	0.0%	0.0%	0.0%	0.0%	94.4%	5.6%	5.3
KSM3A-6	0.0%	2.5%	0.0%	0.0%	1.5%	0.0%	0.0%	0.0%	0.0%	0.0%	96.0%	4.0%	5.0
KSM3A-7	0.0%	0.0%	0.0%	0.0%	1.1%	0.0%	0.0%	0.3%	0.0%	0.0%	98.6%	1.4%	7.2
KSM3A-8	0.0%	0.5%	0.0%	0.0%	1.5%	0.0%	0.0%	0.0%	0.1%	0.0%	97.9%	2.1%	6.3

Mineralogy determined by least squares method, see text for details. n.a. is not available. SSQ is the sum of the squares of the residuals and indicates the goodness of fit to the starting glass composition

Table 2.4 cont.

	Olivine	Plagioclase	Pyroxene	Biotite	Spinel Group	Ilmenite + Rutile	Apatite	Aluminosilicates	Cordierite	Corundum	Glass	Solids	SSQ
Measured Glass													
KSM1C-1	0.0%	0.0%	5.3%	1.5%	5.6%	0.0%	0.0%	0.0%	0.0%	0.0%	87.6%	12.4%	9.3
KSM1C-2	0.0%	0.0%	4.7%	0.4%	6.5%	0.0%	0.0%	0.0%	0.0%	0.0%	88.4%	11.6%	1.8
KSM1C-3	1.6%	27.5%	0.0%	16.9%	10.7%	0.0%	2.3%	0.0%	0.0%	0.0%	41.1%	58.9%	3.1
KSM1C-4	0.0%	29.0%	0.4%	27.9%	9.0%	0.0%	2.6%	0.0%	0.0%	0.0%	31.0%	69.0%	4.6
KSM1C-5	0.0%	31.2%	0.0%	16.4%	10.7%	0.0%	2.4%	0.0%	0.0%	0.0%	39.3%	60.7%	4.7
KSM1C-6	0.8%	18.6%	0.0%	9.2%	10.3%	0.0%	3.6%	0.0%	0.0%	0.0%	57.4%	42.6%	3.5
KSM1C-7	1.7%	15.6%	0.0%	6.1%	10.0%	0.0%	3.4%	0.0%	0.0%	0.0%	63.2%	36.8%	3.4
KSM1C-8	6.1%	55.6%	0.0%	0.0%	11.6%	0.0%	1.3%	0.0%	0.0%	0.0%	25.4%	74.6%	10.6
KSM1C-9	6.5%	35.4%	0.0%	0.0%	6.7%	0.0%	3.5%	0.0%	0.0%	0.0%	47.8%	52.2%	5.7
KSM1C-10	1.8%	14.5%	0.0%	18.5%	8.4%	0.0%	3.7%	0.0%	0.0%	0.0%	53.1%	46.9%	4.1
KSM1C-11	6.9%	31.8%	0.0%	0.0%	8.7%	0.0%	3.7%	0.0%	0.0%	0.0%	48.8%	51.2%	4.3
KSM1C-12	7.7%	39.0%	0.0%	0.0%	8.0%	0.0%	3.4%	0.0%	0.0%	0.0%	41.9%	58.1%	3.5
KSM2A-1	0.0%	5.7%	0.0%	0.0%	0.0%	1.2%	0.0%	3.0%	6.0%	0.0%	84.1%	15.9%	1.2
KSM2A-2	0.0%	7.2%	0.0%	0.0%	3.0%	1.2%	0.0%	0.8%	0.0%	1.4%	86.4%	13.6%	1.0
KSM2C-1	0.0%	10.2%	0.0%	0.0%	3.4%	0.0%	0.0%	0.0%	0.0%	0.0%	86.4%	13.6%	8.0
KSM2C-2	0.0%	12.5%	0.5%	0.0%	3.3%	0.0%	0.0%	0.0%	0.0%	0.0%	83.7%	16.3%	7.9
KSM2C-3	0.0%	11.5%	0.6%	0.0%	2.6%	0.0%	0.0%	0.0%	0.0%	0.0%	85.3%	14.7%	9.5
KSM2C-4	0.0%	5.5%	0.0%	0.0%	1.9%	0.0%	0.0%	0.0%	0.0%	0.0%	92.5%	7.5%	16.8
KSM2C-5	0.0%	14.8%	3.3%	0.0%	1.6%	0.0%	0.0%	0.0%	0.0%	0.0%	80.2%	19.8%	6.0
KSM2C-6	0.0%	11.0%	2.2%	0.0%	1.1%	0.0%	0.0%	0.0%	0.0%	0.0%	85.7%	14.3%	9.4
KSM2C-7	0.0%	13.4%	2.8%	0.0%	1.4%	0.0%	0.0%	0.0%	0.0%	0.0%	82.4%	17.6%	7.4
KSM2C-8	0.0%	9.8%	4.1%	0.0%	0.0%	0.1%	0.0%	0.0%	0.0%	0.0%	85.9%	14.1%	6.8
KSM2C-9	0.0%	17.7%	6.8%	0.0%	0.0%	0.0%	0.0%	0.0%	0.0%	0.0%	75.5%	24.5%	7.7
KSM3A-1	0.0%	2.3%	0.0%	0.0%	0.1%	0.0%	0.0%	0.0%	0.6%	0.0%	97.1%	2.9%	6.2
KSM3A-2	0.0%	0.0%	0.0%	0.0%	0.6%	0.0%	0.0%	0.0%	4.3%	0.0%	95.1%	4.9%	5.5
KSM3A-3	0.0%	6.2%	0.0%	0.0%	2.2%	0.0%	0.0%	0.0%	0.0%	0.0%	91.6%	8.4%	5.5
KSM3A-4	0.0%	0.0%	0.0%	0.0%	0.2%	0.0%	0.0%	0.0%	6.0%	0.0%	93.7%	6.3%	5.5
KSM3A-5	0.0%	0.4%	0.0%	0.0%	2.4%	0.0%	0.0%	0.0%	0.0%	0.0%	97.2%	2.8%	5.2
KSM3A-6	0.0%	0.0%	0.0%	0.0%	1.4%	0.0%	0.0%	0.0%	0.0%	0.0%	98.6%	1.4%	4.9
KSM3A-7	0.0%	0.0%	0.0%	0.0%	0.6%	0.0%	0.0%	0.0%	0.0%	0.0%	99.4%	0.6%	7.3
KSM3A-8	0.0%	0.0%	0.0%	0.0%	1.0%	0.0%	0.0%	0.0%	0.0%	0.0%	99.0%	1.0%	6.3

2.6.1.2. Textures

The textures of the run product crystalline phases range from skeletal to euhedral. Olivine and pyroxene both have skeletal textures, which formed as a result of rapid growth (Figures 2.2 to 2.4) (Shea et al., 2019; Welsch et al., 2014). In addition to skeletal textures, pyroxene often exhibits high aspect ratios (Figure 2.4). Biotite and plagioclase occur as elongated, euhedral crystals. Further, plagioclase generally occurs throughout the run products associated with glass (Figures 2.2 and 2.3). Cordierite, when present, are larger in size relative to other crystals and are euhedral, often rectangular (Figure 2.5). There are two size distributions of spinel. The smaller spinel (< 10 μm) are ubiquitous among all experiments and occur as euhedral and rectangular crystals (Figures 2.2 to 2.5). Larger spinel (> 10 μm) occur in experiments that have residual spinel in the starting material and these spinel have

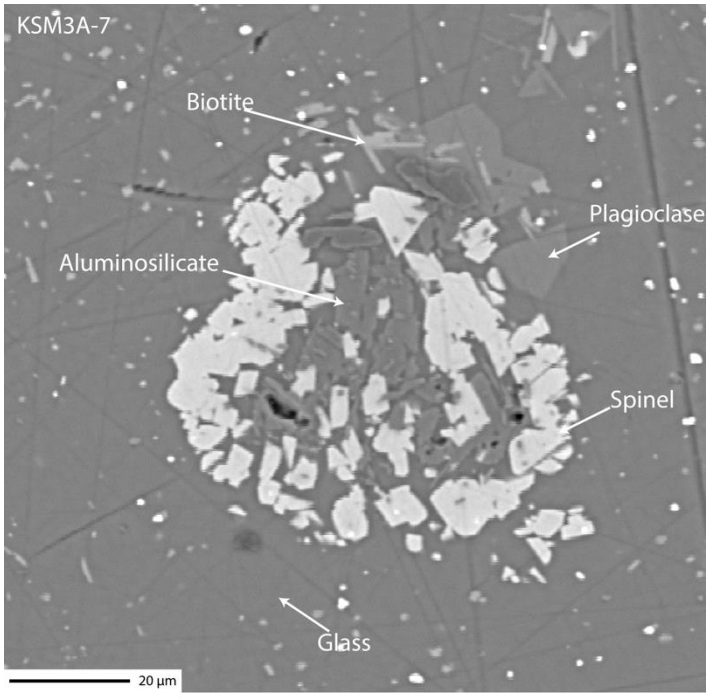

Figure 2.6: Backscatter electron images of KSM3A-7 showing possible miarolitic cavity.

recrystallized during the experiment and occur in clusters (Figure 2.2).

Recrystallization of these spinel is inferred from their welded texture and compositional similarities to smaller spinel crystals (see section 2.6.1.3.5). When present, apatite have an acicular crystal habit (Figure 2.2), which is often interpreted to be the result of rapid cooling and a high growth rate (Höche et al., 2001; Piccoli and Candela, 2002). Additionally, the cores of several run products (polythermal KSM1C experiments) are vesicular and the vesicles are the result of the presence of bubbles at run temperature and pressure, which is due to volatile saturation, as well as partial degassing during quench (Figure 2.3). In the KSM3A experiments that

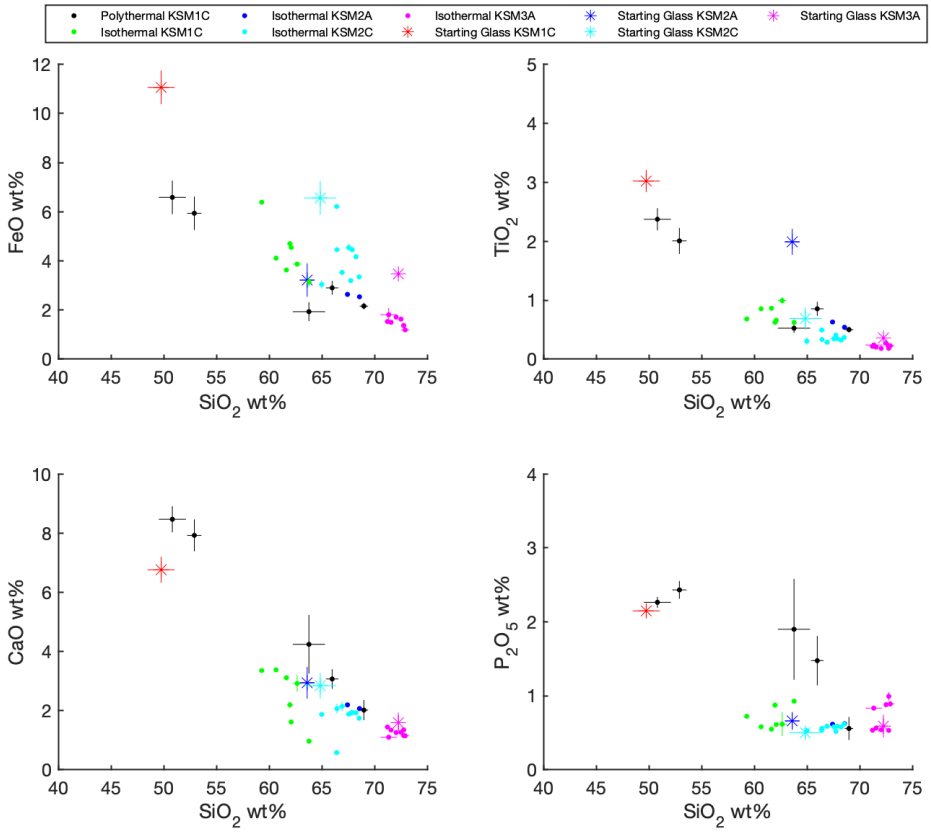

Figure 2.7: Major element (wt%) trends in run-product glass. All plots indicate a decrease in FeO, TiO_2, CaO, and, P_2O_5 as SiO_2 increases. Uncertainty is 1 σ_m.

contained fluorine (KSM3A-7 and -8), there are clusters of aluminosilicates surrounded by spinel, minor biotite, and plagioclase, and these structures may resemble filled miarolitic cavities (Figure 2.6). This may indicate that the crystals within this cavity nucleated on the surface of the melt and grew inward, likely into a bubble (Candela, 1997; London, 1992).

2.6.1.3. Composition of Run-product Phases

2.6.1.3.1. Glass

The compositions of the run-product glasses, which represent the melt at pressure and temperature, are given in Table 2.5. The glass compositions range from ~51 to ~73 wt% SiO_2. As SiO_2 increases in the melt, all other major elements decrease due to the crystallization of minerals (olivine, pyroxene, plagioclase, etc.) and no enrichment trends are observed. FeO, TiO_2, P_2O_5, and CaO exhibit the largest decreases with increasing SiO_2 (Figure 2.7). The range of SiO_2 concentrations of the glasses are produced by variations in the amount of crystallization that has occurred (Figure 2.8), which may be a function of run temperature and duration. Within each experimental set, the SiO_2 concentrations of the glasses increase with increasing crystallization. Longer duration runs broadly have higher mass fractions of total crystals than shorter runs.

The concentration of sodium in the most siliceous experiments (KSM2C-5 to KSM2C -9 and all KSM3A experiments) is lower due to diffusion of sodium away from the electron beam during analyses. This was a consequence of using a small electron beam diameter (1 μm) and high current (20 nA) necessary to analyze the glass and obtain reliable scandium concentrations. In these cases, the sodium

concentrations in Table 2.5 may be ~0.5 to 0.67 of the actual concentrations. This estimate was determined by analyzing Mount St. Helens glass using a 1 μm beam size and 20 nA current and comparing the results to the standard value. The standard value for Na_2O in Mount St. Helens glass is 4.44 wt % (Jochum et al., 2006) and the measured concentration is 2.3 to 2.7 wt% (N=5). However, it should be noted that sodium was the only element affected by the small beam diameter and high current.

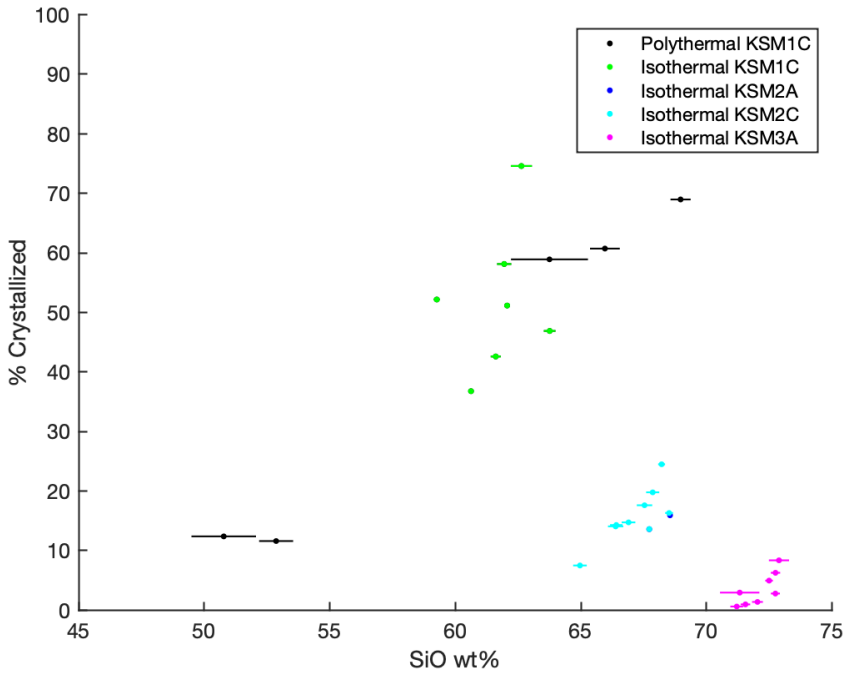

Figure 2.8: SiO_2 (wt%) in run-product glasses plotted against the % crystallized (% solids) as determined by the least-squares method. The trends in the data can only be observed within an experimental set (e.g. a trend when only considering the data for KSM1C experiments). In this figure, there are no meaningful trends when considering all data from different experimental sets. Uncertainty is 1 σ_m.

Table 2.5: Composition of run-product glasses

wt%	KSM1C-1 (N=8)	KSM1C-2 (N=17)	KSM1C-3 (N=7)	KSM1C-4 (N=4)	KSM1C-5 (N=10)	KSM1C-6 (N=13)	KSM1C-7 (N=12)
SiO_2	51 ± 1	52.9 ± 0.7	64 ± 2	69 ± 0.4	66 ± 0.6	61.6 ± 0.2	60.62 ± 0.09
Al_2O_3	20.1 ± 0.4	19.1 ± 0.7	16.7 ± 0.7	15.5 ± 0.5	15.5 ± 0.1	17.72 ± 0.06	17.78 ± 0.06
TiO_2	2.4 ± 0.2	2 ± 0.2	0.5 ± 0.1	0.5 ± 0.05	0.9 ± 0.1	0.86 ± 0.01	0.85 ± 0.01
P_2O_5	2.3 ± 0.1	2.4 ± 0.1	1.9 ± 0.7	0.6 ± 0.2	1.5 ± 0.3	0.55 ± 0.02	0.58 ± 0.01
FeO	6.6 ± 0.7	5.9 ± 0.7	1.9 ± 0.4	2.2 ± 0.1	2.9 ± 0.3	3.63 ± 0.04	4.11 ± 0.03
MgO	1.9 ± 0.3	2.7 ± 0.5	0.4 ± 0.1	0.9 ± 0.1	0.96 ± 0.05	1.58 ± 0.01	1.699 ± 0.005
MnO	0.17 ± 0.01	0.18 ± 0.01	0.11 ± 0.02	0.11 ± 0.01	0.15 ± 0.01	0.15 ± 0.01	0.18 ± 0.01
CaO	8.5 ± 0.4	7.9 ± 0.5	4 ± 1	2 ± 0.3	3.1 ± 0.3	3.11 ± 0.02	3.38 ± 0.01
Na_2O	2.7 ± 0.3	2.1 ± 0.2	1.3 ± 0.3	0.21 ± 0.06	0.56 ± 0.04	1.67 ± 0.08	1.97 ± 0.02
K_2O	2 ± 0.2	3.2 ± 0.4	2.5 ± 0.4	1.1 ± 0.3	2.09 ± 0.04	3.04 ± 0.04	3.14 ± 0.02
Sc_2O_3	0.019 ± 0.003	0.021 ± 0.003	0.012 ± 0.002	0.013 ± 0.003	0.022 ± 0.001	0.018 ± 0.001	0.02 ± 0.001
Total	97 ± 2	99 ± 1	93 ± 2	92 ± 0.8	93.5 ± 0.8	93.9 ± 0.2	94.3 ± 0.1
ASI	1.04	1.04	1.62	3.43	2.22	1.61	1.47

wt%	KSM1C-8 (N=9)	KSM1C-9 (N=10)	KSM1C-10 (N=8)	KSM1C-11 (N=10)	KSM1C-12 (N=8)	KSM2A-1 (N=15)	KSM2A-2 (N=15)
SiO_2	61.4 ± 0.4	59.3 ± 0.1	63.8 ± 0.2	62.06 ± 0.07	61.9 ± 0.3	67.4 ± 0.1	68.5 ± 0.1
Al_2O_3	16.98 ± 0.06	17.40 ± 0.05	18.52 ± 0.04	17.09 ± 0.04	17.7 ± 0.3	16.0 ± 0.1	15.48 ± 0.05
TiO_2	0.85 ± 0.06	0.68 ± 0.01	0.62 ± 0.05	0.660 ± 0.007	0.62 ± 0.02	0.63 ± 0.01	0.54 ± 0.01
P_2O_5	1.0 ± 0.2	0.72 ± 0.02	0.93 ± 0.03	0.611 ± 0.009	0.87 ± 0.04	0.615 ± 0.008	0.62 ± 0.03
FeO	3.7 ± 0.1	6.39 ± 0.06	3.1 ± 0.2	4.55 ± 0.03	4.7 ± 0.1	2.64 ± 0.07	2.54 ± 0.06
MgO	1.58 ± 0.05	1.409 ± 0.008	0.09 ± 0.01	1.252 ± 0.006	1.18 ± 0.03	1.22 ± 0.02	1.18 ± 0.02
MnO	0.164 ± 0.008	0.17 ± 0.01	0.24 ± 0.02	0.15 ± 0.01	0.16 ± 0.01	0.180 ± 0.009	0.17 ± 0.01
CaO	3.80 ± 0.28	3.35 ± 0.01	4.12 ± 0.07	2.78 ± 0.02	3.0 ± 0.3	2.19 ± 0.02	2.07 ± 0.01
Na_2O	2.03 ± 0.05	1.72 ± 0.02	0.96 ± 0.04	1.61 ± 0.03	2.2 ± 0.1	1.19 ± 0.03	1.233 ± 0.008
K_2O	4.0 ± 0.0	3.79 ± 0.01	2.10 ± 0.05	4.21 ± 0.01	4.4 ± 0.1	3.32 ± 0.02	3.45 ± 0.02
Sc_2O_3	0.02 ± 0.00	0.019 ± 0.001	0.02 ± 0.00	0.02 ± 0.00	0.0 ± 0.0	0.042 ± 0.002	0.045 ± 0.001
Total	95.5 ± 0.6	94.9 ± 0.1	94.5 ± 0.3	95.0 ± 0.1	96.8 ± 0.5	95.4 ± 0.2	95.9 ± 0.1
ASI	1.27	1.43	1.81	1.48	1.39	1.82	1.76

Uncertainty is
$1\sigma_m$

Table 2.5 cont.

wt%	KSM2C-1 (N=15)			KSM2C-2 (N=10)			KSM2C-3 (N=8)			KSM2C-4 (N=4)			KSM2C-5 (N=9)			KSM2C-6 (N=10)			KSM2C-7 (N=10)		
SiO_2	67.72	±	0.09	68.5	±	0.2	66.9	±	0.3	65.0	±	0.3	67.9	±	0.3	66.4	±	0.2	67.5	±	0.3
Al_2O_3	14.51	±	0.08	14.1	±	0.1	14.8	±	0.2	14.7	±	0.1	15.3	±	0.2	15.2	±	0.2	14.9	±	0.2
TiO_2	0.41	±	0.02	0.37	±	0.02	0.29	±	0.02	0.31	±	0.07	0.35	±	0.01	0.33	±	0.01	0.35	±	0.01
P_2O_5	0.52	±	0.02	0.62	±	0.02	0.59	±	0.04	0.53	±	0.02	0.59	±	0.01	0.56	±	0.02	0.58	±	0.02
FeO	3.20	±	0.04	3.35	±	0.04	3.53	±	0.08	3.0	±	0.2	4.5	±	0.1	4.46	±	0.06	4.5	±	0.2
MgO	1.08	±	0.01	0.91	±	0.01	1.07	±	0.02	1.21	±	0.02	0.88	±	0.01	0.95	±	0.01	0.94	±	0.02
MnO	0.17	±	0.02	0.17	±	0.02	0.22	±	0.02	0.18	±	0.05	0.19	±	0.01	0.18	±	0.01	0.18	±	0.01
CaO	1.91	±	0.03	1.74	±	0.02	2.1	±	0.2	1.87	±	0.02	1.9	±	0.1	2.1	±	0.2	1.88	±	0.02
Na_2O	1.44	±	0.07	1.49	±	0.06	1.68	±	0.04	1.62	±	0.03	1.0	±	0.1	0.82	±	0.05	0.92	±	0.04
K_2O	2.66	±	0.07	2.77	±	0.03	2.53	±	0.04	3.113	±	0.009	2.69	±	0.03	2.49	±	0.02	2.51	±	0.03
Sc_2O_3	0.069	±	0.002	0.051	±	0.002	0.064	±	0.002	0.062	±	0.002	0.043	±	0.002	0.042	±	0.002	0.042	±	0.002
Total	93.7	±	0.2	94.1	±	0.2	93.8	±	0.4	91.6	±	0.4	95.2	±	0.4	93.5	±	0.4	94.4	±	0.4
ASI	1.79			1.79			1.70			1.67			2.08			2.14			2.14		

wt%	KSM2C-8 (N=10)			KSM2C-9 (N=10)			KSM3A-1 (N=9)			KSM3A-2 (N=10)			KSM3A-3 (N=8)			KSM3A-4 (N=6)		
SiO_2	66.4	±	0.3	68.2	±	0.1	71.3	±	0.8	72.5	±	0.2	72.9	±	0.4	72.7	±	0.2
Al_2O_3	18.1	±	0.2	14.7	±	0.1	13.6	±	0.2	12.7	±	0.1	12.7	±	0.1	12.7	±	0.2
TiO_2	0.50	±	0.03	0.325	±	0.004	0.24	±	0.03	0.27	±	0.07	0.23	±	0.01	0.22	±	0.01
P_2O_5	0.53	±	0.01	0.58	±	0.01	0.83	±	0.03	0.88	±	0.03	0.89	±	0.04	0.99	±	0.06
FeO	6.2	±	0.1	4.17	±	0.05	1.8	±	0.3	1.63	±	0.06	1.19	±	0.03	1.37	±	0.01
MgO	0.86	±	0.02	0.87	±	0.01	0.59	±	0.05	0.39	±	0.01	0.45	±	0.01	0.40	±	0.01
MnO	0.17	±	0.01	0.16	±	0.01	0.20	±	0.01	0.18	±	0.01	0.19	±	0.01	0.20	±	0.01
CaO	0.58	±	0.01	1.92	±	0.01	1.10	±	0.01	1.27	±	0.01	1.15	±	0.02	1.35	±	0.02
Na_2O	1.11	±	0.01	0.88	±	0.03	0.97	±	0.09	0.98	±	0.10	0.87	±	0.08	0.92	±	0.10
K_2O	4.88	±	0.02	2.59	±	0.02	3.04	±	0.05	2.84	±	0.01	2.86	±	0.06	2.62	±	0.09
Sc_2O_3	0.041	±	0.006	0.045	±	0.001	0.056	±	0.003	0.071	±	0.003	0.060	±	0.003	0.053	±	0.003
Total	99.4	±	0.4	94.5	±	0.2	93.8	±	0.9	93.7	±	0.2	93.5	±	0.4	93.6	±	0.3
ASI	2.41			2.09			2.31			2.14			2.30			2.26		

Table 2.5 cont.

wt%	KSM3A-5 (N=10)			KSM3A-6 (N=10)			KSM3A-7 (N=10)			KSM3A-8 (N=10)		
SiO_2	72.74	±	0.18	72.0	±	0.2	71.2	±	0.3	71.6	±	0.2
Al_2O_3	13.04	±	0.05	13.6	±	0.1	13.7	±	0.1	13.7	±	0.1
TiO_2	0.19	±	0.01	0.18	±	0.01	0.22	±	0.01	0.21	±	0.01
P_2O_5	0.53	±	0.03	0.54	±	0.02	0.53	±	0.01	0.56	±	0.01
FeO	1.37	±	0.02	1.71	±	0.04	1.53	±	0.02	1.50	±	0.03
MgO	0.45	±	0.01	0.54	±	0.01	0.55	±	0.01	0.49	±	0.01
MnO	0.14	±	0.01	0.17	±	0.01	0.16	±	0.01	0.18	±	0.01
CaO	1.15	±	0.01	1.25	±	0.03	1.4	±	0.0	1.3	±	0.0
Na_2O	0.89	±	0.02	0.79	±	0.03	0.77	±	0.01	0.87	±	0.02
K_2O	3.07	±	0.02	2.84	±	0.02	2.75	±	0.02	2.98	±	0.01
Sc_2O_3	0.047	±	0.002	0.050	±	0.001	0.054	±	0.001	0.048	±	0.001
F							0.223	±	0.023	0.212	±	0.025
Cl	0.444	±	0.006	0.492	±	0.010	0.442	±	0.007	0.484	±	0.010
F,Cl = O		0.1			0.1			0.2			0.2	
Total	94.0	±	0.2	94.1	±	0.2	93.4	±	0.2	94.0	±	0.2
ASI		2.09			2.26			2.20			2.14	

2.6.1.3.2. Olivine

Olivine is only stable in experiments that reached a temperature of 965 °C. Olivine compositions range from a mole fraction of the forsterite component of the olivine solid solution (X_{Fo}^{Ol}) of 0.537 ± 0.003 (1 σ_m) to 0.73 ± 0.06 (1 σ_m) and are given in Table 2.6. X_{Fo}^{Ol} is strongly a function of f_{O_2} and X_{Fo}^{Ol} is lower in more reduced conditions (Figure 2.9). The observed olivine compositions are consistent with theoretical olivine compositions determined by Roeder and Emslie (1970) for given glass compositions (Figure 2.10), with the exception of experiment KSM1C-10. Experiment KSM1C-10 has olivine with X_{Fo}^{Ol} of 0.549 ± 0.004 (1 σ_m) and experienced a slow quench. During this slow quench, the melt became saturated with biotite,

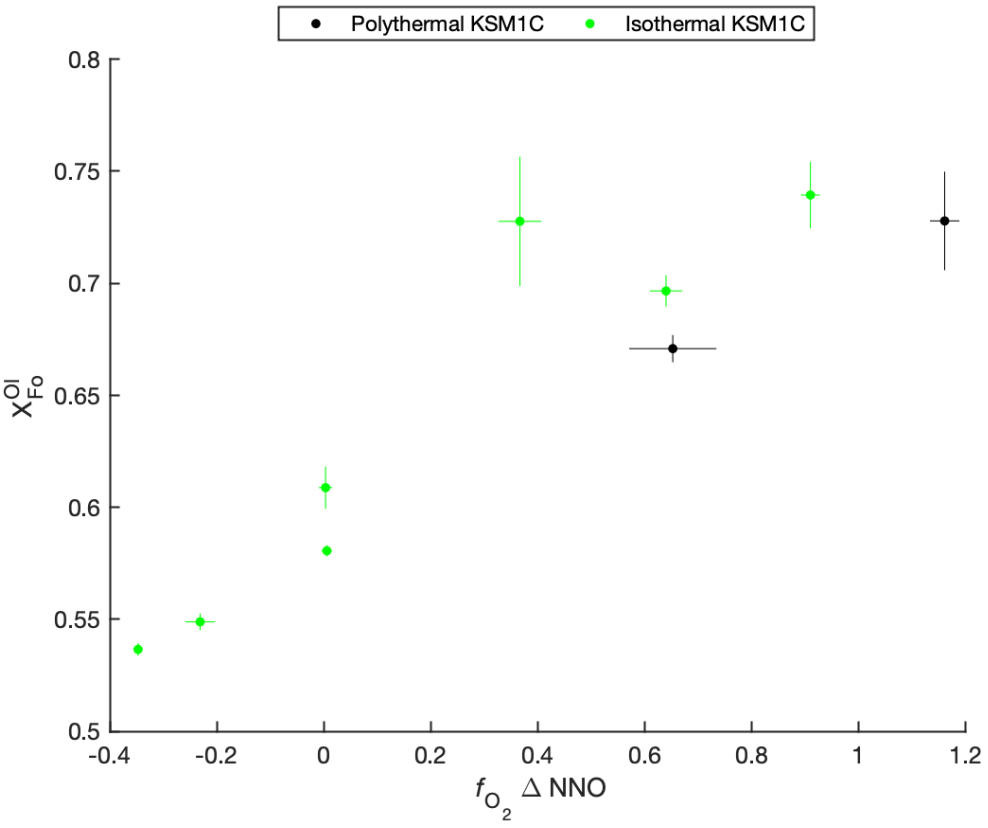

Figure 2.9: X_{Fo}^{Ol} vs. f_{O_2} for experimentally grown olivine

reducing the MgO content of the glass (Table 2.5), and resulted in a glass composition that plots off of the expected X_{Fo}^{Ol} line (Figure 2.10). Given the composition of the olivine, the glass (and at the run conditions the melt) should have a mole % of MgO of ~0.01 instead of the measured 0.002 mole %.

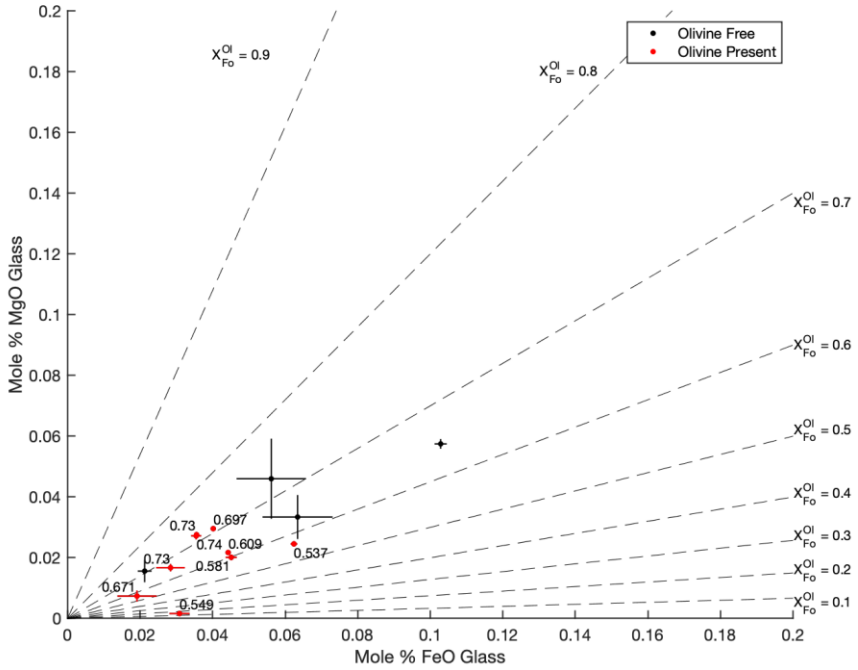

Figure 2.10: Plot of mole % MgO vs mole % FeO in run-product glasses. Numbers next to data points are the X_{Fo}^{Ol} of the olivine present in that experiment. Data points without numbers are from olivine-free. experiments Dashed lines are X_{Fo}^{Ol} as determined by Roeder and Emslie (1970). Uncertainty is 1 σ_m.

2.6.1.3.3. Plagioclase

Run-product plagioclase compositions range from a mole fraction of the anorthite component of the plagioclase solid solution (X_{An}^{Pl}) of 0.59 ± 0.04 (1 σ_m) to 0.80 ± 0.04 (1 σ_m), and are given in Table 2.7. Housh and Luhr (1991) noted that plagioclase compositions are dependent on temperature and the water content of the melt. Thus the run product plagioclase compositions are compared to the temperature of the experiments (Figure 2.11). Given that no attempt has been made to quantify the water concentration of the melt, there are insufficient data to compare plagioclase

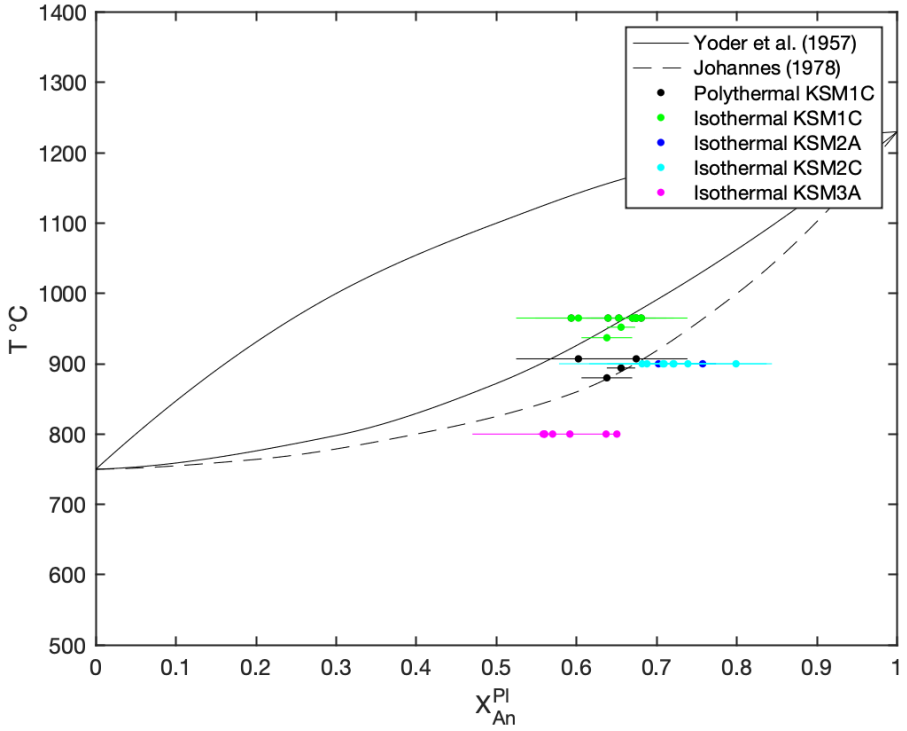

Figure 2.11: Run-product plagioclase compositions as a function of temperature. Upper solid line is the liquidus for the plagioclase solid solution at 500 MPa as determined by Yoder et al. (1957). Lower solid line is the solidus for the plagioclase solid solution at 500 MPa as determined by Yoder et al. (1957). Dashed line is solidus at 500 MPa as determined by Johannes (1978). Uncertainty is 1 σ_m.

compositions to water content of the glasses. However, in each experimental set, the melt was water-saturated and because pressure remained constant, variations in the water content of the melt should have been minor (Papale et al., 2006), and thus had a minor effect on plagioclase composition in these experiments. The run-product plagioclase for KSM1C experiments fall along or between the solidi (Figure 2.11) determined by Yoder et al. (1957) and Johannes (1978) at 500 MPa and are consistent with the observations of Housh and Luhr (1991). However, the run-product plagioclase from KSM2A and KSM2C experiments have higher X_{An}^{Pl} than what is suggested by either Yoder et al. (1957) or Johannes (1978) at 900 °C. Additionally, the plagioclase from KSM3A experiments have significantly higher X_{An}^{Pl} than

suggested (Figure 2.11). The iron content of run product plagioclase is up to ~6 wt%, but is generally < 3 wt%. This is slightly higher than natural plagioclase, which may reach a couple weight percent (Deer et al., 2001). This high iron content may be due to the small grain size or inclusion of spinel.

Table 2.6: Compositions and mineral formulas of run-product olivine

wt%	KSM1C-3 (N=16)			KSM1C-5 (N=9)			KSM1C-6 (N=4)			KSM1C-7 (N=8)			KSM1C-8 (N=6)			KSM1C-9 (N=7)		
SiO_2	35.9	±	0.3	36.9	±	0.1	36.9	±	0.1	36.3	±	0.1	37.5	±	0.2	34.5	±	0.3
Al_2O_3	0.6	±	0.4	0.06	±	0.01	0.08	±	0.04	0.034	±	0.005	0.23	±	0.07	0.09	±	0.01
TiO_2	0.3	±	0.1	0.2	±	0.1	0.17	±	0.04	0.1	±	0.01	0.17	±	0.09	0.3	±	0.2
P_2O_5	1.2	±	0.2	1	±	0.1	0.8	±	0.1	0.6	±	0.1	0.9	±	0.2	0.7	±	0.2
FeO	27.5	±	0.5	24	±	0.6	24.1	±	0.9	26.4	±	0.2	23.1	±	0.4	37.9	±	0.2
MgO	31.5	±	0.5	36	±	0.4	36.1	±	0.6	33.9	±	0.2	36.8	±	0.5	24.6	±	0.1
MnO	1.14	±	0.02	1.22	±	0.01	0.98	±	0.04	0.9	±	0.01	0.93	±	0.02	0.96	±	0.02
Na_2O	0.08	±	0.05	0.02	±	0.005	0.008	±	0.002	0.02	±	0.005	0.0306	±	0.005	b.d. to 0.0403		
CaO	1.1	±	0.4	0.5	±	0.2	0.3	±	0.1	0.19	±	0.01	0.585	±	0.233	0.6	±	0.2
K_2O	0.04	±	0.01	0.016	±	0.003	0.02	±	0.01	0.017	±	0.003	0.0	±	0.0	0.025	±	0.005
Sc_2O_3	0.041	±	0.003	0.043	±	0.004	0.042	±	0.006	0.033	±	0.004	0.036	±	0.004	0.025	±	0.005
Total	99	±	1	100	±	0.8	99	±	1	98.5	±	0.3	100.2	±	0.8	99.6	±	0.5
Formula																		
Si	0.969	±	0.003	0.973	±	0.005	0.978	±	0.004	0.983	±	0.003	0.980	±	0.003	0.980	±	0.008
Al	0.019	±	0.001	0.002	±	0.0004	0.003	±	0.001	0.0011	±	0.0002	0.007	±	0.002	0.0029	±	0.0004
Ti	0.006	±	0.0002	0.005	±	0.002	0.003	±	0.001	0.002	±	0.0002	0.003	±	0.002	0.006	±	0.004
P	0.028	±	0.002	0.022	±	0.003	0.018	±	0.003	0.013	±	0.002	0.01905	±	0.005	0.016	±	0.005
Fe	0.621	±	0.005	0.53	±	0.02	0.53	±	0.02	0.597	±	0.005	0.505	±	0.009	0.900	±	0.004
Mg	1.266	±	0.005	1.41	±	0.01	1.42	±	0.02	1.37	±	0.006	1.43	±	0.01	1.042	±	0.004
Mn	0.0260	±	0.0004	0.0272	±	0.0004	0.022	±	0.001	0.0207	±	0.0003	0.0206	±	0.0004	0.0231	±	0.0005
Na	0.0044	±	0.0003	0.0010	±	0.0002	0.0004	±	0.0001	0.001	±	0.0002	0.0016	±	0.0003	b.d. to 0.002		
Ca	0.0320	±	0.0005	0.013	±	0.004	0.007	±	0.002	0.0055	±	0.0003	0.01642	±	0.007	0.017	±	0.005
K	0.0013	±	0.0001	0.0005	±	0.0001	0.0007	±	0.0003	0.0006	±	0.0001	0.00089	±	0.000	0.0009	±	0.0002
Sc	0.0010	±	0.0001	0.001	±	0.0001	0.001	±	0.0001	0.0008	±	0.0001	0.00083	±	0.0001	0.00062	±	0.00012
X_{Fo}^{Ol}	0.671	±	0.06	0.73	±	0.02	0.73	±	0.03	0.697	±	0.007	0.74	±	0.02	0.537	±	0.003

X_{Fo}^{Ol} is the mole fraction of the forsterite component in the olivine solid solution. Uncertainty is $1\sigma_m$

Table 2.6 cont.

wt%	KSM1C-10 (N=7)			KSM1C-11 (N=5)			KSM1C-12 (N=7)		
SiO_2	34.5	±	0.4	35.7	±	0.1	33.78	±	0.08
Al_2O_3	0.24	±	0.04	0.08	±	0.03	0.18	±	0.02
TiO_2	0.6	±	0.4	0.13	±	0.02	1.1	±	0.1
P_2O_5	0.8	±	0.2	0.57	±	0.08	1.73	±	0.08
FeO	37.2	±	0.1	32.8	±	0.3	34.7	±	0.1
MgO	25.4	±	0.3	28.7	±	0.3	26.91	±	0.09
MnO	0.96	±	0.03	1.08	±	0.02	1.04	±	0.01
Na_2O	0.031	±	0.003	b.d. to 0.0375			0.043	±	0.003
CaO	0.5	±	0.2	0.24	±	0.05	0.698	±	0.105
K_2O	0.0	±	0.0	0.03	±	0.01	0.0	±	0.0
Sc_2O_3	0.036	±	0.004	0.041	±	0.003	0.063	±	0.004
Total	100.3	±	0.7	99.5	±	0.5	100.3	±	0.3
Formula									
Si	0.97	±	0.01	0.989	±	0.001	0.938	±	0.002
Al	0.008	±	0.001	0.003	±	0.001	0.006	±	0.001
Ti	0.012	±	0.008	0.0028	±	0.0005	0.024	±	0.003
P	0.020	±	0.005	0.013419	±	0.002	0.041	±	0.002
Fe	0.874	±	0.003	0.76	±	0.01	0.804	±	0.003
Mg	1.06	±	0.01	1.18	±	0.01	1.113	±	0.004
Mn	0.0228	±	0.0006	0.0253	±	0.0005	0.0244	±	0.0003
Na	0.0017	±	0.0001	b.d. to 0.002			0.0023	±	0.0001
Ca	0.017	±	0.006	0.007	±	0.001	0.021	±	0.003
K	0.0007	±	0.0001	0.0011	±	0.0003	0.0016	±	0.0002
Sc	0.0009	±	0.0001	0.0010	±	0.0001	0.0015	±	0.0001
X_{Fo}^{Ol}	0.548	±	0.004	0.608	±	0.009	0.581	±	0.003

Table 2.7: Compositions and mineral formulas of run-product plagioclase

wt%	KSM1C-1 (N=7)			KSM1C-3 (N=6)			KSM1C-4 (N=6)			KSM1C-5 (N=3)			KSM1C-6 (N=4)			KSM1C-7 (N=2)		
SiO_2	52	±	1	56	±	2	53.8	±	0.6	55	±	2	52.5	±	0.9	50.1	±	0.1
Al_2O_3	24.6	±	0.6	27	±	1	26.7	±	0.7	26	±	1	27.4	±	0.4	28.3	±	0.2
TiO_2	2.6	±	0.4	0.4	±	0.1	0.7	±	0.2	0.4	±	0.1	0.6	±	0.1	0.5	±	0.3
P_2O_5	1.8	±	0.1	0.6	±	0.1	1.2	±	0.2	0.8	±	0.2	0.9	±	0.2	0.72	±	0.03
FeO	5.6	±	0.8	1.1	±	0.1	1.5	±	0.3	1.3	±	0.1	1.8	±	0.1	1.7	±	0.2
MgO	0.5	±	0.1	0.1	±	0.02	0.22	±	0.05	0.4	±	0.1	0.47	±	0.06	0.28	±	0.03
MnO	0.1	±	0.02	0.05	±	0.01	0.07	±	0.02	0.05	±	0.02	0.07	±	0.03	0.03	±	0.001
CaO	10.8	±	0.3	11	±	1	11.5	±	0.2	11.2	±	0.8	12.3	±	0.5	13.1	±	0.02
Na_2O	3	±	0.4	3.3	±	0.3	2.9	±	0.2	2.5	±	0.3	2.8	±	0.2	3.1	±	0.1
K_2O	0.6	±	0.1	1	±	0.3	0.6	±	0.1	0.8	±	0.2	0.7	±	0.1	0.42	±	0.01
Sc_2O_3	0.02	±	0.003	0.006	±	0.001	0.009	±	0.003	0.013	±	0.002	0.007	±	0.001	0.009	±	0.001
Total	101	±	2	101	±	3	99	±	1	99	±	2	99	±	1	98.3	±	0.4
Formula																		
Si	2.36	±	0.04	2.5	±	0.1	2.45	±	0.01	2.51	±	0.07	2.4	±	0.04	2.335	±	0.004
Al	1.33	±	0.03	1.4	±	0.1	1.43	±	0.03	1.41	±	0.07	1.48	±	0.03	1.55	±	0.01
Ti	0.09	±	0.01	0.012	±	0.004	0.024	±	0.007	0.014	±	0.004	0.02	±	0.004	0.02	±	0.01
P	0.07	±	0.005	0.021	±	0.005	0.04	±	0.01	0.029	±	0.009	0.03	±	0.01	0.029	±	0.001
Fe	0.21	±	0.03	0.04	±	0.004	0.06	±	0.01	0.05	±	0.004	0.069	±	0.004	0.065	±	0.006
Mg	0.033	±	0.004	0.007	±	0.001	0.015	±	0.003	0.025	±	0.007	0.032	±	0.004	0.02	±	0.002
Mn	0.004	±	0.001	0.0017	±	0.0005	0.003	±	0.001	0.002	±	0.001	0.003	±	0.001	0.00119	±	0.00004
Ca	0.53	±	0.01	0.5	±	0.1	0.559	±	0.009	0.55	±	0.04	0.6	±	0.03	0.654	±	0.001
Na	0.27	±	0.03	0.28	±	0.02	0.26	±	0.02	0.22	±	0.02	0.25	±	0.02	0.28	±	0.01
K	0.036	±	0.005	0.06	±	0.01	0.035	±	0.004	0.05	±	0.01	0.038	±	0.007	0.0248	±	0.0006
Sc	0.0008	±	0.0001	0.0002	±	0.0001	0.0004	±	0.0001	0.0005	±	0.0001	0.0003	±	0.0001	0.00034	±	0.00002
X_{An}^{Pl}	0.64	±	0.03	0.6	±	0.08	0.66	±	0.02	0.67	±	0.06	0.67	±	0.04	0.681	±	0.007

X_{An}^{Pl} is the mole fraction of the anorthite component in the plagioclase solid solution. Uncertainty is $1\sigma_m$

Table 2.7 cont.

wt%	KSM1C-8 (N=3)	KSM1C-9 (N=9)	KSM1C-10 (N=10)	KSM1C-11 (N=7)	KSM1C-12 (N=7)	KSM2A-1 (N=8)	KSM2A-2 (N=8)
SiO_2	57.22 ± 0.08	54.8 ± 0.7	51.6 ± 0.5	53.3 ± 0.6	55.3 ± 0.7	49.8 ± 0.3	52.0 ± 0.8
Al_2O_3	22 ± 2	24.1 ± 0.6	29.1 ± 0.3	26.5 ± 0.6	24 ± 1	32.0 ± 0.3	30.6 ± 0.6
TiO_2	0.7 ± 0.2	0.58 ± 0.08	0.31 ± 0.08	0.37 ± 0.06	0.78 ± 0.06	0.4 ± 0.2	0.10 ± 0.03
P_2O_5	2 ± 1	0.9 ± 0.1	0.43 ± 0.07	0.9 ± 0.2	1.3 ± 0.3	0.15 ± 0.01	0.18 ± 0.02
FeO	3.0 ± 0.7	3.2 ± 0.3	1.15 ± 0.08	1.8 ± 0.2	2.7 ± 0.4	0.53 ± 0.07	0.55 ± 0.08
MgO	1.0 ± 0.2	0.71 ± 0.07	0.19 ± 0.03	0.37 ± 0.07	0.7 ± 0.1	0.09 ± 0.02	0.16 ± 0.04
MnO	0.13 ± 0.03	0.11 ± 0.02	0.05 ± 0.01	0.08 ± 0.02	0.14 ± 0.02	0.054 ± 0.009	0.054 ± 0.007
CaO	8.8 ± 0.5	9.5 ± 0.5	13.2 ± 0.2	11.6 ± 0.4	9.7 ± 0.6	14.5 ± 0.2	13.5 ± 0.4
Na_2O	1.42 ± 0.02	2.0 ± 0.2	3.15 ± 0.05	3.0 ± 0.2	2.8 ± 0.3	2.4 ± 0.1	2.6 ± 0.1
K_2O	1.5 ± 0.5	1.20 ± 0.07	0.59 ± 0.05	0.92 ± 0.09	1.3 ± 0.2	0.28 ± 0.06	0.5 ± 0.1
Sc_2O_3	0.014 ± 0.004	0.010 ± 0.001	0.006 ± 0.001	0.0080 ± 0.0009	0.007 ± 0.002	0.018 ± 0.005	0.011 ± 0.003
Total	98 ± 2	97 ± 1	99.8 ± 0.6	99 ± 1	99 ± 1	100.2 ± 0.6	100 ± 1
Formula							
Si	2.63 ± 0.02	2.55 ± 0.03	2.36 ± 0.02	2.45 ± 0.02	2.53 ± 0.04	2.27 ± 0.01	2.35 ± 0.03
Al	1.2 ± 0.1	1.32 ± 0.03	1.57 ± 0.02	1.44 ± 0.03	1.32 ± 0.05	1.72 ± 0.02	1.64 ± 0.03
Ti	0.025 ± 0.006	0.020 ± 0.003	0.011 ± 0.003	0.013 ± 0.002	0.027 ± 0.002	0.013 ± 0.006	0.0033 ± 0.0009
P	0.08 ± 0.04	0.036 ± 0.006	0.016 ± 0.003	0.035 ± 0.008	0.05 ± 0.01	0.0059 ± 0.0004	0.0071 ± 0.0009
Fe	0.12 ± 0.03	0.13 ± 0.01	0.044 ± 0.003	0.070 ± 0.008	0.10 ± 0.01	0.020 ± 0.003	0.021 ± 0.003
Mg	0.07 ± 0.01	0.049 ± 0.005	0.013 ± 0.002	0.025 ± 0.005	0.047 ± 0.009	0.006 ± 0.002	0.011 ± 0.003
Mn	0.005 ± 0.001	0.0043 ± 0.0007	0.0010 ± 0.0004	0.0022 ± 0.0007	0.003 ± 0.001	0.0021 ± 0.0003	0.0021 ± 0.0003
Ca	0.43 ± 0.02	0.47 ± 0.03	0.65 ± 0.01	0.57 ± 0.02	0.47 ± 0.03	0.71 ± 0.01	0.66 ± 0.02
Na	0.126 ± 0.002	0.18 ± 0.01	0.280 ± 0.005	0.27 ± 0.02	0.25 ± 0.02	0.211 ± 0.009	0.228 ± 0.009
K	0.09 ± 0.03	0.072 ± 0.004	0.034 ± 0.003	0.054 ± 0.005	0.08 ± 0.01	0.017 ± 0.003	0.026 ± 0.006
Sc	0.0006 ± 0.0001	0.00036 ± 0.00006	0.00023 ± 0.00005	0.00027 ± 0.00005	0.0003 ± 0.0001	0.0007 ± 0.0002	0.0004 ± 0.0001
X_{An}^{Pl}	0.67 ± 0.05	0.65 ± 0.04	0.67 ± 0.01	0.64 ± 0.02	0.59 ± 0.04	0.76 ± 0.02	0.70 ± 0.02

Table 2.7 cont.

wt%	KSM2C-1 (N=8)			KSM2C-2 (N=10)			KSM2C-3 (N=5)			KSM2C-4 (N=4)			KSM2C-5 (N=8)			KSM2C-6 (N=3)		
SiO_2	49.8	±	0.3	49.5	±	0.9	55	±	1	48	±	2	56.0	±	0.9	54	±	1
Al_2O_3	30.3	±	0.4	31.0	±	1.2	26	±	1	31.8	±	2.0	26.9	±	0.7	26.9	±	0.7
TiO_2	0.07	±	0.01	0.26	±	0.06	0.20	±	0.04	0.072	±	0.002	0.18	±	0.05	0.4	±	0.1
P_2O_5	0.14	±	0.02	0.20	±	0.02	0.25	±	0.04	0.17	±	0.01	0.25	±	0.03	0.28	±	0.04
FeO	0.90	±	0.10	1.0	±	0.1	1.6	±	0.3	0.8	±	0.1	1.7	±	0.3	1.8	±	0.2
MgO	0.13	±	0.02	0.15	±	0.02	0.41	±	0.07	0.17	±	0.03	0.30	±	0.05	0.34	±	0.04
MnO	0.13	±	0.05	0.07	±	0.03	0.10	±	0.02	0.044	±	0.006	0.06	±	0.02	0.096	±	0.005
CaO	14.2	±	0.3	13.2	±	0.5	11.1	±	0.9	13.3	±	0.4	11.0	±	0.6	11.3	±	0.5
Na_2O	2.21	±	0.09	2.2	±	0.1	2.0	±	0.2	1.6	±	0.3	2.0	±	0.1	1.77	±	0.05
K_2O	0.45	±	0.06	0.6	±	0.1	1.3	±	0.2	0.37	±	0.07	1.1	±	0.1	1.2	±	0.1
Sc_2O_3	0.011	±	0.003	0.018	±	0.002	0.034	±	0.007	0.013	±	0.002	0.019	±	0.002	0.018	±	0.003
Total	98.3	±	0.6	98.2	±	1.6	98	±	2	97	±	3	100	±	1	98	±	1
Formula																		
Si	2.31	±	0.02	2.30	±	0.05	2.53	±	0.06	2.27	±	0.08	2.53	±	0.04	2.49	±	0.04
Al	1.66	±	0.02	1.69	±	0.06	1.42	±	0.06	1.76	±	0.10	1.43	±	0.04	1.46	±	0.04
Ti	0.0026	±	0.0004	0.009	±	0.002	0.007	±	0.001	0.00253	±	0.00007	0.006	±	0.002	0.015	±	0.004
P	0.0053	±	0.0007	0.0078	±	0.0007	0.010	±	0.002	0.0068	±	0.0003	0.009	±	0.001	0.011	±	0.002
Fe	0.035	±	0.004	0.040	±	0.004	0.06	±	0.01	0.032	±	0.002	0.066	±	0.011	0.068	±	0.008
Mg	0.009	±	0.002	0.011	±	0.002	0.028	±	0.005	0.012	±	0.002	0.020	±	0.003	0.024	±	0.003
Mn	0.005	±	0.001	0.0028	±	0.0009	0.0040	±	0.0009	0.0018	±	0.0002	0.0025	±	0.0007	0.0038	±	0.0002
Ca	0.71	±	0.01	0.66	±	0.02	0.55	±	0.04	0.67	±	0.03	0.54	±	0.03	0.56	±	0.03
Na	0.199	±	0.009	0.20	±	0.01	0.18	±	0.01	0.15	±	0.02	0.18	±	0.01	0.158	±	0.005
K	0.027	±	0.003	0.036	±	0.007	0.08	±	0.01	0.022	±	0.004	0.065	±	0.008	0.070	±	0.007
Sc	0.0004	±	0.0001	0.00073	±	0.00009	0.0014	±	0.0003	0.0005	±	0.0001	0.0008	±	0.0001	0.0007	±	0.0001
X_{An}^{Pl}	0.76	±	0.02	0.74	±	0.03	0.68	±	0.07	0.80	±	0.04	0.69	±	0.05	0.71	±	0.04

Table 2.7 cont.

wt%	KSM2C-7 (N=7)			KSM2C-9 (N=2)			KSM3A-1 (N=1)	KSM3A-2 (N=1)	KSM3A-3 (N=1)	KSM3A-4 (N=1)	KSM3A-6 (N=1)
SiO_2	54	±	1	54	±	1	61.8	54.3	67.0	60.9	55.7
Al_2O_3	28.3	±	0.8	27.20	±	2.50	23.6	29.7	23.0	25.3	28.6
TiO_2	0.22	±	0.08	1.47	±	1.04	0.09	0.03	0.03	1.0	b.d.
P_2O_5	0.22	±	0.02	0.208	±	0.032	0.494	0.3	0.3	0.3	0.206
FeO	1.3	±	0.1	3	±	1	1.13	0.4	0.4	1.7	0.35
MgO	0.25	±	0.03	0.324	±	0.095	0.313	0.05	0.07	0.2	0.038
MnO	0.056	±	0.009	0.096	±	0.030	0.113	0.06	0.08	0.1	0.039
CaO	12.3	±	0.6	11.7	±	1.8	8.6	12.7	9.1	9.0	11.0
Na_2O	2.1	±	0.1	2.0	±	0.3	2.85	3.5	3.2	2.4	4.44
K_2O	0.9	±	0.1	0.98	±	0.29	1.022	0.4	0.4	0.7	0.538
Sc_2O_3	0.011	±	0.003	0.03	±	0.01	0.016	0.01		0.05	0.005
Total	99	±	2	101	±	4	100	101	104	102	101
Formula											
Si	2.45	±	0.05	2.45	±	0.07	2.74	2.4	2.8	2.7	2.49
Al	1.52	±	0.05	1.45	±	0.13	1.23	1.6	1.1	1.3	1.50
Ti	0.008	±	0.003	0.04980	±	0.03561	0.0030	0.001	0.001	0.03	0.0000
P	0.051	±	0.004	0.1044	±	0.0515	0.0185	0.01	0.01	0.01	0.0078
Fe	0.009	±	0.001	0.008	±	0.001	0.042	0.01	0.01	0.06	0.013
Mg	0.017	±	0.002	0.022	±	0.006	0.0206	0.003	0.005	0.01	0.0026
Mn	0.0022	±	0.0004	0.0037	±	0.0012	0.0042	0.002	0.003	0.004	0.0015
Ca	0.60	±	0.03	0.56	±	0.08	0.41	0.6	0.4	0.42	0.52
Na	0.18	±	0.01	0.18	±	0.02	0.245	0.3	0.3	0.2	0.384
K	0.050	±	0.007	0.057	±	0.017	0.0577	0.02	0.0	0.04	0.0307
Sc	0.0004	±	0.0001	0.0013	±	0.0005	0.0006	0.0004	b.d.	0.002	0.0002
X_{An}^{Pl}	0.72	±	0.05	0.71	±	0.13	0.57	0.65	0.59	0.64	0.56

Table 2.7 cont.

wt%	KSM3A-7 (N=2)			KSM3A-8 (N=6)		
SiO_2	53.6	±	0.1	52.6	±	2.0
Al_2O_3	29.0	±	0.1	29.8	±	0.9
TiO_2	b.d. to 0.012			0.13	±	0.09
P_2O_5	0.169	±	0.006	0.20	±	0.01
FeO	0.24	±	0.02	1.5	±	1.0
MgO	0.019	±	0.001	0.5	±	0.3
MnO	0.018	±	0.005	0.08	±	0.02
CaO	11.4	±	0.2	10.3	±	0.5
Na_2O	4.67	±	0.04	4.14	±	0.07
K_2O	0.339	±	0.001	0.42	±	0.02
Sc_2O_3	0.001	±	0.001	0.008	±	0.004
Total	99.4	±	0.2	100	±	2
Formula						
Si	2.438	±	0.007	2.4	±	0.2
Al	1.551	±	0.005	1.6	±	0.1
Ti	0.0004	±	0.0002	0.004	±	0.002
P	0.0065	±	0.0002	0.0075	±	0.0008
Fe	0.009	±	0.001	0.058	±	0.005
Mg	0.0013	±	0.0001	0.035	±	0.005
Mn	0.0007	±	0.0002	0.0030	±	0.0004
Ca	0.55	±	0.01	0.50	±	0.07
Na	0.411	±	0.003	0.36	±	0.05
K	0.0196	±	0.0001	0.024	±	0.009
Sc	0.0001	±	0.0001	0.0003	±	0.0001
X_{An}^{Pl}	0.56	±	0.01	0.56	±	0.09

Table 2.8: Compositions and mineral formulas of run-product biotite

wt%	KSM1C-1 (N=4)	KSM1C-3 (N=8)	KSM1C-4 (N=2)	KSM1C-5 (N=9)	KSM1C-6 (N=3)	KSM1C-7 (N=1)
SiO_2	39.4 ± 0.4	40.2 ± 0.7	42.3 ± 0.2	37 ± 0.7	38.7 ± 0.6	37.5 ± 0.2
Al_2O_3	15.8 ± 0.8	15.6 ± 0.4	15.9 ± 0.9	15.5 ± 0.4	16.4 ± 0.3	16.3 ± 0.1
TiO_2	3.2 ± 0.2	4 ± 0.1	4.2 ± 0.3	4.9 ± 0.2	5.1 ± 0.3	5.26 ± 0.09
P_2O_5	1.8 ± 0.6	0.9 ± 0.3	1.5 ± 0.3	1 ± 0.2	0.3 ± 0.1	0.09 ± 0.04
FeO	12 ± 2	10.8 ± 0.4	11 ± 2	10.6 ± 0.5	10.1 ± 0.4	10.6 ± 0.2
MgO	16 ± 2	13.3 ± 0.3	9.2 ± 0.3	14.2 ± 0.4	14.8 ± 0.8	15.3 ± 0.1
MnO	0.2 ± 0.03	0.18 ± 0.01	0.19 ± 0.05	0.19 ± 0.01	0.13 ± 0.01	0.08 ± 0.04
Na_2O	0.71 ± 0.04	0.89 ± 0.08	1.3 ± 0.5	0.78 ± 0.04	1.19 ± 0.04	0.91 ± 0.04
CaO	2.3 ± 0.9	1.7 ± 0.4	2.7 ± 0.6	1.7 ± 0.3	0.9 ± 0.4	0.51 ± 0.03
K_2O	6.9 ± 0.6	7.6 ± 0.2	6.2 ± 0.3	7.6 ± 0.2	8.1 ± 0.3	8.1 ± 0.05
Sc_2O_3	0.031 ± 0.001	0.048 ± 0.003	0.041 ± 0.003	0.054 ± 0.002	0.037 ± 0.005	0.04 ± 0.01
Total	98 ± 4	95 ± 1	95 ± 3	94 ± 1	96 ± 1	94.7 ± 0.3
Tetrahedral Cations						
Si	2.79 ± 0.05	2.91 ± 0.04	3.043 ± 0.005	2.75 ± 0.04	2.79 ± 0.04	2.723 ± 0.009
Al	1.1 ± 0.08	1.03 ± 0.02	0.87 ± 0.01	1.18 ± 0.01	1.19 ± 0.05	1.272 ± 0.007
Fe^{3+}	-	-	-	-	-	-
P	0.11 ± 0.04	0.06 ± 0.02	0.09 ± 0.02	0.06 ± 0.02	0.018 ± 0.009	0.006 ± 0.002
Total	4 ± 0.1	4 ± 0.05	4 ± 0.02	4 ± 0.04	4 ± 0.06	4 ± 0.01
Octahedral Cations						
Al	0.22 ± 0.05	0.3 ± 0.04	0.48 ± 0.07	0.17 ± 0.04	0.2 ± 0.07	0.126 ± 0.009
Ti	0.17 ± 0.01	0.216 ± 0.008	0.22 ± 0.02	0.27 ± 0.01	0.28 ± 0.01	0.287 ± 0.002
Fe^{2+}	0.7 ± 0.2	0.65 ± 0.03	0.7 ± 0.1	0.66 ± 0.01	0.61 ± 0.04	0.459 ± 0.001
Fe^{3+}	-	-	-	-	-	0.175 ± 0.006
Mg	1.7 ± 0.2	1.44 ± 0.04	0.99 ± 0.03	1.58 ± 0.04	1.59 ± 0.08	1.661 ± 0.002
Mn	0.012 ± 0.002	0.011 ± 0.001	0.012 ± 0.003	0.012 ± 0.001	0.008 ± 0.001	0.005 ± 0.003
Sc	0.002 ± 0.0001	0.003 ± 0.0002	0.003 ± 0.0001	0.004 ± 0.0001	0.002 ± 0.0003	0.003 ± 0.0003
Total	2.8 ± 0.3	2.6 ± 0.1	2.4 ± 0.2	2.7 ± 0.1	2.69 ± 0.04	2.715 ± 0.002
A Site Cations						
K	0.6 ± 0.1	0.7 ± 0.02	0.57 ± 0.02	0.72 ± 0.02	0.75 ± 0.03	0.751 ± 0.001
Ca	0.18 ± 0.07	0.14 ± 0.03	0.21 ± 0.05	0.13 ± 0.02	0.07 ± 0.03	0.04 ± 0.002
Na	0.1 ± 0.01	0.12 ± 0.01	0.2 ± 0.1	0.11 ± 0.01	0.166 ± 0.005	0.128 ± 0.004
Total	0.9 ± 0.1	0.96 ± 0.04	1 ± 0.1	0.97 ± 0.03	0.983 ± 0.006	0.918 ± 0.005
H_2O	4.26 ± 0.03	4.16 ± 0.03	4.19 ± 0.04	4.05 ± 0.02	4.16 ± 0.02	4.1 ± 0.03
X_{Ann}^{Bt}	0.25 ± 0.07	0.25 ± 0.01	0.29 ± 0.06	0.245 ± 0.007	0.23 ± 0.02	0.169 ± 0.0005
$\frac{Fe}{(Fe+Mg)}$	0.29 ± 0.09	0.31 ± 0.02	0.4 ± 0.1	0.3 ± 0.01	0.28 ± 0.02	0.276 ± 0.003
Al Total	1.3 ± 0.1	1.33 ± 0.05	1.4 ± 0.1	1.35 ± 0.04	1.4 ± 0.1	1.4 ± 0.01

Formulas calculated using the method of Dymek (1983). H_2O estimated assuming a filled hydroxyl site. X_{Ann}^{Bt} is the mole fraction of the annite component in the biotite solid solution. Uncertainty is $1\sigma_{m.}$ Dash means data are not present

2.6.1.3.4. Biotite

Biotite is a major phase only in the polythermal KSM1C experiments. In isothermal experiments biotite is a minor phase and nucleates late in the crystallization sequence or during quench. The mole fraction of the annite component of the biotite solid solution (X_{Ann}^{Bt}; defined as the mole fraction of Fe^{2+} in the octahedral site, Table 2.8) ranges from 0.1692 ± 0.0005 (1 σ_m) to 0.29 ± 0.06 (1 σ_m) with a mean X_{Ann}^{Bt} of 0.24 ± .02 (1 σ_m). Biotite compositions are commonly plotted as total octahedral iron over total octahedral iron plus octahedral magnesium (Fe/(Fe+Mg)) vs. total aluminum (Figure 2.12). The difference between the numerical values X_{Ann}^{Bt} and Fe/(Fe+Mg) is small; however, Fe/(Fe+Mg) is useful for

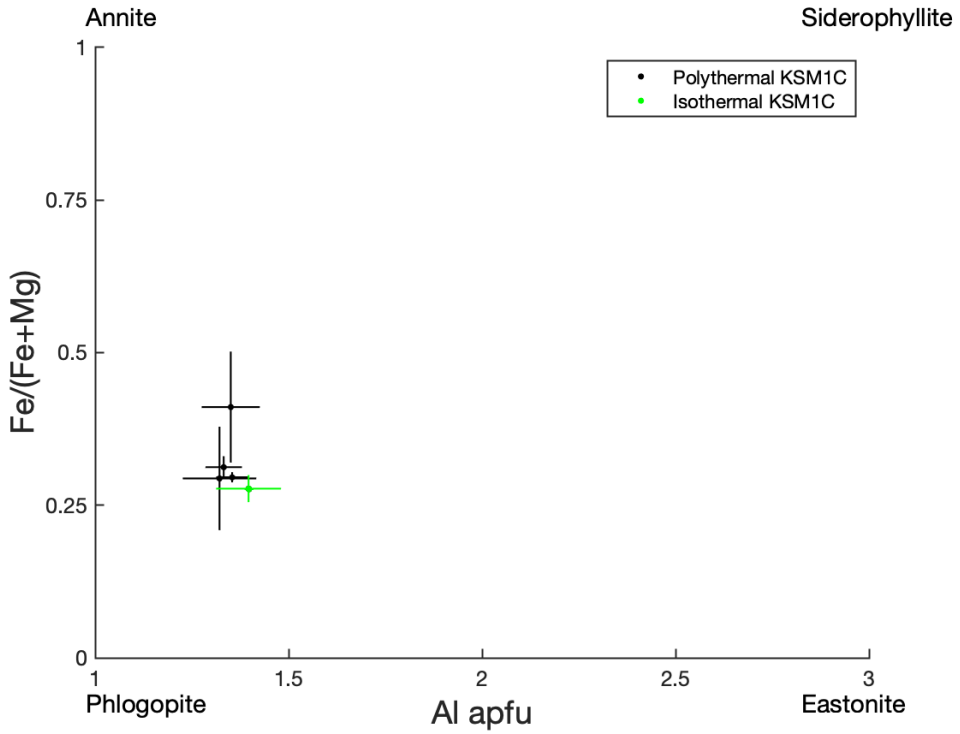

Figure 2.12: Compositions of run-product biotite plotted in terms of octahedral Fe/(Fe+Mg) vs. aluminum apfu. Uncertainty is 1 σ_m.

displaying biotite compositions graphically and X_{Ann}^{Bt} is useful for thermodynamic evaluations. Biotite compositions are consistent and have slightly more magnesium than iron and more aluminum than an idealized phlogopite or annite (Figure 2.12).

2.6.1.3.5. Spinel

Although spinel is a common mineral in the run products, the small grain size make obtaining quality analysis problematic. As a result, the compositions of spinel from several experiments were not obtained, and although analyses were possible in some cases they are few in number. The compositions of run-product spinel are given in Table 2.9 and the phase components of the spinel solid solution that are pertinent to this study include magnetite ($Fe^{2+}Fe_2^{3+}O_4$), ulvöspinel ($Fe_2^{2+}TiO_4$), spinel ($MgAl_2O_4$), hercynite ($FeAl_2O_4$), magnesioferrite ($MgFe_2^{3+}O_4$), and qandilite (Mg_2TiO_4). The components can be best represented by the ratios of cations. The iron and magnesium end-members can be distinguished based on their $Fe^{2+}/(Fe^{2+}+Mg)$ for titanium (ulvöspinel from qandilite), aluminum (hercynite from spinel), and ferric iron (magnetite from magnesioferrite) spinel. The ratios $2Ti/(2Ti+Al)$, $2Ti/(2Ti+Fe^{3+})$, and $Fe^{3+}/(Fe^{3+}+Al)$ can be used to distinguish among spinel that primarily contain titanium, aluminum, and ferric iron. Spinel from KSM1C experiments are primarily ulvöspinel and magnetite with a minor magnesioferrite component (Figure 2.13). There are two coexisting spinel in KSM2A experiments: 1) a spinel with a primarily spinel and hercynite composition; and, 2) a spinel that is primarily magnetite and hercynite with minor ulvöspinel, and magnesioferrite components (Figure 2.13), a composition that is similar to spinel

from other experiments. The composition of these coexisting spinel are consistent with the results of Lehmann and Roux (1986) who described coexisting spinel and miscibility gaps in the $(Mg, Fe)Al_2O_4 - (Mg, Fe)Fe_2^{3+}O_4$ system. Spinel from KSM2C experiments are generally magnetite, ulvöspinel, and hercynite with minor spinel and magnesioferrite components (Figure 2.13). Spinel from KSM3A experiments are primarily hercynite and spinel with a minor ulvöspinel component (Figure 2.13). Spinel compositions vary with glass composition and temperature

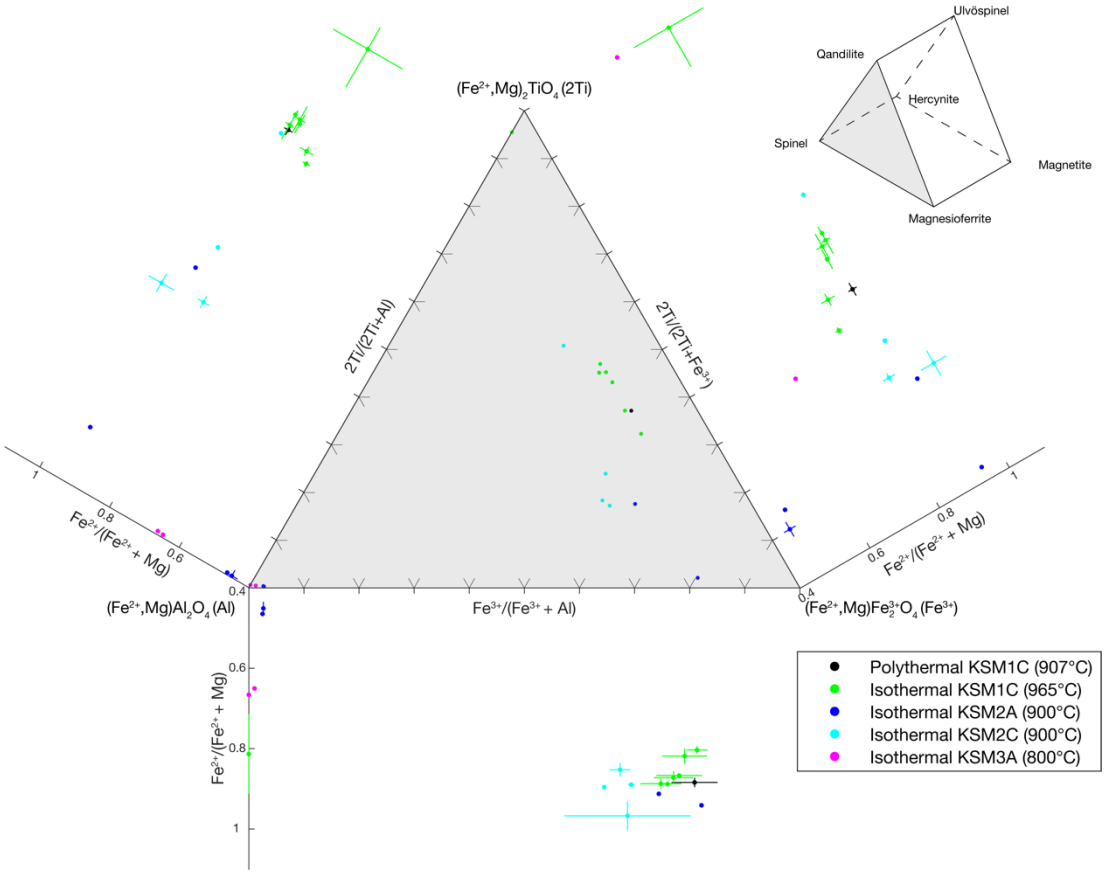

Figure 2.13: Ternary diagram of run-product spinel compositions. Inset is a prism of spinel compositions that are represented by the ternary diagram and projections. Main figure is projected down the $Fe^{2+}/(Fe^{2+}+ Mg)$ axis. The shaded triangle on the main figure is the same shaded triangle in the inset. Cartesian plots on the edges of the ternary are projections of that edge from the opposite corner. Uncertainty is 1 σ_m.

(Figure 2.14). The spinel in high temperature experiments (KSM1C; 965° C) are more magnesium- and aluminum-poor and titanium-rich compared to spinel in low temperature experiments (KSM2A, KSM2C, and KSM3A; 900 and 800°C) (Figures 2.13 and 2.14). Additionally, with the exception of KSM3A experiments and the aluminum-rich spinel in KSM2A experiments, the spinel in the higher temperature experiments contain less Fe^{3+} than lower temperature experiments (Figure 2.13).

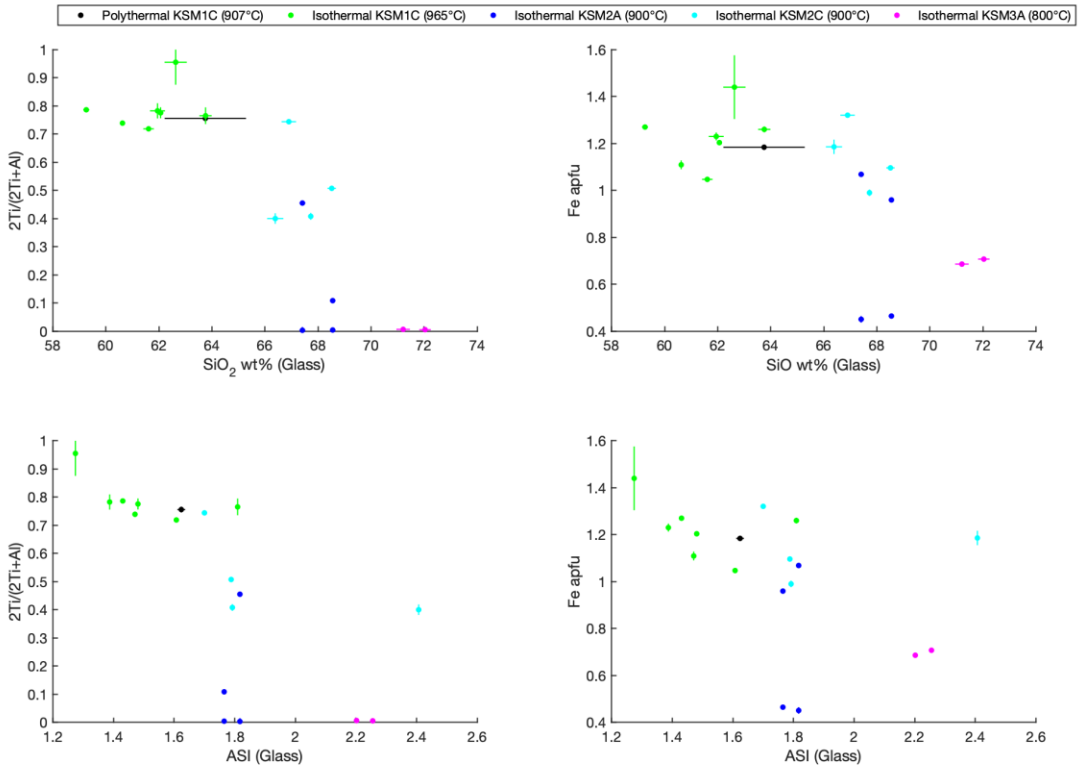

Figure 2.14: Plots of run-product spinel composition vs. composition of run-product glass. Uncertainty is 1 σ_m

2.6.1.3.6. Pyroxene

Pyroxene occurs in both KSM1C and KSM2C experiments, but is primarily observed in experiments conducted at <965 °C. If olivine was not stable at the run temperature (i.e. below ~965 °C), pyroxene was the first ferromagnesian silicate phase to nucleate and grow. The pyroxene compositions can be expressed as phase components of the pyroxene solid solution and are given in Table 2.10. The phase components include enstatite ($Mg_2Si_2O_6$), ferrosilite ($Fe_2^{2+}Si_2O_6$), and wollastonite ($Ca_2Si_2O_6$), where the mole fraction of each component is denoted as X_{En}^{Px}, X_{Fs}^{Px}, X_{Wo}^{Px}, respectively. Pyroxene compositions fall along the enstatite-ferrosilite join and have a minor wollastonite component (Figure 2.15). X_{Wo}^{Px} varies with glass composition and decreases with an increase in SiO_2 (wt%) in the glass and X_{Wo}^{Px} increases with an increase in Al_2O_3 and CaO (wt%) in the glass. Additionally, X_{En}^{Px} increases with an increase in f_{O_2} and X_{En}^{Px} decreases with an increase in FeO (wt%) in the glass. The aluminum concentration of these pyroxene can be quite high (3 to 12 wt%); however, these values are consistent with some natural pyroxenes, which may have up to 6 wt% aluminum (Deer et al., 1997). It is also possible that due to the small grain size of the pyroxene, the pyroxene with greater than 10% aluminum may represent mixed analyses, which may contribute to the high analytical totals in some of the analyses.

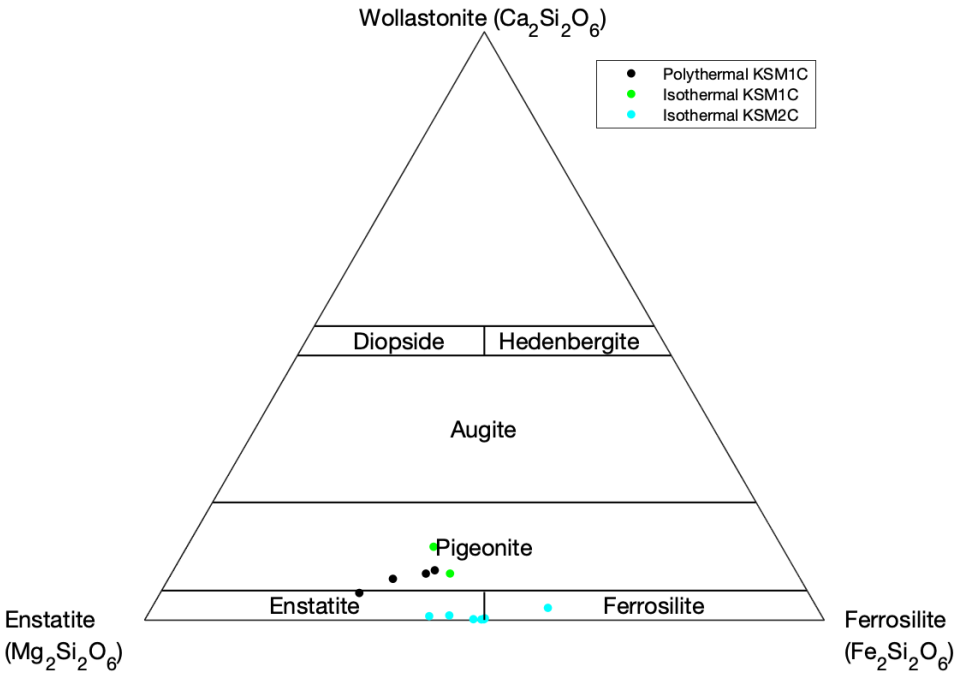

Figure 2.15: Ternary diagram of run-product pyroxene compositions.

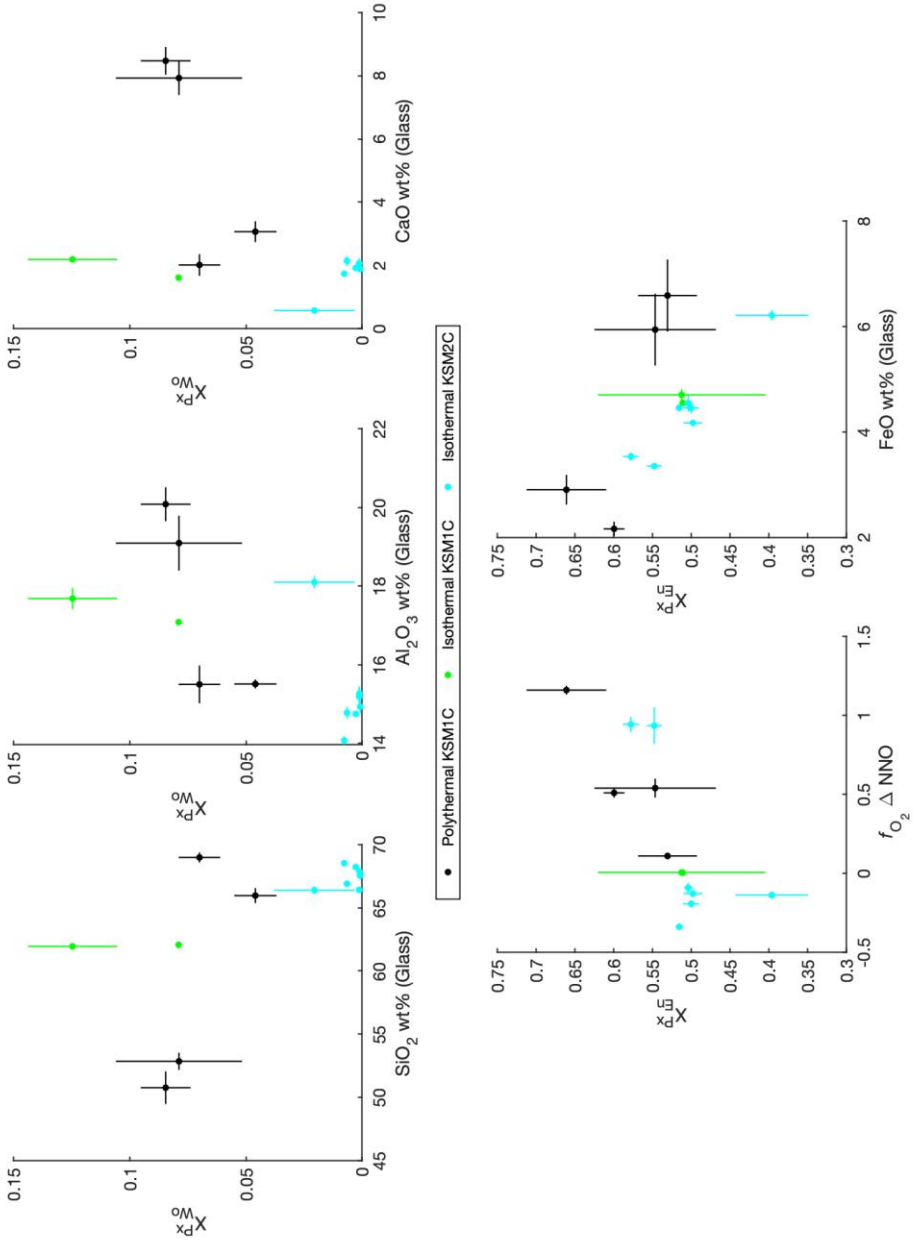

Figure 2.16: Plots of run-product pyroxene composition vs. glass composition and f_{O_2} . Uncertainty is 1 σ_m

Table 2.9: Compositions and mineral formulas of run-product spinel

wt%	KSM1C-3 (N=5)	KSM1C-6 (N=6)	KSM1C-7 (N=4)	KSM1C-8 (N=2)	KSM1C-9 (N=8)	KSM1C-10 (N=10)	KSM1C-11 (N=3)	KSM1C-12 (N=10)
SiO_2	2.3 ± 0.8	1.8 ± 0.3	1.4 ± 0.5	1.7 ± 0.5	0.30 ± 0.09	0.6 ± 0.2	0.8 ± 0.1	0.19 ± 0.02
Al_2O_3	5.2 ± 0.2	5.6 ± 0.1	5.7 ± 0.2	2.00 ± 0.07	5.6 ± 0.1	6.1 ± 0.3	5.4 ± 0.1	5.7 ± 0.1
TiO_2	12.6 ± 0.2	11.2 ± 0.1	12.8 ± 0.2	35 ± 3	16.3 ± 0.2	15.9 ± 0.7	14.6 ± 0.5	16.2 ± 0.6
P_2O_5	b.d.	0.04 ± 0.03	0.24 ± 0.01	b.d.	0.13 ± 0.07	0.10 ± 0.06	0.6 ± 0.6	0.10 ± 0.05
FeO	38.7 ± 0.4	34.8 ± 0.4	36.2 ± 0.8	47 ± 3	27.9 ± 0.3	29 ± 1	30 ± 1	30 ± 1
Fe_2O_3	34 ± 1	38.2 ± 0.6	34 ± 1	-	40.3 ± 0.4	40.8 ± 0.4	38.7 ± 0.2	40.1 ± 0.5
MgO	2.9 ± 0.1	4.77 ± 0.06	4.5 ± 0.2	6.00 ± 0.04	2.92 ± 0.03	2.98 ± 0.09	3.33 ± 0.03	3.33 ± 0.04
MnO	0.98 ± 0.02	0.85 ± 0.02	0.79 ± 0.03	0.85 ± 0.04	0.62 ± 0.01	0.61 ± 0.02	0.80 ± 0.09	0.78 ± 0.01
CaO	0.12 ± 0.03	0.13 ± 0.03	0.3 ± 0.1	0.28 ± 0.08	0.4 ± 0.1	0.3 ± 0.1	1.1 ± 0.9	0.31 ± 0.07
Na_2O	0.3 ± 0.2	0.32 ± 0.07	0.1 ± 0.05	b.d. to 0.13	0.008 ± 0.005	0.02 ± 0.01	0.07 ± 0.03	0.019 ± 0.009
K_2O	0.2 ± 0.1	0.11 ± 0.01	0.08 ± 0.02	0.12 ± 0.04	0.047 ± 0.006	0.08 ± 0.03	0.084 ± 0.002	0.040 ± 0.004
Sc_2O_3	0.049 ± 0.003	0.046 ± 0.003	0.042 ± 0.003	0.15 ± 0.01	0.048 ± 0.001	0.046 ± 0.002	0.046 ± 0.007	0.053 ± 0.002
Total	98 ± 2	97.8 ± 0.8	96 ± 2	93 ± 4	94.5 ± 0.6	96 ± 1	96 ± 2	97 ± 1
Formula								
Si	0.08 ± 0.03	0.06 ± 0.01	0.05 ± 0.02	0.06 ± 0.02	0.011 ± 0.003	0.022 ± 0.008	0.029 ± 0.005	0.0068 ± 0.0007
Al	0.223 ± 0.006	0.238 ± 0.005	0.248 ± 0.009	0.086 ± 0.005	0.248 ± 0.005	0.27 ± 0.01	0.236 ± 0.002	0.247 ± 0.005
Ti	0.345 ± 0.007	0.304 ± 0.004	0.351 ± 0.005	0.96 ± 0.06	0.462 ± 0.005	0.44 ± 0.02	0.41 ± 0.01	0.45 ± 0.02
P	b.d	0.001 ± 0.001	0.0075 ± 0.0003	b.d.	0.009 ± 0.004	0.008 ± 0.004	0.02 ± 0.02	0.008 ± 0.002
Fe	1.18 ± 0.01	1.047 ± 0.009	1.11 ± 0.02	1.4 ± 0.1	1.275 ± 0.004	1.26 ± 0.01	1.204 ± 0.004	1.23 ± 0.02
Fe^{3+}	0.94 ± 0.04	1.04 ± 0.02	0.9 ± 0.04	-	0.794 ± 0.007	0.80 ± 0.03	0.84 ± 0.04	0.84 ± 0.03
Mg	0.155 ± 0.007	0.256 ± 0.004	0.25 ± 0.01	0.327 ± 0.007	0.165 ± 0.003	0.164 ± 0.005	0.185 ± 0.001	0.183 ± 0.002
Mn	0.03 ± 0.001	0.0259 ± 0.0006	0.025 ± 0.001	0.0263 ± 0.0004	0.0199 ± 0.0003	0.0191 ± 0.0007	0.025 ± 0.003	0.0243 ± 0.0005
Ca	0.005 ± 0.001	0.012 ± 0.003	0.013 ± 0.005	0.011 ± 0.003	0.017 ± 0.004	0.013 ± 0.004	0.04 ± 0.03	0.012 ± 0.003
Na	0.02 ± 0.01	0.009 ± 0.002	0.007 ± 0.003	b.d. 0.009	0.0023 ± 0.0008	0.0047 ± 0.0006	0.005 ± 0.002	0.0028 ± 0.0009
K	0.009 ± 0.004	0.0049 ± 0.0006	0.004 ± 0.001	0.005 ± 0.002	0.0023 ± 0.0003	0.004 ± 0.001	0.0040 ± 0.0001	0.0019 ± 0.0002
Sc	0.0016 ± 0.0001	0.0015 ± 0.0001	0.0013 ± 0.0001	0.0048 ± 0.0003	0.00157 ± 0.00004	0.00147 ± 0.00005	0.0015 ± 0.0002	0.00170 ± 0.00007
$Fe^{2+}/(Fe^{2+}+Mg)$	0.88 ± 0.01	0.80 ± 0.01	0.82 ± 0.02	0.8 ± 0.1	0.886 ± 0.004	0.88 ± 0.01	0.867 ± 0.004	0.87 ± 0.02
2Ti/(2Ti+Al)	0.76 ± 0.02	0.72 ± 0.01	0.74 ± 0.01	0.96 ± 0.06	0.79 ± 0.01	0.77 ± 0.03	0.78 ± 0.02	0.78 ± 0.03
$2Ti/(2Ti+Fe^{3+})$	0.42 ± 0.01	0.369 ± 0.007	0.44 ± 0.01	1.00 ± 0.08	0.54 ± 0.01	0.52 ± 0.03	0.49 ± 0.02	0.52 ± 0.03
$Fe^{3+}/(Fe^{3+}+Al)$	0.81 ± 0.04	0.81 ± 0.02	0.78 ± 0.04	0.00	0.76 ± 0.762 ± 0.008	0.75 ± 0.03	0.78 ± 0.04	0.77

Fe_2O_3 calculated after Droop (1987). b.d. is below detection. Uncertainty is $1\sigma_m$

Table 2.9 cont.

wt%	KSM2A-1 Spinel 1 (N=3)	KSM2A-1 Spinel 2 (N=1)	KSM2A-2 Spinel 1 (N=1)	KSM2A-2 Spinel 2 (N=1)	KSM2C-1 (N = 6)	KSM2C-2 (N = 2)	KSM2C-3 (N = 1)	KSM2C-8 (N=3)	KSM3A-6 (N = 1)	KSM3A-7 (N = 1)
SiO_2	0.3 ± 0.2	0.5	0.4	0.6	0.5 ± 0.1	0.88 ± 0.01	0.7	2 ± 1	5.0	8.2
Al_2O_3	64.1 ± 0.4	10.1	63.9	8.3	12.2 ± 0.8	10.56 ± 0.10	7.8	11 ± 1	52.1	49.5
TiO_2	0.15 ± 0.02	6.6	0.2	0.8	6.6 ± 0.2	8.5 ± 0.2	17.7	5.9 ± 0.3	0.2	0.2
P_2O_5	b.d.	b.d.	b.d.	b.d.	b.d.	b.d.	b.d.	0.04 ± 0.02	0.008	0.03
FeO	21.1 ± 0.6	36.8	21.8	32.5	32.6 ± 0.4	36.2 ± 0.1	42.4	40 ± 2	30.3	29.2
Fe_2O_3	2.7 ± 0.3	46.0	2.6	59.5	39.6 ± 0.7	37.52 ± 0.03	22.1	39 ± 4	0.9	-
MgO	14.4 ± 0.3	2.0	14.1	1.1	3.2 ± 0.2	2.52 ± 0.02	2.8	0.8 ± 0.2	9.1	8.2
MnO	0.41 ± 0.02	0.6	0.5	0.3	0.70 ± 0.01	0.7 ± 0.1	0.8	0.31 ± 0.05	0.6	0.7
CaO	0.036 ± 0.008	b.d.	0.03390	b.d.	0.05 ± 0.01	0.10 ± 0.05	0.08	0.08 ± 0.03	0.1	0.2
Na_2O	b.d.	b.d.	0.024	0.08	0.04 ± 0.01	b.d.	0.09	0.02 ± 0.00	0.2	0.3
K_2O	0.02 ± 0.01	0.03	0.05	0.03	0.091 ± 0.009	0.07 ± 0.01	0.07	0.027 ± 0.002	0.3	0.4
Sc_2O_3	0.008 ± 0.002	0.2	0.0	0.1	0.159 ± 0.003	0.153 ± 0.007	0.2	0.11 ± 0.02	0.02	0.03
Total	103.2 ± 0.9	102.7	103.5	103.2	96 ± 1	97.3 ± 0.3	94.7	99 ± 5	98.8	97.0
Formula										
Si	0.007 ± 0.005	0.02	0.01	0.02	0.018 ± 0.005	0.0317 ± 0.0006	0.03	0.08 ± 0.04	0.1	0.2
Al	1.928 ± 0.005	0.4	1.9	0.3	0.52 ± 0.03	0.450 ± 0.001	0.3	0.47 ± 0.05	1.7	1.6
Ti	0.0030 ± 0.0003	0.2	0.0	0.02	0.180 ± 0.006	0.232 ± 0.003	0.5	0.158 ± 0.006	0.004	0.005
P	b.d	b.d.	b.d.	b.d.	b.d.	b.d.	b.d.	0.0012 ± 0.0007	0.0002	0.0007
Fe	0.45 ± 0.01	1.1	0.5	1.0	0.99 ± 0.01	1.096 ± 0.003	1.3	1.19 ± 0.03	0.7	0.7
Fe^{3+}	0.052 ± 0.005	1.2	0.0	1.6	1.08 ± 0.02	1.021 ± 0.007	0.6	1.0 ± 0.1	0.02	-
Mg	0.548 ± 0.010	0.1	0.5	0.06	0.171 ± 0.007	0.13574 ± 0.00006	0.2	0.04 ± 0.01	0.4	0.3
Mn	0.0089 ± 0.0004	0.02	0.01	0.008	0.0216 ± 0.0004	0.022 ± 0.004	0.03	0.009 ± 0.001	0.01	0.02
Ca	0.0010 ± 0.0002	b.d.	0.0	b.d.	0.0018 ± 0.0004	0.004 ± 0.002	0.003	b.d. to 0.003	0.003	0.006
Na	b.d.	b.d.	0.001	0.006	0.0028 ± 0.0009	b.d.	0.006	0.0012 ± 0.0002	0.01	0.02
K	0.0006 ± 0.0004	0.001	0.002	0.001	0.0042 ± 0.0004	0.0030 ± 0.0005	0.003	0.0013 ± 0.0001	0.01	0.01
Sc	0.0002 ± 0.0001	0.005	0.000	0.003	0.0050 ± 0.0001	0.0048 ± 0.0002	0.008	0.0036 ± 0.0005	0.001	0.001
$Fe^{2+}/(Fe^{2+}+Mg)$	0.45 ± 0.02	0.91	0.46	0.94	0.9 ± 0.02	0.890 ± 0.003	0.90	0.97 ± 0.04	0.65	0.67
2Ti/(2Ti+Al)	0.0031 ± 0.0004	0.46	0.004	0.11	0.41 ± 0.02	0.507 ± 0.007	0.74	0.40 ± 0.03	0.01	0.01
$2Ti/(2Ti+Fe^{3+})$	0.10 ± 0.02	0.22	0.14	0.03	0.250 ± 0.009	0.312 ± 0.005	0.62	0.23 ± 0.03	0.33	1.00
$Fe^{3+}/(Fe^{3+}+Al)$	0.026 ± 0.003	0.74	0.02	0.82	0.7 ± 0.02	0.694 ± 0.006	0.64	0.7 ± 0.1	0.0	0.0

Table 2.10: Compositions and mineral formulas of run-product pyroxene

wt%	KSM1C-1 (N=4)	KSM1C-2 (N=13)	KSM1C-4 (N=8)	KSM1C-5 (N=4)	KSM1C-11 (N=4)	KSM1C-12 (N=1)
SiO_2	49 ± 1	48.2 ± 0.7	51 ± 1	53.2 ± 0.5	47 ± 2	47.6
Al_2O_3	5 ± 0.9	3.9 ± 0.6	2.9 ± 0.2	4 ± 0.7	10 ± 3	12.6
TiO_2	1.9 ± 0.3	1.4 ± 0.2	1.1 ± 0.3	0.6 ± 0.1	0.8 ± 0.2	0.3
P_2O_5	1.5 ± 0.2	1.4 ± 0.2	1.2 ± 0.3	0.6 ± 0.2	1.7 ± 0.3	1.0
FeO	21 ± 1	21 ± 0.3	17.9 ± 0.2	15.7 ± 0.6	23 ± 3	18.2
Fe_2O_3	-	1.2 ± 0.5	-	-	-	
MgO	16.6 ± 0.6	18.1 ± 0.6	18.3 ± 0.3	20 ± 1	16 ± 3	14.4
MnO	1.2 ± 0.1	1.37 ± 0.05	1.26 ± 0.03	1.02 ± 0.07	0.7 ± 0.1	0.5
CaO	3.7 ± 0.4	3.6 ± 0.3	3 ± 0.4	1.9 ± 0.3	3.5 ± 0.8	4.9
Na_2O	0.4 ± 0.2	0.22 ± 0.09	0.12 ± 0.02	0.14 ± 0.05	1.1 ± 0.3	2.0
K_2O	0.4 ± 0.1	0.15 ± 0.04	0.14 ± 0.03	0.2 ± 0.1	1.3 ± 0.2	0.8
Sc_2O_3	0.1 ± 0.01	0.121 ± 0.005	0.117 ± 0.005	0.13 ± 0.02	0.039 ± 0.006	0.01
Total	101 ± 2	101 ± 1	97 ± 1	97 ± 1	106 ± 6	102.4
Formula						
Si	1.82 ± 0.06	1.81 ± 0.07	1.94 ± 0.03	1.972 ± 0.004	1.70 ± 0.05	1.73
Al	0.22 ± 0.03	0.2 ± 0.1	0.13 ± 0.01	0.18 ± 0.03	0.4 ± 0.1	0.54
Ti	0.052 ± 0.004	0.04 ± 0.02	0.031 ± 0.009	0.016 ± 0.003	0.021 ± 0.005	0.01
P	0.049 ± 0.002	0.05 ± 0.02	0.03 ± 0.01	0.02 ± 0.01	0.051 ± 0.009	0.03
Fe	0.67 ± 0.06	0.66 ± 0.04	0.57 ± 0.009	0.49 ± 0.02	0.694 ± 0.110	0.55
Fe^{3+}	-	0.03 ± 0.05	-	-	-	-
Mg	0.92 ± 0.05	1 ± 0.1	1.04 ± 0.02	1.1 ± 0.07	0.9 ± 0.2	0.78
Mn	0.037 ± 0.002	0.04 ± 0.01	0.041 ± 0.001	0.032 ± 0.003	0.022 ± 0.003	0.01
Ca	0.15 ± 0.02	0.15 ± 0.05	0.12 ± 0.02	0.08 ± 0.01	0.13 ± 0.03	0.19
Na	0.03 ± 0.01	0.02 ± 0.02	0.009 ± 0.002	0.01 ± 0.004	0.08 ± 0.02	0.14
K	0.017 ± 0.003	0.01 ± 0.01	0.007 ± 0.002	0.012 ± 0.006	0.061 ± 0.009	0.04
Sc	0.0034 ± 0.0003	0.004 ± 0.001	0.0039 ± 0.0002	0.004 ± 0.001	0.0012 ± 0.0002	0.0005
X_{Wo}^{Px}	0.08 ± 0.01	0.08 ± 0.03	0.07 ± 0.009	0.046 ± 0.009	0.08 ± 0.02	0.12
X_{En}^{Px}	0.53 ± 0.04	0.55 ± 0.08	0.6 ± 0.01	0.66 ± 0.05	0.5 ± 0.1	0.51
X_{Fs}^{Px}	0.38 ± 0.04	0.37 ± 0.05	0.33 ± 0.007	0.29 ± 0.02	0.41 ± 0.08	0.36

Fe_2O_3 calculated after Droop (1987). Uncertainty is $1\sigma_m$.

Table 2.10 cont.

wt%	KSM2C-2 (N=8)	KSM2C-3 (N=3)	KSM2C-5 (N=9)	KSM2C-6 (N=9)	KSM2C-7 (N=10)	KSM2C-8 (N=2)	KSM2C-9 (N=9)
SiO_2	45.6 ± 0.4	48.5 ± 0.5	46.4 ± 0.3	46.3 ± 0.4	46.1 ± 0.3	47.4 ± 1.8	48.2 ± 0.6
Al_2O_3	9.9 ± 0.2	6.9 ± 0.8	9.0 ± 0.5	8.2 ± 0.4	8.6 ± 0.4	12.5 ± 0.4	8.1 ± 0.7
TiO_2	0.44 ± 0.02	0.22 ± 0.05	0.6 ± 0.1	0.41 ± 0.02	0.47 ± 0.05	0.53 ± 0.02	0.40 ± 0.04
P_2O_5	0.17 ± 0.03	0.03 ± 0.02	0.15 ± 0.02	0.07 ± 0.02	0.08 ± 0.02	0.47 ± 0.05	0.07 ± 0.02
FeO	23.5 ± 0.3	23.5 ± 0.3	27.0 ± 0.3	26.13 ± 0.09	26.4 ± 0.2	30 ± 1	28.0 ± 0.2
Fe_2O_3	1.4 ± 0.5	0.73 ± 0.01	1.0 ± 0.3	0.77 ± 0.17	2.11 ± 0.21	-	0.5 ± 0.3
MgO	17.2 ± 0.2	18.9 ± 0.3	15.7 ± 0.2	16.1 ± 0.2	16.2 ± 0.2	11 ± 1	15.9 ± 0.3
MnO	0.87 ± 0.01	0.88 ± 0.01	0.78 ± 0.02	0.74 ± 0.02	0.80 ± 0.01	1.1 ± 0.1	0.79 ± 0.02
CaO	0.34 ± 0.03	0.30 ± 0.01	0.40 ± 0.07	0.29 ± 0.02	0.31 ± 0.01	1.2 ± 0.5	0.42 ± 0.09
Na_2O	0.0285 ± 0.006	0.01 ± 0.01	0.03 ± 0.01	0.032 ± 0.007	0.021 ± 0.005	0.5 ± 0.4	0.07 ± 0.02
K_2O	0.09 ± 0.03	0.03 ± 0.02	0.09 ± 0.03	0.06 ± 0.01	0.045 ± 0.004	0.4 ± 0.2	0.12 ± 0.03
Sc_2O_3	0.73 ± 0.05	0.80 ± 0.05	0.77 ± 0.06	0.69 ± 0.04	0.69 ± 0.04	0.29 ± 0.02	0.79 ± 0.05
Total	99.6 ± 0.8	100 ± 1	101 ± 1	99 ± 1	101 ± 1	105 ± 2	103 ± 1
Formula							
Si	1.72 ± 0.01	1.81 ± 0.02	1.74 ± 0.01	1.77 ± 0.01	1.74 ± 0.01	1.73 ± 0.04	1.79 ± 0.02
Al	0.44 ± 0.01	0.30 ± 0.03	0.40 ± 0.02	0.37 ± 0.02	0.38 ± 0.02	0.54 ± 0.01	0.35 ± 0.03
Ti	0.0126 ± 0.0006	0.006 ± 0.001	0.018 ± 0.003	0.012 ± 0.001	0.013 ± 0.001	0.0146 ± 0.0003	0.011 ± 0.001
P	0.006 ± 0.001	0.0011 ± 0.0001	0.0047 ± 0.0007	0.0021 ± 0.0008	0.0024 ± 0.0005	0.014 ± 0.002	0.0021 ± 0.0007
Fe	0.74 ± 0.009	0.74 ± 0.01	0.85 ± 0.01	0.837 ± 0.004	0.83 ± 0.01	0.92 ± 0.04	0.87 ± 0.01
Fe^{3+}	0.04 ± 0.01	0.0205 ± 0.0003	0.029 ± 0.005	0.022 ± 0.004	0.060 ± 0.006		0.015 ± 0.010
Mg	0.97 ± 0.01	1.05 ± 0.02	0.88 ± 0.02	0.92 ± 0.01	0.91 ± 0.01	0.62 ± 0.07	0.88 ± 0.02
Mn	0.0279 ± 0.0004	0.0278 ± 0.0004	0.0250 ± 0.0006	0.0239 ± 0.0006	0.0256 ± 0.0003	0.034 ± 0.004	0.0247 ± 0.0006
Ca	0.014 ± 0.001	0.012 ± 0.001	0.016 ± 0.003	0.012 ± 0.001	0.0125 ± 0.0004	0.05 ± 0.02	0.017 ± 0.003
Na	0.0021 ± 0.0004	0.001 ± 0.001	0.002 ± 0.001	0.002 ± 0.001	0.0015 ± 0.0003	0.03 ± 0.03	0.005 ± 0.002
K	0.004 ± 0.001	0.0016 ± 0.0003	0.0042 ± 0.0013	0.0029 ± 0.0005	0.0022 ± 0.0002	0.017 ± 0.007	0.006 ± 0.002
Sc	0.024 ± 0.002	0.026 ± 0.002	0.025 ± 0.002	0.023 ± 0.001	0.023 ± 0.001	0.009 ± 0.001	0.025 ± 0.002
X^{Px}_{Wo}	0.0078 ± 0.0006	0.0065 ± 0.0003	0.0012 ± 0.0006	0.0013 ± 0.0003	0.0009 ± 0.0002	0.02 ± 0.02	0.003 ± 0.001
X^{Px}_{En}	0.5477 ± 0.0097	0.58 ± 0.01	0.50 ± 0.01	0.516 ± 0.005	0.50 ± 0.01	0.40 ± 0.05	0.50 ± 0.01
X^{Px}_{Fs}	0.44 ± 0.01	0.416 ± 0.006	0.499 ± 0.008	0.483 ± 0.004	0.495 ± 0.006	0.58 ± 0.04	0.50 ± 0.01

2.6.1.3.7. Cordierite

Cordierite occurs in KSM3A experiments and in one KSM2A experiment. The compositions of run-product cordierite are consistent among experiments and have Mg/(Mg + Fe + Mn) of between 0.6 and 0.8 and Na + K of between 0.02 and 0.1 (Table 2.11; Figure 2.17). Additionally, cordierite have CaO + Na_2O +K_2O of between 0.5 and 1 wt% and MnO of between 0.25 and 0.75 wt% (Figure 2.17). The cordierite plot in the metamorphic, anatectic, and magmatic fields of Pereira and Bea (1994) and in the S-type granite fields defined by Bayati et al. (2017), Barbero and Villaseca (1992), and Villaseca and Barbero (1994) (Figure 2.17).

2.6.1.3.8. Miscellaneous Phases

There are several phases that occur in only a few experiments that are worth noting. Aluminosilicates have compositions that are approximately end-member Al_2SiO_5 occur in KSM2A and the fluorine-bearing KSM3A experiments (Table 2.12). Based on the pressure and temperature conditions of the experiments, these aluminosilicates are likely sillimanite. Additionally, ilmenite occurs in three KSM2C experiments and rutile occurs in one KSM2C experiment (Table 2.12). Finally, apatite occurs in two KSM1C experiments (Table 2.13).

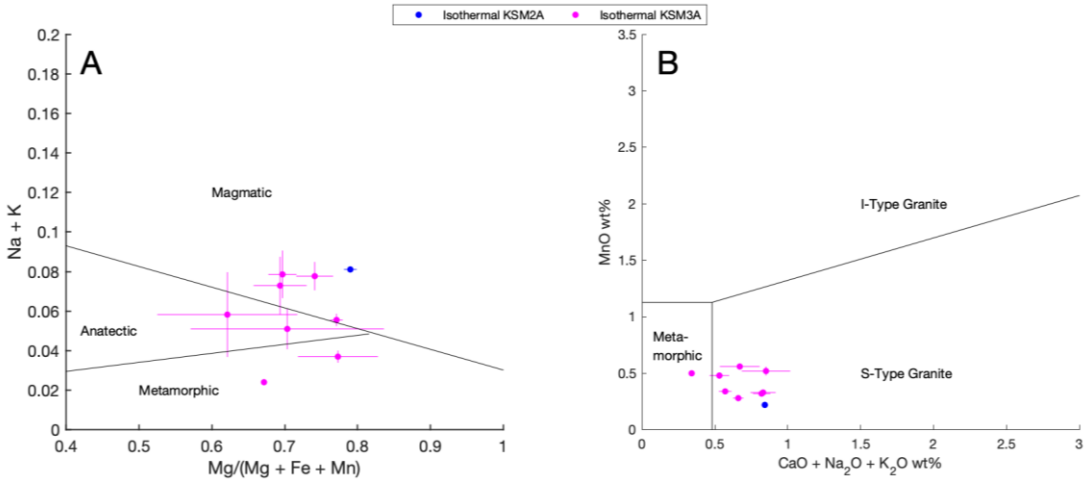

Figure 2.17: Plots of run-product cordierite composition on discriminatory diagram. **A)** Na + K vs Mg/(Mg + Fe + Mn) discriminatory diagram; Magmatic, anatectic, and metamorphic fields are from Pereira and Bea (1994). **B)** MnO (wt%) vs $CaO + Na_2O + K_2O$ (wt%) discriminatory diagram; I- and S-type granite and metamorphic fields are from Bayati et al. (2017), Barbero and Villaseca (1992), and Villaseca and Barbero (1994). Uncertainty is 1 σ_m.

Table 2.11: Compositions and mineral formulas of run-product cordierite

wt%	KSM2A-1 (N=2)			KSM3A-1 (N=3)			KSM3A-2 (N=1)	KSM3A-3 (N=4)			KSM3A-4 (N=2)			KSM3A-5 (N=8)		
SiO_2	47.9	±	0.2	54	±	3	47	51	±	2	48	±	2	47.2	±	0.3
Al_2O_3	34.75	±	0.09	29	±	2	34	32	±	1	37	±	2	34.2	±	0.4
TiO_2	0.10	±	0.02	0.11	±	0.05	0.1	0.06	±	0.01	0.11	±	0.01	0.04	±	0.01
P_2O_5	0.05	±	0.02	0.6	±	0.2	0.2	0.4	±	0.1	0.18	±	0.01	0.05	±	0.01
FeO	4.75	±	0.03	5.9	±	0.4	7.3	5.5	±	0.2	8.0	±	0.4	5.8	±	0.1
MgO	10.49	±	0.02	8.1	±	0.2	9.0	7.9	±	0.8	7.9	±	0.4	9.8	±	0.2
MnO	0.22	±	0.02	0.52	±	0.04	0.5	0.48	±	0.03	0.56	±	0.01	0.32	±	0.01
CaO	0.30	±	0.01	0.4	±	0.1	0.2	0.21	±	0.03	0.31	±	0.03	0.34	±	0.04
Na_2O	0.172	±	0.007	0.23	±	0.05	0.07	0.15	±	0.04	0.2	±	0.1	0.21	±	0.03
K_2O	0.370	±	0.003	0.22	±	0.08	0.07	0.17	±	0.04	0.16	±	0.08	0.27	±	0.04
Sc_2O_3	0.025	±	0.001	0.07	±	0.01	0.05	0.07	±	0.01	0.07	±	0.01	0.04	±	0.01
F		-			-		-		-			-			-	
Cl		-			-		-		-			-		0.17	±	0.05
F,Cl = O		-			-		-		-			-			0.04	
Total	99.1	±	0.3	100	±	4	99	99	±	2	103	±	7	98.37	±	0.51
Formula																
Si	4.8	±	0.0082	5.4	±	0.2	4.8	5.2	±	0.1	4.78	±	0.01	4.84	±	0.04
Al	4.1	±	0.0036	3.5	±	0.3	4.1	3.9	±	0.1	4.3	±	0.1	4.13	±	0.04
Ti	0.008	±	0.0015	0.008	±	0.003	0.007	0.005	±	0.001	0.0081	±	0.0001	0.0032	±	0.0006
P	0.004	±	0.002	0.05	±	0.02	0.02	0.03	±	0.01	0.0153	±	0.0005	0.005	±	0.001
Fe	0.4	±	0.0038	0.49	±	0.04	0.6	0.46	±	0.02	0.66	±	0.06	0.50	±	0.01
Mg	1.6	±	0.0087	1.21	±	0.04	1.4	1.2	±	0.1	1.2	±	0.1	1.50	±	0.03
Mn	0.019	±	0.0012	0.044	±	0.004	0.04	0.041	±	0.003	0.047	±	0.002	0.028	±	0.001
Ca	0.033	±	0.0012	0.04	±	0.01	0.02	0.022	±	0.004	0.034	±	0.004	0.038	±	0.004
Na	0.0333	±	0.0003	0.04	±	0.01	0.01	0.029	±	0.008	0.04	±	0.02	0.04	±	0.01
K	0.0477	±	0.0002	0.03	±	0.01	0.01	0.022	±	0.006	0.020	±	0.009	0.035	±	0.005
Sc	0.0026	±	0.0001	0.006	±	0.001	0.004	0.007	±	0.001	0.006	±	0.001	0.004	±	0.000
F		-			-		-		-			-			-	
Cl		-			-		-		-			-		0.029	±	0.008
Na+K	0.0803	±	0.0003	0.07	±	0.01	0.03	0.04	±	0.01	0.05	±	0.02	0.07	±	0.01
Mg/(Mg+Fe+Mn)	0.79	±	0.01	0.69	±	0.03	0.7	0.70	±	0.10	0.62	±	0.06	0.74	±	0.02

Uncertainty is $1\sigma_m$.

Table 2.11 cont.

wt%	KSM3A-6 (N=7)			KSM3A-7 (N=9)			KSM3A-8 (N=5)		
SiO_2	47	±	1	47.4	±	0.3	48.1	±	0.6
Al_2O_3	34.9	±	0.3	34.2	±	0.1	35.3	±	1.0
TiO_2	0.06	±	0.04	0.03	±	0.01	0.03	±	0.01
P_2O_5	0.07	±	0.03	0.09	±	0.03	0.06	±	0.04
FeO	7	±	1	5.1	±	0.1	4.9	±	0.1
MgO	9.6	±	0.2	10.24	±	0.05	10.12	±	0.23
MnO	0.33	±	0.02	0.28	±	0.02	0.34	±	0.02
CaO	0.36	±	0.04	0.32	±	0.03	0.33	±	0.04
Na_2O	0.24	±	0.05	0.16	±	0.01	0.09	±	0.01
K_2O	0.23	±	0.05	0.18	±	0.01	0.15	±	0.02
Sc_2O_3	0.042	±	0.004	0.034	±	0.006	0.039	±	0.003
F		-		0.05	±	0.01	0.03	±	0.01
Cl	0.12	±	0.02	0.09	±	0.01	0.13	±	0.01
F,Cl = O		0.03			0.04			0.04	
Total	100	±	2	98.1	±	0.3	99.6	±	1.2
Formula									
Si	4.8	±	0.1	4.85	±	0.02	4.84	±	0.01
Al	4.19	±	0.07	4.13	±	0.02	4.18	±	0.06
Ti	0.005	±	0.002	0.002	±	0.001	0.002	±	0.001
P	0.006	±	0.002	0.008	±	0.002	0.005	±	0.003
Fe	0.6	±	0.1	0.44	±	0.01	0.42	±	0.02
Mg	1.46	±	0.02	1.56	±	0.01	1.52	±	0.05
Mn	0.029	±	0.002	0.025	±	0.001	0.029	±	0.002
Ca	0.039	±	0.005	0.035	±	0.003	0.035	±	0.004
Na	0.05	±	0.01	0.032	±	0.003	0.018	±	0.001
K	0.031	±	0.007	0.024	±	0.002	0.019	±	0.003
Sc	0.0037	±	0.0004	0.0031	±	0.0006	0.0034	±	0.0003
F		-		0.016	±	0.003	0.011	±	0.004
Cl	0.020	±	0.003	0.015	±	0.002	0.022	±	0.002
Na+K	0.07	±	0.01	0.058	±	0.003	0.054	±	0.003
Mg/(Mg+Fe+Mn)	0.70	±	0.04	0.77	±	0.01	0.77	±	0.04

Table 2.12: Compositions of miscellaneous run-products

wt%	KSM2A-1 Aluminosilicate (N=2)	KSM2A-2 Aluminosilicate (N=2)	KSM3A-7 Aluminosilicate (N=3)	KSM3A-8 Aluminosilicate (N=1)	KSM2C-2 Ilmenite (N=1)	KSM2C-3 Ilmenite (N=2)	KSM2C-9 Ilmenite (N=2)	KSM2C-2 Rutile (N=1)
SiO_2	26.63 ± 0.04	26 ± 1	24 ± 3	27	0.3	0.7 ± 0.2	3 ± 1	0.06
Al_2O_3	69.0 ± 0.2	66 ± 2	70 ± 2	65	0.8	6.0 ± 0.8	1.2 ± 0.1	0.2
TiO_2	0.49 ± 0.03	1.3 ± 0.1	0.15 ± 0.02	0.1	44.1	32 ± 2	48 ± 1	95.7
P_2O_5	b.d.	b.d.	0.08 ± 0.02	0.06	b.d.	b.d. to 0.05	b.d.	b.d.
FeO	3.89 ± 0.05	5.2 ± 0.2	3.7 ± 0.6	5.0	45	51 ± 1	43 ± 1	1.6
MgO	0.20 ± 0.02	0.23 ± 0.03	0.16 ± 0.02	0.2	2.9	3.34 ± 0.09	2.52 ± 0.02	0.02
MnO	0.013 ± 0.005	b.d. to 0.02	0.03 ± 0.02	0.05	0.9	0.71 ± 0.06	0.87 ± 0.06	0.008
CaO	0.08 ± 0.03	0.09 ± 0.05	0.45 ± 0.23	0.08	0.04	0.08 ± 0.02	0.3 ± 0.1	0.1
Na_2O	0.07 ± 0.02	0.08 ± 0.02	0.25 ± 0.09	0.1	b.d.	0.04 ± 0.01	0.154 ± 0.004	b.d.
K_2O	0.031 ± 0.006	0.08 ± 0.06	0.33 ± 0.21	0.1	0.08	0.10 ± 0.01	0.14 ± 0.06	0.1
Sc_2O_3	0.023 ± 0.002	0.018 ± 0.004	0.025 ± 0.004	0.03	0.7	0.57 ± 0.03	0.37 ± 0.07	0.06
Total	100.4 ± 0.2	99 ± 2	100 ± 4	98	94.9	95 ± 3	99 ± 2	97.9

Table 2.13: Compositions of run-product apatite

wt%	KSM1C-10 (N=4)			KSM1C-11 (N=1)
SiO_2	3.8	±	0.6	4.56
Al_2O_3	1.8	±	0.4	1.5
TiO_2	0.6	±	0.3	0.14
P_2O_5	37.8	±	0.6	38.68
FeO	1.7	±	0.2	1.32
MgO	0.54	±	0.03	0.49
MnO	0.21	±	0.02	0.174
Na_2O	0.13	±	0.07	0.06
CaO	50.3	±	0.5	49.70
K_2O	0.4	±	0.1	0.386
Sc_2O_3	0.024	±	0.005	0.027
H_2O	1.778	±	0.009	1.793
Total	99	±	1	98.9
Formula				
Si	0.32	±	0.05	0.38
Al	0.18	±	0.04	0.15
Ti	0.04	±	0.02	0.01
P	2.70	±	0.04	2.74
Fe	0.12	±	0.02	0.09
Mg	0.068	±	0.005	0.06
Mn	0.015	±	0.001	0.01
Na	0.02	±	0.01	0.01
Ca	4.54	±	0.03	4.45
K	0.04	±	0.01	0.04
Sc	0.0018	±	0.0004	0.002

H_2O calculated assuming the hydroxyl site has 2 OH.

2.6.2. Scandium Partitioning

2.6.2.1. Trends in Scandium Enrichment

On a first order basis, the results of the experiments presented here are consistent with the hypothesis that increased crystallization results in melts that are subsequently poorer in scandium; that is, scandium behaves as a compatible element. This is supported by the decreasing scandium concentration with increasing SiO_2 (wt%) of the run product glass. This is most easily observed by comparing Sc_2O_3 enrichment vs SiO_2, MgO, and FeO enrichment/depletion (Figures 2.18 and 2.19). An enrichment value is calculated by dividing the concentration of the oxide in the run-product glass by the concentration of that oxide in the starting material. For example, if the starting material has 50 wt% SiO_2 and the run-product glass has 60

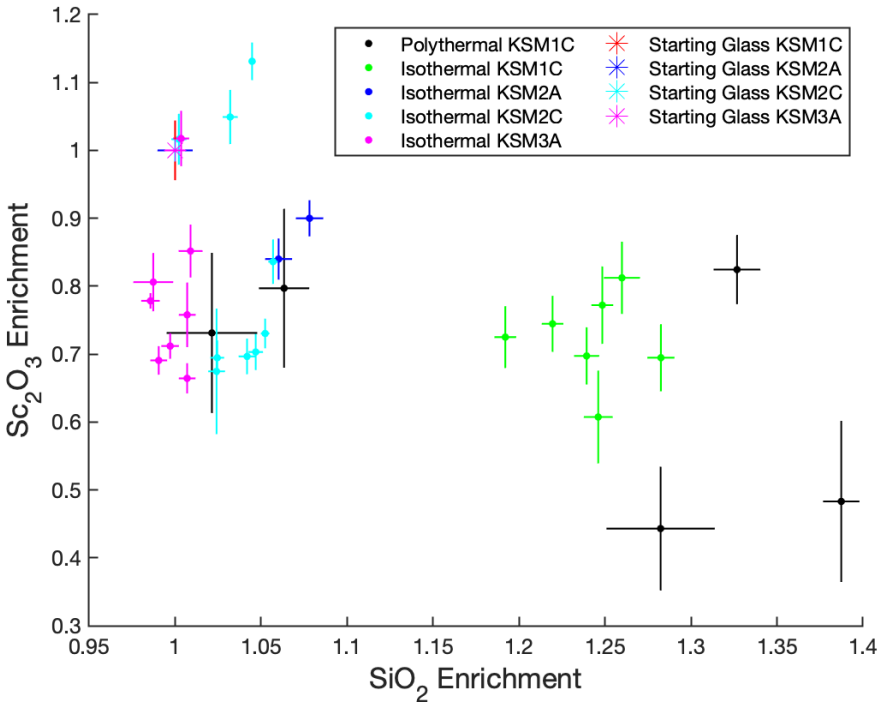

Figure 2.18: Plot of Sc_2O_3 enrichment vs. SiO_2 enrichment of the run-product glasses. See text for examples of the term "enrichment". All of the starting material (asterisk) plot at (1,1). Uncertainty is 1 σ_m.

wt% SiO_2, then the SiO_2 enrichment value is 1.2. Enrichment values greater than 1 indicate an increase in an oxide in the run-product glass relative to the starting materials and values less than 1 indicated a decrease in an oxide in the run-product glass relative to the starting materials. Generally, for each set of experiments the, Sc_2O_3 enrichment value decreases (i.e. less than 1) when the SiO_2 enrichment increases (i.e. greater than 1) (Figure 2.18). However, there are four experiments from the KSM2C and KSM3A sets, wherein the Sc_2O_3 enrichment value increases (i.e. greater than 1), indicating scandium is being concentrated in the glass (Figure 2.18). This is due to either a low modal percent of minerals with high partition coefficients

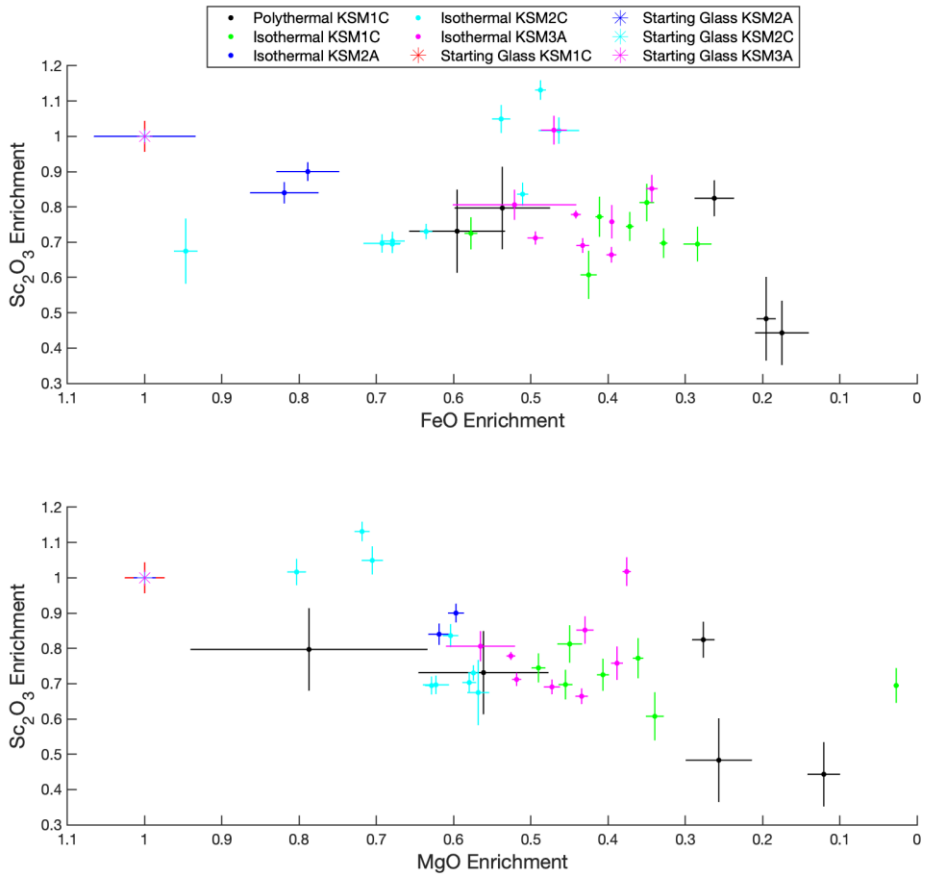

Figure 2.19: Plot of Sc_2O_3 vs. MgO and FeO enrichment of the run-product glasses. Uncertainty is 1 σ_m.

(e.g. pyroxene in KSM2C experiments) or lower partition coefficients (e.g. in cordierite in KSM3A experiments). Additionally, as the FeO and MgO enrichment value decreases (i.e. less than 1), the Sc_2O_3 enrichment value also decreases (Figure 2.19). These trends are primarily due to the compatibility of scandium in crystalline phases relative the melt phase (Table 2.14).

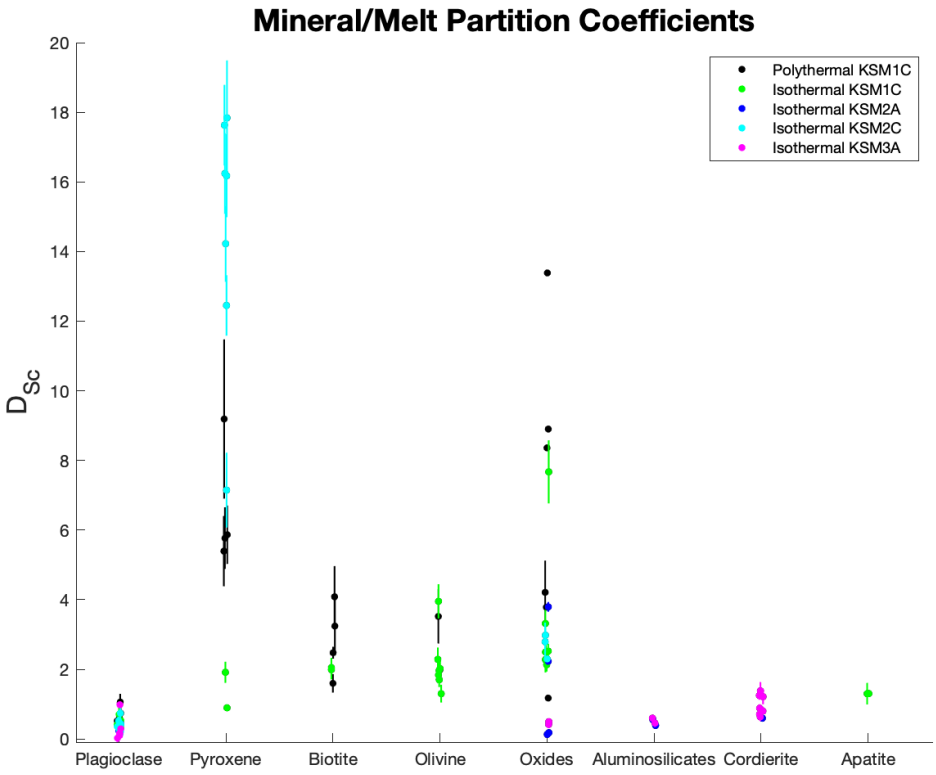

Figure 2.20: Partition coefficients for scandium between run product crystalline phases and melt. Oxides include spinel, ilmenite, and rutile. Uncertainty is 1 σ_m.

2.6.2.2. Mineral/Melt Partition Coefficients

Mineral/melt partition coefficients for scandium vary greatly among experiments and mineral-melt pairs (Table 2.14; Figures 2.20 and 2.21). Generally, partition coefficients for olivine/melt ($D_{Sc}^{Ol/Melt}$), pyroxene/melt ($D_{Sc}^{Px/Melt}$), biotite/melt ($D_{Sc}^{Bt/Melt}$), spinel/melt ($D_{Sc}^{Spl/Melt}$), and ilmenite/melt ($D_{Sc}^{Ilm/Melt}$) are

greater than one; apatite/melt ($D_{Sc}^{Ap/Melt}$) and rutile/melt ($D_{Sc}^{Rt/Melt}$) are approximately one; and plagioclase/melt ($D_{Sc}^{Pl/Melt}$), Al_2SiO_5/melt ($D_{Sc}^{Al_2SiO_5/Melt}$), and cordierite/melt ($D_{Sc}^{Crd/Melt}$) are less than or equal to one. However, the magnitude of partition coefficients is affected by both mineral and glass compositions (Figure 2.21), which may vary as a function of temperature, f_{O_2}, and the percent crystallization (Section 2.6.1.3).

	Mineral Composition								Melt Composition						
	Si	Fe or Mg	Al	Ti	Ca	P	Na	Mn	SiO_2	FeO or MgO	Al_2O_3	TiO_2	CaO	P_2O_5	MnO
Olivine	↓	↓ (Mg)				↑			↑	↓		↓			
Plagioclase		↑		↑	↓	↑			↓	↑	↑	↑	↑	↑	
Biotite		↓ (Mg)		↓					↑	↓	↓	↓			↓
Spinel	↓	↑(Fe)	↓	↑					↓		↓				
Pyroxene		↑ (Fe)		↓	↓	↓	↓	↓	↑	↓?	↓				
Cordierite		↓ (Mg)						↑	↑	↓				↑	

Figure 2.21: Summary of the effect mineral and melt composition have on the partition coefficients for scandium between minerals and melts. Mineral composition is in terms of atoms per formula unit (apfu) and melt composition is in terms of oxide weight %. Red, downward arrows indicate that the partition coefficient decreases as the variable in that column increases (e.g. in olivine the partition coefficient decreases as silicon apfu increases). Green, upward arrows indicate that the partition coefficient increases as the variable in that column increases (e.g. in olivine the partition coefficient increases as phosphorus apfu increases).

2.6.2.2.1. Static and Dynamic Partition Coefficients

In this study, the partition coefficients can be divided into two groups: static and dynamic. Static partition coefficients are from isothermal experiments and dynamic partition coefficients are from polythermal experiments. This distinction was made because as the temperature of the melt decreases, its composition continues to change due to increasing crystallization. The rate at which crystalline phases present prior to the decrease in temperature re-equilibrate with the melt may be slower than the rate at which the melt changes composition due to continuous crystallization. This produces crystals and melt that are coexisting, but may not be in equilibrium, and as a result yield dynamic partition coefficients. How far or if the crystals and melt are out of equilibrium is difficult to quantify. However, partition coefficients can be plotted against the decrease in temperature (ΔT) to compare the

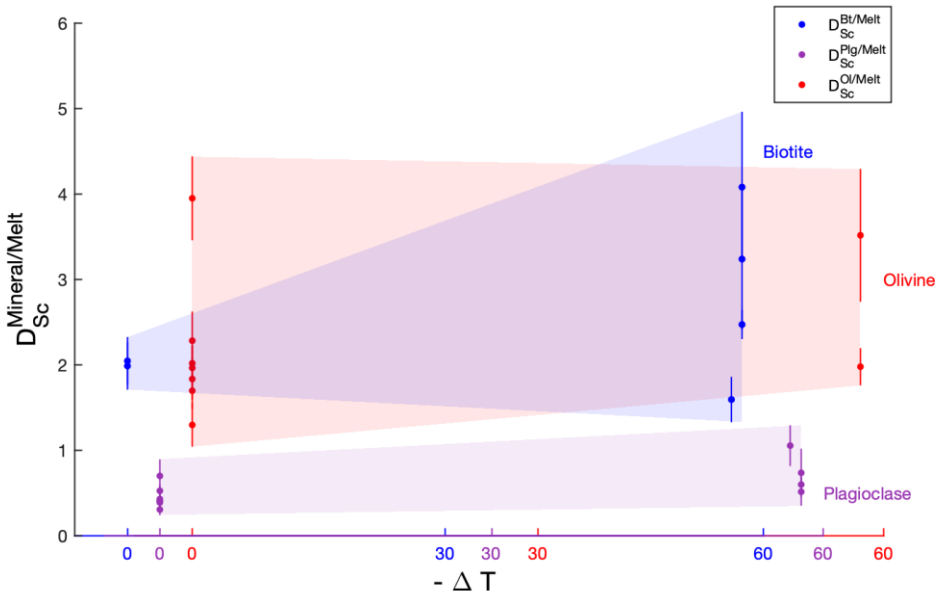

Figure 2.22: Partition coefficients for scandium between biotite/melt, plagioclase/melt, and olivine/melt plotted against the change in temperature (-ΔT) of KSM1C experiments (Table 2.14). Uncertainty is 1 σ_m.

effect of ΔT. The distribution of partition coefficients for plagioclase, biotite, and olivine as a function of ΔT are presented in Figure 2.22. For this comparison only experiments from KSM1C experiments have been plotted, as that is the only set of experiments that contains both iso- and polythermal experiments. As ΔT increases, the variance in the $D_{Sc}^{Bt/Melt}$ increases, but the variance of $D_{Sc}^{Pl/Melt}$ and $D_{Sc}^{Ol/Melt}$remain approximately the same; however, the uncertainty in the partition coefficient for some experiments increases with increasing ΔT (Figure 2.22). Additionally, the scandium concentration of the melt may decrease after the decrease in temperature (Figure 2.23; KSM1C experiments only) due to further crystallization, resulting in slightly increased partition coefficients if the crystalline phases do not have enough time to re-equilibrate with the melt. Partition coefficients from polythermal experiments are thus dynamic and characterize evolving systems. Partition coefficients from isothermal experiments are thus static.

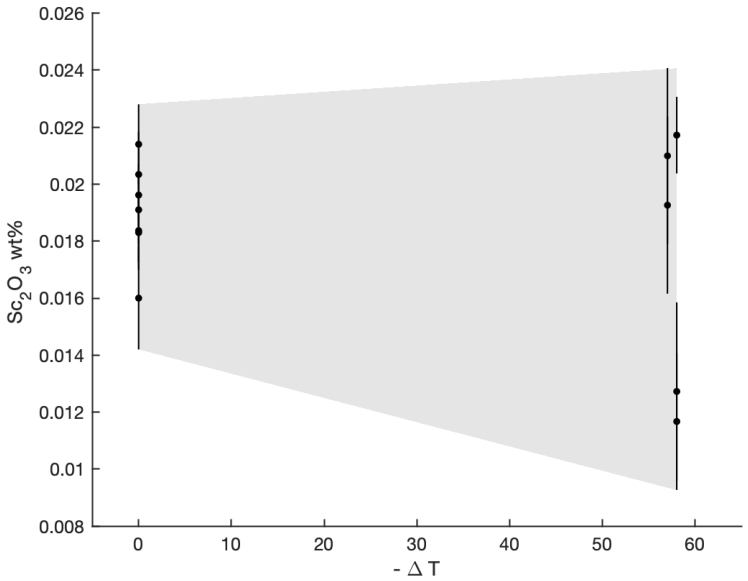

Figure 2.23: Sc_2O_3 (wt%) in the run-product glass plotted against -ΔT for KSM1C experiments. Increasing –ΔT increases the variance in Sc_2O_3 (wt%). Uncertainty is 1 σ_m.

Table 2.14: Mineral/melt partition coefficients

	Plagioclase	Pyroxene	Biotite	Olivine	Spinel	Apatite	Ilmenite	Rutile	Al_2SiO_5	Cordierite	Bulk Partition Coefficient*
KSM1C-1	1.1 ± 0.2	5 ± 1	1.6 ± 0.3		n.a.						4.08 ± 0.4
KSM1C-2	n.a.	5.8 ± 0.9			n.a.						4.27 ± 0.4
KSM1C-3	0.5 ± 0.2		4.1 ± 0.9	3.5 ± 0.8	4.2 ± 0.9						2.34 ± 0.2
KSM1C-4	0.7 ± 0.3	9 ± 2	3.2 ± 0.8		n.a.						2.3 ± 0.2
KSM1C-5	0.6 ± 0.1	5.9 ± 0.8	2.5 ± 0.2	2 ± 0.2	n.a.						1.77 ± 0.1
KSM1C-6	0.41 ± 0.08		2 ± 0.3	2.3 ± 0.3	2.5 ± 0.2						1.46 ± 0.1
KSM1C-7	0.43 ± 0.04		2 ± 0.3	1.7 ± 0.2	2.1 ± 0.2						1.36 ± 0.1
KSM1C-8	0.7 ± 0.2			1.8 ± 0.2	7.7 ± 0.9						2.15 ± 0.2
KSM1C-9	0.53 ± 0.07			1.3 ± 0.3	2.5 ± 0.2						1.04 ± 0.0
KSM1C-10	0.31 ± 0.07		n.a.	2.0 ± 0.3	2.5 ± 0.2	1.3 ± 0.3					1.76 ± 0.1
KSM1C-11	0.39 ± 0.05	1.9 ± 0.3		2.0 ± 0.2	2.3 ± 0.4	1.3 ± 0.1					1.1 ± 0.1
KSM1C-12	0.4 ± 0.1	0.9 ± 0.1		4.0 ± 0.5	3.3 ± 0.4						1.47 ± 0.1
KSM2A-1	0.4 ± 0.1				0.18 ± 0.06[a] & 3.8 ± 0.1[b]				0.55 ± 0.05	0.60 ± 0.04	0.74 ± 0.05
KSM2A-2	0.23 ± 0.06				0.130 ± 0.004 & 2.23 ± 0.07[b]				0.39 ± 0.09		0.46 ± 0.03
KSM2C-1	0.15 ± 0.04				2.30 ± 0.07						0.55 ± 0.02
KSM2C-2	0.35 ± 0.04	14 ± 1			3.0 ± 0.2		13.4 ± 0.5	1.2 ± 0.5			1.46 ± 0.06
KSM2C-3	0.5 ± 0.1	12.4 ± 0.9			3.8 ± 0.1		8.9 ± 0.6				1.33 ± 0.08
KSM2C-4	0.22 ± 0.03				n.a.						0.57 ± 0.05
KSM2C-5	0.45 ± 0.05	18 ± 2			n.a.						2.8 ± 0.2
KSM2C-6	0.41 ± 0.07	16 ± 1			n.a.						1.81 ± 0.1
KSM2C-7	0.26 ± 0.06	16 ± 1			n.a.						2.18 ± 0.11
KSM2C-8	n.a.	7 ± 1			2.8 ± 0.6						1.4 ± 0.2
KSM2C-9	0.7 ± 0.3	18 ± 1			n.a.		8 ± 1				3.8 ± 0.2
KSM3A-1	0.29 ± 0.02				n.a.					1.2 ± 0.2	0.4 ± 0.02
KSM3A-2	0.149 ± 0.006				n.a.					0.70 ± 0.03	0.57 ± 0.02
KSM3A-3	<<1				n.a.					1.2 ± 0.1	0.1 ± 0.02
KSM3A-4	0.98 ± 0.06				n.a.					1.4 ± 0.3	1.3 ± 0.1
KSM3A-5	n.a.				n.a.					0.9 ± 0.1	0.36 ± 0.04
KSM3A-6	0.098 ± 0.003				0.42 ± 0.04					0.84 ± 0.09	0.32 ± 0.05
KSM3A-7	0.02 ± 0.02				0.5 ± 0.09				0.5 ± 0.1	0.6 ± 0.1	0.49 ± 0.07
KSM3A-8	0.17 ± 0.09				n.a.				0.60 ± 0.05	0.80 ± 0.07	0.46 ± 0.04

*The bulk partition coefficient is the average of two bulk partition coefficients calculated for each least-squares method used to determine the mass% of each phase (Table 2.4). For experiments where spinel has been identified by EDS, but partition coefficients are not available (n.a.), the average partition coefficient for that set of experiments is used. For KSM3A experiments the spinel/melt partition coefficient for KSM3A-6 was used for KSM3A-1 to -6, and the spinel/melt partition coefficient for KSM3A-7 was used for KSM3A-8 due to the addition of fluorphlogopite to KSM3A-7 and -8. a = spinel 1, b = spinel 2

2.6.2.2.2. Olivine/Melt Partitioning

$D_{Sc}^{Ol/Melt}$ (value ± 1 σ_m) ranges from 1.3 ± 0.3 to 4 ± 0.8 (Table 2.14), and is dependent on mineral and melt composition. There are two mineral compositional parameters that have a strong effect on $D_{Sc}^{Ol/Melt}$ and one parameter that has minor, possibly insignificant, effects on $D_{Sc}^{Ol/Melt}$ (Figure 2.24). Phosphorus and silicon atoms per formula unit (apfu) have a strong effect on $D_{Sc}^{Ol/Melt}$, such that $D_{Sc}^{Ol/Melt}$ increases with increasing phosphorus apfu and decreases with increasing silicon apfu. X_{Fo}^{Ol} has a minor effect on $D_{Sc}^{Ol/Melt}$, such that $D_{Sc}^{Ol/Melt}$ decreases with increasing X_{Fo}^{Ol}.

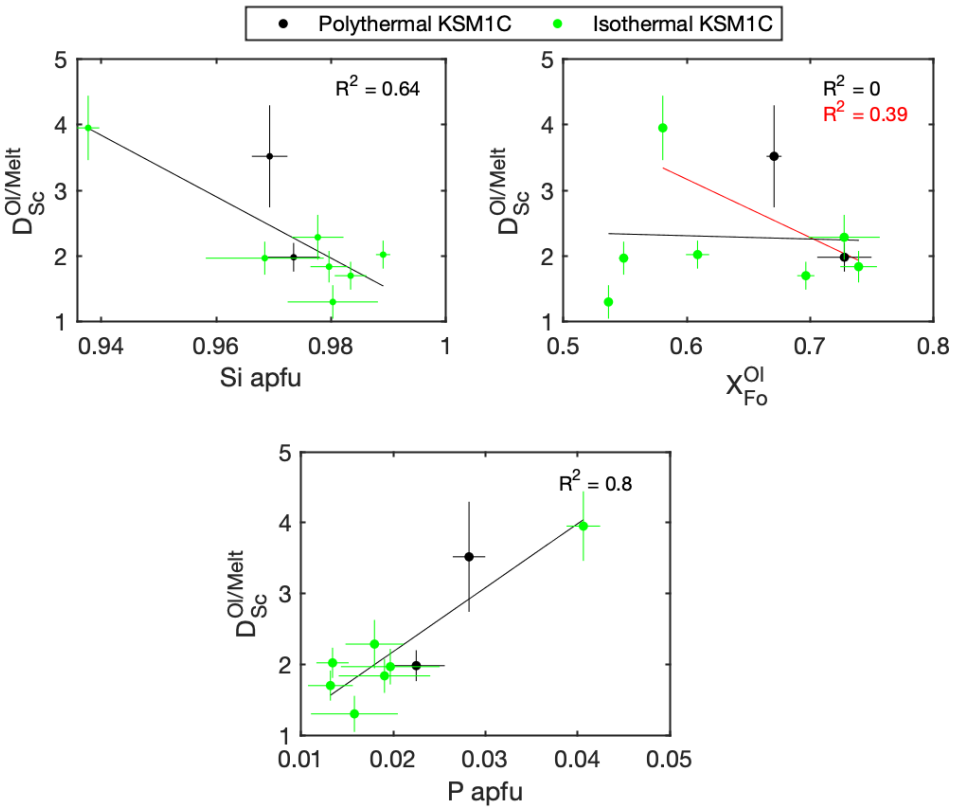

Figure 2.24: Effect of olivine composition on olivine/melt partition coefficients for scandium. $D_{Sc}^{Ol/Melt}$ is plotted against silicon atoms per formula unit (apfu), X_{Fo}^{Ol}, and phosphorus apfu of the run-product olivine. Uncertainty is 1 σ_m. Black lines represent linear regressions of the data. Red line is the liner regression excluding the two most reduced experiments (KSM1C-9 and KSM1C-10; f_{O_2} of <NNO and lowest X_{Fo}^{Ol},).

Although there is a minor correlation between $D_{Sc}^{Ol/Melt}$ and X_{Fo}^{Ol} and there is a strong correlation between X_{Fo}^{Ol} and f_{O_2}, there does not appear to be a strong correlation between $D_{Sc}^{Ol/Melt}$ and f_{O_2} in this dataset. However, in the most reduced experiments (KSM1C-9 and KSM1C-10; f_{O_2} of <NNO) $D_{Sc}^{Ol/Melt}$ does not fall along the trend of decreasing $D_{Sc}^{Ol/Melt}$ with increasing X_{Fo}^{Ol}. The deviation from this trend is consistent

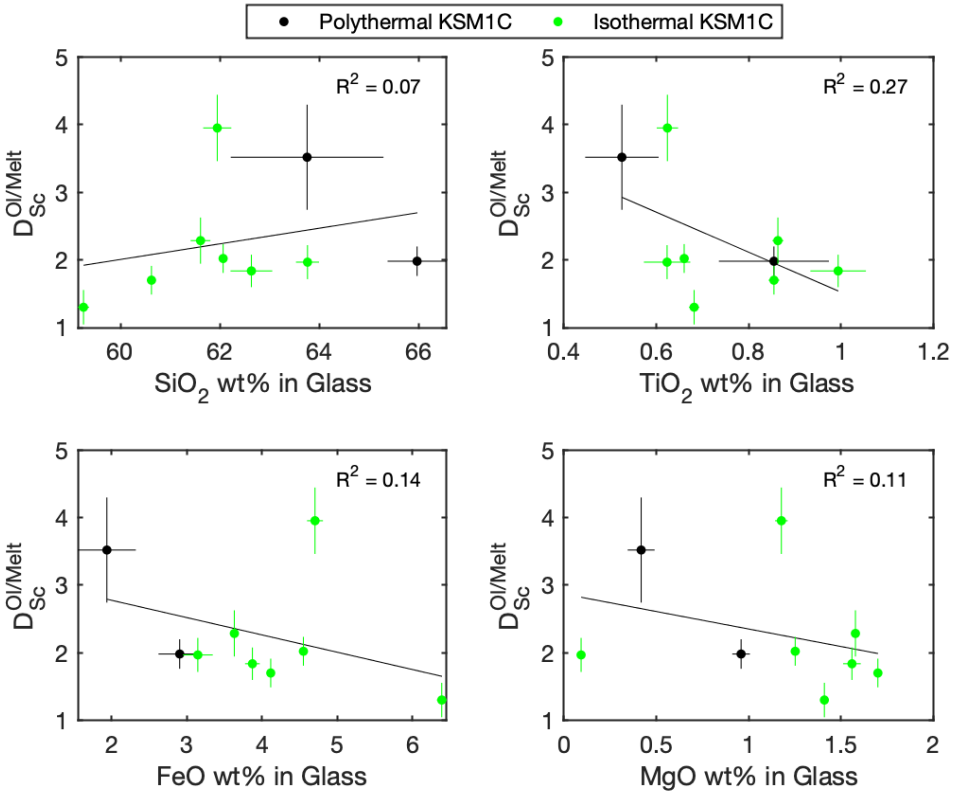

Figure 2.25: Effect of glass composition on olivine/melt partition coefficients for scandium. $D_{Sc}^{Ol/Melt}$ is plotted against SiO_2, TiO_2, FeO, and MgO wt % of the run product melt. Uncertainty is 1 σ_m. Black lines represent linear regressions of the data.

with $D_{Sc}^{Ol/Melt}$ being a function of X_{Fo}^{Ol} only at a given f_{O_2} (or within a sufficiently small range of f_{O_2}). The composition of the run-product glass also has an effect on $D_{Sc}^{Ol/Melt}$ (Figure 2.25). $D_{Sc}^{Ol/Melt}$ tends to increase with increasing SiO_2 of the run-

product glass and decrease with increasing TiO_2, FeO, and MgO of the run-product glass (Figure 2.25).

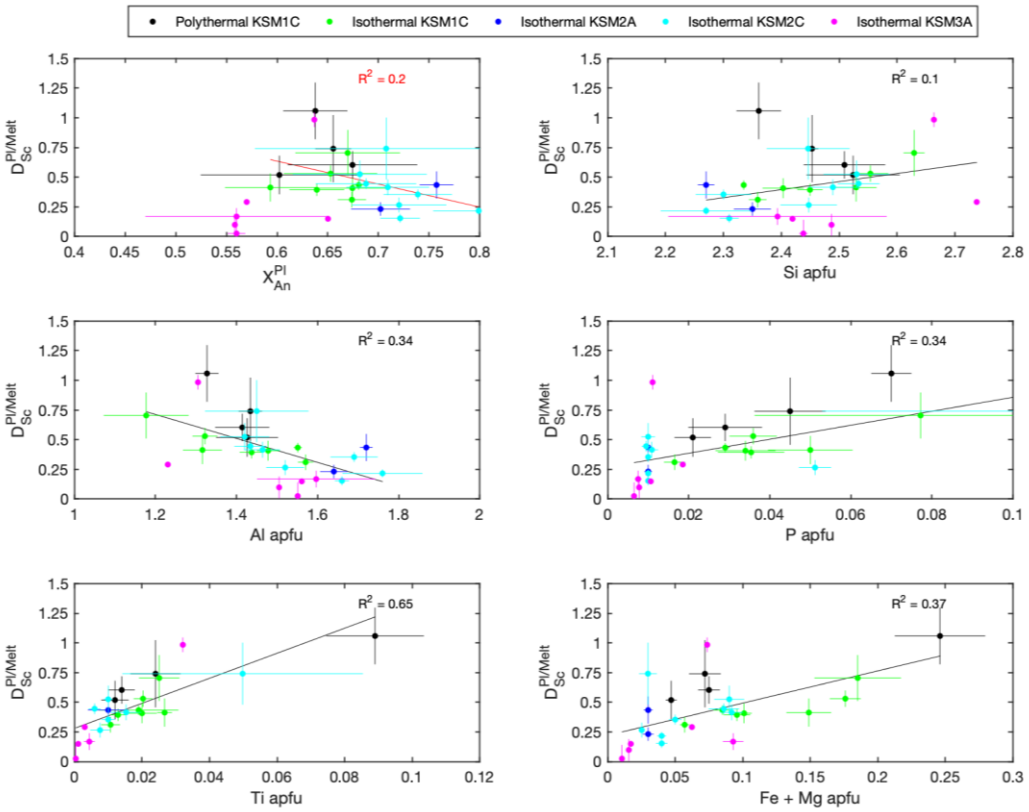

Figure 2.26: Effect of plagioclase composition on plagioclase/melt partition coefficients for scandium. $D_{Sc}^{Plg/Melt}$ is plotted against X_{An}^{Pl}, silicon, aluminum, phosphorus, titanium and iron + magnesium of the run-product plagioclase. Black lines represent linear regressions of the data . Red line is a linear regression excluded KSM3A experiments. Uncertainty is 1 σ_m.

2.6.2.2.3. Plagioclase/Melt Partitioning

$D_{Sc}^{Pl/Melt}$ ranges from 0.02 ± 0.02 to 1.1 ± 0.2 (Table 2.14). $D_{Sc}^{Pl/Melt}$ varies with both essential constituents and minor elements in plagioclase (Figure 2.26). Essential constituents that affect $D_{Sc}^{Pl/Melt}$ include the proportion of calcium, sodium, and potassium represented by X_{An}^{Pl}, and as a result silicon and aluminum apfu. $D_{Sc}^{Pl/Melt}$decreases with increasing X_{An}^{Pl} and aluminum. It should be noted that the relationship of $D_{Sc}^{Pl/Melt}$ to X_{An}^{Pl} only appears to hold when the KSM3A experiments

are excluded. The relationship between $D_{Sc}^{Pl/Melt}$ and silicon apfu is unclear (Figure 2.26). $D_{Sc}^{Pl/Melt}$ more strongly correlates and increases with increasing phosphorus, titanium, and (iron + magnesium) in plagioclase. $D_{Sc}^{Pl/Melt}$ increases with increasing phosphorus, titanium, and iron + magnesium (Figure 2.26). $D_{Sc}^{Pl/Melt}$also varies with run-product glass composition such that $D_{Sc}^{Pl/Melt}$ decreases with

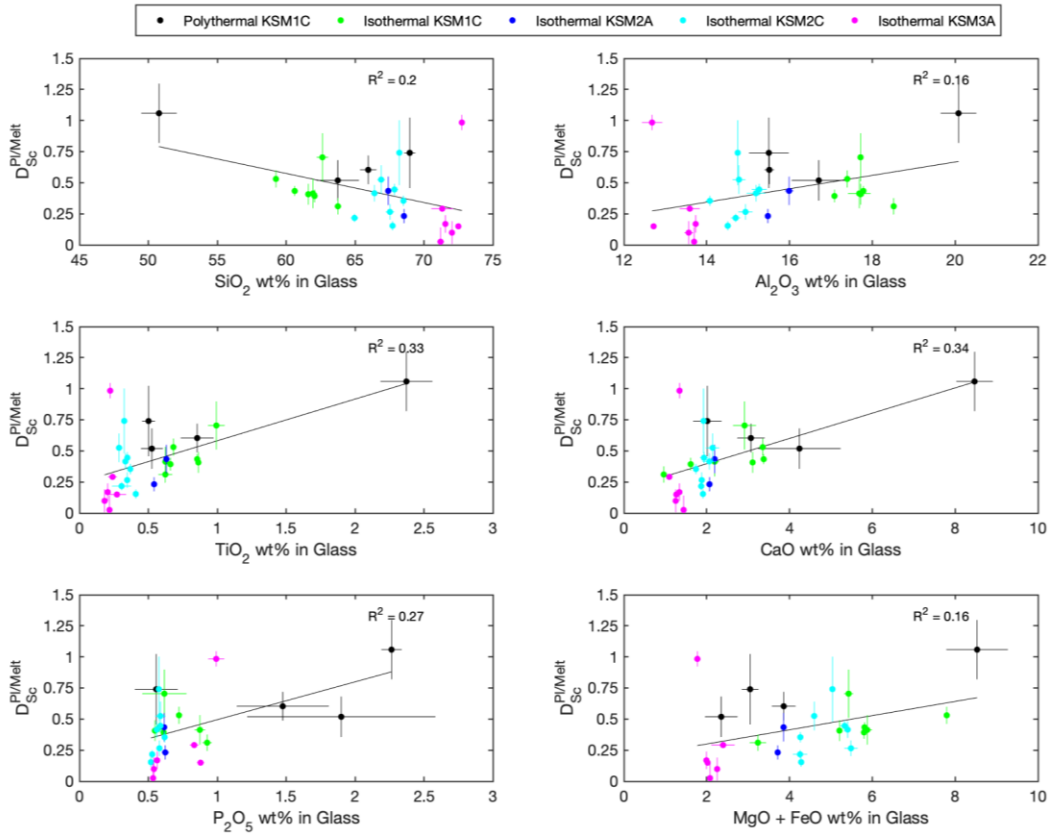

Figure 2.27: Effect of glass composition on plagioclase/melt partition coefficients for scandium. $D_{Sc}^{Plg/Melt}$ is plotted against SiO_2, Al_2O_3, TiO_2, CaO, P_2O_5, and MgO + FeO wt % of the run-product glass. Uncertainty is 1 σ_m. Black lines represent linear regressions of the data.

increasing SiO_2 wt % in the glass and $D_{Sc}^{Pl/Melt}$ increases with increasing Al_2O_3, TiO_2, CaO, P_2O_5, and FeO + MgO wt % in the glass. However, there is considerable

variation in $D_{Sc}^{Pl/Melt}$ and the correlations between $D_{Sc}^{Pl/Melt}$ and glass composition are not as strong as the correlation between $D_{Sc}^{Pl/Melt}$ and minor elements in plagioclase.

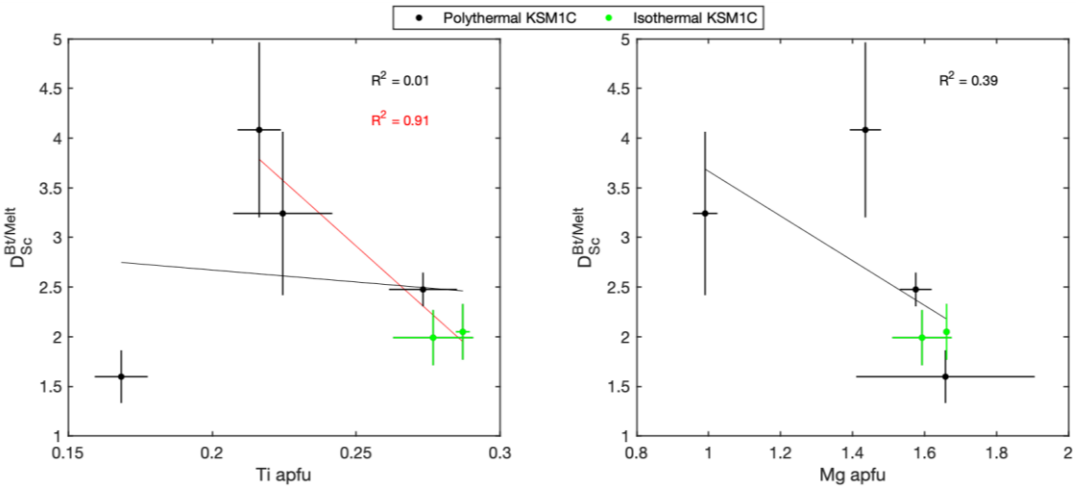

Figure 2.28: Effect of biotite composition on biotite/melt partition coefficients for scandium. $D_{Sc}^{Bt/Melt}$ is plotted against titanium and magnesium apfu of the run-product biotite. Uncertainty is 1 σ_m. Black lines represent linear regressions of the data. Red line is a linear regression excluding the low titanium biotite in experiment KSM1C-1.

2.6.2.2.4. Biotite/Melt Partitioning

$D_{Sc}^{Bt/Melt}$ ranges from 1.6 ± 0.3 to 4.1 ± 0.9 (Table 2.14). The composition of biotite does not vary significantly among experiments (Figure 2.12); however, there are minor compositional changes in the biotite that affect $D_{Sc}^{Bt/Melt}$. Most notably, $D_{Sc}^{Bt/Melt}$ decreases with increasing titanium (excluding the low titanium biotite in experiment KSM1C-1) and magnesium apfu (Figure 2.28). Furthermore, $D_{Sc}^{Bt/Melt}$ increases with increasing SiO_2 (wt%) in the run product glass and decreases with increasing Al_2O_3, MgO, MnO and TiO_2 (wt%) in the run-product glass (Figure 2.29) and also increases with increasing ASI of the run-product glass (Figure 2.29).

2.6.2.2.5. Spinel/Melt Partitioning

$D_{Sc}^{Spl/Melt}$ ranges from 0.130 ± 0.004 to 7.7 ± 0.09 (Table 2.14). Spinel compositions vary significantly among experiments (Figure 2.13) and affect $D_{Sc}^{Spl/Melt}$ (Figure 2.30). $D_{Sc}^{Spl/Melt}$ increases with increasing 2Ti/(2Ti + Al), Fe^{3+}, and titanium apfu and decreases with increasing aluminum apfu (Figure 2.30). Additionally, $D_{Sc}^{Spl/Melt}$ increases with increasing Fe/(Fe + Mg) (Figure 2.30), but to a smaller magnitude than 2Ti/(2Ti + Al). As noted above, spinel composition varies with run-

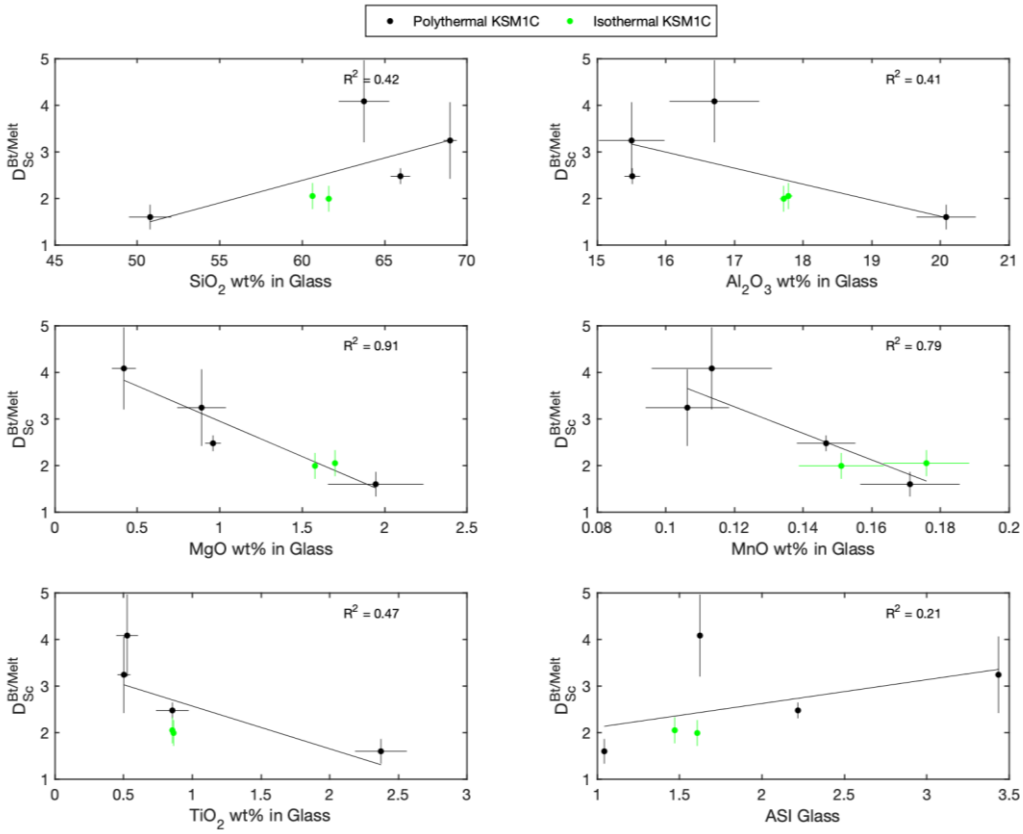

Figure 2.29: Effect of glass composition on biotite/melt partition coefficients for scandium. $D_{Sc}^{Bt/Melt}$ is plotted against SiO_2, Al_2O_3, MgO, MnO, and TiO_2 (wt%), as well as ASI of the run-product glass. Uncertainty is 1 σ_m Black lines represent linear regressions of the data.

product glass composition and temperature (Section 2.6.1.3.5). As a result, $D_{Sc}^{Spl/Melt}$ also varies with run-product glass composition, such that $D_{Sc}^{Spl/Melt}$ decreases with increasing SiO_2 (wt%) and ASI of the glass (Figure 2.31). The magnitude of $D_{Sc}^{Spl/Melt}$ also appears to be related to temperature, such that the lowest $D_{Sc}^{Spl/Melt}$ are found in the lowest temperature experiments (Figure 2.31).

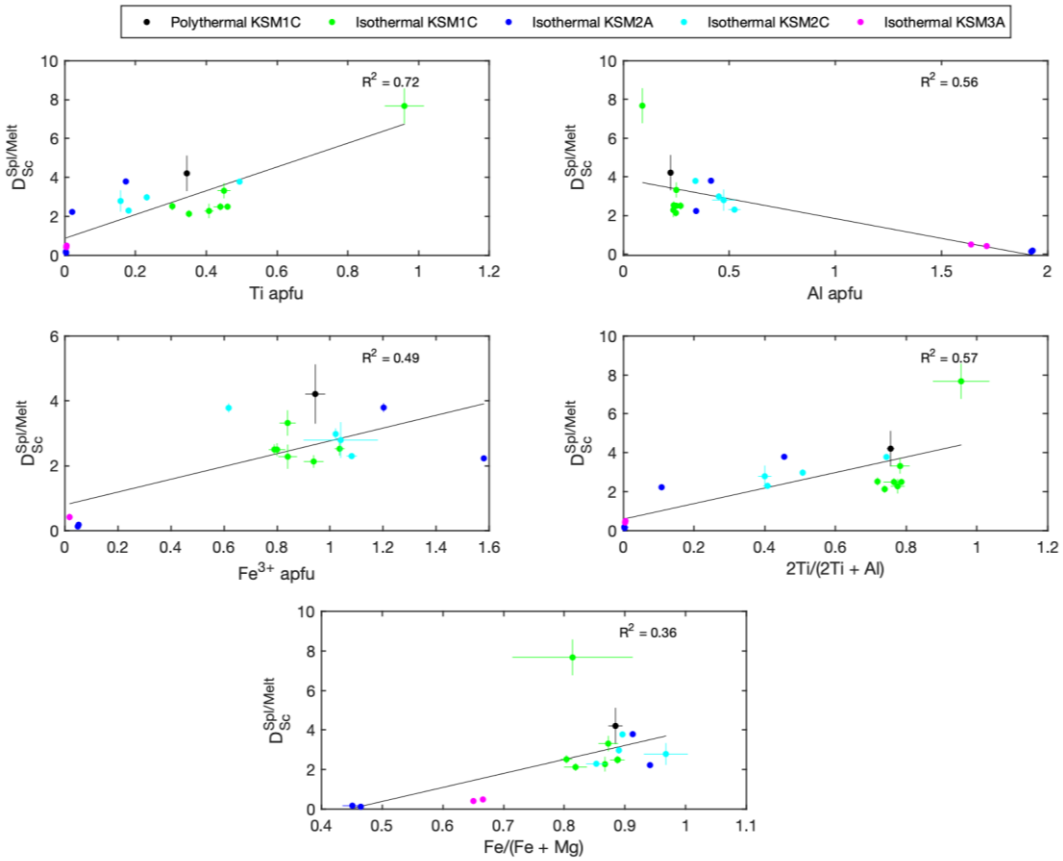

Figure 2.30: Effect of spinel composition on spinel/melt partition coefficients for scandium. $D_{Sc}^{Spl/Melt}$ is plotted against titanium, aluminum, and Fe^{3+}apfu, as well as 2Ti/(2Ti + Al) and Fe/(Fe + Mg) run-product spinel. Uncertainty is 1 σ_m. Black lines represent linear regressions of the data.

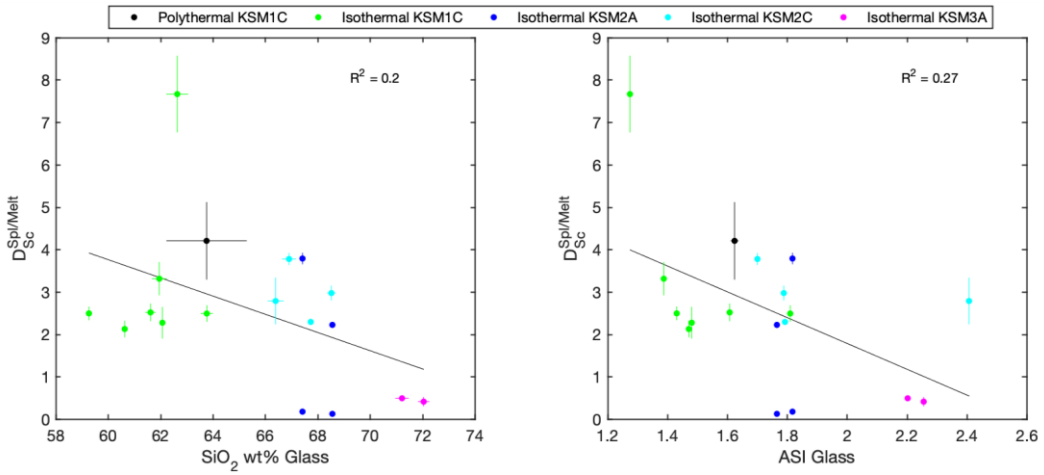

Figure 2.31: Effect of glass composition on spinel/melt partition coefficients for scandium. $D_{Sc}^{Spl/Melt}$ is plotted against SiO_2 (wt%) and ASI of the run-product glass. Uncertainty is 1 σ_m. Black lines represent linear regressions of the data.

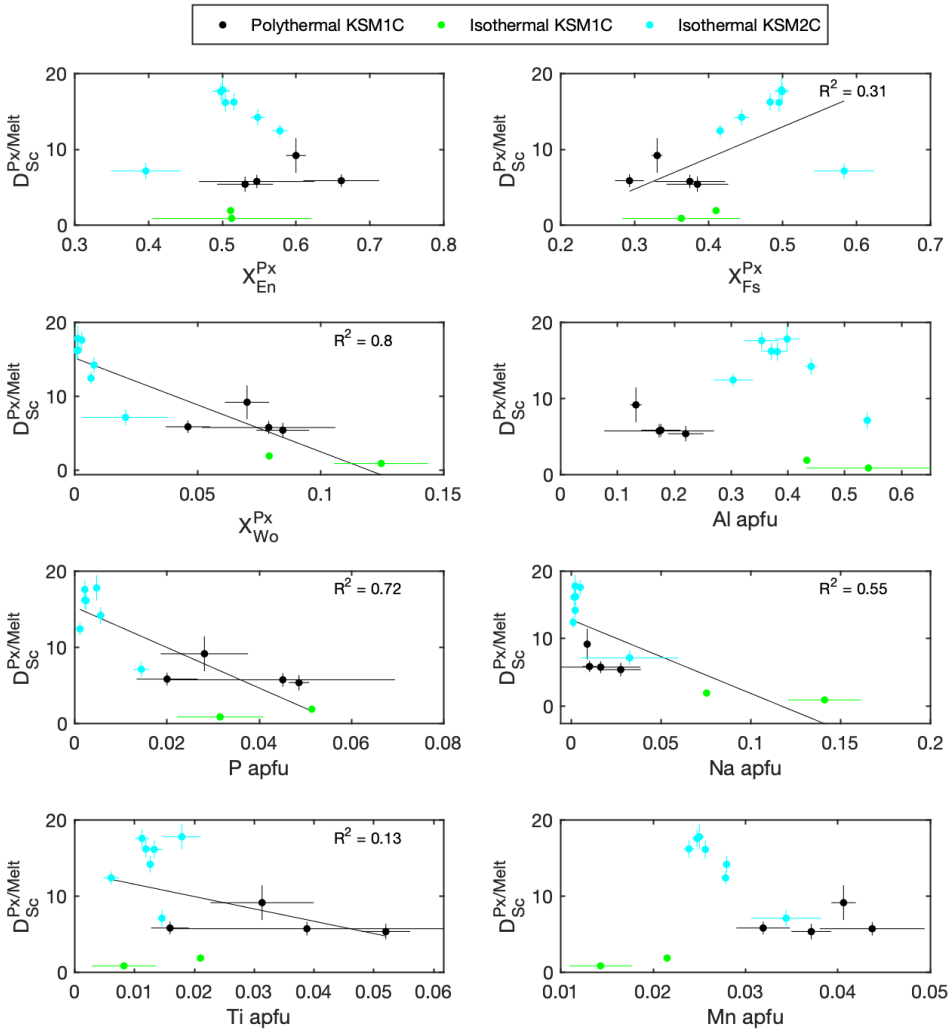

Figure 2.32: Effect of pyroxene composition on pyroxene/melt partition coefficients for scandium. $D_{Sc}^{Px/Melt}$ is plotted against X_{En}^{Px}, X_{Fs}^{Px}, and X_{Wo}^{Px}, as well as aluminum, phosphorus, sodium, titanium, and manganese apfu. Uncertainty is 1 σ_m. Black lines represent linear regressions of the data. Linear regression for X_{En}^{Px} and Mn apfu have been removed as they are strongly influenced by outliers and obscure the general trend. The linear regression aluminum apfu has been removed as the relationship is non-linear.

2.6.2.2.6. Pyroxene/Melt Partitioning

$D_{Sc}^{Px/Melt}$ ranges from 0.9 ± 0.1 to 18 ± 2 (Table 2.14). $D_{Sc}^{Px/Melt}$ varies primarily as a function of pyroxene composition, such that $D_{Sc}^{Px/Melt}$ decreases with increasing X_{En}^{Px} and $D_{Sc}^{Px/Melt}$ increases with increasing X_{Fs}^{Px} (Figure 2.32). Although the pyroxene only have a minor wollastonite component, $D_{Sc}^{Px/Melt}$ best correlates with X_{Wo}^{Px} and $D_{Sc}^{Px/Melt}$ decreases with increasing X_{Wo}^{Px}. $D_{Sc}^{Px/Melt}$ also appears to reach a maximum at a value of between 0.3 and 0.4 aluminum apfu (Figure 2.32). Minor elements in pyroxene also correlate with $D_{Sc}^{Px/Melt}$. $D_{Sc}^{Px/Melt}$ decreases with increasing

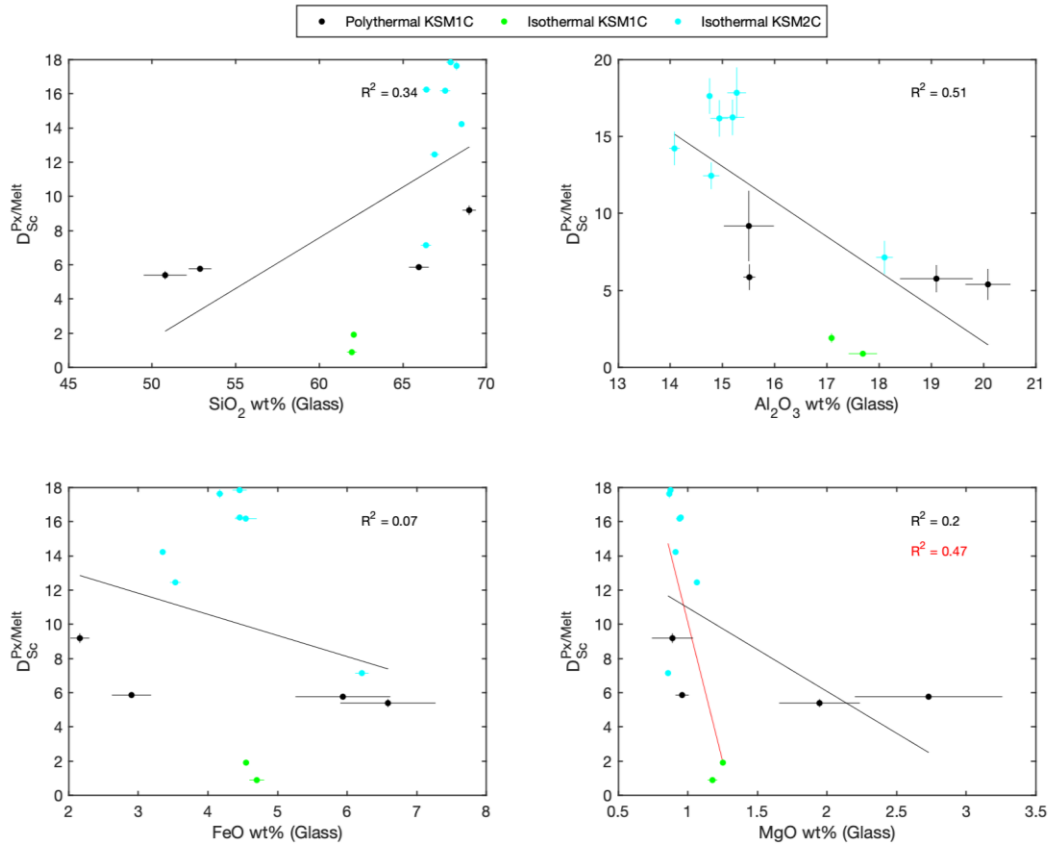

Figure 2.33: Effect of glass composition on pyroxene/melt partition coefficients for scandium. $D_{Sc}^{Px/Melt}$ is plotted against SiO_2, Al_2O_3, FeO, and MgO (wt%) of the run-product glass. Uncertainty is 1 σ_m. Black lines represent linear regressions of the data. Red line is a linear regression excluding KSM1C-1 and KSM1C-2 experiments.

P, Na, Ti, and Mn apfu (Figure 2.32). Additionally, the composition of the run-product glass correlates with the magnitude of $D_{Sc}^{Px/Melt}$. $D_{Sc}^{Px/Melt}$ increases with increasing SiO_2 (wt%) of the glass and $D_{Sc}^{Pyx/Melt}$ decreases with increasing Al_2O_3 (wt%) of the glass (Figure 2.33). $D_{Sc}^{Px/Melt}$ does not correlate strongly with FeO or MgO (wt%) of the run-product glass; however, if two polythermal KSM1C experiments are excluded, $D_{Sc}^{Px/Melt}$ does decrease with increasing MgO (wt%) of the run-product glass.

2.6.2.2.7. Cordierite/Melt Partitioning

$D_{Sc}^{Crd/Melt}$ ranges from 0.60 ± 0.04 to 1.4 ± 0.3 (Table 2.14). $D_{Sc}^{Crd/Melt}$ varies as a function of cordierite composition, such that $D_{Sc}^{Crd/Melt}$ decreases with increasing magnesium apfu and $D_{Sc}^{Crd/Melt}$ increases with increasing manganese apfu (Figure 2.34). $D_{Sc}^{Crd/Melt}$ also varies with the composition of the run-product glass, such that

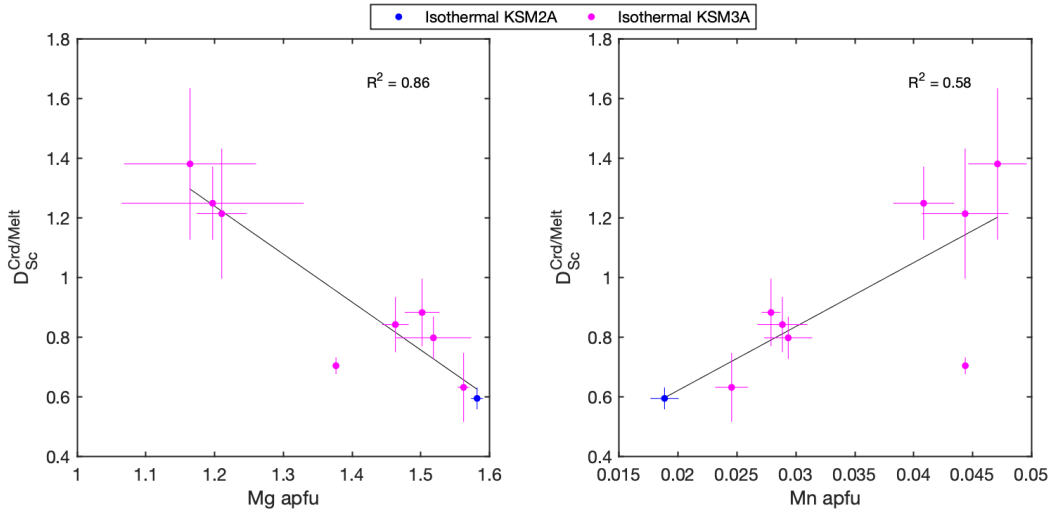

Figure 2.34: Effect of cordierite composition on cordierite/melt partition coefficients for scandium. $D_{Sc}^{Crd/Melt}$ magnesium and manganese apfu. Uncertainty is 1 σ_m. Black lines represent linear regressions of the data.

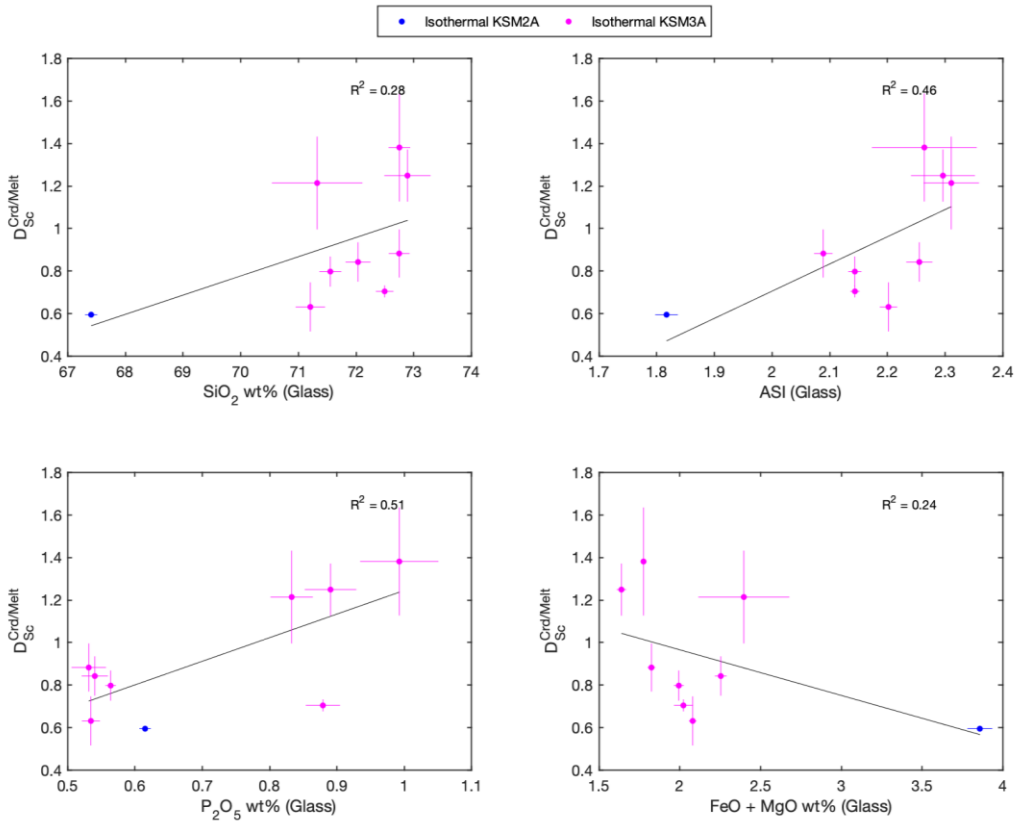

Figure 2.35: Effect of glass composition on cordierite/melt partition coefficients for scandium. $D_{Sc}^{Crd/Melt}$ is plotted against SiO_2, P_2O_5, and FeO, + MgO (wt%), as well as ASI of the run-product glass. Uncertainty is 1 σ_m. Black lines represent linear regressions of the data.

$D_{Sc}^{Crd/Melt}$ increases with increasing SiO_2 and P_2O_5 (wt%), as well as the ASI of the glass (Figure 2.35). Additionally, $D_{Sc}^{Crd/Melt}$ decreases with increasing FeO + MgO (wt%) of the run-product glass (Figure 2.35). $D_{Sc}^{Crd/Melt}$ also depends on the presence or absence of additional volatile elements (fluorine and chlorine). In KSM3A experiments that contain only water as a volatile in the vapor phase (KSM3A-1 through KSM3A-4), $D_{Sc}^{Crd/Melt}$ has a mean value of 1.14 ± 0.09; however, in experiments that contain additional chlorine (KSM3A-5 and KSM3A-6) and fluorine + chlorine (KSM3A-7 and KSM3A-8) $D_{Sc}^{Crd/Melt}$ is 0.79 ± 0.5. This may suggest that

the presence of fluorine and chlorine in the melt may reduce the magnitude of the partition coefficient.

2.6.2.2.8. Miscellaneous Phases/Melt Partitioning

There are not enough data to evaluate the crystal/melt partition coefficients for Al_2SiO_5, ilmenite, rutile, and apatite as a function of the mineral or glass compositions, due to the sparse occurrence of those phases; however, results can be generalized and included here for completeness. $D_{Sc}^{Al_2SiO_5/Melt}$ ranges from 0.39 ± 0.09 to 0.60 ± 0.05, with a mean of 0.50 ± 0.04 (Table 2.14). There is not a significant difference between $D_{Sc}^{Al_2SiO_5/Melt}$ for KSM2A and KSM3A experiments. $D_{Sc}^{Ilm/Melt}$ ranges from 8 ± 1 to 13.4 ±0.5 (Table 2.14). Three $D_{Sc}^{Ilm/Melt}$ were calculated. In two experiments (KSM2C-3 and KSM2C-9) $D_{Sc}^{Ilm/Melt} < 10$ and has a mean of 8.6 ± 0.8. In the third experiment (KSM2C-2) $D_{Sc}^{Ilm/Melt}$ is 13.4 ± 0.5. $D_{Sc}^{Rt/Melt}$ was only calculated for one experiment (KSM2C-2) and is 1.2 ± 0.5 (Table 2.14). $D_{Sc}^{Ap/Melt}$ was calculated for two experiments and the mean of those two values is 1.3 ± 0.2 (Table 2.14).

2.6.2.3. Equilibrium

Equilibrium (thermal, chemical, textural, etc.) requires that the properties of a system do not change with time—a characteristic referred to as time invariance. Time invariance is consistent with, but not sufficient in itself, to demonstrate equilibrium has been attained. Conditions where time invariance is not sufficient to demonstrate equilibrium are a steady state or kinetic unreactivity (Lynton et al., 1993). Systems

out of equilibrium may exhibit changes in composition, rates of reaction, mass of products and reactants, and heat flow, among other properties. One means of assessing equilibrium in experiments is by examining the changes of these properties with time. In the case of the work presented here, the experimentally determined partition coefficients for an otherwise identical set of experiments, can be compared to the duration of the run for each experimental set. If the partition coefficients change with time, then they can be said to be rate dependent or have not reached equilibrium and thus not consistent with the system attaining equilibrium. If the partition coefficients do not change with time, then they are rate independent and are consistent with equilibrium partitioning. Both results can yield useful information. In section 2.6.2.2.1 dynamic vs static experiments have been discussed, but this discussion does not fully address whether the static experiments are at or near equilibrium. For the static experiments, the partition coefficients do not vary systematically with time, but vary with the compositions of the mineral and glass phases. These variations stem from changes in the starting glass composition, temperature, and f_{O_2} (sections 2.6.2), but do not appear to be time dependent. Because there is no systematic variation of the partition coefficients with time, they are consistent with equilibrium partitioning on the timescales that these experiments were conducted. However, there is textural evidence for rapid growth (section 2.6.1.2), which may result in disequilibrium partitioning (Shea et al., 2019). Additionally, the diffusive loss of hydrogen, which is rate dependent, will result in more oxidizing conditions over the course of the experiment (Section 2.3). Thus, although the partition coefficients do not vary with time and are consistent with

equilibrium partitioning, there is not enough evidence to disprove disequilibrium in these experiments.

2.7. Discussion

2.7.1. Composition of the Melt

As mentioned in Section 2.6.1.3.1, run-product glasses become depleted in most of the major elements (Figure 2.7) as the SiO_2 content of the melt increases. Other compositional trends in the melt can be observed that allow the evolution of the melt to be further characterized. The starting glass for KSM1C experiments plots as a trachybasalt on a total alkali verse silica (TAS) diagram (Figure 2.36). As the SiO_2 content of the glass increases due to crystallization, the composition of the glass

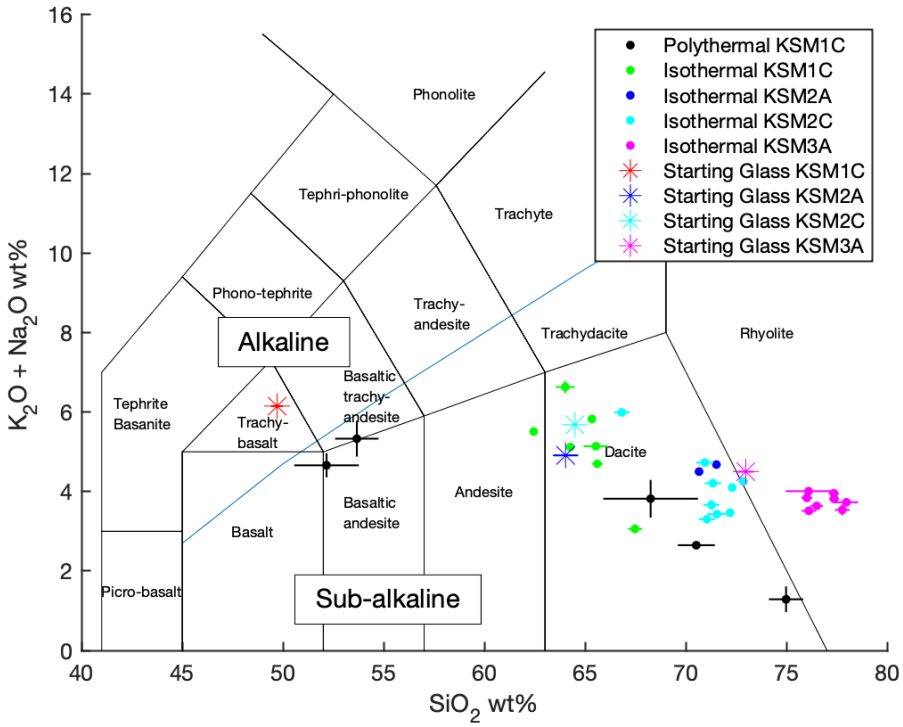

Figure 2.36: Total alkali-silica (TAS) diagram (Le Bas et al., 1986) of run-product glass compositions. Blue line represents the division between alkaline and sub-alkaline rocks as defined by Irvine and Baragar (1971). All glass compositions normalized to 100%. Uncertainty is 1 σ_m.

becomes basaltic and with further crystallization the glass becomes a basaltic trachy-andesite, then dacite, and finally rhyolite (Figure 2.36). The $Na_2O + K_2O$ concentration is relatively constant from SiO_2 concentrations of 50 to 60 wt% and decreases sharply after 60 wt% SiO_2 (Figure 2.36). Because the run-product glasses are sub-alkaline they can also be plotted on an AFM ($Na_2O + K_2O$ vs. total FeO vs. MgO) diagram (Irvine and Baragar, 1971). The starting glass for KSM1C experiments plots in the tholeiitic field and the majority of run-product glasses, and thus starting materials for other experimental sets, plot in the calc-alkaline field of Irvine and Baragar (1971). Some KSM1C isothermal experiments and approximately half of the KSM2C experiments, including the starting material, plot in the tholeiitic

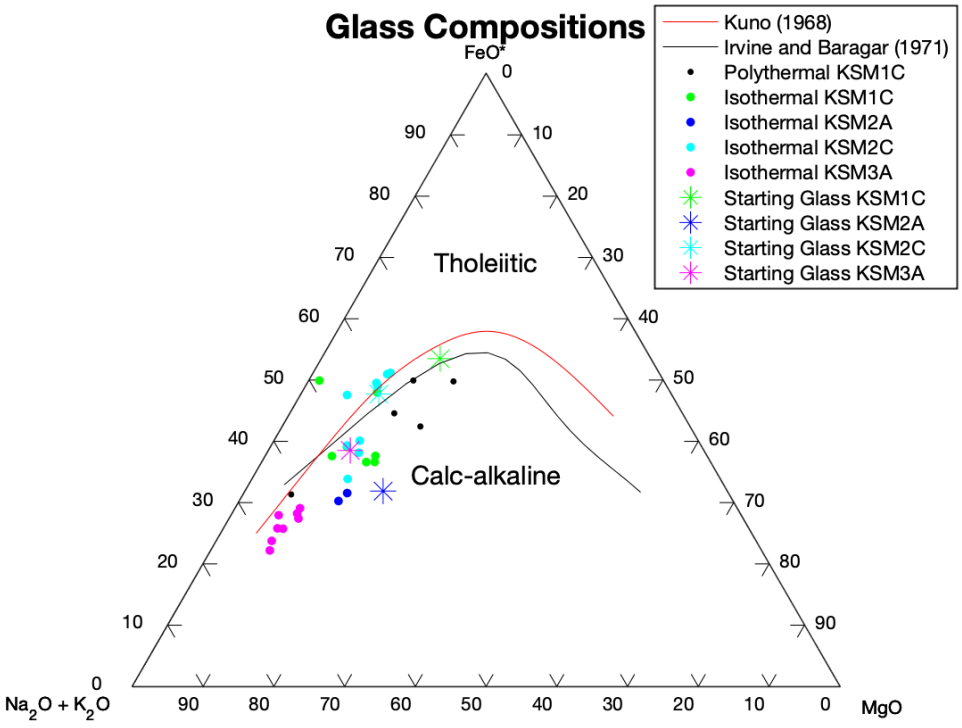

Figure 2.37: Total alkali vs. FeO* vs. MgO diagram for run-product glass. FeO* is total iron. Black line is the division between tholeiitic and calc-alkaline fields as defined by Irvine and Baragar (1971). Red line is the division between tholeiitic and calc-alkaline fields as defined by Kuno (1968).

field of Irvine and Baragar (1971). However, some of the glasses that plot within the tholeiitic field of Irvine and Baragar (1971), plot within the calc-alkaline field of Kuno (1968) or at (slightly above) the division between the tholeiitic and calc-alkaline field (Figure 2.37). Although the majority of the glasses plot within the calc-alkaline field of Kuno (1968) two experiments plot within the tholeiitic field (Figure 2.37). Thus, the run-product glasses in this study can be best classified as sub-alkaline and in the calc-alkaline series, which includes high-aluminum basalts, andesites, dacites, and rhyolites (Irvine and Baragar, 1971).

Although the terms tholeiitic and calc-alkaline are widely used to describe and classify rocks, Arculus (2003) noted that the terms have a variety of meanings, particularly the term calc-alkaline. As a solution to this problem, Arculus (2003)

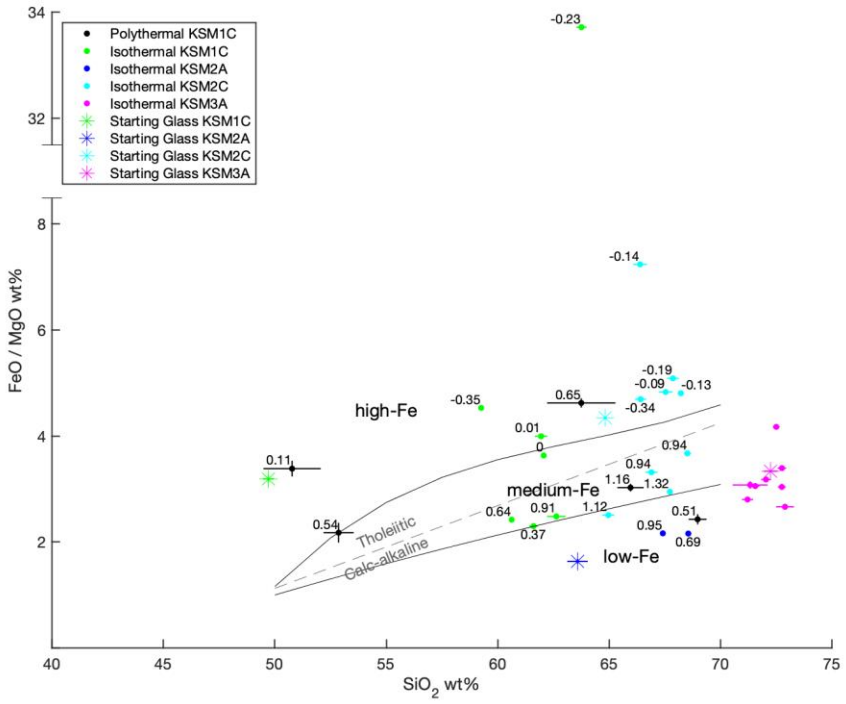

Figure 2.38: FeO/MgO (wt%) vs SiO_2 (wt%) in run-product glass. High-, medium-, and low-Fe fields are separated by solid lines and are defined by Arculus (2003). Dashed line is division of tholeiitic and calc-alkaline fields as defined by Miyashiro (1974). Values next to data points are f_{O_2} for each experiment relative to NNO. KSM3A experiments all have f_{O_2} = NNO +1.3. Uncertainty is 1 σ_m.

suggested classifying sub-alkaline rocks as high-, medium-, or low-Fe on the basis of total FeO/MgO vs SiO_2. The experimental run-product glasses and starting glasses have been plotted on the suggested diagram of Arculus (2003) in Figure 2.38. The starting glasses and the run products for all experiment sets are scattered among the three fields. Examining the distribution of data points in conjunction with the f_{O_2} measured for each experiment explains the large variations in FeO/MgO. With the exception of the polythermal KSM1C, which are dynamic experiments (see Section 2.6.2.2.1), the more reduced ($f_{O_2} \leq$ NNO) experiments plot within the high-Fe field and the more oxidized ($f_{O_2} \geq$ NNO) experiments plot within the medium- or low-Fe fields (Figure 2.38). Thus, a more oxidized melt results in a melt depleted in iron. Further, experiments with $f_{O_2} \leq$ NNO plot within the tholeiitic field and experiments with $f_{O_2} \geq$ NNO plot within the calc-alkaline field as defined by Miyashiro (1974), again excluding polythermal (dynamic) KSM1C experiments (Figure 2.38).

There is one experiment (KSM1C-10) with an abnormally high FeO/MgO of ~34, and as mentioned above (Section 2.6.1.3.2), this experiment underwent a slow quench. During this slow quench a large amount of magnesium-rich biotite crystallized, lowering the concentration of magnesium in the melt, causing an elevated FeO/MgO. There is general agreement between Figures 2.37 and 2.38, in that the experiments that plot within the calc-alkaline field of Figure 2.37 plot within the calc-alkaline field of Figure 2.38. However, this agreement breaks down for KSM1C experiments as the experiments that plot in the tholeiitic field in Figure 2.38 do not plot in the tholeiitic field in Figure 2.37. Taking the above discussion into consideration, the run product glasses are sub-alkaline and form two groups: 1)

reduced high-Fe, tholeiitic glass; and, 2) oxidized medium- to low-Fe, calc-alkaline glasses.

2.7.2. Substitution of Scandium into Crystalline Phases

The mechanisms by which scandium substitutes into the structure of crystalline phases can be determined by evaluating how the partition coefficients vary with changes in composition of those phases and considering site assignments and charge balance. Scandium is most likely to substitute into the octahedral site, because the ionic radius of scandium (0.745 Å) is similar to other octahedrally coordinated cations, such as magnesium (0.720 Å) and iron (0.780 Å; Shannon, 1976). However, in the case of apatite and plagioclase, higher coordination numbers may be possible. Additionally, substitution of scandium into the tetrahedral site may occur in feldspar, as has been proposed for iron and magnesium (Longhi et al., 1976). Scandium is also assumed to be in the three plus oxidation state (Sc^{3+}) only.

Given the relationship between $D_{Sc}^{Ol/Melt}$ and olivine composition, the substitution of scandium into olivine occurs following the coupled substitution

$$\square^{VI} + (Sc^{3+})^{VI} + (P^{5+})^{IV} = 2(Mg^{2+})^{VI} + (Si^{4+})^{IV} \quad , \qquad \text{Eq. (2.1)}$$

where $\square$ is a vacancy. Boesenberg and Hewins (2010) determined that the substitution of phosphorus into olivine is:

$$\square^{VI} + 3(R^{2+})^{VI} + 2(P^{5+})^{IV} = 4(R^{2+})^{VI} + 2(Si^{4+})^{IV} \quad . \qquad \text{Eq. (2.2)}$$

The substitution for phosphorus into olivine (equation 2.2) as proposed by Boesenberg and Hewins (2010) is analogous to equation 2.1, when the three R^{2+} cations on the left side of the equation are replaced by two Sc^{3+} cations. Additionally, Shea et al. (2019) determined that phosphorus zoning in olivine may be a function of growth rate; thus, elevated scandium, and higher partition coefficients, may occur in olivine with high growth rates.

In an effort to evaluate the substitution mechanism proposed above (Eq. 2.1) x-ray maps of an olivine crystal in KSM1C-5 were examined. The olivine exhibits regions of both elevated phosphorus and scandium in olivine, as well as a phase which appears to be a scandium-rich phosphate (Figure 2.39).

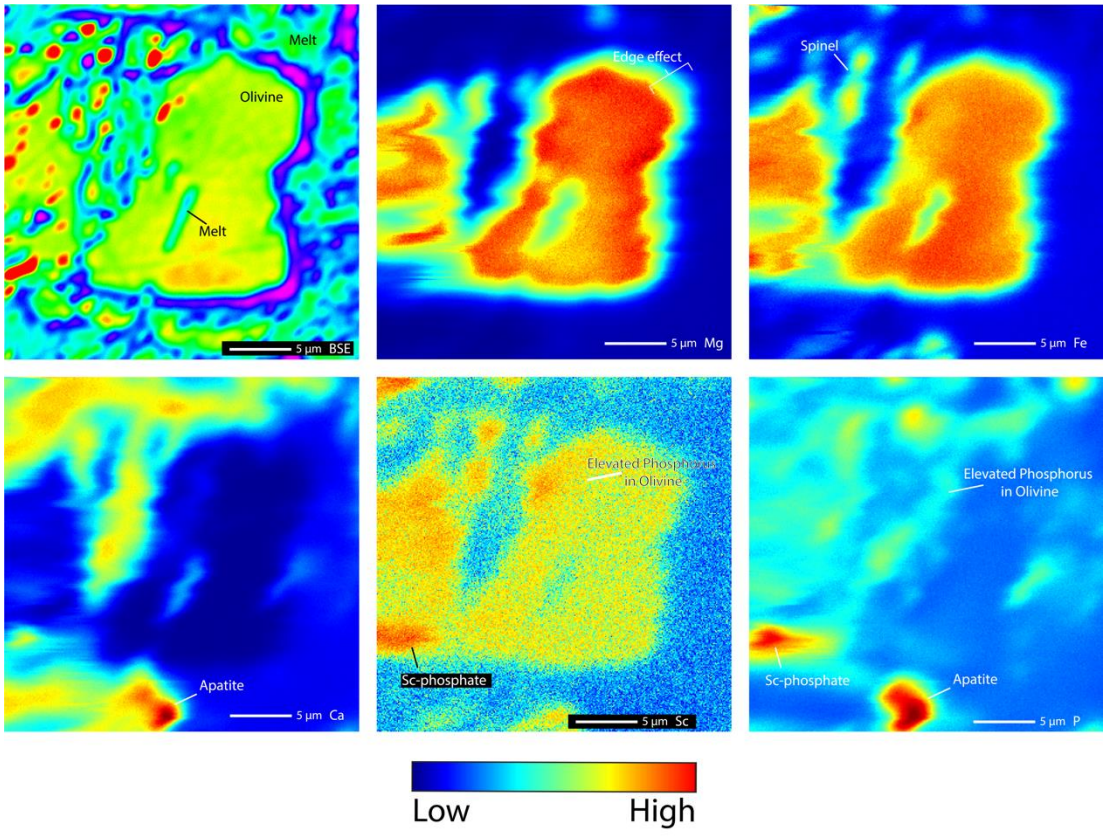

Figure 2.39: WDS x-ray maps for magnesium, iron, calcium, scandium, and phosphorus of an olivine from KSM1C-5. Image in upper left is a pseudocolor BSE image. Warm colors indicated a higher number of x-ray counts than cool colors. Edge effect is the result of small crystal size.

The incorporation of scandium into plagioclase is more complex and involves a series of substitutions. Based on the variation of the partition coefficient with plagioclase composition observed in this study, substitutions may include

$$(Sc^{3+})^{IV} = (Al^{3+})^{IV} \quad , \qquad \text{Eq. (2.3)}$$

$$\square^{VIII} + (Sc^{3+})^{VIII} + (P^{5+})^{IV} = 2(Ca^{2+})^{VIII} + (Si^{4+})^{IV} \quad , \qquad \text{Eq. (2.4)}$$

$$\square^{VIII} + (Sc^{3+})^{VIII} + (Ti^{4+})^{IV} = 2(Ca^{2+})^{VIII} + (Al^{3+})^{IV} \quad , \qquad \text{Eq. (2.5)}$$

and

$$(Sc^{3+})^{VIII} + (R^{2+})^{IV} = (Ca^{2+})^{VIII} + (Al^{3+})^{IV} \quad , \qquad \text{Eq. (2.7)}$$

where $\square$ is a vacancy and R^{2+} is either Mg^{2+} or Fe^{2+}. The preferred site for scandium to substitute into plagioclase is unclear. Longhi et al. (1976) suggested that at least 90% of iron and magnesium in plagioclase from mare basalts substitutes into the tetrahedral site and no more than 10% substitutes for calcium. Thus by analogy scandium may substitute directly for aluminum in the tetrahedral site (equation 2.3). Scandium may also occupy a 7- to 9-fold site when substituting for calcium; calcium coordination in plagioclase has been suggested to range from 7- to 9-fold (Smith and Brown, 1988). The range of possible coordination numbers has been represented here by 8-fold coordination in the equations.

The substitution of scandium into biotite is not as apparent, as the composition of biotite does not vary significantly among experiments. One substitution that may occur is

$$2(Sc^{3+})^{VI} = (Ti^{4+})^{VI} + (Mg^{2+})^{VI} \quad . \qquad \text{Eq. (2.8)}$$

It is also possible that the substitution represented in equation 2.1 occurs for biotite as well. The substitution

$$(Sc^{3+})^{VI} + (Al^{3+})^{IV} = (R^{2+})^{VI} + (Si^{4+})^{IV} \quad , \quad \text{Eq. (2.9)}$$

where R^{2+} is a two-plus metal cation such as Fe^{2+} or Mg^{2+}, and may also occur in biotite as well as other aluminum-bearing ferromagnesian silicates such as amphibole.

There are three substitution mechanisms for scandium into spinel that have been identified and are

$$(Sc^{3+})^{VI} + (Fe^{3+})^{VI} = 2(Al^{3+})^{VI} \quad , \quad \text{Eq. (2.10)}$$

$$(Sc^{3+})^{VI} = (Al^{3+})^{VI} \quad , \quad \text{Eq. (2.11)}$$

and

$$\square^{VI} + (Fe^{2+})^{VI} + (Sc^{3+})^{VI} + (Ti^{4+})^{VI} = (Al^{3+})^{VI} + 3(Mg^{2+})^{VI} \quad , \quad \text{Eq. (2.12)}$$

where $\square$ is a vacancy.

Although $D_{Sc}^{Px/Melt}$ varies with the composition of the pyroxene, the variations are not intuitive. $D_{Sc}^{Px/Melt}$ reported in the literature suggests that when two pyroxenes exist, $D_{Sc}^{Px/Melt}$ for clinopyroxenes is greater than $D_{Sc}^{Px/Melt}$ for orthopyroxenes (Table 2.1); however, the results of this study are consistent with $D_{Sc}^{Px/Melt}$ being higher for calcium-poor pyroxenes. Additionally, the substitution

$$(Na^{+})^{VIII} + (Sc^{3+})^{VI} = 2(R^{2+})^{VI} \quad , \quad \text{Eq. (2.13)}$$

where R^{2+} is either Fe^{2+} or Mg^{2+} in octahedral coordination should be present, as complete replacement of Fe^{2+} or Mg^{2+} would result in the formation of jervisite ($NaScSi_2O_6$), the scandium-bearing pyroxene. However, results of this study are consistent with $D_{Sc}^{Px/Melt}$ decreasing with increasing sodium apfu. From these observations it is clear that $D_{Sc}^{Px/Melt}$ (for orthopyroxene) is more strongly influenced by melt composition. Additionally, because $D_{Sc}^{Px/Melt}$ increases with an increasing

ferrosilite (decreasing enstatite) component (Figure 2.32), it is suggested that scandium prefers to substitute for magnesium. As a result, the substitutions for scandium into pyroxene that are suspected to occur are equivalent to equation 2.1, equation 2.8, and equation 2.13, where the substitution of phosphorus into pyroxene determined by Boesenberg and Hewins (2010) is:

$$\square^{IV} + 3(Si^{4+})^{IV} + 4(P^{5+})^{IV} = 8(Si^{4+})^{IV} \quad . \qquad \text{Eq. (2.14)}$$

The only substitution for scandium into cordierite that is observed in this study is

$$\square^{VI} + 2(Sc^{3+})^{VI} = 3(Mg^{2+})^{VI} \quad . \qquad \text{Eq. (2.15)}$$

The substitution in equation 2.15 may also operate in other ferromagnesian silicates (e.g. olivine, pyroxene, biotite, and amphibole) and may involve iron as well as magnesium. In order to substitute scandium into apatite an oxy- substitution, similar to the substitution of REEs into apatite (e.g. Pan and Fleet, 2002) is needed, which is expressed as:

$$(Sc^{3+})^{9-fold} + O^{2-} = (Ca^{2+})^{9-fold} + OH^{-} \quad , \qquad \text{Eq. (2.16)}$$

and results in the mineral pretulite ($ScPO_4$). Additionally, pretulite has a monazite structure, in which scandium is in 9-fold coordination. Thus, scandium could conceivably be in 9-fold coordination in the ferromagnesian minerals where scandium and phosphorus coupled substitution is present.

The substitution of scandium into the aluminosilicates likely involves a direct replacement of Al^{3+} with Sc^{3+}. For ilmenite the substitution is likely

$$2Sc^{3+} = Ti^{4+} + Fe^{2+} \quad , \qquad \text{Eq. (2.18)}$$

and results in a solid solution between ilmenite and the mineral kangite (Sc_2O_3) although other coupled substitutions may occur. For rutile the substitution may follow equation 2.18.

2.7.3. Discussion of Hypotheses

The null hypotheses (Section 2.3) are both rejected. Scandium behaves as both an incompatible (D < 1) and compatible (D > 1) element (null hypothesis 1) in crystalline phases depending on the composition of both the glass and crystalline phases (null hypothesis 2). Taking into consideration that the partition coefficients for individual phases vary significantly (Table 2.14; Figures 2.20 and 2.21) it is clear that a single partition coefficient for any given phase cannot adequately characterize the behavior of scandium for all situations. Instead consideration must be given to the composition of both the crystalline and glass phases involved.

Further, because the partition coefficients for common rock forming minerals such as olivine, pyroxene, biotite, and amphibole (Nandedkar et al., 2016) are often greater, and in some cases much greater than 1, these phases are expected to sequester large amounts of scandium. In mafic to ultramafic rocks where these phases may reach 30 modal percent or more the bulk partition coefficients will be significantly greater than 1 and thus scandium will be significantly sequestered. If accessory phases such as spinel and other oxides are included, the amount of scandium sequestered will be even greater. Additionally, as melts become more felsic $D_{Sc}^{Mineral/Melt}$ generally becomes larger for any given phase, with the exception of plagioclase, which is consistent with the previous observations of Bédard (2005, 2007, 2014). As a result, any concentration of scandium into a felsic melt by simple

fractionation processes is unlikely. Thus, in general mafic rocks will contain significantly more scandium than felsic rocks. However, this raises serious questions about how scandium-rich deposits associated with granitic magmatism such as the deposits of Kumir, Russia; Misery Lake, Canada; Thomas Range, USA; Erzgebirge, Germany; and granitic pegmatites such as those of the Evje-Iveland, Norway pegmatite field are formed. In order to constrain how these deposits may form, geochemical modeling is required and will be discussed in Chapters 3 and 4.

2.8. Summary of Chapter 2

In order to understand the behavior of scandium in magmatic-hydrothermal systems, cold-seal pressure vessel experiments have been performed to determine mineral/melt partition coefficients for scandium. In total 31 experiments have been completed and partition coefficients for olivine, plagioclase, biotite, spinel, pyroxene, cordierite, an aluminosilicate phase, ilmenite, rutile, and apatite have been determined for basaltic to rhyolitic compositions. The partition coefficients vary as a function of both crystal and glass composition and range from (value ± 1 σ_m): $D_{Sc}^{Ol/Melt}$ of 1.3 ± 0.3 to 4 ± 0.8, $D_{Sc}^{Pl/Melt}$ of 0.02 ± 0.02 to 1.1 ± 0.2, $D_{Sc}^{Bt/Melt}$ of 1.6 ± 0.3 to 4.1 ± 0.9, $D_{Sc}^{Spl/Melt}$ of 0.130 ± 0.004 to 7.7 ± 0.09, $D_{Sc}^{Px/Melt}$ of 0.9 ± 0.1 to 18 ± 2, $D_{Sc}^{Crd/Melt}$ of 0.60 ± 0.04 to 1.4 ± 0.3, $D_{Sc}^{Al_2SiO_5/Melt}$ of 0.39 ± 0.09 to 0.6 ± 0.05, $D_{Sc}^{Ilm/Melt}$ of 8 ± 1 to 13.4 ±0.5, $D_{Sc}^{Rt/Melt}$ of 1.2 ± 0.5, and $D_{Sc}^{Ap/Melt}$ of 1.3 ± 0.2. Generally, partition coefficients are higher in experiments with felsic compositions. As a result, scandium is unlikely to be concentrated in a felsic melt and mafic rocks will have higher concentrations of scandium than felsic rocks. These results raise questions about the

mechanisms that result in the formation of scandium-rich deposits associated with felsic magmatism, and those questions require further exploration.

3. Chapter 3: Geochemical Modeling of Scandium Ore Formation

3.1. Introduction

The formation of ore deposits associated with magmatic-hydrothermal systems requires that metals, in this case scandium, are concentrated into forms that are economically viable to extract. As discussed in Chapter 1 scandium deposits are found in the form of mafic and ultramafic igneous intrusions (and their weathered equivalents; e.g. Nyngan, Australia and Kiviniemi, Finland) and deposits associated with felsic magmatic-hydrothermal systems (e.g. Evje-Iveland, Norway pegmatites; Erzgebirge, Germany; Misery Lake, Canada; and Thomas Range, USA). In order to constrain the formation of these scandium deposits, it necessary to understand the magmatic stage of ore formation. During this stage, scandium can either be depleted in the melt phase and concentrated in coexisting crystalline phases or concentrated in the melt phase. In order to evaluate the distribution of scandium during the magmatic stage of ore formation, the constraints on the partition coefficients for scandium between minerals and melts described in Chapter 2 have been combined with MELTS modeling. In doing so the petrogenesis of scandium-bearing deposits can be constrained.

3.2. Partition Coefficients

As discussed in Chapter 2, mineral/melt partition coefficients for scandium vary as functions of both mineral and melt composition. Thus, it is necessary to extrapolate the experimentally determined partition coefficients to systems of variable composition in order to ensure appropriate values are used in the MELTS modeling.

Toward that end, multiple linear regressions were constructed by using the experimentally determined partition coefficients and the mineral and melt compositions described in Chapter 2 as constraints.

Prior to developing the multiple linear regressions, a series of assumptions must be evaluated. In this study these assumptions are: 1) the partition coefficients (dependent variables) are continuous (numeric variable with an infinite number of values); 2) the partition coefficients vary as a function of two or more mineral and/or melt compositions (independent variables; e.g. Si apfu in a mineral or SiO_2 of the melt); 3) the experiments are independent of one another; 4) the partition coefficients have a linear relationship to the mineral and melt compositions; 5) the variance among the data are homoscedastic (i.e. the variance for the variables is equal); 6) the mineral and melt compositions that are used as independent variables do not strongly correlate with one another (i.e. no multicollinearity); 7) there are no significant outliers; and 8) the residuals in the predicted partition coefficients are normally distributed. Assumptions 1- 4 and 6 are valid for all mineral/melt partition coefficients, as the partition coefficients are continuous, there are two or more mineral or melt compositional variables that correlate with the partition coefficient, the experiments are independent, the partition coefficients and mineral and melt compositions have a linear relationship, and the independent variables used are not multicollinear. Assumption 5 (homoscedastic variables) were not met for any mineral/melt pair; however, it was determined that heteroscedasticity did not significantly affect the predicted partition coefficients by cross-validating the multiple linear regressions. Assumption 7 was not met for any mineral/melt pair; however,

there is at least one independent variable that is not an outlier for each experiment that contains outliers and thus does not significantly affect the regressions. Assumption 8 (normally distributed residuals) was met for all cases except pyroxene. Additional information on how these assumptions were evaluated is given in appendix 3.A.

Table 3.1: Multiple linear regressions for predicting partition coefficients

Mineral (LogD)	Intercept	Standard Error of Intercept	Predictors	Coefficients	Standard Error of Coefficients	R^2	RSME	p-Value for Regression
Olivine	8.199	2.491	Si	-8.441	2.635	0.632	0.106	0.04996
			Fo	0.539	0.484			
Pyroxene (Opx)	1.913	0.981	Fs	1.854	1.110	0.497	0.308	0.0322
			Al_2O_3	-0.112	0.048			
Spinel	-3.841	1.101	2Ti/(2Ti + Al)	0.946	0.218	0.943	0.128	6.3E-09
			Fe/(Fe + Mg)	1.895	0.285			
			SiO_2	0.032	0.016			
Plagioclase	-2.018	0.701	An	1.892	1.002	0.335	0.295	0.02262
			TiO_2	0.207	0.183			
			P_2O_5	0.236	0.189			
Biotite	0.926	0.535	Mg	-0.102	0.123	0.953	0.052	0.07009
			SiO_2	-0.001	0.006			
			MgO	-0.235	0.060			
Cordierite	2.010	0.514	Mg	-1.159	0.254	0.922	0.047	0.00341
			Mn	-9.413	4.412			
			FeO	-0.056	0.031			

Intercepts, coefficients, and statistics for multiple linear regressions used to predict partition coefficients.
Predictors written as an element or component indicate apfu of that element or that component in a mineral.
Predictors written as an oxide indicate the concentration of that oxide in the melt.
All multiple linear regressions were generated using the *fitlm* function in MATLAB

There are some compositional parameters for minerals that correlate with the partition coefficients that cannot be used to predict partition coefficients within the confines of the MELTS program. For example, phosphorus in pyroxene strongly correlates with $D_{Sc}^{Px/Melt}$ (Figure 2.32); however, MELTS does not calculate the phosphorus content of pyroxene and thus phosphorus in pyroxene cannot be used to predict $D_{Sc}^{Px/Melt}$. Additionally, in order to avoid predictions of negative partition coefficients all partition coefficients were log (base 10) transformed prior to

performing the regressions. Although the assumptions are not met in all cases, the multiple linear regressions still have predictive power and can be used to predict the appropriate partition coefficients to be used in the MELTS modeling based on the composition of mineral and melt phases as determined by MELTS. The statistic, coefficients, and intercepts for each regression are given in Table 3.1.

For the cases where multiple linear regressions were not possible due to a small sample size (apatite, rutile, aluminosilicates, and rhombohedral oxides) the average partition coefficient for each mineral was used. The partition coefficients for apatite, rutile, aluminosilicates, and rhombohedral oxides were set to 1.3, 1.2, 0.5, and 10.4, respectively. For partition coefficients that were not determined in Chapter 2 (amphiboles and clinopyroxenes), literature values were used. For amphiboles, the partition coefficients were predicted from amphibole and melt compositions as suggested by Nandedkar et al. (2016; Table 7). For clinopyroxenes, the partition coefficients were predicted from the composition of the pyroxene as suggested by Bédard (2014; equation 629). Additionally, for phases that MELTS calculated to be present, but predictions for that partition coefficient were not available, assumptions were made about the behavior of scandium. This occurred for the minerals whitlockite, leucite, potassium feldspar, sphene, and quartz. For whitlockite, it was assumed that the partition coefficient would be similar to apatite and thus set to 1.3. For potassium feldspar and leucite it was assumed the partition coefficient would be similar to that of plagioclase and thus the multiple linear regression for plagioclase was used to estimate partition coefficients for potassium feldspar and leucite. For sphene it is assumed the partition coefficient will be similar to other 3+ cations such

as the REEs, which have partition coefficients of up to 20 (Green and Pearson, 1986). Thus, the partition coefficient for scandium between sphene and a melt was set to a value of 10; the median value of the REEs. For quartz, it was assumed that the partition coefficient would be << 1 and thus negligible and not considered in the model. Because there is a lack of constraints on the partitioning of scandium between a volatile phase and melt it has been assumed, for these models only, that scandium does not partition into a volatile phase. One limitation when using multiple linear regressions in this manner is the unknown effects that activity coefficients may have on partition coefficients. If the activity coefficients for phase components that contain scandium change significantly, then those components will have different activities and partition coefficients that vary in way that the multiple linear regressions do not account for. Thus, in this study there is an inherent assumption that the activity coefficients for phase components containing scandium do not vary significantly or all vary in a similar way. This assumption will be less problematic if the compositions of the minerals and melts used to predict the partition coefficients fall within the range of the experimentally determined compositions outlined in Chapter 2.

3.3. Description of MELTS Model

The process being modeled in this study is the magmatic stage of ore formation and is constrained by the model of Annen et al. (2006) for the generation of intermediate and siliceous melts. Annen et al. (2006) suggested that incomplete crystallization of a wet basaltic melt (referred to as residual melt), which is emplaced in the lower crust as sills, and the partial melting of pre-existing lower crustal rocks

(referred to as crustal melt) caused by heat, and possibly water transfer (i.e. flux melting), from the basalt to the surrounding rock can generate intermediate to felsic melts. Generally, the crustal melt is volumetrically smaller than the residual melt and is more viscous (Annen et al., 2006). However, Annen et al. (2006) and Annen et al. (2015) acknowledged that flux melting, although difficult to constrain, likely occurs and is an important process in the production of crustal melts. In the case of this study, and to test the hypothesis scandium-rich cumulates may be the source rocks that, when partially melted produce scandium-rich felsic rocks (see Chapter 1), the focus will be on crustal melts produced by fluxing of the pre-existing rock. This crustal melt may also potentially mix with the residual melt, but this mixing is not considered here. Additionally, if the viscosity of the crustal or residual melt is low enough it can be extracted from the source region, rise through the crust adiabatically, decompresses, becomes volatile saturated, crystallizes, which increases its viscosity, and is ultimately emplaced as a granitic pluton (Annen et al., 2006).

Utilizing this sequence, a generalized schematic of the model is presented in Figure 3.1, five models were generated in alphaMELTS for MATLAB. There are a variety of MELTS software formats including MELTS (Asimow and Ghiorso, 1998; Ghiorso and Sack, 1995), pMELTS (Ghiorso et al., 2002), rhyoliteMELTS (Ghiorso and Gualda, 2015; Gualda et al., 2012), and alphaMELTS (Smith and Asimow, 2005). Each version of MELTS is designed for a specific type of calculation. MELTS is designed to perform calculations from 500 to 2000°C and pressure of less than 2 GPa. The pMELTS version is designed for calculations performed for mantle compositions at pressures up to 3 GPa. The rhyoliteMELTS version is used to

perform calculations in water-saturated systems that crystallize at the quartz-two-feldspar ternary. A front end to MELTS was built to perform MELTS calculations in the form of alphaMELTS, which can use MELTS, pMELTS, and rhyoliteMELTS. In this work the term MELTS will refer generally to all MELTS software. Here, MELTS calculations were performed using alphaMELTS for MATLAB (https://gitlab.com/alphaMELTS/MELTS_Matlab) by using rhyolite-MELTS 1.0.2 and 1.2.

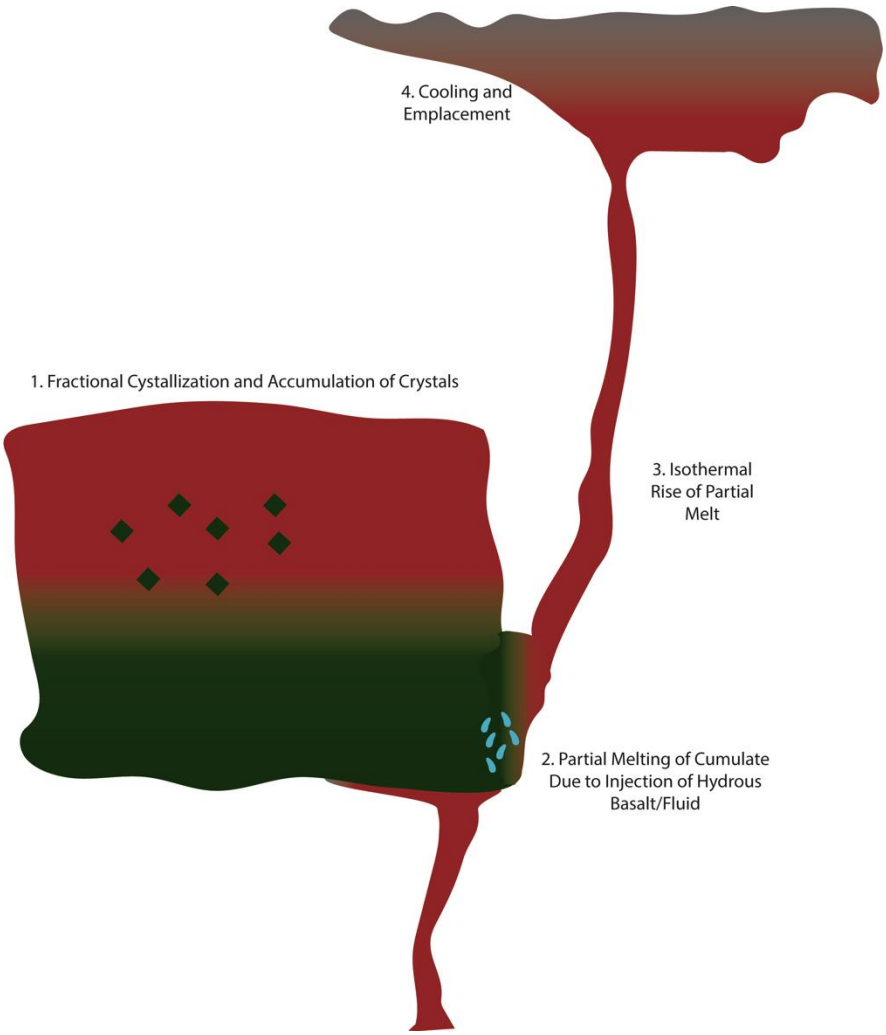

Figure 3.1: Generalized schematic of the generation of a felsic igneous system as modeled in MELTS after Annen et al. (2006). Schematic is not to scale.

Each model begins with a mafic source with compositions that include a MORB (mid-ocean ridge basalt), an estimate of the initial composition of the Skaergaard Layered Intrusion, the composition of a chilled margin of the Skaergaard Layered Intrusion, BCR-2G (analytical standard), and an Aleutian Island basalt (Table 3.2) at a temperature above the liquidus. These compositions were chosen in order to explore the possible bulk compositions that may generate mafic or ultramafic cumulates upon crystallization. The melt then undergoes fractional crystallization where at each step (1°C intervals) the solid phases are removed from the system. An important note in the calculation procedure used by MELTS is that 10^{-5} moles of each solid phase present remains in equilibrium with the melt after fractionation in order to keep those phases in the assemblage and stabilize the calculation.

At a melt fraction of 0.8 (20% crystallization) the bulk composition of all solids fractionated up to that point is taken, equilibrated at the solidus temperature, and then batch melted by increasing its temperature in 1°C increments. A melt fraction of 0.8 was chosen by examination of the phases that occurred in each model during fractionation. At a melt fraction of 0.8, the models generally contained pyroxenes and plagioclase and thus the solid phases are the closest approximation to a mafic or ultramafic clinopyroxenite that occurred in the models. Equilibrating the bulk composition at the solidus does not result in a solid assemblage that has the same minerals in the same proportions as all of the fractionated solids; however, they are broadly consistent. This step is necessary because MELTS does not allow the user to control which phases are present and their proportions at the beginning of a calculation; the user can only provide a bulk composition. A mass of water

Table 3.2: Conditions of MELTS models

wt%	MORB	Skaergaard Layered Intrusion Initial Composition	Skaergaard Layered Intrusion Chilled Margin	BCR-2G	Aleutian Island Basalt
SiO_2	50.47	47.14	48.52	54.4	51.2
TiO_2	1.68	3.75	1.18	2.27	0.75
Al_2O_3	14.7	11.96	17.38	13.4	15.69
FeO	10.43	17.77	9.84	12.4	9.21
MnO	0.184	0.26	0.16	0.19	0.16
MgO	7.58	6.19	8.7	3.56	9.64
CaO	11.39	9.64	11.48	7.06	10.21
Na_2O	2.79	2.49	2.39	3.23	2.77
K_2O	0.16	0.44	0.25	1.74	0.92
P_2O_5	0.184	0.35	0.1	0.37	0.21
Pressure (MPa)	500	400	500	400	950
Liquidus of initial melt (°C)	1266	1217	1266	1194	1381
Solidus of Cumulate (°C)[a]	886	868	927	834	1066
Temperature of Isothermal Rise of Partial Melt (°C)[b]	947	868	927	925	1149
Last Equilibration Temperature or Solidus of Partial Melt at 100 MPa[c]	764	702	740	744	870

Initial melt compositions: MORB - Gale et al. (2013); Skaergaard Layered Intrusion Initial Composition - Nielsen et al. (2009) LZa 13; Skaergaard Layered Intrusion Chilled Margin - Wager and Brown (1968) EG 4509; BCR-2G - Jochum et al. (2005); Aleutian Island Basalt - Perfit (1977) and Gust and Perfit (1987) MK-15. a: Temperature is where liquid disappears from the assemblage or the liquid is less than 0.05 g which prevents the MELTS calculation from being unstable. b: Temperature is the temperature at which the most siliceous melt is produced. In some cases (Aleutian Island Basalt) the MELTS calculation is unstable at the temperature of the most siliceous liquid and was the temperature manually raised until the calculation was stable. c: Temperature at which melt disappears form the assemblage or the lowest temperature at which the MELTS calculation is stable.

equivalent to 0.05 wt% water was added to the cumulate to both lower its melting temperature and simulate injection of a water-bearing magmatic volatile phase or transfer of water from a hydrous basalt to the cumulate. This proportion of water was chosen to allow the melt to be initially vapor undersaturated, and yet permit vapor saturation to take place as the melt decompresses. This model simulates the partial melting of a cumulate, such as those found at Kiviniemi, Finland and the Nyngan and Syerston-Flemington, Australia deposits. Pressure in all models were maintained below the garnet stability and were held constant during fractionation and partial melting. The pressure wherein garnet is stable varies between models, but is

generally above 400 or 500 MPa. This pressure constraint was chosen as scandium-rich pegmatites such as those of the Evje-Iveland pegmatite field are not heavy rare-earth element depleted and therefore garnet cannot be stable in the residue during partial melting of the cumulate. For additional information on this constraint see Chapter 4.

The melt with the highest SiO_2 that is produced by partial melting of the cumulate in 1°C intervals is then isothermally decompressed in 100 MPa intervals to simulate rise through the crust. This melt was chosen as it is roughly andesitic to dacitic in composition and upon further differentiation may produce a granite (*sensu lato*). This melt is ~1 wt% of the mass of the cumulate and ~0.2 wt% or less of the total mass of the system defined at the beginning of the model. These melt fractions may be unrealistically small to be capable of being segregated from the cumulate; however, for this simple model it will be assumed that the melt can be extracted from their source. For the purpose of this model, the calculations in this stage were performed along an isotherm to simulate an adiabatic rise. Changes in temperature during an adiabatic rise have been estimated to be a cooling of between 25 to 60°C/GPa between 1 and 3 GPa; however, at lower pressures and in hydrous magmas this degree of cooling may be higher (Annen et al., 2006; Carmichael, 2002; Clemens et al., 1997; Holtz and Johannes, 1994). During decompression, the melt becomes saturated with an aqueous vapor phase. Once the system is at 100 MPa the system is then cooled to the solidus. Annen et al. (2006) stated that intermediate to felsic melts stall in the crust when the timescale of ascent is longer than the timescale of complete crystallization of the magma. This occurs due to an increase in the viscosity of the

magma due to crystallization and volatile saturation and has been termed "viscous death", which occurs between 4 and 10 km depth (Annen et al., 2006). A pressure of 100 MPa corresponds to between 3 and 4 km depth and thus the magmas in the models presented in this work are emplaced at epizonal levels, which is consistent with Annen et al. (2006). The isothermal rise and cooling of the melt were performed as a batch process. Through the entire model from fractionation to cooling at 100 MPa, the f_{O_2} was constrained to NNO. This f_{O_2} was chosen as natural basaltic melts have f_{O_2} of ranging from NNO - 3 to NNO + 2 (Carmichael, 1991; Christie et al., 1986) and an f_{O_2} of NNO is roughly the center of this range and corresponds to the f_{O_2} of the cold-seal pressure vessel experiments. During fractionation rhyolite-MELTS 1.0.2 was used as no volatile phase is present and the melt does not contain dissolved H_2O. During partial melting of the cumulate and decompression of the partial melt rhyolite-MELTS 1.2 was used because either a volatile phase is present or the melt contains dissolved H_2O.

3.4. Trace Element Model

During fractional crystallization of the mafic melt, partial melting of the cumulate, and rise of the partial melt through the crust, the concentration of scandium in the melt and solid phases was calculated by using the predicted partition coefficients as described above. The initial concentration of scandium in the melt for all models was set to 30 ppm similar to the average concentration of scandium in the lower continental crust is (31 ppm; Rudnick and Gao, 2003). A potential problem with using the partition coefficients discussed in Chapter 2 is extrapolation of the values of the partition coefficients from the experiments performed at 100 MPa to

modeling that is performed at higher pressures (< 1 GPa). In order to estimate the variability in partition coefficients as a function of pressure, $D_{Sc}^{Px/Melt}$ (orthopyroxene) determined in Chapter 2 were compared to partition coefficients in the literature. Bédard (2007) compiled both experimentally determined partition coefficients and partition coefficients from natural samples in order to synthesize a predictive model for $D_{Sc}^{Px/Melt}$ (orthopyroxene) based on the MgO content of the melt. As an example, for the rise and cooling of a partial melt of a cumulate in the Skaergaard Layered Intrusion Initial Composition model, $D_{Sc}^{Px/Melt}$ predicted by the model of Bédard (2007), ranges from 1.6 to 4.4 and $D_{Sc}^{Px/Melt}$ based on the experiments performed in Chapter 2 ranges from 3 to 13.4. Predicted $D_{Sc}^{Px/Melt}$ overlap in both models but the $D_{Sc}^{Px/Melt}$ constrained by the experiments performed in this study are 2 to 4 times greater than those predicted by the model of Bédard (2007) for a given pyroxene composition. $D_{Sc}^{Px/Melt}$ was also compared for the Skaergaard Chilled Margin model. $D_{Sc}^{Px/Melt}$ predicted by Bédard (2007) ranges from 0.6 to 3.9, whereas predicted partition coefficients based on the experimental constraints range from 1.6 to 8.3. Although, there are some differences in the predictive models, $D_{Sc}^{Px/Melt}$ is >1 in most cases and thus pyroxene will still sequester scandium. Thus, if the $D_{Sc}^{Px/Melt}$ predicted by the model of Bédard (2007) are used the results of the trace element modeling will not be significantly different. For example, in modelling of the MORB composition the bulk partition coefficients calculated utilizing the partition coefficients determined in this study range from 0 to 4.13 during partial melting of the cumulate (stage 2) and from 0 to 2.13 during isothermal decompression and cooling (stages 3 and 4). In the

same MORB model the bulk partition coefficients range from 0 to 4.00 during partial melting of the cumulate (stage 2) and range from 0 to 1.17 during isothermal decompression and cooling (stages 3 and 4) if the partition coefficients predicted by the model of Bédard (2007) are used. Thus, the bulk partition coefficients for a given mineral assemblage are not significantly different and will not significantly affect the model. Further, $D_{Sc}^{Sp/Melt}$ determined in the previous chapter study were compared to the $D_{Sc}^{Sp/Melt}$ from Nandedkar (2014) who performed experiments at 0.7 GPa and temperatures of 980 to 730°C with melt compositions from basalt to high-silica rhyolite. $D_{Sc}^{Sp/Melt}$ from Nandedkar (2014) range from 0.6 to 8.17, which are consistent with $D_{Sc}^{Sp/Melt}$ of 0.13 to 7.7 determined here. Thus, although the pressures used in the MELTS modeling are higher than the pressures of the experiments performed in Chapter 2, changes in the partition coefficients at higher pressures are not expected to significantly affect the model. In general, higher pressures are not expected to cause scandium to behave incompatibly, where experiments performed at lower pressures predict compatible behavior or vice versa.

The equations used to calculate the concentration of scandium in the melt and coexisting solid phases during fractionation are

$$\frac{C_{Sc}^{Melt}}{C_{Sc}^{Melt^\circ}} = F^{\overline{D}_{Sc}-1} \quad , \qquad \text{Eq. (3.1)}$$

and

$$C_{Sc}^{Solids} = \frac{C_{Sc}^{Melt^\circ} - F C_{Sc}^{Melt}}{1-F} \quad , \qquad \text{Eq. (3.2)}$$

where $C_{Sc}^{Melt^\circ}$ is the initial concentration of scandium in the melt, C_{Sc}^{Melt} is the concentration of scandium in the melt, F is the melt fraction remaining, $\overline{D}_{Sc}$ is the

bulk partition coefficient for scandium, and C_{Sc}^{Solids} is the concentration of scandium in the solids. The bulk partition coefficient is defined by:

$$\overline{D}_{Sc} = \sum D_{Sc} x_{\phi} \quad , \quad \text{Eq. (3.3)}$$

where D_{Sc} is the Nernst-type partition coefficient for scandium between phase ϕ and the melt and $x_{\phi}$is the mass fraction of phase ϕ in the crystallization products. $\overline{D}_{Sc}$ changes with each temperature step due to the changing proportions of the solid phases and changing D_{Sc} for each mineral as the composition of the melt and mineral phases change. To account for the combination of changing $\overline{D}_{Sc}$ and the removal of the solids during fractionation, at each step F and $C_{Sc}^{Melt^{\circ}}$ is reset. F is calculated as the amount of melt remaining at each step before the solid phases are fractionated and typically ranges from ~0.97 to 0.99. $C_{Sc}^{Melt^{\circ}}$ is the concentration of scandium in the liquid from the previous step. As mentioned above, MELTS retains 10^{-5} moles of each solid phase present in equilibrium with the melt after fractionation. In order to maintain a mass balance, the mass of scandium present in the phases that are kept in equilibrium with the melt is added back into the liquid. The initial concentration in the liquid is then adjusted to reflect the addition of this mass. If this adjustment is not performed the calculation does not close mass balance. Additionally, when performing the mass balance at the end of the calculation it is necessary to determine the sum of the mass of scandium in the phases that remained in equilibrium with the melt at each step and subtract this mass from the total mass. Doing so prevents double counting of the mass of scandium, because the output from the MELTS calculations are prior to fractionation and do not account for the mass of scandium in

the phases kept in equilibrium with the liquid. During batch melting of the cumulate, the concentration of scandium in the melt is calculated by

$$\frac{C_{Sc}^{Melt}}{C_{Sc}^{Cumulate^{\circ}}} = \frac{1}{F+(1-F)\overline{D}_{Sc}} \quad , \qquad \text{Eq. (3.4)}$$

where $C_{Sc}^{Cumulate^{\circ}}$ is the initial concentration of scandium in the cumulate. The concentration of scandium in the remaining solids is calculated by

$$C_{Sc}^{Solids} = \overline{D}_{Sc}\, C_{Sc}^{Melt} \quad . \qquad \text{Eq. (3.5)}$$

$\overline{D}_{Sc}$ varies due to changing mineral and glass compositions (thereby changing D_{Sc}), as well as changing proportions of those phases at each temperature interval. However, because solids were not fractionated, F must vary from 0.0 to 1 and $C_{Sc}^{Cumulate^{\circ}}$ remains constant. $C_{Sc}^{Cumulate^{\circ}}$ was calculated by summing up the mass of the scandium in all of the solids fractionated when the initial mafic melt has crystallized 20% and dividing that mass by the mass of the fractionated phases. During the isothermal decompression and cooling of the partial melt of the cumulate, the concentration of scandium in the melt is calculated by

$$\frac{C_{Sc}^{Melt}}{C_{Sc}^{Melt^{\circ}}} = \frac{1}{F+(1-F)\overline{D}_{Sc}} \quad , \qquad \text{Eq. (3.6)}$$

and the concentration of scandium in the solids is calculated by using equation 3.5. As with the partial melting of the cumulate, because no solids were fractionated during isothermal decompression and cooling of the partial melt, the value of F ranges from 0.0 to 1 and $C_{Sc}^{Melt^{\circ}}$ is constant. $C_{Sc}^{Melt^{\circ}}$ is the concentration of scandium in the melt with the highest SiO_2 (wt%) produced by the partial melting of the cumulate. The concentration of scandium in the individual minerals coexisting with the melt during each interval of fractionation, partial melting, and rise through the

crust were calculated by using the partition coefficient for that mineral at each interval.

3.5. Modeling Results

Figures 3.2, 3.3, 3.4, and 3.5 graphically represent the mineral assemblages that occur during fractionation of a mafic melt, partial melting of the cumulate, isothermal decompression of the partial melt, and cooling of that partial melt, respectively. The following discussion will generally describe the occurrence of phases in each stage of the model. During fractionation of the initial mafic melt, the solid phases that occur (Figure 3.2) include clinopyroxene ± orthopyroxene ± olivine, plagioclase, spinel, rhombohedral oxides, whitlockite (over apatite, as the melts are anhydrous) and rarely sphene, leucite, and quartz.

The phase assemblages produced by batch melting of the cumulate (itself the product of 20% crystallization of the initial basaltic melt) are presented in Figure 3.3. Clinopyroxene, plagioclase (with the exception of the Aleutian Island Basalt model), and orthopyroxene are common to all models and broadly dissolve into the melt in the order: 1) orthopyroxene, 2) plagioclase, and 3) clinopyroxene. Additional phases that occur in minor amounts or in select models include hornblende, biotite, spinel, and olivine. An aqueous vapor phase is also present in the Skaergaard Initial Composition and the MORB models at low melt fractions, but that aqueous vapor phase dissolves into the melt as temperature increases.

As the partial melt of the cumulate rises and is isothermally decompressed, the melt becomes saturated with an aqueous vapor phase after which it begins to crystallize. This is consistent with Annen et al. (2006) and Clemens et al. (1997),

who stated that during an adiabatic rise hydrous melts can become superheated and remain liquid or dissolve any crystals present and only after saturation with a volatile phase will the melt crystallize. Further rise of the melt leads to more crystallization as the aqueous vapor phase is exsolved from the melt, progressively depleting the melt phase in water (Figure 3.4). Plagioclase and orthopyroxene ± clinopyroxene ± spinel also crystallize during decompression. After reaching 100 MPa and subsequently cooling, the melt begins to crystallize further (Figure 3.5). This crystallization generally includes plagioclase, orthopyroxene, clinopyroxene ± spinel ± olivine. In select cases potassium feldspar, quartz, biotite, rhombohedral oxides, and leucite occur at lower temperatures near the solidus.

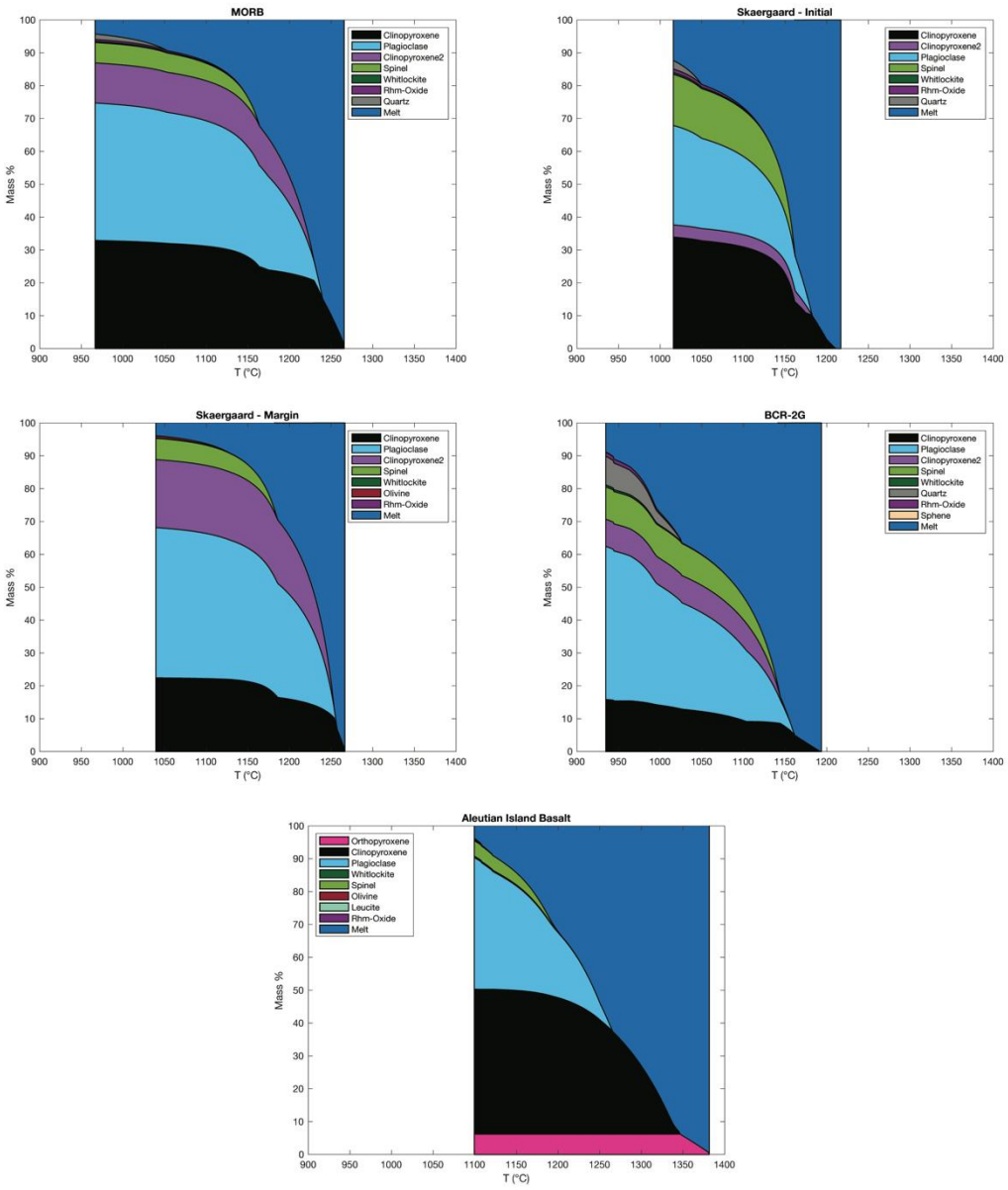

Figure 3.2: Mass % of phases present during fractional crystallization of a mafic melt as calculated by MELTS modeling plotted against temperature. Y-axis is the mass % of phase. The solid phases are the total mass of that phase fractionated up to that point and the mass of that phase in the cumulate. The model begins at the liquidus and decreases in temperature in 1°C intervals. See Table 3.2 for starting compositions, as well as liquidus temperatures and pressure conditions. The x-axis for each plot is the same in order to allow for the model to be easily compared at a given temperature.

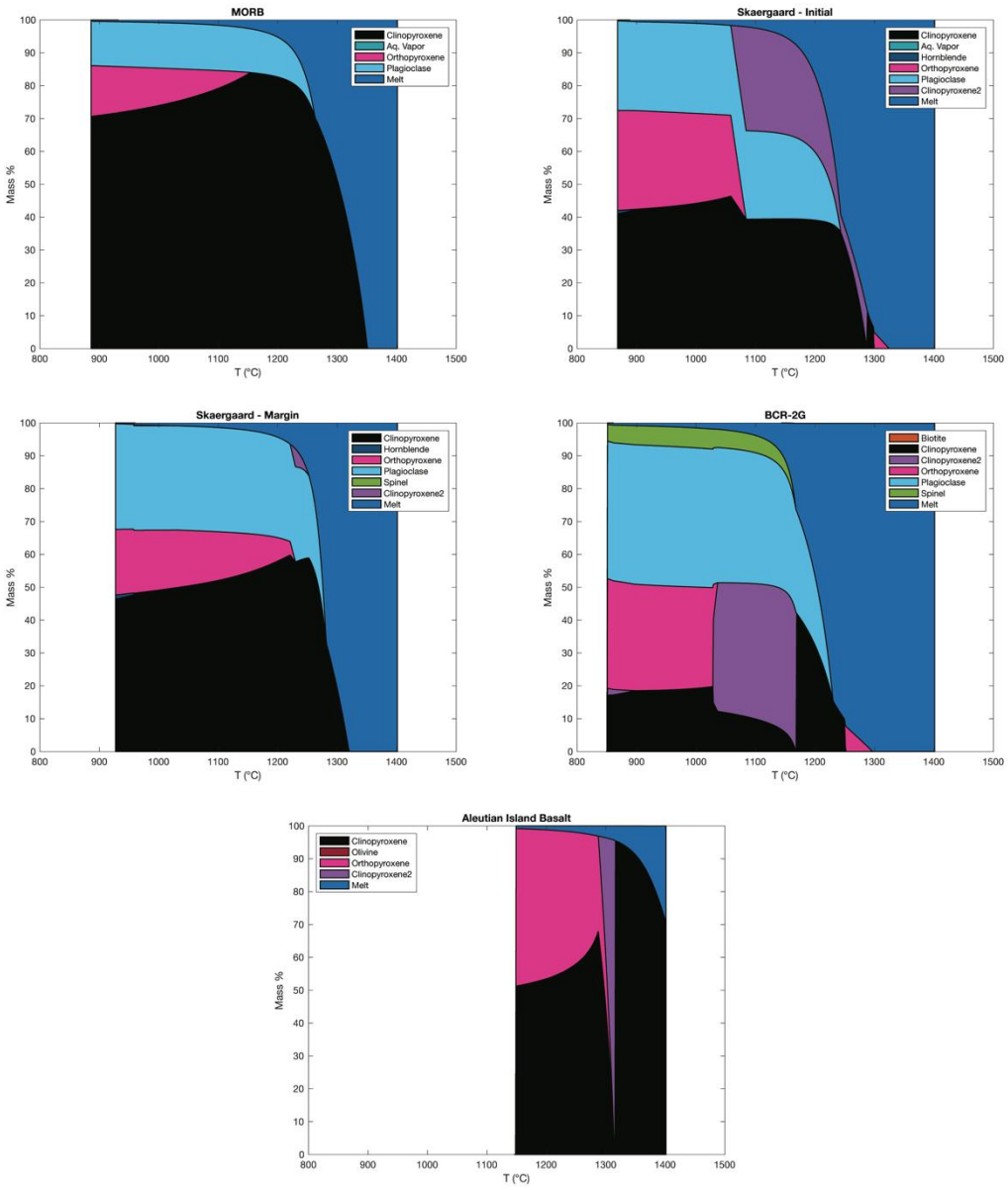

Figure 3.3: Mass % of phases present during batch melting of the cumulate generated by fractional crystallization of a mafic source plotted against temperature. Batch melting occurs at 20% crystallization of the initial mafic source and the cumulate is the composition of all solids fractionated. Batch melting begins at the solidus and the model increases in temperature in 1°C intervals. See Table 3.2 for solidus temperatures and pressure conditions. The x-axis for each plot is the same in order to allow for the model to be easily compared at a given temperature.

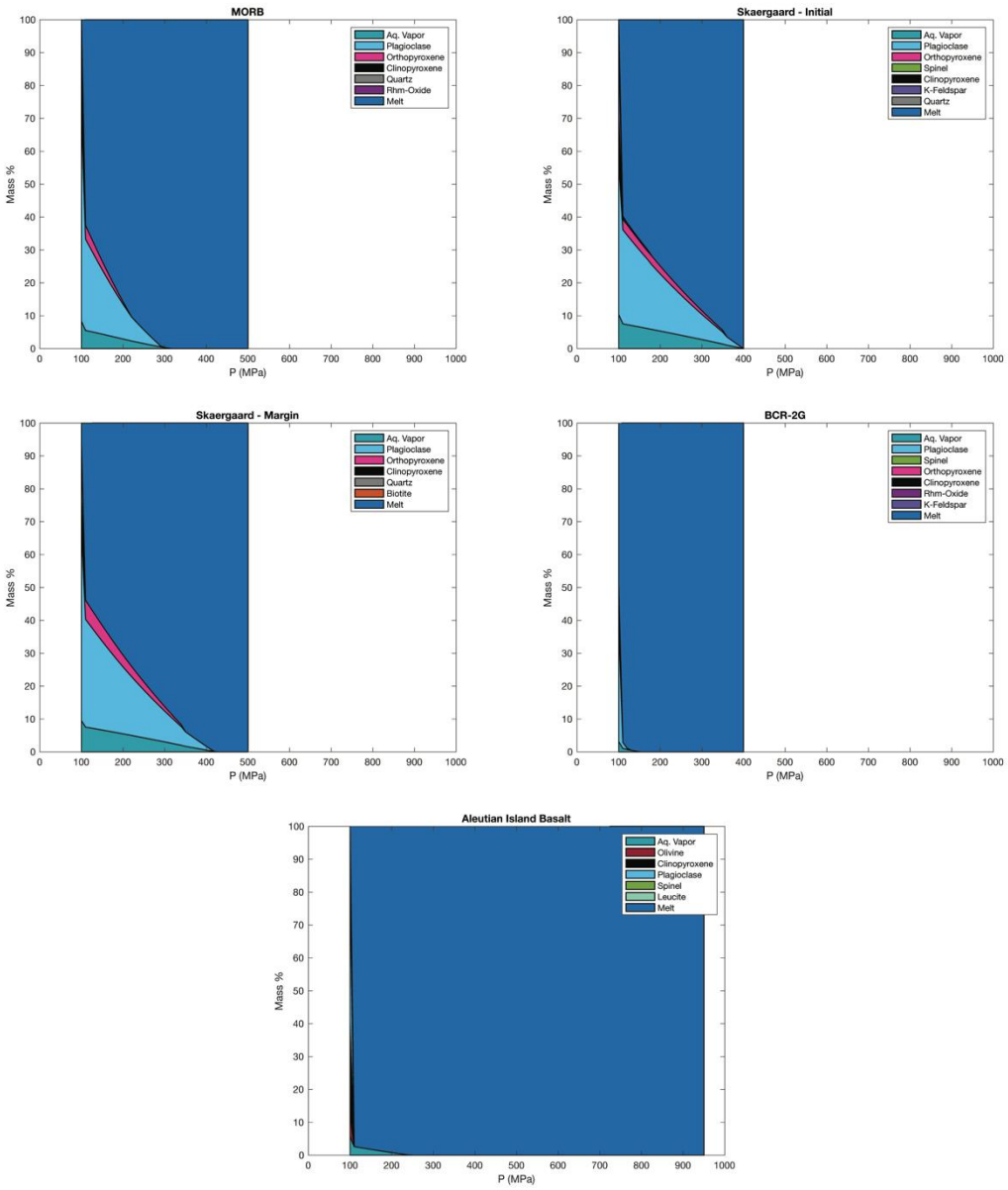

Figure 3.4: Mass % of phases present during isothermal decompression of the most siliceous melt produced by batch melting of a cumulate. Isothermal decompression occurs in 100 MPa intervals and ceases at 100 MPa. See Table 3.2 for temperature of isothermal decompression. The x-axis for each plot is the same in order to allow for the model to be easily compared at a given pressure.

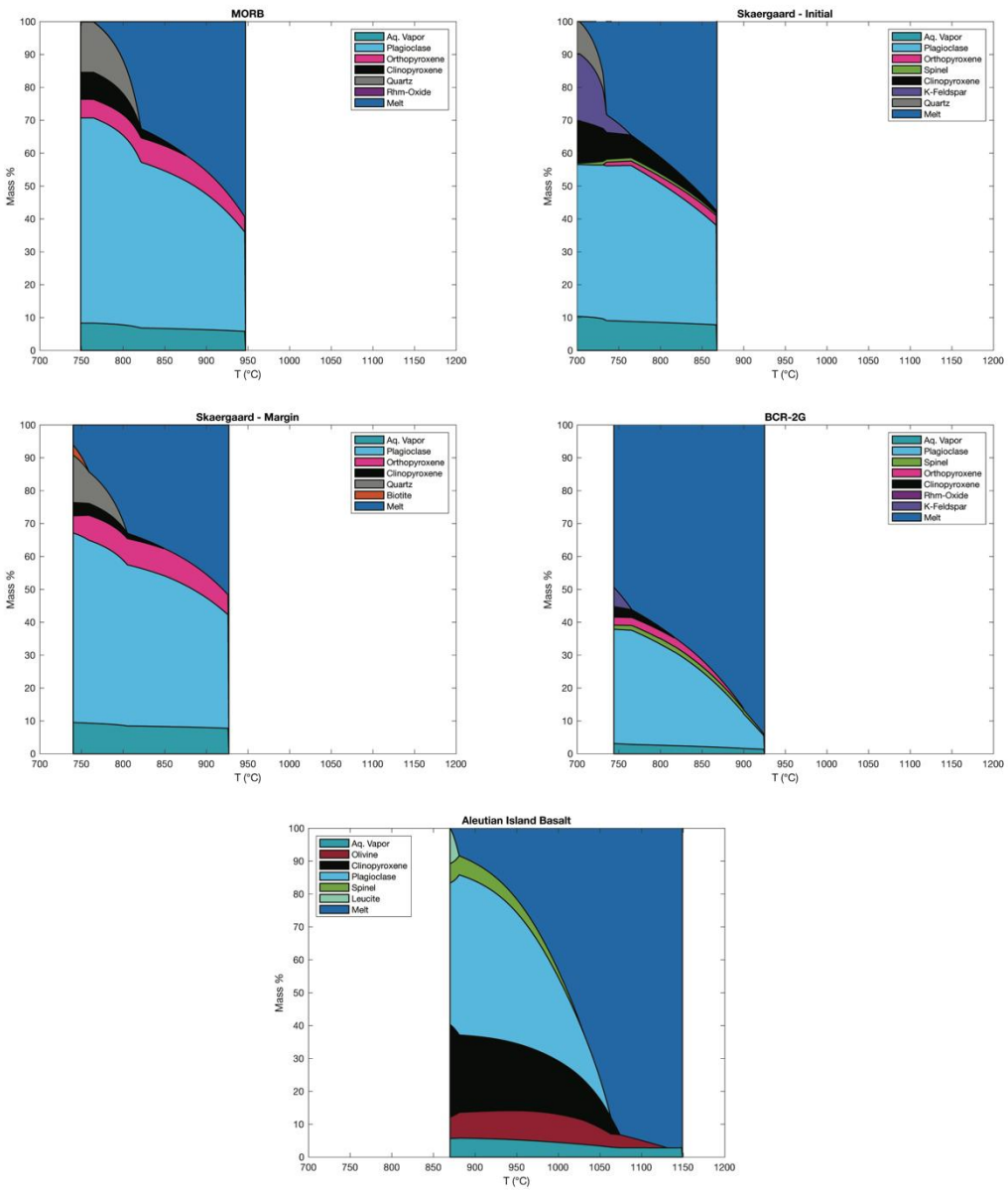

Figure 3.5: Mass % of phases present during cooling at 100 MPa of the most siliceous melt produced by batch melting of the cumulate. Temperature decreases in 1°C intervals. The x-axis for each plot is the same in order to allow for the model to be easily compared at a given temperature.

The bulk partition coefficients ($\overline{D}_{Sc}$) for each model are presented in Figure 3.6. Because the bulk partition coefficient is a function of both the mass fraction of a mineral phase in the crystallization products and the partition coefficient for that phase (equation 3.3) and because each varies with progression of the model, the bulk partition coefficients are not constant. During fractionation $\overline{D}_{Sc}$ is typically between 1 and 10 for all models, increasing to greater than 10 near the solidus in the BCR-2G and MORB model as the melt approaches the solidus and is clinopyroxene saturated. The exception to this is the Aleutian Island Basalt model where $\overline{D}_{Sc}$ is <3 during fractionation and often <1. As the cumulate (20% crystallization) is batch melted, $\overline{D}_{Sc}$ for all models is generally between 1 and 5. However, for the BCR-2G model, $\overline{D}_{Sc}$ <1 over a large temperatures range (~1250 to 1100°C) and the Skaergaard Initial Composition model has a $\overline{D}_{Sc}$ <1 for a brief period at temperatures below 1300°C. During isothermal decompression of the partial melt, $\overline{D}_{Sc}$ < 1 when the phases present in the crystallization assemblages are primarily plagioclase and an aqueous vapor phase (the partition coefficient for the aqueous vapor is not considered). As the melt approaches a pressure of 100 MPa, $\overline{D}_{Sc}$ increases to between 1 and 3.5 for all models except BCR-2G, wherein $\overline{D}_{Sc}$ <0.5. As the melt begins to cool and the melt becomes saturated with ferromagnesian phases $\overline{D}_{Sc}$ > 1. For the Skaergaard Chilled Margin and the MORB model $\overline{D}_{Sc}$ <1 near the solidus.

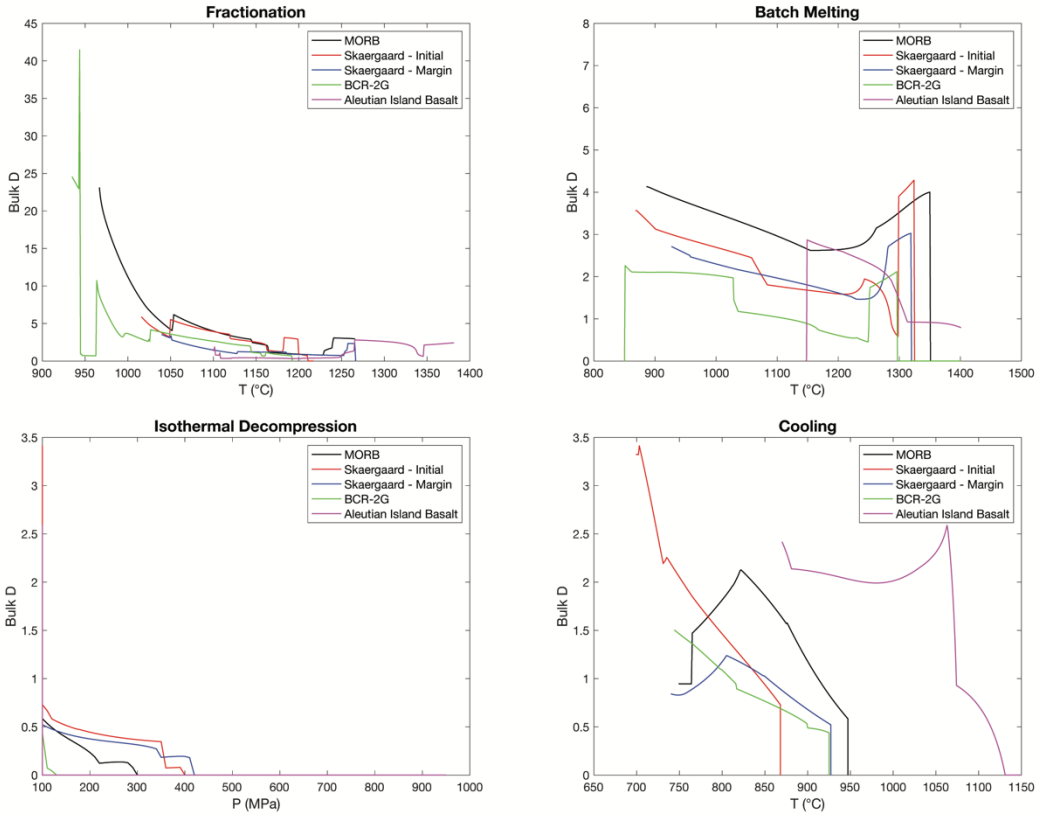

Figure 3.6: $\overline{D}_{Sc}$ calculated for fractionation of a mafic melt, batch partial melting of a cumulate, isothermal decompression of that partial melt, and cooling of that melt at 100 MPa.

The concentration of scandium in all phases present during fractionation, partial melting of the cumulate, isothermal decompression, and cooling are presented in Figure 3.7. Fractionation of the mafic melt initially produces solids that have scandium concentrations approaching 100 ppm. It should be noted that the concentration of scandium in the solids in Figure 3.7 for fractionation is the concentration of scandium in all the solids that are fractionated, whereas for the individual minerals, it is the concentration of scandium at a given temperature. The majority of the scandium is hosted in the pyroxenes and at lower temperatures spinel and rhombohedral oxides may also serve as primary hosts to scandium. Throughout

the entire fractionation process the concentration of scandium in the melt decreases, such that the melt becomes depleted in scandium as it nears the solidus. The Aleutian Island Basalt model is an exception, wherein the scandium concentration in the melt is greater near the solidus than at the liquidus. During batch melting of the cumulate the majority of the scandium is hosted in the pyroxenes and, where present, hornblende. As the temperature increases and the ferromagnesian minerals begin to dissolve in the melt, the scandium concentration in the melt increases. It is also clear that the scandium is retained by the solid phases that are still in equilibrium with the melt and it is not until those phases dissolve that the scandium concentration in the melt can increase. As the partial melt isothermally decompresses, the majority of the scandium is hosted in the pyroxenes; however, the concentration of scandium in the melt and solid phases is relatively constant. This is the result of $\overline{D}_{Sc}$ being close to 1 (Figure 3.7). As the melt cools at a pressure of 100 MPa the concentration of scandium in the melt decreases or remains constant. Similar to fractionation and batch melting of the cumulate, the scandium is primarily hosted in the pyroxenes, as well as the spinel and rhombohedral oxides, where present.

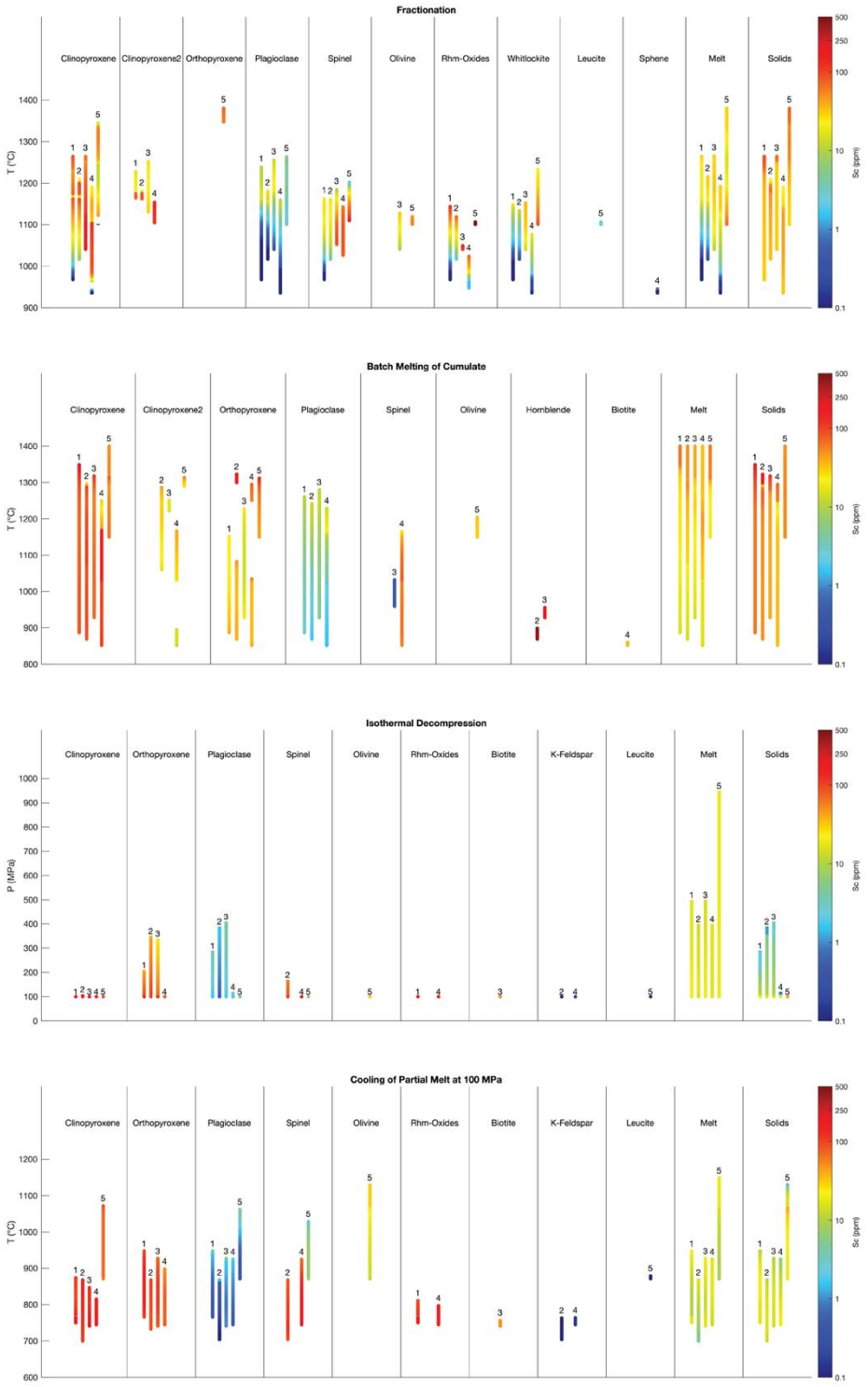

Figure 3.7: Scandium concentrations in mineral and melt phases during fractionation of a mafic source, batch melting of a cumulate, isothermal decompression, and cooling of the partial melt. The scandium concentration in the solids in the fractionation pane represent all solids fractionated to that point. 1 = MORB, 2 = Skaergaard Initial Composition, 3 = Skaergaard Chilled Margin, 4 = BCR-2G, 5 = Aleutian Island Basalt.

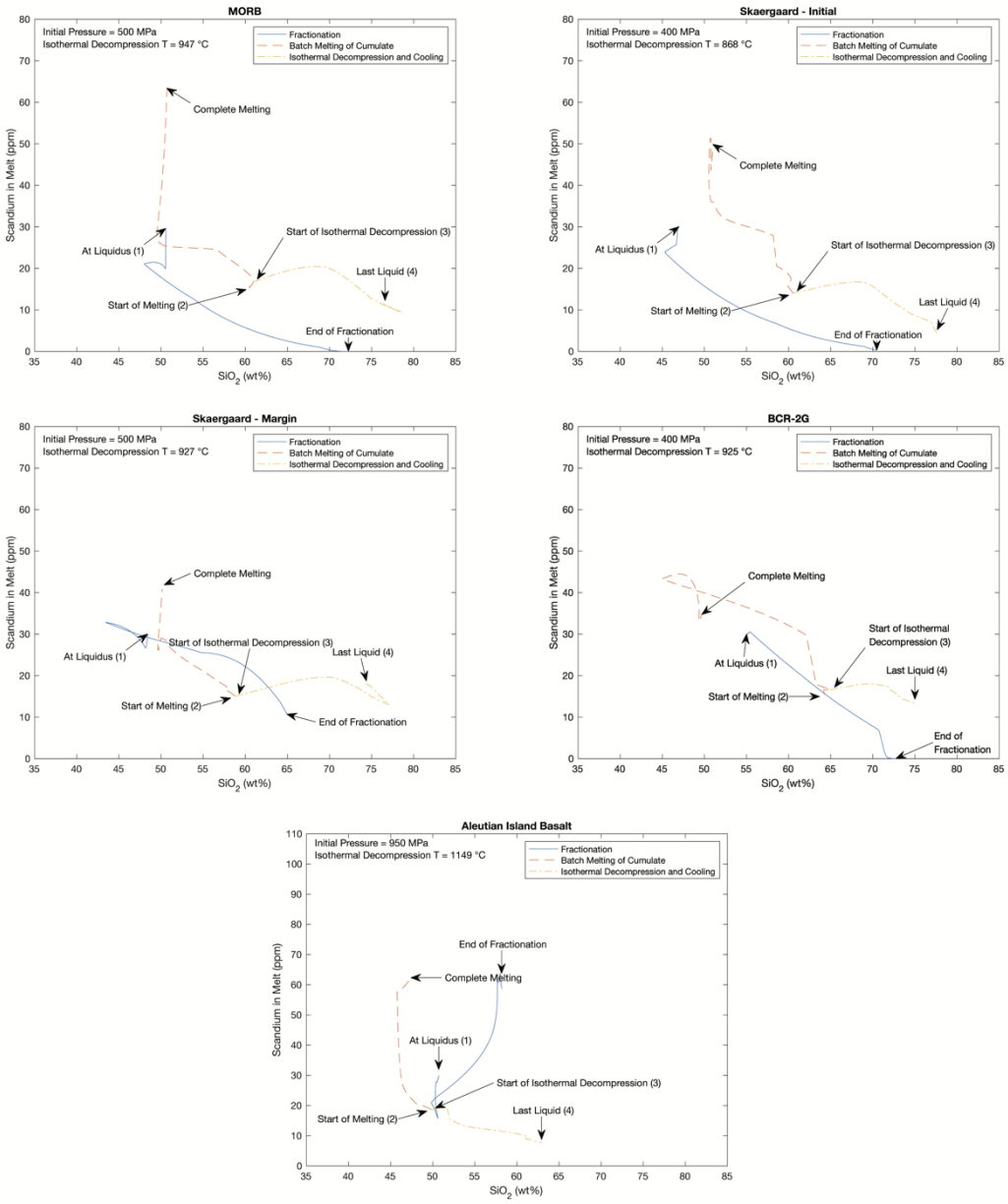

Figure 3.8: Scandium concentration in the melt vs SiO_2 (wt%) for melts produced during fractional crystallization, batch melting of a cumulate, isothermal decompression of the partial melt and final cooling of that melt at 100 MPa. Text labeled 1- 4 corresponds to the stages of the model in Figure 3.1. 1) Liquidus of the mafic source. 2). First melt produced by batch melting of the cumulate produced by 20% fractional crystallization of the melt in stage 1. 3) Melt produced in stage 2 that is isothermally decompressed. 4) Last liquid to be equilibrated in MELTS and is either the liquid present 1°C below the solidus or the last equilibration point before the MELTS calculation fails to converge. End of fractionation is the final melt equilibrated if fractionation of the liquid in stage 1 is carried to completion and is either the liquid present 1°C below the solidus or the last equilibration point before the MELTS calculation fails to converge. Complete melting is the liquid at the liquidus of the cumulate produced by batch melting.

In order to understand the potential of forming a scandium-bearing mineral deposit associate with granitic magmatism, it is important to compare the concentration of scandium in the melts produced as a function of the SiO_2 concentrations of that melt. If the processes modeled in this study are viable mechanisms for forming scandium-bearing deposits, then the scandium concentration in the felsic melts should be significantly higher than the average scandium concentration of barren magmatic systems. Figure 3.8 presents the concentration of scandium in all of the melts produced in the MELTS modeling plotted against the SiO_2 concentration of that melt. It is clear from Figure 3.8 that as soon as a mafic melt begins to crystallize the scandium will be sequestered in the crystalline phases and deplete the melt in scandium. These crystals, if accumulated, will result in a scandium-rich cumulate. When this scandium-rich cumulate is partially melted, the first melt to be produced generally has the highest SiO_2 concentrations. However, this melt is not particularly scandium-rich. The concentration of scandium in this melt is generally higher or has approximately the same as scandium concentration of the melts produced by fractionation alone at comparable SiO_2 concentrations. As this melt is isothermally decompressed and the temperature decreases, the scandium concentration increases slightly, before decreasing due to the crystallization of pyroxenes, yet is typically above the melt produced by fractionation alone. The exception to this is the Aleutian Island Basalt model, wherein the scandium concentration in the melt produced by partial melting of the cumulate is always below that of the melt produced by fractionation alone. The advantage of partial melting a cumulate by injection of a hydrous basalt or addition of water is that the melt can

produce higher-silica rocks than anhydrous fractional crystallization of a mafic melt. Additionally, as expected, if the cumulate is allowed to completely melt, then it is this melt that has the highest concentration of scandium; however, it is still mafic in composition. However, during fractionation of the initial mafic melt and near the solidus, the remaining liquid in the Aleutian Island Basalt model has a higher (approximately double) concentration of scandium than the initial liquid. However, this liquid only has a SiO_2 concentration of ~58 wt% and a temperature of 1100°C. Additionally, the concentration of scandium is beginning to decrease as clinopyroxene re-appears in the crystallization products. Thus, it is likely that this liquid, if fractionated further, will not produce a scandium-rich felsic melt. In this case, the melt could not be further fractionated because the MELTS calculation failed to converge.

3.6. Discussion

The trace element models combined with MELTS modeling provide constraints on the formation of scandium-rich, ultramafic rocks such as those found at Kiviniemi, Finland and the Nyngan and Syerston-Flemington deposits in Australia. The cumulates produced in the MELTS models have scandium concentrations of approaching 100 ppm and potentially higher if that cumulate undergoes some partial melting. Additionally, most of this scandium is hosted in the pyroxenes. The concentration of scandium in the modeled cumulates are consistent with the concentrations of scandium in the ferrodiorite at Kiviniemi (50 to ~300 ppm; Halkoaho et al., 2020), pyroxenite at Nyngan (110 ppm; Rangott et al., 2016), and pyroxenite at Syerston-Flemington (~80 ppm; Chassé et al., 2017). Thus, fractional

crystallization, where the crystallization products are primarily pyroxenes, is a viable mechanism to produce scandium-rich mafic-ultramafic rocks. These results are consistent with the results of Williams-Jones and Vasyukova (2018), who performed trace element modeling for fractional crystallization of the Tammany Creek and the Goose Basalt of the Columbia River Basalts in order to constrain the formation of Alaskan-type ultramafic complexes and calculated that the scandium concentrations of the resulting pyroxenites (cumulates) were 208 and 263 ppm scandium, respectively.

Although fractionation can produce scandium-rich ultramafic rocks, they are unable to produce felsic melts with elevated concentrations of scandium. The magmatic processes that are thought to be common in igneous systems, such as fractionation and partial melting, do not appear to be the operative processes that concentrate scandium in felsic melts. At best, the partial melting of scandium-rich cumulates (such as those a Kiviniemi or Nyngan) is capable of producing felsic rocks with average scandium concentrations. In the five models presented here, the scandium concentration in melts >60 wt% SiO_2 is between 10 and 20 ppm. This is consistent with the concentration of scandium in the upper continental crust of 14 ppm (Rudnick and Gao, 2003). Note, that the concentration of scandium in the average MORB is ~40 ppm (Gale et al., 2013) and had 40 ppm scandium been used as the initial concentration in the model, the final scandium concentration is the felsic melts would be slightly higher, but still consistent with 14 ppm in the upper continental crust.

Williams-Jones and Vasyukova (2018) discussed the formation of the Evje-Iveland, Norway pegmatite field and suggest that a 10% partial melt of a pyroxenite with 100 ppm scandium in Iveland-Gautestad Complex, as it was being metamorphosed by a fluid into the host amphibolite, could produce a melt with ~1000 ppm that is capable of saturating with thortveitite. Williams-Jones and Vasyukova (2018) assumed that all of the scandium is released into the melt as melting begins. However, Williams-Jones and Vasyukova (2018) did not consider that the residual amphibole in equilibrium with that melt will continue to sequester scandium. Amphibole have particularly large scandium partition coefficients, especially when in equilibrium with high-silica melts (Nandedkar et al., 2016) and may be more effective scandium sinks than pyroxenes. Thus, a simple model of partial melting of a cumulate is not likely to be sufficient to produce the Evje-Iveland pegmatites. The formation of the Evje-Iveland pegmatites in Norway will be further discussed in Chapter 4.

One aspect of the behavior of scandium in magmatic systems that remains poorly understood is the role of volatile phases. As discussed in Chapter 1, there is an association of scandium-bearing deposits with fluorine-bearing fluids (i.e. volatile phases), as well as carbonic fluids. The possibility remains that fluorine- or carbon-rich melts may retain their scandium and reduce the ability of ferromagnesian minerals to sequester scandium. This is particularly interesting when considering fluorine and that will be the focus of this discussion. Fluorine prefers to remain in the melt and can have significant effects on melt structure and phase equilibria, as well as complex with cations, such as tungsten and tin (e.g. Manning, 1981). Additionally,

high fluorine concentrations are characteristic of A-type granite systems (Whalen et al., 1987) and as noted in Chapter 1, there is an association of scandium-rich deposits with A-type granites. In order for scandium to be concentrated in a melt, it would require that the partition coefficients for the ferromagnesian minerals be lower than systems with insignificant fluorine. The fluorine-bearing experiments offer a glimpse into this phenomenon. As mentioned above, $D_{Sc}^{Crd/Melt}$ is lower in experiments that contain fluorine and chlorine, than in fluorine- and chlorine-free experiments (Section 2.6.2.2.7). If scandium can complex with fluorine and the fluoride complexes remain in the melt, scandium may remain in melts with significant concentrations of fluorine. Such melts may be produced by partial melting of a scandium-rich cumulate due to the introduction of a fluorine-rich volatile phase followed by fractionation or by fractionation of melts that initially contained significant fluorine, but may not be the result of partial melting of scandium-rich cumulates. Additionally, it is possible that these cumulates already contain fluorine. For example, the gabbros at Kiviniemi contain fluorapatite (Halkoaho et al., 2020) and it has been suggested that the source material for A-type granites may contain fluorine in minerals such as biotite and amphibole, and by extenstion apatite, which enter the melt upon partial melting (see Clemens et al., 1986; Creaser et al., 1991; Dall'Agnol et al., 2012; Whalen et al., 1987 and references therein). It is also unclear how scandium behaves when a melt reaches volatile saturation. If the partition coefficient for scandium between a melt and a magmatic-hydrothermal volatile phase is high enough, it is possible that the scandium can be stripped from the melt, concentrated in a volatile phase, and later deposited. Thus, the role of volatile phases and the effect of anions that can complex with

scandium, such as fluorine, require further research and experimentation. What is clear from the models presented in this study is that relatively common magmatic processes, such as fractionation in either anhydrous systems or systems where the only volatile present is water, are not responsible for the formation of scandium-rich deposits associated with granite magmatism.

3.7. Summary of Chapter 3

Trace element modeling has been combined with MELTS modeling in order to constrain the formation of scandium-rich deposits associated with granitic magmatism. MELTS modeling was performed with five basaltic starting compositions. Modeling including fractional crystallization of a basaltic melt to form a cumulate, which was subsequently partially melted and that melt was isothermally decompressed and then cooled to the solidus. Utilizing the experimentally determined partition coefficients for scandium presented in Chapter 2, as well as data on the partitioning behavior of scandium from the literature, the concentration of scandium in mafic to felsic liquids and the minerals coexisting with those liquids were calculated. Fractional crystallization of a mafic melt can produce scandium-rich cumulates, wherein scandium is primarily hosted in pyroxenes. These cumulates are similar to the mafic and ultramafic rocks found at Kiviniemi, Finland and the Nyngan and Syerston-Flemington complexes of Australia. Although felsic melts were produced by partial melting of scandium-rich cumulate, those melts were not enriched in scandium. Rather, the concentration of scandium in the felsic melts is consistent with the concentration of scandium in the upper continental crust. Thus, partial melting of a scandium-rich cumulate in anhydrous or hydrous systems wherein the

only volatile phase is water can produce felsic rocks with average scandium concentrations, but these melts are not capable of producing scandium-rich felsic rocks. In light of this study it is hypothesized that in order to concentrate scandium in a melt or volatile phase, that melt or volatile phase must be enriched in anions that strongly complex with scandium. These anions may include fluorine, chlorine, or a carbon species. This hypothesis requires further testing and is the next logical step in understanding the behavior of scandium in magmatic-hydrothermal systems.

4. Chapter 4: Experimental Constraints on the Formation of Pegmatite-forming Melts by Anatexis of Amphibolite: A Case Study from Evje-Iveland, Norway

Austin M. Gion[1,2], Philip M. Piccoli[1], Yingwei Fei[2], and Philip A. Candela[1]

[1]Laboratory for Mineral Deposits Research, Department of Geology, University of Maryland, College Park, Maryland

[2]Earth and Planets Laboratory, Carnegie Institution for Science, 5251 Broad Branch Road, N.W.,

Washington, DC 20015, USA

*Corresponding author. Present Address: 8000 Regents Drive, Department of Geology, University of Maryland, College Park, MD 20742, USA. Email: agion@umd.edu

This chapter is presented as a manuscript that is being prepared for submission to be published. The author of the dissertation is the primary author for this work and performed all experiments and analyses, with technical assistance form those listed in the acknowledgements. Philip M. Piccoli, Yingwei Fei, and Philip A. Candela acted as advisors for this work.

4.1. Abstract

The Evje-Iveland pegmatite field in Norway contains rare element pegmatites that are known for their rare scandium mineralization. The petrogenesis of these pegmatites and origin of the scandium mineralization has been debated in the literature for nearly a century. Hypotheses for the origin of pegmatite-forming melt have included both anatexis of the host amphibolite in vapor-absent conditions, wherein scandium is typically scavenged from the host amphibolite; or magmatic differentiation, wherein scandium is magmatically concentrated. In order to test the hypothesis that the pegmatite-forming melt was sourced from the host amphibolite, partial melting experiments on the host amphibolite have been performed in a piston-cylinder apparatus. These experiments were performed at temperatures ranging from 700 to 1064° C and pressures between 400 and 550 MPa. The solidus of the host amphibolite has been determined to be close to 900°C at 500 MPa and is significantly higher than the temperature of pegmatite formation. Partial melting of <40% can produce glasses that are broadly granitic and are aluminum- and sodium-rich; however, they are less siliceous than the Evje-Iveland pegmatites. Further, these glasses are scandium- and REE-poor, and have REE patterns similar to leucosome in vein-type migmatites, produced at low pressures, but dissimilar to the Evje-Iveland pegmatites. The results of partial melting experiments performed on the Evje-Iveland host amphibolite are thus inconsistent with the hypothesis that the Evje-Iveland pegmatites, or other rare element pegmatites, are the result of direct anatexis of common metamorphic rock such as amphibolites. It is proposed that the formation of the Evje-Iveland pegmatites is result of partial melting of a scandium-rich ultramafic

or mafic complex, differentiation of that partial melt, and emplacement of a volatile-saturated melt into the host amphibolite. The role of volatiles during the emplacement of this partial melt is unclear; however, they may play a significant role in complexing with scandium and allowing the melt to retain high concentration of scandium. Additionally, further differentiation of the partial melt may result in the formation of the Flåt metadoritic suite or the Høvringsvatnet granites. The pegmatite-forming melt may then represent the final stages this differentiation. Thus, magmatic differentiation is the preferred model for the formation of the Evje-Iveland pegmatites.

4.2. Introduction

The Sveconorwegian pegmatite province in Norway and Sweden is one of the largest occurrences of pegmatites in the world and contains over 5000 rare-element pegmatites (Müller et al., 2017b). Pegmatites in this province have been mined since the 1860s, for-feldspars, quartz, white mica, and the elements scandium and beryllium (Müller et al., 2017b). Pegmatite formation occurred during the Sveconorwegian (Grenville) Orogeny and continued into a period of post-orogenic quiescence. It has been proposed that there are three groups of pegmatites, which are the result of: 1.) high-pressure, high-temperature metamorphism during the orogeny 2.) low-pressures, high-temperatures post-orogenic extension and 3.) post-orogenic granite magmatism (Müller et al., 2017b). The pegmatites are typically classified as abyssal (barren) or rare element NYF (Niobium-Yttrium-Fluorine) pegmatites (Müller et al., 2017b). NYF and LCT (Lithium-Cesium-Tantalum) pegmatites are common classifications used to describe rare element pegmatites. NYF pegmatites are generally associated with A-type granites and alkaline magmatism, and are alkaline with enrichment of heavy rare earth elements, Be, Ti, Sc, and Zr in addition to Nb, Y, and F (London, 2008). LCT pegmatites are generally associated with S-type granites, and are peraluminous with enrichment of Be, B, P, Rb, Sn among other elements in addition to Li, Cs, and Ta (London, 2008). The mineralogy of NYF and LCT pegmatites is dissimilar, such that NYF pegmatites often have amazonite and sodic pyroxenes and amphiboles, whereas LCT pegmatites often have muscovite, tourmaline, and spessartine-rich garnet (London, 2008). Additionally, LCT pegmatites are more abundant and are more frequently investigated than NYF pegmatites (London, 2008).

The formation of rare element pegmatites, whether NYF, LCT pegmatites, or a mixture of both, is commonly attributed to magmatic differentiation (Černý, 1991; Černý and Ercit, 2005; London, 2005, 2008).

The Evje-Iveland pegmatite field in Norway is a pegmatite field whose petrogenesis has been debated in the literature. The Evje-Iveland pegmatite field hosts some 400 (>1,000 m^3) pegmatites and is located within the Setesdal pegmatite district, in the Telemark Domain, within the Sveconorwegian pegmatite province and (Müller et al., 2015). The Evje-Iveland pegmatites are hosted in Vånne banded gneiss (an amphibolite gneiss), the Iveland-Gautestad gabbro, and the Flåt-Mykleås metadiorite and are spatially associated with the Høvringsvatnet granite (Müller et al., 2015; Pedersen et al., 2009). The mineralogy of the pegmatites includes potassium feldspar (including var. amazonite), plagioclase (including var. cleavelandite), quartz, biotite, and muscovite, as well as accessory minerals such as magnetite, garnet, columbite-group minerals, and beryl (Bjørlykke, 1935; Müller et al., 2015; Müller et al., 2017a; Snook, 2014 and references therein). The pegmatites exhibit internal zonation common to pegmatites and have a granitic wall, a megacrystic intermediate zone, and a core of quartz and feldspar (Müller et al., 2018). The pegmatites have an NYF signature, but are fluorine-poor and have replacement zones with an LCT signature and thus, are classified as mixed NYF (-LCT), rare element pegmatites (Černý, 1991; Müller et al., 2015). Another notable characteristic of the Evje-Iveland pegmatite field is the occurrence of scandium-bearing minerals, in particular the mineral thortveitite ($Sc_2Si_2O_7$), which was first discovered by Schetelig (1911) in an Iveland pegmatite and is now the accepted type-locality.

Past studies have interpreted the Høvringsvatnet granite to be the parental pluton to the Evje-Iveland pegmatites (e.g. Bjørlykke, 1937; Larsen et al., 2000). This interpretation was adopted due in part because the granite is located within the pegmatite field (Müller et al., 2015). Additionally, the oxygen isotopes of mineral separates from the pegmatites range from $\delta^{18}O_{SMOW}$ 0 to ~+11‰ and the hydrogen isotopes for biotite and muscovite from the pegmatites range from δD_{SMOW} -37 to -93 ‰ (Taylor and Friedrichsen, 1983a). These values are comparable with the isotopic signature of the Høvringsvatnet granite but indicate isotopic disequilibrium between the pegmatites and the surrounding wall rocks (Taylor and Friedrichsen, 1983a, b). However, U-Pb dating of zircon from the Høvringsvatnet granite is consistent with a crystallization age of 981 ± 6 Ma (Snook, 2014), whereas the pegmatites have an age of between 900.7 ± 1.8 (from U-Pb dating of columbite; Müller et al., 2017b) and 910.2 ± 14 Ma (from Lu-Hf dating of gadolinite; Scherer et al., 2001). Thus, the minimum age difference is between 52 and 64 Ma and therefore Müller et al. (2017b) has suggested that the Høvringsvatnet granite is unrelated to pegmatite formation. To further complicate the relationship of the granites to the pegmatites, recent U-Pb dating of sphene and U-Th total Pb dating of uraninite within the Evje-Iveland pegmatites has given maximum ages of 964 ± 20 Ma and 989 ± 19 Ma, respectively (Öz et al., 2018; Öz et al., 2019). These new ages overlap with the age of the Høvringsvatnet granite. A population of magmatic sphene and uraninite within the pegmatites have also been dated to an age of 915 ± 19 Ma and 912 ± 3 Ma, respectively, which are consistent with previous younger ages (Öz et al., 2018; Öz et al., 2019). These new data have been interpreted to indicate either two stages of

pegmatite formation or pegmatite formation at 989 ± 19 Ma followed by hydrothermal alteration 912 ± 3 Ma (Öz et al., 2018; Öz et al., 2019).

Due to the possible age difference between spatially associated granites and the Evje-Iveland pegmatites, direct anatexis has been suggested for the formation of the pegmatites (Müller et al., 2015; Müller et al., 2017b; Romer and Smeds, 1996; Snook, 2014). Previously, anatexis of country rocks during granulite (or upper amphibolite) facies metamorphism has been invoked for the formation of abyssal pegmatites and as a result abyssal pegmatites are generally defined as pegmatites that are the result of partial melting or metamorphic re-equilibration (Černý and Ercit, 2005). However, anatexis is not generally invoked for the formation of rare element pegmatites (Černý and Ercit, 2005).

Müller et al. (2015) and Snook (2014) have suggested that the pegmatite-forming melt at Evje-Iveland resulted from the anatexis (15-30% partial melting) of the host amphibolite. This partial melting occurred during the Sveconorwegian Orogeny (the orogeny has an age of 1145 – 900 Ma), wherein heat was provided to the system from crustal underplating (e.g. Andersen et al., 2002; Müller et al., 2017b; Vander Auwera et al., 2011). This petrogenetic model is supported by textural evidence (intermingled restite and leucosome material), the spatial association of the pegmatites to the amphibolites, and initial $^{87}Sr/^{86}Sr$ values of the pegmatites, which are generally consistent with a mantle-derived source (Müller et al., 2015; Müller et al., 2017b). Further, the oxygen and hydrogen isotopes of the Evje-Iveland pegmatites are also similar to the host rock (Taylor and Friedrichsen, 1983a).

The pressure and temperature of pegmatite emplacement in the Evje-Iveland pegmatite field have been estimated to be between 550 to 600° C at a pressure of 400 to 500 MPa (Müller et al., 2015). These emplacement conditions were interpolated from the estimated pressures and temperatures generated during emplacement of Rogaland anorthosite-mangerite-charnockite complex in southwestern Telemark Domain, 100 km west of the Evje-Iveland pegmatite field (Müller et al., 2015). The Rogaland complex is approximately coeval with emplacement of the pegmatites (Schärer et al., 1996; Vander Auwera et al., 2011). The complex is surrounded by a metamorphic aureole, with peak temperature estimates ranging from ~1000°C at the contact of the intrusion to ~750°C near the edges of the aureole (~15 km away from the contact) at a pressure of ~500 MPa (Drüppel et al., 2012; Jansen et al., 1985; Möller et al., 2002; Möller et al., 2003; Westphal et al., 2003). Emplacement of the intrusion was followed by a stage of cooling, wherein the temperature was ~610° C at 918 ± 2 Ma (Bingen and van Breemen, 1998). Further, temperature has been independently estimated by titanium-in-quartz thermometry and is consistent with an emplacement temperature of 613° ± 70°C Müller et al. (2015).

Müller et al. (2018) suggested that the pegmatite-forming melts also underwent melt-melt immiscibility, in a similar manner to what has been observed in pegmatites from the Variscan Ehrenfriedersdorf complex (Thomas et al., 2000). The immiscibility resulted in the separation of a sodium-dominated, water- and fluorine-rich melt from the main alkali and water-poor pegmatite forming melt (Müller et al., 2018). This sodium-dominated melt was responsible for the formation of the albite

(cleavelandite) zone (crystallization temperature of ~600° C) within the host pegmatite (crystallization temperature of ~680° C) (Müller et al., 2018).

If direct anatexis of the host rock was the petrogenetic mechanism that produced the pegmatites, several key questions need to be addressed: 1) What is the required pressure and temperature to partially melt the amphibolite?; 2) What is the bulk composition of that melt?; and 3) Does the melt have the trace element budget (e.g. scandium) required to generate rare element mineralization (e.g. thortveitite) in the pegmatites? Scandium is of particular interest in this study and may act as a tracer during the pegmatite forming process. Goldschmidt (1934) first hypothesized that the scandium enrichment in the pegmatites was the result of scandium being scavenged from the country rock (host amphibolite) by the pegmatite-forming melt. Bjørlykke (1935) agreed with Goldschmidt (1934) and stated that thortveitite ($Sc_2Si_2O_7$) formed as an early- to middle-stage mineral. Neumann (1961) disagreed with the Goldschmidt's hypothesis noting that the host amphibolite is not enriched in scandium and that minerals (including biotite, beryl, and columbite) from thortveitite-bearing pegmatites have higher scandium concentrations than the same minerals in thortveitite-absent pegmatites. Given that scandium is compatible in amphibole compared to a melt, particularly at lower temperatures and higher SiO_2 concentrations (Nandedkar et al., 2016), a pegmatite-forming melt in equilibrium with a residue containing amphibole is unlikely to be enriched in scandium. These issues are not exclusive to the Evje-Iveland pegmatite field or the Sveconorwegian pegmatite province. As noted above, the generation of pegmatite-forming melts by anatexis at granulite to amphibolite facies metamorphic conditions may generate abyssal

pegmatites, but is not typically associated with rare metal pegmatites (Černý and Ercit, 2005). Thus, evaluating the role of anatexis in the formation of rare element pegmatites is important to understanding the generation of pegmatites unrelated to plutonism.

In an effort to test the hypothesis that the Evje-Iveland pegmatites formed as a result of direct anatexis of the amphibolite host rock, experiments were performed in order to determine the phase relations at pressures and temperatures corresponding to amphibolite and granulite metamorphic facies. The experiments reported here elucidate the pressure and temperature conditions where melting begins, as well as the major and trace element composition of that melt.

Results of this study build on previous studies that examined the partial melting of amphibolites. Partial melting experiments have been performed on a variety of amphibolite (or basaltic) compositions at amphibolite to granulite facies pressures and temperatures in vapor-absent systems (Beard and Lofgren, 1989, 1991; Rapp, 1995; Rapp and Watson, 1995; Rapp et al., 1991; Winther and Newton, 1991; Wolf and Wyllie, 1994, 1995; Wyllie and Wolf, 1993). The results and interpretation of these previous studies can be generalized into a few important points. First, the vapor-absent solidus for a given amphibolite is strongly a function of bulk composition, and solidi have been estimated to be <750°C and up to 975° C (Rapp et al., 1991; Wolf and Wyllie, 1994; Wyllie and Wolf, 1993). Second, the temperature of the solidus is a function of pressure. Wyllie and Wolf (1993) noted that at pressures where garnet is stable, the solidus abruptly "backbends" to significantly lower temperatures. Further, Petford and Gallagher (2001), utilizing available

experimental data, determined an average global solidus for an amphibolite is ~822°C and that temperatures when partial melting occurs may exceed 900°C. Third, less than ~40% partial melting can generate melts with tonalitic-trondhjemitic compositions that are depleted in heavy rare earth elements (HREEs) (e.g. Beard and Lofgren, 1991; Rapp et al., 1991; Wolf and Wyllie, 1995). Fourth, melting first occurs at the contact between plagioclase and amphibole and the amount of melt generated is controlled by the breakdown of amphibole, with the largest melt fractions occurring after complete consumption of amphibole (Rapp et al., 1991). Reactions that occur during melting involve the consumption of amphibole and plagioclase and the production of melt and minerals including more aluminous amphibole, more calcic or chemically similar plagioclase, clinopyroxene (diopsidic augite), magnesium-rich orthopyroxene, garnet, iron-titanium oxides, and olivine (Beard and Lofgren, 1991; Rapp, 1995; Rapp and Watson, 1995; Wolf and Wyllie, 1994). Finally, in natural settings, the generation of a melt in vapor-absent systems may be the result of underplating of the crust by a basaltic magma (Petford and Gallagher, 2001; Rapp and Watson, 1995).

There is significant variability in the solidus temperature and reaction products among experimental studies. It is clear that extrapolation of experimental studies to natural processes requires that the experiments be performed on material that is compositionally similar to the study site. Extrapolation of experimental studies to natural systems with dissimilar compositions is likely to lead to inaccurate interpretations. In the case of the Evje-Iveland pegmatite field, it is not known what the composition of the unmetamorphosed amphibolite was, although it was likely

gabbroic. However, the amphibolite is the best representation of this composition. In order to elucidate the role of direct anatexis on the formation of the Evje-Iveland pegmatites partial melting experiments on the host amphibolite have been performed.

4.3. Experimental Methods

The starting material for all experiments in this study was from a massive amphibolite provided courtesy of Axel Müller, University of Oslo. The sample locality (sample 23051707b; Rosing-Schow *et al.* 2018) is 80 m from the contact of the Steli pegmatite in the Evje-Iveland pegmatite field. The whole rock composition is given in Rosing-Schow et al. (2018), as well as presented in the supplementary files. This amphibolite represents the potential source of the pegmatite-forming melt (Müller et al., 2015).

The amphibolite was processed into three physical forms: as a core, as a powder, and a powder that was sieved to produce a uniformly smaller grain size. Cores of the amphibolite were acquired using 1 or 2 mm coring drill bit. Additionally, the amphibolite sample was powdered in an alumina grinding dish within a shatterbox and an aliquot was sieved. The majority of the grains of the unsieved portion were <200 μm with a small portion between 200-400 μm and the grains of the sieved portion are <53 μm.

All experiments were conducted in a Boyd-England style end-loaded, piston-cylinder apparatus (Boyd and England, 1960), in ½ or ¾ inch talc-Pyrex assemblies. The starting material was loaded into either 3 mm outer diameter (0.126 mm wall thickness) gold capsules or 2 mm outer diameter (0.126 mm wall thickness) platinum capsules that were 4-6 mm in length and sealed by welding. Capsules were placed in

an outer MgO sleeve and packed with MgO powder, both of which were fired at 1000° C. The MgO sleeves, along with fired MgO plugs, were then placed in a graphite, a Pyrex, and a talc sleeve, and finally wrapped in thin lead foil. In each experiment either two or four capsules were included, wherein the starting material in each capsule was either a core, unsieved powder, or sieved powder (Figure 4.1; Table 4.1). In experiments containing sieved and unsieved powder, the sieved powder was placed inside of a platinum capsule to allow for easy identification after completion of the experiment. Core and unsieved powder experiments were contained in gold capsules.

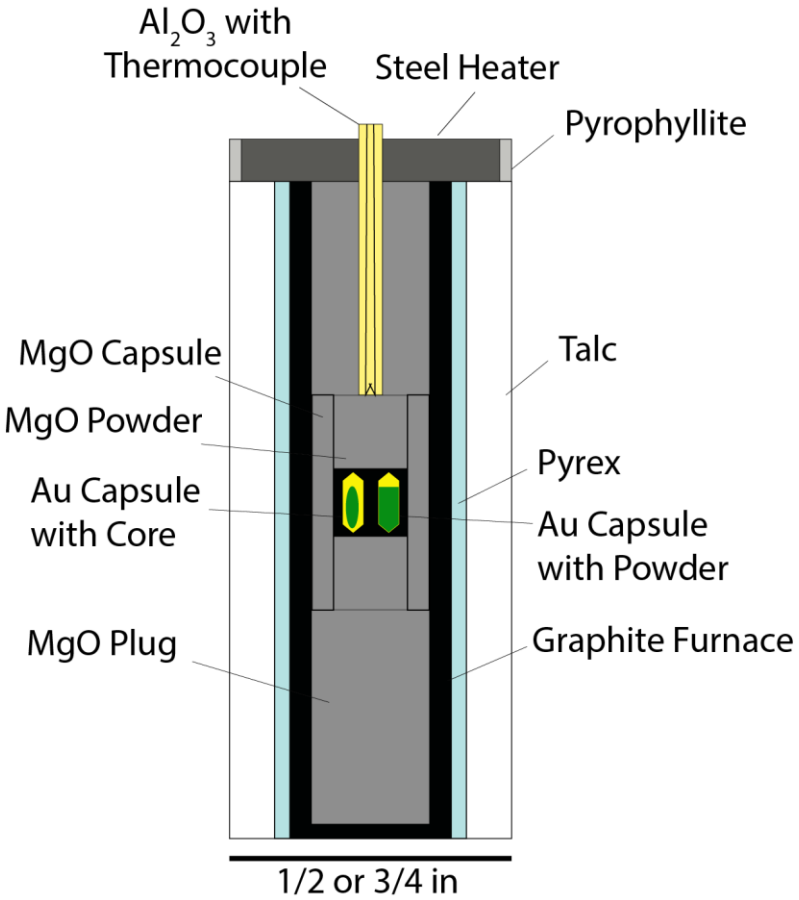

Figure 4.1: Schematic of piston-cylinder assembly. Standard ½ or ¾ inch diameter assemblies were used. .

Experiments were conducted at temperatures ranging from 700 to 1064° C and pressures between 400 and 550 MPa (Table 4.1). Temperature was measured using type-C (95%W5%Re -74%W26%Re) thermocouple. The pressure reported in Table 4.1 is the average pressure over the duration of the run. Run durations were up to 117.2 hours. A friction correction of -10% and -7.5% was used for ½ and ¾ inch assemblies, respectively. In all experiments, the assembly was first overpressurized at

Table 4.1: Experimental conditions, run products, and notes

Run	Replicates	Capsule	Starting Material	Temperature (°C)	Pressure (MPa)	Duration (Hours)	Run Product Mineralogy	Assembly Size	Notes
EIP-1	Ca	Gold	Core	700	400	117.2	No Reaction: Original Plg and Am	3/4 in	
	Pa	Gold	Powder						
	Cb	Gold	Core						
	Pb	Gold	Powder						
EIP-3	Ca	Gold	Core	800	510	24	No Reaction: Original Plg and Am	3/4 in	Thermocouple failed after 24 hours. Run spent and additional 45 hours <800°C
	Pa	Gold	Powder						
	Cb	Gold	Core						
	Pb	Gold	Powder						
EIP-4	a	Gold	Powder	900	550	69.5	Gl, Am, Pyx, Ol, Bt	1/2 in	Temperature spike at hour 19.3 to 958°C before returning to 900°C
	b	Gold	Core				Gl, Am, Pyx, Ol, Bt		
EIP-5	a	Gold	Powder	850 to 1064	520	70.6	Gl, Pyx,Ol, residual Plg	1/2 in	Temperature spike to 1064°C ~10 minutes before quenching
	b	Gold	Core				Gl, Pyx,Ol, residual Plg and Ap		
EIP-6	a	Gold	Powder	900	480	25	Trace melt, Original Plg and Am	1/2 in	Thermocouple failed after 48 hours. Run spent and additional 45 hours <900°C
	b	Platinum	Powder (<53 μm)				No Reaction: Original Plg and Am		
EIP-7	a	Gold	Powder	900	500	70.17	Gl, Plg, Am, Pyx, Sp	3/4 in	
	b	Platinum	Powder (<53 μm)				Gl, Plg, Am, Pyx, Sp, Ap		
EIP-8	b	Platinum	Powder (<53 μm)	950	510	70.3	Gl, Plg, Am, Pyx, Sp	3/4 in	Replicate "a" not recovered
EIP-9	a	Gold	Powder	950	530	71.6	Gl, Plg, Pyx	3/4 in	
	b	Platinum	Powder (<53 μm)				Gl, Plg, Pyx		

Pressure is the average pressure over the duration of each experiment. Gl = glass, Am = amphibole, Plg = plagioclase, Ol = olivine, Bt = biotite, Ap = apatite, Sp = Spinel

room temperature to allow for relaxation of the assembly during heating. The target pressure was achieved when the run reached the target temperature. At the completion of the experiment, power to the apparatus was turned off and the experiment was rapidly quenched to <100°C in several seconds by water circulating around the assembly. After quenching, the experimental capsules were mounted in epoxy and polished for analysis.

4.4. Analytical Techniques

Major element analysis and x-ray mapping were performed by using a JEOL JXA 8900R electron probe microanalyzer at the Advanced Imaging and Microscopy Laboratory, University of Maryland and a JEOL 8530F field-emission electron probe microanalyzer at the Earth and Planets Laboratory, Carnegie Institution for Science. Wavelength dispersive spectroscopy (WDS) was used to determine the concentration of Si, P, Ti, Al, Fe, Mg, Mn, Ca, Na, K, F, and Cl in the experimental run products. The electron beam conditions were an accelerating voltage of 15 kV, a current of 5 (all run product and some standards) or 20 nA (standards), and a beam size of 1-10 μm depending on the phase being analyzed and the size of that phase. Standards included Makaopuhi basalt, microcline, rhodonite, topaz, scapolite, Indian Ocean basalt, Durango apatite, Clear Lake plagioclase, Kakanui hornblende, fayalite, forsterite, fluorapatite, albite, San Carlos olivine, EnAl10 enstatite glass, TiO_2, orthoclase, sodalite, Basalt 812, Bear Lake hornblende, magnetite, and MnO_2. Elemental mapping was conducted by both wavelength dispersive spectroscopy and energy dispersive spectroscopy (EDS). All major elements that were quantitatively measured were mapped by EDS. Mg, Na, P, Ti, and Sc were mapped by WDS. The

electron beam condition for mapping was an accelerating voltage of 15 kV, a current of 20 nA, a dwell time of 20 ms, and a pixel size of 1 μm.

The abundance or mass fraction of each phase present in the run product assemblage was determined by a constrained linear least-squares method. Inherent in the application of the least-squares method is the assumption that there was no exchange of mass across the capsule walls. Given this assumption, the bulk composition of the run products is equivalent to the bulk composition of the starting material. Thus, the sum of the mass fraction of each run product phase multiplied by the composition of that phase (determined by using WDS), for each major element, should equal the bulk composition of the starting material. In order to perform this calculation, identification of all phases and the composition of those phases, as well as the bulk composition of the starting material is required. To solve these linear least-squares equations the MATLAB function *lsqlin* was used and was constrained such that the mass fraction of each phase present is greater than zero and the sum of all mass fractions is equal to one. For all least-squares calculations, iron was assumed to be FeO.

Glass and crystalline run products were analyzed by using laser ablation inductively coupled plasma mass spectrometry (LA-ICP-MS) to determine trace element abundances. LA-ICP-MS was performed using a New Wave UP213 Nd:YAG laser ablation system coupled to a ThermoFisher Element2 ICP-MS at the Plasma Mass Spectrometry Laboratory, University of Maryland. The laser spot sizes were 25 μm (15 μm in one case) for the unknowns, 80 μm for standards, and 40 μm for BHVO2G analyzed as an unknown to evaluate accuracy. The operating conditions

for the laser were 7 Hz and a power of between 2 and 4 J cm^{-1}. The standard for all analyses was NIST610 and silicon was used as the internal reference. Data reduction was performed using LAMTRACE (Jackson, 2008).

4.5. Results

4.5.1. Phase Assemblages and the Solidus

The results of the experiments are summarized in Table 4.1 and Figure 4.2. Successful experiments performed at temperatures below 900°C exhibited no observable reaction or melting. In all 700 and 800°C experiments, the original plagioclase and amphibole were the only phases present. Additionally, the texture at the end of the experiments was unchanged from the original material (Figure 4.2). In two experiments performed at 900°C (EIP-4 and EIP-7), the run products included glass (Figure 4.2A). In experiment EIP-4, glass was found in discreet pockets and the run product assemblage also included amphibole, clinopyroxene, olivine, and minor biotite. The clinopyroxene in experiment EIP-4 is found in the core of run product amphibole. The presence of olivine is thought to result from a short duration temperature spike to 958°C during the run, before returning to 900°C: it is likely that olivine is not a stable phase at 900°C. In experiment EIP-7, the glass is intermingled with plagioclase and the run products also included amphibole, clinopyroxene, plagioclase, spinel ± apatite. Unlike experiment EIP-4, the clinopyroxene is found as a discreet phase. In one experiment (EIP-6), one replicate did not show evidence of melting or subsolidus reactions; the second replicate had minor melting within plagioclase but no other reactions (Figure 4.2A). In experiments performed above 900°C all run products included a glass (Figure 4.2B). In the experiments performed

at 950°C, the minerals in the run products include plagioclase, clinopyroxene, amphibole and spinel (EIP-8), or plagioclase and clinopyroxene (EIP-9). In experiment EIP-8 the glass is intermingled with plagioclase and the clinopyroxene is found within the cores of amphibole. In experiment EIP-9, the glass is found in pockets and the clinopyroxene is present as a discreet phase. Experiment EIP-5 suffered a thermocouple failure that resulted in a runaway temperature at the completion of the experiment. The temperature of experiment EIP-5 for the majority (70.43 hours) of the run was 850°C and, after failure of the thermocouple, the temperature reached at least 1064°C (for 0.16 hours), estimated by the presence of gold spheres within the experiment, indicating the temperature was approximately the melting point of gold (Figure 4.2). The run products in experiment EIP-5 include glass, olivine, and clinopyroxene (as a discreet phase) with residual plagioclase and apatite. The texture of the residual plagioclase indicates that it was dissolving into the melt, but dissolution was halted during quench (Figure 4.2). With the failure of experiment EIP-5, constraining the solidus to a great degree of accuracy is difficult. However, the solidus is clearly greater than 800°C and in light of the phases present in the run products and the textures in experiment EIP-5, the solidus of the Evje-Iveland amphibolite at 500 MPa in vapor-absent conditions is likely close to 900°C.

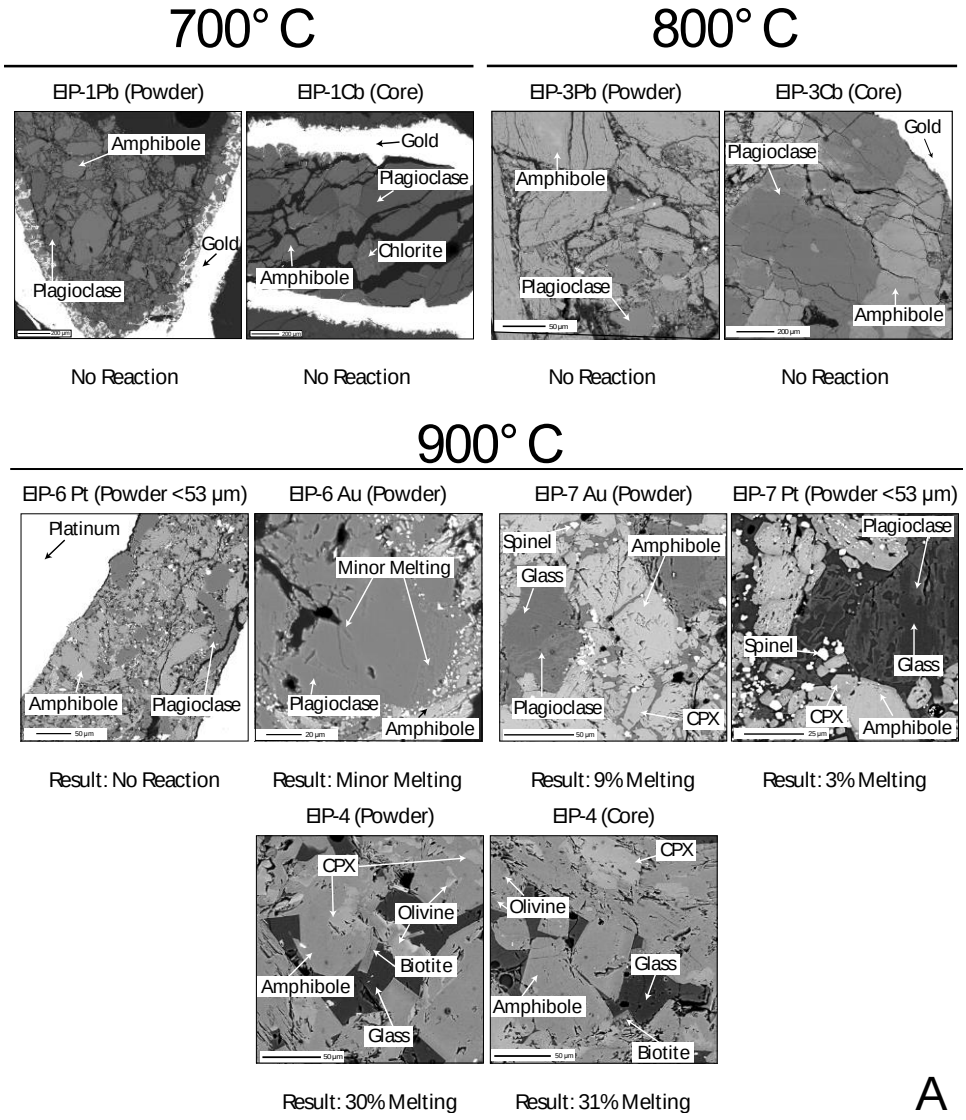
700° C
800° C
EIP-1Pb (Powder)
EIP-1Cb (Core)
EIP-3Pb (Powder)
EIP-3Cb (Core)
Amphibole
Gold
Plagioclase
Chlorite
Amphibole
Plagioclase
Amphibole
Gold
Plagioclase
Amphibole
Plagioclase
Gold
Amphibole
No Reaction
No Reaction
No Reaction
No Reaction
900° C
EIP-6 Pt (Powder <53 µm)
EIP-6 Au (Powder)
EIP-7 Au (Powder)
EIP-7 Pt (Powder <53 µm)
Platinum
Amphibole
Plagioclase
Minor Melting
Plagioclase
Amphibole
Spinel
Amphibole
Glass
Plagioclase
CPX
Plagioclase
Spinel
Glass
CPX
Amphibole
Result: No Reaction
Result: Minor Melting
Result: 9% Melting
Result: 3% Melting
EIP-4 (Powder)
EIP-4 (Core)
CPX
Olivine
Biotite
Amphibole
Glass
CPX
Olivine
Glass
Amphibole
Biotite
Result: 30% Melting
Result: 31% Melting
A

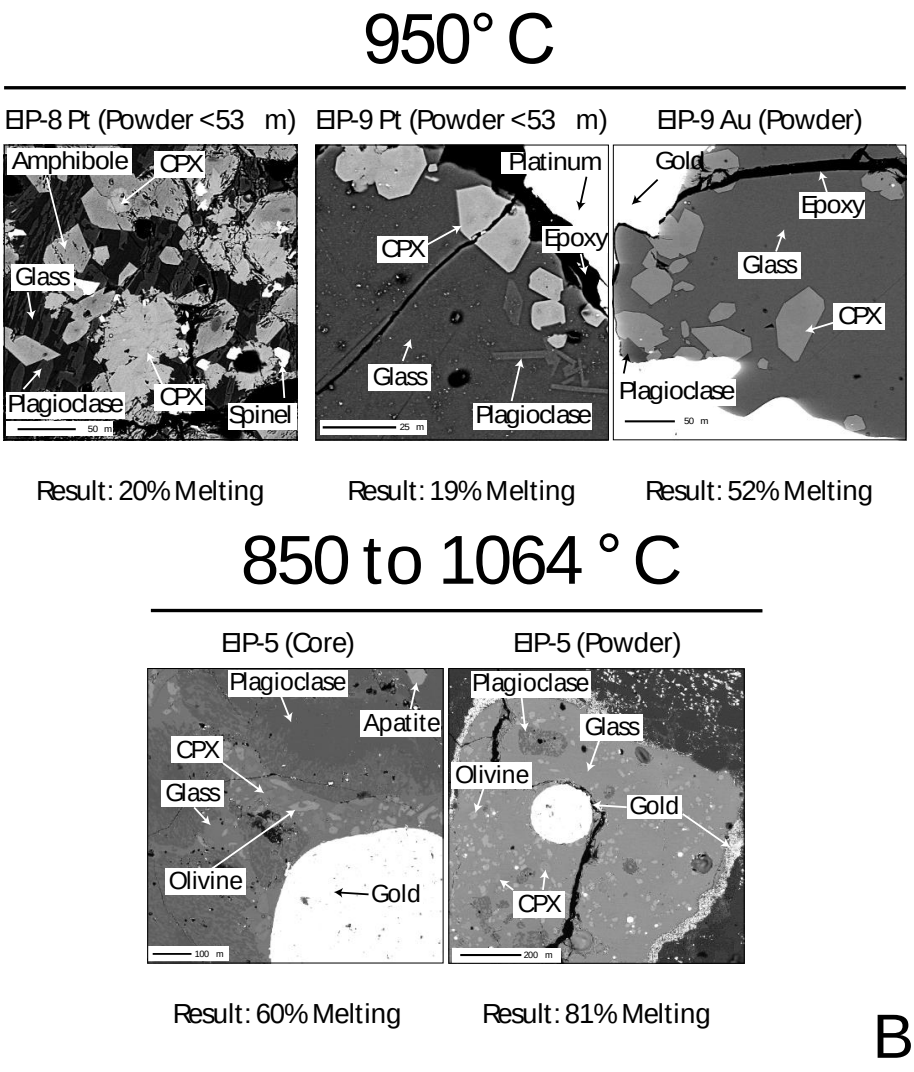

Figure 4.2: Backscatter electron images of piston-cylinder run products. Percent melting was determined by a constrained linear least-squares method (see text for details). Panel **A** are from experiments run at 700 to 900° C. Panel **B** are experiments >900° C. .

4.5.2. Major Element Composition of Run Products

4.5.2.1. Glass

The compositions of run product glasses are reported in Table 4.2 and vary in SiO_2 from 47.5 to 65.7 wt% and plotted on an anhydrous basis (normalized to 100%) in Figure 4.3. The glass at the solidus (900°C) plots as a trachyandesite (Figure 4.4). The minor amount of glass in experiment EIP-6a was not analyzed quantitatively due to the small size, but a semi-quantitative EDS analysis suggests that the SiO_2 concentration of the glass is >75% and the K_2O + Na_2O concentration is ~6 wt%. At temperatures between 900 and 950°C the glasses are trachyandesitic to dacitic in composition. At temperatures above 950°C the glasses are dacitic to basaltic (trachy) andesite. At temperatures approaching the liquidus the glasses are basaltic in composition and approaching the bulk composition of the starting material (Figure 4.4). The Al_2O_3 and Na_2O concentration of the run product glasses are also noteworthy. The run product glasses are more aluminous than the starting material with Al_2O_3 reaching up to 23 wt% (Figure 4.5) and the ASI (aluminum saturation index; molar $Al_2O_3/\left(Na_2O + K_2O + (CaO - 1.67 \cdot P_2O_5)\right)$ of the melt ranges from 0.62 to 1.91 across the range of melt compositions in different experiments (Table 4.2). Additionally, the Na_2O concentration of the glass decreases with decreasing Al_2O_3 and near the solidus is greater than 5 wt% (Figure 4.5). These changes in glass composition are the result of variations in the run temperature. The temperature of the experiments controls which phases coexists with the melt, and ultimately the proportion of melt generated. For instance, the melting of plagioclase and amphibole

results in a more aluminous and sodic melt coexisting with pyroxene, more aluminous amphibole, and less sodic plagioclase.

Early analyses of the glass in experiment EIP-4 at the University of Maryland yielded Na_2O concentrations of 11 to 12 wt%; however, repeat analyses, both at the University of Maryland and at the Earth and Planets Laboratory, prior to and after repolishing the sample yielded lower analytical totals and lower Na_2O concentrations (Table 4.2). It is likely that between analyses, the glass became hydrated and began to break down, potentially undergoing perlitization. Regardless of the cause of this breakdown, it is clear that the glasses produced at the solidus are both aluminous and sodic. It should also be noted that in the experiments performed in platinum capsules, there is significant iron loss from the glass to the platinum capsule. This phenomenon is most evident in experiment EIP-9, wherein the glass in replicate "b" (in platinum capsule) has less than half of the iron of replicate "a" (in gold capsule) (Table 4.2).

Table 4.2: Major element composition of run product glass

	EIP-4 Early Analysis		EIP-4		EIP-5		EIP-7		EIP-8	EIP-9	
Replicate	a	b	a	b	a	b	a	b	b	a	b
N	10	10	19	20	19	22	4	10	9	10	10
SiO_2	61.2 ± 0.2	59.9 ± 0.3	57.3 ± 0.2	56.2 ± 0.671	47.5 ± 0.2	49.4 ± 0.4	55.4 ± 0.4	62.0 ± 0.5	64.7 ± 0.6	53.3 ± 0.1	57.4 ± 0.2
Al_2O_3	23.9 ± 0.2	24.7 ± 0.2	21.5 ± 0.1	22.8 ± 0.537	16.8 ± 0.1	16.5 ± 0.2	21.6 ± 0.4	15.5 ± 0.2	14.8 ± 0.4	18.23 ± 0.05	17.34 ± 0.04
TiO_2	0.05 ± 0.02	0.03 ± 0.01	0.04 ± 0.01	0.2 ± 0.132	1.18 ± 0.03	0.75 ± 0.04	0.32 ± 0.05	0.53 ± 0.03	0.27 ± 0.01	0.62 ± 0.02	0.76 ± 0.02
FeO	1.35 ± 0.03	1.00 ± 0.07	1.41 ± 0.04	1.3 ± 0.371	10.7 ± 0.3	10.5 ± 0.2	4.3 ± 0.2	3.1 ± 0.2	1.65 ± 0.03	7.62 ± 0.04	2.89 ± 0.04
MgO	0.08 ± 0.02	0.04 ± 0.01	0.18 ± 0.06	0.7 ± 0.635	5.35 ± 0.09	5.0 ± 0.2	1.4 ± 0.3	2.0 ± 0.3	0.63 ± 0.02	2.35 ± 0.02	3.0 ± 0.1
MnO	0.08 ± 0.02	0.05 ± 0.01	0.058 ± 0.005	0.1 ± 0.009	0.197 ± 0.008	0.18 ± 0.01	0.08 ± 0.01	0.13 ± 0.01	0.14 ± 0.01	0.19 ± 0.01	0.16 ± 0.01
CaO	0.17 ± 0.02	0.28 ± 0.03	0.23 ± 0.04	0.9 ± 0.559	11.49 ± 0.08	9.8 ± 0.2	1.5 ± 0.2	4.5 ± 0.1	4.0 ± 0.2	5.40 ± 0.02	5.41 ± 0.04
Na_2O	11.6 ± 0.1	11.78 ± 0.08	5.6 ± 0.2	8.4 ± 0.853	3.21 ± 0.05	3.79 ± 0.09	5.7 ± 0.6	2.2 ± 0.1	1.4 ± 0.2	3.55 ± 0.03	3.1 ± 0.1
K_2O	1.68 ± 0.02	2.30 ± 0.07	1.76 ± 0.02	1.9 ± 0.201	0.77 ± 0.02	0.85 ± 0.04	2.9 ± 0.1	2.05 ± 0.03	1.91 ± 0.04	1.71 ± 0.01	1.84 ± 0.02
Cl	0.43 ± 0.01	0.32 ± 0.03	0.475 ± 0.009	0.3 ± 0.033	0.054 ± 0.004	0.076 ± 0.004	0.12 ± 0.02	0.110 ± 0.005	0.17 ± 0.01	0.11 ± 0.01	0.13 ± 0.01
F	0.06 ± 0.03	0.14 ± 0.05	0.08 ± 0.01	0.1 ± 0.000	0.29 ± 0.04	0.28 ± 0.03	b.d. to 0.08	0.12 ± 0.01	0.06 ± 0.01	0.07 ± 0.01	0.06 ± 0.01
P_2O_5	0.15 ± 0.03	0.16 ± 0.02	0.25 ± 0.03	0.3 ± 0.023	0.11 ± 0.02	0.11 ± 0.02	0.08 ± 0.03	0.17 ± 0.01	0.38 ± 0.02	0.24 ± 0.01	0.28 ± 0.02
-(F,Cl) = O	0.1	0.1	0.1	0.1	0.1	0.1	0.06	0.08	0.06	0.05	0.05
Total	100.7 ± 0.3	100.5 ± 0.4	88.8 ± 0.3	92.9 ± 1.5	97.5 ± 0.4	97.0 ± 0.6	93.4 ± 0.9	92.4 ± 0.6	90.0 ± 0.8	93.3 ± 0.1	92.3 ± 0.3
ASI	1.14	1.11	1.91	1.34	0.62	0.66	1.41	1.13	1.32	1.06	1.04

b.d. is below detection. Uncertainty is the standard deviation of the mean ($1\sigma_m$). "Early Analysis" indicates analyses of glass prior to breakdown and perlitization.

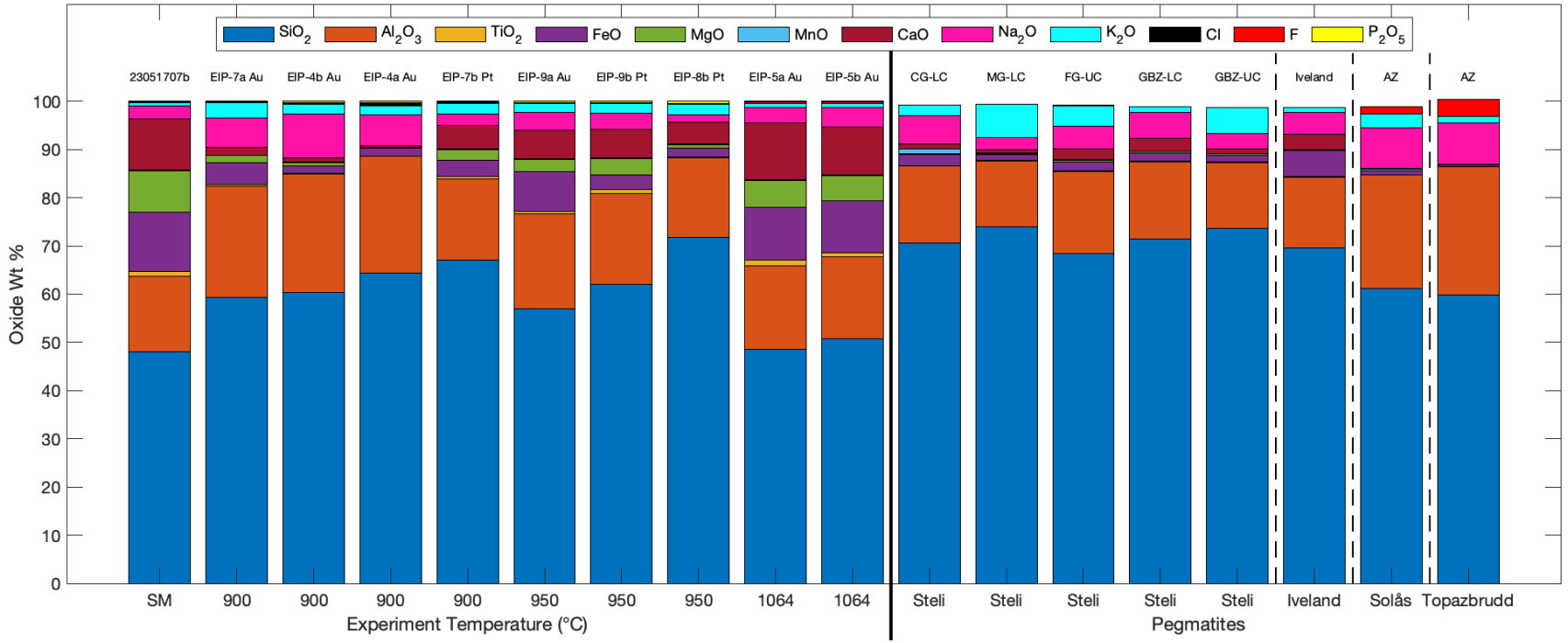

Figure 4.3: Compositions of run product glasses, the Steli and Iveland pegmatites from the Evje-Iveland pegmatite field plotted as stacked bars. All composition are normalized to 100% on an anhydrous basis. Compositions of the Steli and Iveland pegmatites are from Snook (2014) and are given in Table 4.D1. Compositions from the Solås and Topazbrudd albite zones are from Müller et al. (2018) and are given in table 4.D1. Labels along the x-axis are the temperatures (SM = starting material) of the experiments or the name of the naturally occurring pegmatite. Experiments and pegmatites are separated by a solid vertical line. Compositions of the pegmatites are separated by dashed vertical lines. Labels above the bars are the experiment or sample number, or zone from the pegmatite. CG = coarse grained, MG = medium grained, FG = Fine grained, LC = lower contact, UC = upper contact, BZ = boarder zone, AZ = albite zone

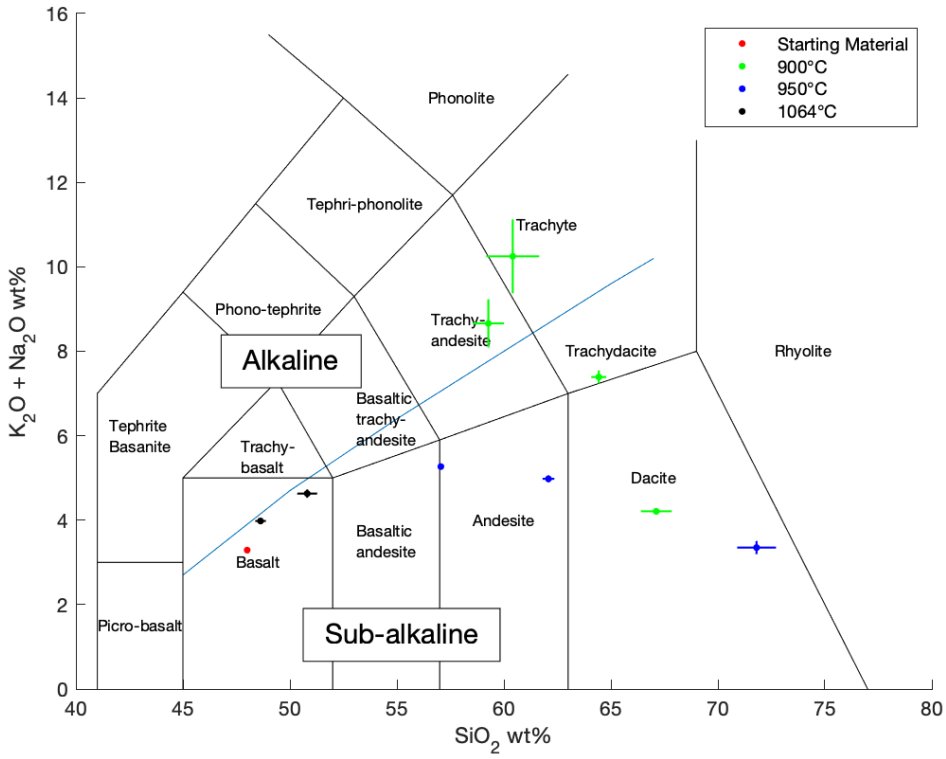

Figure 4.4: Total alkali vs silica (TAS) diagram of run product glass and starting material compositions. Uncertainty is reported as the standard deviation of the mean ($1\sigma_m$).

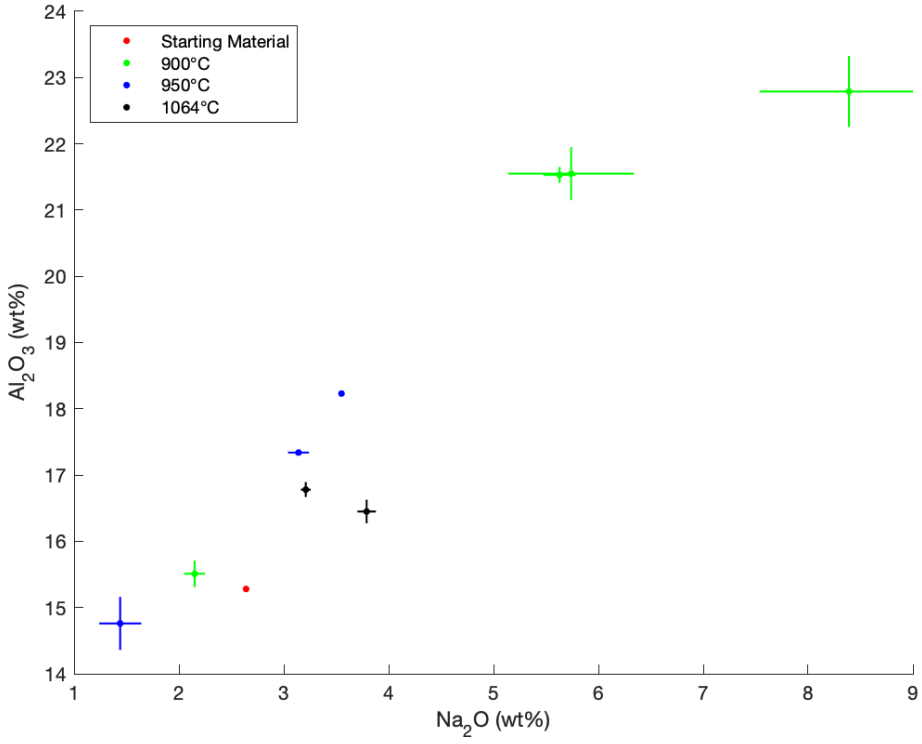

Figure 4.5: Al_2O_3 vs Na_2O (wt%) plot for run product glasses and starting material. Uncertainty is the standard deviation of the mean ($1\sigma_m$).

4.5.2.2. Amphibole

The starting amphibole is magnesiohornblende. The newly crystallized amphibole in the run products are pargasite and are more aluminous (11.5 to 17.2 wt% Al_2O_3) and sodic (1.71 to 3.18 wt% Na_2O) than the starting material (10.0 wt % Al_2O_3; 1.66 wt % Na_2O) (Table 4.3; Figure 4.6). Additionally, the starting amphibole has Fe/(Fe+Mg) of 0.46, whereas run product amphibole have Fe/(Fe+Mg) that are generally lower, ranging from 0.22 to 0.47, where Fe/(Fe+Mg) is total iron divided by total iron plus magnesium. Amphibole from experiment EIP-7 (900°C) are only slightly more aluminous (11.5 to 12.0 wt% Al_2O_3) than the starting amphibole and are

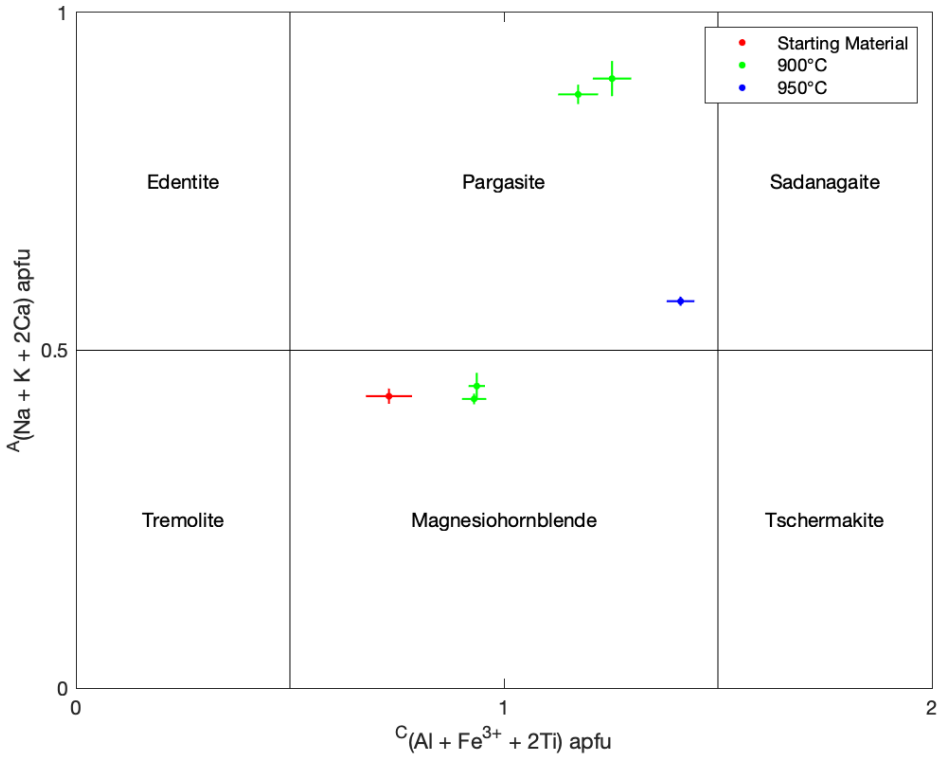

Figure 4.6: Plot of amphibole compositions for run products and starting material. Fields from Hawthorne et al. (2012). The y-axis is the (Na + K + 2Ca) in the A site. The x- axis is (Al + Fe^{3+} + 2Ti) in the C (octahedral) site. Uncertainty is the standard deviation of the mean ($1\sigma_m$).

the closest in composition to the starting amphibole (Table 4.3). As temperature increases, the amphibole become increasingly pargasitic.

4.5.2.3. Plagioclase

Plagioclase in the starting material has a composition of X_{An}^{Pl}= 0.41 to 0.45, where X_{An}^{Pl} is the mole fraction of the anorthite component in the plagioclase solid solution (Table 4.4 and supplementary files). Generally, the run product plagioclase increases in X_{An}^{Pl} with increasing temperature (Figure 4.7); however, the plagioclase composition is variable and in some cases, two plagioclase compositions coexist. For example, in both replicates of experiment EIP-7 (900°C), plagioclase exists with two distinct compositions, one with moderate X_{An}^{Pl} (0.52 and 0.56, respectively) and the other with lower X_{An}^{Pl} (0.39 and 0.46, respectively). The high X_{An}^{Pl} plagioclase represents newly crystallized plagioclase, which falls near the plagioclase solidus (Figure 4.7) and the low X_{An}^{Pl} may represent residual plagioclase, which may not have reacted completely. Experiments conducted at 950°C yield plagioclase compositions that are broadly consistent with the plagioclase solidus (X_{An}^{Pl} ranging from 0.55 to 0.66; Figure 4.7). In the highest temperature experiment (EIP-5; 1064°C) plagioclase in one replicate has an X_{An}^{Pl}= 0.76 and the other replicate has an X_{An}^{Pl}= 0.52 (Table 4.4). The large difference in plagioclase composition in experiment EIP-5 is likely due to the kinetics of crystallization and the grain size of the starting material. In this experiment, the failure of the thermocouple resulted in an abrupt increase in temperature and rapid dissolution of the starting plagioclase. As the temperature increased rapidly, the composition of the plagioclase changed and approached equilibrium with the melt, but equilibration of the larger grains was slower than the

rate of temperature increase. In replicate EIP-5a the starting material was a powder, with smaller grain size than the core in replicate EIP-5b, and the result was a shorter equilibration time in replicate EIP-5a and higher X_{An}^{Pl} than replicate EIP-5b.

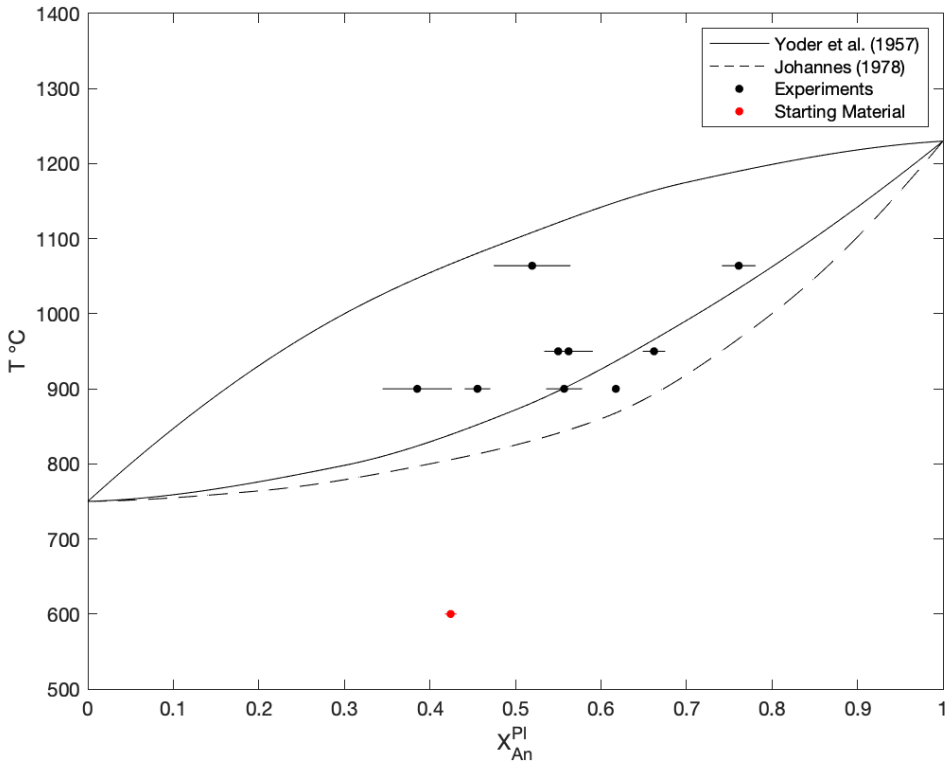

Figure 4.7: Phase diagram for run product and starting material plagioclase. X_{An}^{Pl} is the mole fraction of the anorthite component in the plagioclase solid solution. Solid lines are the solidus and liquids determined by Yoder et al. (1957) at 500 MPa. Dashed line represents the solidus determined by Johannes (1978) at 500 MPa. Uncertainty is the standard deviation of the mean ($1\sigma_m$). Temperature of the starting material is arbitrary.

Table 4.3: Major element composition and formulas of starting and run product amphibole

	23051707b	EIP-4		EIP-7		EIP-8
Replicate		a	b	a	b	b
N	10	23	19	10	9	8
SiO_2	44.9 ± 0.3	40.6 ± 0.3	41.1 ± 0.3	44.7 ± 0.1	44.3 ± 0.2	41.0 ± 0.3
Al_2O_3	10.0 ± 0.3	17.1 ± 0.4	17.2 ± 0.4	11.5 ± 0.1	12.0 ± 0.2	15.0 ± 0.3
TiO_2	1.12 ± 0.05	1.7 ± 0.2	1.3 ± 0.2	1.20 ± 0.02	1.22 ± 0.03	2.18 ± 0.06
FeO	17.1 ± 0.2	8.7 ± 0.2	8.0 ± 0.2	16.9 ± 0.2	17.6 ± 0.2	9.5 ± 0.2
MgO	11.0 ± 0.1	14.9 ± 0.1	15.7 ± 0.1	11.6 ± 0.1	11.0 ± 0.1	17.3 ± 0.3
MnO	0.29 ± 0.02	0.145 ± 0.008	0.14 ± 0.01	0.269 ± 0.006	0.27 ± 0.01	0.21 ± 0.02
CaO	11.59 ± 0.06	12.8 ± 0.4	12.4 ± 0.1	11.82 ± 0.02	11.73 ± 0.04	11.7 ± 0.1
Na_2O	1.66 ± 0.04	3.01 ± 0.09	3.18 ± 0.05	1.71 ± 0.03	1.82 ± 0.07	2.72 ± 0.03
K_2O	0.57 ± 0.03	0.65 ± 0.03	0.66 ± 0.02	0.62 ± 0.01	0.61 ± 0.03	0.39 ± 0.01
Cl	n.a.	0.023 ± 0.002	0.020 ± 0.002	0.07 ± 0.01	0.077 ± 0.006	0.026 ± 0.005
F	n.a.	0.30 ± 0.03	0.22 ± 0.02	0.07 ± 0.02	b.d. to 0.1	b.d. to 0.05123
P_2O_5	0.03 ± 0.01	0.051 ± 0.009	0.05 ± 0.01	b.d. to 0.02	0.06 ± 0.02	0.07 ± 0.01
-(F,Cl) = O	0	0.1	0.1	0.02	0.06	0.03
Total	98.2 ± 0.5	99.8 ± 0.7	99.9 ± 0.6	100.4 ± 0.3	100.8 ± 0.4	100.2 ± 0.5
H_2O	1.77 ± 0.01	1.59 ± 0.04	1.72 ± 0.05	1.76 ± 0.01	1.74 ± 0.01	1.62 ± 0.09
Formula						
Tetrahedral (T Site) Cations						
Si	6.68 ± 0.04	5.78 ± 0.05	5.82 ± 0.05	6.47 ± 0.01	6.43 ± 0.02	5.76 ± 0.04
Al	1.32 ± 0.04	2.21 ± 0.05	2.17 ± 0.05	1.53 ± 0.01	1.57 ± 0.03	2.23 ± 0.04
P	0.0034 ± 0.0009	0.006 ± 0.001	0.00658 ± 0.00168	b.d. to 0.002	0.007 ± 0.002	0.00849 ± 0.00134
Total	8.00 ± 0.06	8.00 ± 0.07	8.00 ± 0.08	8.00 ± 0.02	8.00 ± 0.03	8.00 ± 0.05
Octahedral (C Site) Cations						
Al	0.42 ± 0.02	0.66 ± 0.02	0.70 ± 0.02	0.44 ± 0.02	0.490 ± 0.009	0.26 ± 0.02
Ti	0.125 ± 0.006	0.18 ± 0.02	0.14 ± 0.02	0.131 ± 0.003	0.133 ± 0.004	0.230 ± 0.006
Fe^{3+}	0.06 ± 0.05	0.24 ± 0.02	0.20 ± 0.01	0.23 ± 0.02	0.18 ± 0.02	0.70 ± 0.03
Fe^{2+}	2.07 ± 0.03	0.80 ± 0.05	0.75 ± 0.05	1.82 ± 0.02	1.95 ± 0.03	0.41 ± 0.03
Mg	2.45 ± 0.03	3.16 ± 0.03	3.32 ± 0.03	2.51 ± 0.02	2.39 ± 0.03	3.62 ± 0.05
Mn	0.036 ± 0.002	0.017 ± 0.001	0.017 ± 0.001	0.033 ± 0.001	0.034 ± 0.002	0.025 ± 0.002
Total	5.15 ± 0.07	5.05 ± 0.06	5.11 ± 0.07	5.17 ± 0.04	5.18 ± 0.04	5.24 ± 0.07
B Site Cations						
Ca	1.846 ± 0.008	1.95 ± 0.05	1.89 ± 0.01	1.835 ± 0.003	1.823 ± 0.005	1.76 ± 0.02
Na	0.15 ± 0.01	0.05 ± 0.03	0.11 ± 0.01	0.165 ± 0.007	0.18 ± 0.02	0.24 ± 0.01
Total	2.00 ± 0.01	2.00 ± 0.06	2.00 ± 0.02	2.000 ± 0.008	2.00 ± 0.02	2.00 ± 0.02
A Site Cations						
Na	0.32 ± 0.01	0.78 ± 0.03	0.76 ± 0.01	0.314 ± 0.007	0.33 ± 0.02	0.50 ± 0.01
K	0.107 ± 0.005	0.119 ± 0.005	0.119 ± 0.003	0.114 ± 0.003	0.113 ± 0.005	0.071 ± 0.002
Total	0.43 ± 0.01	0.90 ± 0.03	0.88 ± 0.01	0.428 ± 0.008	0.45 ± 0.02	0.573 ± 0.007
Hydroxyl Site						
Cl	n.a.	0.0056 ± 0.0004	0.0047 ± 0.0005	0.017 ± 0.002	0.019 ± 0.001	0.006 ± 0.001
F	n.a.	0.13 ± 0.01	0.095 ± 0.009	0.030 ± 0.008	b.d. to 0.04	b.d. 0.02
OH	1.75 ± 0.01	1.49 ± 0.04	1.61 ± 0.05	1.680 ± 0.008	1.66 ± 0.01	1.48 ± 0.01
Total	1.75 ± 0.01	1.63 ± 0.04	1.71 ± 0.05	1.73 ± 0.01	1.72 ± 0.01	1.51 ± 0.01
Fe/(Fe+Mg)	0.46 ± 0.01	0.25 ± 0.01	0.22 ± 0.01	0.45 ± 0.01	0.47 ± 0.01	0.23 ± 0.01

Amphibole formulas calculated after the method of Hawthorne et al. (2012). n.a. is not analyzed. b.d. is below detection. Fe/(Fe+Mg) is total iron divided by total iron plus magnesium. Uncertainty is the standard deviation of the mean ($1\sigma_m$)

Table 4.4: Major element composition of run product plagioclase

	23051707b	EIP-5		EIP-7			EIP-8		EIP-9	
Replicate		a	b	a	a	b	b	b	a	b
N	8	10	8	7	3	6	1	7	3	1
SiO_2	57.4 ± 0.2	49.2 ± 0.4	55 ± 1	57.6 ± 0.7	54 ± 1	56.7 ± 0.3	53.5	54.7 ± 0.2	53.7 ± 0.4	50.07
Al_2O_3	26.7 ± 0.1	30.4 ± 0.8	27.4 ± 0.5	27.0 ± 0.8	29.8 ± 0.1	28.0 ± 0.2	28.6	27.9 ± 0.4	28.8 ± 0.9	29.95
TiO_2	0.03 ± 0.01	0.17 ± 0.06	0.08 ± 0.04	0.04 ± 0.02	0.05104 ± 0.01511	0.04 ± 0.01	0.09	0.06 ± 0.01	0.07 ± 0.05	0.06
FeO	0.06 ± 0.02	2.1 ± 0.5	0.7 ± 0.5	0.8 ± 0.2	0.70 ± 0.02	0.30 ± 0.02	0.97	0.97 ± 0.07	0.9 ± 0.3	0.79
MgO	0.01 ± 0.00	0.7 ± 0.3	0.3 ± 0.3	0.06 ± 0.04	0.047 ± 0.007	b.d. to 0.03	0.3	0.1 ± 0.0	0.2 ± 0.1	1.13
MnO	0.03 ± 0.01	0.04 ± 0.01	0.07 ± 0.02	0.02 ± 0.01	b.d.	b.d. to 0.02	b.d.	0.039 ± 0.007	b.d. to 0.05	b.d.
CaO	8.6 ± 0.1	14.9 ± 0.3	10.1 ± 0.7	7.9 ± 0.8	11.6 ± 0.2	9.7 ± 0.3	12.5	11.1 ± 0.2	11.6 ± 0.5	13.54
Na_2O	6.41 ± 0.06	2.5 ± 0.1	5.1 ± 0.4	6.7 ± 0.4	4.9 ± 0.2	6.3 ± 0.2	4.0	4.9 ± 0.2	4.9 ± 0.1	3.70
K_2O	0.086 ± 0.006	0.17 ± 0.03	0.14 ± 0.03	0.5 ± 0.2	0.2 ± 0.1	0.12 ± 0.02	0.43	0.28 ± 0.04	0.25 ± 0.08	0.17
Cl	n.a.	b.d.	b.d.	0.022 ± 0.007	0.0267 ± 0.0006	b.d.	0.03	0.03 ± 0.01	0.03 ± 0.01	0.08
F	n.a.	b.d.	b.d.	b.d.	b.d. to 0.05441	0.07 ± 0.01	b.d.	b.d.	b.d.	b.d.
P_2O_5	0.02 ± 0.02	b.d.	b.d.	0.06 ± 0.01	0.08679 ± 0.00865	b.d. to 0.03	0.04	0.07 ± 0.01	0.06 ± 0.05	0.03
-(F,Cl) =	-	-	-	0.005	0.03	0.03	0.01	0.006	0.006	0.02
Total	99.3 ± 0.3	100 ± 1	99 ± 1	101 ± 1	101 ± 1	101.3 ± 0.4	100.4	100.1 ± 0.5	101 ± 1	99.54
					Formulas					
Si	2.585 ± 0.006	2.27 ± 0.01	2.51 ± 0.04	2.57 ± 0.03	2.41 ± 0.01	2.52 ± 0.01	2.4	2.47 ± 0.01	2.43 ± 0.03	2.30
Al	1.416 ± 0.006	1.65 ± 0.04	1.47 ± 0.03	1.42 ± 0.03	1.57 ± 0.01	1.47 ± 0.01	1.5	1.49 ± 0.01	1.53 ± 0.04	1.63
Ti	0.0009 ± 0.0002	0.006 ± 0.002	0.003 ± 0.001	0.0015 ± 0.0005	0.0017 0.0008	0.0012 ± 0.0003	0.003	0.0022 ± 0.0005	0.002 ± 0.001	0.002
Fe	0.0024 ± 0.0006	0.08 ± 0.02	0.03 ± 0.02	0.028 ± 0.008	0.026 ± 0.001	0.0112 ± 0.0009	0.04	0.037 ± 0.003	0.03 ± 0.01	0.03
Mg	0.0008 ± 0.0002	0.05 ± 0.02	0.02 ± 0.01	0.004 ± 0.002	0.0032 0.0006	0.0021 ± 0.0005	0.02	0.007 ± 0.001	0.013 ± 0.007	0.08
Mn	0.0010 ± 0.0003	0.0016 ± 0.0005	0.003 ± 0.001	0.0008 ± 0.0002	b.d.	0.0006 ± 0.0001	b.d.	0.0015 ± 0.0003	0.0020 ± 0.0007	
Ca	0.416 ± 0.006	0.74 ± 0.01	0.49 ± 0.03	0.38 ± 0.03	0.555 ± 0.014	0.46 ± 0.01	0.6	0.54 ± 0.01	0.56 ± 0.02	0.67
Na	0.560 ± 0.005	0.22 ± 0.01	0.45 ± 0.03	0.58 ± 0.04	0.426 ± 0.024	0.54 ± 0.01	0.4	0.43 ± 0.02	0.42 ± 0.01	0.33
K	0.0049 ± 0.0003	0.010 ± 0.002	0.008 ± 0.002	0.03 ± 0.01	0.014 ± 0.004	0.0067 ± 0.0009	0.02	0.016 ± 0.003	0.014 ± 0.004	0.01
Cl	0.0007 ± 0.0006	n.a.	n.a.	0.002 ± 0.001	0.00203 ± 0.00083	b.d.	0.002	0.0022 ± 0.0005	0.0020 ± 0.0008	0.01
F	n.a.	n.a.	n.a.	b.d.	b.d. to 0.008	0.010 ± 0.002	b.d.	b.d.	b.d.	b.d.
P	n.a.	b.d.	n.a.	0.0023 ± 0.0006	0.003 ± 0.001	0.0013 ± 0.0002	0.002	0.0026 ± 0.0006	0.002 ± 0.001	0.001
X_{An}^{Plag}	0.424 ± 0.007	0.76 ± 0.02	0.52 ± 0.04	0.39 ± 0.04	0.557 ± 0.021	0.46 ± 0.01	0.6	0.55 ± 0.01	0.56 ± 0.03	0.66
X_{Ab}^{Plag}	0.571 ± 0.007	0.23 ± 0.01	0.47 ± 0.04	0.59 ± 0.05	0.43 ± 0.03	0.54 ± 0.02	0.4	0.44 ± 0.01	0.42 ± 0.02	0.33
X_{Or}^{Plag}	0.0050 ± 0.0003	0.010 ± 0.002	0.009 ± 0.002	0.03 ± 0.01	0.014 ± 0.004	0.007 ± 0.001	0.03	0.017 ± 0.003	0.014 ± 0.004	0.01

n.a. is not available. b.d. is below detection. Uncertainty is the standard deviation of the mean ($1\sigma_m$)

4.5.2.4. Pyroxene

Run product pyroxene is present in all experiments containing glass. The run product pyroxene has a composition that plots within the enstatite-ferrosilite-hedenbergite-diopside quadrilateral, and are augite and diopside (Figure 4.8). All run product pyroxene is aluminum-rich with between 0.1 (2.5 wt% Al_2O_3) and 0.56 (12.8 wt% Al_2O_3) aluminum per formula unit (apfu) (Table 4.5). In four experiments two pyroxenes coexist, wherein one is a low-aluminum pyroxene and the other is a high-aluminum pyroxene relative to each other, e.g. 6.4 vs 12.8 wt% Al_2O_3 in replicate EIP-4a. Generally, the low-aluminum pyroxene is less abundant than the high-aluminum pyroxene.

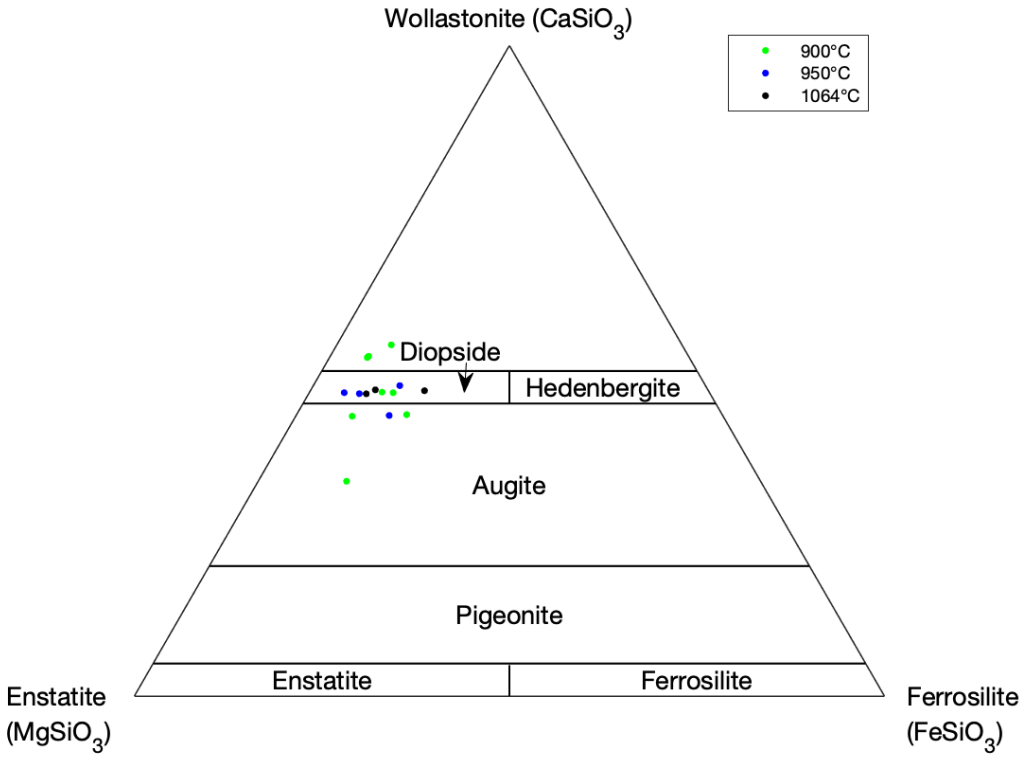

Figure 4.8: Ternary diagram of pyroxene compositions.

Table 4.5: Major element composition of run product pyroxene

	EIP-4					EIP-5			EIP-7	
Replicate	a	a	b	b	a	a	b		a	
N	15	1	13	1	10	1	11		8	
SiO_2	43.5 ± 0.3	49.0	44.8 ± 0.4	45.9	47.9 ± 0.7	47.9	48.5 ± 0.3		51.9 ± 0.3	
Al_2O_3	12.8 ± 0.3	6.4	11.5 ± 0.6	4.7	5.2 ± 0.3	10.1	4.8 ± 0.2		2.9 ± 0.2	
TiO_2	2.18 ± 0.07	1.2	1.62 ± 0.09	0.72	0.83 ± 0.04	1.2	0.61 ± 0.03		0.50 ± 0.05	
FeO	3.8 ± 0.4	3.0	2.7 ± 0.3	8.5	4.2 ± 0.6	7.9	4.8 ± 0.3		6.4 ± 0.1	
Fe_2O_3	3.8 ± 0.5	3.2	3.8 ± 0.4	b.d.	7 ± 1	0.91	6.4 ± 0.3		4.0 ± 0.1	
MgO	11.3 ± 0.3	14.3	12.7 ± 0.2	22.5	14.3 ± 0.9	11.0	13.8 ± 0.3		13.5 ± 0.1	
MnO	0.12 ± 0.01	0.13	0.134 ± 0.007	0.19	0.23 ± 0.02	0.16	0.22 ± 0.01		0.42 ± 0.02	
CaO	22.0 ± 0.4	24.1	21.6 ± 0.7	18.8	20.1 ± 0.8	19.1	20.4 ± 0.3		20.8 ± 0.1	
Na_2O	0.7 ± 0.1	0.39	0.7 ± 0.1	0.26	0.36 ± 0.02	1.2	0.31 ± 0.01		1.4 ± 0.1	
K_2O	0.08 ± 0.03	b.d.	0.14 ± 0.04	0.04	0.018 ± 0.004	0.25	0.028 ± 0.005		0.03 ± 0.01	
Cl	0.014 ± 0.001	b.d.	0.019 ± 0.003	b.d.	0.017 ± 0.002	0.04	0.012 ± 0.001		0.018 ± 0.005	
F	0.14 ± 0.02	b.d.	0.30 ± 0.04	b.d.	0.14 ± 0.02	b.d.	0.28 ± 0.03		0.07 ± 0.01	
P_2O_5	0.051 ± 0.002	0.08	0.056 ± 0.008	b.d.	0.11 ± 0.01	b.d.	0.044 ± 0.008		0.07 ± 0.01	
-(F,Cl) = O	0.06	-	0.13	-	0.06	0.01	0.12		0.03	
Total	100.4 ± 0.9	101.8	100 ± 1	101.7	100 ± 2	99.8	100.1 ± 0.7		102.0 ± 0.4	
Formulas										
Si	1.61 ± 0.01	1.8	1.66 ± 0.01	1.7	1.79 ± 0.03	1.8	1.811 ± 0.007		1.890 ± 0.009	
Al	0.56 ± 0.01	0.27	0.50 ± 0.03	0.2	0.23 ± 0.01	0.44	0.21 ± 0.01		0.124 ± 0.008	
Ti	0.061 ± 0.002	0.03	0.045 ± 0.003	0.02	0.023 ± 0.001	0.03	0.017 ± 0.001		0.014 ± 0.001	
Fe	0.12 ± 0.01	0.09	0.083 ± 0.008	0.26	0.13 ± 0.02	0.24	0.15 ± 0.01		0.195 ± 0.004	
Fe^{3+}	0.10 ± 0.01	0.09	0.105 ± 0.009	-	0.19 ± 0.03	0.03	0.179 ± 0.006		0.110 ± 0.004	
Mg	0.63 ± 0.01	0.77	0.70 ± 0.01	1.2	0.79 ± 0.04	0.61	0.77 ± 0.02		0.736 ± 0.006	
Mn	0.0037 ± 0.0003	0.00	0.0042 ± 0.0002	0.006	0.0072 ± 0.0004	0.005	0.0069 ± 0.0002		0.0130 ± 0.0006	
Ca	0.87 ± 0.02	0.94	0.86 ± 0.03	0.74	0.80 ± 0.04	0.76	0.82 ± 0.01		0.814 ± 0.005	
Na	0.050 ± 0.008	0.03	0.051 ± 0.009	0.02	0.026 ± 0.001	0.09	0.0226 ± 0.0007		0.100 ± 0.008	
K	0.004 ± 0.002	b.d.	0.006 ± 0.002	0.002	0.0009 ± 0.0002	0.01	0.0014 ± 0.0002		0.0013 ± 0.0004	
Cl	0.0009 ± 0.0001	b.d.	0.0012 ± 0.0002	b.d.	0.0011 ± 0.0001	0.003	0.0007 ± 0.0001		0.0011 ± 0.0003	
F	0.01604 ± 0.00001	b.d.	0.035 ± 0.003	b.d.	0.017 ± 0.004	b.d.	0.033 ± 0.002		0.008 ± 0.002	
P	0.00160 ± 0.00008	0.003	0.0018 ± 0.0003	b.d.	0.0033 ± 0.0003	b.d.	0.0014 ± 0.0003		0.0020 ± 0.0004	
X_{Wo}^{Pyx}	0.54 ± 0.01	0.52	0.52 ± 0.02	0.33	0.47 ± 0.03	0.47	0.471 ± 0.009		0.467 ± 0.004	
X_{En}^{Pyx}	0.39 ± 0.01	0.43	0.43 ± 0.01	0.55	0.46 ± 0.03	0.38	0.44 ± 0.01		0.422 ± 0.004	
X_{Fs}^{Pyx}	0.072 ± 0.008	0.05	0.051 ± 0.005	0.12	0.08 ± 0.01	0.15	0.086 ± 0.008		0.112 ± 0.002	
Q	1.62 ± 0.03	1.8	1.64 ± 0.03	2.2	1.73 ± 0.06	1.6	1.74 ± 0.02		1.744 ± 0.009	
J	0.10 ± 0.02	0.05	0.10 ± 0.02	0.04	0.052 ± 0.003	0.18	0.045 ± 0.001		0.20 ± 0.02	

Fe_2O_3 calculated after the method of Droop (1987). Q = Fe + Mg + Ca. J = 2Na. n.a. is not available. b.d. is below detection. Uncertainty is the standard deviation of the mean ($1\sigma_m$)

Table 4.5 cont.

	EIP-7		EIP-8			EIP-9		
Replicate	a	b	b	b	a	a	b	
N	2	1	2	6	6	11	9	
SiO_2	51 ± 3	52.6	50.7 ± 0.7	45.8 ± 0.3	51.5 ± 0.3	49.0 ± 0.1	50.5 ± 0.4	
Al_2O_3	6.5 ± 0.8	2.5	5.2 ± 0.2	8.1 ± 0.3	2.9 ± 0.4	5.6 ± 0.2	4.2 ± 0.4	
TiO_2	0.7 ± 0.2	0.32	0.68 ± 0.03	1.45 ± 0.09	0.41 ± 0.05	0.76 ± 0.03	0.58 ± 0.06	
FeO	7 ± 2	4.7	5.7 ± 0.8	3.8 ± 0.1	7.5 ± 0.2	6.7 ± 0.2	2.8 ± 0.3	
Fe_2O_3	4.2	3.1	3 ± 1	6.2 ± 0.1	2.9 ± 0.2	4.2 ± 0.2	3.8 ± 0.3	
MgO	11.9 ± 0.5	17.2	14.58 ± 0.01	14.8 ± 0.3	15.2 ± 0.3	13.3 ± 0.2	16.3 ± 0.3	
MnO	0.3 ± 0.0	0.50	0.41 ± 0.03	0.27 ± 0.02	0.33 ± 0.01	0.27 ± 0.01	0.37 ± 0.03	
CaO	17 ± 2	20.9	21.8 ± 0.4	20.5 ± 0.2	20.5 ± 0.2	21.7 ± 0.2	21.7 ± 0.2	
Na_2O	2.5 ± 0.5	0.40	0.54 ± 0.01	0.48 ± 0.02	0.42 ± 0.04	0.55 ± 0.03	0.50 ± 0.02	
K_2O	0.35 ± 0.01	b.d.	b.d. 0.05	0.026 ± 0.004	0.02 ± 0.01	0.025 ± 0.004	0.04 ± 0.01	
Cl	b.d. to 0.04	0.01	b.d.	0.016 ± 0.001	0.016 ± 0.001	0.015 ± 0.001	0.03 ± 0.01	
F	b.d.	b.d.	b.d.	b.d. to 0.05	0.07 ± 0.03	0.07 ± 0.01	b.d. to 0.08341	
P_2O_5	b.d.	b.d.	0.046 ± 0.004	b.d. to 0.07	0.04 ± 0.01	0.033 ± 0.008	0.05 ± 0.01	
-(F,Cl) = O	0.01	0.00	-	0.03	0.04	0.03	0.04	
Total	102 ± 5	102.2	103 ± 2	101.5 ± 0.6	101.8 ± 0.7	102.1 ± 0.4	100.8 ± 0.8	
Si	1.9 ± 0.1	1.9	1.83 ± 0.02	1.67 ± 0.01	1.88 ± 0.01	1.791 ± 0.004	1.84 ± 0.01	
Al	0.28 ± 0.04	0.11	0.22 ± 0.01	0.35 ± 0.01	0.13 ± 0.02	0.24 ± 0.01	0.18 ± 0.02	
Ti	0.01 ± 0.005	0.01	0.018 ± 0.001	0.040 ± 0.002	0.011 ± 0.001	0.021 ± 0.001	0.016 ± 0.002	
Fe	0.22 ± 0.06	0.14	0.17 ± 0.02	0.116 ± 0.004	0.23 ± 0.01	0.20 ± 0.01	0.08 ± 0.01	
Fe^{3+}	0.12	0.08	0.08 ± 0.03	0.170 ± 0.003	0.08 ± 0.01	0.115 ± 0.004	0.10 ± 0.01	
Mg	0.64 ± 0.03	0.92	0.783 ± 0.003	0.80 ± 0.02	0.83 ± 0.02	0.73 ± 0.01	0.88 ± 0.01	
Mn	0.01 ± 0.001	0.02	0.013 ± 0.001	0.008 ± 0.001	0.0101 ± 0.0003	0.01 ± 0.00	0.011 ± 0.001	
Ca	0.66 ± 0.07	0.80	0.84 ± 0.02	0.80 ± 0.01	0.80 ± 0.01	0.85 ± 0.01	0.85 ± 0.01	
Na	0.17 ± 0.04	0.03	0.0376 ± 0.0003	0.034 ± 0.002	0.030 ± 0.003	0.039 ± 0.002	0.036 ± 0.001	
K	0.01 ± 0.0006	b.d.	b.d. 0.0023	b.d. to 0.001	0.0011 ± 0.0003	0.0011 ± 0.0002	0.0019 ± 0.0004	
Cl	b.d. to 0.0027	0.001	b.d.	b.d. to 0.001	0.0010 ± 0.0000	0.0009 ± 0.0001	0.0019 ± 0.0003	
F	b.d.	b.d.	b.d.	b.d. to 0.0063	0.009 ± 0.003	0.008 ± 0.002	b.d. to 0.0096	
P	b.d.	b.d.	0.0014 ± 0.0001	b.d. to 0.0021	0.0014 ± 0.0002	0.0010 ± 0.0003	0.0015 ± 0.0005	
X_{Wo}^{Pyx}	0.43 ± 0.05	0.43	0.47 ± 0.01	0.465 ± 0.007	0.432 ± 0.006	0.478 ± 0.005	0.467 ± 0.006	
X_{En}^{Pyx}	0.42 ± 0.04	0.49	0.44 ± 0.01	0.468 ± 0.011	0.445 ± 0.009	0.41 ± 0.01	0.49 ± 0.01	
X_{Fs}^{Pyx}	0.15 ± 0.04	0.07	0.10 ± 0.01	0.067 ± 0.002	0.124 ± 0.003	0.115 ± 0.004	0.046 ± 0.004	
Q	1.5 ± 0.1	1.9	1.80 ± 0.03	1.72 ± 0.02	1.86 ± 0.02	1.78 ± 0.01	1.81 ± 0.02	
J	0.35 ± 0.07	0.06	0.075 ± 0.001	0.068 ± 0.003	0.060 ± 0.005	0.078 ± 0.005	0.071 ± 0.003	

4.5.2.5. Olivine

Olivine is only present as a run product phase in two experiments: EIP-4 and EIP-5. Run product olivine in experiment EIP-4 (900°C) has X_{Fo}^{Ol} that ranges from 0.67 to 0.8, where X_{Fo}^{Ol} is defined as the mole fraction of the forsterite (Mg_2SiO_4) component in the olivine solid solution. In replicate EIP-4a, there are coexisting olivine with variable X_{Fo}^{Ol}, one with a X_{Fo}^{Ol} = 0.80 and one with a X_{Fo}^{Ol} = 0.67; whereas in replicate EIP-4b the olivine has X_{Fo}^{Ol} = 0.74 (Table 4.6). The low X_{Fo}^{Ol} olivine is less abundant than the high X_{Fo}^{Ol} in replicate EIP-4a. As mentioned the olivine in experiment is likely the result of a short duration temperature spike to above 950° C. Upon cooling to the run temperature (950° C) after this spike the olivine attempts to re-equilibrate resulting in two olivine compositions. In experiment EIP-5 (1064°C), where olivine did not undergo re-equilibration at a lower temperature the olivine has an X_{Fo}^{Ol} that range from 0.63 to 0.67.

4.5.2.6. Miscellaneous Crystalline Phases

There are several additional crystalline phases that occur as minor phases in the starting material and as run products in a small number of experiments. These phases include biotite, oxides, and apatite. Biotite is only present in experiment EIP-4 (900°C) and has a X_{Phl}^{Bt} of 0.74 to 0.77 (Table 4.7), where the X_{Phl}^{Bt} is the mole fraction of the phlogopite component in the biotite solid solution, which is defined as the fraction of magnesium in the octahedral site. The limited occurrence of biotite in the run products is likely due to the minor concentration of K_2O (0.65 wt%) in the starting material. The starting material contains ilmenite (Table 4.8); however, oxides are absent the in the majority of experimental run products, occurring only in

experiments EIP-7 and EIP-8. In replicates EIP-7a and EIP-8b the oxides are titanium-rich magnetite and in replicate EIP-7b the oxides are iron-rich ulvöspinel (Table 4.8). Apatite occurs in the starting material and as a residual unreacted phase in replicate EIP-5a, whereas newly crystallized apatite is only found in replicate EIP-7b (Table 4.9).

Table 4.6: Major element composition of run product olivine

	EIP-4							EIP-5						
Replicate	a			a			b	a			b			
N	6			2			1	12			12			
SiO_2	39.11	±	0.04	37.1	±	0.9	38.6	37.39	±	0.08	36.6	±	0.2	
Al_2O_3	0.084	±	0.008	1	±	1	0.41	0.24	±	0.08	0.20	±	0.08	
TiO_2	0.06	±	0.01	b.d. to 0.0069			0.06	0.06	±	0.01	0.07	±	0.01	
FeO	18.9	±	0.3	27.8	±	0.3	23.1	28.76	±	0.42	31.7	±	0.3	
Fe_2O_3	1.4	±	0.1	b.d. to 1.27			-	-			0.2	±	0.3	
MgO	41.5	±	0.2	32.3	±	0.6	37.7	33.1	±	0.2	30.4	±	0.4	
MnO	0.33	±	0.01	0.738	±	0.001	0.69	0.44	±	0.02	0.47	±	0.01	
CaO	0.445	±	0.002	0.331	±	0.001	0.56	0.43	±	0.04	0.5	±	0.2	
Na_2O	0.004	±	0.001	0.2	±	0.2	0.1	0.07	±	0.02	0.04	±	0.01	
K_2O	0.0107	±	0.0006	0.07	±	0.06	0.02	0.024	±	0.005	0.020	±	0.002	
Cl	0.019	±	0.001	0.022	±	0.005	b.d.	0.016	±	0.002	0.019	±	0.003	
F	0.050	±	0.008	b.d.			b.d.	b.d.			b.d.			
P_2O_5	b.d. to 0.04			b.d.			b.d.	0.12	±	0.01				
-(F,Cl) = O	0.03			-			-	0.004			0.004			
Total	101.9	±	0.4	100	±	2	101.2	100.6	±	0.5	100.4	±	0.7	
Si	0.987	±	0.001	1.00	±	0.01	1.00	0.998	±	0.002	1.00	±	0.01	
Al	0.0025	±	0.0002	0.04	±	0.03	0.01	0.007	±	0.003	0.007	±	0.002	
Ti	0.0011	±	0.0002	b.d. 0.00014			0.00	0.0011	±	0.0002	0.0014	±	0.0002	
Fe	0.398	±	0.006	0.62	±	0.01	0.50	0.642	±	0.009	0.721	±	0.009	
Fe^{3+}	0.026	±	0.002	b.d. to 0.026			-	-			0.005	±	0.007	
Mg	1.561	±	0.006	1.29	±	0.04	1.45	1.318	±	0.005	1.24	±	0.02	
Mn	0.0071	±	0.0002	0.0168	±	0.0002	0.02	0.0099	±	0.0004	0.0108	±	0.0003	
Ca	0.01203	±	0.00004	0.0095	±	0.0001	0.02	0.012	±	0.001	0.016	±	0.005	
Na	0.00018	±	0.00004	0.01	±	0.01	0.00	0.003	±	0.001	0.002	±	0.001	
K	0.00034	±	0.00002	0.002	±	0.002	0.00	0.0008	±	0.0001	0.0007	±	0.0001	
Cl	0.0008	±	0.0001	0.0010	±	0.0002	b.d.	b.d. 0.0007			0.00088	±	0.00002	
F	b.d. to 0.004			b.d.			b.d.	b.d.			b.d.			
P	0.0009	±	0.0002	b.d.			b.d.	b.d. to 0.00267			b.d.			
X_{Fo}^{Ol}	0.80	±	0.01	0.67	±	0.02	0.74	0.67	±	0.01	0.63	±	0.01	
X_{Fa}^{Ol}	0.203	±	0.003	0.33	±	0.01	0.26	0.328	±	0.005	0.369	±	0.006	

Fe^{3+} calculated after the method of Droop (1987). b.d. is below detection. Uncertainty is the standard deviation of the mean ($1\sigma_m$)

Table 4.7: Major element composition and formulas of run product biotite

	EIP-4			
Replicate	a			b
N	2			1
SiO_2	38.4	±	0.3	37.7
Al_2O_3	17.0	±	0.3	17.4
TiO_2	0.18	±	0.05	0.3
FeO	10.64	±	0.08	9.2
MgO	21.1	±	0.6	21.7
MnO	0.10	±	0.01	0.07
CaO	0.10	±	0.03	0.07
Na_2O	2.38	±	0.04	2.3
K_2O	6.8	±	0.2	7.1
Cl	0.09	±	0.01	0.09
F	b.d.			b.d.
P_2O_5	b.d.			b.d.
-(F,Cl) = O	0.02			0.02
Total	96.8	±	0.7	95.8
H_2O	4.21	±	0.03	4.2
	Formulas			
	Tetrahedral Cations			
Si	2.711	±	0.001	2.7
Al	1.289	±	0.001	1.3
Total	4.000	±	0.002	4.00
	Octahedral Cations			
Al	0.13	±	0.03	0.12
Ti	0.010	±	0.003	0.02
Fe^{3+}	0.20	±	0.02	0.24
Fe^{2+}	0.43	±	0.03	0.30
Mg	2.22	±	0.05	2.3
Mn	0.006	±	0.001	0.00
Total	2.99	±	0.07	3.0
	A Site Cations			
K	0.62	±	0.01	0.64
Ca	0.007	±	0.002	0.01
Na	0.326	±	0.003	0.31
Total	0.95	±	0.01	0.96
	Hydroxyl Site Cations			
Cl	0.011	±	0.002	0.01
OH	1.989	±	0.002	2.0
F	b.d			b.d
X_{Ann}^{Bt}	0.14	±	0.01	0.1
$X_{Fe^{3+}}^{Bt}$	0.07	±	0.02	0.08
X_{Phl}^{Bt}	0.741	±	0.005	0.77

Formulas calculated after the method of Dymek (1983). b.d. is below detection. Uncertainty is the standard deviation of the mean ($1\sigma_m$)

Table 4.8: Major element composition and formulas of starting and run product oxides

	23051707b (Ilmenite)	EIP-7	EIP-7	EIP-8
Replicate	-	a	b	b
N	1	6	3	5
SiO_2	0.03	0.9 ± 0.2	0.4 ± 0.3	0.4 ± 0.1
Al_2O_3	0.01	3.4 ± 0.4	1.1 ± 0.1	6 ± 1
TiO_2	50.8	4.5 ± 0.2	22 ± 2	2.1 ± 0.3
FeO	43.8	29.9 ± 0.4	45 ± 2	27.2 ± 0.9
Fe_2O_3	-	54.6 ± 0.5	24 ± 4	57 ± 1
MgO	0.04	2.5 ± 0.1	2.7 ± 0.4	3.0 ± 0.9
MnO	2.6	0.46 ± 0.01	0.23 ± 0.05	0.9 ± 0.1
CaO	0.17	0.38 ± 0.04	0.4 ± 0.2	0.26 ± 0.01
Na_2O	b.d.	0.22 ± 0.06	0.04 ± 0.02	0.042 ± 0.009
K_2O	b.d.	0.05 ± 0.01	0.04 ± 0.01	0.040 ± 0.009
Cl	n.a.	0.04 ± 0.01	b.d. to 0.03	0.020 ± 0.005
F	n.a.	b.d.	b.d.	b.d.
P_2O_5	b.d.	b.d.	b.d.	b.d. to 0.03
-(F,Cl) = O	-	0.01	0.01	0.005
Total	97 ± 1	97 ± 1	95 ± 5	97 ± 2
		Formula		
Si	0.00	0.03 ± 0.01	0.01 ± 0.01	0.01 ± 0.00
Al	0.00	0.15 ± 0.02	0.048 ± 0.005	0.25 ± 0.04
Ti	0.991	0.128 ± 0.005	0.63 ± 0.07	0.06 ± 0.01
Fe	0.95	0.94 ± 0.02	1.44 ± 0.04	0.85 ± 0.04
Fe^{3+}	-	1.55 ± 0.02	0.68 ± 0.11	1.61 ± 0.05
Mg	0.00	0.14 ± 0.01	0.16 ± 0.02	0.17 ± 0.05
Mn	0.06	0.0146 ± 0.0003	0.007 ± 0.001	0.029 ± 0.004
Ca	0.0047	0.015 ± 0.002	0.01 ± 0.01	0.010 ± 0.001
Na	b.d.	0.016 ± 0.005	0.003 ± 0.002	0.0031 ± 0.0007
K	b.d.	0.002 ± 0.001	0.0019 ± 0.0001	0.0019 ± 0.0003
Cl	n.a.	0.002 ± 0.001	b.d. to 0.0021	0.0013 ± 0.0003
F	n.a.	b.d.	b.d.	b.d.
P	b.d.	b.d.	b.d.	b.d. to 0.001
X^{Sp}_{Mag}		0.66 ± 0.02	0.19 ± 0.07	0.68 ± 0.06
X^{Sp}_{Sp}		0.020 ± 0.002	0.0066 ± 0.0005	0.034 ± 0.008
X^{Sp}_{He}		0.06 ± 0.01	0.022 ± 0.003	0.10 ± 0.01
X^{Sp}_{Uv}		0.120 ± 0.007	0.62 ± 0.06	0.044 ± 0.009
X^{Sp}_{Mfr}		0.126 ± 0.009	0.15 ± 0.02	0.134 ± 0.037
X^{Sp}_{Qd}		0.012 ± 0.003	0.01 ± 0.00	0.01 ± 0.00

Fe_2O_3 calculated after the method of Droop (1987). Mole fractions are a best fit. n.a. is not available. b.d. is below detection. Uncertainty is the standard deviation of the mean ($1\sigma_m$)

Table 4.9: Major element composition and formulas of starting and run product apatite

	23051707b			EIP-5			EIP-7		
Replicate				a			b		
N	10			4			2		
SiO_2	b.d.			b.d.			0.7	±	0.6
Al_2O_3	0.41	±	0.08	0.06	±	0.02	0.4	±	0.1
TiO_2	0.02	±	0.01	0.04	±	0.00	b.d. to 0.05		
FeO	0.16	±	0.03	0.09	±	0.04	0.7	±	0.1
MgO	0.034	±	0.006	0.06	±	0.02	0.3	±	0.2
MnO	0.16	±	0.03	0.05	±	0.01	0.074	±	0.002
CaO	55.3	±	0.2	55.0	±	0.1	56	±	1
Na_2O	b.d.			b.d.			b.d. to 0.03		
K_2O	n.a.			n.a.			0.05	±	0.03
Cl	0.199	±	0.009	0.220	±	0.003	0.35	±	0.08
F	4.5	±	0.2	5.2	±	0.1	1.9	±	0.3
P_2O_5	41.61	±	0.07	41.2	±	0.1	44.92	±	0.03
SO_3	0.018	±	0.004	0.016	±	0.006	n.a.		
-(F,Cl) = O	1.9			2.3			0.9		
Total	100.5	±	0.3	99.7	±	0.2	104	±	1
H_2O	-			1.0	±	0.1	2.8	±	0.1
				Formulas					
Si	b.d.			b.d.			0.06	±	0.05
Al	0.041	±	0.008	0.006	±	0.002	0.04	±	0.01
Ti	0.0014	±	0.0004	0.002	±	0.001	b.d. to 0.003		
Fe	0.011	±	0.002	0.007	±	0.003	0.045	±	0.008
Mg	0.004	±	0.001	0.008	±	0.003	0.03	±	0.03
Mn	0.011	±	0.002	0.004	±	0.001	0.0050	±	0.0001
Ca	4.991	±	0.009	5.028	±	0.004	4.7	±	0.1
Na	b.d.			n.a.			b.d. to 0.005		
K	n.a.			n.a.			0.005	±	0.003
Cl	0.028	±	0.001	0.0318	±	0.0005	0.05	±	0.01
F	1.19	±	0.05	1.41	±	0.03	0.48	±	0.06
P	2.967	±	0.006	2.976	±	0.004	3.01	±	0.02
OH	-			0.56	±	0.03	1.47	±	0.07

Water calculated by assuming a filled hydroxyl site. n.a. is not available. b.d. is below

4.5.3. Proportion of Phases and Mass Balance

The results of the least-squares calculations are given in Table 4.10 and Figure 4.9 along with the residuals of the fits in Table 4.11. The residual is the difference between the concentration of a given major oxide in the starting material and the estimation of the concentration of that oxide from the least-squares calculation. The least-squares calculation has a good fit (residuals are typically below 1% for each major element) for the starting materials and all of the replicates in experiments EIP-5 and EIP-7. For replicates in experiment EIP-4 and replicates EIP-8b and EIP-9a there is a poor fit for several oxides (FeO, and MgO in experiment EIP-4; TiO_2 and FeO in replicate EIP-8b; SiO_2, FeO, and CaO in replicate EIP-9a), but for most of the major elements the residual is generally less than 2% and often less than 1%. The sum of the squares for replicate EIP-9b would indicate a poor fit, but on examination of the residuals, the goodness of the fit is dominated by the residual for FeO, CaO, and SiO_2, whereas the residual for all the other oxides is less than 1%. The large residual for FeO is likely due to iron loss to the platinum capsule (Table 4.2). The least-squares technique does not account for this iron loss and underestimates the proportion of glass and overestimates the proportion of pyroxene in experiment. If the replicate EIP-9a (gold capsule) is compared to the replicate EIP-9b (platinum capsule) the SSQ for replicate EIP-9a is ~1/3 that of EIP-9b. This also occurs in replicates EIP-7b and EIP-8b, but to a lesser extent; the SSQ for the replicate EIP-7a (gold capsule) is ~1/2 of replicate EIP-7b (platinum capsule). Thus, it is assumed that the replicates performed in a gold capsule are more accurate representations of the mineral proportions.

Table 4.10: Mineralogy of run products (mass %)

	23051707b	EIP-4		EIP-5		EIP-7		EIP-8	EIP-9	
Replicate		a	b	a	b	a	b	b	a	b
Glass	0%	37.5%	36.2%	82.6%	62.0%	13.1%	8.0%	23.2%	60.8%	34.2%
Plagioclase (Low Ca)	29%	0.0%	0.0%	0.0%	15.8%	0.0%	18.2%	0.0%	0.0%	0.0%
Plagioclase (High Ca)	0%	0.0%	0.0%	4.6%	0.0%	15.5%	2.2%	20.3%	0.0%	23.8%
Amphibole	70%	1.2%	13.6%	0.0%	0.0%	70.5%	70.5%	29.6%	0.0%	0.0%
Pyroxene (High Al)	0%	43.7%	37.6%	0.0%	0.0%	0.0%	0.0%	18.0%	39.2%	0.0%
Pyroxene (Low Al)	0%	0.0%	0.0%	2.0%	5.6%	0.9%	0.0%	0.0%	0.0%	42.0%
Olivine 1	0%	0.0%	12.6%	10.7%	14.6%	0.0%	0.0%	0.0%	0.0%	0.0%
Olivine 2	0%	17.5%	0.0%	0.0%	0.0%	0.0%	0.0%	0.0%	0.0%	0.0%
Biotite	0%	0.0%	0.0%	0.0%	0.0%	0.0%	0.0%	0.0%	0.0%	0.0%
Apatite	0%	0.0%	0.0%	0.0%	2.0%	0.0%	0.8%	0.0%	0.0%	0.0%
Spinel	1%	0.0%	0.0%	0.0%	0.0%	0.0%	0.3%	9.0%	0.0%	0.0%

See text for details of calculation

Table 4.11: Residuals of least-square calculation

	23051707b	EIP-4		EIP-5		EIP-7		EIP-8	EIP-9	
Replicate		a	b	a	b	a	b	b	a	b
SiO_2	-1.07	-0.74	-0.81	0.32	-0.55	-0.75	-0.86	0.33	-4.77	-5.92
Al_2O_3	0.67	1.15	0.31	-0.11	0.46	-0.30	-0.17	0.18	1.98	0.47
TiO_2	-0.46	0.01	0.14	0.00	0.48	0.10	0.02	-1.92	0.33	0.48
FeO	-0.56	3.37	5.23	-0.27	0.13	-0.68	-0.95	1.01	3.27	8.22
MgO	0.63	-2.49	-3.54	0.08	-0.04	-0.14	0.41	0.19	1.73	0.22
MnO	-0.03	0.01	0.03	-0.01	0.01	0.01	0.00	0.04	-0.01	0.00
CaO	-0.27	0.41	0.13	-0.32	0.33	-0.19	-0.81	-0.02	-1.46	-3.88
Na_2O	-0.36	0.15	-1.11	-0.14	-0.53	-0.09	-0.05	0.42	0.26	0.47
K_2O	0.23	-0.07	-0.17	0.01	0.10	-0.20	0.02	0.02	-0.40	-0.04
Cl	0.00	-0.19	-0.11	-0.05	-0.06	-0.07	-0.07	-0.06	-0.07	-0.08
F	0.16	0.07	-0.02	-0.09	-0.13	0.09	0.12	0.15	0.09	0.14
P_2O_5	0.07	-0.04	-0.04	-0.02	-0.84	0.06	-0.36	-0.04	-0.08	-0.04
SSQ	2.82	19.66	41.91	0.32	1.89	1.24	2.65	5.10	42.86	118.48

Negative values indicate an over estimation of the given oxide. Positive values indicate and underestimation of the given oxide.

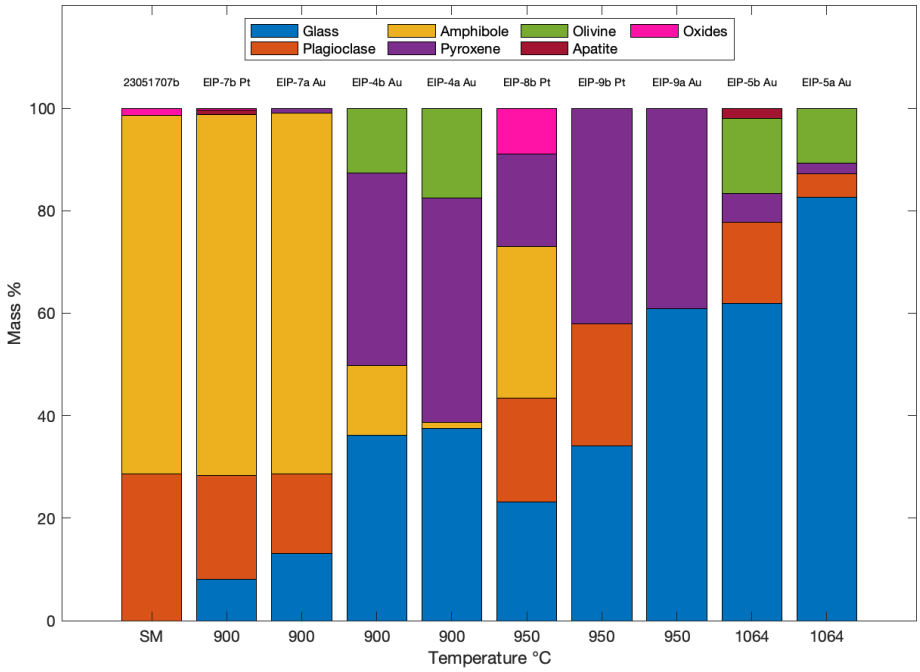

Figure 4.9: Mineralogy in mass % of the run products and starting material as determined by a constrained linear least-squares method (see text for details) plotted as stacked bars. Along the x-axis is the temperature of the experiments. From left to right bars are plotted in increasing temperature and increasing proportion of glass. SM is the starting material. Biotite is << 1% in EIP-4a and EIP-4b and excluded from the figure.

Examining the results of the least-squares calculations (Table 4.10 and Figure 4.9), the proportion of glass present: at 900°C is between ~10 and 40%; at 950°C is ~35 to 50%; and above 1000°C is 60 to 80%. At 900°C, pyroxene begins to crystallize (~1%) at the expense of amphibole and increases to 30 to 40% between 900 and 950°C. Pyroxene begins to disappear at temperatures above 1000°C. The amount of amphibole decreases with increasing temperature and ultimately disappears as the temperature approaches 950°C. Olivine is only stable at temperatures greater than 950°C, as olivine is not present in other 900 or 950°C experiments (with the exception of experiment EIP-4, which was the result of a temperature spike to 958°C). The presence of biotite, oxides, and apatite is

inconsistent and may reflect heterogeneities in the starting material, level of exposure in the mounted run products, or in the case of biotite low concentrations of primary constituents in the starting material (i.e. K_2O in the starting material may not be sufficient to saturate a melt with biotite). These phases are visible in the backscatter electron images (Figure 4.2), but are predicted to be significantly less than 1% by the least-squares calculation in most cases. In the case of the oxides, the effect of iron loss to the capsule may result in the stabilization of titanium-rich spinel (e.g. replicate EIP-7b).

4.5.4. Approach to Equilibrium

In order to assess equilibrium, two techniques were utilized: replicate experiments and experiments with different physical forms of the starting materials (cores, powdered, and powdered and sieved). Run products were compared from experiments at a given temperature. Replicates in experiments are comparable in terms of composition of run products and mass percent of those run products regardless of the physical form of the starting material. There are differences among experiments performed at the same temperature; however, these differences can generally be explained by variations in temperature for short durations during the run (see comments and discussion of experiment EIP-4). In several experiments, there is a bimodal distribution of pyroxene and plagioclase compositions; however, one composition typically dominates. Further, the presence of zoning of pyroxene and amphibole may not suggest disequilibrium and may be the result of growth along different crystallographic faces (i.e. sector zoning in amphibole). Similarly, for experiments performed at 950°C (experiments EIP-8 and -9), the compositional

differences of the run products between replicates is the result of the choice of capsule material and the loss of iron to the platinum capsule. In the experiments performed in platinum capsules (replicates EIP-8b and EIP-9b), results are similar in terms of both mass percent of phases and composition. Thus, it can be concluded that experiments approach equilibrium.

4.5.5. Elemental Mapping

WDS and EDS maps for Al, Ca, Na, Mg, and Sc are presented in Figure 4.10. These maps illustrate a variety of textural and compositional characteristics of the run products. Amphibole in experiments EIP-4 and EIP-8 are sector zoned, whereas amphibole in experiment EIP-7 are relatively unzoned. The sector zoning is most visible in the aluminum maps, but is also present in the magnesium and silicon maps, which is consistent with a Tschermak exchange (i.e. Mg + Si = 2 Al). The maps also highlight the occurrence of pyroxene in amphibole cores, as well as the presence of both high- and low-aluminum pyroxenes (Table 4.5; Figure 4.10b). These high- and low-aluminum pyroxenes are also zoned with respect to magnesium (Figure 4.10b) and silicon (Table 4.5), which is also consistent with a Tschermak exchange. Plagioclase, when present, forms bands intermingled within the glass and zonation is not apparent. The exception is residual plagioclase in experiment EIP-5 (Figure 4.10a). The plagioclase is heterogeneous in composition and has lower sodium and higher calcium in the rim compared to the core: the interpretation is that the rims are dissolving and forming melt. It is also evident from the elemental maps that olivine occurs within amphibole and as a discreet phase above 1000°C. In these high-temperature experiments the olivine has magnesium and iron zoning (Figure 4.10b).

The glass in experiments EIP-4 and EIP-7 are also zoned, whereas all other glasses are homogeneous. The zonation in the melt is primarily reflected in concentrations of sodium and aluminum. Additionally, in experiment EIP-4 low sodium spots are visible within the glass, which has broken down and become hydrated (see above) and maybe the result of sodium diffusion away from the electron beam. As noted above, the results of early analyses glasses from experiment EIP-4 are consistent with the glass being anhydrous with no evidence of breakdown (Table 4.2). The elemental maps were performed after repolishing and WDS analyses, and the breakdown is visible at a deeper level within the glass (Figure 4.10a). Another notable result of the mapping is the distribution of scandium among the phases. In all experiments the glass has the lowest count rate for scandium and thus likely has the lowest abundance of scandium, except for plagioclase where the abundance is roughly equal. The platinum and gold capsules, although not run products, have the highest relative concentration of scandium. The oxide phases, where present, have the highest relative abundance of scandium of the run products. Pyroxene and olivine have the next highest scandium concentration, which is slightly higher than the scandium concentration in amphibole.

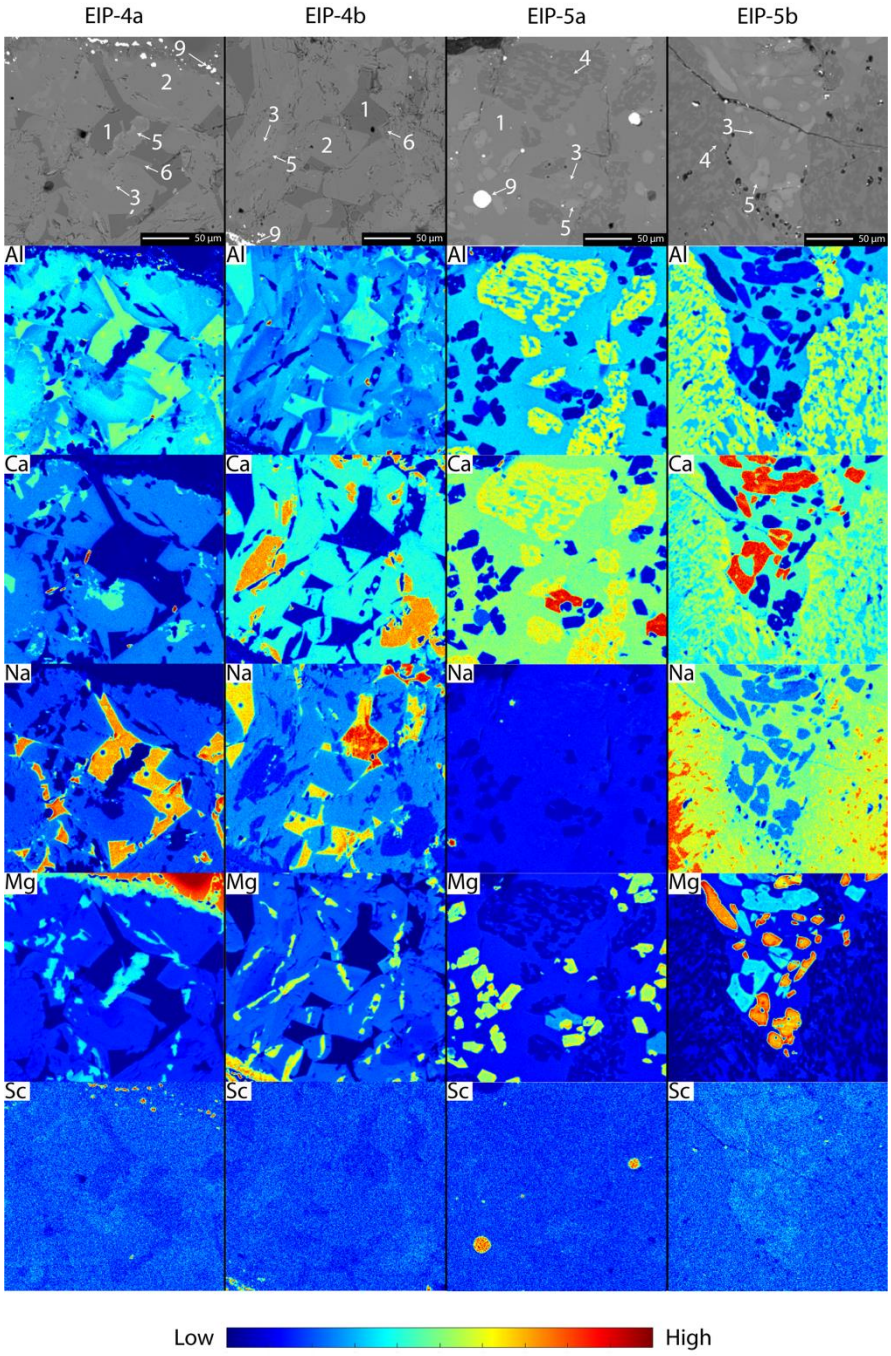

Figure 4.10: Elemental x-ray maps of run products. Scandium x-ray map was collected using WDS: all other maps were collected using EDS analysis. Cool colors indicate low count rates. Warm colors indicate high count rates. Number indicate phase: 1 = Glass; 2 = Amphibole; 3 = Pyroxene; 4 = Plagioclase; 5 = Olivine; 6 = Biotite; 7 = Oxides; 8 = Apatite; 9 = Gold; 10 = Platinum.

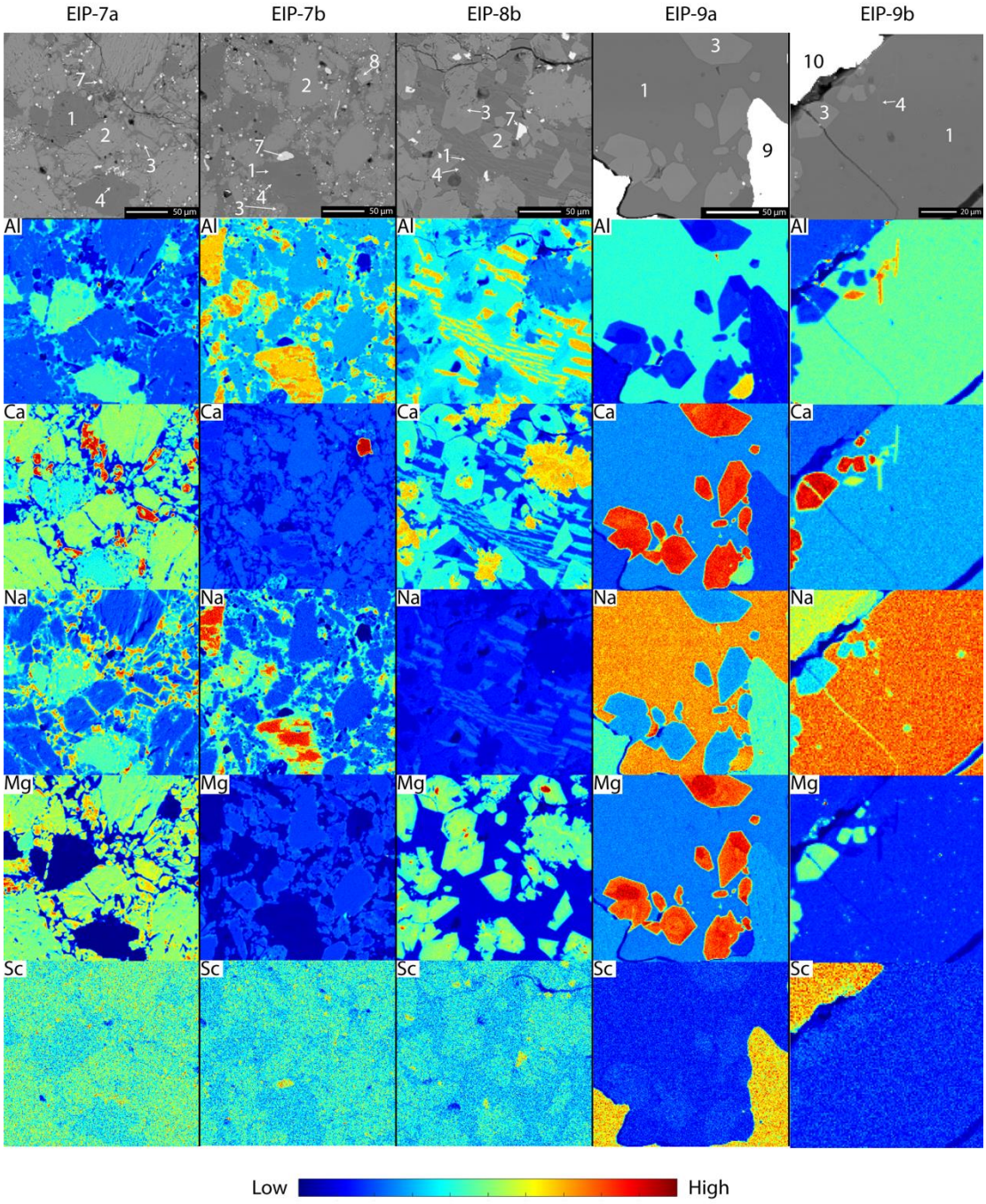

Figure 4.10 continued.

4.5.6. Trace Elements

The trace element concentrations determined by using LA-ICP-MS are presented in Table 4.12 and the supplementary files (for individual data points and limits of detection). The run product glasses from experiments with low degrees of partial melting (experiments EIP-4 and EIP-7) are devoid of trace elements which are often below the detection limit of the ICP-MS. As the glass reaches >40% (replicate EIP-9a and experiment EIP-5) the concentration of the trace elements increase as the fraction of amphibole and pyroxene decreases (Table 4.12 and Figure 4.10). Notably, the concentration of scandium in the run product glasses is below detection (typically between 15 and 30 ppm; see supplementary files) in the majority of cases. The only run product glasses with scandium consistently above the limit of detection are those glasses from experiment EIP-5. In this experiment the starting material has undergone up to 80% partial melting and the scandium concentration is approximately equal to that of the bulk starting material (39 ppm). Replicate EIP-9b had a range of scandium concentration from below detection to 16.2 ppm. Clinopyroxene and amphibole are the primary hosts for the trace elements (Sc, Y, V, REEs). Scandium concentrations in run product clinopyroxene and amphibole range from 54 to 120 ppm and 28 to 81 ppm, respectively.

Chondrite normalized rare earth element (REE) patterns for the run product glasses, clinopyroxene, and amphibole are presented in Figure 4.11 and 4.12. The REE patterns for both clinopyroxene and amphibole are flat and contain little enrichment in either the light rare earth elements (LREEs) or the heavy rare earth elements (HREEs) relative to each group of REEs. The REE patterns for run product

glasses are generally flat with minor LREE enrichment compared to the HREEs (Figure 4.12). Glasses from experiments with low degrees of partial melting (experiments EIP-4 and EIP-7) have more variable REE patterns. Glasses from experiments with larger degrees of partial melting have less variable and REE patterns similar to the starting material, with only minor LREE enrichment. Additionally, there is a lack of a europium anomaly in the run product glasses; although, it may be argued that replicates EIP-4a and EIP-7b may have minor positive europium anomalies (Figure 4.12).

Table 4.12: Trace elements in run products and starting material

	Glass								
	EIP-4		EIP-5		EIP-7	EIP-8	EIP-9		
Replicate	a	b	a	b	a	b	b	a	b
N	2	3	2	3	2	1	1	2	2
Li	37 ± 7	35 ± 2	b.d. to 17.9	b.d.	b.d.	b.d.	20	27 ± 4	28 ± 7
Sc	b.d.	b.d.	37 ± 5	50 ± 10	b.d.	b.d.	b.d.	b.d.	b.d. to 16.3
V	b.d.	b.d. to 67.9	300 ± 70	214 ± 3	b.d.	b.d.	66	56.5 ± 0.4	240 ± 30
Ga	70 ± 1	70 ± 20	70 ± 20	40 ± 5	51 ± 21	49	115	200 ± 2	180 ± 20
Ge	b.d.	b.d.	b.d t 12.9	b.d.	b.d.	37.5	b.d.	b.d.	b.d.
Rb	35 ± 5	53 ± 7	13 ± 3	5 ± 1	6 ± 3	b.d.	29	45.6 ± 0.5	47 ± 6
Sr	230 ± 40	270 ± 50	200 ± 50	195 ± 29	400 ± 100	828	122	225 ± 3	210 ± 10
Y	3 ± 2	5 ± 3	22 ± 5	26 ± 1	b.d. to 0.7	b.d.	14	31 ± 1	34 ± 2
Zr	b.d. to 11.1	13 ± 6	43 ± 8	42 ± 4	b.d.	b.d.	105	123.5 ± 0.4	150 ± 20
Nb	b.d. to 0.2	b.d. to 0.9	3 ± 1	2.9 ± 0.7	0.10 ± 0.03	b.d.	5.7	6.5 ± 0.6	7 ± 2
Cd	b.d. to 1.6	b.d.	b.d. to 2	b.d.	b.d. to 0.3	b.d.	b.d.	b.d.	b.d.to 1.4
In	b.d.	0.08 ± 0.01	b.d.	b.d. to 0.1	b.d. to 0.3	b.d.	b.d.	b.d.	b.d.
Sn	b.d.	b.d.	b.d.	b.d.	b.d.	b.d.	b.d.	b.d.	b.d.
Cs	2.70 ± 0.08	3.2 ± 0.5	b.d. to 0.4	b.d.	b.d.	b.d.	b.d.	1.95 ± 0.06	2.0 ± 0.6
La	10 ± 8	12 ± 6	18 ± 5	10 ± 5	1.4 ± 0.3	3.5	18	12.8 ± 0.5	18.2 ± 0.6
Ce	5 ± 4	5 ± 3	16 ± 5	15 ± 2	1.9 ± 0.4	3.9	31	35.0 ± 0.2	36 ± 2
Pr	b.d. to 0.3	0.8 ± 0.5	3 ± 1	2.9 ± 0.4	0.24 ± 0.09	0.5	3.4	4.8 ± 0.3	5.2 ± 0.7
Nd	b.d. to 1.5	b.d. to 5.5	14 ± 4	15 ± 1	0.42 ± 0.06	0.7	13	23.3 ± 0.9	22.0 ± 0.7
Sm	b.d to 0.5	b.d. to 2.2	5 ± 2	4.5 ± 0.4	0.3	0.9	b.d.	5.3 ± 0.2	5.0 ± 0.4
Eu	b.d. to 0.3	b.d. to 0.6	1.8 ± 0.9	1.44 ± 0.09	b.d.	0.7	1.2	2.03 ± 0.09	2.00 ± 0.06
Gd	b.d.	b.d. to 1.4	b.d. to 3	4.4 ± 0.4	0.5 ± 0.2	b.d.	b.d.	6.7	5.0 ± 0.5
Tb	0.05 ± 0.01	0.2 ± 0.1	b.d. to 1	0.85 ± 0.02	0.03 ± 0.01	0.3	b.d.	0.89 ± 0.01	0.94 ± 0.01
Dy	0.3 ± 0.2	b.d. to 0.5	5 ± 1	5.3 ± 0.5	b.d.	0.8	4.0	5.1 ± 0.9	5.7 ± 0.6
Ho	0.10 ± 0.08	b.d. to 0.4	0.8 ± 0.1	1.0 ± 0.1	b.d.	b.d.	0.4	1.05 ± 0.08	1.1 ± 0.1
Er	b.d. to 0.2	b.d. to 0.6	2.2 ± 0.3	2.6 ± 0.1	b.d.	b.d.	1.4	3.36 ± 0.06	3.4 ± 0.2
Tm	b.d. to 0.02	0.2 ± 0.1	0.39 ± 0.02	0.34 ± 0.05	0.02 ± 0.01	b.d.	b.d.	0.45 ± 0.03	0.53 ± 0.01
Yb	0.6 ± 0.2	0.8 ± 0.4	2.4 ± 0.4	2.2 ± 0.2	0.3 ± 0.1	b.d.	1.2	3.1 ± 0.6	2.43 ± 0.03
Lu	0.03 ± 0.01	b.d. to 0.3	b.d. to 0.1	0.28 ± 0.09	b.d.	b.d.	0.1	0.63 ± 0.02	0.38 ± 0.05
Hf	b.d.	b.d. to 0.5	1.1 ± 0.3	1.309 ± 0.002	0.6 ± 0.5	b.d.	2.3	4.0 ± 0.3	3.7 ± 0.6
Ta	b.d. to 0.02	b.d. to 0.2	0.21 ± 0.08	0.16 ± 0.03	0.04 ± 0.03	b.d.	0.4	b.d. to 0.6	0.30 ± 0.01

b.d. is below detection. Uncertainty is the standard deviation of the mean ($1\sigma_m$)

Table 4.12 cont.

	Pyroxene								Plagioclase	Olivine		
	EIP-4		EIP-5		EIP-7	EIP-8	EIP-9		23051707b	EIP-4	EIP-5	
Replicate	a	b	a	b	a	b	a	b	-	a	a	b
N	1	2	2	2	1	2	2	1	2	1	1	2
Li	b.d.	7.8	b.d.	b.d.	b.d.	9 ± 3	b.d.	b.d.	b.d. to 2.6	12	b.d.	b.d.
Sc	98	110 ± 30	90 ± 10	82 ± 2	54	97 ± 9	105 ± 6	120	b.d. to 3.4	b.d.	23	b.d to 13
V	825	722 ± 8	390 ± 70	210 ± 10	210	129 ± 4	200 ± 30	112	b.d.	10	129	50 ± 20
Ga	18	15 ± 3	30 ± 10	18 ± 2	73	20 ± 10	9.2 ± 0.5	b.d.	38 ± 5	4.5	23	5 ± 1
Ge	b.d.	b.d.	b.d.	b.d.	b.d.	b.d.	b.d.	b.d.	b.d.	b.d.	b.d.	b.d. to 9.2
Rb	b.d.	b.d. to 0.3	5 ± 2	2.5 ± 0.1	26	b.d. to 8	b.d.	b.d.	b.d. to 23	2.6	5.1	b.d.
Sr	49	40 ± 10	90 ± 40	85 ± 2	72	40.0 ± 30.0	22 ± 1	27	350 ± 300	17	74	22 ± 4
Y	31	35.9 ± 0.4	22.6 ± 0.9	23 ± 3	41	44 ± 3	46 ± 3	68	b.d. to 0.8	1.0	12	3.5 ± 0.7
Zr	83	67 ± 1	26 ± 6	32 ± 3	177	69.3 ± 0.4	50 ± 2	61	b.d. to 102	b.d.	19	b.d. to 5.4
Nb	1.2	b.d. to 1	1.3 ± 0.8	1.2 ± 0.1	b.d.	b.d. to 0.3	0.12 ± 0.07	0.4	b.d. to 0.2	b.d.	1.7	0.4 ± 0.3
Cd	b.d.	b.d.	0.6 ± 0.1	b.d.	b.d.	b.d. to 0.8	0.8 ± 0.6	7.5	b.d. to b.d.	b.d.	0.4	b.d. to 0.5
In	b.d.	b.d.	b.d.	b.d.	b.d.	b.d.	b.d.	b.d.	b.d. to 84	b.d.	b.d.	b.d.
Sn	b.d.	b.d.	b.d.	b.d.	b.d.	b.d.	b.d.	b.d.	b.d. to 43	b.d.	b.d.	b.d.
Cs	b.d.	b.d.	b.d.	b.d.	1.1	b.d.	b.d.	b.d.	b.d. to 0.2	b.d.	b.d.	b.d.
La	4.3	10 ± 2	9 ± 4	2.2 ± 0.2	7.8	5 ± 2	2.1 ± 0.1	3.7	1.6 ± 0.8	0.7	8.8	0.6 ± 0.1
Ce	9.9	13 ± 1	9 ± 2	8.1 ± 0.9	20	13 ± 2	8.7 ± 0.9	11	2.0 ± 0.3	0.1	6.5	2.0 ± 0.3
Pr	2.1	3.2 ± 0.3	1.8 ± 0.6	1.61 ± 0.02	3.9	2.6 ± 0.3	2.2 ± 0.5	b.d.	0.24 ± 0.03	b.d.	0.7	0.33 ± 0.05
Nd	15	16.9 ± 0.7	9 ± 1	10.7 ± 0.2	26	17 ± 2	15.0 ± 0.7	13	b.d. to 0.5	b.d.	5.2	2.1 ± 0.6
Sm	5.4	6.1 ± 0.2	5 ± 1	3.3 ± 0.3	7.0	6 ± 1	6.5 ± 0.2	6.8	b.d.	b.d.	2.3	0.6 ± 0.3
Eu	1.7	1.9 ± 0.2	b.d. to 1.3	1.31 ± 0.08	2.0	1.74 ± 0.08	1.8 ± 0.2	4.1	b.d. to 0.08	b.d.	0.8	0.174 ± 0.002
Gd	5.5	9 ± 1	b.d.	4 ± 1	8.7	8.1 ± 0.2	8.6 ± 0.1	23	b.d. to 0.1	0.7	b.d.	b.d. to 0.5
Tb	1	1.5 ± 0.1	0.7 ± 0.1	0.8 ± 0.2	1.2	1.5 ± 0.3	1.5 ± 0.1	2.6	0.07 ± 0.05	b.d.	0.5	0.13 ± 0.01
Dy	7.3	9.4 ± 0.2	4.83 ± 0.06	4.8 ± 0.6	b.d.	9 ± 1	8.7 ± 0.4	16	b.d. to o.06	b.d.	2.4	0.65 ± 0.09
Ho	1.5	1.66 ± 0.02	0.94 ± 0.07	1.0 ± 0.1	1.4	1.66 ± 0.05	2.01 ± 0.06	3.3	0.07 ± 0.05	b.d.	0.4	0.17 ± 0.04
Er	4	4.9 ± 0.4	3.0 ± 0.1	2.31 ± 0.02	4.4	4.8 ± 0.4	4.4 ± 0.6	11	b.d. to 0.1	0.1	1.6	0.35 ± 0.02
Tm	0.6	0.49 ± 0.02	0.45 ± 0.01	0.33 ± 0.04	0.7	0.529 ± 0.005	0.6 ± 0.1	1.5	b.d. to 0.02	b.d.	0.3	0.07 ± 0.01
Yb	3.3	2.9 ± 0.5	2.29 ± 0.03	1.67 ± 0.06	b.d.	3.9 ± 0.3	4.0 ± 0.2	b.d.	b.d. to 0.05	0.1	1	b.d. to 0.6
Lu	0.4	0.50 ± 0.08	0.40 ± 0.05	0.25 ± 0.06	0.7	0.67 ± 0.01	0.43 ± 0.04	0.7	b.d.	0.07	0.2	0.08 ± 0.02
Hf	3.6	3.2 ± 0.1	1.6 ± 0.6	1.2 ± 0.1	4.8	2.4 ± 0.2	2.8 ± 0.2	2	b.d. to 3	b.d.	0.9	0.3 ± 0.1
Ta	0.2	0.19 ± 0.06	0.092 ± 0.002	0.043 ± 0.001	b.d.	0.15 ± 0.04	0.09 ± 0.04	0.2	b.d. to 0.02	b.d.	0.1	0.03 ± 0.02

Table 4.12 cont.

	Amphibole				
	23051707b	EIP-4		EIP-7		EIP-8
Replicate	-	a	b	a	b	b
N	3	2	3	2	2	2
Li	b.d. to 2.34	b.d.	b.d. to 8.3	21 ± 3	8.9 ± 0.8	b.d.
Sc	52.0 ± 0.5	28 ± 1	21 ± 2	81 ± 9	49 ± 2	60 ± 20
V	370 ± 30	190 ± 40	140 ± 15	410 ± 6	281 ± 4	360 ± 80
Ga	29 ± 2	60 ± 10	53 ± 9	42 ± 9	20 ± 2	44.4 ± 0.7
Ge	b.d. 7.1	b.d. to 20.3	b.d. to 10.8	b.d.	b.d.	b.d.
Rb	1.9 ± 0.4	2.57 ± 0.02	2.4 ± 0.3	6 ± 3	b.d. 2.4	b.d. to 7.9
Sr	24 ± 1	170 ± 40	200 ± 20	38 ± 4	23 ± 1	126 ± 12
Y	36 ± 6	36 ± 7	19 ± 3	52 ± 9	29 ± 2	42 ± 7
Zr	25 ± 1	140 ± 40	38 ± 7	39 ± 5	25 ± 3	66 ± 16
Nb	2.8 ± 0.7	6.7 ± 0.8	4.9 ± 0.8	4 ± 2	2 ± 0	3.0 ± 0.9
Cd	b.d.	b.d.	b.d. to 0.2	b.d. to 1.1	b.d. to 1.1	b.d. to 1.1
In	b.d. to 0.2	b.d. to 0.1	b.d. to 0.1	b.d.	b.d.	b.d.
Sn	30 ± 10	b.d.	b.d.	b.d.	b.d.	b.d.
Cs	b.d.	b.d.	b.d.	b.d.	b.d.	b.d.
La	5.8 ± 0.5	12.3 ± 0.5	36 ± 6	7.26 ± 0.04	5.6 ± 0.4	4 ± 1
Ce	19 ± 2	20.0 ± 1.0	26 ± 3	22 ± 2	17 ± 2	12 ± 2
Pr	3.1 ± 0.3	3.5 ± 0.3	3.9 ± 0.3	3.9 ± 0.3	2.8 ± 0.1	2.5 ± 0.1
Nd	16 ± 2	19 ± 2	19 ± 4	25 ± 5	13 ± 2	18.4 ± 0.1
Sm	4.5 ± 0.4	6 ± 1	4.2 ± 0.5	7 ± 2	4.3 ± 0.5	5.0 ± 0.3
Eu	1.5 ± 0.2	1.5 ± 0.4	1.4 ± 0.5	1.86 ± 0.02	1.40 ± 0.08	1.9 ± 0.1
Gd	6 ± 1	6 ± 2	5.3 ± 0.2	9 ± 3	4.8 ± 0.1	8.0 ± 2.0
Tb	0.9 ± 0.1	1.0 ± 0.3	0.66 ± 0.08	1.4 ± 0.3	0.73 ± 0.04	1.5 ± 0.4
Dy	7 ± 2	6 ± 1	3.7 ± 0.6	10 ± 2	5.99 ± 0.01	8.7 ± 2.0
Ho	1.5 ± 0.3	1.4 ± 0.4	0.83 ± 0.13	1.9 ± 0.2	1.19 ± 0.01	1.7 ± 0.2
Er	3.8 ± 0.7	3.5 ± 0.6	2.1 ± 0.3	5.1 ± 0.9	3.1 ± 0.7	4.9 ± 0.5
Tm	0.455 ± 0.005	0.5 ± 0.1	0.22 ± 0.02	0.7 ± 0.1	0.43 ± 0.01	0.60 ± 0.07
Yb	3.7 ± 0.3	4 ± 1	2.2 ± 0.3	5.2 ± 0.7	3.0 ± 0.1	4.1 ± 0.5
Lu	0.39 ± 0.03	0.46 ± 0.02	0.30 ± 0.04	0.7 ± 0.3	0.43 ± 0.07	0.61 ± 0.09
Hf	1.40 ± 0.03	4 ± 1	1.2 ± 0.2	2.402 ± 0.003	1.00 ± 0.07	2.9 ± 0.3
Ta	0.12 ± 0.02	0.8 ± 0.2	0.42 ± 0.08	0.26 ± 0.06	b.d. to 0.12	b.d. to 0.3

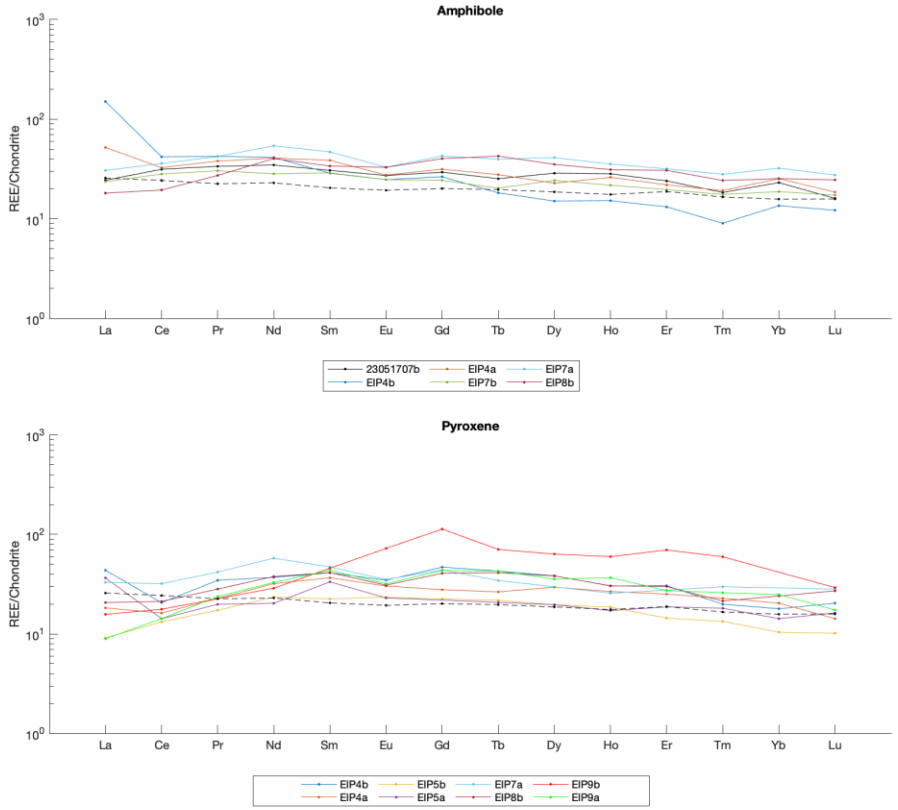

Figure 4.11: Chondrite normalized REE plots for run product amphiboles and pyroxenes. Chondrite values from McDonough and Sun (1995)**.** Dashed line is the bulk chondrite normalized REE pattern for the starting materials (sample 23051707b).

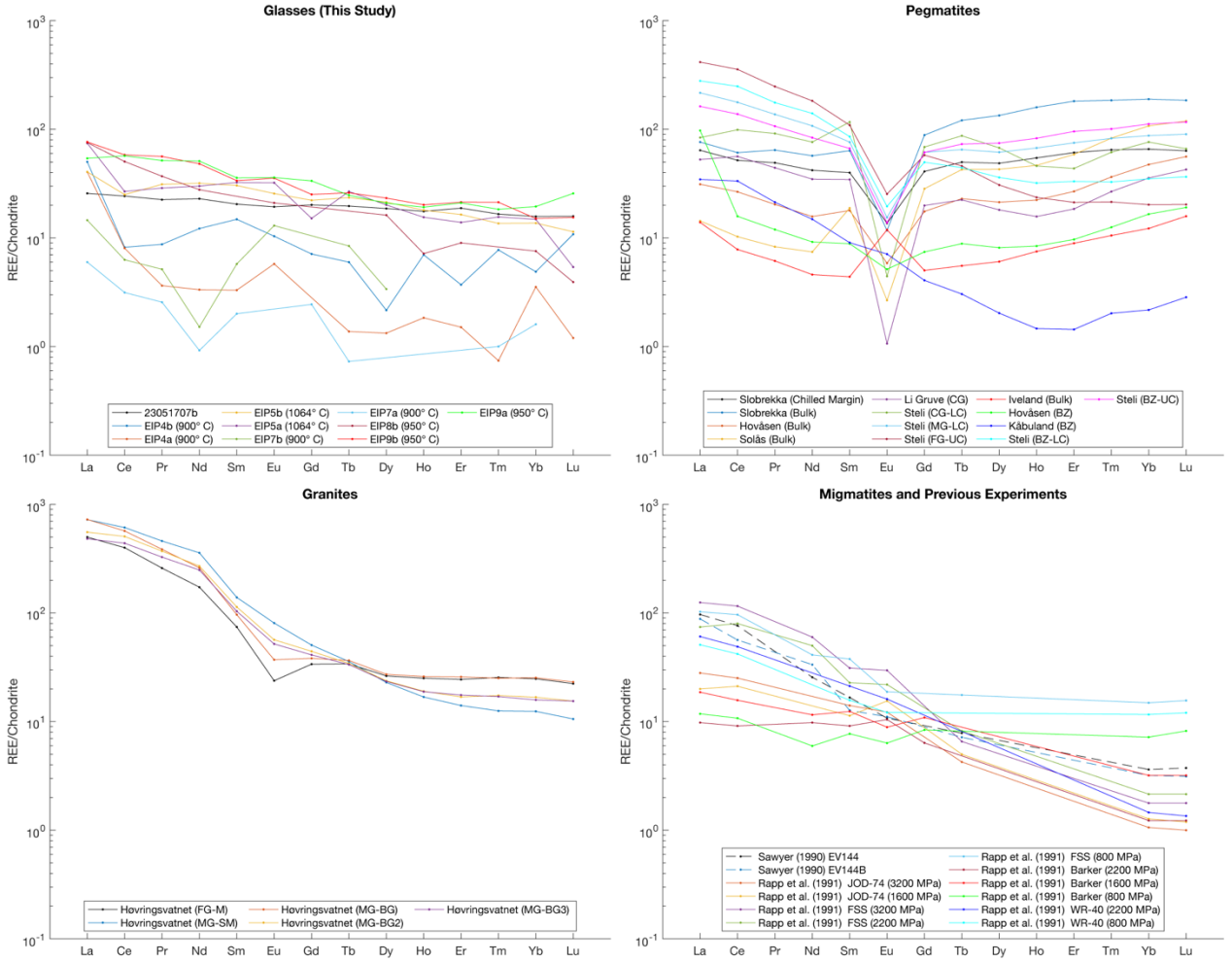

Figure 4.12: Chondrite normalized REE plots for run product glasses, Evje-Iveland pegmatites (Snook, 2014)**,**vein-type migmatites from the Grenville Front , Quebec (Sawyer, 1991), and previous partial melting experiments Rapp et al. (1991). Chondrite values from McDonough and Sun (1995). CG = coarse grained, MG = medium grained, FG = Fine grained, LC = lower contact, UC = upper contact, BZ = boarder zone, M = monzonite, SM = syenomonzonite, BG = biotite granite.

4.6. Discussion

4.6.1. Melt Formation

The solidus of the Evje-Iveland amphibolite at vapor absent conditions is at or near 900°C at a pressure of 500 MPa. During partial melting, the first reaction to occur is the breakdown of amphibole (magnesiohornblende) and generation of a sodium-rich, high-aluminum melt at or near amphibole-plagioclase grain boundaries. The initial melt is water undersaturated and any water in the system is transferred directly into the melt. This reaction also produces more-aluminous amphibole (pargasite) and less-sodic plagioclase, as well as an aluminum-rich diopside in the core of the pargasite. One reaction to describe this relationship is:

magnesiohornblende + plagioclase $\rightarrow$ pargasite + less sodic plagioclase + aluminian diopside + melt .

This reaction reaches completion at approximately 900°C. Between 900 and 950°C the pargasite and less-sodic plagioclase react to yield additional melt and aluminian diopside:

pargasite + less sodic plagioclase $\rightarrow$ aluminian diopside + melt .

Above 950°C, the amphibole and plagioclase are consumed and the reaction products are an aluminian diopside, a melt phase, as well as olivine. These results are in good agreement with previous studies. The solidus as determined from the results of the experiments presented here, as well as the position of the clinopyroxene-in (900° C) and hornblende-out (950° C) reactions, are in agreement with results of Wyllie and Wolf (1993) and reference therein. Additionally, crystallization of clinopyroxene within the core of amphibole was also observed by Wolf and Wyllie (1991). The

increase in the aluminum content of the amphibole and the aluminum-rich pyroxene, are consistent with the results of Rapp et al. (1991), Rushmer (1991), Rapp (1995), and Wolf and Wyllie (1994).

4.6.2. Composition of Pegmatite-forming Melts

4.6.2.1. Major Elements

The composition of the run product glass is of particular interest in this study. A comparison of the experimental glasses in this study to the bulk composition of the granitic border zones of the Steli pegmatite, the "Iveland Wall" (a roadcut displaying the relationship of the pegmatites and the host amphibolite) in the Evje-Iveland pegmatite field (Snook, 2014), and two albite zones from the Solås and Topazbrudd pegmatites (Müller et al., 2018) is given in Figure 4.3.

Snook (2014) assumed that the border zones of the pegmatites in the Evje-Iveland field are representative of the bulk pegmatite, but this assumption is not without problems. As discussed by London (2008), and noted by Jahns (1982) and Jolliff et al. (1992), the border zones of pegmatites are chilled margins; however, unlike chilled margins, e.g. in mafic rocks, pegmatite border zones do not efficiently incorporate trace elements and fluxes (i.e. H_2O, F, B, and P) as they are incompatible in border zone minerals. Pegmatite-forming melts are often enriched in fluxes and trace elements (e.g. Li, F, Cs etc.) that are incompatible in the minerals in border zones of pegmatites (London, 2008). Thus, it is likely that the bulk composition of the border zones has a lower concentration of fluxes and incompatible trace elements than the initial melt (London, 2008). Müller et al. (2018) used modal analyses of the pegmatite and image analyses to determine the bulk composition of the coarse-

grained albite zones by modal recombination, which may represent some portion of the initial pegmatite-forming melt. However, determination of the initial melt compositions by other means, has not been performed for bulk compositions of the Evje-Iveland pegmatites. Determining the bulk composition of the pegmatite by modal recombination as done by Müller et al. (2018) would provide an additional estimate of the bulk composition that may be able to account for lower concentration of fluxes or incompatible trace elements as noted by London (2008). Such modal recombination attempts have been successful in previous studies such at the Tanco pegmatite in Manitoba, Canada (Stilling et al., 2006). Because this type of modal recombination hasn't been completed for the bulk composition of the Evje-Iveland pegmatite the composition of the border zones as determined by Snook (2014) is thought to be the best estimate. However, the modal recombination of the albite zones from Müller et al. (2018) will also be considered.

The compositions of experimental glasses are compared to pegmatites in Figure 4.3 and they are less siliceous than the Steli and the "Iveland Wall" pegmatites; however, the experimental glasses have approximately the SiO_2 concentrations as the albite zones. Only one experiment (EIP-8b) has an SiO_2 concentration greater than 70 wt% and experiment EIP-7b has approximately the same SiO_2 concentration as the fine-grained granitic facies in the upper contact (border zone) of the Steli pegmatite (FG-UC). The glasses in the remainder of the experiments have SiO_2 concentrations more than 5 wt% lower than the Steli and the "Iveland Wall" pegmatites. The glass from experiments performed at temperatures above 950°C generally have Al_2O_3 concentrations comparable to the Steli and the

"Iveland Wall" pegmatites, whereas the experiments performed at 900° C are more aluminous. The same is observed for Na_2O. The elevated Na_2O concentrations are particularly notable in the 900° C experiments. Müller et al. (2018) suggested that melt-melt immiscibility resulted in the generation of an alkali-water-poor melt and an alkali (sodium-dominated)-water-fluorine-rich melt and the formation of albite zone. The low-degree partial melts in the 900° C experiments are aluminous and sodium-rich and are compositionally similar to the albite zones. However, they are fluorine-poor and water-undersaturated and are thus unlikely to be directly responsible for the generation of the albite zones. Instead, as suggested by Müller et al. (2018), melt-melt immiscibility was likely to occur at late stages of pegmatite formation as a result of magmatic differentiation. The remaining major elements in experiments performed at 900 and 950°C are comparable to the Steli and "Iveland Wall" pegmatites and are greater than the albite zones. The Steli and the "Iveland Wall" pegmatites have approximately the same bulk composition, but are more siliceous, aluminous, and sodic than the albite zones. Based on the bulk composition, it is not unreasonable to conclude that partial melting of <40% by mass of an amphibolite host rock may produce pegmatite-forming (i.e. granitic) melts. This degree of partial melting is consistent with the conclusions of Rapp et al. (1991) and Rapp and Watson (1995), which suggest 10% to 40% and 10 to 55% of partial melting to produce granitic melts, respectively.

4.6.2.2. Trace Elements

There are also differences in the trace element signatures among the experimental glasses and the Evje-Iveland pegmatites. The experimental glasses in this study are strongly depleted in scandium and many of the REEs and are below detection in low-degree partial melts (Table 4.12). As noted by London (2005), Černý et al. (2005), and London (2018), the concentration of essential constituents (e.g. Nb, Ta, Be, etc.) in a melt, at anatectic temperatures (>700°C), needed to saturate with minerals (e.g. columbite, beryl, etc. both of which are found in Evje-Iveland pegmatites (Müller et al., 2015)) often found in pegmatites are significantly higher than the protolith. As such, large degrees of differentiation are needed to reach the saturation point for these minerals. Thus, it is unlikely that the low-degree partial melts generated in the experiments discussed here, or in natural settings, have high enough concentrations to be saturated with minerals such as thortveitite, the columbite-group minerals, or beryl. It should be noted that at very low melt fractions, for elements with partition coefficients << 1, there could be a large enrichment of that element in the melt; however, there are no indications that this is the case in the experiments discussed in this study.

The REE patterns of the run product glasses are compared to the REE patterns of the border and wall zones of pegmatites found in the Evje-Iveland pegmatite field and the Høvringsvatnet granites in Figure 4.12. The first clear difference is that the pegmatites have significant negative europium anomalies that are not present in the REE patterns of the run product glasses. The exception to this is the bulk "Iveland Wall" sample (Snook, 2014), which has a positive europium anomaly and roughly

similar chondrite normalized REE values to the low-degree partial melts (experiments EIP-4 and EIP-7). Snook (2014) noted that LREE or HREE enrichment relative to each REE group in the pegmatites is minimal, but variable. Although the experimental glasses in this study are not LREE or HREE enriched, the pegmatites have greater chondrite normalized REE values than the run product glasses. The REE patterns for the Høvringsvatnet granites, the source of the pegmatitic melts proposed by some, are LREE enriched and HREE depleted with no europium anomaly, which are significantly different from the pegmatites and experimental glasses.

In order to further examine the hypothesis that the petrogenesis of the pegmatites involved anatexis, it is useful to compare the experimental glasses and pegmatites to rocks that are known to have an anatectic origin. Such rocks include migmatites, such as the leucosomes in vein-type migmatites in Archean rocks from the Grenville Front, Quebec (Sawyer, 1991). These migmatites are of particular interest because the leucosomes (see Figure 3d of Sawyer, 1991) and the "Iveland Wall" outcrop (see Figure 12 of Müller et al. 2017b) have similar textural relationships to their host rock. Sawyer (1991) concluded that the Grenville Front leucosomes are the result of equilibrium partial melting, with a garnet and hornblende residue, and migration and intrusion of those melts into the host rock as vein networks. The leucosomes have strong LREE enrichment, as well as a lack of europium anomaly. The REE patterns of the leucosomes and the majority of the pegmatites are not similar (with the exception of Kåbuland (BZ)). However, the REE patterns of the leucosomes are similar to the higher pressure (> 800 MPa) experiments of Rapp et al. (1991), wherein garnet is stable. It is important to note that

the 800 MPa experiments of Rapp et al. (1991) are not LREE enriched and have flat REE patterns with no europium anomalies, which are similar to the experimental glasses in this study. It can be concluded that the LREE enrichment in the leucosomes of the vein-type migmatites is a consequence of garnet in the residue. If the leucosomes were generated at lower pressures, wherein garnet was not stable, they would have similar REE patterns to both the 800 MPa experiments of Rapp et al. (1991), the experimental glasses of this study, and the "Iveland Wall" sample (Snook, 2014). Thus, it is suggested that the felsic material at the "Iveland Wall" has a similar petrogenesis to the leucosomes in the vein-type migmatites of the Grenville Front, albeit at lower pressures. This petrogenesis includes equilibrium partial melting of a basaltic like material with hornblende ± clinopyroxene in the residue followed by melt migration and intrusion of that melt into the host rock. This is supported by the REE patterns of the experimental glasses derived in this study; however, the REE patterns do not support formation of rare element pegmatites by direct anatexis of amphibolite. The REE patterns of the Høvringsvatnet granites are similar to the REE patterns of the leucosomes from the Grenville Front. Generation of a partial melt as noted above, followed by magmatic differentiation may result in a melt that has a REE pattern similar to the Høvringsvatnet granites. Further differentiation, may ultimately produce a melt that has a similar REE pattern to the pegmatites at the Evje-Iveland pegmatite field, where as direct anatexis cannot.

Based on the REE patterns, the petrogenetic sequence described above, without a need for magmatic differentiation, is only present in two pegmatites: the "Iveland Wall" and potentially Kåbuland (BZ; due to is strong LREE enrichment) in

the Evje-Iveland pegmatite field. For the remaining pegmatite border zones where data are available, there is no LREE enrichment and strong negative europium anomalies are not observed in the experimental glasses in this study or in previous studies. Taking into consideration the low concentrations of scandium and the REEs in the run product glasses of this study, and the differences among the REE patterns as compared to the pegmatites, there is no evidence to support the formation of the rare element pegmatites within the Evje-Iveland pegmatite field by direct anatexis of the host amphibolite and consideration of an alternative petrogenesis, such as magmatic differentiation, is warranted.

4.6.3. Solidus Temperature

The vapor-absent solidus temperature of close to 900° C determined here is significantly higher than the temperatures of pegmatite emplacement at 613° ± 70° C determined by titanium-in-quartz thermometry for the Evje-Iveland pegmatites (Müller et al., 2015). The emplacement temperatures (550 to 600°C) of the pegmatites estimated from the metamorphic aureole surrounding the Rogaland complex (Müller et al., 2015) are not well constrained. The estimates of the temperature near the edge of the metamorphic aureole (~750°C) extend, at most, a few tens of kilometers away from the contact of the intrusion (Jansen et al., 1985; Westphal et al., 2003), whereas the Evje-Iveland pegmatite field is ~100 km away from the intrusion. However, heat provided to the region by underplating of mafic magma (Müller et al., 2015) cannot be ruled out. It can be argued that the solidus temperature and pegmatite emplacement temperature shouldn’t be consistent if the melt was generated distal to the emplacement location of the pegmatites, with

significant melt migration. This is common in the generation of granitic pegmatites as the melt migrates away from the source pluton and crystallize as a result of undercooling during emplacement in a colder host rock (London, 2008). However, Müller et al. (2015) suggested that melting and pegmatite emplacement occurred in approximately the same location. If pegmatite formation by direct anatexis is assumed, it could then be concluded that the temperature of emplacement and the temperature of amphibolite melting should be approximately the same, which is not supported by the experiments conducted in this study.

A lower solidus temperature could be achieved by increasing the pressure. An increase in pressure, such that garnet is stable instead of clinopyroxene (between 700 MPa and 1 GPa), can reduce the solidus temperature to ~650° C at 700 MPa (Wyllie and Wolf, 1993). This pressure and temperature estimate is similar to the emplacement conditions suggested by Müller et al. (2015); however, the stabilization of garnet in the residue would significantly impact the trace element signature of the melt. First, the REE patterns of the melt would be LREE enriched and HREE depleted (e.g. Rapp et al., 1991), which is inconsistent with the REE patterns of the pegmatites (with exception of Kåbuland, BZ). Secondly, scandium is compatible in garnet relative to a silicate melt (Chassé et al., 2018; Steffenssen et al., 2019; Westrenen Wim et al., 1999) and will be depleted in the melt, similar to the experiments performed in this study. Thus, higher pressures, although capable of reducing the solidus temperature, are not supported by trace element abundances observed.

A second possibility for lowering the solidus temperature is the introduction of an externally derived fluid to the system. The introduction of a fluid containing fluxing agents (water, fluorine, boron, lithium etc.) may reduce the solidus temperature to the wet basalt solidus, which is ~700° C at 500 MPa (e.g. Holloway and Burnham, 1972; Tuthill, 1968; Yoder and Tilley, 1962). An externally derived fluid could also introduce trace elements, such as scandium, that would otherwise be sequestered in the residue during partial melting. It has been proposed that scandium can be transported by fluorine-rich hydrothermal fluids (Gramaccioli et al., 2004; Guastoni et al., 2012; Kempe and Wolf, 2006; Pezzotta et al., 2005) and thus similar fluids may be required to provide scandium to the Evje-Iveland pegmatite system.

4.6.4. Petrogenetic Model

The introduction of an externally derived melt, in addition to an externally derived fluid, must be considered for the generation of the Evje-Iveland pegmatites. The experiments conducted in this study offer little support to the hypothesis that the pegmatites were derived by direct anatexis of host amphibolite, because the melt compositions (major and trace elements; particularly scandium and the REEs) and the solidus temperatures are not consistent with previous observations. As such, it is suggested that the pegmatite-forming melt was not a result of direct anatexis of the host amphibolite, but instead an externally derived melt generated by melting of a scandium-rich source rock (several hundreds of ppm scandium), differentiation of that melt resulting in scandium enrichment, and emplacement of that melt in the host amphibolite. A scandium-rich source rock is required to generate a melt that is capable of saturation with thortveitite upon emplacement. This melt must be

scandium-rich compared to average felsic rocks, which do not saturate with thortveitite (i.e. the average scandium concentration in the upper continental crust is 14 ppm; Rudnick and Gao, 2003) although the melt will be scandium-poor relative to any residue generated during melting. Additionally, any residue must be garnet-absent and contain plagioclase. The presence of garnet in the residue would produce a LREE enriched and HREE depleted REE pattern, which is not seen in the REE patterns of the Evje-Iveland pegmatites (Figure 4.12); therefore, garnet must be absent. Plagioclase must also be present in the residue in order to produce the negative europium anomalies observed in the pegmatites (Figure 4.12). The constraints of garnet absent and plagioclase present make the assumption that the source material has not been previously been depleted in HREEs or already has a negative europium anomaly and that these features are derived from the partial meting event. Scandium-enrichment due to differentiation of a melt requires that the crystallization products of the melt contain minimal ferromagnesian minerals, such as biotite, amphibole, and pyroxenes, as these minerals will sequester scandium. It can be speculated that a melt or coexisting fluid, if the melt is volatile saturated, contains anions that may strongly complex with scandium (e.g. F, Cl, C-species). Such scandium complexes may allow scandium to remain in a melt or fluid, even if ferromagnesian minerals are present. One anion of particular interest is fluorine as fluorine-rich fluids have often been associated with scandium-bearing deposits (Gramaccioli et al., 2004; Guastoni et al., 2012; Kempe and Wolf, 2006; Pezzotta et al., 2005). Additionally, fluorine prefers to remain in the melt and can have significant effects on melt structure and phase equilibria, as well as complex with

cations, such as tungsten and tin (e.g. Manning, 1981). If scandium can complex with fluorine and those complexes remain in the melt, then scandium could be concentrated in melts with significant levels of fluorine more efficiently than fluorine-poor melts. A scandium-rich cumulate that is fluxed by a fluorine-rich fluid and partially melted, resulting in a fluorine-rich partial melt may yield the best scenario for forming a scandium-rich felsic melt. It is also unclear how scandium behaves when a melt reaches volatile saturation. If the partition coefficients for scandium between a magmatic-hydrothermal fluid and a melt is high enough, it is possible that the scandium can be stripped from the melt, concentrated in a fluid, and later deposited.

Thus, it is suggested that formation of the Evje-Iveland pegmatites was the result of the partial (or complete) melting of a scandium-rich source rock, which leaves a garnet-absent and plagioclase-present residue; followed by magmatic differentiation, wherein the crystallization products contained minor ferromagnesian minerals or the melt contains anions that strongly complex with scandium and prefer to remain in the melt; and subsequent emplacement of a volatile- and scandium-rich melt. This model is consistent with previous suggestions that rare element pegmatites are the result of magmatic differentiation.

Partial melting of a scandium rich-source rock would also leave behind a residue containing elevated concentrations of scandium. The host amphibolite is, again, unlikely to be the source of the pegmatites as it, at present, has a scandium concentration (39 ppm scandium; Rosing-Schow *et al.*, 2018) that is typical of basaltic rocks (40 ppm scandium in MORB; Gale et al., 2013). The scandium-rich

source rock likely was an ultramafic or mafic pyroxene-rich complex. Such complexes have been observed at the Kiviniemi intrusion in Finland (Ahven, 2012), as well as the Gilgai (Nyngan) and Tout Intrusive Complexes of the Fifield platinum district in eastern Australia, which have been prospected for scandium, in addition to nickel, cobalt, and platinum (Chassé et al., 2017; Fairfield et al., 2018; Johan et al., 1989; Rangott et al., 2016). The Kiviniemi intrusion has a reported scandium concentration that reaches at maximum of ~200 ppm in a fayalite ferrogabbro unit (Halkoaho et al., 2020). Within the intrusion, the major scandium-bearing phases are amphibole, clinopyroxene, and apatite, which have concentrations of Sc_2O_3 that range from 103-2088 ppm, 610-1740 ppm, and 940-1133 ppm, respectively (Ahven, 2016). The apatite at Kiviniemi is fluorapatite, which may also be a potential source of fluorine that can complex with scandium (Halkoaho et al., 2020). Additionally, any amphibole or mica within the cumulates or intrusions may also be as source of fluorine, and during partial melting that fluorine enters the melt. The Gilgai and Tout Intrusive Complexes are Alaskan-type complexes that contain pyroxenites, hornblende pyroxenites, olivine pyroxenites, and dunites (Chassé et al., 2017; Johan et al., 1989; Rangott et al., 2016). Alaskan-type complexes are ultramafic-mafic cumulates that occur as the result of fractional crystallization of basaltic magmas and contain forsteritic olivine, diopsidic and augitic clinopyroxene, magnetite, and hornblende (Himmelberg and Loney, 1995). It is conceivable that a complex similar in composition to the Kiviniemi Intrusion or Gilgai and Trout Complexes was or is present at depth in the region of the Evje-Iveland pegmatite field and partial melting of this complex, followed by magmatic differentiation was responsible for the

formation of the pegmatites. This petrogenic model is similar to that suggested by Williams-Jones and Vasyukova (2018) for the formation of scandium-rich pegmatites, with one key difference. Williams-Jones and Vasyukova (2018) accepted that the host amphibolite is the metamorphic equivalent of the source rock for the pegmatite-forming melt. In their model they suggest that a clinopyroxenite (i.e. ultramafic cumulate) was fluxed by metamorphic fluid and partial melting, wherein all of the scandium present in the clinopyroxenite was released into the partial melt. Williams-Jones and Vasyukova (2018) did not recognize that the efficiency that scandium is removed from the source rock into the melt, wherein that source rock contains amphibole, is far below 100%. In order to reach scandium concentrations in the melt high enough to be saturated with thortveitite, magmatic differentiation is required. The model proposed in this study agrees with the model of Williams-Jones and Vasyukova (2018) in that a pyroxene-rich cumulate was the source rock for the pegmatite-forming melt, but disagrees that, that the melt did not undergo differentiation and that the host amphibolite is the metamorphic equivalent of this pyroxene-rich cumulate.

A notable intrusive body that may be related to the formation of the pegmatites is the Flåt metadioritic suite, comprising the Mykleås diorite, the Flåt ore diorite, and the Fennefoss metagranodiorite (augen gneiss). Although, the Flåt suite is substantially older (age of ~1030 Ma) than the Evje-Iveland pegmatites and is not particularly rich in scandium, it is unique in that it is host to a nickel deposit hosted in felsic rocks (Pedersen, 1993). The nickel mineralization has been interpreted to be the result of immiscibility of a sulfide melt from the magma (Pedersen, 1993); a similar

process for base metal sulfide mineralization in Alaskan-type platinum deposits (e.g. Kelvin Grove, Owendale Intrusive Complex, Australia, which is spatially associated with Gilgai and Tout Intrusive Complexes; Johan et al., 1989). Pedersen (1993) also concluded that the Flåt metadioritic suite was formed by partial melting of a mantle-derived magma. Thus, it can be speculated that the formation of the Flåt metadioritic suite may be related to the partial melting of an ultramafic (possibly Alaskan-type) complex rich in nickel and scandium. Partial melting of this complex may result in a melt, which undergoes magmatic differentiation that concentrates scandium and nickel. During the final stages of crystallization, the nickel is removed by an immiscible sulfide melt (Pedersen, 1993) and the scandium-rich melt may form the Evje-Iveland pegmatites. More data are required to test this hypothesis; however, the close spatial association of the nickel-bearing Flåt diorite to the pegmatites is worthy of further investigation.

The role of the Høvringsvatnet granite in the formation of the pegmatites remains uncertain. The granites may be the partial melts of complexes such as the Gilgai and Tout Complexes and the pegmatites may represent the final stages of magmatic differentiation of that partial melt. However, the Høvringsvatnet granite contains both biotite and amphibole (Pedersen, 1975), which will sequester scandium during differentiation, and have relatively low concentrations of scandium (Snook, 2014). Regardless of the role the Høvringsvatnet granite have in pegmatite formation, there is enough variation in the interpreted ages of the pegmatites, such that age alone cannot exclude the granites as the source of the pegmatites.

4.6.5. Implications Outside of the Evje-Iveland Pegmatite Field

This study also has implications for the formation of pegmatites outside of the Evje-Iveland pegmatite field. The generation of rare element, usually LCT, pegmatites by direct anatexis has been suggested for other localities such as Kings Mountain, North Carolina, USA (Norton, 1973) and the Mt. Mica pegmatite in Maine, USA (Simmons et al., 2016), as well as from experimental data on LCT pegmatites (Stewart, 1978). As discussed above for the Evje-Iveland pegmatite field, generation of a volatile- and trace element-rich melt by direct anatexis without magmatic differentiation is problematic. The melts generated are often in equilibrium with a residue that contain ferromagnesian phases that sequester trace elements. Additionally, the temperatures produced during low-pressure metamorphism are, generally, not high enough to produce felsic melts without the introduction of a volatile phase or by direct transfer of volatiles from hydrous minerals (such as amphibole) to a melt. This study shows that even in the latter case, the melts produced are not volatile- or trace element-rich and without further differentiation the formation of rare element pegmatites and saturation with phases commonly found in rare element pegmatites is unlikely. These observations echo the observations of Černý et al. (2005) and London (2018), and references therein, who outlined these and additional problems with anatectic origins of rare element pegmatites. As such, it can be concluded that the origin of rare element pegmatites by direct anatexis is unlikely; however, direct anatexis may generate barren pegmatites.

4.7. Conclusions

The results of partial melting experiments performed on the Evje-Iveland host amphibolite are inconsistent with the hypothesis that the Evje-Iveland pegmatites are the result of direct anatexis of that amphibolite. The solidus of the amphibolite is close to 900°C at 500 MPa. The run product glasses generated are broadly granitic and are aluminum- and sodium-rich; however, they are less siliceous than the Evje-Iveland pegmatites. Additionally, the solidus temperature of 900° C is significantly higher than the suggested emplacement temperature of 613° ± 70° C (Müller et al., 2015). At the solidus, magnesiohornblende and plagioclase react to produce a melt and a residue of pargasite and less sodic plagioclase. At temperatures above the solidus, pargasite and the less-sodic plagioclase react to generate larger melt fractions and a residue containing aluminian diopside. The glasses are depleted in trace elements, notably scandium and the REEs. REE patterns of the run product glasses are generally flat with minor LREE enrichment and minor positive europium anomalies at low degrees of partial melting. These REE patterns are significantly different from the REE patterns of the Evje-Iveland pegmatites, but are similar to leucosomes in vein-type migmatites produced at low pressures. The differences in major and trace elements, as well as the high solidus temperature of the experimentally derived glasses, as compared to the Evje-Iveland pegmatites, do not support the hypothesis that the rare element pegmatites were generated by direct anatexis of the host amphibolite. The exception to this may be the leucosomes found at the “Iveland Wall”, which in light of this study, have been interpreted to have a similar petrogenesis to the leucosomes in vein-type migmatites (e.g. Sawyer, 1991).

Thus, it is suggested that two generations of melts are present in the Evje-Iveland pegmatite field. One generation of melt is related to direct anatexis and formation of barren pegmatites (leucosomes) such as those found at the “Iveland Wall” and a rare element pegmatite-forming melt.

An alternate hypothesis for the generation of the rare element pegmatite-forming melt is the partial melting of a scandium-rich ultramafic or mafic complex, differentiation of the partial melt wherein that melt may contain anions that readily complex with scandium, and emplacement of a volatile-saturated melt into the host amphibolite. Such complexes are commonly early crystallization and cumulate products during magmatic differentiation. The partial melting of these complexes and magmatic differentiation of those melts may result in the formation of the Flåt metadoritic suite or the Høvringsvatnet granites and the pegmatites may represent the final stages this differentiation. This hypothesis and the connection between the Flåt diorite, Høvringsvatnet granites, and the Evje-Iveland pegmatites warrant further consideration.

The generation of rare element pegmatite-forming melt by direct anatexis of the host rocks at Evje-Iveland or other localities is not support by this study. These partial melting experiments demonstrate that melts produced by anatexis of common metamorphic rocks, although broadly granitic in composition, lack the enrichment of volatiles and trace elements commonly seen in LCT and NYF pegmatites. Instead, magmatic differentiation is the preferred model for the formation of rare element pegmatites.

4.8. Acknowledgments

The authors thank Axel Müller for providing the samples necessary for completion of these experiments. Amanda Lindoo and Jing Yang are thanked for technical assistance for performing the piston-cylinder experiments. Emma Bullock and Richard Ash are thanked for assistance in performing electron microprobe analyses and analysis by LA-ICP-MS, respectively. A. Jay Kaufman, Richard J. Walker, Sarah C. Penniston-Dorland, and Andrew Houston are also thanked for providing the necessary equipment and assistance in order to process the starting material. Austin M. Gion is supported by the National Science Foundation [grant EAR 1348010] and the Department of Geology, University of Maryland.

5. Chapter 5: Ferromagnesian Silicates: Fingerprints of Felsic-Magmatic Systems

Austin M. Gion[1], Philip M. Piccoli[1], and Philip A. Candela[1]

[1]Laboratory for Mineral Deposits Research, Department of Geology, University of Maryland, College Park, Maryland

*Corresponding author. Present Address: 8000 Regents Drive, Department of Geology, University of Maryland, College Park, MD 20742, USA. Email: agion@umd.edu Phone: (301) 405-4082

This chapter is presented as a manuscript that is being prepared for submission to be published. The author of the dissertation is the primary author for this work. Philip M. Piccoli and Philip A. Candela acted as advisors for this work.

5.1. Abstract

Implicit in the S-, I-, and A-type genetic classification of granitic rocks is information about the compositional characteristics of the source rocks and related granitic magmas. Given that biotite and amphibole are common accessory minerals in granites, the question arises as to whether these minerals can fingerprint aspects (composition and intensive parameters) of the magma from which they crystallize. In order to address this question, a database of biotite and amphibole compositions has been compiled and scrutinized. In this work, nearly 1750 analyses (1215 biotite and 525 amphibole) were compiled from previously classified I-, S- and A-type granites. Several identifying compositional characteristics of biotite and amphibole were determined and a bootstrap random forest technique was utilized to evaluate if these minerals reflect the characteristics of source rocks and the related granitic magma. Six characteristics of biotite and three characteristics of amphibole composition have been identified.

In the case of biotite, results show that $X_{\mathrm{Annite}}^{\mathrm{Bt}}$ (fraction of Fe^{2+} in the octahedral site), $X_{\mathrm{Fe^{VI*}}}^{\mathrm{Bt}}$ (fraction of total iron in the octahedral site), and total aluminum (apfu) can be used to distinguish between A- and S-type granites, whereas the fluorine intercept values (IV[F]) and the associated $\frac{f_{\mathrm{H_2O}}}{f_{\mathrm{HF}}}$ are useful discriminators between I- and A-type granites. The composition of biotite from S- and I-type granites overlap considerably for the aforementioned variables. However, a bootstrap random forest model based on biotite composition can be used to as a discriminator between S-, I-, and A-type granites with 83.7% accuracy.

The presence of amphibole in granitic rocks is an indicator that host rocks are derived from either I- or A-type sources. The dearth of natural examples of amphibole in S-type systems is striking; however, the lack of amphibole is not an effective indicator of the granite type. Total aluminum of amphibole, Fe/(Fe+Mg), and NK/CNK [defined as (Na + K)/(Ca + Na +K) in atoms per formula unit of amphibole can be used to distinguish between I- and A-type granites. The bootstrap random forest model based on amphibole composition can be used as a discriminator between (S-) I- and A-type granites with 96% accuracy.

Both biotite and amphibole compositions can yield estimates of a variety of intensive magmatic parameters, including f_{O_2}, $\frac{f_{H_2O}}{f_{HF}}$, $\frac{f_{H_2O}}{f_{Cl}}$, and $\frac{f_{HF}}{f_{HCl}}$ given appropriate mineral assemblages and for given temperatures and pressures. Based on these constraints, S-type granites are generally the most reduced, I-type granites are generally more oxidized, and A-type granites exhibit variable f_{O_2}. A-type granites exhibit lower $\frac{f_{H_2O}}{f_{HF}}$ and $\frac{f_{H_2O}}{f_{Cl}}$ compared to S- and I-type granites, whereas S- and I-type granites exhibit broadly similar $\frac{f_{H_2O}}{f_{HF}}$ and $\frac{f_{H_2O}}{f_{Cl}}$. Finally, the iron content of biotite and amphibole increases with increasing whole rock SiO_2, such that the most iron-rich ferromagnesian minerals are found in the most siliceous granites. Given the results of the bootstrap random forest modelling, as applied to a database of published analyses from known granite types, biotite and amphibole, the most common accessory phases in granites (*s.l.*), can independently be used to determine the characteristic of the source rock and related granitic magmas.

Keywords: amphibole; biotite; felsic; ferromagnesian; granite, A-type, I-type, S-type

5.2. Introduction

Granites *(s.l.)* are plutonic igneous rocks that exhibit a phaneritic texture and, by definition, comprise quartz (or rarely feldspathoids) and feldspar. Beyond these minerals granites contain a variety of accessory minerals including, but not limited to, biotite, amphibole, pyroxene, zircon, magnetite, ilmenite, sphene, and apatite. These phases may reach abundances of tens of modal (volume) percent and become major rock forming minerals. These accessory phases are often the primary hosts of trace elements and are thus the focus of many geochemical studies. Additionally, they may be used to refine the granite naming scheme (e.g. Glazner et al., 2019). Of these minerals, biotite and amphibole are arguably the most abundant and well studied, and can be used to calculate intensive (e.g. temperature) properties of magmatic systems. Studies have examined the use of biotite as an oxybarometer (Bucholz et al., 2018; Czamanske and Wones, 1973) and geothermometer (Patiño Douce, 1993). Biotite composition has also been used to obtain estimates of crustal contamination (Ague and Brimhall, 1988), as an indicator of tectonic setting (Shabani et al., 2003), and to infer magma composition (e.g. Abdel-Rahman, 1994). A complete review of previous studies is beyond the scope of this paper; however, a few notable works require more elaboration. Czamanske and Wones (1973) utilized the biotite solution model of Wones and Eugster (1965) and Wones (1972), together with the composition of the biotite, to estimate the partial pressure of water during the crystallization of the Finnmarka Complex, Norway. Ague and Brimhall (1987, 1988) used biotite composition to determine the degree of crustal contamination of granites in the Sierra Nevada Batholith. Their study determined that biotite composition reflects

contamination of subduction zone/mantle wedge-derived parental magma by incorporation of varying proportions of continental crust components. Abdel-Rahman (1994) suggested that biotite composition reflects the composition of the parental magma. Abdel-Rahman (1994) showed biotite composition graphically on a ternary diagram defined by the proportion of FeO* (total iron), MgO, and Al_2O_3 in mass units normalized to 100 (Figure 5.1). Three fields are evident, and correspond to alkaline granites and A-type granites (A) such as the Mulanje complex, Malawi; peraluminous and S-type granites (P) such as the Strathbogie Batholith, Australia; and calc-alkaline and I-type granites (C) such as the Sierra Nevada Batholith (Abdel-Rahman, 1994).

Amphibole composition has provided a basis for a geobarometer (e.g. Hammarstrom and Zen, 1986; Mutch et al., 2016), as well as a proxy for temperature and melt composition (Barnes et al., 2020; Putirka, 2016; Werts et al., 2020; Zhang et al., 2017). As a result amphibole composition has been used to constrain the thermal history of magmas and to gain an understanding of amphibole-melt equilibria. For example, Putirka (2016) calibrated thermometers and geobarometers based on amphibole composition, as well as determined the pressure and degree of cooling in pre-eruptive magmas of the Augustine and Merapi volcanos as recorded by the amphiboles in the eruption products. Werts et al. (2020) utilized the equations of Putirka (2016) and determined that amphibole from the Tuolumne Intrusive Suite are generally in equilibrium with melts that are more siliceous than the bulk-rock compositions of their hosts. Werts et al. (2020) interpreted this observation to be the result of crystal accumulation and (or) melt loss. Additionally, Barnes et al. (2020) used trace elements in hornblende to support the hypothesis that most granites have

undergone melt loss and that bulk rock compositions of granitic rocks do not represent melt compositions. This indicates that amphibole composition reflects the composition of their parental magma and gives insight into the true composition of a magma (Barnes et al., 2020; Werts et al., 2020).

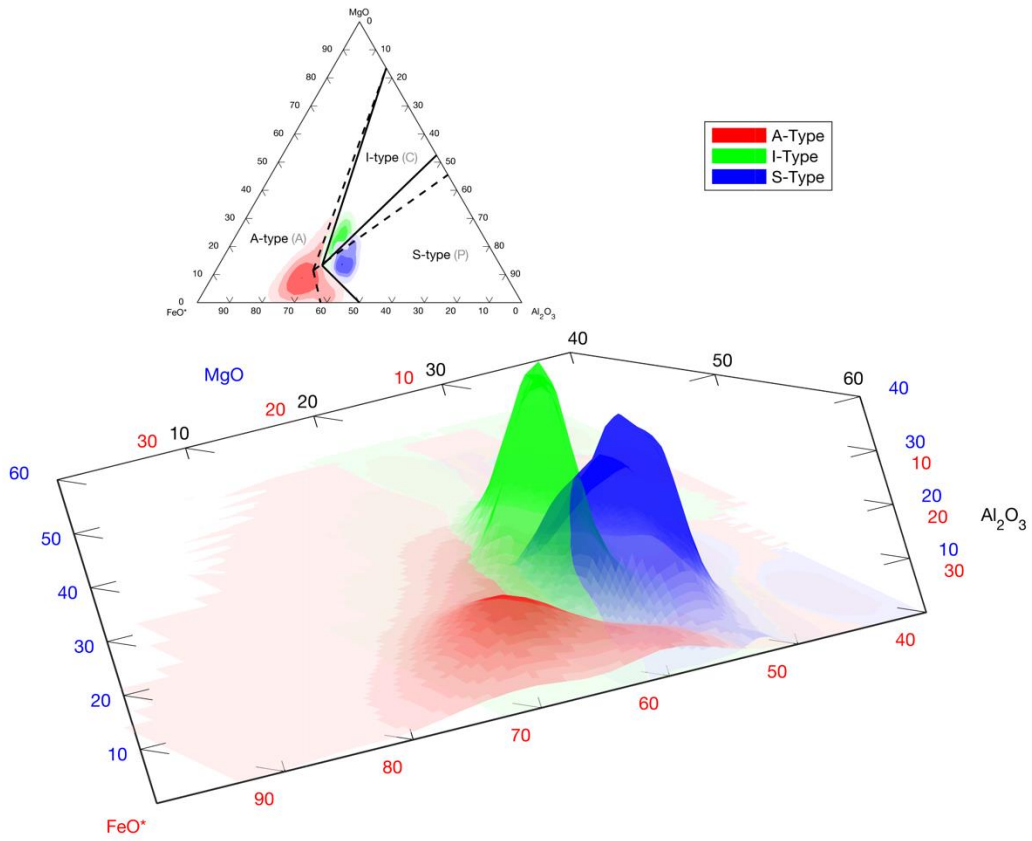

Figure 5.1: 3-D rendering of a FeO-MgO-Al_2O_3 (wt%) ternary diagram of biotite compositions included in this study. FeO* is total iron. Each volume is a three-dimensional surface of a kernel density estimate (KDE), representing the distribution of biotite compositions. The KDE and bandwidth (smoothing factor) are calculated after the method of Bowman and Foster (1993). Axes for the ternary diagram have been truncated and color coded; MgO is blue, Al_2O_3 is black, and FeO* is red. The upper ternary is modified from Abdel-Rahman (1994). Dashed lines are the original divisions determined by Abdel-Rahman (1994) for alkaline (A), calc-alkaline (C), and peraluminous (P) fields. Solid lines are new divisions proposed in this study to separate A-type, I-type, and S-type fields. See text for justification of new field and field names. End points for divisions of new fields are: Center = 56 FeO*, 32.5 Al_2O_3, 13.5 MgO; A-S dividing line = 50 FeO*, 50 Al_2O_3, 0 MgO; A-I dividing line = 0 FeO*, 16.5 Al_2O_3, 83.5 MgO; I-S dividing line = 50 FeO*, 47.5 Al_2O_3, 52.5 MgO. Contours are a two-dimensional representation of the 3-D rendering. The contour lines are drawn in 25% intervals. For example, approximately 75% of the data, given the distribution of the data and the probability density function determined by KDE, lies inside the lowest contour.

As outlined above, various authors have proposed that biotite and amphibole are the fingerprints of magmatic systems and that careful analysis and petrologic observations can elucidate the P-T-X conditions of the magmas from which they crystallize. We further suggest that biotite and amphibole compositions may be used as discriminators among S-, I-, and A- type granites (*s.l.*). S- and I-type granites are classified on the basis of their chemical composition and mineralogy, and those characteristics are used to infer the source material for those granites, whether sedimentary or igneous, respectively (Chappell and Stephens, 2011; Chappell and White, 1974, 2001). A-type granites were later included in this classification scheme and though their composition and mineralogy are reflective of their source material and they are distinct from S- and I-type granites, a specific sedimentary or igneous source is not inferred. Instead, a tectonic setting or a variety of sources, such as rift related (anatectic) melting of lower crustal (granulite) material, fractionation of mantle derived basaltic magmas, or partial melting of crustal (tonalitic or granodioritic) material is inferred (Anderson and Bender, 1989; Clemens et al., 1986; Collins et al., 1982; Eby, 1990; Frost and Frost, 2011; Loiselle and Wones, 1979; Whalen et al., 1987). Thus, the goal of this study is to examine and test the proposal that ferromagnesian minerals, such as biotite and amphibole in felsic-magmatic systems can be used as fingerprints of the magmas from which they crystallize and can be used as a discriminator of granite type.

5.3. Data and Methods

The data used in this study have been compiled through an extensive literature search, and although not exhaustive, represent a global distribution of biotite and

amphibole compositions from previously classified S-, I-, and A-type granites. Biotite and amphibole compositions in this study only include analyses from granites that are reported as S-, I-, and A-type granites in the literature and no additional effort has been made to further classify the granites. The database used here comprises 1215 biotite analyses (S-type: 299, I-type: 669, A-type: 247) from 47 sources, and 525 amphibole analyses (I-type: 368, A-type: 157) from 17 sources. A complete list of references is given in the supplementary files (Appendix 5.A). In order to compare data from different studies on a similar basis, all biotite and amphibole mineral formulas were calculated after the method of Dymek (1983) and Hawthorne et al. (2012), respectively. Mineral formulas and additional information on calculation procedure are given in the supplementary files (Appendix 5.B and 5.C).

In order to evaluate how well biotite and amphibole compositions can be used to classify granites as either S-, I-, and A-type granites, two predictive models were constructed by using a bootstrap random forest technique for biotite and amphibole, respectively. The models were trained by using the *Classification Learner* app and exported as a function into MATLAB, where the *Bagged Tree* classifier was used. Cross-validation was used and set to five folds, i.e. the data were partitioned into five folds (five groups) and for each fold a model is trained on out-of-fold observations and evaluated on in-fold observations. Cross-validation generated five separate models and the average error across those models was taken to assess the accuracy of a model trained on all of the training data, prevent overfitting, and tune model parameters. After assessing the accuracy by cross-validation, a final model was trained using all of the data in the training data set. This final model was then tested

against a data set not used for training. This process was carried out for both biotite and amphibole, resulting in two predictive models. For the predictive model based on biotite composition, 1000 data points were used for training and 215 data points were withheld for testing. For the predictive model based on amphibole composition, 425 data points were used for training and 100 data points were withheld for testing.

5.4. Results

5.4.1. Biotite

The biotite compositions considered in this study are plotted on the ternary diagram of Abdel-Rahman (1994) (Figure 5.1). Biotite from A-type granites generally plot within the alkaline field, but extend into the peraluminous and calc-alkaline field. Biotite from I-type granites significantly overlap with both the S- and A- type granite fields and extend into the peraluminous field. Biotite from S-type granites generally fall within the peraluminous field, but do extend into the calc-alkaline field. Overall, there is considerable overlap amongst the S-, I-, and A-type granites with the alkaline, calc-alkaline, and peralumious fields as defined by Abdel-Rahman (1994). Previous studies have interpreted the alkaline field to be analogous to A-type granites, the peraluminous field to be analogous to S-type granites, and the calc-alkaline field to be analogous to I-type granites; however, this is not consistent with the results of this study. Thus, in light of the biotite compositions considered in this study, the fields determined by Abdel-Rahman (1994) do not adequately define S-, I-, and A-type granites.

Biotite compositions can also be compared on the basis of mineral formulas (Figure 5.2a and 5.2b). Each granite type has distinctly different biotite compositions

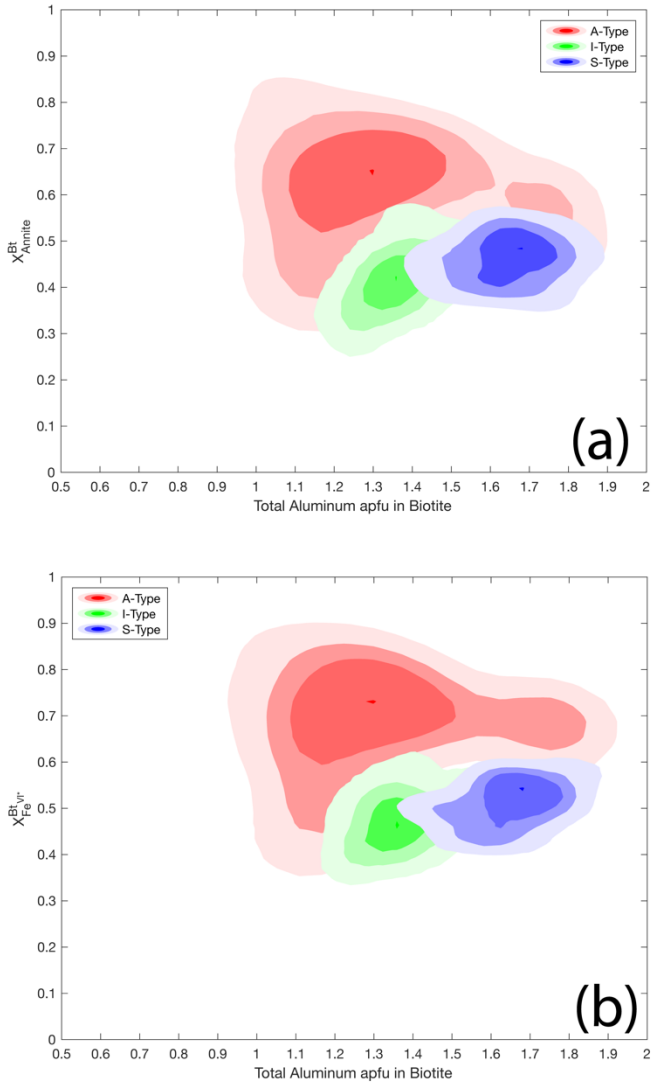

Figure 5.2: Plots of **(a)** X^{Bt}_{Annite} (fraction of the annite component in biotite defined as the fraction of Fe^{2+} in the octahedral site) and **(b)** $X^{Bt}_{Fe^{VI*}}$ [Fe^{VI*} is Fe^{2+} + Fe^{3+} in the octahedral site of biotite] versus total aluminum per formula unit (apfu) in biotite for S-, I-, and A-type granites. Formulas calculated after the method of Dymek (1983). See caption for Figure 5.1 for information on contours.

when evaluated on the basis of the mole fraction of the annite component in biotite (X^{Bt}_{Annite}; fraction of Fe^{2+} in the octahedral site), the fraction of total iron in octahedral site $X^{Bt}_{Fe^{VI*}}$ (wherein Fe^{VI*} is the fraction of Fe^{2+} + Fe^{3+} in the octahedral site), and aluminum atoms per formula unit (apfu), here after referred to as total aluminum. All three granite groups have broadly similar, but statistically different X^{Bt}_{Annite} and $X^{Bt}_{Fe^{VI*}}$

(see supplementary files (Appendix 5.C) for appropriate F- and t-tests). However, for a given total aluminum, biotite from A-type granites have a higher $X^{\mathrm{Bt}}_{\mathrm{Annite}}$ and $X^{\mathrm{Bt}}_{\mathrm{Fe^{VI*}}}$ than S- or I-type granites. Biotite from S-type granites are typically more aluminous than biotite from I- or A-type granites. Although the distribution of biotite compositions are comparable when plotted as either $X^{\mathrm{Bt}}_{\mathrm{Annite}}$ or $X^{\mathrm{Bt}}_{\mathrm{Fe^{VI*}}}$, at elevated total aluminum (>~1.6 apfu) the A-type field is separated from the S-type field when plotted as $X^{\mathrm{Bt}}_{\mathrm{Fe^{VI*}}}$. This feature is due to an increase in the amount of estimated Fe^{3+} (see Dymek (1983) for estimation procedure), that is, A-type granites contain biotite that is more iron-rich than biotite from I- or S-type granites.

Observed biotite compositions can also be compared to theoretical biotite compositions (represented as curves in Figure 5.3) that satisfy the equation

$$\log f_{H_2O} = \frac{7409}{T} + 4.25 + \frac{1}{2}\log f_{O_2} + 3\log X_{Fe^{2+}} + 2\log X_{OH}^{Bt} - \log a_{KAlSi_3O_6} - \log a_{Fe_3O_4} \quad \text{Eq. (5.1)}$$

from Czamanske and Wones (1973) at a given temperature, where $f_{\mathrm{H_2O}}$ is the fugacity of water, T is temperature, $f_{\mathrm{O_2}}$is oxygen fugacity , $X_{Fe^{2+}}$ is $X^{\mathrm{Bt}}_{\mathrm{Annite}}$, X_{OH}^{Bt} is the mole fraction of OH in the hydroxyl site, $a_{KAlSi_3O_6}$ is the activity of sanidine, and $a_{Fe_3O_4}$ is the activity of magnetite, and the total pressure (fluid pressure) is 200 MPa. The activities of magnetite and sanidine were set to 0.7 and 0.8, respectively. These values were shown to be consistent across a wide range of $f_{\mathrm{O_2}}$ for the crystallization of melts and were calculated by using alphaMELTS for MATLAB for each temperature, $f_{\mathrm{O_2}}$, and melt composition. The input compositions for the MELTS calculations were those of the average S-, I-, and A-type granites from Chappell and

White (1992) and Whalen et al. (1987). Observed biotite compositions from each granite are consistent with a wide range of possible pressure, temperature, f_{H_2O}, and f_{O_2} conditions (Figure 5.3). However, for a given temperature (800° C), biotite from S-type granites plot at an f_{O_2} of less than QFM (quartz-fayalite-magnetite), biotite from I-type granites are variable, but tend to plot at an f_{O_2} of between QFM and QFM+1, and biotite from A-type granites are variable and tend to plot between QFM and QFM+1. The reader should note that the P-T-f_{O_2} conditions are not necessarily

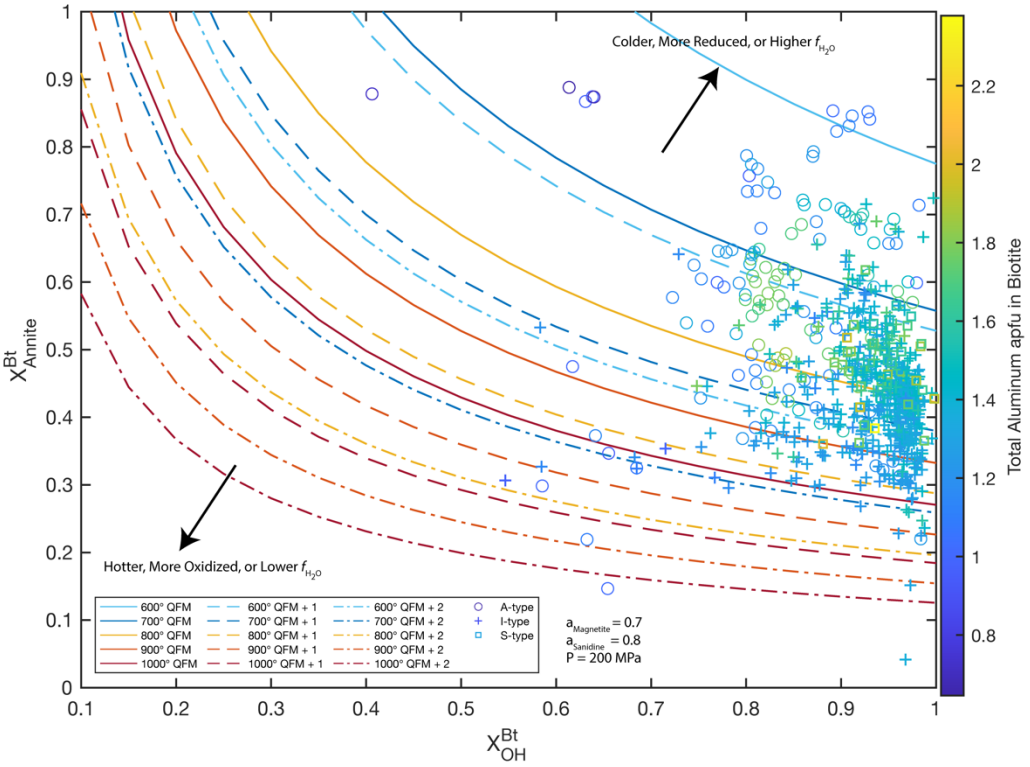

Figure 5.3: Plot of X^{Bt}_{Annite} vs X^{Bt}_{OH} for biotite compositions in this study. Curves are combinations of X^{Bt}_{Annite} and X^{Bt}_{OH} that satisfy the equation of Czamanske and Wones (1973) for determining f_{H_2O} at variable temperature and f_{O_2}. Pressure for all calculations is 200 MPa. The activities of magnetite and activity of sanidine were calculated using alphaMELTS for MATLAB for each temperature, f_{O_2}, and melt condition. Input for MELTS were average S-, I-, and A-type granites from Chappell and White (1992) and Whalen et al. (1987). Variations in the calculated activity of magnetite and activity of sanidine among each group at different temperatures and f_{O_2} are minor and thus were set to 0.7 and 0.8, respectively. See supplementary files (Appendix 5.D) for additional curves and individual figures. Only biotite where fluorine and chlorine were analyzed have been plotted.

the conditions at the time of biotite crystallization, but represent possible P-T-f_{O_2} conditions that satisfy equation 5. 1. See supplementary files (Appendix 5.D) for individual plots of each granite type.

Chlorine (IV[Cl]), fluorine (IV[F]), and fluorine/chlorine (IV[F/Cl]) intercepts are numerical values that define the degree of chlorine and fluorine enrichment and the ratio of the fluorine and chlorine enrichment in micas (Munoz, 1984). Such values were derived to account for the tendency of micas to exhibit Fe-F and Mg-Cl avoidances (Munoz, 1984). The intercept values also provide an estimate of the fugacities of hydrofluoric acid and hydrochloric acid relative to water fugacity. Intercept values were calculated after Munoz (1984) and were used to determine fugacity ratios given the equations

$$\log\left(\frac{f_{\mathrm{HCl}}}{f_{\mathrm{HF}}}\right) = \frac{-3501}{\mathrm{T}} + \mathrm{IV}\left[\frac{\mathrm{F}}{\mathrm{Cl}}\right] \quad , \qquad \text{Eq. (5.2)}$$

$$\mathrm{Log}\left(\frac{f_{\mathrm{H_2O}}}{f_{\mathrm{HCl}}}\right) = \frac{5151}{\mathrm{T}} + \mathrm{IV[Cl]} \quad , \qquad \text{Eq. (5.3)}$$

$$\log\left(\frac{f_{\mathrm{H_2O}}}{f_{\mathrm{HF}}}\right) = \frac{2100}{\mathrm{T}} + \mathrm{IV[F]} \quad , \qquad \text{Eq. (5.4)}$$

where

$$\mathrm{IV}\left[\frac{\mathrm{F}}{\mathrm{Cl}}\right] = 3.45\,X_{Mg} + 0.41\,X_{An} + 0.20\,X_{Sid} - \log\left(\frac{X_F}{X_{Cl}}\right) + 5.1 \quad , \qquad \text{Eq. (5.5)}$$

$$\mathrm{IV[Cl]} = -5.01 - 1.93\,X_{Mg} - \log\left(\frac{X_{Cl}}{X_{OH}}\right) \quad , \qquad \text{Eq. (5.6)}$$

and

$$\mathrm{IV[F]} = 1.52\,X_{Mg} + 0.42\,X_{An} + 0.20\,X_{Sid} - \log\left(\frac{X_F}{X_{OH}}\right) \quad . \qquad \text{Eq. (5.7)}$$

In these equations, as used by Munoz (1984) and as determined by Gunow et al. (1980), X_{Mg} is the mole fraction of phlogopite, X_{Sid} is the mole fraction of siderophyllite, and X_{An} is the mole fraction of annite as defined by

$$X_{Mg} = \frac{\text{Mg}}{\sum \text{Octahedral Cations}} \quad , \qquad \text{Eq. (5.8)}$$

$$X_{Sid} = \frac{\left(3 - \frac{Si}{Al}\right)}{1.75}\left[1 - X_{Mg}\right] \qquad \text{Eq. (5.9)}$$

and,

$$X_{An} = 1 - X_{Mg} - X_{Sid} \quad . \qquad \text{Eq. (5.10)}$$

Note that in these equations X_{An} is not equivalent to X_{Annite}^{Bt} and is only defined as X_{An} for the purposes of the calculations in equations 5.2 to 5.10.

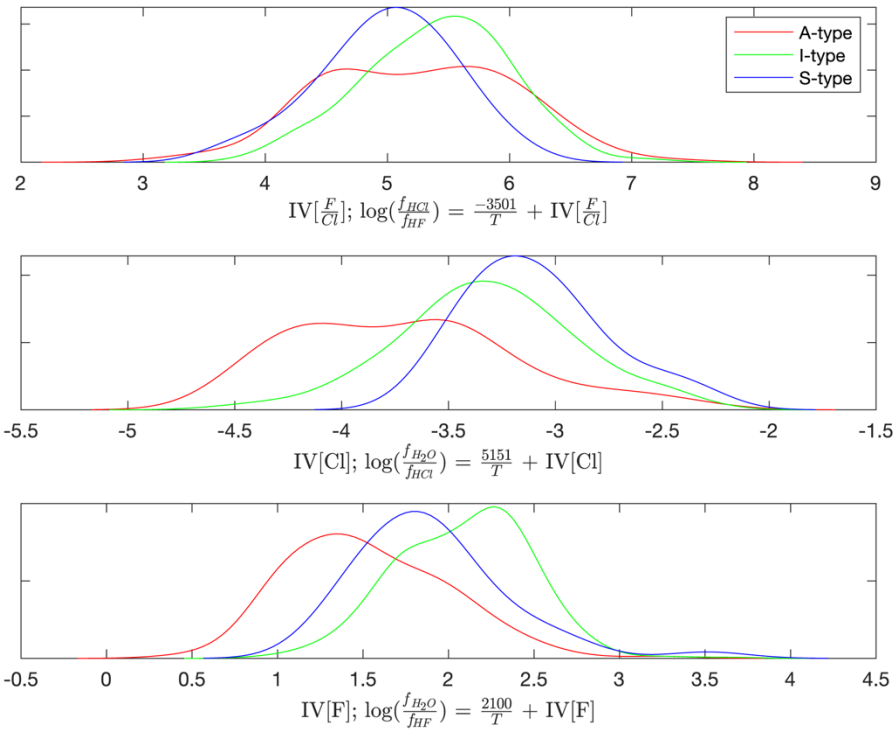

Figure 5.4: Chlorine (IV[Cl]), fluorine (IV[F]), and fluorine/chlorine (IV[F/Cl]) intercepts calculated after Munoz (1984) for biotite in this study (see text for details of calculations). Curves are a kernel density estimate (KDE); see caption to Figure 5.1. Only biotite where fluorine and chlorine were analyzed have been plotted.

There is significant overlap in all intercept values, particularly for IV[F/Cl] (Figure 5.4). Biotite from A-type granites have approximately the same IV[F/Cl] as both biotite from S- and I-type granites and there is only a minor separation in biotite from S- and I-type granites at a IV[F/Cl] of ~5.25. For both IV[Cl] and IV[F] biotite from A-type granites tend to have lower and more negative values. Biotite from S-type granites tend to have slightly lower IV[F] and slightly higher, but roughly equivalent IV[Cl] than biotite from I-type granites.

Approximately 36% of the biotite compositions in this study have corresponding whole rock data. When $X_{Fe^{VI*}}^{Bt}$ from this subset of data, are plotted against their corresponding whole rock SiO_2 (wt%) (Figure 5.5a), each granite type does not form a discrete field as seen in Figure 5.1 and 5.2. However, $X_{Fe^{VI*}}^{Bt}$ increases with increasing whole rock SiO_2 such that the most iron-rich biotite, for each granite type, occur in rocks with SiO_2 >70%. Further, whole rock ASI [aluminum saturation index defined as the molar $Al_2O_3/(Na_2O + K_2O + CaO)$] and total aluminum of biotite are also positively correlated (Figure 5.5b).

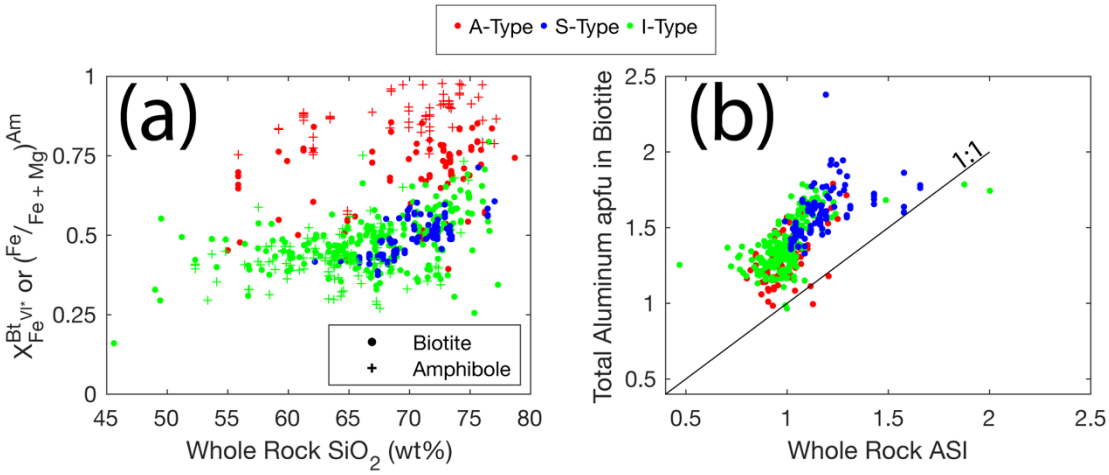

Figure 5.5: Variations in biotite and amphibole composition for S-, I-, and A- type granites**. a)** Plot of $X_{Fe^{VI}}^{Bt}$ and Fe/(Fe+Mg) in amphibole versus the SiO_2 (wt%) in whole rock samples. **b)** Plot of total aluminum apfu in biotite versus ASI [molar ratio of $Al_2O_3/(Na_2O + K_2O + CaO)$] in whole rock samples.

5.4.2. Amphibole

A comparison of amphibole compositions from S-, I-, and A-type granites is given in Figure 5.6. For amphibole from I-type granites, total aluminum and Fe/(Fe+Mg) [defined as $(Fe^{2+} + Fe^{3+})/ Fe^{2+} + Fe^{3+}+Mg$) in atoms per formula unit] increase with increasing NK/CNK [defined as (Na + K)/(Ca + Na +K) in atoms per formula unit of the amphibole]. However, for amphibole from A-type granites, as NK/CNK of the amphibole increases, amphibole total aluminum decreases, and Fe/(Fe+Mg) of the amphibole remains approximately constant. Additionally, there is

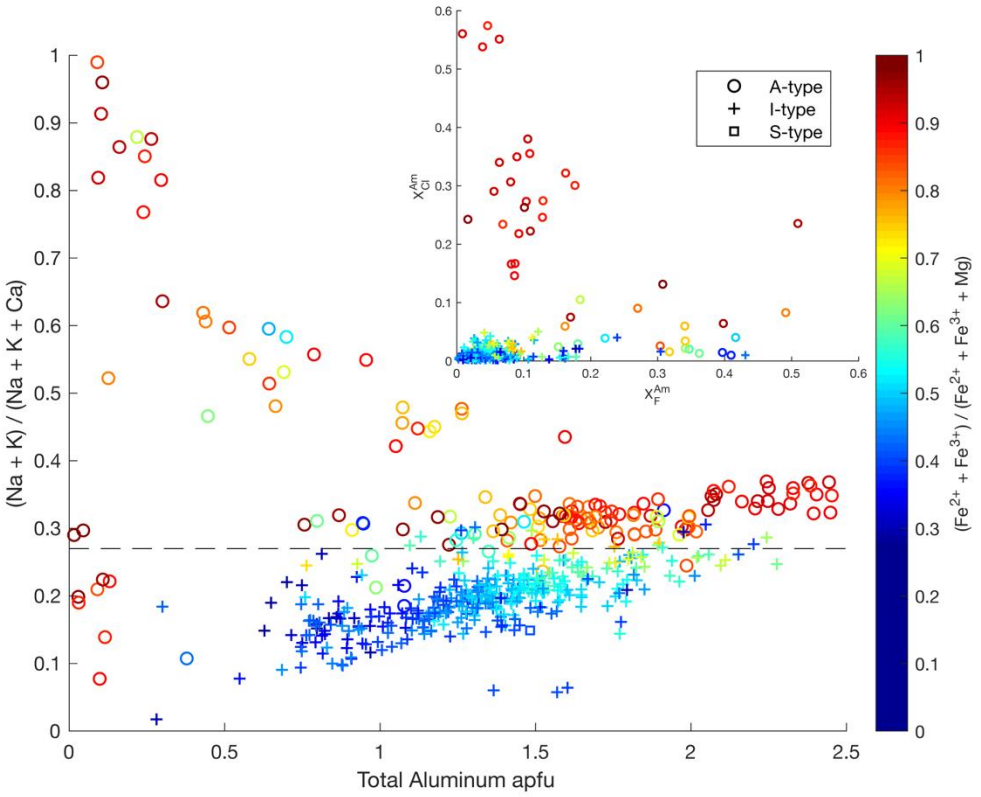

Figure 5.6: Plot of (Na + K)/ (Ca + Na + K) vs total aluminum apfu and colored by the ratio of $(Fe^{2+} + Fe^{3+})/(Fe^{2+} + Fe^{3+} +$ Mg) for amphibole in S-, I-, and A-type granites. Dashed line is the demarcation of amphibole from I- and A-type granites at NK/CNK = 0.27. Formulas calculated after the method of Hawthorne et al. (2012). All ratios are on the basis of atoms per formula unit. **Inset** is the variation in X_F^{Am} and X_{Cl}^{Am}, fractions of fluorine and chlorine in the hydroxyl site of amphibole, respectively, for analyses wherein both fluorine and chlorine were analyzed and colored by $(Fe^{2+} + Fe^{3+})/(Fe^{2+} + Fe^{3+} + Mg)$. The one amphibole from the S-type granites is of unclear origin, possibly xenocrystic (Joyce, 1970) and is not included in the count of amphibole compositions.

a group of amphibole from A-type granites that are aluminum-poor and have low

NK/CNK (Figure 5.6). These amphibole have been interpreted to be subsolidus or secondary grunerite (Wolf River Batholith; Anderson, 1975 and Pikes Peak; Barker et al. 1975). There is a clear demarcation of amphibole compositions at NK/CNK of the amphibole of 0.27, where non-gruneritic amphibole from A-type granites plot above 0.27 and amphibole from I-type granites plot below 0.27. Amphibole from I- and A-type granites thus form two distinct trends: 1). Increasing total aluminum of the amphibole with increasing NK/CNK of the amphibole and 2). Decreasing total aluminum of the amphibole with increasing NK/CNK of the amphibole. Additionally, amphibole from A-type granites generally have higher Fe/(Fe+Mg) than amphibole from I-type granites. Variations in $X_{\mathrm{F}}^{\mathrm{Am}}$ and $X_{\mathrm{Cl}}^{\mathrm{Am}}$, defined as the mole fraction of fluorine and chlorine in the hydroxyl site of amphibole, respectively, are plotted in the inset of Figure 5.6 and color coded by Fe/(Fe+Mg) of the amphibole. Amphibole from A-type granites are more variable in $X_{\mathrm{F}}^{\mathrm{Am}}$ and $X_{\mathrm{Cl}}^{\mathrm{Am}}$ than amphibole from I-type granites and $X_{\mathrm{F}}^{\mathrm{Am}}$ increases with decreasing Fe/(Fe+Mg). As with biotite, 36% of amphibole compositions have whole rock data available and Fe/(Fe+Mg) increases with increasing whole rock SiO_2, for each granite type (Figure 5.5a).

5.4.3. Predictive Modeling: Bootstrap Random Forest

The predictive model, generated by a bootstrap random forest technique, that is used to predict granite type based on biotite composition was trained by using 1000 randomly selected data points from the database presented above, wherein the predictors used were $X_{\mathrm{Annite}}^{\mathrm{Bt}}$, $X_{\mathrm{Fe}^{\mathrm{VI}*}}^{\mathrm{Bt}}$, total aluminum of biotite, IV[F], IV[Cl], IV[F/Cl]. The results of the model training are presented as a confusion matrix in Figure 5.7. In the training dataset, 206 data points are from A-type granites, 550 are

from I-types granites, and 244 are from S-types granites. Figure 5.7 also includes the positive predictive values (percentage that a predicted granite type matches the known granite type), false discovery rate (percentage that a predicted granite type does not match the known granite type), the true positive rate (percentage that the known granite type matches the predicted granite type), and false negative rate (percentage that the known granite type does not match the predicted granite type) for each granite type. During training, the model had a positive predictive value, based on biotite composition alone, of 78.5% for A-type granites, 82.1% for I-type granites, and 81.6% for S-type granites and a false discovery rate of 21.5%, 17.9%, and 18.4%, respectively. In order to test the model against a dataset not used for training, predictions were made on the remaining data (215 data points from the database presented above). Figure 5.7 contains a confusion matrix of the results of the test dataset. The model was able to predict the correct granite type with an overall accuracy of 83.7%. The positive predictive values and false discovery rates provide estimates on how well the model correctly predicts the granite type for a given unknown. For example, if the model predicts that the granite is an A-type granite based on the biotite composition, then the true granite type will be an A-type

granite 90.3% (positive predictive values) of the time and will be misclassified as an A-type granite 9.7% (false negative rate) of the time. For I- and S-types the positive predictive values are 83.2% and 81.1%, respectively with false discovery rates of 16.8% and 18.9%, respectively. If the model is trained by only considering total aluminum the total accuracy during training is ~70%. The addition of $X^{\mathrm{Bt}}_{\mathrm{Annite}}$ and $X^{\mathrm{Bt}}_{\mathrm{Fe^{VI*}}}$increase the accuracy to ~80% and the addition of the halogen intercept values increases the accuracy again by several percent more.

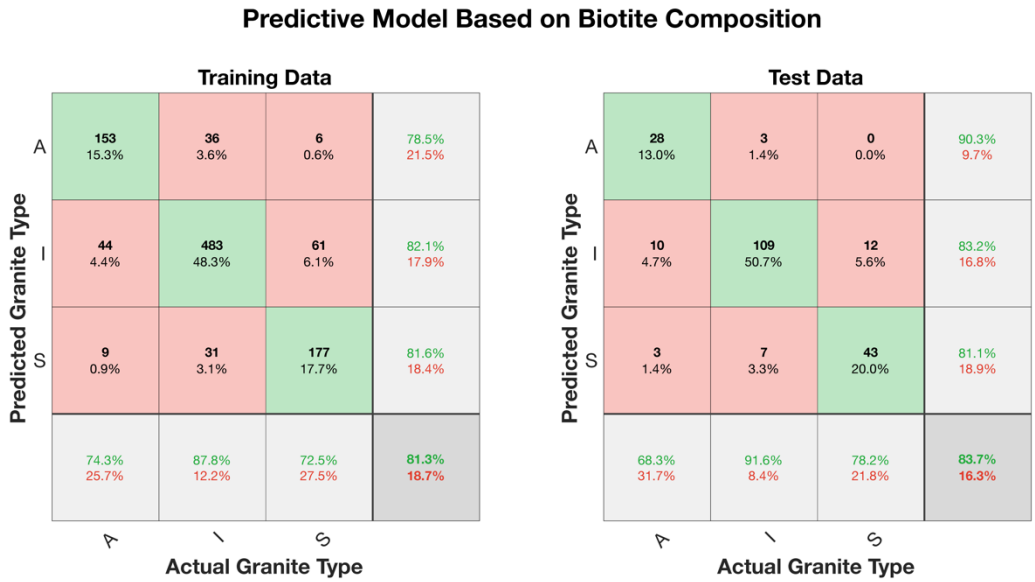

Figure 5.7: Confusion matrix for the training and test data sets classified by the predictive model based on biotite composition. The y-axis is the granite type predicted by the trained model. The x-axis is the granite type recorded in the literature. Numbers in bold are the number of observations that fall within that box; below the number of observations is the percentage of observation that fall within that box. The right most column are the positive predictive values (in green) and false discovery rate (in red). The bottom most row are the true positive rate (in green) and false negative rate (in red). The square in the bottom right (in dark grey) is the total accuracy of the predictions for the test data set. The confusion matrix for the training data set was generated by using the five models generated during cross-validation.

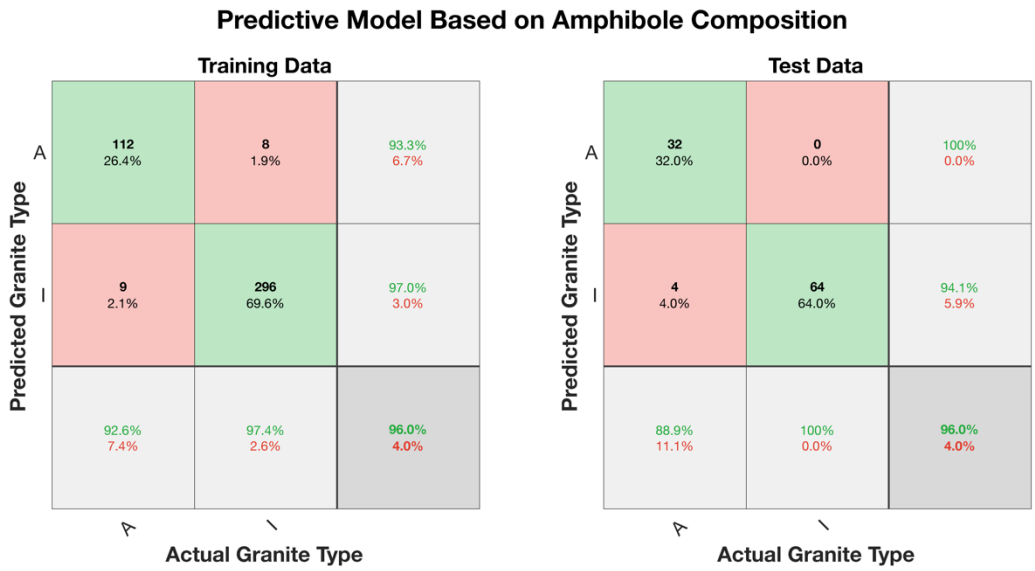

Figure 5.8: Confusion matrix for the training and test data sets classified by the predictive model based on amphibole composition. See caption of Figure 5.7 for further details.

A predictive model was also trained to predict granite type based on amphibole composition and the predictors included total aluminum of the amphibole, NK/CNK of the amphibole, and Fe/(Fe+Mg) of the amphibole. In this model 425 randomly selected data points were used for training and 100 data points were withheld for testing. In the training dataset 121 data points are amphibole from A-type granites and 304 data points are amphibole from I-type granites. The results of the model training are presented as a confusion matrix in Figure 5.8. During training the positive predictive values of the model were 93.3% and 97.0% with a false discovery rate of 6.7% and 3.0%, for amphibole from A- and I-type granites, respectively. The results of predictions for the 100 data points withheld from training are presented in Figure 5.8. The model was able to predict the correct granite type for the test data with an overall accuracy of 96%. The positive predictive values for A- and I-type granites are 100% and 94.1%, respectively with false discovery rates of 0% and 5.9%, respectively. If the model is trained by only considering NK/CNK the

total accuracy of the training is ~90%. The addition of the total aluminum of the amphibole, and Fe/(Fe+Mg) of the amphibole increase the accuracy of the model between ~2 and 6%.

5.5. Discussion

The results of this study are consistent with the hypothesis that the composition of biotite and amphibole in granitic rocks can be used as a discriminator of granite type. Biotite composition is best examined on the basis $X^{\mathrm{Bt}}_{\mathrm{Annite}}$ or $X^{\mathrm{Bt}}_{\mathrm{Fe^{VI*}}}$ versus total aluminum (Figure 5.2a and 5.2b). Examination of biotite composition, in consideration with halogen ratios, can provide insight on the intensive variables of a magmatic system, such as $f_{\mathrm{O_2}}$, $\frac{f_{\mathrm{HCl}}}{f_{\mathrm{HF}}}$, $\frac{f_{\mathrm{H_2O}}}{f_{\mathrm{HCl}}}$, $\frac{f_{\mathrm{H_2O}}}{f_{\mathrm{HF}}}$ and potentially temperature and pressure. Examining Figure 5.2a and 5.2b on a first order basis, A-type granites have the most variable $f_{\mathrm{O_2}}$. A-type granites containing biotite with >1.6 total aluminum and significant Fe^{3+} are more oxidized than granites containing biotite with <1.6 total aluminum and $X^{\mathrm{Bt}}_{\mathrm{Annite}}$ > ~0.5 (or $X^{\mathrm{Bt}}_{\mathrm{Fe^{VI*}}}$ > ~0.6) and are more reduced than granites containing biotite with <1.6 total aluminum and $X^{\mathrm{Bt}}_{\mathrm{Annite}}$ < ~0.5 (or $X^{\mathrm{Bt}}_{\mathrm{Fe^{VI*}}}$ <~0.6). I-type granites are more oxidized than S-type granites, this is reflected in the differences in $X^{\mathrm{Bt}}_{\mathrm{Annite}}$ and $X^{\mathrm{Bt}}_{\mathrm{Fe^{VI*}}}$ and is consistent with previous observations (Chappell and White, 1992, 2001). The conditions that the biotite from A-type granites satisfy equation 5.1 vary in $f_{\mathrm{O_2}}$ at a given temperature (800° C). Additionally, the biotite with total aluminum > 1.6 apfu tend to satisfy equation 5.1 at an intermediate $f_{\mathrm{O_2}}$at 800° C. Further, biotite from S-type granites tend to be the most restricted in $f_{\mathrm{O_2}}$ and satisfy equation 5.1 at the most reduced conditions, whereas

biotite from I-type granites tend to satisfy equation 5.1 at the most oxidized conditions. The relationship between $X^{\mathrm{Bt}}_{\mathrm{Annite}}$ and $X^{\mathrm{Bt}}_{\mathrm{Fe^{VI*}}}$ and total aluminum may also elucidate the oxidation state of a magmatic system. Whalen and Chappell (1988) and Mason (1978) noted that increasing ΣFe/(Fe +Mg) with increasing octahedral aluminum is the result of more reducing conditions and decreasing ΣFe/(Fe +Mg) with increasing octahedral aluminum is the result of more oxidizing conditions. However, this study suggests that an increasing $X^{\mathrm{Bt}}_{\mathrm{Annite}}$ with increasing total aluminum is indicative of more reducing conditions; whereas a decreasing $X^{\mathrm{Bt}}_{\mathrm{Annite}}$ and increasing or flattening of $X^{\mathrm{Bt}}_{\mathrm{Fe^{VI*}}}$ is indicative of more oxidizing conditions. By considering only ΣFe/(Fe +Mg), wherein iron is all Fe^{2+}, an increasing ΣFe/(Fe +Mg) may be mistaken for more reducing conditions, when in actuality it represents more oxidizing conditions. Additionally, a decreasing $X^{\mathrm{Bt}}_{\mathrm{Annite}}$ and $X^{\mathrm{Bt}}_{\mathrm{Fe^{VI*}}}$ with increasing total aluminum would be indicative of highly oxidized conditions.

Fugacity ratios of f_{HF} and f_{HCl} relative to $f_{\mathrm{H_2O}}$ can also be inferred from biotite composition, based on their IV[Cl], IV[F], and IV[F/Cl] values. At a given temperature A-type granites have the lowest $\frac{f_{\mathrm{H_2O}}}{f_{\mathrm{HF}}}$ and $\frac{f_{\mathrm{H_2O}}}{f_{\mathrm{HCl}}}$, whereas I- and S-type granites have similar $\frac{f_{\mathrm{H_2O}}}{f_{\mathrm{HF}}}$ and $\frac{f_{\mathrm{H_2O}}}{f_{\mathrm{HCl}}}$; I-type granites have slightly higher $\frac{f_{\mathrm{H_2O}}}{f_{\mathrm{HF}}}$ and lower $\frac{f_{\mathrm{H_2O}}}{f_{\mathrm{HCl}}}$ than S-type granites. Thus, of the three intercept values, IV[F], and as a result $\frac{f_{\mathrm{H_2O}}}{f_{\mathrm{HF}}}$, is the most useful discriminator between granite types, particularly between A- and I-type granites.

Temperature and pressure cannot be determined based on the biotite composition alone. Temperature plays an important role in determining which biotite compositions satisfy equation 5.1, as well as the fugacity ratios. If the temperature at which biotite crystallized is assumed to be 800° C, the biotite plotting above the 800° C isotherm (i.e. at isotherms corresponding to <800°C in Figure 5.3) represent systems that are more reduced than QFM or are at higher pressures, which would result in a higher f_{H_2O} assuming the system is water saturated. Conversely, biotite plotting below the 800° C isotherm (i.e. at isotherms corresponding to >800°C in Figure 5.3) likely represent systems that are more oxidized than QFM or at lower pressures, which would result in lower f_{H_2O} assuming the system is water saturated. The curves in Figure 5.3 were calculated at a pressure of 200 MPa, but higher or lower pressures may move the positioning of these curves (see the supplementary files (Appendix 5.D) for calculations at 100 MPa). A pressure of 200 MPa is assumed to be representative of the conditions of epizonal granite emplacement and used in this study.

The FeO*-MgO-Al_2O_3 ternary of biotite composition originally defined by Abdel-Rahman (1994) requires re-evaluation in light of the larger dataset considered here. Additional data indicate that the peraluminous, calc-alkaline, and alkaline fields as defined by Abdel-Rahman (1994) are not directly analogous to S-, I-, and A-type granites, respectively. Given the significant overlap between the alkaline and peraluminous fields and the peraluminous and calc-alkaline fields in Figure 5.1, the fields defining S-, I-, and A-type granites have been redefined (Figure 5.1). In part, this is due to the larger and more global dataset compiled here and more careful

consideration of the granite type. In some cases the S-, I-, and A-type granites included by Abdel-Rahman (1994) were of questionable classification. For example, the Hercynian granites of Morocco in Mahmood (1983) were considered calc-alkaline by Abdel-Rahman (1994) but were given S-type characteristics by Mahmood and Bennani (1984). Additionally, some Hercynian granites of Portugal were included by Abdel-Rahman (1994), but Neiva (1981) refer to them as hybrid granites. Although there is still some overlap in biotite from I- and S-type granites even after redefining the fields, this overlap is primarily due to the presence of peraluminous (Chappell et al., 2012) and contaminated (Ague and Brimhall, 1987; Whalen, 1993) I-type granites.

This study shows that $X^{\mathrm{Bt}}_{\mathrm{Annite}}$, $X^{\mathrm{Bt}}_{\mathrm{Fe^{VI}}}$, and total aluminum may serve as a discriminator between S- and A-type granites (Figure 5.1 and 5.2), whereas IV[F], and thus $\frac{f_{\mathrm{H_2O}}}{f_{\mathrm{HF}}}$, may serve as a discriminator between A- and I-type granites (Figure 5.2). Additional information, outside of ferromagnesian mineral composition, may be required to distinguish peraluminous or contaminated I-type granites from S-type granites. However, a note of caution is required when using the composition of biotite as a discriminator of granite type. Biotite composition from individual granites may correspond to S-, I-, or A-type granites; however, a single criterion, such as biotite composition, may not warrant classification. As discussed in detail by White et al. (1986), the term “two-mica granite” has erroneously become synonymous with S-type granites because of the presence of muscovite, despite evidence that rocks such as those in the Peninsular Range are gradational with metaluminous, hornblende-bearing granites and fractionated I-type granites may contain muscovite.

Additionally, White et al. (1986) noted that muscovite occurs in less than 1% of the S-type granites found in the Lachlan Fold Belt, where the distinction between S- and I-type granites was first made. Further, the S- and I-type classification was intended to be applied to granitic suites as opposed to individual granitic units. Thus, biotite composition, in addition to other mineralogical and compositional criteria, from granitic suites should be used as a discriminatory tool for S-, I-, or A-type granites.

This study demonstrates that amphibole from I- and A-type granites form two distinct trends: one trend of increasing NK/CNK of the amphibole with increasing total aluminum (I-type granite trend) and one trend with decreasing NK/CNK of the amphibole with increasing total aluminum (A-type granite trend) (Figure 5.6). These trends, in addition to the iron-rich nature of amphibole from A-type granites and a boundary of NK/CNK = 0.27, allows for amphibole in I- and A-type granites to be clearly distinguished from one another. Little attention has been paid to the effect of $\frac{f_{\mathrm{HCl}}}{f_{\mathrm{HF}}}$, $\frac{f_{\mathrm{H_2O}}}{f_{\mathrm{HCl}}}$, and $\frac{f_{\mathrm{H_2O}}}{f_{\mathrm{HF}}}$, as well as amphibole composition on the halogen ratios of amphibole as done by Munoz (1984) for mica. However, similar behavior of halogens can be assumed, particularly in those systems that contain both biotite and amphibole (I- and A-type granites). Similar to the lower IV[Cl] and IV[F] in biotite, which are consistent with elevated $X_{\mathrm{F}}^{\mathrm{Bt}}$and $X_{\mathrm{Cl}}^{\mathrm{Bt}}$, the elevated $X_{\mathrm{F}}^{\mathrm{Am}}$and $X_{\mathrm{Cl}}^{\mathrm{Am}}$ in A-type granites (Figure 5.6) may indicate lower $\frac{f_{\mathrm{H_2O}}}{f_{\mathrm{HF}}}$ and $\frac{f_{\mathrm{H_2O}}}{f_{\mathrm{HCl}}}$ as compared to I-type granites. Further, $X_{\mathrm{F}}^{\mathrm{Am}}$and $X_{\mathrm{Cl}}^{\mathrm{Am}}$ also appear to vary with Fe/(Fe +Mg), such that $X_{\mathrm{F}}^{\mathrm{Am}}$ increases with decreasing Fe/(Fe +Mg), which is also consistent with Fe-F and Mg-Cl avoidance described by Munoz (1984) for mica. However, the Fe-F and Mg-Cl avoidance suggested by Munoz (1984) for biotite is not observed in the data presented here.

Additionally, amphibole, by analogy to biotite composition, with higher Fe/(Fe +Mg) are indicative of more reducing conditions (Krawczynski et al., 2012; Popp et al., 1977), but only if the appropriate low-variance assemblages constrained by mineral equilibria are present; consideration of these systematics are beyond the scope of this paper. Additionally, if a granite contains amphibole it is not an S-type granite, as S-type granites are amphibole-free (the one occurrence found here is considered a xenocryst and is not utilized in this study). However, the absence of amphibole does not indicate that a granite is an S-type granite, as both I- and A-type granites can lack amphibole. Overall the presence of amphibole can be used to eliminate classification as an S-type granite and amphibole composition may be used to discriminate between I- and A-type granite.

The results of the predictive modeling are consistent with the hypothesis that biotite and amphibole may be used to discriminate among S-, I-, and A-type granites. A combination of approaches can be used. For example, if a granite contains both biotite and amphibole, then it is not an S-type granite, as S-type granites do not contain amphibole. Further, the composition of the biotite and amphibole can be used to distinguish I- from A-type granites. Greater weight should be given to the predictive model that is based on amphibole composition due to its higher accuracy (96%). If a granite does not contain amphibole, then the predictive model based on biotite composition should be used. However, for granites (s.s.), which contain biotite and no amphibole, it is important to consider other petrologic observations as the granite could belong to any of three considered categories. In such cases, the predictive model based on biotite composition will correctly classify a granite with an

accuracy of approximately 83.7 %, but additional characteristics (e.g. characteristic mineralogy; see Chappell and White, 1974, 2001; Collins et al., 1982) should be used to confirm the classification.

A problem noted by Chappell and White (2001) is the difficulty in distinguishing between S- and I-type granites based on composition and mineralogy as they approach a minimum melt composition. The accuracy of the predictive models based on biotite and amphibole composition can be evaluated for granites of varying whole rock SiO_2 (wt%). The results of the model predictions for granites at varying whole rock SiO_2 (wt%) concentrations, based on biotite and amphibole composition, for the test data sets are presented in Figure 5.9. At a whole rock SiO_2 of >70 wt% the predictive model based on biotite composition has a positive prediction value of near 70% and the predictive model based on amphibole composition has a positive prediction value of 100%. In order to increases the accuracy of the model for granites at high SiO_2 concentrations, a second model was trained by using only biotite from granites with >70% SiO_2. This model had a total accuracy of 64.3% during training (168 data points) and the granite type was only predicted correctly 64% of the time for the test data set (25 data points). During testing of this model, the S-, I- and A-type granites had positive predictive values of 87.5%, 46.7%, and 100%, respectively. Training on this small subset of data does not increase the accuracy of the model at a high SiO_2 (wt%) of the whole rock. In order to increase the accuracy of the model at high (>70 wt% SiO_2) more data are needed. Overall, these models

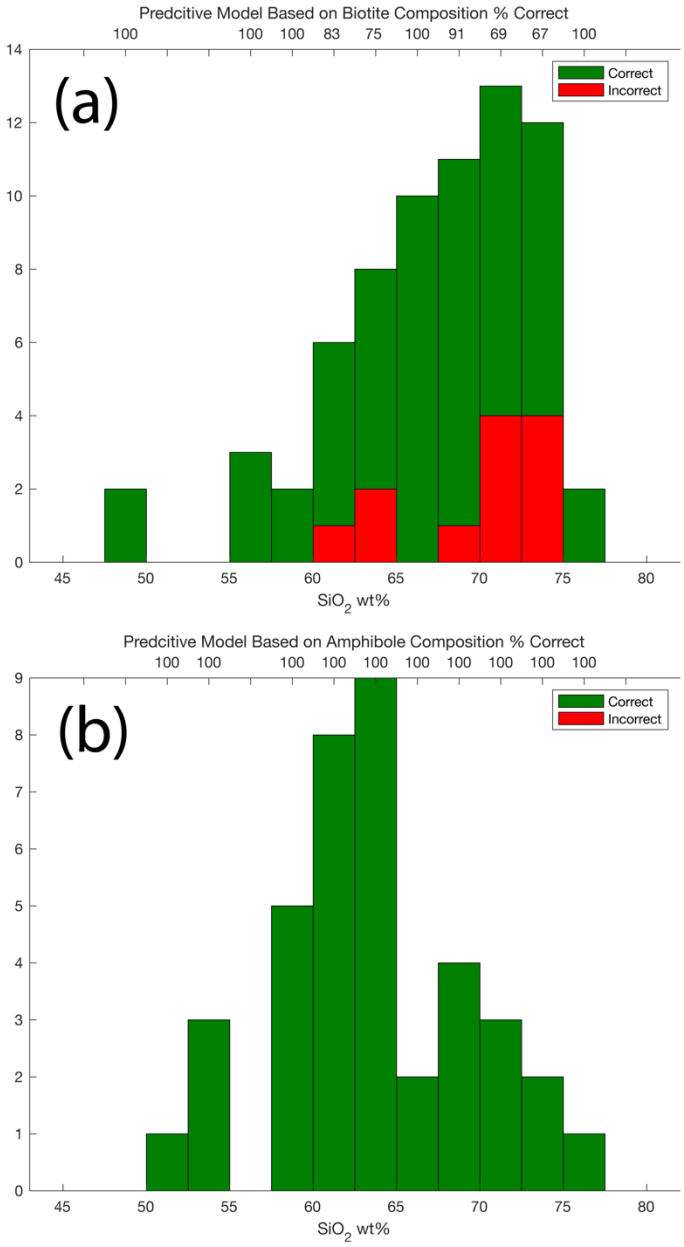

Figure 5.9: Histogram of whole rock SiO_2 in the test data sets for **(a)** biotite and **(b)** amphibole compositions binned in 2.5 wt% intervals. The top x-axis the percent correct for each SiO_2 bin. Each bar is colored by number of correct and incorrect predictions.

provide excellent predictions based on the composition of amphibole and reasonably accurate predictions based on the composition of biotite, regardless of the whole rock composition. As a result, both biotite and amphibole composition can be used to aid

in the classification of evolved S-, I-, and A-type granites at high (>70 wt%). whole rock SiO_2.

The predictive models based on both biotite and amphibole composition are provided in the supplementary files (Appendix 5.E) for use by the reader. In order to apply these predictive models to new data sets, only electron microprobe analyses and calculated mineral formulas for biotite and amphibole are required. For the best results quantitative measurements of the halogens in biotite should be acquired; however, without these data the predictive models will still have an accuracy of ~80% for biotite composition. Note that when using the *Classification Learner* app or exported function to train the model, the model is retrained each time and variations in the model accuracy (several %; e.g. 80% vs 82% total accuracy) will occur.

An increase in the iron content of biotite and amphibole with increasing SiO_2 in the whole rock (Figure 5.5) indicates that, for the compositions examined in this study, the most iron-rich biotite and amphibole are found in the most felsic members of each granite type. This trend is consistent with Whalen and Chappell (1988) who recorded similar observations in rocks from the Lachlan Fold Belt. In general, a trend of increasing iron in biotite with increasing SiO_2 in the whole rock, within a suite of genetically related rocks, would indicate that the parental melts evolved to more reducing conditions (Whalen and Chappell, 1988). Conversely, a trend of decreasing iron in biotite with increasing SiO_2 in the whole rock, within a suite of genetically related rocks, would indicate that the parental melts evolved to more oxidizing conditions (Czamanske and Wones, 1973). Similar conclusions may be drawn by analogy for amphibole, but more work is required.

The correlation between increasing total aluminum of biotite and whole rock ASI may not be as clear. The ASI of biotite along the phlogopite-annite join is ideally 1, but often ranges from 1.3 to 1.5 (Zen, 1986) and is effectively equal to the total aluminum (assuming potassium apfu equals one) and should approximate the ASI of the magma and thus the whole rock. However, the ratio of total aluminum to whole rock ASI is 1.2:1, when excluding rocks with an ASI >1.4. Although an increasing ASI of the magma would result in more aluminous biotite the presence of large amounts of biotite will result in a higher whole rock ASI and as noted by Chappell et al. (2012) excess aluminum in S-type granites is often hosted in biotite. Aluminous biotite is almost certainty the result of crystallization from aluminous magma, but elevated whole rock ASI may simply be due to a high modal proportion of biotite and not a true reflection of the ASI of the parental magma, particularly in more mafic granites.

5.6. <u>Conclusions</u>

The global compilation of biotite and amphibole from S-, I-, and A-type granites in this study has revealed that biotite and amphibole can often serve as fingerprints of the magmas from which they crystallize. Biotite composition can be used as a discriminator between A- and S-type granites when the iron content ($X^{\mathrm{Bt}}_{\mathrm{Annite}}$ or $X^{\mathrm{Bt}}_{\mathrm{Fe^{VI*}}}$) and the total aluminum content are considered. Biotite composition can also be used as a discriminator between I- and A-type granites by evaluating the fluorine intercept values (IV[F]), and the associated $\frac{f_{\mathrm{H_2O}}}{f_{\mathrm{HF}}}$. Biotite compositions in S- and I-type granites overlap considerably. However, a bootstrap random forest model based on biotite composition can be used to as a discriminator between S-, I-, and A-type

granites with 83.7% accuracy. Amphibole composition can also be used to discriminate between I- and A-type granites based on whether the NK/CNK of the amphibole increases (I-type granites) or decreases (A-type granites) with increasing total aluminum of the amphibole. Further, a bootstrap random forest model based on amphibole composition can be used to as a discriminator between S-, I-, and A-type granites with 96% accuracy. Biotite composition may yield an estimate of magmatic f_{O_2}, $\frac{f_{H_2O}}{f_{HF}}$, $\frac{f_{H_2O}}{f_{Cl}}$, and $\frac{f_{HF}}{f_{HCl}}$ given the presence of appropriate mineral assemblages and appropriate estimates of temperature and pressure. Amphibole composition by analogy may yield similar information on intensive variables, but more work is required. Generally, S-type granites are the most reduced, I-type granites are more oxidized, and A-type granites have variable f_{O_2}. Further, A-type granites exhibit lower $\frac{f_{H_2O}}{f_{HF}}$ and $\frac{f_{H_2O}}{f_{Cl}}$ than S- and I-type granites and S- and I-type granites exhibit broadly similar $\frac{f_{H_2O}}{f_{HF}}$ and $\frac{f_{H_2O}}{f_{Cl}}$. Finally, the iron content of biotite and amphibole increases with increasing whole rock SiO_2, such that the most iron-rich ferromagnesian minerals are found in the most siliceous granites. Overall, the composition of biotite and amphibole can be used to constrain the composition of their parental melts, as well as distinguish between S-, I-, and A-type granites, so long as other petrologic factors such as modal mineralogy, whole rock chemistry, trace element signatures, and isotopic data are not ignored.

5.7. <u>Acknowledgments</u>

We would like to thank Phil Blevin, Colleen Bryant, Penelope King, David Lescinsky, Joseph Whalen, and Lesley Wyborn for assisting the authors in locating

data on granites in Australia and Canada and providing some of the data in this study. Austin M. Gion is supported by the National Science Foundation [grant EAR 1348010] and the Department of Geology, University of Maryland

Appendices

Chapter 2 Appendices

Appendix 2.A: Target (ideal) starting glass compositions

Table 2.A1: Bulk (ideal) composition of glass mixtures

	KSM1C	KSM2A	KSM2C	KSM3A
SiO_2	47.8	64.8	64.8	71.7
Al_2O_3	15.3	18.8	17.7	15.4
TiO_2	3.6	1.0	0.8	0.3
P_2O_5	1.8	0.58	0.5	0.6
FeO	13.5	3.8	4.5	3.5
MgO	3.0	1.8	1.5	1.1
MnO	0.3	0.2	0.2	0.2
Sc_2O_3	0.040	0.028	0.020	0.065
Na_2O	2.9	1.9	2.1	1.7
CaO	7.5	3.4	3.9	2.0
K_2O	2.6	3.2	3.4	2.9
Total	98.3	99.5	99.4	99.5

Iron is calculated as ferrous iron (ferric iron powder was used) in order to calculated modal mineralogy. It was assumed all water (added as hydroxide powders) was lost during heating.

Appendix 2.B: Crystal Settling and Melt Migration

A primary texture of the run products, as mentioned in the main text, is a spinel-rich core with a spinel- and crystal-poor rim. One potential cause for this texture is crystal settling. The rate at which crystals settle can be determined by using Stoke's Law given in equation 2.B.1

$$V_{\mathrm{Xl}} = \frac{1}{18}\frac{(\rho_{\mathrm{xl}}-\rho_{\mathrm{melt}})}{\eta_{\mathrm{melt}}} g d^2 \qquad \text{Eq. (2.B.1)}$$

where V_{Xl} is the settling velocity of the crystals (m/s), ρ_{xl} is the density (kg/m^3) of the crystalline phase, ρ_{melt} is the density (kg/m^3) of the melt, η_{melt} is the viscosity (Pa s) of the melt, g is the acceleration due to gravity (m/s^2), and d is the diameter (m) of the crystal. In order to calculate the density of each crystalline phase in each experiment, a linear relationship between composition and density of the end-members is assumed. The density of end-members for all phases was calculated from the molar weight and volume reported by Robie and Hemingway (1995). For example, the density of the olivine end-members is approximately 3220 and 4400 kg/m^3 for forsterite and fayalite, respectively. If the percent forsterite component is 70, then the density is 70% of the difference between the forsterite and fayalite end-members subtracted from the density of fayalite and would equal approximately 3574 kg/m^3. If the percent forsterite component is 100 the density would be 3220 kg/m^3, likewise if the percent forsterite component is 0 the density would be 4400. This method was applied for other crystalline phases with the exception of spinel and apatite. In these cases the density of end-member magnetite and hydroxyapatite were used. The densities determined here serve only as approximations to determine an estimated settling velocity. The density of the melt was calculated by using the method of

Bottinga and Weill (1970). Melt density calculations were performed in a Microsoft Excel spreadsheet designed by J.D. Winter (available at https://www.whitman.edu/geology/winter/ and described in Winter (2010)). The spreadsheet utilizes molar volumes and thermal expansion values from Lange and Carmichael (1987), as well as Lange (1994). Values for compressibility are from Kress and Carmichael (1991). All melt viscosity calculations were performed using the method of Giordano et al. (2008) and performed in a Microsoft Excel spreadsheet (available at https://www.eoas.ubc.ca/~krussell/VISCOSITY/grdViscosity.html). The diameter of the crystals was set to 10 microns for all calculations. Parameters used in calculating the settling velocity, as well as the results of the calculations are given in Table C1. The largest distance settled by an individual phase, for the experimental run time, is ~5 microns for the spinel phase. This estimation is not without problems. The calculation described would require that the composition of the run-product melt is instantaneously achieved and remains constant, such that any changes in viscosity and density are a function of temperature only. A more likely scenario would involve a time dependent composition, viscosity, and density of the melt, wherein viscosity increases and density decreases with crystallization through time at a constant temperature (assuming cooling is instantaneous). This scenario would result in dynamic settling rates and may produce larger distances settled by individual phases. However, the relationship of viscosity, density, and/or composition to time, at a constant temperature, is difficult to ascertain for these experiments. A maximum possible settling rate and distance settled for an individual phase can be calculated by allowing the most dense phase (spinel) to settle for 48

hours (longest run time) in the least viscous melt (KSM1C-1 at 937°C). This calculation results in a distance settled of ~45 microns. This distance is similar to the thickness of the crystal-poor rims. It should also be noted that the density of the melt and crystalline phases can be calculated by MELTS (Gualda and Ghiorso, 2015), as can melt viscosities from the calculated equilibrium melt compositions. The settling rates and distances calculated using the results of the MELTS calculation are similar to those described above. Thus, crystal setting is a reasonable method by which the crystal-poor, melt-rich rims may form.

A second potential process for producing melt-rich and crystal-poor regions is through melt migration, which may form silicic segregations. Silicic segregations have been observed and detailed in large mafic systems whether in emplaced plutons or in active lava lakes (Marsh, 1996). In large magma chambers, silicic segregations can form through solidification front instability (SFI), by which the crystallizing roof of a magma chamber is pulled downward due to gravity; tears under its own weight; and because the crystal content is high (> 55%) and the crystal network is rigid, melt flows into the void space (Marsh, 1996). In lava lakes silicic segregations are observed, and have been artificially produced, as a result of drilling into the partially molten rock (Helz, 1987; Helz and Wright, 1983; Wright et al.). Both types of segregations form by filter pressing, similar to that described by Marsh (1996), in which melt flows through a rigid crystal network due to a pressure gradient caused by the presence and exsolution of a vapor in the magma (Anderson et al., 1984). In these small-scale experiments filter pressing due to the presence of a vapor phase is more probable than segregation due to a SFI. The exsolution of a vapor bubble on

quench or the motion of vapor throughout the melt may result in melt flowing through the crystal network and into melt channels (Marsh, 2019). Marsh (2019) also suggested that melt may be transported on the surface of the vapor bubbles, which aids in the formation of crystal-poor regions. The process of filter pressing and melt transport by vapor bubbles is also supported by the occurrence of these melt-rich regions at grain boundaries and near vesicles (Figure 2.1 (Marsh, 2019). Thus, melt migration (by filter pressing and/or bubble transport) offers a second possible mechanism by which melt-rich and crystal-poor regions can form.

Table 2.B1: Parameters and results for crystal settling calculations

	KSM1C-1	KSM1C-2	KSM1C-3	KSM1C-4	KSM1C-5	KSM1C-6	KSM1C-7	KSM1C-8
Density of Crystalline Phase (kg/m^3)								
Olivine	-	-	3611	-	3544	3544	3580	3541
Plagioclase	2728	2670	2725	2729	2731	2731	2732	2670
Pyroxene	3578	3565	-	3523	3474	-	-	3998
Biotite	2944	2788	2954	3006	2945	2935	2934	2788
Spinel	5201	5201	5201	5201	5201	5201	5201	5201
Apatite	3147	3147	3147	3147	3147	3147	3147	3147
Before temperature decrease								
Density of Melt (kg/m^3)	2544	2528	2358	2302	2352	2362	2375	2365
Log Viscosity of Melt (Pa s)	2.7	2.9	3.7	4.6	4.1	3.5	3.3	3.5
Time (hours)	1	1	2	1	1	0	0	0
Distance settled (µm)								
Olivine	-	-	-	0.10	0.02	-	-	-
Plagioclase	0.06	0.04	0.00	0.03	0.01	-	-	-
Pyroxene	0.36	0.27	0.01		0.02	-	-	-
Biotite	0.14	0.07	0.00	0.05	0.01	-	-	-
Spinel	0.94	0.71	0.01	0.23	0.04	-	-	-
Apatite	0.21	0.16	0.00	0.06	0.01	-	-	-
After temperature decrease								
Density of Melt (kg/m^3)	2552	2535	2362	2305	2356	2362	2375	2365
Viscosity of Melt (Pa s)	3.3	3.4	4.2	5.1	4.6	3.5	3.3	3.5
Time (hours)	6.5	20.5	24	24	48	24	16	24
Distance settled (µm)								
Olivine	-	-	0.4	-	0.3	1.6	1.7	1.7
Plagioclase	0.1	0.2	0.1	0.01	0.1	0.5	0.5	0.4
Pyroxene	0.7	1.7	-	0.04	0.2	-	-	2.3
Biotite	0.3	0.4	0.2	0.02	0.1	0.8	0.8	0.6
Spinel	1.8	4.4	0.9	0.1	0.6	3.9	4.0	4.0
Apatite	0.4	1.0	0.2	0.03	0.2	1.1	1.1	1.1
Total Distance settled (µm)								
Olivine			0.4	0.1	0.3	1.6	1.7	1.7
Plagioclase	0.2	0.3	0.1		0.1	0.5	0.5	0.4
Pyroxene	1.1	2.0	0.0	0.0	0.3			2.3
Biotite	0.4	0.5	0.2	0.1	0.1	0.8	0.8	0.6
Spinel	2.8	5.2	0.9	0.3	0.7	3.9	4.0	4.0
Apatite	0.6	1.2	0.2	0.1	0.2	1.1	1.1	1.1

The density of the melt is calculated after Bottinga and Weil (1970). The viscosity of the melt is calculated after Giordano et al. (2006). See text for details on density of crystalline phase. Diameter for crystalline phases is 10 µm for all calculations.

Appendix 2.C: Comparison to MELTS Calculation

In order to compare the results of the partitioning experiments to theoretical calculations, the mineralogy and composition of the phases present in the run products were compared to calculations performed in the software package MELTS. MELTS uses a thermodynamic database and model to calculate equilibrium phase assemblages at specified temperatures, pressures, and redox conditions for given bulk compositions by minimization of Gibbs free energy. There are a variety of MELTS software including MELTS (Asimow and Ghiorso, 1998; Ghiorso and Sack, 1995), pMELTS (Ghiorso et al., 2002), rhyoliteMELTS (Ghiorso and Gualda, 2015; Gualda et al., 2012), and alphaMELTS (Smith and Asimow, 2005). Each version of melts is designed for a specific type of calculation. MELTS is designed to perform calculations from 500 to 2000°C and pressure of 0 to 2 GPa. The pMELTS version is designed for calculations performed for mantle compositions at up to 3GPa. The rhyoliteMELTS version is used to perform calculations in water-saturated systems that crystallize at the quartz-two-feldspar ternary. A front end to MELTS was built to perform MELTS calculations in the form of alphaMELTS, which can use MELTS, pMELTS, and rhyoliteMELTS. In this work the term MELTS will refer generally to all MELTS software. MELTS calculations were performed using alphaMELTS for MATLAB (https://gitlab.com/alphaMELTS/MELTS_Matlab). Four calculations were performed by using the rhyolite-MELTS 1.2.0 MELTS model and the compositions of the starting materials presented in Table 2.2, which were converted to grams. All calculations were performed at a pressure of 100 MPa, a temperature corresponding the temperature of the experimental set (e.g. KSM2C experiments T =

900°C), and an f_{O_2} of NNO. Four grams of water were added to the bulk starting composition to ensure the melt was saturated with a volatile phase. For KSM3A experiments containing chlorine and/or fluorine, the amount of chlorine and fluorine present in the run-product melt was added to the bulk composition for each calculation.

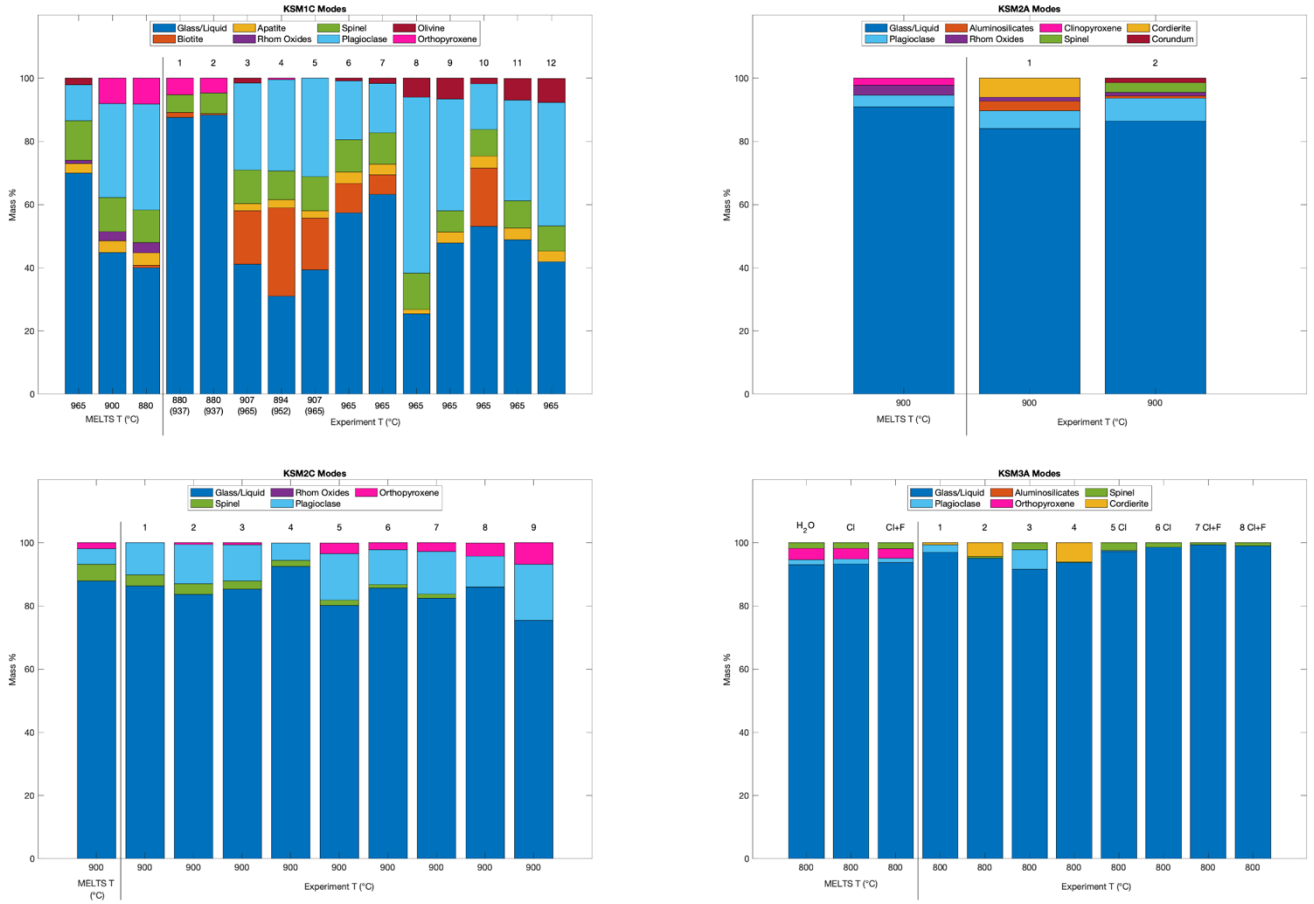

Figure 2.C1: Comparison of mineralogy (mass %) for MELTS and least-squares calculations. Starting composition for MELTS calculation is the starting glass compositions in Table 2. Pressure for all MELTS calculations was set to 100 MPa and oxygen fugacity was set to NNO. Temperatures of the MELTS calculations and experiments are on the x-axis in °C. The y-axis is in mass %. The labels above the stacked bars are the experiment number for each set, respectively. For KSM3A runs containing fluorine and chlorine are marked. The mineralogy plotted corresponds to the least-squares calculation which utilizes the measured composition of the starting material.

The mineralogy in mass % frlom the MELTS calculation is compared to the run-products, as determined by the least-squares calculation using the measured starting material composition in Figure 2.C1. The MELTS and least-squares calculations for isothermal KSM1C experiments have broadly similar mineralogy; however, MELTS calculates less plagioclase and olivine and more glass/liquid. Additionally, rhombohedral oxides are present in the MELTS calculations and these phases were not observed in the run products. The MELTS and least-squares calculations for polythermal KSM1C experiments are similar with the exception of the main ferromagnesian silicate present. MELTS calculates that pyroxene should be the main ferromagnesian silicate; however, in KSM1C-3 to KSM1C-7 and KSM1C-10 biotite is the main ferromagnesian silicate. Orthopyroxene is present in KSM1C-1 and KSM1C-2, whereas biotite is a minor phase. There is also a lack of rhombohedral oxides in the run-products of polythermal KSM1C experiments whereas the MELTS calculations include rhombohedral oxides. The MELTS and least-squares calculations for KSM2A experiments have similar proportions of glass/liquid and plagioclase (Figure 2.C1). However, the MELTS calculations lack aluminosilicates, cordierite, and spinel, which are present in the run-products; and have clinopyroxene, which is absent in the run products. The MELTS calculations for KSM2C experiments are comparable to the least-squares calculation, with the MELTS calculations having slightly less pyroxene and plagioclase, and slightly more spinel (Figure 2.C1). For KSM3A experiments the proportion of glass and spinel are broadly similar; however, the run-products and least-squares calculations lack orthopyroxene and contain less plagioclase than the MELTS calculations (Figure 2.C1).

Additionally, the MELTS calculations lack cordierite, which is present in the run products.

The mineralogy presented in Figure 2.C1 is only that calculated by using the least-squares method that utilizes the measured glass composition, and therefore only represents one of the two calculated mineralogies (Table 2.4; Section 2.6.1.1). The mineralogy calculated using the target glass composition more closely matches the MELTS calculations in several regards. Namely, with respect to KSM1C experiments and plagioclase in KSM3A experiments. In KSM1C experiments, the least-squares calculation that uses the target glass composition (Appendix 2.A), more closely matches the MELTS calculation with respect to the proportion of plagioclase, glass, olivine, pyroxene, and biotite. By using the target glass composition, the proportion of plagioclase, biotite, and olivine decreases and the proportion of glass and pyroxene increases. For KSM3A experiments, the amount of plagioclase calculated by the least-squares calculation that utilizes the target starting material composition is greater and is comparable to MELTS. Although, the residual sum of the squares for the least-squares calculations that utilize the measured starting material composition are generally lower (Table 2.4), the least-squares calculations that utilize the target composition appear to more closely match the MELTS calculations. The discrepancy between the two least-squares calculations and the MELTS calculation is particularly problematic for KSM1C experiments due to the residual spinel in the starting material. One explanation for this discrepancy is that during the experiment, the residual spinel does not significantly interact with the melt chemically because the melt is spinel-saturated or the kinetics are too slow compared

to the duration of the experiment. However, this comparison highlights potential problems with utilizing a least-squares calculation, whereby some phases are under or overestimated and may not match observations.

The compositions of the run-product glasses are compared to the composition of the liquid calculated by MELTS in Figure 2.C2. The composition of the glasses in all experimental sets matches the composition of the liquid composition calculated by MELTS remarkably well. The main difference between the liquid compositions from the MELTS calculations and the run-product glasses is that concentration of total iron is generally lower in the MELTS calculations than in the run product glasses. Additionally, for KSM1C experiments there is greater variability in SiO_2 (wt%) concentrations of the run-product glasses that is not observed in the MELTS calculation; although, the concentrations are similar.

The compositions of the run-product plagioclase are compared to the composition of plagioclase from the MELTS calculations in Figure C3. Plagioclase compositions determined by MELTS are similar in composition; however, the plagioclase compositions calculated by MELTS have a greater amount of sodium and less calcium than the run-product plagioclase. Additionally, MELTS does not take into consideration the concentration of FeO in plagioclase and thus the plagioclase from the run-products have greater FeO concentrations than the plagioclase compositions calculated by MELTS.

Run-product spinel compositions are compared to the compositions of run-product spinel calculated by MELTS in Figure 2.C4. Run-product spinel compositions are comparable to the spinel compositions calculated by MELTS for

both KSM1C and KSM2C experiments with two exceptions. Spinel from KSM1C-8 and KSM2C-3 contain more TiO_2 than the MELTS calculations, as well as more TiO_2 than other experiments in their respective experimental sets. Run-product spinel from KSM3A experiments do not match the calculated spinel compositions by MELTS. The run-product spinel in KSM3A experiments are significantly more aluminous and less iron-rich than the spinel composition calculated by MELTS.

The compositions of run-product ferromagnesian silicates are compared to the compositions of ferromagnesian silicates calculated by MELTS in Figure 2.C5. Pyroxene compositions in KSM1C experiments are more aluminous, calcic, and iron-rich than the composition of pyroxene calculated by MELTS. Additionally, pyroxene from KSM2C experiments are also more aluminous and iron-rich than the composition of pyroxene calculated by MELTS. The composition of both run-product olivine and biotite in KSM1C experiments are more iron-rich than the composition of olivine and biotite calculated by melts. There are also a number of elements that have significant concentrations in the ferromagnesian silicates that are not considered by the MELTS calculations. Such elements include TiO_2 in biotite and pyroxene, as well as CaO and Na_2O in biotite. The differences in the iron content of the ferromagnesian minerals is likely due to the choice of oxygen fugacity for the MELTS calculation. For simplicity, a buffer of NNO was used for all calculations; however, the experiments are both more oxidized and more reduced than the NNO buffer. Thus, changes to the f_{O_2} used in the MELTS calculation will vary the iron content of the silicates (i.e. more reduced system will produce more iron-rich silicates; for example see Figure 2.9) and may account for these discrepancies.

The compositions of miscellaneous phases that occur in the run products are compared to the MELTS calculation in Figure 2.C6. The composition of apatite calculated by MELTS is end-member hydroxyapatite with no impurities, whereas the run product apatite are hydroxyapatite that contain minor amount of SiO_2, Al_2O_3, and FeO. The rhombohedral oxide phases calculated by MELTS are ilmenite with minor Fe_2O_3, whereas the rhombohedral oxides in the run-products are ilmenite with no Fe_2O_3 and the non-rhombohedral oxide rutile. The aluminosilicate minerals calculated by MELTS are sillimanite with no impurities; however, the run-product aluminosilicates contain significant amount of FeO for both KSM2A and KSM3A experiments and minor amounts of TiO_2 in KSM2A experiments.

Not all run-product phases can be compared to calculated mineral compositions determined by MELTS. Because the mineralogy calculated by MELTS and the mineral assemblages present in the run products are not always equivalent there may not be a direct comparison. Such examples include cordierite in KSM2A and KSM3A experiments and pyroxene in KSM3A experiment, which are both absent the MELTS calculations. Additionally, in some cases a phase is present in the run products, but that phase does not appear in the crystallization sequence determined by MELTS until a much lower temperature. For example, in KSM1C experiments biotite is present at 965°C; however, biotite does not enter the crystallization sequence, according to MELTS, until 887 °C. The same occurs for rhombohedral oxides in KSM2A experiments and the aluminosilicates in KSM2C and KSM3A experiments. Although these compositions can be compared, the comparison may not equivalent.

Overall, the experimental results are consistent with the MELTS calculations in both the proportion of the phases and the composition of those phases. The discrepancies between the MELTS calculations and observations generally stem from uncertainties in the least-squares calculations, variations in f_{O_2}, and the fact that MELTS does not incorporate minor elements in many of the phases.

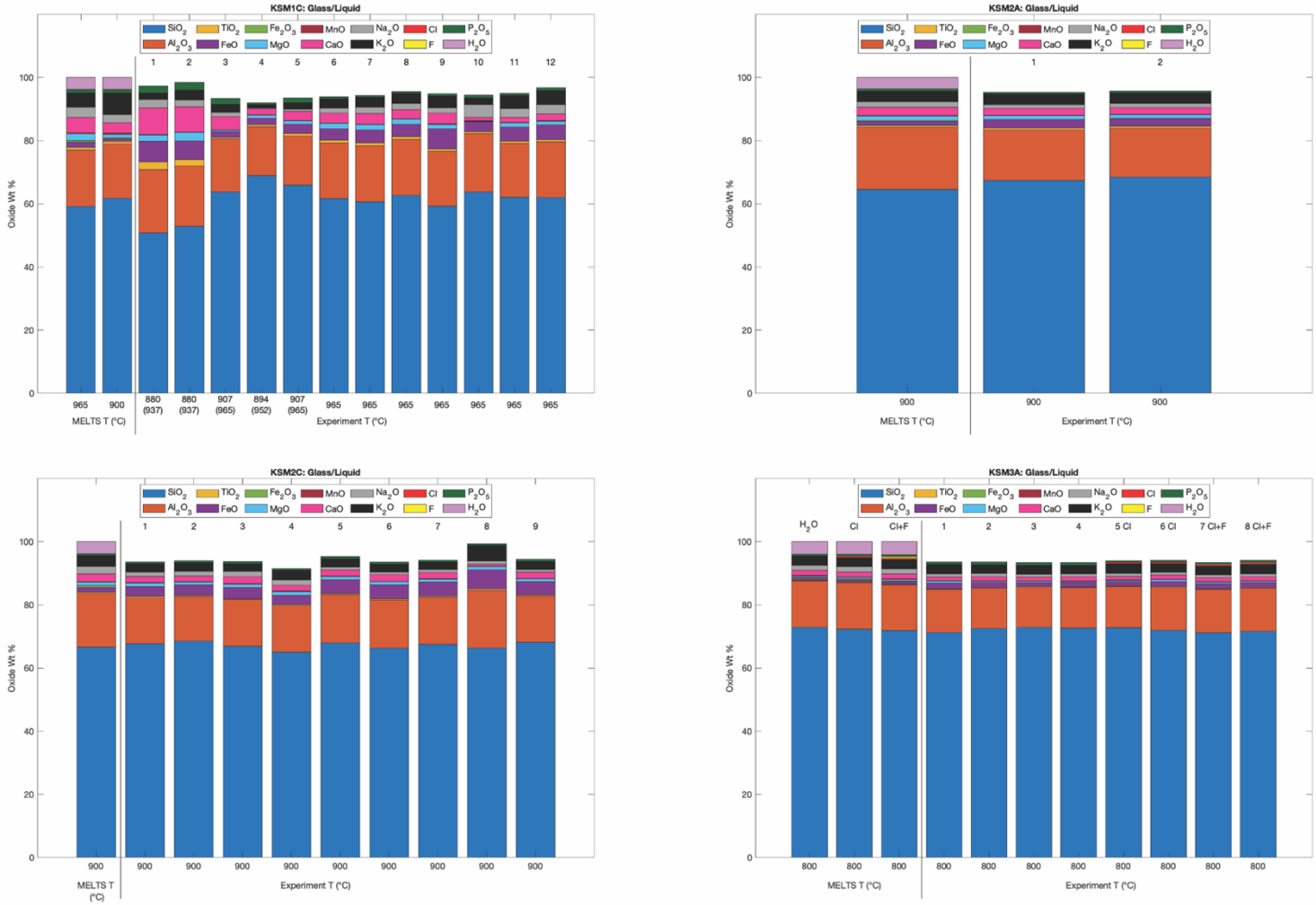

Figure 2.C2: Comparison of the compositions of run-product glasses to liquid compositions calculated by MELTS. See Figure 2.C1 and text for additional detail on MELTS calculations and figure labeling.

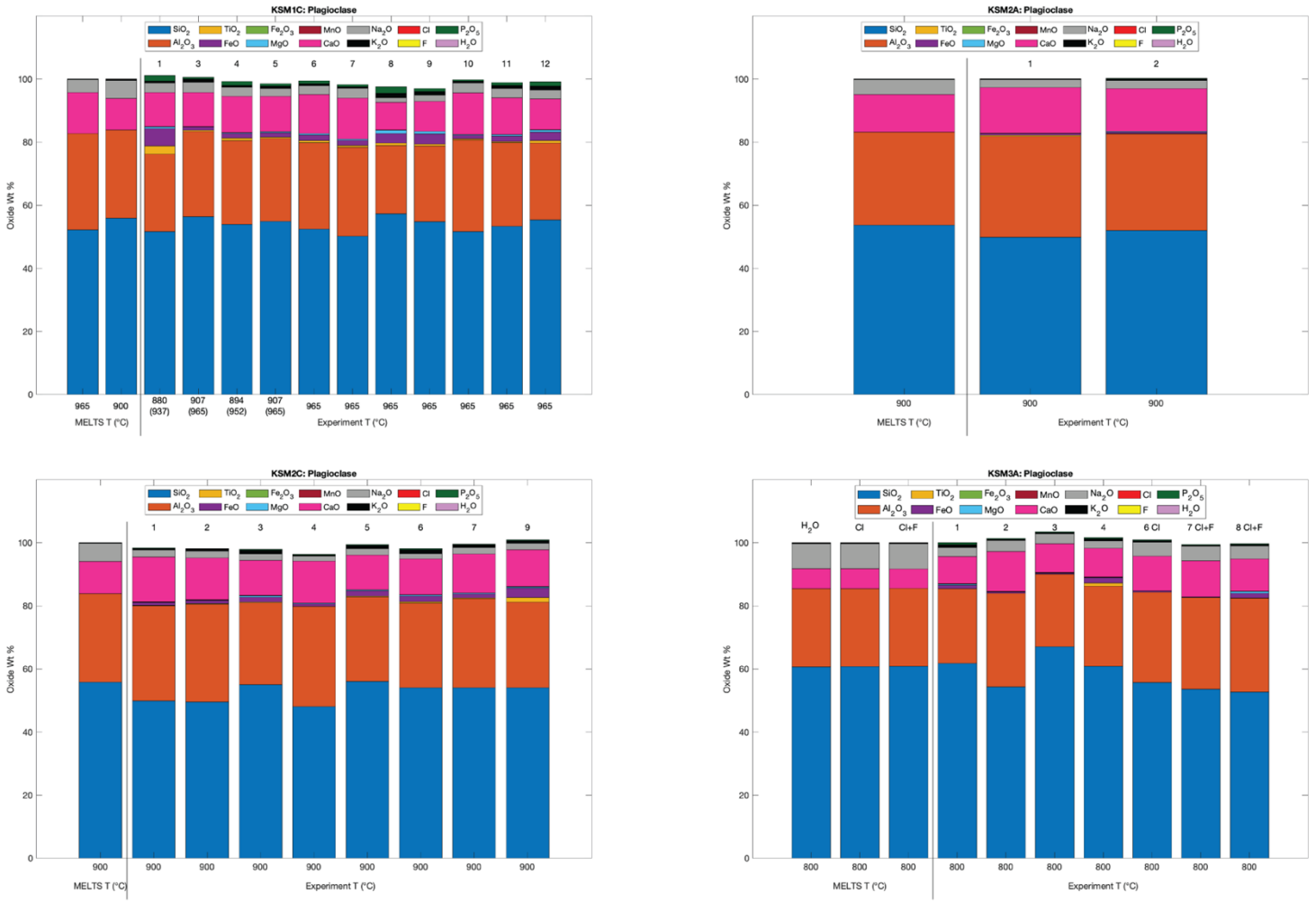

Figure 2.C3: Comparison of the compositions of run-product plagioclase to compositions calculated by MELTS. See Figure 2.C1 and text for additional detail on MELTS calculations and figure labeling.

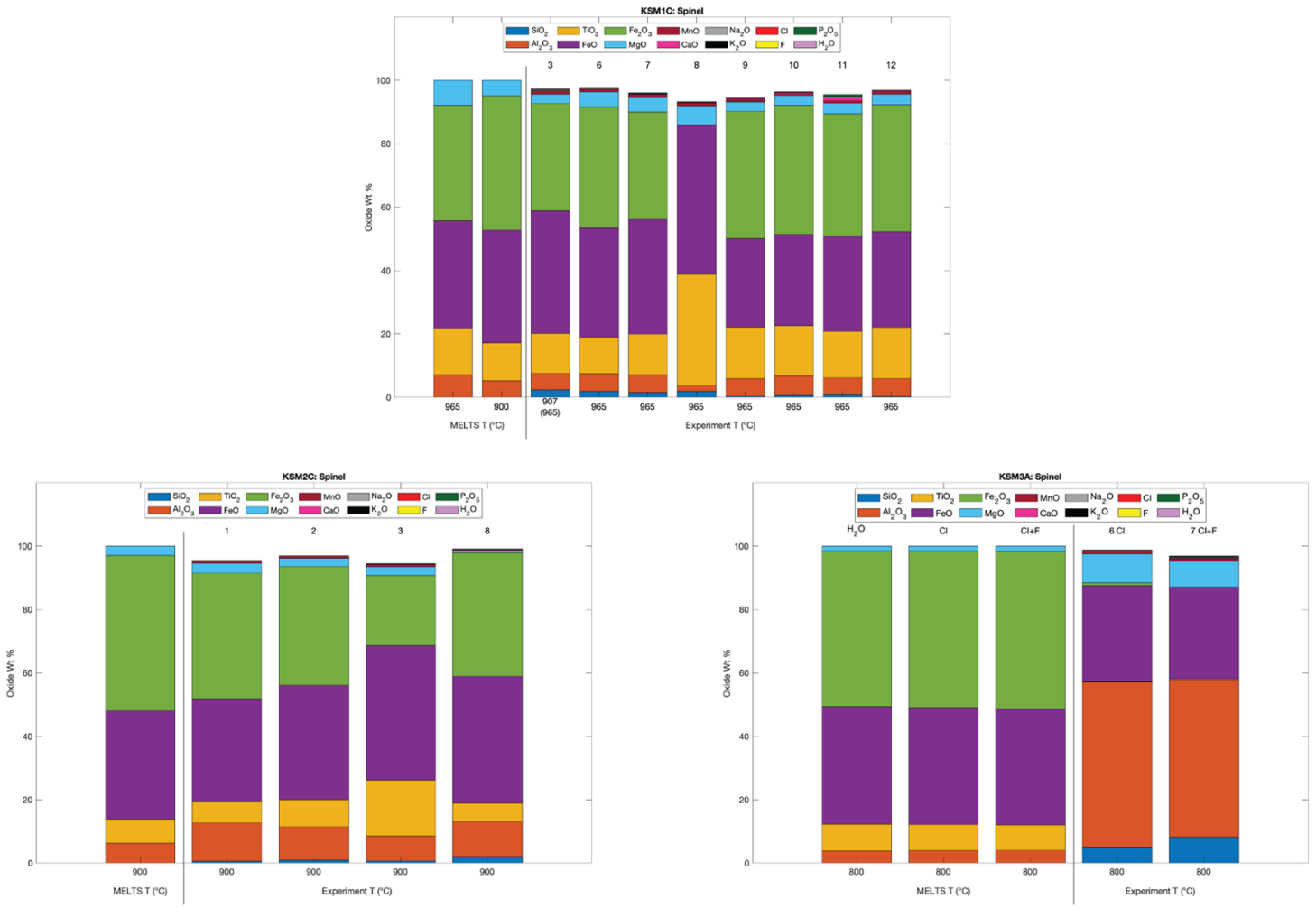

Figure 2.C4: Comparison of the compositions of run-product spinel to compositions calculated by MELTS. See Figure 2.C1 and text for additional detail on MELTS calculations and figure labeling.

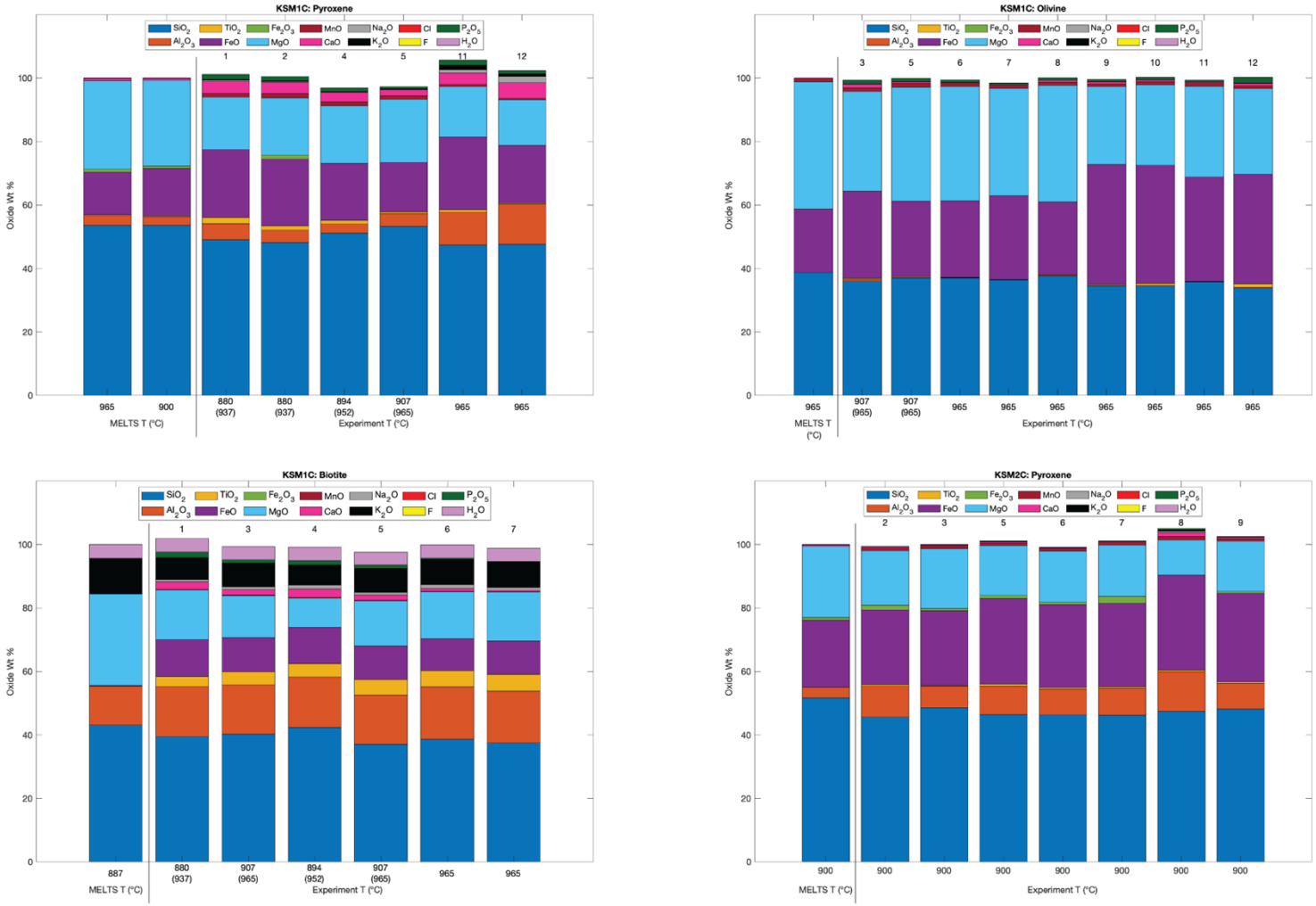

Figure 2.C5: Comparison of the compositions of run-product ferromagnesian silicates to compositions calculated by MELTS. See Figure 2.C1 and text for additional detail on MELTS calculations and figure labeling.

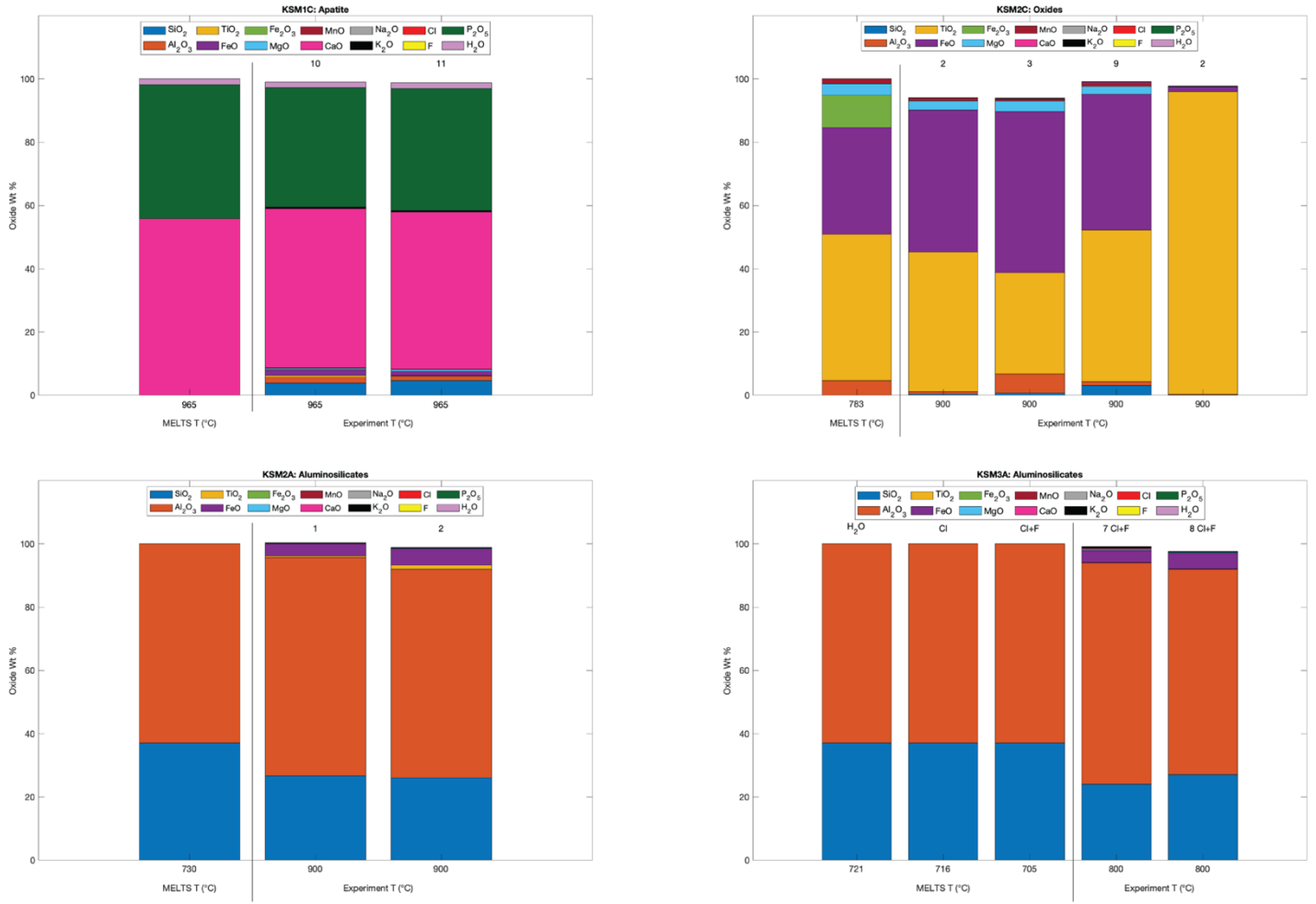

Figure 2.C6: Comparison of the compositions of miscellaneous run-product phases to compositions calculated by MELTS. See Figure 2.C1 and text for additional detail on MELTS calculations and figure labeling.

Appendix 2.D All Electron Microprobe Analyses for Chapter 2.

The tables that follow are individual electron microprobe analyses for all phases described in Chapter 2. b.d. denotes that the concentration was below detection. Mixed analyses are not reported.

Table 2.D1: EPMA analyses for Chapter 2

Starting Glass

Run	Na_2O	K_2O	CaO	MnO	P_2O_5	MgO	Sc_2O_3	TiO_2	FeO	Al_2O_3	SiO_2	Total
KSM1C												
	2.94	3.45	6.44	0.26	2.07	3.19	0.03	3.53	10.44	17.42	50.81	100.57
	2.93	3.39	6.59	0.27	2.15	3.17	0.02	3.36	10.65	17.30	50.90	100.74
	2.94	3.42	6.63	0.24	2.09	3.24	0.03	3.49	10.46	17.26	50.67	100.46
	3.04	3.42	6.60	0.21	2.14	3.23	0.03	3.49	10.66	17.29	50.94	101.06
	3.09	3.43	6.56	0.28	2.10	3.18	0.03	3.33	10.65	17.32	50.74	100.70
	2.94	3.56	6.39	0.30	2.01	3.15	0.02	3.43	10.44	17.23	50.75	100.24
	2.92	3.57	6.23	0.25	2.00	3.04	0.02	3.31	10.48	17.33	50.69	99.83
	2.75	3.09	7.02	0.32	2.21	3.82	0.02	3.04	11.23	16.89	48.72	99.10
	2.72	2.96	7.06	0.23	2.30	3.92	0.02	3.12	11.97	16.86	47.68	98.85
	2.84	2.97	6.95	0.30	2.29	3.85	0.02	3.08	11.85	16.72	47.63	98.51
	2.84	3.22	6.91	0.25	2.21	3.66	0.03	2.69	11.40	17.64	49.61	100.45
	2.93	3.27	7.08	0.32	2.15	3.58	0.02	2.67	11.25	17.66	49.33	100.25
	2.91	3.19	6.93	0.27	2.24	3.64	0.03	2.67	11.21	17.70	49.12	99.92
	2.85	3.20	6.83	0.31	2.19	3.57	0.03	2.67	11.14	17.58	49.38	99.75
	2.87	3.26	6.86	0.30	2.09	3.56	0.02	2.64	11.09	17.62	49.50	99.80
	2.86	3.27	6.82	0.27	2.10	3.51	0.03	2.65	11.44	17.70	49.22	99.87
	2.88	3.20	6.83	0.28	2.17	3.51	0.03	2.62	11.25	17.82	49.51	100.09
	2.44	3.26	6.94	0.32	2.16	3.57	0.03	2.58	11.46	17.75	49.62	100.14
KSM2A												
	1.84	3.32	3.01	0.19	0.68	1.96	0.06	0.65	2.71	19.81	65.26	99.48
	1.89	3.29	2.91	0.18	0.65	1.94	0.05	0.94	2.73	19.52	65.56	99.69
	1.80	3.24	2.98	0.20	0.66	2.02	0.04	1.26	2.70	19.73	65.50	100.14
	1.79	3.20	3.01	0.15	0.65	2.02	0.06	1.80	2.80	19.59	64.34	99.41
	1.67	3.15	3.08	0.21	0.63	2.06	0.07	2.35	2.91	20.02	63.58	99.71
	1.76	3.08	2.86	0.14	0.63	1.94	0.05	3.04	3.60	19.70	62.49	99.27
	1.68	3.03	2.82	0.21	0.65	1.93	0.05	2.92	3.73	19.95	62.49	99.45
	1.74	3.04	2.86	0.25	0.63	1.94	0.05	2.61	3.59	19.85	61.87	98.43
	1.76	3.02	2.91	0.22	0.65	1.98	0.05	2.28	3.68	19.91	62.17	98.64
	1.75	3.12	2.91	0.17	0.75	1.89	0.06	2.04	3.69	19.91	62.56	98.86

Run	Na_2O	K_2O	CaO	MnO	P_2O_5	MgO	Sc_2O_3	TiO_2	FeO	Al_2O_3	SiO_2	Total
KSM2C												
	2.42	3.17	2.70	0.14	0.50	1.44	0.06	0.86	6.49	17.93	65.32	100.98
	2.40	3.14	2.47	0.31	0.51	1.51	0.06	0.97	6.30	17.73	64.70	100.03
	2.34	3.25	2.82	0.16	0.52	1.52	0.05	0.76	6.61	17.48	64.40	99.86
	2.53	3.26	2.87	0.24	0.50	1.52	0.06	0.92	6.47	17.83	64.84	100.99
	2.42	3.23	2.76	0.26	0.51	1.50	0.06	0.94	6.38	17.94	64.65	100.59
	2.39	3.19	2.79	0.10	0.48	1.57	0.06	0.73	6.54	18.01	64.83	100.62
	2.36	3.17	2.63	0.30	0.52	1.46	0.07	0.59	6.57	17.93	64.74	100.26
	2.45	3.25	2.85	0.13	0.50	1.51	0.06	0.71	6.65	17.57	64.65	100.27
	2.40	3.19	2.82	0.20	0.48	1.48	0.05	0.73	6.55	17.74	64.98	100.56
	2.47	3.25	2.72	0.26	0.48	1.46	0.07	0.64	6.50	17.77	64.57	100.14
	2.42	3.20	2.80	0.28	0.54	1.51	0.08	0.61	6.70	17.82	64.40	100.28
	2.43	3.20	2.91	0.20	0.47	1.49	0.06	0.63	6.85	17.47	64.78	100.41
	2.41	3.20	2.75	0.22	0.52	1.45	0.07	0.63	6.50	17.72	64.87	100.24
	2.40	3.30	2.94	0.27	0.45	1.55	0.06	0.74	6.71	17.93	65.99	102.28
	2.49	3.20	2.84	0.18	0.45	1.48	0.06	0.53	6.72	17.35	64.68	99.91
	2.30	3.30	2.91	0.15	0.49	1.52	0.06	0.75	7.01	18.26	65.60	102.29
	2.56	3.24	2.93	0.24	0.53	1.51	0.05	0.60	6.55	17.76	64.95	100.87
	2.46	3.33	2.75	0.23	0.49	1.54	0.06	0.66	6.55	17.65	64.33	100.00
	2.45	3.32	2.98	0.12	0.54	1.53	0.06	0.58	6.45	17.54	64.97	100.48
	2.51	3.32	2.97	0.14	0.53	1.68	0.06	0.59	6.56	17.42	65.47	101.20
	2.58	3.32	2.86	0.23	0.53	1.57	0.06	0.67	6.45	17.31	64.37	99.89
	2.42	3.27	2.94	0.17	0.46	1.58	0.05	0.70	6.37	17.19	64.78	99.88
	2.40	3.31	2.88	0.19	0.53	1.55	0.06	0.65	6.46	17.47	64.36	99.78
	2.46	3.35	3.04	0.25	0.52	1.50	0.06	0.59	6.56	17.35	65.19	100.80
	2.35	3.33	2.97	0.18	0.49	1.45	0.06	0.55	6.45	17.34	64.47	99.59
	2.36	3.32	2.84	0.30	0.49	1.44	0.06	0.61	6.58	17.40	64.46	99.81
KSM3A												
	1.67	2.86	1.39	0.13	0.71	1.01	0.07	0.25	3.23	14.44	73.97	99.65
	1.65	2.75	1.73	0.21	0.62	1.04	0.07	0.29	3.56	15.47	70.19	97.49
	1.61	2.89	1.42	0.22	0.41	0.95	0.06	0.43	3.14	13.73	73.38	98.20
	1.59	2.86	1.50	0.13	0.60	1.03	0.07	0.40	3.54	14.93	72.14	98.72
	1.66	2.75	1.61	0.31	0.62	1.10	0.07	0.26	3.68	15.20	72.05	99.23
	1.78	2.80	1.70	0.26	0.64	1.14	0.07	0.35	3.63	15.68	71.03	99.01
	1.72	2.91	1.58	0.14	0.65	1.04	0.05	0.39	3.25	14.88	72.60	99.15
	1.60	2.82	1.62	0.21	0.60	1.03	0.07	0.48	3.43	14.95	71.67	98.43
	1.73	2.85	1.59	0.22	0.60	0.98	0.07	0.37	3.59	15.03	73.15	100.12
	1.62	2.86	1.48	0.26	0.59	0.93	0.06	0.30	3.55	14.60	73.80	100.00
	1.67	2.75	1.66	0.09	0.56	0.98	0.06	0.33	3.22	15.04	71.88	98.18
	1.78	2.79	1.69	0.24	0.57	1.17	0.07	0.34	3.43	15.48	71.91	99.42
	1.69	2.86	1.69	0.09	0.56	1.13	0.07	0.44	3.45	15.40	71.78	99.09
	1.83	2.84	1.61	0.28	0.65	1.06	0.07	0.36	3.58	14.55	72.36	99.13
	1.59	2.67	1.58	0.24	0.47	1.04	0.07	0.46	3.76	14.90	71.68	98.39

Glass												
Run	**Na_2O**	**K_2O**	**CaO**	**MnO**	**P_2O_5**	**MgO**	**Sc_2O_3**	**TiO_2**	**FeO**	**Al_2O_3**	**SiO_2**	**Total**
KSM1C - 1												
	2.00	2.97	7.12	0.22	2.52	3.05	0.022	2.80	9.73	17.63	50.31	98.36
	0.96	2.95	6.72	0.24	2.63	4.29	0.025	2.61	7.81	18.81	53.16	100.21
	2.38	2.28	8.17	0.14	2.42	1.78	0.014	1.97	5.54	18.85	52.98	96.53
	2.00	3.29	6.42	0.17	2.07	3.46	0.014	2.45	10.42	18.49	52.06	100.84
	4.02	0.60	11.16	0.14	1.94	0.46	0.020	2.79	7.06	23.39	44.87	96.45
	3.27	1.25	9.00	0.17	2.19	0.63	0.025	2.47	3.73	20.90	52.23	95.86
	2.55	1.74	8.01	0.18	2.31	1.49	0.030	2.59	4.94	19.85	54.99	98.69
	4.34	0.69	11.16	0.11	2.03	0.40	0.005	1.31	3.45	22.73	45.61	91.85
KSM1C - 2												
	2.00	3.51	8.54	0.14	2.52	2.88	0.014	1.55	4.85	20.12	53.67	99.79
	1.24	5.93	5.89	0.13	2.98	6.48	0.027	2.64	9.00	16.41	49.04	99.78
	1.87	3.68	8.06	0.15	2.72	3.10	0.021	1.90	4.67	18.22	52.09	96.49
	2.61	2.09	9.98	0.15	2.47	1.30	0.016	1.03	4.55	21.61	52.67	98.48
	3.05	1.00	11.12	0.17	1.97	0.96	0.008	2.14	3.40	23.73	52.52	100.08
	1.52	5.30	5.25	0.23	2.31	4.68	0.035	2.26	6.97	17.70	54.52	100.78
	2.25	2.51	7.70	0.18	2.38	0.58	0.020	1.92	3.04	18.83	57.90	97.32
	1.56	4.21	7.36	0.16	2.76	3.95	0.018	1.71	5.37	18.48	51.90	97.49
	2.36	2.93	7.85	0.20	1.86	2.56	0.034	4.65	7.72	20.16	51.27	101.58
	3.01	1.74	9.57	0.12	1.68	0.75	0.002	0.77	1.98	22.24	54.74	96.60
	1.85	2.08	7.23	0.34	2.31	2.82	0.040	1.57	6.54	16.55	56.54	97.88
	3.19	1.49	9.75	0.18	1.82	1.16	0.008	1.63	6.38	22.96	52.97	101.54
	3.22	1.19	11.31	0.15	2.52	0.34	0.007	1.39	2.89	23.03	52.74	98.79
	2.15	2.38	9.06	0.14	3.31	0.49	0.010	1.25	3.02	18.31	57.69	97.79
	2.19	2.93	7.78	0.19	3.08	1.56	0.019	2.10	10.53	16.63	50.00	97.02
	1.06	5.25	5.66	0.18	2.92	5.54	0.036	2.32	8.51	15.47	50.13	97.08
	0.67	6.50	2.63	0.20	1.74	7.26	0.043	3.26	11.51	14.13	48.26	96.20
KSM1C - 3												
	1.18	1.07	8.74	0.12	5.23	0.48	0.014	0.47	1.63	17.46	57.95	94.34
	2.07	3.58	3.50	0.13	1.28	0.67	0.006	0.96	4.05	16.28	60.73	93.24
	0.97	3.56	5.46	0.11	3.40	0.60	0.015	0.59	1.77	13.87	61.64	91.99
	1.10	2.15	3.56	0.05	1.80	0.38	0.015	0.35	1.27	16.62	64.06	91.35
	2.60	2.07	5.69	0.07	0.93	0.09	0.000	0.34	0.89	19.71	64.25	96.64
	0.60	3.41	1.35	0.18	0.29	0.39	0.013	0.50	2.19	16.48	68.75	94.15
	0.52	1.85	1.38	0.15	0.38	0.32	0.019	0.47	1.74	16.53	68.87	92.21
KSM1C - 4												
	0.31	0.84	2.95	0.08	0.97	1.32	0.011	0.61	2.46	16.91	69.36	95.82
	0.07	0.50	1.38	0.11	0.22	0.66	0.014	0.41	1.90	15.27	69.81	90.36
	0.16	0.98	1.66	0.10	0.48	0.73	0.006	0.44	1.97	14.88	68.74	90.15
	0.33	1.98	2.07	0.13	0.55	0.85	0.021	0.54	2.31	14.94	67.96	91.69
KSM1C - 5												
	0.54	2.14	1.88	0.15	0.28	0.80	0.014	0.59	2.31	15.93	67.97	92.61
	0.55	2.16	1.94	0.14	0.31	0.78	0.018	0.55	2.33	15.73	68.06	92.57
	0.59	1.94	3.76	0.15	2.01	1.04	0.020	1.73	3.72	15.07	64.12	94.15
	0.61	2.10	2.10	0.10	0.48	0.97	0.024	0.57	2.27	15.80	67.79	92.80
	0.59	2.29	2.28	0.16	0.72	0.94	0.022	1.01	2.72	15.93	67.26	93.91
	0.53	1.96	4.84	0.18	3.33	0.84	0.021	0.64	2.86	15.12	64.03	94.36
	0.43	2.09	4.07	0.11	2.27	1.21	0.027	0.74	2.27	15.36	65.92	94.49
	0.34	1.88	3.07	0.17	1.51	1.19	0.022	0.62	2.23	15.57	66.94	93.55
	0.63	2.12	4.00	0.15	2.59	0.90	0.029	0.88	3.34	14.97	63.94	93.57
	0.78	2.21	2.76	0.16	1.25	0.90	0.021	1.21	4.98	15.65	63.52	93.44

Glass												
Run	**Na_2O**	**K_2O**	**CaO**	**MnO**	**P_2O_5**	**MgO**	**Sc_2O_3**	**TiO_2**	**FeO**	**Al_2O_3**	**SiO_2**	**Total**
KSM1C - 6												
	1.97	3.36	3.25	0.26	0.50	1.66	0.021	0.88	3.93	18.03	63.17	97.03
	1.99	3.32	3.22	0.15	0.58	1.58	0.019	0.89	3.55	17.89	61.74	94.91
	1.84	3.16	3.17	0.11	0.44	1.59	0.025	0.78	3.63	17.56	61.01	93.30
	1.48	2.99	3.11	0.13	0.55	1.58	0.013	0.92	3.74	18.10	62.74	95.35
	1.36	2.92	2.99	0.12	0.54	1.56	0.018	0.83	3.58	17.61	60.61	92.12
	1.37	2.98	3.03	0.12	0.59	1.57	0.023	0.82	3.66	17.71	61.63	93.48
	1.38	2.93	3.10	0.16	0.64	1.60	0.019	0.84	3.65	17.41	61.46	93.18
	1.21	2.86	2.94	0.11	0.61	1.50	0.011	0.86	3.52	17.58	60.84	92.03
	1.39	2.90	3.14	0.18	0.48	1.62	0.021	0.94	3.66	17.84	61.90	94.06
	2.00	2.99	3.14	0.10	0.58	1.49	0.016	0.87	3.88	17.51	61.07	93.65
	1.85	2.96	3.09	0.19	0.52	1.56	0.015	0.86	3.40	17.59	61.44	93.48
	1.91	3.05	3.09	0.16	0.58	1.60	0.018	0.90	3.46	17.72	61.72	94.19
	1.89	3.03	3.15	0.16	0.51	1.58	0.021	0.84	3.50	17.75	61.58	93.99
KSM1C - 7												
	1.95	3.02	3.35	0.10	0.50	1.71	0.016	0.81	4.07	17.68	60.52	93.72
	1.95	3.11	3.44	0.15	0.54	1.67	0.021	0.91	3.93	17.90	60.69	94.31
	1.91	3.12	3.30	0.14	0.60	1.68	0.019	0.86	4.11	17.83	60.74	94.30
	1.97	3.16	3.41	0.12	0.62	1.70	0.017	0.91	4.03	17.58	60.45	93.95
	2.01	3.15	3.43	0.19	0.62	1.70	0.021	0.85	3.96	17.91	60.87	94.68
	2.01	3.23	3.43	0.18	0.60	1.70	0.029	0.82	4.35	18.16	60.85	95.33
	2.04	3.15	3.34	0.16	0.60	1.74	0.018	0.90	4.14	18.10	61.19	95.36
	2.10	3.16	3.36	0.23	0.57	1.71	0.016	0.79	4.14	17.65	60.02	93.72
	1.98	3.17	3.34	0.24	0.57	1.69	0.017	0.86	4.10	17.70	60.38	94.02
	1.82	3.12	3.36	0.18	0.55	1.71	0.017	0.83	4.24	17.46	60.37	93.64
	1.98	3.22	3.39	0.24	0.55	1.70	0.021	0.87	4.03	17.63	60.74	94.35
	1.95	3.11	3.37	0.19	0.65	1.68	0.024	0.86	4.23	17.81	60.65	94.51
KSM1C - 8												
	2.04	4.14	3.04	0.20	0.56	1.54	0.019	0.75	3.44	17.26	62.43	95.40
	1.92	4.16	3.03	0.19	0.50	1.52	0.019	0.82	3.59	17.06	62.67	95.47
	1.76	4.03	3.88	0.18	1.22	1.52	0.015	0.78	3.59	16.85	61.67	95.49
	2.18	3.89	3.89	0.15	0.94	1.78	0.021	0.78	3.64	17.15	60.79	95.22
	2.33	3.84	3.87	0.13	1.10	1.87	0.024	1.32	4.40	16.86	59.89	95.62
	2.10	3.73	5.82	0.14	2.14	1.43	0.016	0.75	3.40	17.03	58.98	95.53
	2.02	4.10	3.36	0.15	0.79	1.54	0.016	0.76	3.59	17.01	62.24	95.58
	1.95	3.93	3.79	0.18	1.02	1.52	0.026	0.85	3.70	16.95	61.87	95.78
	2.00	4.04	3.49	0.18	0.98	1.51	0.023	0.82	3.72	16.66	62.09	95.52
KSM1C - 9												
	1.78	3.81	3.40	0.13	0.74	1.38	0.015	0.68	6.43	17.48	59.11	94.96
	1.72	3.76	3.27	0.22	0.67	1.43	0.018	0.67	6.44	17.50	59.39	95.08
	1.81	3.76	3.39	0.12	0.67	1.43	0.022	0.69	6.55	17.32	58.83	94.60
	1.73	3.80	3.32	0.22	0.70	1.45	0.018	0.74	6.71	17.65	59.77	96.11
	1.71	3.83	3.34	0.23	0.71	1.37	0.023	0.67	5.96	17.38	58.99	94.22
	1.59	3.76	3.37	0.17	0.73	1.41	0.013	0.68	6.44	17.33	59.14	94.64
	1.68	3.78	3.40	0.16	0.84	1.38	0.016	0.66	6.42	17.19	58.75	94.28
	1.74	3.80	3.35	0.13	0.69	1.42	0.021	0.63	6.22	17.12	59.45	94.58
	1.67	3.80	3.38	0.13	0.75	1.42	0.024	0.73	6.28	17.42	59.39	94.97
	1.74	3.83	3.31	0.19	0.73	1.41	0.020	0.67	6.42	17.55	59.76	95.63
KSM1C - 10												
	0.87	1.91	4.46	0.16	1.15	0.07	0.020	0.32	2.08	18.51	65.07	94.62
	1.11	2.08	3.81	0.29	0.95	0.08	0.017	0.55	2.82	18.48	63.63	93.81
	0.95	2.24	4.20	0.22	0.87	0.11	0.022	0.74	3.39	18.56	63.27	94.56
	1.10	2.13	4.13	0.29	0.85	0.13	0.020	0.66	3.91	18.38	63.26	94.88
	0.99	2.31	4.18	0.23	0.89	0.14	0.022	0.74	3.68	18.70	63.08	94.98
	0.84	2.08	4.25	0.27	0.86	0.05	0.015	0.70	3.00	18.69	64.27	95.03
	0.78	1.95	3.93	0.23	0.92	0.07	0.020	0.58	3.04	18.41	63.57	93.51
	1.06	2.10	3.99	0.23	0.92	0.09	0.011	0.69	3.23	18.41	63.88	94.61

Glass												
Run	**Na_2O**	**K_2O**	**CaO**	**MnO**	**P_2O_5**	**MgO**	**Sc_2O_3**	**TiO_2**	**FeO**	**Al_2O_3**	**SiO_2**	**Total**
KSM1C - 11												
	1.66	4.24	2.75	0.13	0.60	1.25	0.021	0.65	4.37	17.13	62.03	94.83
	1.68	4.18	2.93	0.14	0.61	1.26	0.018	0.67	4.74	17.05	62.43	95.71
	1.68	4.18	2.72	0.13	0.65	1.26	0.028	0.64	4.51	17.22	62.01	95.03
	1.58	4.18	2.79	0.17	0.64	1.27	0.020	0.64	4.51	17.00	62.08	94.87
	1.57	4.22	2.69	0.13	0.58	1.21	0.014	0.64	4.54	16.96	61.93	94.48
	1.72	4.27	2.81	0.22	0.64	1.27	0.023	0.70	4.53	17.20	61.77	95.15
	1.59	4.26	2.81	0.18	0.61	1.25	0.016	0.65	4.51	17.05	62.23	95.14
	1.45	4.18	2.79	0.12	0.57	1.26	0.015	0.66	4.60	16.96	61.73	94.34
	1.56	4.22	2.83	0.15	0.62	1.26	0.022	0.69	4.50	17.02	62.03	94.90
	1.65	4.19	2.71	0.17	0.60	1.22	0.026	0.68	4.67	17.27	62.37	95.56
KSM1C - 12												
	1.83	4.64	2.34	0.19	0.85	1.29	0.015	0.59	4.87	17.24	62.11	95.97
	2.79	3.64	5.09	0.17	1.09	1.02	0.013	0.55	4.06	19.51	60.29	98.21
	2.01	4.60	2.42	0.15	0.90	1.30	0.020	0.59	4.93	17.31	62.55	96.77
	2.11	4.56	2.68	0.20	0.86	1.21	0.018	0.66	4.95	17.48	62.16	96.88
	2.27	4.49	2.72	0.20	0.80	1.16	0.022	0.72	4.58	17.59	61.74	96.29
	2.32	4.44	3.00	0.10	0.76	1.17	0.010	0.71	4.59	17.86	62.00	96.95
	2.01	4.67	2.39	0.15	0.77	1.19	0.022	0.61	4.73	17.12	63.02	96.68
	2.21	4.45	3.06	0.16	0.96	1.08	0.010	0.57	4.91	17.37	61.69	96.47
KSM2A - 1												
	1.06	3.20	2.04	0.12	0.63	1.14	0.045	0.54	3.21	15.44	67.29	94.73
	1.00	3.20	2.07	0.15	0.56	1.17	0.039	0.66	3.15	15.34	67.71	95.06
	0.99	3.16	2.09	0.20	0.63	1.12	0.039	0.54	2.94	15.47	67.76	94.93
	1.28	3.33	2.27	0.19	0.66	1.33	0.028	0.63	2.74	16.13	67.22	95.81
	1.29	3.31	2.18	0.20	0.62	1.46	0.043	0.57	2.86	16.83	66.34	95.70
	1.22	3.34	2.23	0.19	0.60	1.22	0.049	0.66	2.45	15.99	67.21	95.15
	1.26	3.32	2.29	0.19	0.67	1.33	0.043	0.66	2.64	16.46	66.84	95.70
	1.21	3.36	2.25	0.22	0.56	1.26	0.034	0.68	2.57	15.94	67.47	95.55
	1.22	3.30	2.27	0.22	0.59	1.26	0.041	0.71	2.52	16.29	67.82	96.23
	1.18	3.40	2.16	0.15	0.65	1.13	0.042	0.60	2.47	15.75	67.44	94.96
	1.30	3.37	2.28	0.14	0.59	1.18	0.050	0.70	2.34	16.22	67.33	95.49
	1.23	3.39	2.19	0.17	0.61	1.16	0.042	0.62	2.41	15.91	67.65	95.37
	1.17	3.32	2.16	0.24	0.61	1.18	0.047	0.63	2.35	15.96	67.97	95.63
	1.17	3.29	2.22	0.20	0.61	1.16	0.041	0.62	2.43	16.06	67.50	95.33
	1.22	3.43	2.19	0.14	0.63	1.19	0.049	0.65	2.48	16.08	67.57	95.61
KSM2A - 2												
	1.27	3.38	2.09	0.14	0.70	1.21	0.043	0.48	2.69	15.35	68.40	95.76
	1.23	3.45	2.15	0.20	0.59	1.21	0.045	0.50	2.69	15.50	69.05	96.61
	1.20	3.45	2.08	0.17	0.65	1.17	0.041	0.52	2.70	15.35	68.90	96.23
	1.21	3.48	2.03	0.21	0.61	1.19	0.045	0.53	2.70	15.24	68.74	95.98
	1.20	3.37	2.10	0.23	0.60	1.15	0.048	0.54	2.72	15.39	68.92	96.27
	1.22	3.43	2.05	0.19	0.69	1.18	0.036	0.57	2.90	15.22	68.56	96.05
	1.28	3.47	2.06	0.20	0.60	1.27	0.041	0.50	2.55	15.83	68.15	95.95
	1.27	3.52	2.10	0.11	0.64	1.20	0.050	0.64	2.43	15.61	68.60	96.17
	1.22	3.48	2.11	0.11	0.75	1.14	0.052	0.55	2.46	15.52	68.57	95.96
	1.26	3.50	2.09	0.18	0.69	1.16	0.055	0.54	2.27	15.47	68.21	95.43
	1.18	3.45	1.99	0.15	0.59	1.29	0.051	0.56	2.68	15.95	67.58	95.48
	1.27	3.50	2.06	0.17	0.63	1.12	0.042	0.56	2.56	15.56	68.99	96.47
	1.23	3.53	2.01	0.15	0.67	1.18	0.041	0.53	2.30	15.50	68.77	95.91
	1.22	3.22	1.99	0.12	0.30	1.01	0.043	0.52	2.08	15.24	68.14	93.87
	1.23	3.45	2.10	0.20	0.63	1.17	0.049	0.57	2.36	15.46	68.66	95.87

Glass												
Run	**Na_2O**	**K_2O**	**CaO**	**MnO**	**P_2O_5**	**MgO**	**Sc_2O_3**	**TiO_2**	**FeO**	**Al_2O_3**	**SiO_2**	**Total**
KSM2C - 1												
	1.45	2.70	2.15	0.30	0.51	1.12	0.06	0.26	3.07	14.95	68.04	94.54
	1.62	2.72	1.90	0.08	0.48	1.05	0.08	0.36	3.27	14.99	67.75	94.24
	1.49	2.66	1.91	0.19	0.59	1.04	0.06	0.39	2.97	14.34	67.43	93.01
	1.50	2.70	1.93	0.18	0.47	1.13	0.06	0.43	3.21	14.68	67.27	93.50
	1.48	2.81	1.89	0.08	0.69	1.04	0.07	0.44	2.92	14.20	67.81	93.37
	1.45	2.78	1.90	0.18	0.47	1.07	0.07	0.43	3.24	14.31	67.12	92.95
	1.48	2.71	1.85	0.26	0.49	1.11	0.08	0.46	3.00	14.41	67.45	93.21
	1.49	2.60	2.18	0.16	0.42	1.02	0.07	0.33	3.40	15.01	67.75	94.36
	1.50	2.79	1.85	0.24	0.55	1.11	0.07	0.54	3.03	14.57	68.22	94.40
	1.46	2.75	1.95	0.12	0.55	1.13	0.07	0.37	3.34	14.44	68.02	94.13
	1.46	2.73	1.89	0.13	0.47	1.19	0.06	0.40	3.45	14.50	67.84	94.05
	1.55	2.80	1.89	0.21	0.64	1.00	0.07	0.45	3.25	14.41	67.92	94.13
	1.58	2.68	1.77	0.13	0.50	1.12	0.08	0.44	3.11	14.01	67.08	92.43
	1.60	2.78	1.84	0.11	0.45	1.09	0.07	0.43	3.32	14.73	67.99	94.33
	0.43	1.77	1.73	0.11	0.50	1.06	0.08	0.40	3.38	14.09	68.14	91.62
KSM2C - 2												
	1.54	2.79	1.79	0.30	0.63	0.91	0.04	0.38	3.30	14.03	67.75	93.44
	1.33	2.82	1.77	0.13	0.59	0.85	0.05	0.31	3.44	14.25	68.18	93.67
	1.78	2.86	1.71	0.06	0.67	0.98	0.05	0.27	3.27	13.58	68.82	93.99
	1.57	2.92	1.70	0.16	0.62	0.97	0.05	0.44	3.27	14.23	68.97	94.84
	1.55	2.74	1.70	0.08	0.58	0.86	0.04	0.30	3.30	13.80	68.78	93.70
	1.51	2.68	1.88	0.17	0.51	0.87	0.06	0.36	3.54	14.31	68.30	94.13
	1.00	2.54	1.71	0.20	0.59	0.92	0.05	0.45	3.54	13.81	68.00	92.75
	1.44	2.80	1.66	0.16	0.61	0.91	0.05	0.38	3.49	14.71	68.15	94.33
	1.54	2.81	1.67	0.19	0.64	0.93	0.05	0.45	3.15	13.98	68.90	94.24
	1.60	2.79	1.81	0.25	0.74	0.92	0.05	0.35	3.20	14.09	69.27	95.02
KSM2C - 3												
	1.73	2.71	1.93	0.23	0.57	1.11	0.07	0.34	3.56	14.39	67.75	94.32
	1.64	2.55	2.10	0.16	0.64	1.01	0.06	0.14	3.57	14.80	67.04	93.65
	1.46	2.55	1.88	0.21	0.72	1.08	0.05	0.35	3.41	14.69	67.69	94.03
	1.67	2.58	1.90	0.25	0.56	1.12	0.07	0.34	3.95	14.43	66.61	93.41
	1.61	2.46	1.97	0.13	0.61	1.12	0.07	0.27	3.58	14.71	66.77	93.24
	1.71	2.33	3.23	0.24	0.37	0.97	0.06	0.26	3.18	15.66	65.28	93.22
	1.78	2.49	2.18	0.26	0.57	1.02	0.07	0.33	3.49	15.17	67.18	94.47
	1.82	2.59	1.96	0.25	0.66	1.08	0.06	0.28	3.52	14.40	66.85	93.41
KSM2C - 4												
	1.64	3.09	1.91	0.32	0.52	1.22	0.06	0.33	2.81	14.69	65.18	91.71
	1.62	3.11	1.87	0.08	0.58	1.21	0.06	0.10	3.19	14.96	65.00	91.73
	1.67	3.14	1.87	0.19	0.53	1.25	0.06	0.40	3.46	14.75	64.20	91.45
	1.53	3.11	1.83	0.12	0.48	1.17	0.07	0.39	2.71	14.40	65.46	91.21
KSM2C - 5												
	0.61	2.83	1.87	0.23	0.53	0.84	0.04	0.34	4.05	14.88	68.42	94.65
	1.28	2.72	1.84	0.20	0.56	0.86	0.04	0.38	4.34	15.03	68.45	95.68
	0.63	2.75	1.89	0.21	0.56	0.85	0.05	0.33	4.32	14.91	68.23	94.72
	0.55	2.69	1.79	0.18	0.59	0.87	0.05	0.35	4.25	15.13	68.41	94.87
	1.20	2.67	1.84	0.17	0.60	0.96	0.04	0.36	5.10	15.80	66.96	95.71
	1.45	2.53	2.69	0.14	0.61	0.86	0.04	0.33	4.30	16.51	66.15	95.62
	1.26	2.66	1.79	0.23	0.64	0.89	0.05	0.39	4.68	15.02	67.99	95.59
	1.22	2.66	1.87	0.17	0.58	0.87	0.05	0.34	4.62	15.03	68.10	95.51
	0.61	2.66	1.83	0.17	0.62	0.88	0.04	0.31	4.44	15.11	68.02	94.68
KSM2C -6												
	0.43	2.56	1.95	0.17	0.53	1.01	0.04	0.37	4.57	15.15	66.68	93.46
	0.84	2.51	1.87	0.18	0.58	1.01	0.04	0.36	4.80	15.29	66.53	94.01
	0.86	2.48	1.91	0.21	0.59	0.96	0.03	0.33	4.45	14.90	66.28	93.00
	0.81	2.49	1.87	0.15	0.52	0.96	0.05	0.33	4.42	14.96	66.69	93.25
	0.82	2.48	1.94	0.17	0.61	0.93	0.04	0.36	4.44	14.85	66.79	93.42
	0.78	2.48	1.86	0.23	0.68	0.92	0.04	0.27	4.36	14.82	66.44	92.87
	0.83	2.52	1.89	0.18	0.54	0.91	0.05	0.34	4.55	14.87	66.45	93.14
	0.85	2.48	1.90	0.23	0.53	0.93	0.04	0.35	4.38	14.93	66.96	93.57
	0.84	2.51	1.91	0.13	0.53	0.94	0.04	0.36	4.57	14.95	66.99	93.76
	1.11	2.35	3.56	0.17	0.50	0.92	0.03	0.28	4.04	17.17	64.29	94.44

Glass												
Run	**Na_2O**	**K_2O**	**CaO**	**MnO**	**P_2O_5**	**MgO**	**Sc_2O_3**	**TiO_2**	**FeO**	**Al_2O_3**	**SiO_2**	**Total**
KSM2C -7												
	0.84	2.41	1.90	0.17	0.62	0.87	0.04	0.33	4.40	14.69	68.08	94.34
	1.01	2.59	1.82	0.12	0.60	1.06	0.05	0.35	4.89	15.22	66.24	93.94
	0.88	2.41	1.88	0.15	0.62	0.89	0.04	0.42	4.35	14.59	68.28	94.50
	0.87	2.46	1.95	0.16	0.59	0.90	0.04	0.32	4.36	14.56	67.74	93.95
	1.09	2.58	1.90	0.18	0.56	0.96	0.04	0.36	4.60	15.42	67.26	94.96
	0.76	2.46	1.90	0.24	0.52	0.91	0.05	0.31	4.21	14.44	67.87	93.67
	0.85	2.49	1.90	0.14	0.57	0.90	0.04	0.36	4.57	14.76	68.15	94.73
	1.20	2.68	1.77	0.18	0.50	1.10	0.04	0.34	5.79	16.21	65.40	95.22
	0.85	2.50	1.90	0.19	0.68	0.90	0.05	0.32	4.16	14.63	68.02	94.18
	0.87	2.54	1.88	0.22	0.55	0.91	0.05	0.37	4.12	14.85	68.29	94.64
KSM2C -8												
	1.14	5.01	0.59	0.13	0.54	0.88	0.05	0.44	6.27	18.53	65.44	99.03
	1.10	4.81	0.57	0.22	0.55	0.92	0.04	0.48	6.49	18.64	65.67	99.50
	1.11	4.79	0.58	0.18	0.51	0.93	0.04	0.43	6.53	18.40	65.81	99.30
	1.09	4.81	0.59	0.18	0.58	0.91	0.05	0.52	6.44	18.59	65.56	99.32
	1.01	4.82	0.60	0.18	0.61	0.92	0.02	0.48	6.63	18.54	65.69	99.50
	1.14	4.96	0.59	0.20	0.49	0.86	0.08	0.62	5.89	17.88	66.28	98.99
	1.14	4.88	0.54	0.16	0.55	0.83	0.05	0.73	5.92	17.93	66.73	99.45
	1.14	4.86	0.56	0.10	0.50	0.79	0.02	0.42	6.19	17.66	66.65	98.89
	1.11	4.89	0.61	0.16	0.45	0.75	0.02	0.44	5.94	17.20	67.97	99.54
	1.14	4.95	0.56	0.14	0.58	0.78	0.03	0.40	5.81	17.64	68.06	100.08
KSM2C -9												
	0.95	2.53	1.93	0.18	0.54	0.85	0.04	0.34	4.27	14.70	68.11	94.45
	0.95	2.55	1.90	0.13	0.59	0.85	0.05	0.34	4.23	14.51	68.05	94.16
	0.98	2.55	1.94	0.16	0.57	0.86	0.05	0.32	4.22	14.85	68.68	95.19
	0.80	2.56	1.87	0.21	0.55	0.85	0.04	0.33	4.23	14.61	67.80	93.85
	0.78	2.53	1.88	0.13	0.58	0.88	0.04	0.32	4.40	14.67	68.46	94.68
	0.94	2.66	1.91	0.15	0.58	0.92	0.04	0.33	4.32	15.00	67.37	94.22
	0.90	2.67	1.96	0.17	0.60	0.90	0.05	0.33	4.07	14.74	68.22	94.60
	0.75	2.63	1.90	0.17	0.58	0.85	0.04	0.32	4.07	14.64	68.07	94.03
	0.81	2.62	1.98	0.16	0.59	0.82	0.05	0.32	4.00	14.71	68.56	94.61
	0.93	2.58	1.97	0.15	0.59	0.88	0.05	0.30	3.89	15.06	68.82	95.23
KSM3A-1												
	1.24	3.04	1.09	0.25	0.87	0.47	0.07	0.26	1.12	12.99	73.08	94.47
	1.05	2.85	1.04	0.22	0.92	0.67	0.05	0.15	1.06	12.96	70.17	91.14
	0.72	3.14	1.11	0.15	0.93	0.43	0.05	0.24	1.24	12.90	73.02	93.92
	0.96	3.19	1.09	0.25	0.92	0.65	0.06	0.36	3.06	14.57	71.21	96.31
	0.79	3.06	1.15	0.20	0.86	0.51	0.05	0.18	1.39	13.40	72.16	93.75
	1.41	3.28	1.11	0.18	0.70	0.71	0.07	0.43	2.41	14.33	68.90	93.52
	0.68	2.86	1.07	0.21	0.73	0.85	0.05	0.22	3.14	14.66	66.64	91.11
	1.18	2.97	1.11	0.16	0.85	0.51	0.05	0.16	1.56	13.41	73.17	95.12
	0.71	2.98	1.12	0.20	0.71	0.48	0.06	0.16	1.31	13.12	73.56	94.42
KSM3A-2												
	0.70	2.80	1.24	0.21	0.84	0.39	0.06	0.22	1.59	12.77	73.07	93.89
	1.31	2.83	1.27	0.17	0.80	0.40	0.06	0.19	1.53	12.69	72.95	94.21
	0.77	2.87	1.28	0.25	0.76	0.39	0.07	0.18	1.61	12.71	72.25	93.14
	0.75	2.83	1.27	0.18	0.87	0.40	0.06	0.21	1.66	12.60	72.46	93.28
	0.74	2.88	1.28	0.14	0.96	0.37	0.07	0.21	1.56	12.47	72.68	93.37
	1.44	2.83	1.27	0.15	0.92	0.35	0.09	0.87	2.14	12.65	71.72	94.44
	1.37	2.85	1.30	0.18	0.81	0.39	0.08	0.20	1.61	13.06	73.05	94.89
	0.73	2.81	1.28	0.21	1.00	0.40	0.07	0.23	1.52	12.68	72.05	92.99
	1.30	2.83	1.23	0.17	0.97	0.40	0.07	0.23	1.59	12.94	71.96	93.70
	0.70	2.84	1.27	0.18	0.85	0.41	0.06	0.18	1.50	12.61	72.74	93.34
KSM3A-3												
	0.71	2.90	1.18	0.20	0.85	0.45	0.06	0.22	1.20	12.94	72.15	92.86
	0.73	2.94	1.19	0.20	0.90	0.47	0.06	0.23	1.28	12.62	71.55	92.16
	0.67	3.00	1.15	0.19	0.90	0.46	0.05	0.22	1.14	13.16	75.14	96.07
	0.85	2.50	1.22	0.22	1.10	0.46	0.07	0.19	1.33	13.17	72.78	93.89
	1.10	2.97	1.11	0.15	0.81	0.44	0.05	0.27	1.15	12.54	73.44	94.04
	1.05	2.85	1.03	0.17	0.73	0.37	0.06	0.22	1.11	11.94	73.54	93.06
	0.63	2.83	1.19	0.20	0.91	0.47	0.07	0.21	1.18	12.77	72.10	92.56
	1.24	2.88	1.08	0.21	0.93	0.45	0.05	0.27	1.16	12.66	72.41	93.35

Glass

Run	Na_2O	K_2O	CaO	MnO	P_2O_5	MgO	Sc_2O_3	TiO_2	FeO	Al_2O_3	SiO_2	Total
KSM3A-4												
	1.02	2.33	1.25	0.21	0.97	0.40	0.04	0.23	1.35	11.51	72.10	91.40
	0.77	2.82	1.39	0.20	0.95	0.44	0.06	0.26	1.42	12.99	73.08	94.37
	0.57	2.70	1.32	0.17	1.09	0.39	0.06	0.25	1.38	12.57	73.11	93.61
	1.24	2.81	1.34	0.23	0.75	0.39	0.05	0.20	1.34	12.91	73.10	94.35
	0.81	2.36	1.40	0.21	1.17	0.42	0.05	0.21	1.36	13.08	72.86	93.91
	1.10	2.71	1.37	0.20	1.02	0.39	0.06	0.21	1.39	13.04	72.25	93.74

Run	Na_2O	K_2O	CaO	MnO	P_2O_5	MgO	Sc_2O_3	TiO_2	FeO	Al_2O_3	SiO_2	F	Cl	Total
KSM3A-5														
	0.73	2.96	1.21	0.14	0.62	0.46	0.05	0.18	1.41	13.10	72.14	n.a.	0.47	93.36
	0.88	3.08	1.18	0.15	0.55	0.47	0.05	0.19	1.42	13.10	72.75	n.a.	0.45	94.17
	0.87	3.03	1.17	0.19	0.58	0.48	0.05	0.22	1.41	12.99	72.27	n.a.	0.44	93.60
	0.96	3.10	1.20	0.16	0.58	0.42	0.06	0.23	1.51	13.25	72.64	n.a.	0.46	94.47
	0.92	3.08	1.17	0.11	0.55	0.46	0.05	0.18	1.40	13.10	72.54	n.a.	0.46	93.92
	0.83	3.02	1.15	0.12	0.54	0.46	0.05	0.21	1.33	12.78	73.56	n.a.	0.46	94.40
	0.98	3.08	1.12	0.15	0.43	0.46	0.04	0.16	1.31	12.99	73.42	n.a.	0.45	94.49
	0.89	3.14	1.12	0.12	0.39	0.43	0.04	0.15	1.32	12.86	72.73	n.a.	0.40	93.51
	0.94	3.09	1.10	0.15	0.45	0.39	0.04	0.15	1.27	12.96	73.45	n.a.	0.43	94.31
	0.88	3.08	1.12	0.13	0.62	0.48	0.05	0.20	1.36	13.21	71.94	n.a.	0.42	93.40
KSM3A-6														
	0.61	2.69	1.19	0.15	0.46	0.53	0.05	0.23	1.47	13.34	72.04	n.a.	0.48	93.12
	0.87	2.91	1.29	0.23	0.62	0.55	0.06	0.17	1.75	13.75	71.41	n.a.	0.49	93.98
	0.76	2.88	1.27	0.16	0.55	0.55	0.04	0.19	1.80	13.75	71.45	n.a.	0.49	93.78
	0.95	2.92	1.31	0.20	0.62	0.54	0.05	0.19	1.81	13.80	71.55	n.a.	0.53	94.33
	0.76	2.82	1.30	0.12	0.60	0.53	0.06	0.15	1.76	13.81	71.98	n.a.	0.54	94.29
	0.89	2.91	1.05	0.20	0.47	0.50	0.05	0.20	1.55	12.75	73.51	n.a.	0.43	94.42
	0.79	2.80	1.31	0.14	0.49	0.53	0.05	0.17	1.72	13.45	72.53	n.a.	0.48	94.35
	0.73	2.84	1.27	0.16	0.47	0.55	0.05	0.23	1.79	13.60	71.90	n.a.	0.50	93.98
	0.84	2.87	1.25	0.17	0.57	0.54	0.05	0.14	1.73	13.59	71.35	n.a.	0.48	93.48
	0.75	2.81	1.29	0.16	0.55	0.58	0.05	0.17	1.77	13.84	72.59	n.a.	0.52	94.94
KSM3A-7														
	0.79	2.71	1.31	0.19	0.48	0.50	0.06	0.24	1.44	13.27	72.78	0.34	0.46	94.32
	0.79	2.76	1.44	0.13	0.50	0.54	0.05	0.21	1.46	13.65	72.06	0.23	0.40	94.04
	0.75	2.66	1.45	0.10	0.48	0.55	0.06	0.21	1.47	13.74	71.44	0.21	0.42	93.34
	0.75	2.77	1.46	0.18	0.50	0.55	0.06	0.20	1.47	13.90	71.36	0.30	0.44	93.71
	0.73	2.69	1.51	0.16	0.54	0.55	0.05	0.20	1.52	13.78	71.72	0.16	0.44	93.89
	0.73	2.74	1.44	0.12	0.58	0.56	0.06	0.25	1.61	13.69	70.75	0.16	0.44	92.96
	0.79	2.77	1.44	0.19	0.61	0.56	0.06	0.19	1.61	13.71	70.42	0.20	0.47	92.82
	0.79	2.82	1.46	0.22	0.56	0.56	0.06	0.23	1.60	13.77	70.58	0.14	0.46	93.09
	0.79	2.78	1.43	0.14	0.54	0.55	0.05	0.23	1.60	13.73	70.48	0.33	0.46	92.86
	0.77	2.75	1.50	0.21	0.56	0.55	0.05	0.23	1.54	13.73	70.47	0.17	0.44	92.81
KSM3A-8														
	0.77	2.96	1.34	0.19	0.55	0.49	0.05	0.19	1.46	13.59	71.19	0.27	0.46	93.27
	0.87	2.95	1.34	0.21	0.62	0.46	0.05	0.21	1.43	14.02	72.28	0.26	0.49	94.95
	0.93	2.98	1.35	0.21	0.56	0.48	0.05	0.23	1.50	13.76	71.37	0.25	0.46	93.91
	0.82	3.00	1.37	0.18	0.53	0.48	0.05	0.22	1.49	13.86	71.18	0.05	0.47	93.60
	0.95	2.95	1.47	0.21	0.55	0.53	0.04	0.24	1.65	14.02	70.75	0.14	0.48	93.80
	0.86	2.90	1.36	0.11	0.54	0.52	0.05	0.18	1.41	13.80	71.69	0.28	0.46	93.94
	0.92	3.01	1.33	0.19	0.58	0.44	0.05	0.17	1.46	13.50	71.04	0.18	0.56	93.23
	0.92	2.99	1.33	0.18	0.57	0.53	0.05	0.20	1.62	13.84	71.33	0.31	0.49	94.11
	0.83	3.02	1.33	0.18	0.58	0.45	0.06	0.18	1.60	13.61	72.03	0.18	0.51	94.36
	0.80	3.00	1.18	0.11	0.56	0.53	0.05	0.24	1.40	13.36	72.66	0.20	0.46	94.37

Plagioclase

Run	Na_2O	K_2O	CaO	P_2O_5	MnO	MgO	Sc_2O_3	TiO_2	FeO	Al_2O_3	SiO_2	Total
KSM1C - 1												
	2.05	0.88	9.97	2.38	0.10	0.45	0.013	1.98	5.27	23.78	54.52	101.39
	4.09	0.41	11.64	1.86	0.05	0.33	0.013	1.83	5.25	25.16	49.64	100.27
	3.79	0.46	11.24	1.49	0.07	0.34	0.018	1.92	4.56	25.53	51.40	100.84
	2.10	0.52	10.76	1.30	0.14	0.39	0.012	2.27	4.44	25.20	53.25	100.37
	2.07	0.74	11.39	1.87	0.04	0.79	0.026	1.89	3.97	26.70	54.13	103.61
	3.91	0.37	10.88	1.87	0.07	0.41	0.034	4.25	10.35	24.15	45.74	102.04
	2.97	0.93	9.95	1.88	0.20	0.65	0.028	4.01	5.20	21.75	52.45	100.02
KSM1C - 3												
	3.75	0.44	13.27	0.22	0.04	0.05	b.d.	0.14	0.73	30.89	53.07	102.60
	3.08	1.88	8.41	0.92	0.08	0.16	0.011	0.31	1.23	23.24	59.63	98.96
	3.87	0.74	12.63	0.71	0.01	0.05	0.006	0.17	0.88	28.33	53.62	101.01
	2.28	0.57	12.20	0.72	0.09	0.11	0.007	0.27	1.34	28.41	55.13	101.13
	3.84	0.64	12.02	0.21	0.02	0.07	0.008	0.93	1.28	29.43	53.08	101.53
	2.84	1.73	6.17	0.56	0.04	0.17	0.006	0.31	0.95	21.96	63.94	98.68
KSM1C - 4												
	3.08	0.41	11.90	1.10	0.05	0.16	0.002	0.72	1.70	26.74	51.94	97.81
	3.00	0.65	11.23	0.95	0.04	0.32	0.012	1.22	2.25	25.77	53.06	98.51
	2.04	0.66	11.04	1.39	0.17	0.30	0.016	1.41	2.33	24.54	53.08	96.98
	3.17	0.81	10.82	1.99	0.07	0.37	0.014	0.51	1.11	26.47	54.44	99.78
	3.13	0.41	12.13	0.29	0.05	0.05	0.000	0.13	0.77	30.02	55.39	102.36
	3.20	0.63	11.63	1.27	0.04	0.15	0.012	0.27	0.86	26.72	55.09	99.88
KSM1C - 5												
	2.07	1.08	10.43	1.23	0.07	0.56	0.013	0.33	1.20	24.62	56.81	98.42
	2.37	0.88	10.44	0.46	0.02	0.35	0.009	0.29	1.22	25.77	56.59	98.41
	2.93	0.46	12.78	0.58	0.05	0.20	0.017	0.64	1.51	28.42	51.39	98.97
KSM1C - 6												
	2.49	0.77	11.23	0.78	0.10	0.60	0.007	0.92	2.01	26.42	54.18	99.51
	3.36	0.27	13.56	1.09	0.01	0.30	0.005	0.61	1.92	28.40	49.83	99.37
	2.77	0.78	11.94	0.41	b.d.	0.47	0.006	0.36	1.56	27.69	53.05	99.02
	2.76	0.78	12.31	1.28	0.10	0.51	0.012	0.40	1.74	27.09	52.86	99.85
KSM1C - 7												
	3.23	0.43	13.12	0.75	0.03	0.26	0.008	0.20	1.50	28.44	50.23	98.20
	3.02	0.41	13.09	0.70	0.03	0.31	0.009	0.87	1.83	28.09	50.07	98.42
KSM1C - 8												
	1.46	2.29	8.47	4.08	0.17	1.40	0.021	1.00	4.48	18.11	57.09	98.57
	0.61	1.96	4.85	2.58	0.16	1.63	0.013	1.37	7.90	16.26	56.62	93.96
	1.39	0.72	9.87	0.74	0.06	0.70	0.010	0.41	2.00	24.93	57.21	98.03
	1.41	1.49	8.16	1.13	0.16	0.91	0.011	0.78	2.61	22.19	57.36	96.20
KSM1C - 9												
	2.28	0.99	10.05	0.54	0.06	0.56	0.012	0.35	3.04	25.03	54.05	96.94
	2.61	0.99	11.38	0.66	0.04	0.45	0.015	0.42	2.23	26.41	53.77	98.98
	2.33	1.08	9.64	0.69	0.14	0.65	0.004	0.92	3.31	24.79	53.80	97.35
	2.13	1.05	11.65	1.58	0.14	0.58	0.009	0.91	3.09	24.64	51.09	96.87
	1.49	1.47	7.30	0.64	0.15	0.95	0.011	0.57	4.28	22.45	57.58	96.88
	1.36	1.36	8.01	1.66	0.14	0.96	0.008	0.52	4.49	21.52	55.82	95.85
	1.77	1.30	8.21	0.68	0.13	0.80	0.011	0.46	3.71	23.46	55.96	96.48
	2.54	1.10	10.75	0.61	0.03	0.53	b.d.	0.31	2.40	26.09	53.58	97.95
KSM1C - 10												
	3.04	0.74	13.04	0.73	b.d.	0.16	0.005	0.30	1.37	28.68	52.87	100.92
	3.51	0.88	12.07	0.52	b.d.	0.37	0.010	0.19	1.42	27.82	53.70	100.50
	3.07	0.41	14.21	0.47	0.07	0.12	0.003	0.32	1.07	30.27	51.19	101.21
	3.07	0.74	12.77	0.81	0.05	0.30	0.004	0.21	1.23	27.59	53.13	99.90
	3.31	0.64	12.75	0.39	b.d.	0.15	0.010	0.28	1.23	28.96	53.01	100.75
	3.24	0.55	13.04	0.35	0.06	0.19	0.005	0.09	0.88	29.04	51.38	98.81
	2.94	0.58	13.45	0.31	0.04	0.19	0.002	0.31	1.14	29.80	50.24	98.99
	3.09	0.51	13.57	0.16	b.d.	0.18	0.012	0.13	0.75	29.66	50.76	98.82
	3.07	0.36	14.03	0.16	b.d.	0.13	0.002	0.29	0.90	30.60	50.08	99.61
	2.05	0.88	9.97	2.38	0.10	0.45	0.013	1.98	5.27	23.78	54.52	101.39

Plagioclase

Run	Na_2O	K_2O	CaO	P_2O_5	MnO	MgO	Sc_2O_3	TiO_2	FeO	Al_2O_3	SiO_2	Total
KSM1C - 11												
	2.55	1.02	11.85	1.96	0.06	0.49	0.010	0.62	2.43	24.46	51.52	96.96
	2.62	1.13	10.64	0.74	0.12	0.62	0.008	0.50	2.12	25.45	54.32	98.28
	3.62	0.77	12.00	0.78	b.d.	0.26	0.008	0.38	1.82	27.19	52.62	99.48
	3.20	0.73	12.77	1.03	0.03	0.21	0.006	0.19	1.20	27.76	52.35	99.47
	3.65	0.57	12.44	0.14	b.d.	0.09	0.006	0.16	0.91	29.06	52.88	99.90
	2.91	0.97	11.43	0.84	0.11	0.36	b.d.	0.40	2.03	26.56	53.12	98.74
	2.58	1.23	10.04	0.85	0.09	0.55	0.011	0.35	2.28	25.21	56.13	99.33
KSM1C - 12												
	3.82	0.63	12.51	1.03	b.d.	0.20	0.006	0.53	1.21	28.31	52.26	100.53
	3.34	1.02	10.97	0.69	b.d.	0.35	0.003	0.78	1.72	26.87	54.93	100.69
	3.07	1.09	9.42	0.72	0.14	0.96	0.003	0.73	2.79	25.23	55.49	99.64
	2.32	1.65	9.29	2.34	0.18	0.70	0.010	0.99	3.37	22.30	55.33	98.49
	2.93	1.40	9.42	1.38	0.14	1.20	0.011	0.93	3.43	23.43	54.56	98.82
	2.65	1.56	8.48	0.69	b.d.	0.51	0.001	0.64	2.40	24.00	57.25	98.23
	1.59	1.79	7.80	2.16	0.10	0.88	0.013	0.86	3.68	20.95	57.43	97.24
KSM2A - 1												
	2.73	0.29	13.99	0.14	0.07	0.06	0.005	0.02	0.44	32.29	50.76	100.80
	2.49	0.35	14.17	0.14	0.03	0.06	0.013	0.09	0.49	31.59	50.49	99.92
	2.53	0.24	14.27	0.19	0.03	0.10	0.015	0.39	0.46	31.73	49.41	99.37
	2.21	0.17	14.76	0.16	0.04	0.12	0.043	1.26	0.86	32.78	48.38	100.78
	1.83	0.65	13.48	0.19	0.10	0.24	0.036	1.03	0.85	29.94	50.57	98.91
	2.51	0.19	15.15	0.09	0.08	0.04	0.012	0.05	0.33	32.61	49.60	100.67
	2.60	0.21	14.92	0.17	0.04	0.04	0.008	0.07	0.39	32.20	50.15	100.78
	2.18	0.18	15.51	0.15	0.05	0.05	0.014	0.04	0.40	32.79	48.92	100.29
KSM2A - 2												
	2.47	0.76	12.58	0.21	0.05	0.22	0.018	0.24	0.64	29.15	54.36	100.70
	2.99	0.29	13.93	0.16	0.03	0.05	b.d.	0.04	0.31	31.10	51.39	100.27
	2.43	0.34	14.23	0.12	0.05	0.09	0.009	0.07	0.41	31.60	50.61	99.96
	2.76	0.24	13.97	0.14	0.06	0.18	0.007	0.01	0.65	31.41	50.41	99.84
	2.76	0.24	13.98	0.18	b.d.	0.29	0.008	0.10	0.78	31.92	50.07	100.31
	2.83	0.29	14.25	0.15	0.09	0.06	0.002	0.05	0.28	31.34	51.18	100.51
	2.10	1.07	11.14	0.34	0.06	0.34	0.021	0.19	0.92	27.27	56.76	100.22
	2.41	0.39	14.32	0.19	0.04	0.09	0.008	0.06	0.39	31.41	50.94	100.24
KSM2C - 1												
	2.33	0.33	14.26	0.17	b.d.	0.13	0.012	0.05	0.76	30.70	50.18	98.86
	2.60	0.63	12.57	0.15	0.01	0.16	0.017	0.07	1.49	28.51	49.77	95.96
	1.81	0.45	14.66	0.10	b.d.	0.13	0.012	b.d.	0.81	30.21	49.73	97.80
	2.03	0.68	13.70	0.03	0.20	0.25	0.022	0.11	0.91	29.49	50.78	98.18
	2.40	0.37	14.86	0.18		0.10	0.001	0.05	0.99	31.45	48.98	99.32
	2.10	0.24	15.00	0.15	0.08	0.02	0.005	0.10	0.68	31.71	48.11	98.19
	2.05	0.58	13.56	0.12	0.21	0.17	0.014	0.09	0.93	29.75	50.95	98.39
	2.39	0.33	14.76	0.18	b.d.	0.06	0.002	0.05	0.63	30.73	49.53	98.63
KSM2C - 2												
	2.56	0.35	13.13	0.10	0.14	0.09	0.014	0.33	1.02	33.12	48.96	99.82
	2.31	0.47	13.84	0.22	0.12	0.11	0.016	0.44	0.92	29.91	49.65	97.99
	2.38	0.98	12.29	0.26	0.16	0.25	0.019	0.08	0.93	27.38	52.18	96.88
	2.22	0.77	12.96	0.24	0.01	0.16	0.017	0.13	0.93	28.88	51.16	97.44
	2.19	0.83	12.57	0.20	0.04	0.18	0.013	0.11	0.90	31.94	49.71	98.68
	1.86	0.22	14.41	0.20	0.00	0.11	0.019	0.53	1.04	34.72	46.98	100.08
	1.43	0.20	15.51	0.18	b.d.	0.10	0.016	0.28	0.76	35.30	44.91	98.64
	2.55	1.01	11.18	0.19	0.02	0.23	0.032	0.16	1.76	26.74	52.36	96.22
KSM2C - 3												
	2.12	1.09	11.71	0.19	0.07	0.35	0.015	0.14	1.33	27.11	53.30	97.42
	1.82	1.59	9.74	0.37	0.05	0.47	0.041	0.18	1.81	24.50	56.53	97.07
	2.54	0.60	13.83	0.13	0.18	0.21	0.024	0.08	0.70	29.58	51.25	99.11
	1.65	1.90	8.89	0.31	0.11	0.63	0.057	0.31	2.18	23.32	58.91	98.21
	1.93	1.31	11.36	0.24	0.11	0.38	0.032	0.28	1.97	26.43	54.22	98.23

Plagioclase

Run	Na_2O	K_2O	CaO	P_2O_5	MnO	MgO	Sc_2O_3	TiO_2	FeO	Al_2O_3	SiO_2	Total
KSM2C -4												
	1.14	0.23	14.01	0.16	0.04	0.07	0.012	0.66	35.85	0.11	44.46	96.73
	1.64	0.45	13.05	0.19	0.04	0.07	0.017	0.90	30.05	0.20	49.86	96.46
	2.01	0.45	12.74	0.16	0.06	0.08	0.011	0.89	29.54	0.20	50.49	96.60
	2.06	0.50	11.36	0.18	0.03	0.27	0.024	0.08	0.87	27.43	51.80	94.58
KSM2C -5												
	2.47	0.64	13.33	0.01	0.17	0.16	0.012	0.09	0.87	29.56	53.41	100.72
	2.08	1.29	10.09	0.15	0.31	0.37	0.018	0.17	1.92	25.63	57.36	99.38
	1.54	1.67	8.22	0.11	0.36	0.55	0.027	0.52	3.23	24.30	58.57	99.09
	1.53	1.51	10.00	0.07	0.29	0.39	0.017	0.15	2.13	25.26	58.17	99.52
	2.53	0.61	12.98	0.01	0.12	0.13	0.014	0.06	0.81	29.38	52.61	99.24
	2.46	0.83	12.47	0.02	0.21	0.16	0.018	0.08	1.06	28.49	53.60	99.39
	1.80	1.20	11.04	0.08	0.29	0.31	0.021	0.19	1.99	26.80	55.88	99.61
	1.82	1.28	10.25	0.07	0.23	0.35	0.026	0.15	1.86	25.70	58.29	100.02
KSM2C -6												
	1.69	1.23	10.38	0.09	0.30	0.42	0.022	0.59	2.16	25.59	55.72	98.19
	1.87	0.98	11.34	0.11	0.20	0.30	0.013	0.18	1.43	27.11	54.07	97.60
	1.75	1.37	12.06	0.10	0.34	0.30	0.018	0.55	1.71	28.04	51.96	98.19
KSM2C -7												
	1.81	1.29	10.27	0.03	0.31	0.36	0.016	0.13	1.78	25.95	56.99	98.93
	2.40	0.86	12.25	0.05	0.28	0.23	0.002	0.12	1.14	28.19	54.85	100.38
	2.00	0.25	15.49	0.04	0.14	0.09	0.012	0.67	1.29	32.67	47.04	99.71
	2.06	0.93	11.45	0.08	0.20	0.27	0.020	0.33	1.56	27.09	54.23	98.22
	2.31	0.79	12.13	0.02	0.22	0.24	0.002	0.08	1.19	28.11	53.92	99.04
	1.86	1.09	11.93	0.09	0.24	0.30	0.016	0.15	1.46	27.50	55.44	100.07
	2.13	0.79	12.80	0.08	0.17	0.22	0.011	0.06	0.98	28.81	53.85	99.91
KSM2C -8												
	2.29	0.70	13.41	0.07	0.18	0.23	0.021	0.42	1.41	29.71	52.73	101.15
	1.74	1.27	9.90	0.13	0.24	0.42	0.045	2.51	4.11	24.70	55.47	100.54
KSM3A-1												
	2.85	1.02	8.61	0.11	0.49	0.31	0.016	0.09	1.13	23.58	61.82	100.04
KSM3A-2												
	3.53	0.38	12.73	0.06	0.28	0.05	0.011	0.03	0.37	29.72	54.29	101.45
KSM3A-3												
	3.20	0.44	9.14	0.08	0.34	0.07	b.d.	0.03	0.41	22.99	66.97	103.66
KSM3A-4												
	2.36	0.72	9.01	0.12	0.30	0.17	0.052	0.98	1.71	25.30	60.86	101.57
KSM3A-6												
	4.44	0.54	10.97	0.04	0.21	0.04	0.005	b.d.	0.35	28.60	55.70	100.88
KSM3A-7												
	4.71	0.34	11.22	0.02	0.16	0.02	0.000	0.01	0.22	28.85	53.79	99.33
	4.63	0.34	11.52	0.01	0.17	0.02	0.003	b.d.	0.27	29.06	53.49	99.48
KSM3A-8												
	4.17	0.41	10.28	0.06	0.21	0.02	0.002	0.01	0.27	28.41	56.16	100.00
	4.32	0.49	11.06	0.05	0.19	0.02	b.d.	b.d.	0.31	28.42	55.57	100.43
	4.26	0.40	10.95	0.05	0.21	b.d.	0.007	0.02	0.29	28.64	54.96	99.77
	3.92	0.41	10.93	0.03	0.13	0.02	b.d.	0.05	0.24	28.41	55.13	99.26
	3.97	0.41	10.42	0.10	0.22	0.76	0.016	0.49	1.75	31.46	49.58	99.18
	4.17	0.37	7.89	0.18	0.22	1.73	b.d.	0.08	6.33	33.24	44.14	98.35

Pyroxene

Run	Na_2O	K_2O	CaO	MnO	P_2O_5	MgO	Sc_2O_3	TiO_2	FeO	Al_2O_3	SiO_2	Total
KSM1C - 1												
	0.26	0.34	3.71	1.19	1.82	17.78	0.11	1.66	24.62	4.41	46.95	102.85
	0.07	0.05	3.09	1.47	1.10	17.18	0.13	2.77	22.10	2.79	49.36	100.11
	0.41	0.61	3.26	0.98	1.65	15.14	0.08	1.30	17.88	6.01	53.14	100.46
	0.78	0.46	4.66	1.08	1.62	16.27	0.10	1.73	21.17	6.88	46.99	101.73
KSM1C - 2												
	0.06	0.11	3.26	1.34	1.45	18.43	0.12	2.09	27.13	2.71	45.10	101.79
	0.11	0.54	3.14	1.43	1.48	18.38	0.14	1.74	22.31	3.54	47.11	99.93
	0.06	0.05	3.49	1.68	1.56	18.37	0.12	2.12	25.69	2.58	45.86	101.57
	0.07	0.04	3.55	1.41	1.49	19.26	0.11	0.74	21.20	3.16	50.48	101.50
	0.07	0.05	5.45	1.37	3.21	18.71	0.11	0.54	21.15	1.85	48.00	100.51
	0.04	0.07	2.99	1.61	1.31	19.56	0.13	1.41	23.93	2.27	47.08	100.40
	0.20	0.13	2.23	1.45	0.26	19.09	0.13	0.46	21.41	3.98	52.58	101.92
	0.16	0.07	3.02	1.28	0.93	18.34	0.16	0.97	22.31	4.34	48.64	100.22
	0.30	0.21	2.68	1.32	0.65	18.34	0.11	0.65	21.10	4.82	51.83	102.01
	1.11	0.22	6.25	0.94	1.71	12.42	0.07	2.37	18.61	10.06	46.52	100.29
	0.03	0.12	2.77	1.42	0.71	20.74	0.12	0.43	21.20	2.14	50.24	99.92
	0.09	0.10	3.19	1.35	1.29	18.81	0.12	1.60	22.72	3.23	48.05	100.57
	0.59	0.26	5.31	1.34	2.45	15.50	0.12	2.87	19.50	6.31	47.71	101.98
KSM1C - 4												
	0.13	0.05	1.86	1.19	b.d.	19.72	0.11	0.40	18.62	2.82	52.93	97.80
	0.12	0.22	1.60	1.11	b.d.	17.19	0.09	0.22	17.68	3.97	56.30	98.46
	0.12	0.08	3.73	1.33	1.47	18.34	0.12	2.22	18.07	2.67	48.43	96.58
	0.05	0.08	2.50	1.39	0.36	17.67	0.11	0.50	18.43	2.66	50.90	94.66
	0.09	0.14	4.03	1.29	1.81	17.17	0.12	1.55	17.05	2.83	49.20	95.27
	0.26	0.33	2.49	1.18	0.42	19.13	0.12	0.44	17.54	4.04	53.23	99.19
	0.13	0.11	3.15	1.31	0.97	18.53	0.12	1.17	18.88	2.61	49.80	96.77
	0.04	0.08	4.37	1.26	2.02	18.31	0.14	2.27	17.13	1.99	47.86	95.46
KSM1C - 5												
	0.25	0.51	2.49	0.89	1.12	17.19	0.10	0.87	15.34	5.42	54.22	98.40
	0.23	0.40	2.64	0.86	0.77	19.01	0.09	0.64	14.10	5.49	53.88	98.10
	0.04	0.03	1.04	1.18	0.09	21.78	0.16	0.41	17.09	2.47	52.49	96.78
	0.05	0.03	1.52	1.15	0.57	21.55	0.16	0.36	16.25	2.76	52.13	96.53
KSM1C - 11												
	0.55	1.22	2.22	0.83	44.06	20.93	0.05	1.24	28.26	5.97	1.88	107.22
	1.12	1.96	3.19	0.60	51.13	12.16	0.04	0.86	18.88	12.02	1.74	103.69
	1.97	1.25	5.90	0.48	51.18	10.80	0.02	0.31	15.76	17.54	0.87	106.10
	0.74	0.95	2.72	0.90	42.94	20.15	0.04	0.68	28.73	5.92	2.21	105.97
KSM1C - 12												
	2.00	0.81	4.88	0.46	47.62	14.43	0.01	0.30	18.21	12.64	1.02	102.40
KSM2C-2												
	0.02	0.06	0.29	0.85	0.01	0.98	0.44	25.15	9.26	17.12	45.32	98.53
	0.02	0.06	0.30	0.84	0.19	0.65	0.46	25.26	9.56	17.64	45.06	99.38
	0.03	0.04	0.27	0.84	0.11	0.57	0.38	25.58	11.26	17.33	43.92	99.76
	0.01	0.04	0.49	0.89	0.24	0.71	0.56	24.29	9.80	17.44	44.88	98.63
	0.02	0.03	0.32	0.92	0.22	0.58	0.48	24.93	9.06	17.85	45.18	99.01
	0.07	0.22	0.37	0.89	0.24	0.74	0.39	24.26	10.10	16.79	47.29	100.62
	0.04	0.09	0.30	0.86	0.27	0.78	0.39	24.34	10.29	16.91	45.77	99.25
	0.03	0.19	0.38	0.92	0.12	0.83	0.45	24.89	9.95	16.28	47.05	100.27
KSM2C-3												
	0.01	b.d.	0.32	0.90	0.05	19.12	0.83	0.22	23.57	6.68	48.25	99.11
	0.04	0.06	0.30	0.88	0.06	19.15	0.86	0.13	24.68	5.64	49.55	100.49
	b.d.	0.04	0.27	0.86	b.d.	18.34	0.71	0.30	24.30	8.34	47.74	100.17

Pyroxene

Run	Na_2O	K_2O	CaO	MnO	P_2O_5	MgO	Sc_2O_3	TiO_2	FeO	Al_2O_3	SiO_2	Total
KSM2C-5												
	0.03	0.12	0.37	0.79	0.29	15.76	0.93	0.51	26.47	10.07	46.31	101.67
	0.03	0.10	0.34	0.82	0.08	15.57	0.73	0.46	29.15	6.89	47.48	101.66
	0.00	0.03	0.31	0.77	0.17	15.96	1.13	0.54	27.33	9.91	45.29	101.46
	0.01	0.07	0.39	0.84	0.05	15.80	0.72	0.50	29.09	7.55	46.84	101.85
	0.01	0.07	0.28	0.81	0.17	15.99	0.60	0.39	28.12	8.49	45.91	100.82
	b.d.	0.03	0.31	0.71	0.15	16.25	0.59	0.42	28.13	9.31	45.61	101.52
	b.d.	0.04	0.31	0.81	0.15	15.88	0.62	1.32	28.68	9.67	45.18	102.65
	0.11	0.28	0.94	0.70	0.16	13.96	0.95	0.46	26.12	11.72	47.69	103.09
	0.00	0.03	0.35	0.81	0.11	16.43	0.61	1.11	28.52	7.23	47.03	102.23
KSM2C-6												
	0.05	0.04	0.28	0.81	b.d.	15.60	0.66	0.41	27.08	7.96	45.67	98.52
	0.02	0.06	0.32	0.72	0.05	16.16	0.58	0.37	26.50	9.14	46.04	99.96
	b.d.	0.04	0.24	0.78	0.02	15.59	0.86	0.39	26.76	9.02	45.58	99.28
	0.01	0.05	0.21	0.67	b.d.	15.75	0.62	0.45	27.06	9.61	44.85	99.28
	0.01	0.04	0.27	0.75	0.01	16.61	0.63	0.29	27.62	6.10	47.05	99.37
	0.02	0.05	0.29	0.75	0.08	16.03	0.84	0.52	26.95	8.02	45.89	99.45
	0.04	0.05	0.33	0.66	0.21	16.36	0.84	0.44	26.13	8.76	46.32	100.14
	0.05	0.11	0.35	0.78	0.06	16.80	0.63	0.41	26.18	6.56	49.44	101.37
	0.06	0.11	0.33	0.69	0.03	15.63	0.53	0.44	27.13	8.70	45.82	99.47
KSM2C-7												
	0.01	0.04	0.36	0.83	0.13	16.47	0.79	0.45	27.71	7.59	46.99	101.38
	0.04	0.04	0.31	0.84	0.08	17.05	0.51	0.33	28.10	6.81	47.59	101.69
	0.02	0.03	0.33	0.74	0.08	16.29	0.87	0.50	27.57	8.11	46.26	100.80
	0.00	0.05	0.31	0.82	0.02	16.25	0.59	0.34	28.64	9.69	45.20	101.91
	0.02	0.03	0.31	0.80	b.d.	15.92	0.85	0.47	28.80	8.51	46.25	101.96
	0.02	0.04	0.26	0.81	0.07	15.57	0.60	0.34	28.31	10.58	44.46	101.04
	0.01	0.04	0.32	0.77	0.04	16.66	0.58	0.29	28.43	7.13	47.46	101.74
	0.02	0.08	0.32	0.81	0.17	15.76	0.80	0.59	28.55	8.95	45.58	101.64
	0.05	0.05	0.30	0.81	0.06	15.83	0.54	0.76	28.26	9.52	44.88	101.05
	0.02	0.05	0.28	0.78	0.04	15.72	0.74	0.61	28.51	8.81	46.20	101.76
KSM2C-8												
	0.06	0.21	0.70	1.22	0.52	12.48	0.31	0.51	31.11	12.15	45.58	104.86
	0.85	0.52	1.65	1.00	0.42	10.39	0.28	0.55	28.93	12.87	49.14	106.59
KSM2C-9												
	0.01	0.02	0.26	0.83	b.d.	15.45	1.01	0.52	29.70	8.86	45.98	102.64
	0.09	0.14	0.33	0.79	0.06	15.99	0.88	0.35	28.32	7.38	49.08	103.40
	0.21	0.16	1.10	0.80	0.03	15.49	0.72	0.31	27.02	8.01	50.78	104.63
	0.14	0.34	0.41	0.69	0.09	14.45	0.79	0.38	27.60	11.23	49.02	105.14
	b.d.	0.05	0.35	0.85	b.d.	17.22	0.60	0.22	29.30	3.89	49.95	102.42
	0.01	0.05	0.28	0.79	0.00	15.53	0.87	0.45	29.30	9.18	45.99	102.45
	0.07	0.17	0.39	0.78	0.18	16.17	0.71	0.44	27.82	8.89	47.92	103.52
	0.01	0.03	0.31	0.77	0.09	16.26	0.88	0.65	28.45	9.36	45.87	102.69
	0.02	0.10	0.32	0.78	0.03	16.64	0.61	0.29	28.50	5.85	48.89	102.02

Biotite

Run	Na_2O	K_2O	CaO	MnO	Al_2O_3	MgO	Sc_2O_3	TiO_2	FeO	SiO_2	P_2O_5	Total
KSM1C - 1												
	0.75	7.98	1.61	0.20	17.47	18.56	0.03	3.16	9.25	38.53	1.42	98.95
	0.71	7.44	0.91	0.20	16.33	20.03	0.03	3.25	8.64	38.94	0.72	97.19
	0.60	7.25	1.92	0.13	15.67	15.27	0.03	2.71	10.16	40.38	1.59	95.72
	0.80	5.13	4.87	0.29	13.83	8.91	0.03	3.53	18.52	39.78	3.54	99.24
KSM1C - 3												
	0.82	7.75	3.04	0.21	14.80	14.74	0.05	4.88	13.06	34.94	2.39	96.67
	0.84	8.53	0.41	0.20	15.83	15.53	0.06	4.34	12.04	37.13	0.21	95.12
	0.85	6.69	1.14	0.17	15.38	9.81	0.05	2.94	8.53	48.01	0.53	94.09
	1.17	8.16	1.55	0.17	16.60	14.46	0.05	4.52	11.51	38.35	0.61	97.14
	1.07	7.12	3.19	0.20	16.92	13.75	0.04	4.02	10.26	39.49	1.01	97.07
	0.79	8.24	2.25	0.15	14.83	15.74	0.06	4.17	11.58	35.00	1.49	94.31
	0.66	8.14	1.65	0.17	15.50	14.85	0.05	4.58	11.97	36.84	0.98	95.40
	0.87	5.89	0.73	0.14	15.08	7.53	0.03	2.38	7.24	51.93	0.14	91.96
KSM1C - 4												
	0.77	5.96	2.09	0.15	15.07	9.48	0.04	4.44	13.73	42.05	1.20	94.98
	1.80	6.48	3.38	0.24	16.78	8.98	0.04	3.86	9.22	42.53	1.77	95.09
KSM1C - 5												
	0.71	7.77	1.09	0.22	15.03	15.04	0.06	4.77	10.94	37.18	0.71	93.50
	0.74	7.99	0.71	0.15	14.95	15.44	0.06	4.36	10.17	38.37	0.41	93.33
	0.71	6.82	2.74	0.24	13.80	13.96	0.05	5.97	14.03	32.78	2.03	93.14
	0.71	7.80	1.32	0.22	14.87	15.09	0.06	4.87	10.98	37.23	1.01	94.16
	0.72	7.45	2.41	0.22	15.41	14.29	0.05	3.84	10.27	36.50	1.75	92.92
	1.10	6.65	2.64	0.18	18.23	11.74	0.05	4.61	9.19	39.33	-0.04	93.67
	0.80	7.78	2.08	0.20	15.12	14.28	0.05	5.01	9.72	35.99	1.66	92.68
	0.76	8.10	1.82	0.16	15.23	14.57	0.06	5.17	10.47	36.20	1.26	93.80
	0.75	7.92	0.43	0.16	16.45	13.51	0.05	5.43	9.99	39.77	0.19	94.67
KSM1C - 6												
	1.26	7.45	1.69	0.14	16.87	13.29	0.03	4.60	9.51	39.68	0.57	95.06
	1.16	8.48	0.43	0.14	16.00	15.75	0.04	5.43	9.88	37.70	0.07	95.04
	1.14	8.42	0.59	0.11	16.39	15.37	0.04	5.28	10.96	38.59	0.24	97.09
KSM1C - 7												
	0.91	8.10	0.51	0.08	16.33	15.34	0.04	5.26	10.59	37.48	0.09	94.70

Olivine

Run	Na_2O	K_2O	CaO	MnO	Al_2O_3	MgO	Sc_2O_3	TiO_2	FeO	SiO_2	P_2O_5	Total
KSM1C - 3												
	b.d.	0.01	0.19	1.22	0.02	32.13	0.03	0.07	29.06	35.98	0.29	98.99
	0.03	0.00	0.26	1.24	0.20	32.26	0.04	0.08	28.51	36.70	0.65	99.96
	0.06	0.02	0.25	1.21	0.39	32.79	0.03	0.06	27.71	36.86	0.32	99.69
	0.02	0.01	0.38	1.12	0.06	32.51	0.02	0.13	28.34	36.79	0.55	99.93
	0.00	0.02	0.20	1.05	0.04	32.40	0.03	0.11	28.31	36.61	0.57	99.33
	0.00	0.02	0.21	1.12	0.05	32.14	0.04	0.15	28.63	36.00	1.00	99.35
	0.04	0.04	1.97	1.24	0.32	29.81	0.05	0.72	28.54	33.59	2.12	98.45
	0.03	0.02	0.76	1.17	0.10	33.02	0.05	0.17	26.84	36.06	1.22	99.44
	0.14	0.06	4.73	1.07	1.02	29.71	0.05	0.16	24.30	34.01	3.66	98.91
	0.04	0.03	0.33	1.14	0.27	34.50	0.05	0.11	27.79	36.26	0.90	101.42
	0.03	0.03	0.23	1.20	0.03	31.87	0.04	0.14	29.10	36.32	0.64	99.64
	0.02	0.01	0.29	1.15	0.05	31.48	0.04	0.06	28.49	35.38	1.09	98.05
	0.00	0.04	0.22	1.10	0.04	31.85	0.03	0.12	28.83	36.18	0.72	99.13
	0.00	0.00	0.20	1.15	0.08	31.95	0.04	0.12	28.85	35.43	1.00	98.83
	0.79	0.21	4.57	0.90	5.66	26.04	0.04	0.22	20.72	38.17	2.03	99.34
	0.21	0.08	2.91	1.14	1.46	29.03	0.08	2.30	26.44	34.26	3.02	100.94
KSM1C - 5												
	0.02	0.03	1.15	1.22	0.05	37.72	0.07	1.07	20.80	36.33	1.69	100.16
	0.03	0.01	0.21	1.16	0.17	36.58	0.05	0.11	23.11	37.47	0.59	99.49
	b.d.	0.02	0.48	1.19	0.04	36.44	0.04	0.12	24.26	37.23	0.61	100.43
	0.02	0.00	0.30	1.28	0.05	34.02	0.03	0.11	26.09	36.94	0.69	99.53
	0.00	0.02	0.17	1.29	0.06	34.26	0.04	0.10	26.70	36.61	1.23	100.48
	0.03	0.01	0.17	1.23	0.06	35.36	0.05	0.09	24.82	36.75	1.23	99.80
	b.d.	0.02	1.39	1.17	0.06	36.24	0.04	0.35	21.81	36.67	1.33	99.07
	0.01	0.02	0.17	1.23	0.05	36.12	0.03	0.11	24.62	37.37	0.48	100.22
	0.01	0.02	0.15	1.21	0.03	36.95	0.05	0.12	23.59	37.05	1.21	100.40
KSM1C - 6												
	b.d.	0.00	0.17	0.96	0.04	35.12	0.04	0.15	25.05	37.14	0.67	99.33
	0.01	0.02	0.17	1.07	0.02	35.20	0.03	0.12	26.06	36.70	0.50	99.90
	0.00	0.03	0.18	0.87	0.07	36.83	0.06	0.12	22.77	36.93	0.85	98.72
	0.01	0.03	0.49	1.00	0.19	37.29	0.04	0.30	22.51	36.99	1.18	100.03
KSM1C - 7												
	b.d.	0.01	0.19	0.88	0.03	33.65	0.05	0.08	26.87	35.97	1.03	98.76
	0.00	0.02	0.16	0.92	0.03	33.26	0.03	0.06	26.85	36.27	0.47	98.09
	0.02	0.01	0.19	0.97	0.04	33.93	0.03	0.07	26.59	36.62	0.33	98.81
	b.d.	b.d.	0.21	0.86	0.03	34.80	0.02	0.15	25.76	36.80	0.26	98.90
	b.d.	0.01	0.18	0.92	0.02	33.98	0.04	0.14	26.11	35.89	0.80	98.10
	0.03	0.01	0.23	0.89	0.07	34.43	0.05	0.11	25.33	36.07	0.92	98.12
	0.02	0.02	0.21	0.90	0.02	34.04	0.03	0.10	26.19	36.63	0.30	98.48
	0.02	0.03	0.15	0.88	0.03	33.47	0.03	0.08	27.19	36.39	0.47	98.74
KSM1C - 8												
	0.02	0.01	0.22	0.92	0.08	37.43	0.03	0.09	24.32	37.86	0.27	101.25
	b.d.	b.d.	0.20	1.01	0.14	36.66	0.02	0.07	23.76	37.71	0.36	99.95
	0.04	0.04	1.33	0.96	0.36	36.95	0.03	0.09	21.85	37.30	1.42	100.38
	0.03	0.03	1.31	0.90	0.53	34.51	0.04	0.61	21.67	36.78	1.55	97.96
	b.d.	b.d.	0.20	0.91	0.12	37.94	0.05	0.09	23.21	37.94	0.59	101.07
	b.d.	b.d.	0.25	0.88	0.12	37.02	0.04	0.10	23.74	37.34	0.97	100.45
KSM1C - 9												
	b.d.	b.d.	1.37	0.98	0.06	24.68	0.01	0.15	38.04	34.33	1.10	100.73
	b.d.	0.03	1.07	0.88	0.12	24.04	0.05	1.27	36.80	32.91	1.59	98.76
	0.04	0.01	0.50	0.90	0.13	24.92	0.03	0.13	37.81	34.62	0.53	99.62
	b.d.	0.01	0.30	1.04	0.09	24.50	0.02	0.14	37.89	34.57	0.63	99.18
	b.d.	0.03	0.21	0.99	0.07	24.59	0.02	0.13	38.21	34.77	0.35	99.39
	b.d.	0.04	0.24	0.98	0.09	24.28	0.02	0.08	37.87	34.98	0.19	98.79
	b.d.	0.02	0.21	0.93	0.04	25.14	0.02	0.13	38.41	35.28	0.20	100.39

Olivine

Run	Na_2O	K_2O	CaO	MnO	Al_2O_3	MgO	Sc_2O_3	TiO_2	FeO	SiO_2	P_2O_5	Total
KSM1C - 10												
	0.03	0.02	1.36	0.95	0.31	23.86	0.03	2.78	37.17	32.48	1.14	100.12
	b.d.	b.d.	1.23	0.81	0.37	24.72	0.05	0.54	36.86	33.45	1.85	99.90
	0.03	0.03	0.25	0.95	0.36	25.60	0.02	0.09	37.29	35.38	0.13	100.14
	0.04	0.01	0.24	1.02	0.08	25.64	0.04	0.25	37.51	35.10	0.64	100.57
	0.03	0.02	0.23	0.95	0.11	25.79	0.04	0.14	37.66	34.69	0.92	100.58
	b.d.	0.03	0.34	0.98	0.28	25.84	0.04	0.08	36.77	34.86	0.91	100.15
	b.d.	b.d.	0.19	1.04	0.17	26.21	0.03	0.14	37.07	35.42	0.19	100.45
KSM1C - 11												
	b.d.	0.03	0.18	1.12	0.03	27.41	0.04	0.07	33.94	35.29	0.45	98.57
	b.d.	0.02	0.21	1.06	0.05	28.95	0.04	0.18	33.04	35.82	0.39	99.75
	0.04	0.07	0.44	1.03	0.20	28.97	0.05	0.18	32.05	36.00	0.71	99.73
	b.d.	0.02	0.20	1.07	0.05	29.23	0.03	0.09	32.75	35.89	0.54	99.87
	b.d.	0.03	0.18	1.13	0.05	28.84	0.05	0.14	32.44	35.61	0.79	99.25
KSM1C - 12												
	b.d.	0.01	0.30	1.08	0.11	27.23	0.05	0.65	34.73	33.61	1.96	99.75
	0.04	0.06	1.01	1.00	0.12	26.92	0.05	0.83	34.68	33.80	2.06	100.57
	0.04	0.04	0.97	1.03	0.24	27.00	0.06	1.21	34.05	33.80	1.52	99.95
	b.d.	0.05	0.56	1.01	0.24	26.97	0.07	1.32	34.86	33.51	1.70	100.30
	0.05	0.06	0.63	1.03	0.19	26.75	0.06	0.99	34.72	34.09	1.58	100.14
	b.d.	0.04	0.48	1.04	0.12	27.03	0.08	1.24	35.16	33.98	1.66	100.83
	b.d.	0.05	0.94	1.09	0.21	26.46	0.06	1.80	34.40	33.70	1.61	100.33

Apatite

Run	Na_2O	K_2O	CaO	MnO	Al_2O_3	MgO	Sc_2O_3	TiO_2	FeO	SiO_2	P_2O_5	Total
KSM1C - 10												
	0.29	0.69	48.83	0.24	2.00	0.63	0.03	0.11	1.53	4.82	36.66	95.83
	0.03	0.28	51.15	0.17	1.36	0.46	0.03	0.25	1.49	3.67	39.02	97.93
	b.d.	0.25	50.91	0.25	1.04	0.54	0.02	1.50	2.35	2.13	38.72	97.71
	0.22	0.24	50.27	0.20	2.74	0.54	0.01	0.37	1.46	4.44	36.83	97.32
KSM1C - 11												
	0.06	0.39	49.70	0.17	1.54	0.49	0.03	0.14	1.32	4.56	38.68	97.09

Spinel

Run	Na_2O	K_2O	CaO	MnO	P_2O_5	MgO	Sc_2O_3	TiO_2	FeO	Al_2O_3	SiO_2	Total
KSM1C - 3												
	0.82	0.23	0.20	1.01	b.d.	2.52	0.05	12.35	68.14	5.72	3.42	94.41
	0.14	0.45	0.15	0.99	b.d.	2.70	0.05	11.98	68.77	5.18	2.98	93.34
	0.01	0.01	0.02	0.99	b.d.	2.75	0.06	12.84	71.22	4.88	0.37	93.02
	0.32	0.27	0.14	0.92	b.d.	3.20	0.04	12.57	68.27	5.21	4.15	95.03
	0.01	0.04	0.07	1.02	b.d.	3.09	0.04	13.15	71.59	4.85	0.57	94.37
KSM1C - 6												
	0.09	0.09	0.36	0.82	0.00	4.94	0.05	11.24	68.79	5.72	0.97	93.09
	0.05	0.12	0.49	0.80	0.12	4.72	0.04	10.86	68.27	5.37	2.46	93.29
	0.06	0.06	0.11	0.91	b.d.	4.95	0.05	11.72	70.30	5.18	0.74	93.99
	0.14	0.13	0.18	0.88	b.d.	4.71	0.04	11.25	69.05	5.48	1.57	93.37
	0.20	0.14	0.23	0.79	b.d.	4.66	0.05	11.10	69.14	5.69	2.57	94.54
	0.27	0.09	0.55	0.89	0.15	4.65	0.05	11.23	69.34	6.18	2.34	95.73
KSM1C - 7												
	b.d.	0.13	0.56	0.79	0.24	4.50	0.04	12.83	65.82	6.08	2.53	93.53
	0.04	0.07	0.51	0.74	0.25	4.69	0.04	12.66	65.83	5.41	0.50	90.74
	0.20	0.07	0.14	0.75	b.d.	4.08	0.05	12.30	67.22	6.17	1.77	92.67
	0.07	0.05	0.11	0.89	b.d.	4.78	0.04	13.28	68.40	5.30	0.61	93.47
KSM1C - 8												
	b.d.	0.08	0.20	0.81	1.22	5.96	0.14	32.17	50.20	2.07	b.d.	92.83
	0.13	0.16	0.36	0.89	2.23	6.04	0.17	38.17	43.94	1.93	b.d.	93.98
KSM1C - 9												
	0.04	0.08	0.12	0.62	0.72	2.95	0.05	15.78	66.55	5.95	b.d.	92.85
	0.02	0.03	0.26	0.60	0.71	2.76	0.05	15.57	66.26	5.90	0.05	92.22
	b.d.	0.05	0.44	0.59	0.18	2.90	0.05	16.71	66.08	5.53	0.14	92.68
	b.d.	0.05	0.29	0.66	0.17	2.95	0.04	16.55	66.23	5.43	b.d.	92.33
	b.d.	0.04	0.79	0.59	0.13	2.92	0.05	16.31	65.39	5.39	0.32	91.93
	b.d.	0.05	0.21	0.63	0.14	2.84	0.04	16.58	66.18	5.39	b.d.	92.04
	b.d.	0.04	0.97	0.67	0.15	2.96	0.05	16.89	65.09	5.09	0.57	92.47
	b.d.	0.03	0.26	0.59	0.19	3.09	0.05	15.63	61.52	5.81	b.d.	87.14
KSM1C - 10												
	0.05	0.02	0.02	0.55	0.52	2.71	0.05	13.67	69.95	7.09	b.d.	94.60
	0.08	0.13	0.10	0.49	1.41	2.64	0.05	13.20	68.42	7.67	b.d.	94.17
	b.d.	0.01	0.00	0.61	0.42	2.47	0.05	11.81	70.78	7.21	b.d.	93.31
	b.d.	0.05	0.52	0.60	0.28	3.10	0.05	16.53	66.15	5.71	0.12	93.12
	b.d.	0.07	0.18	0.55	0.17	2.96	0.05	17.08	64.84	5.37	b.d.	91.23
	b.d.	0.03	0.10	0.62	0.25	3.23	0.05	17.04	66.26	5.65	b.d.	93.18
	b.d.	0.08	1.01	0.64	0.18	3.11	0.04	16.77	64.74	5.92	0.52	93.02
	b.d.	0.06	0.70	0.64	0.16	3.03	0.04	17.65	65.13	5.79	0.37	93.57
	b.d.	0.05	0.23	0.66	0.21	3.09	0.04	17.58	66.79	5.13	b.d.	93.76
	0.07	0.34	0.30	0.73	2.33	3.43	0.04	17.22	64.24	5.88	0.02	94.59
KSM1C - 11												
	0.08	0.10	0.12	0.84	2.23	5.61	0.05	14.43	64.45	5.57	b.d.	93.45
	0.10	0.08	1.94	0.71	0.91	3.30	0.04	14.11	64.32	5.32	1.19	92.03
	0.05	0.09	0.24	0.89	0.67	3.36	0.05	15.09	67.16	5.45	0.02	93.06
KSM1C - 12												
	0.03	0.03	0.56	0.84	0.11	3.27	0.05	16.25	68.05	5.71	0.32	95.22
	b.d.	0.03	0.15	0.77	0.15	3.16	0.05	15.79	67.53	5.80	b.d.	93.38
	0.05	0.03	0.44	0.86	0.18	3.28	0.05	15.45	67.13	5.79	0.14	93.39
	0.01	0.05	0.17	0.72	0.18	3.23	0.05	15.04	68.17	6.03	b.d.	93.64
	b.d.	0.05	0.09	0.71	0.17	3.41	0.05	15.65	68.12	5.79	b.d.	94.00
	b.d.	0.03	0.21	0.76	0.20	3.26	0.07	15.40	68.71	5.96	b.d.	94.57
	b.d.	0.05	0.73	0.76	0.25	3.35	0.05	15.40	67.42	5.70	0.37	94.09
	0.03	0.06	0.51	0.80	0.17	3.33	0.06	15.18	67.25	5.66	0.17	93.22
	b.d.	0.02	0.09	0.77	0.11	3.65	0.06	21.91	62.79	4.63	b.d.	94.00
	0.08	0.05	0.16	0.79	0.33	3.40	0.05	15.58	67.33	5.83	b.d.	93.56

Spinel

Run	Na_2O	K_2O	CaO	MnO	P_2O_5	MgO	Sc_2O_3	TiO_2	FeO	Al_2O_3	SiO_2	Total
KSM2A - 1												
	0.01	0.03	b.d.	0.57	b.d.	1.98	0.16	6.62	78.16	10.10	0.53	98.11
	0.00	0.01	0.04	0.38	b.d.	14.49	0.01	0.18	23.32	63.98	0.10	102.47
	0.00	0.01	0.02	0.45	b.d.	14.86	0.00	0.12	23.06	64.77	0.03	103.31
	b.d.	0.04	0.05	0.41	0.00	13.85	0.01	0.16	24.23	63.46	0.68	102.91
KSM2A - 2												
	0.08	0.03	b.d.	0.25	b.d.	1.14	0.10	0.79	86.01	8.25	0.55	97.15
	0.00	0.00	0.00	0.00	b.d.	0.00	0.00	0.00	0.00	0.00	0.00	0.00
KSM2C- 1												
	0.01	0.10	0.01	0.65	b.d.	3.10	0.16	5.95	65.39	11.92	0.93	88.00
	0.07	0.06	0.04	0.71	b.d.	3.08	0.16	7.13	67.54	11.21	0.51	90.29
	0.03	0.13	0.04	0.76	b.d.	3.06	0.16	7.23	69.55	11.48	0.85	93.07
	0.05	0.09	0.08	0.69	0.01	3.90	0.16	6.09	66.19	16.04	0.17	93.31
	b.d.	0.08	0.04	0.72	b.d.	2.85	0.17	6.50	70.31	10.99	0.23	91.64
	b.d.	0.09	0.08	0.68	b.d.	2.98	0.14	6.79	70.30	11.82	0.29	92.95
KSM2C- 2												
	0.00	0.08	0.05	0.58	b.d.	2.50	0.15	8.37	69.90	10.47	0.89	92.78
	0.00	0.06	0.14	0.85	b.d.	2.53	0.16	8.69	70.11	10.66	0.86	93.88
KSM2C- 3												
	0.09	0.07	0.08	0.81	b.d.	2.77	0.24	17.67	62.27	7.75	0.75	92.23
	0.05	0.09	0.06	0.77	0.05	3.42	0.60	34.52	49.86	5.22	0.53	94.55
	0.03	0.11	0.11	0.64	0.00	3.25	0.54	29.72	52.18	6.81	0.88	93.69
KSM2C- 8												
	0.01	0.03	b.d.	0.37	0.06	0.83	0.15	6.38	73.49	11.56	2.95	95.82
	0.02	0.03	b.d.	0.21	b.d.	0.29	0.10	5.33	78.29	8.47	0.12	92.83
	0.01	0.03	0.08	0.35	0.02	1.13	0.10	5.85	70.68	13.54	3.89	95.67
KSM3A-6												
	0.19	0.27	0.10	0.62	0.01	9.14	0.02	0.21	31.07	52.06	5.02	98.71
KSM3A-7												
	0.29	0.41	0.20	0.72	0.03	8.21	0.03	0.25	29.19	49.49	8.19	97.01

Ilmenite

Run	Na_2O	K_2O	CaO	MnO	P_2O_5	MgO	Sc_2O_3	TiO_2	FeO	Al_2O_3	SiO_2	Total
KSM2C-2												
	b.d.	0.08	0.04	0.92	0.01	2.95	0.69	44.14	45.02	0.81	0.26	94.23
KSM2C-3												
	0.05	0.09	0.06	0.77	0.05	3.42	0.60	34.52	49.86	5.22	0.53	94.55
	0.03	0.11	0.11	0.64	0.00	3.25	0.54	29.72	52.18	6.81	0.88	93.69
KSM2C-9												
	0.16	0.08	0.41	0.80	b.d	2.49	0.31	49.05	42.10	1.09	1.51	98.00
	0.15	0.20	0.13	0.93	b.d	2.54	0.44	47.37	43.40	1.23	3.81	100.18

Rutile

Run	Na_2O	K_2O	CaO	MnO	P_2O_5	MgO	Sc_2O_3	TiO_2	FeO	Al_2O_3	SiO_2	Total
KSM2C-2												
	b.d.	0.10	0.14	0.01	b.d	0.02	0.06	95.75	1.59	0.21	0.06	97.85

Cordierite

Run	Na_2O	K_2O	CaO	MnO	P_2O_5	MgO	Sc_2O_3	TiO_2	FeO	Al_2O_3	F	Cl	SiO_2	Total
KSM2A-1														
	0.16	0.37	0.31	0.21	0.03	10.51	0.03	0.12	4.78	34.67	n.a.	n.a.	47.62	98.80
	0.18	0.37	0.29	0.24	0.07	10.47	0.02	0.08	4.72	34.84	n.a.	n.a.	48.09	99.37
KSM3A-1														
	0.24	0.18	0.63	0.59	1.07	8.04	0.05	0.16	5.83	27.99	n.a.	n.a.	54.69	99.47
	0.31	0.38	0.32	0.54	0.34	8.46	0.09	b.d.	6.55	33.54	n.a.	n.a.	48.90	99.40
	0.14	0.11	0.17	0.45	0.51	7.91	0.07	0.06	5.24	26.63	n.a.	n.a.	59.24	100.53
KSM3A-2														
	0.07	0.07	0.19	0.51	0.22	9.02	0.05	0.10	7.35	34.21	n.a.	n.a.	47.18	98.98
KSM3A-3														
	0.09	0.11	0.18	0.52	0.42	8.89	0.07	0.04	5.73	30.91	n.a.	n.a.	51.57	98.54
	0.13	0.13	0.17	0.51	0.49	7.43	0.06	0.05	5.14	33.07	n.a.	n.a.	52.50	99.67
	0.27	0.30	0.29	0.48	0.20	9.53	0.09	0.10	5.79	33.58	n.a.	n.a.	46.29	96.92
	0.10	0.14	0.17	0.40	0.37	5.92	0.07	0.06	5.27	31.74	n.a.	n.a.	54.90	99.15
KSM3A-4														
	0.31	0.23	0.28	0.55	0.19	7.49	0.06	0.11	7.59	38.86	n.a.	n.a.	49.77	105.46
	0.09	0.08	0.34	0.57	0.17	8.23	0.09	0.10	8.36	34.36	n.a.	n.a.	46.53	98.92
KSM3A-5														
	0.22	0.23	0.37	0.34	b.d.	9.79	0.04	0.03	6.14	34.48	n.a.	0.17	46.87	98.63
	0.35	0.51	0.51	0.27	0.03	8.63	0.06	0.06	6.15	31.72	n.a.	0.49	49.01	97.68
	0.23	0.21	0.22	0.33	0.06	9.91	0.03	0.04	5.35	34.35	n.a.	0.09	46.86	97.67
	0.20	0.23	0.23	0.31	0.03	10.07	0.02	0.04	5.75	34.41	n.a.	0.09	47.30	98.67
	0.27	0.33	0.45	0.37	0.04	10.04	0.05	0.07	5.94	34.94	n.a.	0.14	46.31	98.92
	0.20	0.21	0.23	0.31	0.01	10.22	0.03	b.d.	5.28	34.35	n.a.	0.07	47.07	97.96
	0.12	0.21	0.32	0.31	0.08	10.01	0.03	0.02	5.70	34.25	n.a.	0.14	46.74	97.92
	0.13	0.20	0.40	0.32	0.12	9.90	0.06	0.05	6.02	34.74	n.a.	0.15	47.35	99.40
KSM3A-6														
	0.24	0.21	0.38	0.25	0.09	9.81	0.04	0.01	5.98	34.73	n.a.	0.14	46.49	98.36
	0.50	0.53	0.53	0.28	0.03	9.39	0.04	0.02	5.60	33.74	n.a.	0.17	49.62	100.42
	0.33	0.25	0.38	0.41	0.02	9.68	0.04	0.05	5.77	34.63	n.a.	0.12	47.34	99.00
	0.16	0.13	0.17	0.34	b.d.	10.12	0.02	0.02	5.55	34.46	n.a.	0.04	47.90	98.86
	0.10	0.09	0.25	0.41	0.21	8.80	0.06	0.20	14.69	36.58	n.a.	0.08	39.26	100.72
	0.20	0.22	0.36	0.30	0.03	9.80	0.04	b.d.	6.16	34.91	n.a.	0.12	48.00	100.09
	0.18	0.21	0.43	0.34	0.07	9.75	0.05	b.d.	6.12	34.99	n.a.	0.15	47.62	99.87
KSM3A-7														
	0.13	0.08	0.13	0.27	b.d.	10.46	0.00	0.01	5.05	33.94	b.d.	0.03	47.92	97.97
	0.15	0.18	0.34	0.28	0.15	10.21	0.04	0.06	5.40	34.33	0.00	0.13	46.67	97.90
	0.12	0.20	0.41	0.28	0.22	9.96	0.07	0.06	5.13	33.70	0.07	0.11	48.07	98.35
	0.21	0.23	0.21	0.24	b.d.	10.16	0.01	0.05	4.92	33.87	b.d.	0.07	49.10	99.05
	0.18	0.19	0.37	0.39	0.04	10.27	0.04	0.02	5.36	34.73	0.04	0.08	46.45	98.12
	0.19	0.21	0.32	0.25	0.03	10.15	0.02	0.01	4.98	34.04	0.05	0.09	47.01	97.30
	0.16	0.18	0.39	0.33	0.05	10.22	0.04	0.03	5.38	34.40	b.d.	0.08	46.52	97.74
	0.20	0.20	0.33	0.28	0.05	10.41	0.04		5.01	34.43	0.05	0.10	46.83	97.88
	0.10	0.16	0.35	0.24	0.09	10.34	0.04	0.02	4.97	34.54	0.08	0.11	47.68	98.66
KSM3A-8														
	0.08	0.16	0.33	0.31	0.02	10.47	0.04	0.02	5.16	34.05	b.d.	0.11	47.09	97.83
	0.08	0.18	0.42	0.44	0.02	10.10	0.04	0.05	5.39	34.71	0.02	0.12	47.82	99.36
	0.09	0.11	0.19	0.33	b.d.	10.42	0.03	0.01	4.79	33.75	0.01	0.08	47.56	97.33
	0.09	0.09	0.32	0.33	0.18	9.23	0.04	0.05	4.64	39.25	0.05	0.16	50.43	104.81
	0.11	0.19	0.37	0.31	0.03	10.35	0.04	b.d.	4.76	34.55	0.06	0.16	47.51	98.38

Aluminosilicates

Run	Na_2O	K_2O	CaO	MnO	P_2O_5	MgO	Sc_2O_3	TiO_2	FeO	Al_2O_3	SiO_2	Total
KSM2A-1												
	0.05	0.03	0.12	0.01	0.01	0.18	0.03	0.51	3.84	68.75	26.58	100.11
	0.09	0.04	0.05	0.02	b.d.	0.21	0.02	0.46	3.94	69.20	26.67	100.67
KSM2A-2												
	0.33	0.15	1.47	0.04	0.05	0.33	0.02	0.31	4.04	64.14	28.52	99.39
	0.09	0.14	0.14	0.02	b.d.	0.26	0.02	1.41	5.36	64.77	26.75	98.97
	0.01	0.01	0.01	0.06	b.d.	0.07	0.00	0.31	2.97	91.97	5.61	101.00
	0.06	0.03	0.04	b.d.	0.00	0.20	0.01	1.26	5.05	67.81	24.84	99.29
KSM2A-2												
	0.10	0.13	0.07	0.06	0.04	0.12	0.03	0.12	3.97	71.89	22.91	99.44
	0.27	0.76	0.41	0.00	0.12	0.17	0.02	0.19	2.50	73.40	19.90	97.73
	0.39	0.10	0.85	0.04	0.08	0.19	0.03	0.14	4.61	65.53	29.84	101.79
KSM2A-2												
	0.11	0.10	0.08	0.05	0.06	0.16	0.03	0.12	4.99	65.31	27.36	98.36

CoPd			
Run	Co	Pd	Total
KSM1C - 1			
	16.45	83.37	99.82
	16.26	83.72	99.98
	16.17	82.17	98.34
	16.71	83.14	99.85
	16.38	83.41	99.79
	16.07	84.64	100.70
	15.10	86.03	101.13
	15.73	84.73	100.46
	17.01	82.81	99.82
	16.46	84.41	100.86
KSM1C - 2			
	13.92	86.93	100.84
	13.89	86.74	100.63
	13.38	88.86	102.24
	13.50	87.20	100.69
	13.62	87.08	100.71
	11.76	87.17	98.93
	10.34	90.69	101.03
	13.85	87.57	101.43
	13.84	87.23	101.07
	11.80	89.85	101.65
KSM1C - 3			
	12.61	87.25	99.87
	12.85	87.42	100.27
	12.92	87.81	100.73
	12.23	87.90	100.13
	11.80	89.76	101.56
	12.73	88.37	101.10
	12.45	86.97	99.42
	12.66	88.08	100.74
	7.42	93.55	100.96
	12.02	87.66	99.68
	13.10	88.94	102.04
	13.22	88.28	101.50
KSM1C - 4			
	13.65	86.30	99.95
	13.69	86.53	100.22
	13.58	86.83	100.41
	12.36	88.27	100.63
	13.50	86.35	99.85
	13.07	84.57	97.63
	12.65	87.80	100.45
	11.71	88.23	99.94
	12.54	84.72	97.26
	12.71	87.44	100.15
KSM1C - 5			
	8.78	91.19	99.97
	8.72	90.98	99.70
	8.69	89.16	97.85
	9.77	89.57	99.34
	9.89	90.42	100.32
	9.29	89.59	98.88
	8.83	89.83	98.66
	8.76	90.40	99.16
	8.63	90.57	99.21
	8.65	89.82	98.46

CoPd			
Run	Co	Pd	Total
KSM1C - 6			
	13.56	84.38	97.94
	13.59	86.91	100.50
	14.45	85.57	100.02
	13.38	85.64	99.02
	12.97	86.05	99.02
	11.60	87.28	98.88
	15.03	84.47	99.50
	14.58	84.88	99.45
	13.82	84.93	98.75
	13.60	83.51	97.10
KSM1C - 7			
	12.38	87.77	100.16
	11.91	87.11	99.03
	12.10	87.40	99.49
	12.42	86.88	99.30
	12.29	86.93	99.21
	12.12	87.04	99.17
	11.42	87.46	98.88
	10.84	88.43	99.27
	11.15	88.82	99.97
	10.90	88.45	99.35
KSM1C - 9			
	20.39	78.48	98.87
	20.30	79.12	99.42
	20.13	78.36	98.48
	20.41	78.15	98.55
	20.28	77.78	98.06
	20.48	78.87	99.34
KSM1C - 10			
	19.49	78.67	98.16
	19.50	79.77	99.27
	18.84	79.52	98.36
	19.62	79.48	99.10
	20.30	79.76	100.05
	18.77	79.40	98.18
	17.70	81.15	98.85
	17.87	81.14	99.01
KSM1C - 11			
	16.60	82.11	98.71
	17.37	81.96	99.33
	16.16	82.47	98.63
	16.34	82.58	98.92
	16.39	81.80	98.19
	16.86	81.26	98.12
	16.94	82.37	99.31
	16.89	82.17	99.07
	16.63	82.45	99.08
	16.24	83.51	99.75
KSM1C - 12			
	16.56	82.35	98.91
	16.77	82.13	98.90
	15.92	82.09	98.00
	17.01	82.73	99.73
	16.57	83.34	99.90
	16.61	82.46	99.07
	16.93	82.37	99.30
	16.56	82.24	98.80
	17.02	82.63	99.65

CoPd			
Run	**Co**	**Pd**	**Total**
KSM2A-1			
	7.49	92.68	100.16
	8.63	90.89	99.51
	11.90	88.05	99.95
	10.69	90.07	100.76
	10.13	89.76	99.89
	12.25	88.52	100.77
	11.96	87.98	99.94
	12.53	87.81	100.34
	12.37	89.64	102.01
KSM2A-2			
	10.79	88.55	99.35
	11.14	89.35	100.49
	11.29	88.29	99.59
	11.04	89.15	100.18
	12.06	87.78	99.83
	14.95	85.94	100.89
	15.13	85.80	100.93
	13.77	85.45	99.22
	12.12	88.88	101.00
	12.61	88.24	100.85
KSM2C-1			
	8.87	88.20	97.07
	9.19	88.73	97.93
	9.49	88.60	98.10
	9.53	89.84	99.36
	9.49	88.70	98.19
	7.96	89.22	97.17
	7.55	90.32	97.87
	8.44	91.01	99.45
	7.62	90.39	98.01
	8.47	88.77	97.24
KSM2C - 2			
	11.06	86.42	97.48
	10.62	87.56	98.18
	9.19	88.14	97.32
	10.56	88.22	98.79
	11.12	87.98	99.10
	11.50	88.15	99.65
	11.10	87.59	98.70
	11.05	88.02	99.07
KSM2C - 3			
	11.76	86.92	98.68
	11.02	88.40	99.42
	10.65	86.81	97.46
	10.76	88.40	99.17
	12.06	86.84	98.90
	11.09	87.86	98.95
	11.27	90.20	101.47
	10.30	89.16	99.46
	9.09	90.85	99.95
	10.01	88.66	98.67

CoPd			
Run	**Co**	**Pd**	**Total**
KSM2C - 4			
	8.50	89.68	98.18
	8.93	89.57	98.50
	9.88	90.38	100.26
	9.80	88.87	98.67
	9.85	89.80	99.65
	10.13	89.02	99.15
	10.02	85.69	95.71
	10.17	89.09	99.26
	9.72	89.72	99.44
	10.70	88.58	99.28
KSM2C - 5			
	18.56	80.38	98.93
	18.71	80.41	99.12
	17.50	81.05	98.55
	17.45	80.68	98.13
	19.02	79.59	98.61
	19.00	80.57	99.57
	19.12	79.17	98.29
	19.19	79.34	98.53
KSM2C - 6			
	20.06	79.73	99.79
	19.33	79.20	98.53
	20.67	78.50	99.17
	20.42	78.79	99.21
	20.67	78.61	99.28
	20.40	79.66	100.05
	19.56	79.23	98.79
	21.69	78.28	99.96
KSM2C - 7			
	16.65	82.45	99.10
	16.74	81.48	98.22
	16.53	81.65	98.18
	17.08	83.01	100.08
	18.15	80.56	98.71
	18.40	79.63	98.03
	18.34	80.50	98.84
	18.34	80.53	98.88
KSM2C - 8			
	18.46	80.69	99.15
	18.69	80.93	99.62
	18.22	81.20	99.42
	16.39	81.91	98.30
	18.57	80.53	99.10
	18.35	79.39	97.74
	18.22	80.28	98.50
	17.77	80.96	98.73
	17.36	81.15	98.51
KSM2C - 9			
	17.75	80.38	98.14
	17.61	81.35	98.96
	17.60	81.11	98.71
	17.63	80.37	98.00
	19.04	80.30	99.34
	18.82	83.01	101.83
	18.64	80.77	99.41
	16.52	81.71	98.24

Chapter 3 Appendices

Appendix 3.A Multiple Linear Regression Assumptions

Prior to developing the multiple linear regressions, a series of assumptions must be evaluated. In this study these assumptions are: 1) the partition coefficients (dependent variables) are continuous; 2) the partition coefficients vary as a function of two or more mineral and/or melt composition (independent variables); 3) the experiments are independent of one another; 4) the partition coefficients have a linear relationship to the mineral and melt compositions; 5) the variance among the data are homoscedastic (i.e. the variance for the variables is equal); 6) the mineral and melt composition do not strongly correlate with one another (i.e. no multicollinearity); 7) there are no significant outliers; and 8) the residuals in the predicted partition coefficients are normally distributed. Assumptions 1- 4 are valid for all mineral/melt partition coefficients, as the partition coefficients are continuous, there are two or more mineral or melt compositional variables that correlate with the partition coefficient, the experiments are independent, and the partition coefficients and mineral and melt compositions have a linear relationship.

There are a number of independent variables, which may be correlated to each other (e.g. SiO_2 and Al_2O_3 (wt%) in the glass), and thus it is necessary to evaluate if the independent variables exhibit multicollinearity and eliminate multicollinearity where possible. The MATLAB function *collintest* was used to evaluate multicollinearity and remove independent variables where necessary. In order to remove multicollinearity, not all variables that correlate strongly with the partition coefficients (see Chapter 2) can used to predict a partition coefficient. For each

mineral/melt partition coefficient, multicollinearity was reduced, such that the maximum condition index was less than 30 and thus the assumption of multicollinearity was met.

Homoscedasticity of the data sets was tested by using the *vartestn* function in MATLAB. For all mineral/melt partition coefficients the data are heteroscedastic. In order to evaluate the effect of the heteroscedasticity, the multiple linear regressions were evaluated in the regressionLearner app in MATLAB. The regressionLearner app performs a multiple linear regression with cross validation. Cross-validation was used and set to five folds, i.e. the data were partitioned into five folds (five groups) and for each fold a model is trained on out-of-fold observations and evaluated on in-fold observations. Cross-validation generated five separate models and the average error across those models was taken to assess the accuracy of a model trained on all of the training data, prevent overfitting, and tune model parameters. By using cross-validation the predictors that generate a model with the lowest RSME (root-mean-square-error) were used. As a result, the effect of heteroscedasticity can be reduced when training using the *fitlm* function.

There are also outliers present in the datasets for each mineral/melt pair. Outliers were determined by using the *isoutlier* function in MATLAB. Although there are outliers in the dataset, for each data set there is at least one independent variable that is not an outlier for each experiment containing outliers. The final assumption of normally distributed residuals holds true for all multiple linear regression except for pyroxene.

Appendix 3.B Trace Element Model

This appendix contains MATLAB scripts and variables required to perform the trace element model in alphaMELTS for MATLAB described in Chapter 3, as well as a REAME file describing what each file contains. The information is electronically available on https://drum.lib.umd.edu/ or upon request.

Appendix 4.A Analysis of Evje-Iveland Amphibolite

Table 4.A1: Analysis of Evje-Iveland Amphibolite

	23051707b
SiO_2 (wt%)	46.81
Al_2O_3 (wt%)	15.28
Fe_2O_3 (wt%)	13.33
MgO (wt%)	8.37
CaO (wt%)	10.32
Na_2O (wt%)	2.64
K_2O (wt%)	0.65
TiO_2 (wt%)	1.00
P_2O_5 (wt%)	0.08
MnO (wt%)	0.21
Sc (ppm)	39

Analysis from Rosing-Schow et al. (2018)

Appendix 4.B All Electron Microprobe Analyses for Chapter 4.

The following tables contain individual electron microprobe analyses for all phases described in Chapter 4. b.d. denotes elements at concentrations below detection. n.a. is not analyzed

Table 4.B1: EPMA analyses for Chapter 4

	Glass												
Run	**F**	**Na_2O**	**MgO**	**P_2O_5**	**CaO**	**Al_2O_3**	**SiO_2**	**Cl**	**K_2O**	**TiO_2**	**FeO**	**MnO**	**Total**
EIP-4a Powder (Early Analysis)													
	0.04	10.84	0.05	0.17	0.16	25.00	61.66	0.40	1.73	0.04	1.35	0.07	101.39
	0.16	11.36	0.21	0.09	0.28	24.35	60.50	0.40	1.73	0.07	1.15	0.06	100.21
	b.d.	11.45	0.03	0.14	0.16	23.74	61.45	0.43	1.76	b.d.	1.32	0.17	100.52
	0.00	11.66	0.08	0.16	0.16	23.81	61.26	0.42	1.74	b.d.	1.43	0.12	100.70
	b.d.	11.89	0.12	0.31	0.12	23.78	61.95	0.44	1.63	0.07	1.31	b.d.	101.48
	0.10	11.84	0.11	0.25	0.16	23.74	60.56	0.40	1.61	0.05	1.28	0.03	99.99
	0.02	11.86	0.07	0.03	0.14	23.81	60.83	0.43	1.60	0.13	1.43	b.d.	100.24
	b.d.	11.79	0.01	0.11	0.19	23.72	60.71	0.44	1.70	b.d.	1.46	0.02	99.96
	b.d.	11.79	0.05	b.d.	0.21	24.00	60.99	0.42	1.68	0.02	1.37	b.d.	100.27
	b.d.	11.22	0.11	0.12	0.08	23.15	62.51	0.51	1.60	0.00	1.41	0.08	100.66
EIP-4b Core (Early Analysis)													
	0.12	11.83	0.04	0.16	0.34	24.94	59.32	0.31	2.21	b.d.	0.81	0.00	99.94
	b.d.	11.93	0.04	0.12	0.32	24.54	59.82	0.32	2.30	0.01	0.93	0.01	100.25
	b.d.	11.71	0.02	0.11	0.34	24.68	59.33	0.27	2.29	0.04	0.92	0.04	99.65
	0.22	11.82	0.03	0.19	0.35	24.95	59.07	0.27	2.36	0.05	0.94	0.14	100.23
	0.02	11.90	0.00	0.08	0.29	25.26	59.39	0.31	2.35	0.02	1.05	0.11	100.68
	b.d.	11.65	0.06	0.18	0.32	24.34	61.01	0.30	2.31	0.05	0.96	0.06	101.16
	b.d.	11.78	0.05	0.19	0.32	24.41	60.24	0.32	2.35	0.03	0.88	0.04	100.53
	0.00	11.37	0.03	0.22	0.22	24.17	60.54	0.33	2.32	b.d.	1.12	b.d.	100.18
	b.d.	12.03	0.09	0.32	0.09	24.55	60.36	0.46	2.25	b.d.	1.44	0.06	101.46
	0.32	11.80	0.02	0.06	0.22	24.84	59.55	0.28	2.26	b.d.	1.01	0.02	100.15

Glass													
Run	**F**	**Na_2O**	**MgO**	**P_2O_5**	**CaO**	**Al_2O_3**	**SiO_2**	**Cl**	**K_2O**	**TiO_2**	**FeO**	**MnO**	**Total**
EIP-4a Powder													
	0.10	5.43	0.09	0.17	0.21	21.03	55.20	0.48	1.87	b.d.	1.50	0.05	86.09
	b.d.	5.20	0.04	0.09	0.23	21.71	58.31	0.46	1.84	b.d.	1.30	0.03	89.14
	b.d.	5.67	0.09	0.15	0.27	21.35	57.33	0.38	1.76	0.08	1.47	0.08	88.58
	b.d.	5.81	0.12	b.d.	0.26	22.16	57.34	0.45	1.73	0.05	1.43	0.04	89.38
	b.d.	6.05	0.23	0.36	0.14	21.98	57.91	0.41	1.79	0.04	1.43	0.05	90.34
	b.d.	5.66	0.19	0.38	0.11	21.39	55.71	0.51	1.74	0.03	1.33	0.06	87.11
	b.d.	5.60	0.12	0.39	0.13	20.47	56.28	0.48	1.75	b.d.	1.26	b.d.	86.52
	b.d.	5.64	0.21	0.29	0.21	21.35	58.14	0.49	1.88	0.03	1.45	0.09	89.80
	b.d.	7.32	0.11	0.11	0.31	21.87	55.22	0.45	1.94	b.d.	1.39	0.06	88.83
	b.d.	7.35	0.11	0.42	0.13	21.87	58.48	0.48	1.71	b.d.	1.38	0.07	92.04
	b.d.	5.69	0.04	0.27	0.27	22.37	57.14	0.51	1.76	0.08	1.30	0.04	89.45
	0.10	5.27	0.07	0.35	0.21	22.37	57.42	0.49	1.81	0.02	1.24	0.07	89.43
	b.d.	5.30	0.13	0.22	0.18	21.53	58.21	0.47	1.76	b.d.	1.28	0.05	89.10
	b.d.	5.58	0.08	0.34	0.13	21.39	57.87	0.47	1.78	b.d.	1.28	0.04	88.96
	0.06	4.99	0.08	0.14	0.24	21.38	57.53	0.50	1.79	b.d.	1.61	0.04	88.37
	b.d.	5.22	0.10	0.10	0.12	21.52	57.96	0.50	1.67	b.d.	1.39	0.07	88.54
	b.d.	4.78	0.11	0.25	0.12	21.24	58.55	0.56	1.59	b.d.	1.27	0.03	88.42
	b.d.	5.21	0.14	0.20	0.14	21.35	58.57	0.52	1.60	b.d.	1.48	0.07	89.21
	b.d.	4.95	1.36	0.23	0.93	20.72	56.41	0.43	1.67	0.03	2.10	0.10	88.84
EIP-4b Core													
	b.d.	8.40	0.07	0.28	0.32	23.16	56.80	0.34	2.48	b.d.	0.95	b.d.	92.87
	b.d.	8.12	0.08	0.19	0.30	22.88	54.63	0.35	2.56	b.d.	1.14	0.03	90.21
	b.d.	8.10	0.09	0.30	0.36	22.75	56.43	0.30	2.42	0.04	1.09	0.04	91.79
	b.d.	8.22	0.03	0.26	0.31	23.39	55.45	0.33	2.56	b.d.	0.95	0.06	91.54
	0.13	8.43	0.04	0.19	0.44	21.97	55.44	0.31	2.26	b.d.	1.09	0.04	90.36
	b.d.	2.95	12.81	0.09	11.45	15.09	44.11	0.02	0.63	0.56	8.26	0.17	96.08
	b.d.	7.83	0.15	0.27	0.27	21.65	54.95	0.30	2.47	b.d.	1.05	0.10	88.99
	b.d.	15.50	0.08	0.10	0.13	26.64	58.32	0.02	0.35	b.d.	0.48	0.03	101.58
	b.d.	16.61	0.21	b.d.	0.13	27.05	57.88	b.d.	0.42	b.d.	0.44	b.d.	102.80
	0.13	7.91	0.30	0.21	0.42	22.66	55.82	0.33	2.44	b.d.	1.30	0.03	91.54
	b.d.	14.17	0.07	0.50	0.97	24.67	59.64	0.05	0.24	b.d.	0.40	0.02	100.71
	0.06	14.77	0.03	0.05	0.19	24.83	59.80	0.02	0.35	b.d.	0.48	0.05	100.61
	b.d.	5.74	0.08	0.44	0.26	22.24	56.58	0.44	2.20	0.02	1.06	0.04	89.07
	b.d.	5.45	0.01	0.32	0.23	22.44	57.41	0.39	2.35	b.d.	1.20	0.08	89.79
	b.d.	5.57	0.07	0.31	0.22	22.30	57.39	0.38	2.21	b.d.	1.24	0.04	89.72
	b.d.	5.54	0.05	0.27	0.22	22.25	57.07	0.41	2.17	b.d.	1.22	b.d.	89.18
	b.d.	6.12	0.06	0.30	0.17	22.29	56.85	0.42	2.33	b.d.	0.99	0.08	89.62
	b.d.	5.72	0.04	0.36	0.24	22.37	56.95	0.39	2.20	0.07	1.08	0.04	89.36
	b.d.	6.46	0.05	0.26	0.28	22.71	55.25	0.30	2.22	b.d.	1.10	0.02	88.62
	b.d.	6.22	0.09	0.29	0.20	22.52	56.38	0.29	2.33	b.d.	0.96	b.d.	89.33

Glass													
Run	**F**	**Na_2O**	**MgO**	**P_2O_5**	**CaO**	**Al_2O_3**	**SiO_2**	**Cl**	**K_2O**	**TiO_2**	**FeO**	**MnO**	**Total**
EIP-5a Powder													
	0.50	3.15	5.55	0.24	11.74	16.60	47.46	0.04	0.87	1.22	11.27	0.23	98.66
	0.57	3.12	5.12	0.08	11.52	17.36	47.92	0.08	0.83	1.27	11.11	0.27	98.99
	b.d.	2.97	5.09	0.12	12.16	16.32	47.87	0.06	0.70	1.25	11.90	0.19	98.60
	0.10	2.79	5.85	0.03	12.09	16.00	47.74	0.06	0.68	1.28	12.33	0.20	99.10
	0.08	2.97	5.67	0.10	11.90	16.73	48.01	0.05	0.66	1.14	11.25	0.17	98.70
	0.51	3.28	5.72	0.17	11.28	17.87	48.87	0.05	0.84	0.99	10.03	0.20	99.58
	0.21	3.37	4.87	b.d.	11.37	16.95	47.72	0.05	0.76	0.95	11.70	0.19	98.01
	b.d.	3.32	5.65	0.01	11.27	17.15	48.86	0.05	0.78	0.99	10.20	0.24	98.52
	0.08	3.08	5.15	0.05	11.73	16.58	48.16	0.03	0.76	1.21	11.91	0.12	98.83
	b.d.	3.55	5.67	0.13	11.05	16.89	46.84	0.05	0.78	1.06	9.55	0.17	95.69
	b.d.	3.40	4.56	0.11	10.84	16.52	45.06	0.05	0.77	1.09	8.96	0.21	91.47
	0.16	3.75	5.73	0.17	10.63	16.70	48.13	0.05	0.93	0.92	7.34	0.19	94.68
	b.d.	3.43	5.94	b.d.	11.08	17.49	48.12	0.05	0.85	1.15	9.36	0.21	97.46
	b.d.	3.17	4.99	0.12	11.75	16.64	47.12	0.06	0.76	1.34	11.57	0.20	97.61
	b.d.	3.16	5.00	0.08	11.55	16.14	47.38	0.10	0.78	1.43	11.21	0.22	96.98
	b.d.	3.10	5.14	0.07	11.49	16.74	46.42	0.06	0.67	1.24	11.38	0.22	96.46
	b.d.	3.10	5.38	b.d.	11.65	16.83	46.78	0.06	0.74	1.26	11.04	0.14	97.10
	b.d.	3.25	5.56	0.12	11.25	16.18	45.86	0.04	0.63	1.34	11.08	0.18	95.48
	b.d.	3.11	4.86	b.d.	11.68	16.96	47.30	0.04	0.76	1.25	10.39	0.19	96.51
EIP-5b Core													
	0.44	3.46	5.96	0.12	9.87	16.25	48.95	0.07	0.72	0.98	11.48	0.03	98.12
	0.37	3.46	5.78	0.17	10.03	16.25	48.77	0.09	0.72	0.88	11.77	0.34	98.45
	0.60	3.64	5.75	0.01	9.89	16.55	49.43	0.10	0.81	0.79	11.29	0.20	98.77
	0.44	4.03	5.18	b.d.	9.52	16.36	51.05	0.07	0.91	0.56	10.12	0.13	98.16
	b.d.	3.49	5.11	b.d.	10.07	15.52	49.80	0.08	0.79	0.64	10.95	0.08	96.51
	0.31	3.48	4.92	b.d.	10.76	15.80	49.57	0.08	0.73	0.74	12.17	0.19	98.55
	0.02	3.73	5.45	b.d.	10.01	17.16	49.58	0.06	0.87	0.49	10.13	0.01	97.47
	0.04	3.72	5.23	0.05	10.09	16.76	49.41	0.08	0.83	0.55	10.31	0.20	97.22
	0.02	3.45	5.07	0.08	10.88	16.31	48.53	0.08	0.63	1.04	12.06	0.15	98.27
	0.00	4.14	4.38	0.03	8.46	17.34	51.56	0.08	1.07	0.72	9.69	0.19	97.66
	0.42	4.91	2.53	0.24	7.02	18.24	54.85	0.10	1.46	0.43	8.18	0.24	98.42
	0.38	4.69	2.64	0.26	6.43	17.76	54.41	0.08	1.57	0.45	8.61	0.10	97.20
	0.13	3.17	5.43	0.14	11.30	15.06	48.08	0.09	0.70	1.15	11.95	0.21	97.41
	b.d.	3.32	5.44	b.d.	10.81	15.22	45.89	0.07	0.78	0.82	10.22	0.16	92.68
	b.d.	3.47	5.26	0.13	10.38	15.32	47.03	0.11	0.67	0.82	11.17	0.24	94.59
	b.d.	3.88	5.53	0.07	10.27	15.68	48.54	0.06	0.75	0.79	10.62	0.19	96.38
	b.d.	3.61	5.52	b.d.	10.46	16.65	48.80	0.07	0.74	0.76	10.61	0.17	97.39
	b.d.	3.96	5.18	b.d.	9.72	17.29	47.83	0.03	0.82	0.66	9.38	0.13	94.93
	b.d.	3.82	5.08	b.d.	10.25	16.58	49.09	0.08	0.74	0.65	10.65	0.17	97.12
	b.d.	4.16	4.79	0.04	9.36	16.71	49.51	0.05	0.92	0.64	9.71	0.21	96.14
	b.d.	4.05	4.95	0.07	8.79	17.43	49.57	0.07	0.88	0.75	9.42	0.25	96.31
	b.d.	3.78	5.48	0.17	9.82	16.19	48.31	0.08	0.71	1.02	10.56	0.23	96.38

Glass													
Run	**F**	**Na_2O**	**MgO**	**P_2O_5**	**CaO**	**Al_2O_3**	**SiO_2**	**Cl**	**K_2O**	**TiO_2**	**FeO**	**MnO**	**Total**
EIP-7a Powder													
	0.08	6.45	0.83	b.d.	1.37	22.56	55.62	0.17	2.87	0.18	3.81	0.06	94.01
	b.d.	4.07	1.97	0.15	1.89	21.17	56.03	0.10	2.83	0.42	4.85	0.10	93.57
	b.d.	6.44	1.76	0.05	1.88	21.76	54.32	0.11	2.82	0.36	4.14	0.10	93.75
	b.d.	6.02	1.00	0.04	1.02	20.73	55.69	0.10	3.13	0.33	4.27	0.07	92.38
EIP-7b Powder <53 µm													
	0.11	2.13	1.68	0.12	4.28	15.25	62.69	0.12	2.12	0.46	2.86	0.13	91.95
	b.d.	1.93	1.47	0.19	4.38	15.68	62.42	0.12	2.11	0.50	2.70	0.13	91.68
	b.d.	2.11	4.02	0.24	5.56	14.99	60.04	0.08	1.91	0.68	3.62	0.16	93.38
	b.d.	2.22	1.71	0.23	4.20	15.56	62.87	0.11	2.07	0.52	2.72	0.15	92.37
	b.d.	1.90	2.84	0.17	4.81	14.50	58.82	0.11	1.88	0.68	5.08	0.13	90.95
	b.d.	2.01	1.64	0.18	4.23	15.65	62.94	0.11	2.03	0.51	2.99	0.14	92.47
	0.13	2.61	1.55	0.11	4.89	16.74	62.24	0.09	2.02	0.44	2.74	0.11	93.66
	b.d.	2.22	1.80	0.13	4.32	15.38	62.28	0.11	2.08	0.49	2.98	0.13	91.96
	b.d.	2.27	1.64	0.16	4.21	15.69	63.29	0.13	2.11	0.53	2.82	0.14	93.02
	b.d.	2.15	1.58	0.20	4.24	15.64	62.81	0.11	2.21	0.49	2.72	0.10	92.27
EIP-8b Powder <53 µm													
	b.d.	0.85	0.63	0.43	3.73	14.16	66.19	0.16	1.81	0.27	1.57	0.17	89.89
	b.d.	1.35	0.61	0.41	3.63	14.07	65.21	0.19	1.88	0.24	1.68	0.09	89.40
	b.d.	1.25	0.63	0.26	3.72	13.96	65.79	0.15	1.99	0.28	1.52	0.17	89.77
	b.d.	2.53	0.53	0.35	4.99	16.96	62.70	0.16	1.74	0.22	1.55	0.07	91.79
	b.d.	1.39	0.64	0.44	3.66	14.13	65.78	0.15	2.09	0.29	1.61	0.13	90.30
	0.05	1.32	0.60	0.49	3.71	14.07	64.82	0.20	2.03	0.32	1.71	0.16	89.47
	0.07	1.40	0.63	0.41	3.65	14.14	64.90	0.15	2.01	0.25	1.66	0.12	89.38
	b.d.	1.31	0.63	0.32	3.68	14.24	65.93	0.18	1.94	0.33	1.72	0.20	90.47
	b.d.	1.51	0.79	0.31	5.02	17.15	60.68	0.19	1.73	0.24	1.85	0.18	89.63
EIP-9a Powder													
	0.09	3.53	2.36	0.28	5.47	18.40	53.38	0.11	1.73	0.59	7.49	0.21	93.63
	b.d.	3.60	2.40	0.24	5.41	18.29	53.07	0.10	1.70	0.70	7.60	0.16	93.09
	0.06	3.47	2.42	0.18	5.41	18.05	53.01	0.09	1.65	0.65	7.82	0.18	93.00
	0.06	3.37	2.34	0.25	5.41	18.04	53.13	0.12	1.77	0.59	7.43	0.23	92.74
	b.d.	3.65	2.30	0.31	5.34	18.41	53.28	0.13	1.73	0.62	7.74	0.15	93.72
	b.d.	3.63	2.38	0.26	5.44	18.23	53.53	0.08	1.72	0.55	7.46	0.20	93.45
	b.d.	3.62	2.39	0.28	5.37	18.25	53.12	0.16	1.74	0.65	7.62	0.17	93.42
	b.d.	3.49	2.29	0.25	5.48	18.30	53.35	0.08	1.67	0.52	7.78	0.22	93.36
	b.d.	3.60	2.29	0.20	5.29	18.04	53.39	0.08	1.74	0.63	7.55	0.18	93.02
	b.d.	3.57	2.30	0.16	5.40	18.32	53.36	0.11	1.70	0.72	7.68	0.22	93.53

	Glass												
Run	**F**	**Na_2O**	**MgO**	**P_2O_5**	**CaO**	**Al_2O_3**	**SiO_2**	**Cl**	**K_2O**	**TiO_2**	**FeO**	**MnO**	**Total**
EIP-9b Powder <53 μm													
	b.d.	3.14	2.89	0.27	5.36	17.20	58.14	0.11	1.94	0.68	2.74	0.19	92.63
	b.d.	3.13	2.94	0.32	5.27	17.42	57.87	0.12	1.82	0.88	2.75	0.16	92.71
	0.07	3.26	2.91	0.30	5.31	17.22	57.75	0.13	1.89	0.72	2.73	0.21	92.49
	b.d.	2.49	2.98	0.36	5.42	17.51	58.20	0.12	1.84	0.73	2.83	0.10	92.51
	0.07	3.29	3.01	0.35	5.31	17.24	57.67	0.11	1.87	0.82	2.83	0.13	92.70
	b.d.	3.24	2.91	0.27	5.37	17.55	57.03	0.15	1.83	0.71	2.90	0.13	92.13
	b.d.	3.04	2.94	0.14	5.52	17.27	57.33	0.14	1.85	0.74	3.06	0.18	92.23
	0.03	3.30	3.55	0.24	5.50	17.39	56.42	0.15	1.70	0.72	2.95	0.18	92.13
	b.d.	3.28	3.26	0.27	5.63	17.19	55.95	0.15	1.82	0.71	3.11	0.17	91.46
	0.07	3.20	2.94	0.29	5.40	17.38	57.36	0.15	1.83	0.85	2.97	0.14	92.58

Amphibole

Run	F	Na_2O	MgO	P_2O_5	CaO	Al_2O_3	SiO_2	Cl	K_2O	TiO_2	FeO	MnO	Total
23051707b													
	n.a.	1.67	11.34	b.d.	11.51	9.61	45.06	n.a.	0.51	0.95	17.34	0.25	98.24
	n.a.	1.73	10.56	0.02	11.68	10.07	44.70	n.a.	0.57	1.27	17.25	0.34	98.19
	n.a.	1.70	10.57	b.d.	11.64	10.86	43.96	n.a.	0.65	1.27	17.12	0.24	98.01
	n.a.	1.80	10.72	b.d.	11.52	10.25	44.67	n.a.	0.54	1.11	17.22	0.32	98.15
	n.a.	1.47	11.93	b.d.	11.82	8.18	47.34	n.a.	0.37	0.84	16.04	0.28	98.23
	n.a.	1.53	11.02	b.d.	11.75	9.93	43.49	n.a.	0.57	1.27	17.54	0.33	97.29
	n.a.	1.70	11.16	b.d.	11.43	10.59	44.77	n.a.	0.61	1.04	17.05	0.27	98.61
	n.a.	1.66	10.66	0.04	11.66	10.07	45.20	n.a.	0.55	1.13	17.13	0.36	98.46
	n.a.	1.82	11.24	0.05	11.74	10.99	44.96	n.a.	0.67	1.30	17.65	0.30	100.72
	n.a.	1.53	11.18	0.00	11.19	9.04	44.99	n.a.	0.61	1.06	16.36	0.16	96.12
EIP-4a Powder													
	0.60	2.75	19.20	0.02	12.10	14.11	38.12	0.01	0.73	2.69	8.07	0.09	98.24
	0.59	2.84	18.16	0.05	12.19	14.44	39.43	0.01	0.72	1.90	8.45	0.11	98.64
	0.07	3.19	14.27	0.04	11.68	14.83	42.27	0.02	0.58	0.92	10.05	0.20	98.08
	0.27	3.00	16.81	0.05	11.83	14.51	40.65	0.02	0.68	1.14	8.83	0.11	97.77
	0.55	2.71	19.29	0.04	11.80	13.77	37.70	0.02	0.76	1.91	7.86	0.14	96.32
	0.72	2.88	19.30	b.d.	12.12	14.58	40.74	0.01	0.72	1.52	8.10	0.10	100.49
	0.42	2.95	17.79	0.02	12.05	14.53	40.43	0.01	0.70	1.00	8.53	0.13	98.40
	0.28	2.92	16.83	0.01	12.27	14.32	40.48	0.02	0.73	1.18	8.83	0.17	97.92
	0.14	3.00	14.87	b.d.	12.66	17.90	39.49	0.04	0.64	0.90	9.00	0.14	98.76
	0.14	3.04	14.97	0.04	12.58	17.91	42.31	0.04	0.76	1.07	8.63	0.12	101.61
	b.d.	3.03	14.62	b.d.	13.00	18.51	40.98	b.d.	0.69	1.67	8.90	0.15	101.53
	0.18	3.10	14.39	0.06	13.11	19.86	39.36	0.02	0.72	2.96	8.52	0.14	102.41
	0.16	3.09	14.70	b.d.	13.07	18.69	39.13	b.d.	0.70	2.89	8.52	0.14	101.10
	b.d.	3.35	15.09	0.07	12.02	13.20	43.98	0.05	0.57	0.45	10.75	0.24	99.77
	b.d.	3.24	14.39	0.06	12.41	15.76	41.53	0.02	0.64	0.94	10.97	0.22	100.04
	0.16	3.10	15.13	0.05	12.93	16.37	41.00	0.03	0.63	1.52	8.20	0.19	99.31
	b.d.	2.83	15.08	b.d.	13.10	18.28	40.11	b.d.	0.70	2.47	7.87	0.17	100.50
	b.d.	0.47	12.27	b.d.	23.68	11.55	46.72	b.d.	0.04	1.40	6.36	0.12	102.62
	b.d.	3.36	15.84	0.12	12.57	16.32	40.36	b.d.	0.59	2.42	8.54	0.14	100.29
	b.d.	3.40	16.25	0.03	12.48	15.70	41.00	b.d.	0.59	2.24	8.55	0.16	100.45
	0.09	3.11	15.26	0.04	12.74	18.59	38.92	0.03	0.79	2.49	8.40	0.14	100.60
	b.d.	3.30	15.25	b.d.	12.49	17.72	40.01	0.02	0.70	1.14	8.91	0.18	99.68
	b.d.	3.39	16.02	b.d.	12.26	15.17	41.82	0.02	0.59	1.26	9.15	0.09	99.81

Amphibole													
Run	**F**	**Na_2O**	**MgO**	**P_2O_5**	**CaO**	**Al_2O_3**	**SiO_2**	**Cl**	**K_2O**	**TiO_2**	**FeO**	**MnO**	**Total**
EIP-4b Core													
	0.51	2.93	15.74	0.03	12.04	16.20	40.85	0.01	0.63	1.85	7.14	0.14	97.86
	0.24	3.15	15.18	0.01	11.95	15.97	41.39	0.01	0.59	0.83	8.73	0.17	98.12
	0.08	3.28	14.70	0.03	11.72	14.89	42.44	0.02	0.60	0.38	9.97	0.23	98.30
	0.34	2.77	14.80	0.04	12.63	17.95	40.31	0.01	0.77	1.30	7.44	0.09	98.32
	0.43	3.00	15.47	0.04	12.20	18.03	40.72	0.01	0.72	1.15	7.48	0.12	99.19
	0.40	2.96	15.16	0.05	12.15	18.04	40.27	0.02	0.65	1.27	7.10	0.11	97.99
	0.11	2.95	15.52	b.d.	12.83	19.14	40.45	0.03	0.75	1.73	7.52	0.11	101.13
	b.d.	3.29	15.11	0.05	12.62	17.88	40.76	0.03	0.69	1.16	8.16	0.17	99.88
	b.d.	2.97	15.19	0.04	13.25	19.88	39.83	b.d.	0.75	2.10	7.68	0.09	101.79
	b.d.	3.31	16.28	0.07	13.12	17.32	42.21	b.d.	0.62	1.88	7.49	0.13	102.41
	b.d.	3.25	15.10	b.d.	12.66	16.60	42.27	0.03	0.62	0.62	9.23	0.13	100.48
	0.09	3.20	15.32	0.10	12.75	18.74	40.37	0.02	0.71	1.11	8.05	0.18	100.64
	b.d.	3.19	16.09	b.d.	13.18	17.54	41.22	b.d.	0.62	2.62	7.09	0.12	101.66
	b.d.	2.98	15.03	b.d.	12.88	19.43	40.09	b.d.	0.76	2.19	7.80	0.09	101.19
	b.d.	3.19	15.90	b.d.	12.80	19.02	38.54	b.d.	0.69	2.95	7.01	0.15	100.22
	b.d.	3.33	16.49	b.d.	12.39	15.74	42.20	b.d.	0.67	0.51	8.82	0.16	100.31
	b.d.	3.26	16.10	0.03	12.60	17.34	41.05	0.02	0.69	0.82	8.24	0.13	100.17
	b.d.	3.35	16.43	0.03	12.22	16.81	41.17	b.d.	0.55	0.98	7.92	0.15	99.63
	b.d.	3.86	17.56	0.14	11.34	13.17	44.26	0.03	0.55	0.23	8.86	0.22	100.25
EIP-7a Powder													
	b.d.	1.68	11.86	b.d.	11.84	11.53	44.61	0.09	0.63	1.28	16.19	0.24	100.00
	b.d.	1.57	11.84	b.d.	11.76	11.32	44.55	0.06	0.59	1.23	17.25	0.31	100.45
	b.d.	1.70	11.74	b.d.	11.90	11.12	44.91	0.07	0.55	1.21	16.92	0.27	100.34
	b.d.	1.58	11.52	b.d.	11.73	11.96	44.63	0.08	0.64	1.24	15.94	0.27	99.60
	b.d.	1.67	11.94	b.d.	11.77	10.82	45.40	0.03	0.56	1.14	17.03	0.27	100.48
	b.d.	1.71	12.00	b.d.	11.81	11.26	44.95	0.04	0.64	1.11	16.74	0.27	100.50
	0.05	1.79	12.04	b.d.	11.88	11.19	44.94	0.07	0.60	1.10	16.70	0.23	100.58
	b.d.	1.77	10.95	0.02	11.75	12.03	44.24	0.10	0.61	1.12	17.80	0.27	100.60
	0.09	1.78	11.18	b.d.	11.88	11.86	44.13	0.07	0.70	1.31	17.54	0.26	100.79
	b.d.	1.79	11.26	b.d.	11.84	11.92	44.23	0.08	0.64	1.26	16.92	0.27	100.18

Amphibole

Run	F	Na_2O	MgO	P_2O_5	CaO	Al_2O_3	SiO_2	Cl	K_2O	TiO_2	FeO	MnO	Total
EIP-7b Powder <53 μm													
	b.d.	1.58	11.01	0.04	11.97	11.69	44.76	0.08	0.54	1.21	17.82	0.22	100.91
	0.10	2.17	10.76	0.06	11.78	12.06	43.92	0.09	0.58	1.20	18.23	0.31	101.25
	b.d.	1.86	11.04	b.d.	11.79	12.61	43.89	0.11	0.74	1.39	17.39	0.25	101.03
	b.d.	1.87	11.23	b.d.	11.79	12.51	44.21	0.06	0.67	1.35	17.35	0.24	101.29
	b.d.	1.66	11.51	0.03	11.66	12.19	44.61	0.07	0.67	1.21	16.90	0.27	100.80
	b.d.	1.81	10.79	b.d.	11.59	11.97	44.17	0.08	0.55	1.12	17.66	0.25	99.84
	b.d.	2.06	10.54	b.d.	11.65	12.14	44.05	0.05	0.60	1.16	18.11	0.27	100.47
	b.d.	1.75	10.61	b.d.	11.68	12.26	43.50	0.09	0.68	1.29	17.96	0.33	100.06
	b.d.	1.62	11.81	0.10	11.69	10.94	45.62	0.07	0.46	1.08	16.89	0.32	100.65
EIP-8b Powder <53 μm													
	b.d.	2.78	17.68	b.d.	11.50	15.41	40.69	0.02	0.45	2.23	9.09	0.16	99.86
	0.05	2.59	15.73	0.06	12.28	15.45	40.53	0.02	0.40	1.99	10.72	0.28	100.10
	b.d.	2.70	17.17	0.09	11.73	15.64	40.57	0.04	0.40	2.39	9.33	0.25	100.33
	b.d.	2.71	16.96	0.04	11.90	15.67	40.52	b.d.	0.40	2.37	9.33	0.20	100.13
	b.d.	2.66	17.74	b.d.	11.47	15.25	40.48	0.02	0.38	2.22	9.25	0.14	99.56
	b.d.	2.70	18.09	0.10	11.45	13.52	42.62	b.d.	0.33	1.90	9.06	0.18	99.93
	b.d.	2.79	18.01	b.d.	11.71	14.15	42.15	0.02	0.36	2.12	9.35	0.21	100.94
	b.d.	2.79	16.86	0.06	11.74	15.20	40.77	b.d.	0.44	2.24	9.55	0.22	99.85

Pyroxene

Run	F	Na_2O	MgO	P_2O_5	CaO	Al_2O_3	SiO_2	Cl	K_2O	TiO_2	FeO	MnO	Total
EIP-4a Powder (1)													
	0.14	1.46	12.57	0.08	18.78	14.23	42.04	b.d.	0.27	2.08	7.24	0.11	98.94
	0.14	1.00	12.35	0.06	20.43	13.04	43.72	0.006	0.16	1.90	6.58	0.11	99.45
	b.d.	0.40	10.61	0.08	22.73	13.47	43.41	0.001	0.00	2.32	7.32	0.15	100.50
	b.d.	0.47	9.98	b.d.	21.37	13.14	44.39	b.d.	0.02	2.14	7.08	0.08	98.69
	b.d.	0.42	12.28	0.04	23.35	11.31	45.45	b.d.	0.02	1.84	5.59	0.06	100.25
	b.d.	0.74	12.10	0.06	20.94	12.76	44.77	b.d.	0.07	2.25	6.47	0.07	100.20
	b.d.	0.48	11.79	b.d.	22.07	9.98	46.71	b.d.	0.02	1.27	6.04	0.12	98.55
	b.d.	0.41	9.79	0.04	21.57	13.09	43.74	b.d.	b.d.	2.05	7.87	0.11	98.62
	b.d.	0.56	9.69	0.05	22.96	13.84	43.18	b.d.	0.06	2.42	7.78	0.07	100.56
	b.d.	0.47	11.42	b.d.	22.89	12.14	43.85	b.d.	b.d.	2.36	5.81	0.10	99.14
	b.d.	0.50	11.50	0.03	23.53	11.17	44.05	b.d.	b.d.	2.24	7.47	0.13	100.49
	b.d.	1.08	11.54	0.03	21.51	12.72	43.00	0.032	0.13	2.20	8.09	0.20	100.58
	b.d.	0.46	10.92	b.d.	23.76	12.88	42.68	0.023	b.d.	2.48	7.71	0.09	101.00
	b.d.	0.52	10.56	b.d.	23.71	13.29	42.03	0.021	0.02	2.68	7.60	0.16	100.61
	b.d.	0.39	14.29	0.08	24.12	6.43	49.04	b.d.	b.d.	1.16	5.83	0.13	101.52
EIP-4a Powder (1)													
	b.d.	0.39	14.29	0.08	24.12	6.43	49.04	b.d.	b.d.	1.16	5.83	0.13	101.52
EIP-4b Core (1)													
	b.d.	0.44	12.41	0.08	23.20	11.80	45.23	b.d.	0.00	1.86	5.02	0.11	100.14
	0.22	1.41	12.95	0.07	17.90	13.74	42.66	0.003	0.31	1.43	5.80	0.08	96.48
	0.37	1.60	12.32	0.01	16.82	17.19	40.84	0.009	0.34	2.25	5.72	0.12	97.43
	b.d.	1.03	12.29	0.07	20.18	11.95	45.36	0.028	0.13	1.32	7.09	0.15	99.56
	b.d.	0.47	11.53	b.d.	23.03	12.08	45.09	0.016	0.02	1.92	6.88	0.14	101.13
	b.d.	0.44	14.30	0.06	20.81	11.33	43.41	b.d.	b.d.	2.08	7.41	0.17	99.96
	b.d.	0.48	11.35	b.d.	21.69	10.92	44.37	b.d.	b.d.	1.80	6.66	0.13	97.38
	b.d.	0.51	10.66	b.d.	22.28	12.13	44.47	b.d.	b.d.	2.28	6.60	0.16	99.08
	b.d.	0.49	12.60	b.d.	22.90	10.78	45.13	b.d.	0.02	1.46	6.10	0.16	99.69
	b.d.	0.48	13.01	b.d.	24.40	10.02	46.56	b.d.	b.d.	1.24	4.79	0.12	100.54
	b.d.	0.43	12.94	b.d.	23.23	9.31	46.23	0.038	b.d.	1.20	6.49	0.18	99.94
	b.d.	0.33	13.44	b.d.	23.74	8.06	46.93	0.021	b.d.	1.15	6.25	0.12	100.06
	0.13	0.37	13.95	b.d.	23.46	7.49	47.42	b.d.	b.d.	1.17	6.27	0.18	100.41
EIP-4b Core (2)													
	b.d.	0.26	22.53	b.d.	18.76	4.68	45.94	b.d.	0.04	0.72	8.55	0.19	101.59

Pyroxene

Run	F	Na_2O	MgO	P_2O_5	CaO	Al_2O_3	SiO_2	Cl	K_2O	TiO_2	FeO	MnO	Total
EIP-5a Powder (1)													
	b.d.	0.36	13.06	0.12	21.16	6.37	47.66	0.011	0.01	0.98	9.41	0.06	99.19
	0.09	0.41	12.49	0.10	21.33	6.40	47.25	b.d.	0.01	1.08	11.16	0.30	100.58
	b.d.	0.31	13.63	b.d.	20.29	4.57	48.38	0.002	0.01	0.72	11.27	0.17	99.32
	b.d.	0.45	13.26	0.09	20.36	4.60	49.28	0.002	0.06	0.63	9.96	0.24	98.89
	0.04	0.29	12.99	0.05	21.23	5.71	47.85	b.d.	0.00	0.90	10.71	0.32	100.08
	0.29	0.45	12.84	0.16	21.60	5.48	47.99	b.d.	b.d.	0.95	9.40	0.24	99.26
	b.d.	0.31	14.81	b.d.	21.32	3.96	50.74	b.d.	b.d.	0.75	8.57	0.17	100.61
	b.d.	0.31	13.53	b.d.	21.05	4.35	47.20	b.d.	b.d.	0.79	10.06	0.22	97.55
	b.d.	0.40	13.09	b.d.	20.16	5.34	48.61	0.025	b.d.	0.77	10.34	0.28	99.13
	b.d.	0.34	20.48	b.d.	14.49	5.87	44.54	0.031	0.04	0.86	13.88	0.27	100.73
EIP-5a Powder (2)													
	b.d.	1.22	11.04	b.d.	19.06	10.13	47.94	0.044	0.25	1.22	8.71	0.16	99.82
EIP-5b Core													
	0.24	0.33	12.77	0.04	20.20	5.59	47.64	b.d.	b.d.	0.73	11.88	0.23	99.53
	b.d.	0.32	13.13	b.d.	21.42	4.72	48.42	b.d.	b.d.	0.57	11.11	0.24	99.88
	b.d.	0.28	12.58	0.05	20.68	5.27	47.70	b.d.	0.03	0.63	11.18	0.24	98.59
	b.d.	0.34	13.08	0.12	21.10	5.52	47.81	0.003	b.d.	0.70	11.43	0.15	100.22
	b.d.	0.31	13.16	0.05	21.39	4.62	48.72	0.003	b.d.	0.62	10.75	0.16	99.77
	0.32	0.22	14.47	0.03	18.72	3.30	49.66	0.016	0.02	0.47	13.07	0.31	100.44
	b.d.	0.33	15.14	0.03	20.14	4.82	49.79	0.014	0.02	0.51	9.58	0.24	100.58
	b.d.	0.31	12.64	b.d.	19.68	5.30	47.48	0.018	0.05	0.69	11.17	0.19	97.49
	b.d.	0.34	13.68	b.d.	21.38	5.54	48.02	0.019	0.03	0.72	10.15	0.19	100.01
	b.d.	0.32	14.81	b.d.	20.70	4.51	49.65	b.d.	b.d.	0.56	10.00	0.19	100.74
	b.d.	0.31	16.06	b.d.	19.66	3.91	48.74	0.014	b.d.	0.53	9.33	0.25	98.73
EIP-7a Powder (1)													
	b.d.	1.58	13.17	0.03	20.79	2.82	52.22	b.d.	0.03	0.60	9.97	0.38	101.54
	b.d.	1.40	13.23	0.02	21.07	3.28	51.74	0.023	0.06	0.58	9.99	0.42	101.86
	0.05	1.54	13.61	0.03	20.85	1.71	53.05	b.d.	0.02	0.27	9.40	0.39	100.93
	b.d.	0.94	13.95	0.09	20.52	3.11	50.56	b.d.	b.d.	0.42	10.59	0.54	100.78
	b.d.	1.34	13.88	0.10	20.83	2.99	51.83	0.014	0.02	0.42	10.04	0.37	101.82
	b.d.	1.31	13.57	b.d.	20.70	3.49	51.49	b.d.	b.d.	0.69	10.31	0.46	101.92
	0.08	1.99	13.20	0.08	20.27	2.55	52.39	b.d.	b.d.	0.52	10.02	0.40	101.50
	b.d.	1.24	13.72	0.11	21.70	3.12	51.70	b.d.	0.01	0.52	9.69	0.42	102.17
EIP-7a Powder (2)													
	b.d.	2.96	12.41	b.d.	15.11	7.38	47.47	0.044	0.36	0.86	13.43	0.34	100.37
	b.d.	2.00	11.31	b.d.	18.87	5.72	54.39	b.d.	0.34	0.51	8.90	0.28	102.26
EIP-7b Powder <53 μm (1)													
	b.d.	0.40	17.23	b.d.	20.87	2.53	52.56	0.013	b.d.	0.32	7.48	0.50	101.86

Pyroxene

Run	F	Na_2O	MgO	P_2O_5	CaO	Al_2O_3	SiO_2	Cl	K_2O	TiO_2	FeO	MnO	Total
EIP-7b Powder <53 μm (2)													
	b.d.	0.53	14.57	0.05	22.20	5.01	49.98	b.d.	b.d.	0.65	8.57	0.38	101.92
	b.d.	0.55	14.59	0.04	21.30	5.49	51.36	b.d.	0.05	0.72	8.42	0.45	103.02
EIP-8b Powder <53 μm													
	b.d.	0.50	15.04	b.d.	20.41	7.77	46.43	0.01	0.02	1.22	8.87	0.31	100.55
	0.05	0.58	13.97	b.d.	20.84	9.33	45.31	b.d.	0.01	1.82	9.10	0.30	101.25
	b.d.	0.41	16.02	b.d.	20.03	6.86	46.81	b.d.	0.03	1.22	8.84	0.31	100.49
	b.d.	0.43	14.14	0.07	21.21	7.95	45.47	b.d.	0.04	1.47	9.81	0.22	100.75
	b.d.	0.46	14.97	b.d.	20.12	8.28	45.73	0.02	b.d.	1.44	9.64	0.25	100.93
	b.d.	0.49	14.57	b.d.	20.15	8.67	45.22	b.d.	0.04	1.51	9.95	0.23	100.82
EIP-9a Powder (1)													
	0.11	0.35	15.23	0.03	21.25	2.67	51.35	0.02	b.d.	0.41	9.69	0.29	101.42
	b.d.	0.45	15.12	0.05	20.59	2.95	51.20	b.d.	b.d.	0.41	10.38	0.34	101.40
	b.d.	0.39	15.08	b.d.	20.28	2.87	51.83	b.d.	0.02	0.38	9.87	0.30	100.99
	0.04	0.44	15.19	0.06	20.59	2.78	51.67	b.d.	b.d.	0.38	10.04	0.29	101.46
	b.d.	0.44	15.16	b.d.	20.26	3.18	51.53	b.d.	0.02	0.44	10.17	0.42	101.60
	b.d.	0.46	15.32	b.d.	20.07	3.01	51.42	0.02	0.03	0.42	10.64	0.32	101.61
EIP-9a Powder (2)													
	b.d.	0.66	13.25	b.d.	20.78	5.90	48.30	b.d.	b.d.	0.81	10.81	0.28	100.82
	b.d.	0.68	13.59	b.d.	21.94	5.54	48.99	b.d.	b.d.	0.66	10.21	0.25	101.86
	0.05	0.34	14.63	b.d.	21.98	4.08	49.71	b.d.	0.01	0.70	10.22	0.30	102.03
	b.d.	0.59	13.09	0.04	21.14	6.06	48.17	b.d.	0.02	0.90	11.06	0.28	101.20
	b.d.	0.45	13.34	b.d.	22.09	5.27	49.04	0.01	0.04	0.62	9.64	0.29	100.77
	b.d.	0.55	13.48	b.d.	22.03	5.60	48.98	0.02	b.d.	0.70	10.03	0.26	101.58
	b.d.	0.43	12.88	b.d.	22.51	6.09	48.63	b.d.	b.d.	0.77	10.40	0.29	101.87
	b.d.	0.49	12.93	b.d.	22.34	5.99	49.12	b.d.	0.03	0.84	10.12	0.24	102.08
	0.08	0.59	12.79	0.02	21.33	5.77	49.16	b.d.	0.03	0.68	10.87	0.27	101.60
	b.d.	0.56	13.17	b.d.	21.39	5.98	49.06	b.d.	b.d.	0.84	10.73	0.24	101.88
	b.d.	0.68	13.16	b.d.	21.05	5.73	49.39	b.d.	0.02	0.79	10.68	0.25	101.69
EIP-9b Powder <53 μm													
	b.d.	0.48	15.05	b.d.	22.06	5.56	48.60	0.03	0.04	0.90	7.73	0.41	100.85
	b.d.	0.43	17.16	b.d.	20.87	3.03	52.55	b.d.	b.d.	0.42	6.10	0.46	101.02
	b.d.	0.49	17.39	0.08	21.12	2.47	52.01	b.d.	b.d.	0.42	6.23	0.53	100.75
	b.d.	0.49	16.87	0.04	21.76	4.02	50.64	b.d.	0.02	0.52	5.94	0.34	100.68
	b.d.	0.53	15.87	b.d.	21.62	4.69	50.04	0.02	0.03	0.72	6.48	0.37	100.33
	b.d.	0.48	16.94	0.03	22.36	3.09	51.42	0.04	0.02	0.41	5.33	0.30	100.29
	0.08	0.49	16.59	b.d.	21.44	4.15	50.39	0.02	b.d.	0.58	6.02	0.30	99.99
	b.d.	0.61	15.35	b.d.	22.20	5.48	49.41	b.d.	0.05	0.70	6.13	0.32	100.07
	b.d.	0.54	15.46	b.d.	22.14	5.02	49.14	0.05	0.08	0.57	5.69	0.31	99.03

Apatite

Run	F	Na_2O	MgO	P_2O_5	CaO	Al_2O_3	SiO_2	Cl	K_2O	TiO_2	FeO	MnO	SO_3	Total
23051707b														
	4.29	b.d.	0.06	41.87	55.88	0.75	b.d.	0.16	n.a.	b.d.	0.25	0.32	0.02	101.50
	3.62	b.d.	0.03	41.35	55.89	0.21	b.d.	0.23	n.a.	b.d.	b.d.	0.07	0.03	99.66
	5.01	b.d.	0.06	41.64	55.12	0.59	b.d.	0.17	n.a.	0.00	0.28	b.d.	0.01	100.56
	4.12	b.d.	0.05	41.79	55.99	0.21	b.d.	0.20	n.a.	b.d.	0.16	0.05	b.d.	100.55
	3.92	b.d.	0.01	41.92	54.88	0.21	b.d.	0.23	n.a.	0.01	0.17	0.21	b.d.	99.69
	4.41	b.d.	0.05	41.46	54.88	b.d.	b.d.	0.22	n.a.	0.06	0.10	0.14	b.d.	98.96
	4.63	b.d.	b.d.	41.29	54.52	b.d.	b.d.	0.19	n.a.	b.d.	0.10	0.14	0.01	98.67
	4.37	b.d.	0.03	41.55	55.46	0.43	b.d.	0.17	n.a.	0.02	0.16	0.18	0.03	100.39
	5.41	b.d.	0.02	41.66	54.93	b.d.	b.d.	0.23	n.a.	b.d.	b.d.	0.09	0.00	99.49
	4.77	b.d.	0.01	41.58	55.51	0.48	b.d.	0.20	n.a.	b.d.	0.05	0.22	b.d.	100.58
EIP-5b Core														
	5.45	b.d.	0.06	41.11	54.87	0.02	b.d.	0.21	n.a.	0.04	0.01	0.04	0.01	99.37
	5.27	b.d.	0.02	41.64	55.31	b.d.	b.d.	0.22	n.a.	b.d.	0.05	b.d.	0.01	100.05
	4.91	b.d.	0.04	41.12	54.82	0.07	b.d.	0.23	n.a.	0.03	0.13	b.d.	0.00	99.02
	5.28	b.d.	0.10	40.96	55.00	0.09	b.d.	0.22	n.a.	b.d.	0.20	0.07	0.03	99.56
EIP-7b														
	1.7	b.d.	0.1	44.9	56.7	0.3	0.1	0.3	0.0	0.0	0.5	0.1	b.d.	104.8
	2.2	0.0	0.5	44.9	54.7	0.5	1.3	0.4	0.1	b.d.	0.8	0.1	b.d.	105.5

Oxides (Ilmenite and Spinel)

Run	F	Na_2O	MgO	P_2O_5	CaO	Al_2O_3	SiO_2	Cl	K_2O	TiO_2	FeO	MnO	Total
23051707b													
	n.a.	b.d.	0.04	b.d.	0.17	0.01	0.03	n.a.	b.d.	50.83	43.77	2.64	101.50
EIP-7a Powder													
	b.d.	0.39	3.19	b.d.	0.43	5.39	1.24	0.06	0.09	4.22	75.71	0.45	91.09
	b.d.	b.d.	2.40	b.d.	0.31	2.92	0.22	b.d.	0.02	4.50	80.83	0.46	91.71
	b.d.	0.15	2.51	b.d.	0.40	3.32	1.09	0.03	0.05	4.81	78.72	0.50	91.49
	b.d.	0.08	2.51	b.d.	0.28	3.28	0.62	b.d.	0.05	4.86	79.61	0.45	91.59
	b.d.	b.d.	2.18	b.d.	0.29	2.38	0.37	0.03	b.d.	4.81	80.44	0.45	90.87
	b.d.	0.26	2.36	b.d.	0.57	3.26	1.63	b.d.	0.03	3.87	78.73	0.43	91.08
EIP-7b Powder <53 μm													
	b.d.	0.07	3.48	b.d.	0.14	0.87	0.07	b.d.	0.04	26.06	62.59	0.30	93.50
	b.d.	b.d.	2.27	b.d.	0.66	1.21	0.91	b.d.	0.04	17.82	68.26	0.14	91.31
	b.d.	0.02	2.48	b.d.	0.27	1.11	0.09	0.03	b.d.	20.87	66.74	0.23	91.73
EIP-8b Powder <53 μm													
	b.d.	0.06	1.82	b.d.	0.29	3.60	0.69	0.01	0.05	1.89	80.70	1.03	90.01
	b.d.	0.05	2.29	b.d.	0.27	5.65	0.15	b.d.	0.02	1.61	79.85	1.06	90.86
	b.d.	0.03	2.15	b.d.	0.26	5.07	0.29	b.d.	0.05	1.71	80.14	0.97	90.53
	b.d.	0.06	2.21	0.03	0.25	3.81	0.57	b.d.	0.04	2.05	81.40	1.04	91.49
	b.d.	0.01	6.48	b.d.	0.23	9.63	0.11	0.03	b.d.	3.12	70.63	0.47	90.70

Plagioclase

Run	F	Na_2O	MgO	P_2O_5	CaO	Al_2O_3	SiO_2	Cl	K_2O	TiO_2	FeO	MnO	Total
23051707b													
	n.a.	6.45	b.d.	b.d.	8.18	26.37	57.70	n.a.	0.08	0.01	0.06	0.01	98.83
	n.a.	6.69	b.d.	b.d.	8.42	26.80	58.23	n.a.	0.12	b.d.	0.00	b.d.	100.17
	n.a.	6.34	0.01	b.d.	8.40	26.44	57.14	n.a.	0.07	0.06	0.15	0.06	98.64
	n.a.	6.26	0.01	b.d.	9.10	27.49	57.06	n.a.	0.06	b.d.	0.07	0.02	99.98
	n.a.	6.50	b.d.	0.00	8.77	26.15	57.06	n.a.	0.08	b.d.		b.d.	98.43
	n.a.	6.28	0.02	b.d.	8.95	26.52	56.72	n.a.	0.10	b.d.	0.07	0.02	98.61
	n.a.	6.57	b.d.	b.d.	8.33	26.61	57.71	n.a.	0.09	0.03	0.08	0.03	99.40
	n.a.	6.18	0.01	0.03	8.84	26.92	57.25	n.a.	0.09	0.02	0.03	0.02	99.38
EIP-5a Powder													
	n.a.	2.59	0.14	n.a.	15.36	32.06	49.64	n.a.	0.09	0.06	0.84	0.07	100.86
	n.a.	3.01	0.71	n.a.	14.18	30.02	50.92	n.a.	0.16	0.06	1.35	0.01	100.42
	n.a.	2.74	2.33	n.a.	13.84	25.20	49.46	n.a.	0.35	0.63	5.48	0.02	100.03
	n.a.	2.95	1.99	n.a.	13.83	26.61	47.92	n.a.	0.33	0.44	4.09	0.03	98.19
	n.a.	2.78	0.21	n.a.	14.15	31.56	50.93	n.a.	0.15	0.12	1.13	n.a.	100.96
	n.a.	1.87	0.11	n.a.	16.34	32.19	48.13	n.a.	0.10	0.00	0.96	0.00	99.70
	n.a.	2.12	0.38	n.a.	15.97	31.41	48.63	n.a.	0.12	0.14	1.61	0.02	100.40
	n.a.	2.23	0.51	n.a.	15.19	31.10	48.00	n.a.	0.13	0.14	2.05	0.07	99.41
	n.a.	2.09	0.11	n.a.	15.71	32.65	48.42	n.a.	0.12	0.07	0.94	0.02	100.13
	n.a.	2.45	0.65	n.a.	14.89	31.05	49.64	n.a.	0.12	0.06	2.08	0.12	101.07
EIP-5b Core													
	n.a.	5.39	0.03	n.a.	9.04	27.30	56.33	n.a.	0.16	0.04	0.04	b.d.	98.32
	n.a.	5.43	0.01	n.a.	9.20	26.96	56.45	n.a.	0.08	b.d.	0.04	b.d.	98.11
	n.a.	5.52	0.00	n.a.	9.46	27.29	56.50	n.a.	0.12	b.d.	0.08	0.09	99.03
	n.a.	5.79	b.d.	n.a.	9.26	27.03	56.43	n.a.	0.08	b.d.	0.03	b.d.	98.46
	n.a.	6.01	b.d.	n.a.	8.96	26.83	56.34	n.a.	0.07	b.d.	0.22	b.d.	98.36
	n.a.	3.40	1.68	n.a.	12.69	26.19	50.44	n.a.	0.27	0.21	4.22	0.12	99.21
	n.a.	5.70	0.00	n.a.	8.60	26.92	57.51	n.a.	0.21	0.05	0.11	0.01	99.12
	n.a.	3.33	0.14	n.a.	13.62	30.75	51.14	n.a.	0.12	0.03	0.83	0.07	100.01
EIP-7a Powder (1)													
	b.d	6.85	0.02	b.d	9.05	27.34	56.65	b.d	0.11	0.03	0.42	b.d	100.36
	b.d	6.75	0.03	0.07	8.03	26.71	56.31	0.02	0.47	0.06	0.65	b.d	99.11
	b.d	6.37	b.d	b.d	9.79	28.85	55.93	b.d	0.21	0.02	0.66	b.d	101.85
	b.d	5.55	0.13	b.d	6.85	25.71	58.66	b.d	0.74	0.04	1.07	b.d	98.72
	b.d	7.38	0.02	b.d	8.01	27.46	59.30	0.02	0.27	b.d	0.60	0.02	103.04
	b.d	6.08	0.01	b.d	8.62	28.34	58.22	0.01	0.26	b.d	0.38	b.d	101.95
	b.d	7.91	0.17	0.05	5.23	24.33	58.45	0.04	1.16	0.08	1.53	0.03	98.98

Plagioclase

Run	F	Na_2O	MgO	P_2O_5	CaO	Al_2O_3	SiO_2	Cl	K_2O	TiO_2	FeO	MnO	Total
EIP-7a Powder (2)													
	b.d	4.76	0.04	b.d	11.91	29.95	54.49	0.03	0.14	0.04	0.67	b.d	101.97
	b.d	5.37	0.06	0.08	11.14	29.61	54.26	b.d	0.32	0.07	0.71	b.d	101.62
	0.05	4.59	0.04	0.10	11.62	29.83	52.82	0.03	0.28	b.d	0.72	b.d	100.10
EIP-7b Powder <53 μm (1)													
	0.07	6.44	b.d	0.03	9.85	27.91	56.91	b.d	0.08	0.04	0.31	b.d	101.62
	0.09	6.22	0.03	b.d	9.90	27.90	57.00	b.d	0.12	b.d	0.35	0.02	101.60
	b.d	6.02	b.d	b.d	10.11	28.32	56.25	b.d	0.11	0.05	0.29	b.d	101.13
	0.05	5.80	0.03	b.d	10.44	28.63	55.57	b.d	0.19		0.38	b.d	101.08
	b.d	6.78	b.d	b.d	8.77	27.68	57.03	b.d	0.10	0.02	0.24	b.d	100.62
	b.d	6.64	b.d	b.d	9.03	27.60	57.50	b.d	0.11		0.24	b.d	101.14
EIP-7b Powder <53 μm (2)													
	b.d	3.99	0.30	0.04	12.47	28.62	53.49	0.03	0.43	0.09	0.97	b.d	100.40
EIP-8b Powder <53 μm													
	b.d	5.44	0.10	0.06	11.06	28.44	54.87	b.d	0.20	0.07	1.12	0.02	101.33
	b.d	4.43	0.11	0.04	11.88	28.50	54.10	0.02	0.27	0.02	0.88	0.05	100.33
	b.d	4.66	0.10	0.07	10.59	26.89	55.04	0.03	0.43	0.02	0.99	0.03	98.83
	b.d	5.41	0.06	0.04	10.91	28.22	55.12	b.d	0.23	b.d	0.75	0.03	100.68
	b.d	5.08	0.05	b.d	11.39	28.62	54.00	b.d	0.20	0.10	0.76	0.05	100.16
	b.d	4.04	0.18	0.12	10.47	26.34	55.40	0.05	0.47	0.07	1.01	0.05	98.22
	b.d	5.09	0.08	b.d	11.27	28.61	54.32	0.01	0.20	0.09	1.30	b.d	100.92
EIP-9a Powder													
	b.d	4.62	0.08	b.d	12.48	30.06	52.99	0.02	0.14	0.02	0.62	b.d	100.95
	b.d	4.83	0.10	0.11	11.82	29.27	53.74	b.d	0.21	b.d	0.67	b.d	100.71
	b.d	5.11	0.38	0.02	10.65	27.08	54.46	0.04	0.40	0.12	1.45	0.05	99.72

Olivine

Run	F	Na_2O	MgO	P_2O_5	CaO	Al_2O_3	SiO_2	Cl	K_2O	TiO_2	FeO	MnO	Total
EIP-4a Powder (1)													
	0.05	0.01	42.92	b.d.	0.38	0.07	38.92	0.00	0.00	0.02	17.47	0.28	100.05
	b.d.	0.00	41.61	b.d.	0.37	0.04	38.70	0.00	0.01	b.d.	18.88	0.32	99.88
	b.d.	b.d.	41.37	0.03	0.48	0.11	39.95	0.03	0.02	0.06	20.08	0.36	102.49
	b.d.	b.d.	41.41	0.09	0.48	0.12	38.62	0.02	b.d.	b.d.	20.74	0.29	101.80
	b.d.	0.02	40.68	0.04	0.49	0.06	38.45	0.03	b.d.	0.08	21.13	0.38	101.24
	b.d.	b.d.	40.62	0.02	0.47	0.07	38.68	b.d.	0.02	0.02	20.68	0.35	100.95
EIP-4a Powder (2)													
	b.d.	0.34	31.66	b.d.	0.33	2.44	38.02	0.03	0.13	b.d.	26.89	0.74	100.55
	b.d.	0.02	32.90	b.d.	0.33	0.34	36.26	0.02	0.01	0.01	28.61	0.74	99.20
EIP-4b Core													
	b.d.	0.10	37.69	b.d.	0.56	0.41	38.57	b.d.	0.02	0.06	23.12	0.69	101.16
EIP-5a Powder													
	n.a.	b.d.	32.89	n.a.	0.37	0.06	37.10	n.a.	0.03	0.00	29.97	0.40	100.82
	n.a.	b.d.	33.17	n.a.	0.35	0.07	37.17	n.a.	b.d.	0.12	30.38	0.45	101.68
	n.a.	0.02	33.78	n.a.	0.38	0.03	37.07	n.a.	0.02	0.03	27.64	0.43	99.40
	n.a.	0.06	33.61	n.a.	0.54	0.33	37.86	n.a.	0.02	b.d.	27.57	0.37	100.35
	n.a.	b.d.	33.01	n.a.	0.31	0.15	36.85	n.a.	0.01	0.05	30.18	0.52	101.07
	n.a.	b.d.	33.04	n.a.	0.31	0.04	36.77	n.a.	0.01	0.11	28.88	0.48	99.64
	n.a.	0.00	32.47	n.a.	0.35	0.10	37.17	n.a.	0.02	0.05	31.03	0.46	101.65
	n.a.	b.d.	32.11	n.a.	0.34	0.13	36.89	n.a.	0.00	0.05	29.12	0.43	99.05
	b.d.	0.04	33.13	b.d.	0.32	0.09	37.69	b.d.	0.03	b.d.	29.65	0.50	101.51
	b.d.	0.11	32.84	0.12	0.59	0.60	37.36	b.d.	0.02	0.09	27.15	0.40	99.26
	b.d.	0.17	33.90	b.d.	0.65	0.67	37.81	0.02	0.04	0.03	26.82	0.37	100.56
	b.d.	b.d.	32.96	b.d.	0.38	0.08	37.82	b.d.	b.d.	0.04	29.10	0.45	100.78
EIP-5b Core													
	n.a.	0.02	31.54	n.a.	0.34	b.d.	35.99	n.a.	0.02	0.08	32.83	0.36	101.15
	n.a.	0.04	30.50	n.a.	0.43	0.07	35.89	n.a.	0.04	0.09	31.71	0.43	99.21
	n.a.	0.09	27.11	n.a.	3.06	1.00	38.46	n.a.	b.d.	0.13	30.26	0.43	100.53
	n.a.	0.01	32.47	n.a.	0.43	0.07	37.04	n.a.	0.01	b.d.	29.48	0.32	99.75
	n.a.	0.12	31.28	n.a.	0.54	0.39	37.49	n.a.	0.03	0.02	30.70	0.40	100.97
	n.a.	b.d.	30.62	n.a.	0.30	b.d.	36.46	n.a.	0.02	0.08	31.72	0.40	99.55
	n.a.	0.01	31.52	n.a.	0.38	0.11	36.56	n.a.	0.01	0.06	31.62	0.49	100.74
	n.a.	b.d.	29.52	n.a.	0.25	0.01	36.54	n.a.	0.01	0.05	31.64	0.55	98.56
	b.d.	b.d.	31.21	b.d.	0.34	0.12	36.03	b.d.	b.d.	0.05	32.96	0.51	101.18
	b.d.	0.06	30.62	b.d.	0.33	0.16	36.16	b.d.	b.d.	b.d.	31.07	0.48	98.93
	b.d.	0.02	30.98	b.d.	0.27	0.16	36.75	0.02	b.d.	0.08	32.03	0.54	100.83
	b.d.	b.d.	28.42	b.d.	0.58	0.10	36.98	0.02	b.d.	b.d.	33.29	0.53	99.81

Biotite

Run	F	Na_2O	MgO	P_2O_5	CaO	Al_2O_3	SiO_2	Cl	K_2O	TiO_2	FeO	MnO	Total
EIP-4a Powder													
	b.d.	2.42	21.64	b.d.	0.07	16.72	38.63	0.08	7.01	0.13	10.57	0.09	97.37
	b.d.	2.34	20.47	b.d.	0.12	17.35	38.13	0.10	6.69	0.23	10.72	0.11	96.19
EIP-4b Core													
	b.d.	2.26	21.71	b.d.	0.07	17.39	37.70	0.09	7.07	0.29	9.22	0.07	95.80

Appendix 4.C All LA-ICP-MS Analyses for Chapter 4.

Values with "<" indicate they are below detection. The value following the "<" is the detection limit for that individual analysis.

Table 4.C1: LA-ICP-MS analyses for Chapter 4

	Amphibole													
	23051707b	**23051707b**	**23051707b**	**EIP4b**	**EIP4b**	**EIP4b**	**EIP4a**	**EIP4a**	**EIP7b**	**EIP7b**	**EIP7a**	**EIP7a**	**EIP8b**	**EIP8b**
Li	<26.57	2.3	<4.48	8.3	<8.07	<10.33	<6.70	<9.74	8.1	9.7	18.3	23.7	<10.25	<11.75
Al_2O_3	15.5	11.1	11.7	16.8	11.2	14.1	12.8	17.0	10.4	11.0	12.0	14.5	17.0	13.0
SiO_2	<78.25	44.9	44.9	41.1	41.1	41.1	40.6	40.6	44.3	44.3	44.7	44.7	41.0	41.0
Sc	<89.67	51.5	52.6	22.1	23.0	17.4	28.8	26.6	51.1	46.9	89.8	71.9	81.3	41.4
V	435.6	329.7	336.0	142.7	114.7	164.4	151.6	228.9	285.5	277.2	404.2	415.4	442.4	282.3
Ga	26.0	32.8	27.2	58.3	35.1	64.6	43.5	70.8	21.8	18.5	33.0	50.9	43.6	45.1
Ge	<92.70	7.1	<22.11	<51.54	<25.57	10.8	<25.69	20.3	<17.23	<25.50	<29.94	<32.51	<36.39	<34.62
Rb	<11.20	2.3	1.4	2.8	1.9	2.6	2.6	2.5	2.4	<1.50	3.0	9.4	<2.11	7.9
Sr	25.8	23.9	21.1	233.8	152.7	211.9	133.1	212.5	21.7	24.7	33.6	41.8	137.8	113.3
Y	47.3	27.5	31.9	23.0	13.4	22.0	29.1	43.0	31.3	27.4	61.6	43.1	49.5	35.1
Zr	<36.43	26.5	23.2	40.5	24.7	47.8	97.1	181.8	21.5	27.9	34.0	43.0	49.8	81.3
Nb	4.2	2.2	2.0	5.6	3.3	5.9	5.9	7.6	2.6	1.9	6.1	2.7	2.1	4.0
Cd	<350.22	<0.34	<3.30	0.2	<7.46	<9.24	<3.27	<7.94	1.1	<7.76	<7.25	1.1	1.1	<3.74
In	<1.78	0.2	<0.61	0.1	<0.59	<0.54	0.1	<0.34	<0.55	<0.40	<0.74	<0.43	<0.80	<0.31
Sn	59.7	12.4	26.8	<7.28	<4.81	<7.80	<4.69	<5.33	<4.79	<4.38	<7.75	<4.63	<7.26	<3.96
Cs	<2.03	<0.10	<0.36	<1.17	<0.52	<0.83	<0.45	<1.24	<0.52	<0.50	<0.73	<1.33	<1.21	<0.95
La	6.8	5.2	5.4	45.7	36.0	25.4	12.8	11.9	6.0	5.2	7.3	7.2	3.2	5.4
Ce	23.6	17.7	16.5	32.1	23.2	21.8	19.0	21.1	18.8	15.8	23.8	20.3	10.1	13.8
Pr	3.7	2.9	2.8	4.5	3.6	3.7	3.2	3.8	3.0	2.7	4.3	3.6	2.4	2.7
Nd	19.8	14.2	13.6	20.4	11.0	25.3	16.2	21.0	15.1	10.8	29.7	19.8	18.3	18.5
Sm	5.4	4.2	4.0	5.1	3.4	4.2	4.3	7.2	4.8	3.8	9.3	4.6	5.3	4.7
Eu	1.9	1.4	1.4	2.0	0.8	<1.18	1.1	2.0	1.3	1.5	1.9	1.8	2.0	1.7
Gd	8.3	4.4	4.8	5.0	<4.26	5.6	4.5	8.1	4.9	4.7	11.4	5.7	10.0	6.0
Tb	<2.11	0.8	1.1	0.7	0.5	0.8	0.7	1.3	0.8	0.7	1.8	1.1	1.9	1.2
Dy	10.6	5.2	5.4	3.7	2.7	4.7	4.5	6.7	6.0	6.0	12.4	7.9	10.6	6.7
Ho	2.0	1.0	1.6	1.0	0.6	0.9	1.1	1.8	1.2	1.2	2.2	1.7	1.9	1.5
Er	5.2	3.2	3.2	2.8	1.6	1.9	2.9	4.1	2.5	3.8	5.9	4.2	5.4	4.4
Tm	0.5	0.4	0.5	0.2	0.2	0.3	0.4	0.5	0.4	0.4	0.8	0.6	0.7	0.5
Yb	4.2	3.1	3.8	2.7	1.6	2.2	2.6	5.5	2.9	3.1	5.9	4.5	4.6	3.5
Lu	0.4	0.4	0.4	0.3	0.2	0.3	0.4	0.5	0.4	0.5	0.9	0.4	0.7	0.5
Hf	<13.31	1.4	1.4	1.2	0.8	1.4	2.3	5.1	1.1	0.9	2.4	2.4	2.6	3.3
Ta	<2.31	0.1	0.1	0.5	0.3	0.5	0.6	1.0	<0.60	0.1	0.3	0.2	<0.65	0.3

	Glass																	
	EIP4b	**EIP4b**	**EIP4b**	**EIP4a**	**EIP4a**	**EIP5b**	**EIP5b**	**EIP5b**	**EIP5a**	**EIP5a**	**EIP7b**	**EIP7a**	**EIP7a**	**EIP8b**	**EIP8b**	**EIP9b**	**EIP9b**	**EIP9a**	**EIP9a**
Li	32.7	<19.48	37.6	30.4	43.9	<11.14	<4.83	<14.48	17.9	<14.02	<115.42	<13.84	<12.60	<20.62	19.6	34.7	21.7	30.6	22.4
Al_2O_3	19.9	16.9	21.7	16.4	19.1	18.6	12.6	15.7	21.2	13.2	35.1	27.4	13.2	22.8	14.3	21.1	18.4	19.4	19.4
SiO_2	56.2	56.2	56.2	57.3	57.3	49.7	49.7	49.7	47.5	47.5	62.0	55.4	55.4	64.7	64.7	57.4	57.4	53.3	53.3
Sc	<19.32	<36.33	<18.06	<26.22	<13.02	32.5	74.3	35.2	41.5	32.2	<107.17	<30.05	<13.22	65.0	<31.59	16.3	<15.59	<15.01	<15.83
V	67.9	<10.76	<5.55	<8.60	<5.23	209.1	216.9	216.9	363.1	232.8	<35.25	<11.67	<3.74	522.4	65.9	273.6	209.4	56.8	56.1
Ga	82.3	23.2	88.3	68.2	70.9	44.2	29.3	46.3	86.8	57.6	48.6	71.5	30.1	102.9	114.9	192.0	159.7	202.8	198.1
Ge	<55.81	<92.41	<16.41	<87.45	<28.64	<15.66	<44.21	<21.12	12.9	<21.09	37.5	<43.81	<59.29	17.2	<91.54	<33.72	<23.30	<24.58	<15.72
Rb	44.1	<3.79	62.4	30.2	39.4	6.6	3.5	6.3	16.5	10.2	<9.76	8.4	3.2	23.9	29.1	52.3	40.9	46.1	45.1
Sr	225.5	364.3	223.1	272.5	185.3	237.6	139.0	209.4	245.8	145.5	828.3	484.0	245.6	218.9	122.3	225.7	197.9	228.3	222.4
Y	9.6	<2.34	1.2	4.2	0.8	27.8	23.4	26.3	27.5	16.7	<10.48	<4.62	0.7	59.9	13.8	35.4	31.6	32.4	30.5
Zr	19.9	<14.60	6.1	11.1	<8.94	44.3	35.0	46.4	51.1	34.6	<61.06	<13.46	<7.48	130.7	105.4	167.6	133.3	123.9	123.1
Nb	0.8	0.0	0.0	0.2	0.0	4.0	1.6	3.3	4.2	1.8	0.0	0.1	0.1	6.7	5.7	8.4	5.0	7.2	5.9
Cd	<10.10	<26.02	<5.40	1.6	<4.00	<10.86	<5.05	<4.83	2.0	<10.60	<79.25	<8.66	0.3	0.7	0.0	1.4	<9.31	0.0	<12.69
In	0.1	0.1	0.0	<1.00	<0.64	<0.84	0.1	<0.90	<0.73	<0.82	<3.25	0.3	<0.79	<0.47	<1.37	<0.57	<0.97	<0.68	<1.74
Sn	<4.94	<19.82	<8.97	<7.32	<6.50	<9.54	<3.29	<7.45	<4.92	<6.36	<33.13	<9.25	<7.50	<5.39	<14.17	<7.30	<6.99	<2.06	<5.65
Cs	2.5	<3.50	3.8	2.6	2.8	<0.72	<0.91	<0.87	<1.73	0.4	<6.74	<1.50	<1.74	<0.73	<2.42	2.6	1.5	2.0	1.9
La	22.7	0.7	12.3	17.4	1.8	5.2	3.2	20.5	22.5	12.8	3.5	1.7	1.1	14.1	17.9	18.8	17.5	12.3	13.3
Ce	11.2	0.3	3.6	9.1	0.8	18.1	11.0	17.0	21.6	11.3	3.9	2.4	1.5	35.1	31.0	37.6	33.8	34.8	35.2
Pr	1.4	0.0	0.2	0.3	<0.30	3.6	2.1	3.0	3.6	1.7	0.5	0.3	0.1	6.1	3.4	5.9	4.6	5.1	4.5
Nd	5.6	0.0	0.0	1.5	0.0	16.5	12.2	15.1	17.6	9.8	0.7	0.5	0.4	27.7	12.7	21.3	22.7	24.3	22.4
Sm	2.2	0.0	0.0	0.5	0.0	5.0	4.9	3.6	6.3	3.3	0.9	0.3	0.0	11.6	<6.84	5.4	4.6	5.1	5.5
Eu	0.6	0.0	0.0	0.3	<1.23	1.6	1.3	1.5	2.7	0.9	0.7	<1.39	<0.94	2.7	1.2	1.9	2.1	2.1	1.9
Gd	1.4	<3.74	0.0	<3.87	<2.30	4.3	3.9	5.1	<7.88	3.0	<18.10	0.7	0.2	11.8	<13.00	4.5	5.5	6.7	<6.39
Tb	0.3	<0.56	0.1	0.0	0.1	0.9	0.9	0.8	1.0	<0.64	0.3	0.0	0.0	2.0	<0.80	0.9	0.9	0.9	0.9
Dy	0.5	0.0	0.0	0.6	0.1	6.2	5.0	4.6	6.3	3.6	0.8	<2.36	0.0	10.6	4.0	5.2	6.3	4.3	6.0
Ho	0.4	0.0	<0.33	0.2	0.0	1.2	1.0	0.8	1.0	0.7	<3.63	0.0	0.0	2.5	0.4	1.2	1.0	1.0	1.1
Er	0.6	0.0	0.0	0.2	0.0	2.6	2.8	2.5	2.5	2.0	<7.81	0.0	0.0	5.9	1.4	3.7	3.2	3.4	3.3
Tm	0.4	0.0	0.0	0.0	0.0	<0.30	0.3	0.4	0.4	0.4	<4.94	0.0	0.0	0.8	<0.75	0.5	0.5	0.4	0.5
Yb	1.3	0.0	0.3	0.7	0.4	2.6	2.1	1.9	2.8	2.0	0.0	0.1	0.4	6.5	1.2	2.4	2.5	2.5	3.7
Lu	0.3	0.0	0.0	0.0	0.0	0.5	0.2	0.2	<2.24	0.1	<6.11	0.0	0.0	0.9	0.1	0.4	0.3	0.6	0.7
Hf	0.5	0.0	0.0	0.0	0.0	1.3	<1.27	1.3	1.4	0.8	<10.17	1.1	0.1	3.2	2.3	3.0	4.3	4.4	3.7
Ta	0.2	<0.59	0.0	0.0	0.0	0.2	0.2	0.1	0.3	0.1	0.0	0.1	0.0	0.1	0.4	0.3	0.3	<0.37	0.6

	Pyroxene													Plagioclase	
	EIP4b	**EIP4b**	**EIP4a**	**EIP5b**	**EIP5b**	**EIP5a**	**EIP5a**	**EIP7a**	**EIP8b**	**EIP8b**	**EIP9b**	**EIP9a**	**EIP9a**	**23051707b**	**23051707b**
Li	7.8	<6.49	<6.08	<7.20	<5.05	<8.82	<12.67	<17.21	5.8	11.5	<44.58	<19.89	<10.70	<22.96	2.6
Al_2O_3	12.2	12.5	10.2	9.2	8.6	7.7	11.7	9.4	11.1	12.1	6.6	6.0	7.1	36.7	0.9
SiO_2	44.8	44.8	43.5	48.5	48.5	47.9	47.9	51.9	50.7	50.7	50.5	49.0	51.5	<81.50	57.4
Sc	78.3	136.0	98.3	79.8	83.9	103.1	77.7	54.0	106.9	87.9	119.7	99.4	110.5	<87.33	3.4
V	730.0	713.6	825.4	201.4	222.9	461.5	326.7	209.9	132.8	125.5	112.3	174.2	228.2	<15.94	<0.84
Ga	18.2	11.9	18.3	15.7	19.8	20.4	44.4	72.9	11.7	36.3	<12.16	8.7	9.7	32.9	42.2
Ge	<29.88	<30.57	<9.58	<40.57	<12.14	<23.97	<54.35	<85.31	<21.53	<39.17	<87.08	<15.42	<20.77	<106.09	<3.07
Rb	0.3	<1.18	<0.60	2.4	2.6	3.2	7.8	25.7	<1.71	8.0	<6.88	<1.86	<1.64	<6.38	23.1
Sr	52.2	28.2	48.6	83.0	87.6	54.3	129.9	72.0	16.8	70.1	27.3	20.8	23.4	678.1	18.2
Y	35.5	36.2	31.0	19.8	25.4	21.8	23.5	41.5	46.9	41.1	68.5	42.4	49.1	0.0	0.8
Zr	65.4	67.9	83.1	29.6	34.8	20.0	32.5	177.3	68.9	69.8	60.5	48.1	52.1	<24.53	101.8
Nb	<2.71	0.9	1.2	1.1	1.4	0.5	2.1	<3.65	0.3	<2.52	0.4	0.2	0.0	<3.85	0.2
Cd	<7.47	<8.60	<6.34	<7.52	<7.69	0.8	0.5	<23.70	<11.16	0.8	7.5	1.4	0.2	<23.26	<0.78
In	<0.87	<0.63	<0.25	<0.70	<0.45	0.0	<1.37	<0.89	<0.42	<0.58	<1.75	<0.59	<0.92	83.8	<0.12
Sn	<11.51	<9.73	<3.66	<4.62	<7.99	<4.21	<9.45	<15.79	<7.87	<5.83	<17.19	<6.61	<5.99	<39.60	42.9
Cs	<0.38	<0.42	<0.93	<1.02	<0.95	<1.34	<1.56	1.1	<0.91	<1.43	<3.20	<0.71	<0.96	<3.78	0.2
La	8.7	12.0	4.3	2.0	2.4	4.5	12.8	7.8	2.9	6.8	3.7	2.0	2.2	2.4	0.8
Ce	11.2	14.1	9.9	7.2	9.0	6.6	10.9	19.6	11.2	14.7	10.8	7.9	9.6	2.3	1.7
Pr	2.9	3.5	2.1	1.6	1.6	1.3	2.4	3.9	2.3	2.9	<4.81	1.7	2.7	0.3	0.2
Nd	16.2	17.6	14.6	10.9	10.5	8.1	10.4	26.4	19.2	15.3	13.2	14.3	15.8	0.0	0.5
Sm	5.9	6.3	5.4	3.1	3.6	3.6	6.2	7.0	7.4	4.8	6.8	6.6	6.3	0.0	<0.77
Eu	1.7	2.2	1.7	1.4	1.2	1.3	<1.63	2.0	1.7	1.8	4.1	1.6	2.0	<2.32	0.1
Gd	8.3	10.4	5.5	3.5	5.4	<4.17	<6.74	8.7	8.3	7.9	22.5	8.5	8.8	<7.05	0.1
Tb	1.4	1.7	1.0	0.6	0.9	0.9	0.6	1.2	1.7	1.2	2.6	1.4	1.7	0.1	0.0
Dy	9.2	9.6	7.3	4.3	5.4	4.8	4.9	<5.89	10.5	8.3	15.6	9.2	8.3	0.0	0.1
Ho	1.6	1.7	1.5	0.9	1.1	1.0	0.9	1.4	1.7	1.6	3.3	1.9	2.1	0.1	0.0
Er	5.3	4.5	4.0	2.3	2.3	2.9	3.1	4.4	5.2	4.4	11.2	3.7	5.0	0.0	0.1
Tm	0.5	0.5	0.6	0.3	0.4	0.5	0.4	0.7	0.5	0.5	1.5	0.5	0.7	0.0	0.0
Yb	3.4	2.4	3.3	1.6	1.7	2.3	2.3	<3.00	4.2	3.5	<11.19	4.2	3.8	0.0	0.1
Lu	0.6	0.4	0.4	0.2	0.3	0.4	0.4	0.7	0.7	0.7	0.7	0.5	0.4	0.0	<0.05
Hf	3.1	3.3	3.6	1.1	1.3	1.0	2.3	4.8	2.7	2.2	2.0	3.0	2.6	<9.01	3.0
Ta	0.1	0.3	0.2	0.0	0.0	0.1	0.1	<0.72	0.1	0.2	0.2	0.0	0.1	0.0	0.0

	Olivine				BHVO2G			
	EIP4a	**EIP5b**	**EIP5b**	**EIP5a**	**BHVO2G**	**BHVO2G**	**BHVO2G**	**BHVO2G**
Li	11.9	<4.34	<7.43	<11.14	4.3	4.7	3.9	4.1
Al_2O_3	1.2	1.6	2.5	6.6	14.3	14.3	14.9	14.5
SiO_2	39.1	36.6	36.6	37.4	49.3	49.3	49.3	49.3
Sc	<12.10	12.8	<12.79	22.8	30.6	31.3	30.4	30.2
V	10.0	26.9	71.8	128.8	309.9	317.8	322.6	310.3
Ga	4.5	4.2	6.3	23.5	47.6	50.7	58.0	51.9
Ge	<24.22	<22.91	9.2	<35.34	9.1	9.6	12.2	9.1
Rb	2.6	<1.32	<1.73	5.1	8.7	9.0	10.0	7.3
Sr	16.8	18.7	25.7	74.3	383.1	399.4	419.2	374.5
Y	1.0	2.8	4.3	12.0	19.9	21.2	23.0	22.6
Zr	<7.55	5.4	<9.33	19.4	146.0	148.9	166.6	149.5
Nb	0.0	0.1	0.7	1.7	17.2	18.6	18.7	16.7
Cd	<4.29	<4.53	0.5	0.4	0.2	<1.36	0.6	<0.82
In	<0.68	<0.46	<0.91	<0.52	<0.09	<0.21	<0.82	<0.49
Sn	<5.02	<4.29	<3.55	<5.61	1.5	1.6	2.1	1.4
Cs	<0.70	<0.74	<0.57	<1.48	0.1	<0.20	<0.75	<0.43
La	0.7	0.5	0.7	8.8	15.4	14.9	15.3	15.3
Ce	0.1	1.7	2.3	6.5	38.2	37.1	37.9	37.9
Pr	0.0	0.3	0.4	0.7	5.2	5.3	5.3	5.5
Nd	0.0	1.6	2.7	5.2	24.6	23.7	26.0	25.4
Sm	0.0	0.3	0.9	2.3	6.3	6.1	6.3	5.8
Eu	0.0	0.2	0.2	0.8	2.0	2.0	2.2	1.9
Gd	0.7	0.5	<1.76	<2.79	5.9	5.4	5.6	5.8
Tb	0.0	0.1	0.1	0.5	0.9	0.7	0.9	0.9
Dy	<2.15	0.6	0.7	2.4	4.9	4.4	5.6	5.6
Ho	<0.27	0.1	0.2	0.4	0.9	<0.81	1.0	0.9
Er	0.1	0.4	0.3	1.6	2.5	2.0	2.7	2.6
Tm	0.0	0.1	0.1	0.3	0.3	0.3	<0.77	<0.41
Yb	0.1	<0.89	0.6	1.0	1.9	1.8	1.9	1.8
Lu	0.1	0.1	0.1	0.2	0.3	0.2	<0.67	<0.25
Hf	0.0	0.2	0.4	0.9	4.5	4.3	4.3	4.2
Ta	0.0	0.0	0.1	0.1	1.2	1.1	1.2	1.0

Appendix 4.D Composition of Steli and “Iveland Wall” pegmatites.

The following compositions are bulk rock compositions of the border zones from the Steli and the “Iveland Wall’ outcrop from Snook (2014) and albite zones from Müller et al. (2018). CG = coarse grained, MG = medium grained, FG = Fine grained, LC = lower contact, UC = upper contact, BZ = boarder zone, AZ = albite zone

Table 4.D1: Composition of Steli and “Iveland Wall” pegmatites

Wt%	**Steli CG-LC**	**Steli MG-LC**	**Steli FG-UC**	**Steli GBZ-LC**	**Steli GBZ-UC**	**Iveland Wall**	**Solaås AZ**	**Topazbrudd AZ**
SiO_2	70.52	73.99	68.47	71.45	73.63	69.58	61.1	59.8
Al_2O_3	16.01	13.58	16.97	15.97	13.68	14.63	23.7	26.6
TiO_2	0.07	0.12	0.21	0.18	0.14	0.15	-	-
FeO	2.39	1.26	1.78	1.61	1.39	5.46	0.7	0.3
MgO	0.17	0.24	0.42	0.4	0.28	0.05	0	0
MnO	0.91	0.04	0.04	0.04	0.05	0.05	0.5	0.2
CaO	1.14	0.67	2.29	2.69	0.98	3.17	0.1	0.1
Na_2O	5.74	2.66	4.64	5.35	3.21	4.69	8.4	8.5
K_2O	2.26	6.77	4.3	1.19	5.3	0.98	2.8	1.3
F	-	-	-	-	-	-	1.5	3.6
P_2O_5	0.02	0.03	0.04	0.03	0.03	0.01	-	-

Chapter 5 Appendices

Appendix 5.A: Additional References for Chapter 5

The following references are all of the sources used to compile the database of biotite and amphibole compositions in this study. The following sources are cited in Appendix 5.B.

Ague, J. J., and Brimhall, G. H., 1988, Magmatic arc asymmetry and distribution of anomalous plutonic belts in the batholiths of California: Effects of assimilation, crustal thickness, and depth of crystallization: Geological Society of America Bulletin, v. 100, no. 6, p. 912-927, doi:10.1130/0016-7606(1988)100<0912:MAAADO>2.3.CO;2.

Allan, B., and Clarke, D., 1981, Occurrence and origin of garnet in the South Mountain Batholith, Nova Scotia: The Canadian Mineralogist, v. 19, no. 1, p. 19-24.

Anderson, J. L., 1975, Petrology and geochemistry of the Wolf River Batholith [Ph.D.]:The University of Wisconsin-Madison, 297 p.

Anderson, J. L., and Bender, E. E., 1989, Nature and origin of Proterozoic A-type granitic magmatism in the southwestern United States of America: Lithos, v. 23, no. 1, p. 19-52, doi:10.1016/0024-4937(89)90021-2.

Antunes, I. M. H. R., Neiva, A. M. R., Silva, M. M. V. G., and Corfu, F., 2008, Geochemistry of S-type granitic rocks from the reversely zoned Castelo Branco pluton (central Portugal): Lithos, v. 103, no. 3, p. 445-465, doi:10.1016/j.lithos.2007.10.003.

Barker, F., Wones, D. R., Sharp, W. N., and Desborough, G. A., 1975, The Pikes Peak batholith, Colorado front range, and a model for the origin of the gabbro—anorthosite—syenite—potassic granite suite: Precambrian Research, v. 2, no. 2, p. 97-160, doi:10.1016/0301-9268(75)90001-7.

Bennett, V. W., 1990, Mineralogy and chemistry of biotite and muscovite from the granitoid rocks of the Bay d'Espoir Area, Newfoundland [B.Sc.]:Memorial University, 92 p.

Bikramaditya Singh, R. K., 2013, Origin and emplacement of the Higher Himalayan Leucogranite in the eastern Himalaya: Constraints from geochemistry and mineral chemistry: Journal of the Geological Society of India, v. 81, no. 6, p. 791-803, doi:10.1007/s12594-013-0104-9.

Burkhard, D. J. M., 1991, Temperature and redox path of biotite-bearing intrusives: A method of estimation applied to S- and I-type granites from Australia: Earth and Planetary Science Letters, v. 104, no. 1, p. 89-98, doi:10.1016/0012-821X(91)90240-I.

Chappell, B. W., Bryant, C. J., and Bultitude, R. J., CHAPGRAN: Geochemical database of the granites of eastern Australia: Australian Journal of Earth Sciences. (in prep.).

Chappell, B. W., and White, A. J. R., 1976, Plutonic Rocks of the Lachlan Mobile Zone, Canberra, 25th International Geological Congress, Excursion Guide No 13C, 40 p.

Clarke, D. B., 1995, Unpublished Data.

Cunha, I. R. V. d., Dall'Agnol, R., and Feio, G. R. L., 2016, Mineral chemistry and magnetic petrology of the Archean Planalto Suite, Carajás Province – Amazonian Craton: Implications for the evolution of ferroan Archean granites: Journal of South American Earth Sciences, v. 67, p. 100-121, doi:10.1016/j.jsames.2016.01.007.

Czamanske, G. K., and Wones, D. R., 1973, Oxidation during magmatic differentiation, Finnmarka complex, Oslo area, Norway: Part 2, the mafic silicates: Journal of Petrology, v. 14, no. 3, p. 349-380, doi:10.1093/petrology/14.3.349.

Dahlquist, J. A., Alasino, P. H., and Bello, C., 2014, Devonian F-rich peraluminous A-type magmatism in the proto-Andean foreland (Sierras Pampeanas, Argentina): geochemical constraints and petrogenesis from the western-central region of the Achala batholith: Mineralogy and Petrology, v. 108, no. 3, p. 391-417, doi:10.1007/s00710-013-0308-0.

Dahlquist, J. A., Alasino, P. H., Eby, G. N., Galindo, C., and Casquet, C., 2010, Fault controlled Carboniferous A-type magmatism in the proto-Andean foreland (Sierras Pampeanas, Argentina): Geochemical constraints and petrogenesis: Lithos, v. 115, no. 1, p. 65-81, doi:10.1016/j.lithos.2009.11.006.

Dahlquist, J. A., Rapela, C. W., and Baldo, E. G., 2005, Petrogenesis of cordierite-bearing S-type granitoids in Sierra de Chepes, Famatinian orogen, Argentina: Journal of South American Earth Sciences, v. 20, no. 3, p. 231-251, doi:10.1016/j.jsames.2005.05.014.

Dall'Agnol, R., Teixeira, N. P., Rämö, O. T., Moura, C. A. V., Macambira, M. J. B., and de Oliveira, D. C., 2005, Petrogenesis of the Paleoproterozoic rapakivi A-type granites of the Archean Carajás metallogenic province, Brazil: Lithos, v. 80, no. 1, p. 101-129, doi:10.1016/j.lithos.2004.03.058.

De Pieri, R., and Jobstraibizer, P. G., 1977, On some biotites from Adamello massif (northern Italy): Neues Jahrbuch fr Mineralogie, v. 27, p. 15-24.

Ding, Y., 1995, AFM minerals in the Halifax Pluton, Nova Scotia, Canada [M.Sc.]:Dalhousie University, 203 p.

Dodge, F. C. W., Smith, V. C., and Mays, R. E., 1969, Biotites from granitic rocks of the central Sierra Nevada Batholith, California: Journal of Petrology, v. 10, no. 2, p. 250-271, doi:10.1093/petrology/10.2.250.

Douma, S. L., 1988, The Mineralogy, Petrology, and Geochemistry of the Port Mouton Pluton, Nova Scotia, Canada [M.Sc.]:Dalhousie University, 343 p.

Esmaiel, D., Mahmoud, K., Roy, B., and Mohammad, S., 2015, Petrology and mineral chemistry of peraluminous Marziyan granites, Sanandaj-Sirjan metamorphic belt (NW Iran): Geologica Carpathica, v. 66, no. 5, p. 361-374, doi:10.1515/geoca-2015-0031.

Gulson, B. L., 1968, The evolution of dioritic rocks with special reference to the high potassium diorites of the Yeoval Igneous Complex, N.S.W. [Ph.D.]:Australian National University, 318 p.

Ham, L. J., 1988, The mineralogy, petrology, and geochemistry of the Halfway Cove - Queensport Pluton, Nova Scotia, Canada [M.Sc.]:Dalhousie University, 314 p.
Haslam, H. W., 1968, The crystallization of intermediate and acid magmas at Ben Nevis, Scotland: Journal of Petrology, v. 9, no. 1, p. 84-104, doi:10.1093/petrology/9.1.84.
Joyce, A. S., 1970, Geochemistry of the Murrumbidgee Batholith [Ph.D.]:Australian National University, 219 p.
Kinnaird, J. A., Bowden, P., Ixer, R. A., and Odling, N. W. A., 1985, Mineralogy, geochemistry and mineralization of the Ririwai complex, northern Nigeria: Journal of African Earth Sciences (1983), v. 3, no. 1, p. 185-222, doi:10.1016/0899-5362(85)90036-3.
Kleemann, G. J., and Twist, D., 1989, The Compositionally-zoned Sheet-like Granite Pluton of the Bushveld Complex: Evidence Bearing on the Nature of A-type Magmatism: Journal of Petrology, v. 30, no. 6, p. 1383-1414, doi:10.1093/petrology/30.6.1383.
Lalonde, A. E., and Martin, R. F., 1983, The Baie-des-Moutons syenitic complex, La Tabatiere, Quebec; II, The ferromagnesian minerals: The Canadian Mineralogist, v. 21, no. 1, p. 81-91.
MacDonald, M. A., 1981, The mineralogy, petrology, and geochemistry of the Musquodoboit Batholith, Nova Scotia, Canada [M.Sc.]:Dalhousie University, 288 p.
Maillet, L., 1984, The origin and occurrence of cordierite in the South Mountain Batholith, Nova Scotia [B.Sc.]:Dalhousie University.The c
Morales Cámera, M. M., Dahlquist, J. A., Basei, M. A. S., Galindo, C., da Costa Campos Neto, M., and Facetti, N., 2017, F-rich strongly peraluminous A-type magmatism in the pre-Andean foreland Sierras Pampeanas, Argentina: Geochemical, geochronological, isotopic constraints and petrogenesis: Lithos, v. 277, p. 210-227, doi:10.1016/j.lithos.2016.10.035.
Neiva, A. M. R., 1976, The geochemistry of biotites from granites of northern Portugal with special reference to their tin content: Mineralogical Magazine, v. 40, no. 313, p. 453-466, doi:10.1180/minmag.1976.040.313.04.
Papoutsa, A., and Pe-Piper, G., 2014, Geochemical variation of amphiboles in A-type granites as an indicator of complex magmatic systems: Wentworth pluton, Nova Scotia, Canada: Chemical Geology, v. 384, p. 120-134, doi:10.1016/j.chemgeo.2014.07.001.
Parsons, I., 1981, The Klokken Gabbro-Syenite Complex, South Greenland: Quantitative interpretation of mineral chemistry: Journal of Petrology, v. 22, no. 2, p. 233-260, doi:10.1093/petrology/22.2.233.
Pattison, D. R. M., Carmichael, D. M., and St -Onge, M. R., 1982, Geothermometry and geobarometry applied to early proterozoic “S-type” granitoid plutons, Wopmay Orogen, Northwest Territories, Canada: Contributions to Mineralogy and Petrology, v. 79, no. 4, p. 394-404, doi:10.1007/bf01132069.
Persson, P., 2017, The geochemical and mineralogical evolution of the Mount Rosa Complex, El Paso County, Colorado, USA [M.S.]:Colorado School of Mines, 133 p.

Phillips, G. N., Wall, V. J., and Clemens, J. D., 1981, Petrology of the Strathbogie Batholith; a cordierite-bearing granite: The Canadian Mineralogist, v. 19, no. 1, p. 47-63.
Platt, R. G., and Woolley, A. R., 1986, The mafic mineralogy of the peralkaline syenites and granites of the Mulanje complex, Malawi: Mineralogical Magazine, v. 50, no. 355, p. 85-99.
Price, R. C., 1983, Geochemistry of a peraluminous granitoid suite from North-eastern Victoria, South-eastern Australia: Geochimica et Cosmochimica Acta, v. 47, no. 1, p. 31-42, doi:10.1016/0016-7037(83)90088-1.
Sapountzis, E. S., 1976, Biotites from the Sithonia igneous complex (north Greece): Neues Jahrbuch fur Mineralogie, v. 126, p. 327-341.
Schneiderman, J. S., 1991, Petrology and mineral chemistry of the Ascutney Mountain igneous complex: American Mineralogist, v. 76, no. 1-2, p. 218-229.
Shabani, A. A. T., 1999, Mineral chemistry and Mossbauer spectroscopy of micas from granitic rocks of the Canadian Appalachians [PhD]:University of Ottawa, 309 p.
Shabani, A. A. T., Lalonde, A. E., and Whalen, J. B., 2003, Composition of biotite from granitic rocks of the Canadian Appalachian Orogen: A potential tectonomagmatic indicator?: The Canadian Mineralogist, v. 41, no. 6, p. 1381-1396, doi:10.2113/gscanmin.41.6.1381.
Speer, J. A., 1981, Petrology of cordierite- and almandine-bearing granitoid plutons of the southern Appalachian Piedmont, U.S.A: The Canadian Mineralogist, v. 19, no. 1, p. 35-46.
Stallard, V. A., 1975, Geochemistry of biotites as a guide to the differentiation of the South Mountain Batholith, Nova Scotia [B.Sc.]:Dalhousie University, 43 p.
Wallace, G. M. B., 1988, Petrogenesis of the McGerrigle Plutonic Complex: Mineralogical and oxygen isotopic constraints [M.Sc.]:McGill University, 330 p.
Whalen, J. B., 1980, Aspects of granites and associated mineralization [PhD]:Australian National University, 381 p.
Whalen, J. B., 1993, Geology, petrography, and geochemistry of Appalachian granites in New Brunswick and Gaspésie, Quebec, Bulletin 436, Geologic Survey of Canada, p. 124.
White, A. J. R., and Chappell, B. W., 1989, Geology of the Numbla 1:100,000 Sheet 8625: New South Wales Geological Survey, 160.
White, A. J. R., Williams, I. S., and Chappell, B. W., 1977, Geology of the Beridale 1:100000 Sheet 8625: Geological Survey of New South Wales Department of Mines, 138.
Yaowanoiyothin, W., and Barr, S. M., 1991, Petrology of the Black Brook granitic suite, Cape Breton Island, Nova Scotia: The Canadian Mineralogist, v. 29, no. 3, p. 499-515.

Appendix 5.B: Biotite and Amphibole Mineral Formulas and Statistics

This appendix is an Excel spreadsheet that is electronically available on https://drum.lib.umd.edu/ or upon request. The Excel spreadsheet contains the biotite and amphibole formulas, references for the compositions of the minerals from the literature (full citations in appendix 5.A), and F- and t-test results used to compare biotite formulas from S-, I-, and A-type granites. Further text on the contents of this Excel file are located in appendix 5.C.s

Appendix 5.C: Additional Text for Chapter 5

Additional Text for Biotite and Amphibole Formulas

Biotite Formulas: Biotite formulas were calculated after the method of Dymek (1983), which allows for the estimation of Fe^{3+}. $X_{Annnite}^{Bt}$ is the mole fraction of the annite component in the biotite (fraction of Fe^{2+} in the octahedral site). $X_{Phlogopite}^{Bt}$is the mole fraction of the phlogopite component in biotite (fraction of magnesium in the octahedral site). X_{Fe3+} is the fraction of Fe^{3+} in the octahedral site. X_{OH}^{Bt}, X_{Cl}^{Bt}, and $X_{F}^{Bt}$are the mole fractions of OH, C, and F in the hydroxyl site, respectively. X_{OH}^{Bt}, X_{Cl}^{Bt}, and X_{F}^{Bt} were only calculated when Cl and F were both analyzed. The concentration of water (wt%) was calculated assuming the hydroxyl site is full. Fe/(Fe+Mg) is the molar ratio of total iron to total iron plus magnesium. Sample numbers are original sample numbers in the original publication. Some sample numbers have been annotated to distinguish between samples from different publications that use identical sample numbers. Only whole rock SiO_2 (wt%) required for generating the figures are included in the Excel supplementary file.

Amphibole Formulas: Amphibole formulas were calculated after the method of Hawthorne et al. (2012), which allows for the estimation of Fe^{3+}. X_{OH}^{Am}, X_{Cl}^{Am}, and $X_{F}^{Am}$are the mole fractions of OH, Cl, and F in the hydroxyl site, respectively. X_{OH}^{Am}, X_{Cl}^{Am}, and X_{F}^{Am}were only calculated when Cl and F were both analyzed. Water (wt%) was calculated assuming the hydroxyl site is full. Fe/(Fe+Mg) is the ratio of total iron to total iron plus magnesium. Some sample numbers have been annotated to distinguish between samples from different publications that use identical sample numbers. Only whole rock SiO_2 (wt%) required for generating the figures are included in the Excel supplementary file.

F- and t-tests

F- and t-test were performed to test the significance of differences in $X_{\mathrm{Annite}}^{\mathrm{Bt}}$. First F-tests were performed to determine whether the variance between each group (A- vs I-type, A- vs S-type, and I- vs S-type) were heteroscedastic or homoscedastic. If the F-value was greater than the critical F-value at the 0.05 level of significance then the null hypothesis (that the variances are homoscedastic) was rejected. For all F-tests the variances were heteroscedastic. After determining the variance for each comparison, a two-tailed t-test, assuming heteroscedastic variance, was performed. If the t-test value was greater than the critical p-value then the null hypothesis (there is no difference between the groups being compared) was rejected. In all cases the null was rejected at the 0.05 level of significance. The results of the F- and t-tests, as well as the mean, standard deviation, and variance for each group are included in Appendix 5.B.

Random Forest

The scripts and data used to generate the random forest models are located in the folder "Appendix 5.E". Instructions on how to train the models (not necessary for making predictions) are provided in the "trainModel_Biotite.m" and "trainModel_Amphibole.m" files. An example and explanation of how to use the model to make new predictions is given in the "ModelExample.m" file. All required variables are located in the ".mat" files.

Appendix 5.D: Supplementary Figures for Chapter 5

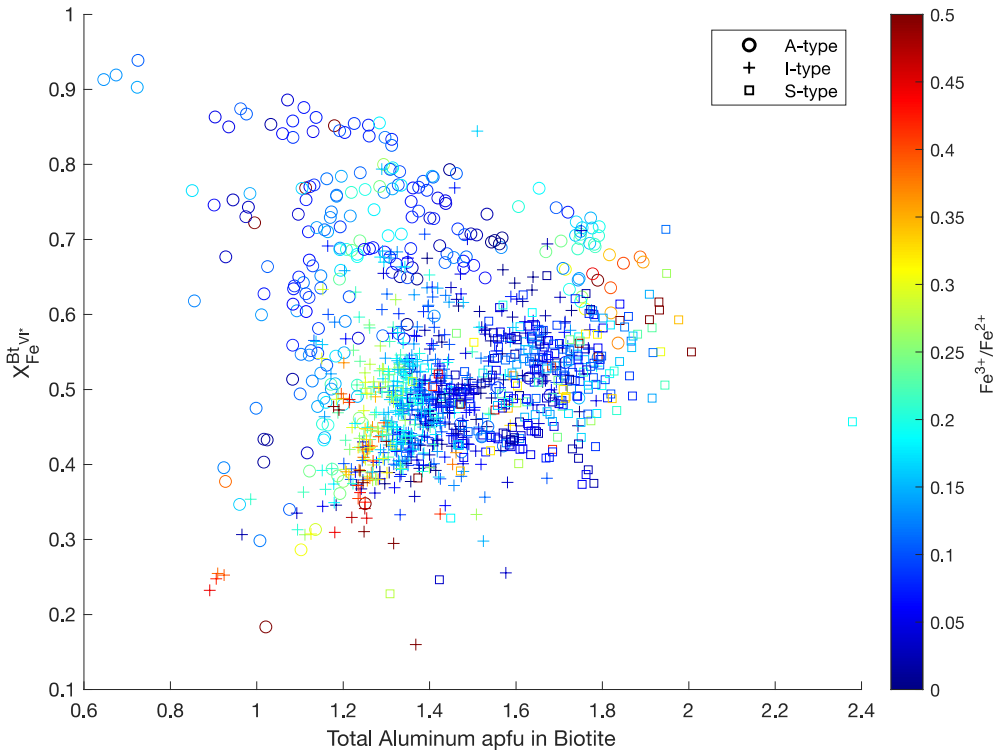

Figure 5.D1: $\boldsymbol{X^{Bt}_{Annite}}$ (fraction of the annite component in biotite defined as the fraction of Fe^{2+} in the octahedral site) vs. total aluminum colored by the ratio of Fe^{3+} to Fe^{2+} (Fe^{3+}/Fe^{2+}) in biotite. .

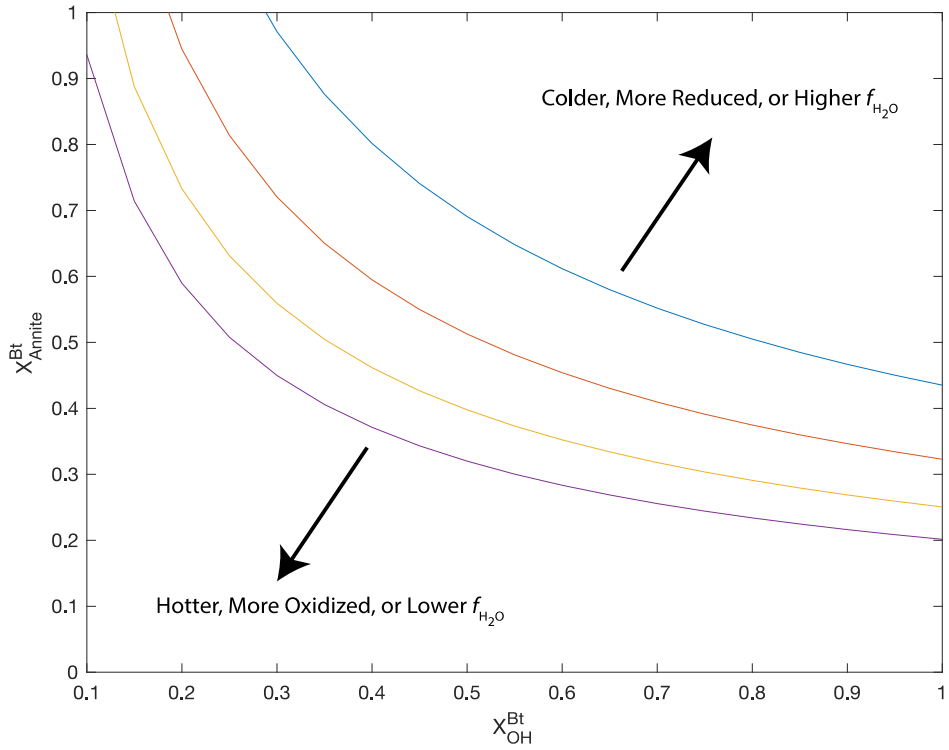

Figure 5.D2: Generalized effect of temperature, $\boldsymbol{f_{O_2}}$, and $\boldsymbol{f_{H_2O}}$ on curves that satisfy the equation of Czamanske and Wones (1973).

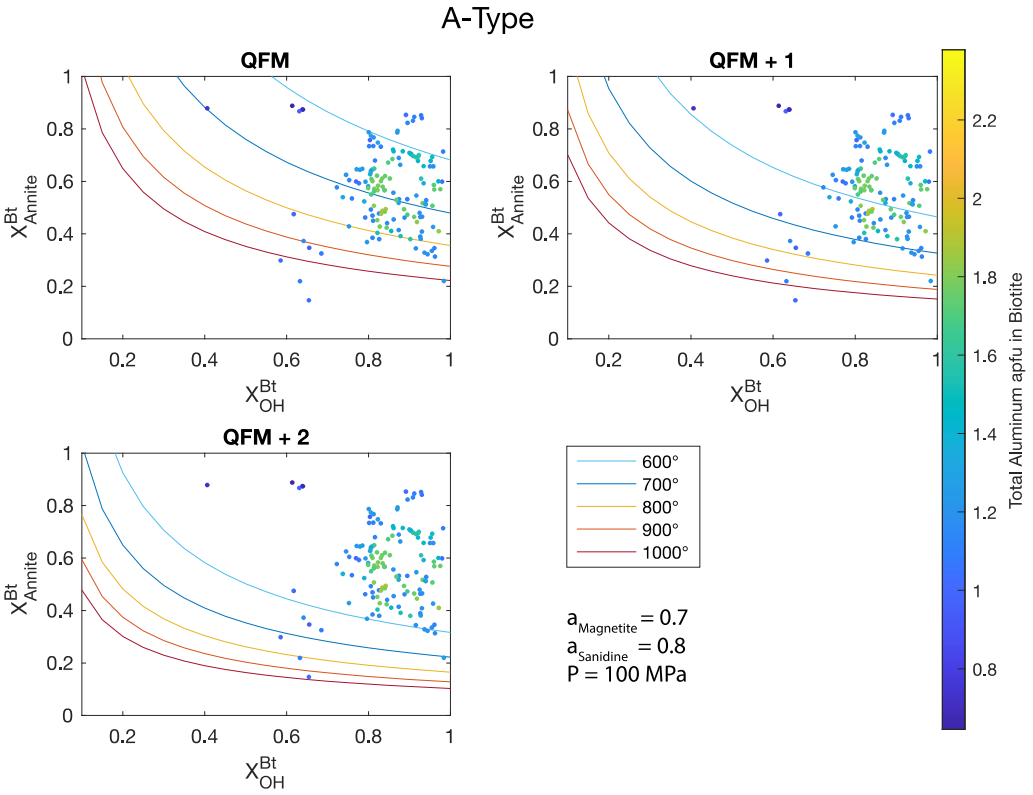

Figure 5.D3: Plot of $\boldsymbol{X^{Bt}_{Annite}}$ vs $\boldsymbol{X^{Bt}_{OH}}$ for biotite compositions from A-type granites at 100 MPa. Curves are combinations of $\boldsymbol{X^{Bt}_{Annite}}$ and $\boldsymbol{X^{Bt}_{OH}}$ that satisfy the equation of Czamanske and Wones (1973) for determining $\boldsymbol{f_{H_2O}}$ at variable temperatures and $\boldsymbol{f_{O_2}}$. The activity of magnetite and activity of sanidine were calculated using alphaMELTS for Matlab for each temperature and $\boldsymbol{f_{O_2}}$. Input for MELTS was the average A-type granite from Whalen et al. (1987). Variations in the calculated activity of magnetite and activity of sanidine among each group at different temperatures and $\boldsymbol{f_{O_2}}$ are minor and thus were set to 0.7 and 0.8.

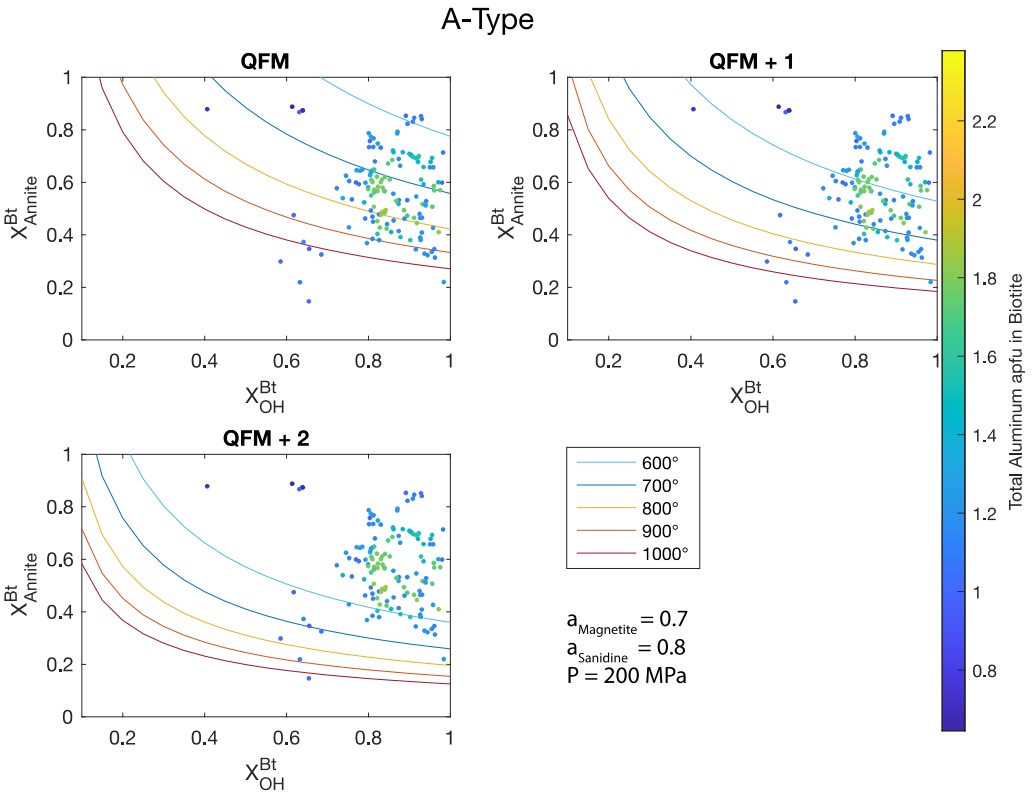

Figure 5.D4: Plot of $\boldsymbol{X^{Bt}_{Annite}}$ vs $\boldsymbol{X^{Bt}_{OH}}$ for biotite compositions from A-type granites at 200 MPa. See caption for Figure 5.D3 for details on curves, activity of magnetite, and activity of sanidine. Input for MELTS calculations was the average A-type granite from Whalen et al. (1987).

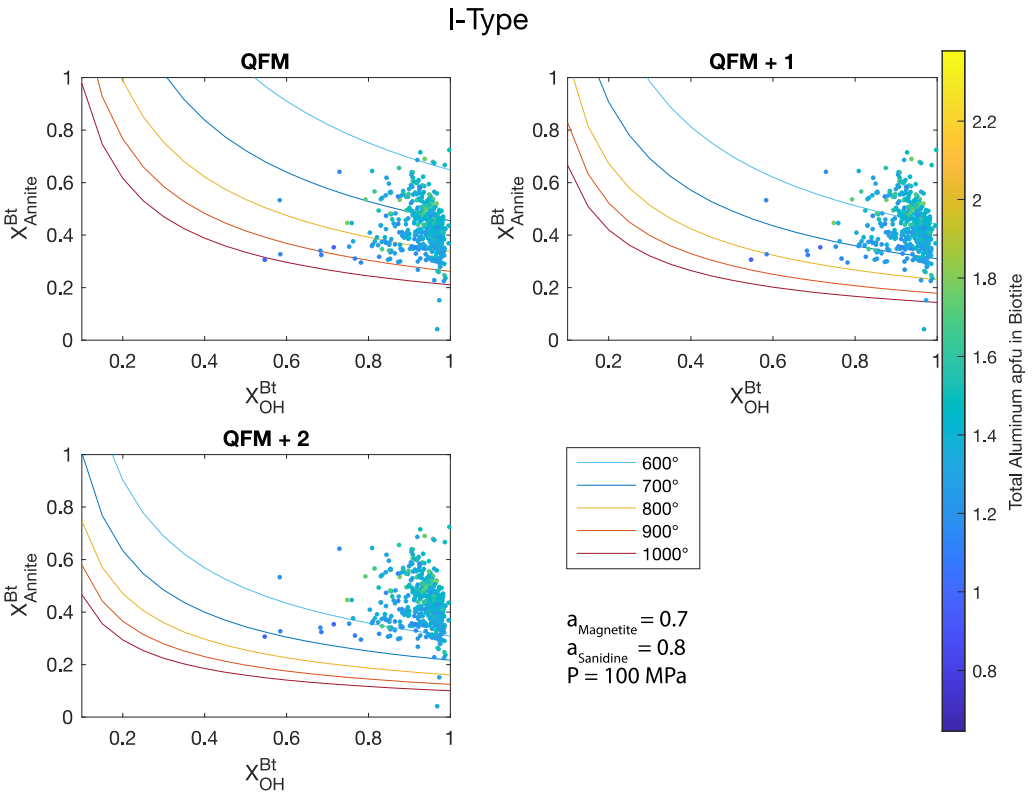

Figure 5.D5: Plot of $\boldsymbol{X^{Bt}_{Annite}}$ vs $\boldsymbol{X^{Bt}_{OH}}$ for biotite compositions from I-type granites at 100 MPa. See caption for Figure 5.D3 for details on curves, activity of magnetite, and activity of sanidine. Input for MELTS calculations was the average I-type granite from Chappell and White (1992).

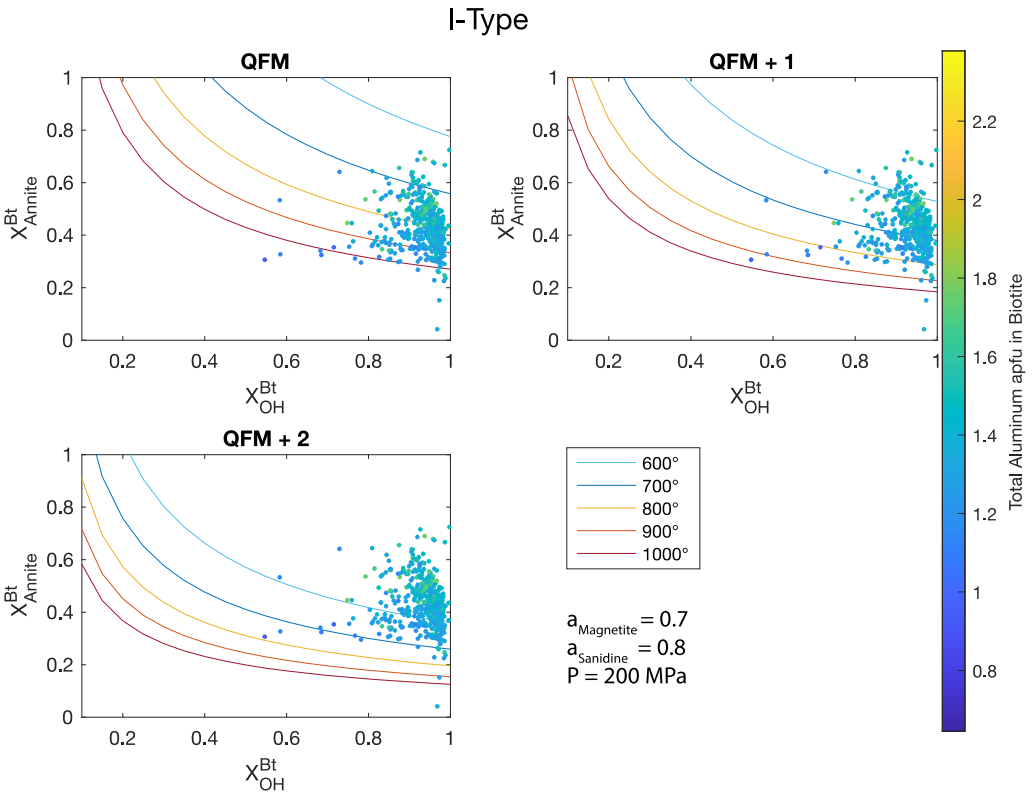

Figure 5.D6: Plot of $\boldsymbol{X^{Bt}_{Annite}}$ vs $\boldsymbol{X^{Bt}_{OH}}$ for biotite compositions from I-type granites at 200 MPa. See caption for Figure 5.D3 for details on curves, activity of magnetite, and activity of sanidine. Input for MELTS calculations was the average I-type granite from Chappell and White (1992).

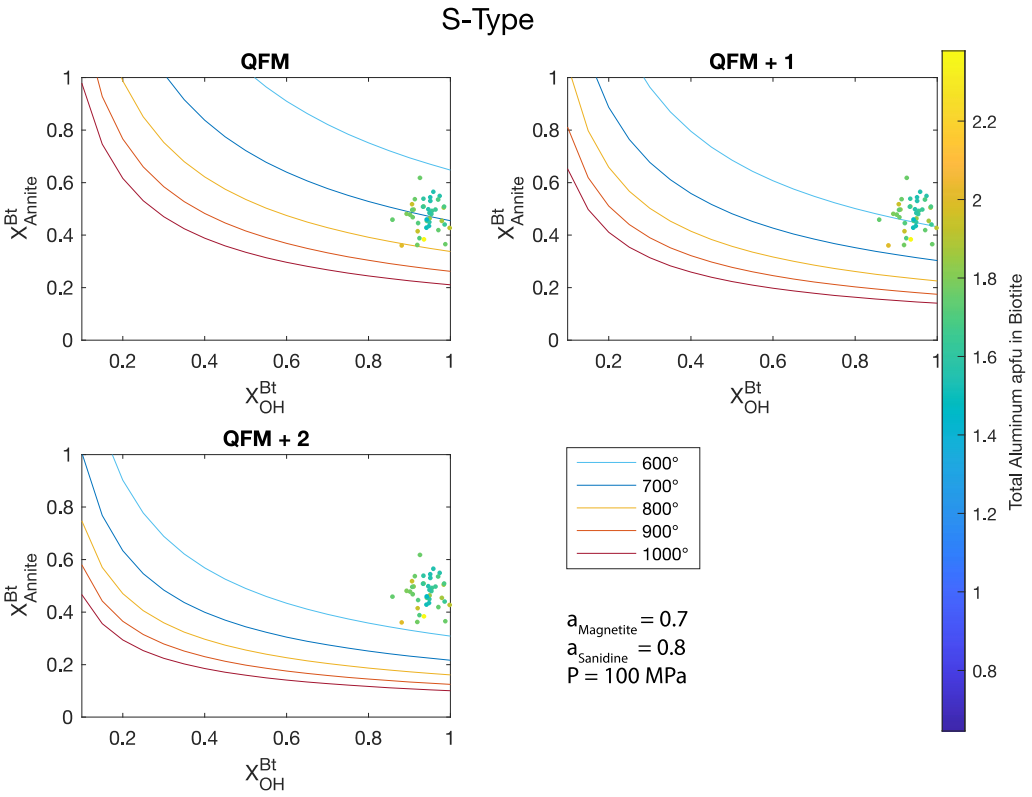

Figure 5.D7: Plot of $\boldsymbol{X^{Bt}_{Annite}}$ vs $\boldsymbol{X^{Bt}_{OH}}$ for biotite compositions from S-type granites at 100 MPa. See caption for Figure 5.D3 for details on curves, activity of magnetite, and activity of sanidine. Input for MELTS calculations was the average S-type granite from Chappell and White (1992).

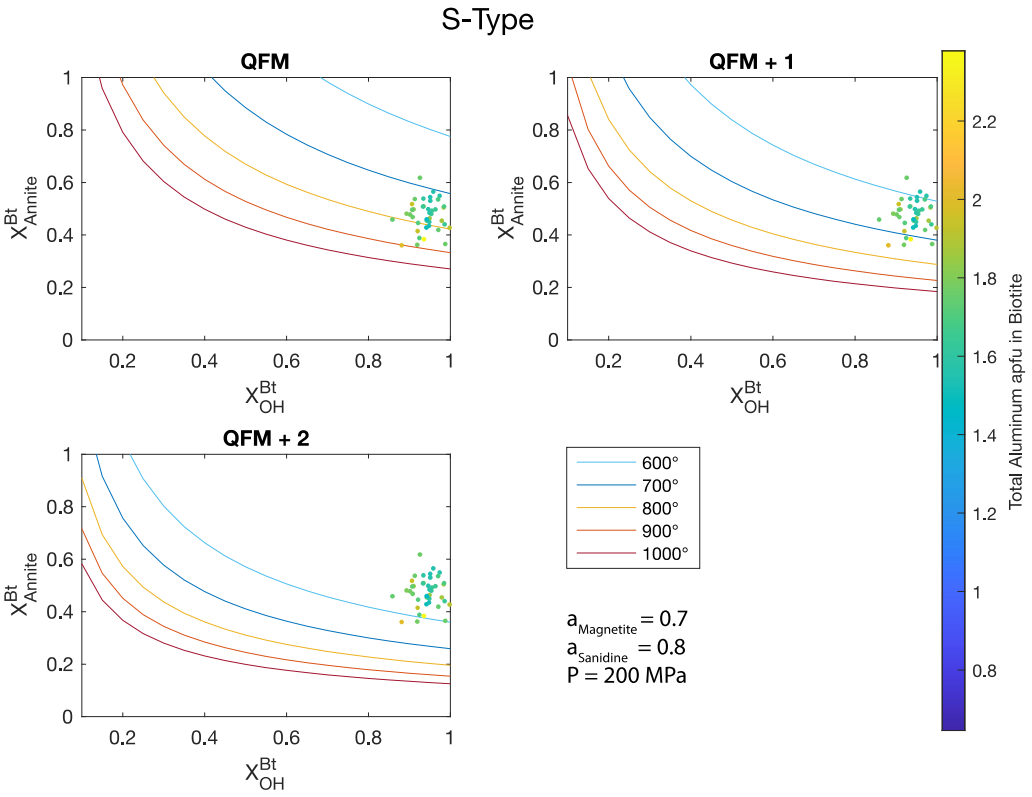

Figure 5.D8: Plot of $\boldsymbol{X^{Bt}_{Annite}}$ vs $\boldsymbol{X^{Bt}_{OH}}$ for biotite compositions from S-type granites at 200 MPa. See caption for Figure 5.D3 for details on curves, activity of magnetite, and activity of sanidine. Input for MELTS calculations was the average S-type granite from Chappell and White (1992).

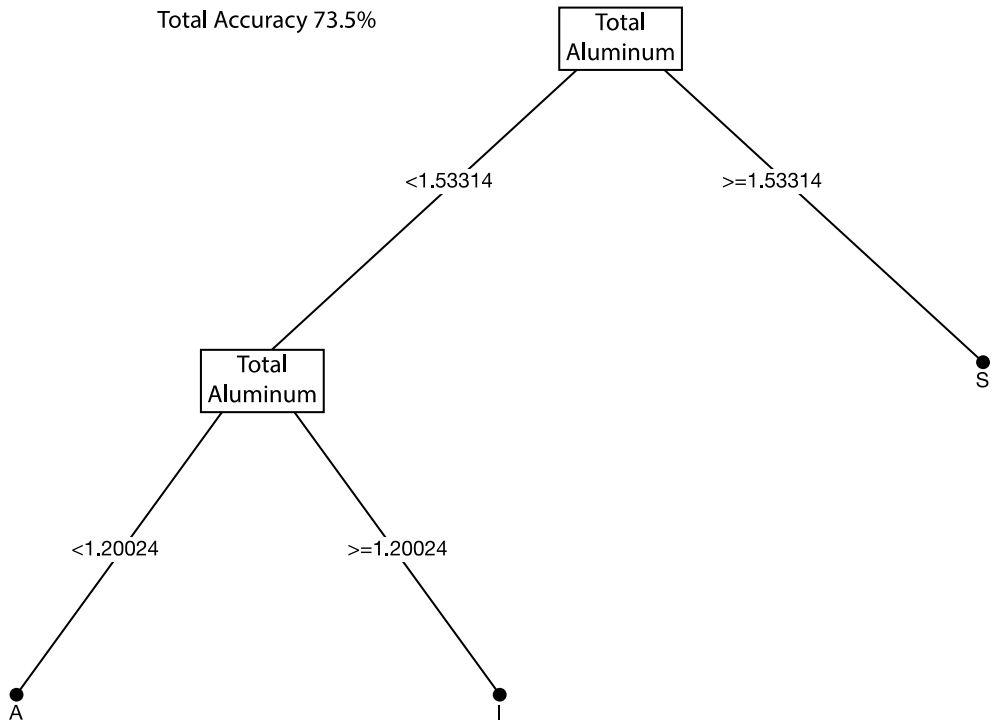

Figure 5.D9: Example decision tree for predictive model based on biotite composition. This decision tree is one tree in the "forest" of bagged trees. The total accuracy for this model is 73.5%.

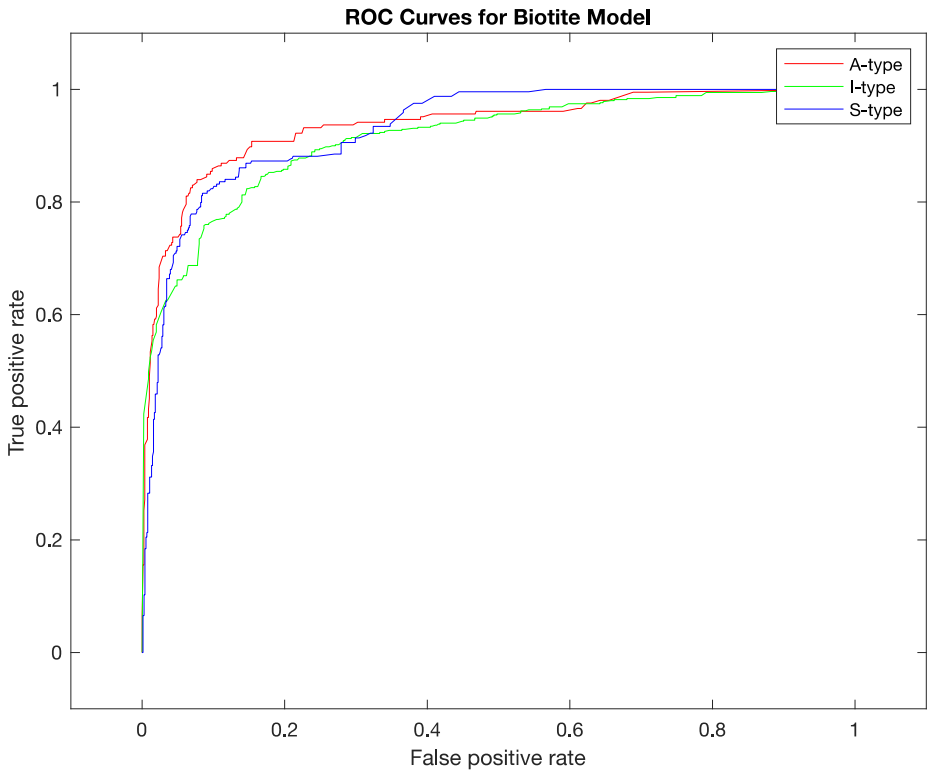

Figure 5.D10: ROC (Receiver Operating Characteristic) for the predictive model based on biotite composition. The y-axis is the true positive rate (i.e. the rate at which the model correctly classifies a granite). The x-axis is the false positive rate (i.e. the rate at which the model incorrectly classifies a granite). The curve shows the rate at which the model generates false positive for each true positive.

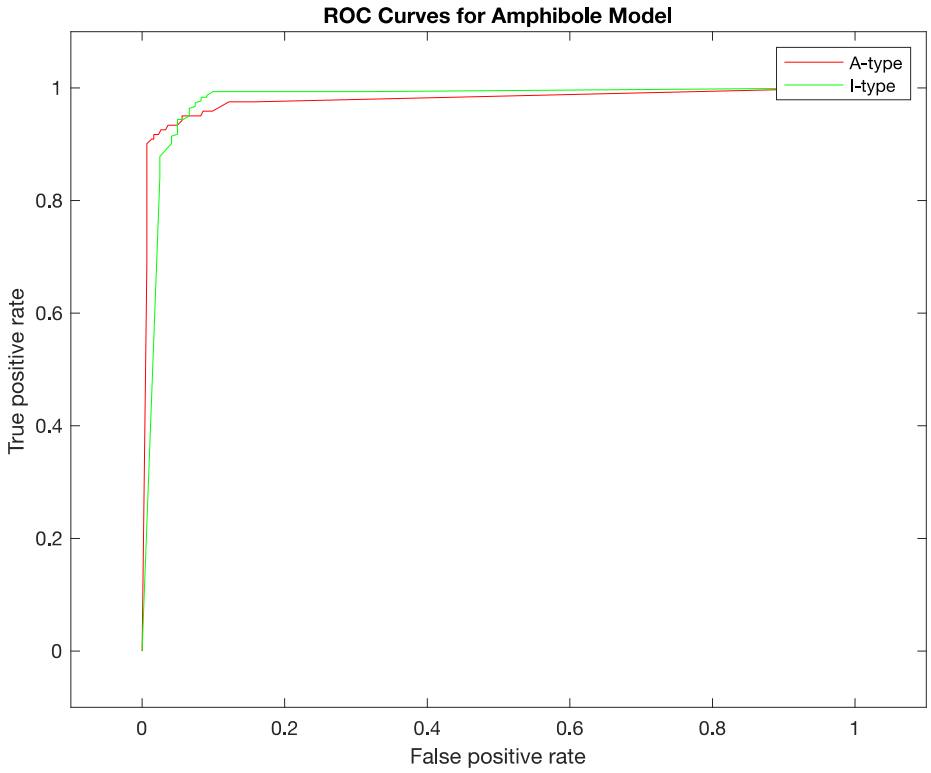

Figure 5.D11: ROC (Receiver Operating Characteristic) for the predictive model based on amphibole composition. See caption for Figure 5.D10 for additional details.

Appendix 5.E: Predictive Bootstrap Models

This appendix contains a series of MATLAB scripts and variables that are electronically available on https://drum.lib.umd.edu/ or upon request. This appendix contains the bootstrap models described in Chapter 5, an example of how to use these models, and the scripts and data used to train the models.

References

Abdel-Rahman, A.-F.M. (1994) Nature of biotites from alkaline, calc-alkaline, and peraluminous magmas. *Journal of Petrology* **35**, 525-541.

Adam, J. and Green, T. (2006) Trace element partitioning between mica- and amphibole-bearing garnet lherzolite and hydrous basanitic melt: 1. Experimental results and the investigation of controls on partitioning behaviour. *Contributions to Mineralogy and Petrology* **152**, 1-17.

Adam, J., Oberti, R., Cámara, F. and Green, T.H. (2007) An electron microprobe, LAM-ICP-MS and single-crystal X-ray structure refinement study of the effects of pressure, melt-H_2O concentration and fO_2 on experimentally produced basaltic amphiboles. *European Journal of Mineralogy* **19**, 641-655.

Ague, J.J. and Brimhall, G.H. (1987) Granites of the batholiths of California: Products of local assimilation and regional-scale crustal contamination. *Geology* **15**, 63-66.

Ague, J.J. and Brimhall, G.H. (1988) Regional variations in bulk chemistry, mineralogy, and the compositions of mafic and accessory minerals in the batholiths of California. *GSA Bulletin* **100**, 891-911.

Ahven, M. (2012) *Rautalammin Kiviniemen granaattipitoinen fayaliittiferrogabro (Petrology and geochronology of the Kiviniemi garnet-bearing fayalite ferrogabbro, Rautalampi)* [M.Sc.]:University of Helsinki, 62 p.

Ahven, M. (2016) Scandium deposits and potential in Finland. 32nd Nordic Geological Winter Meeting, Helsinki, Finland.

Andersen, T., Griffin, W.L. and Pearson, N.J. (2002) Crustal Evolution in the SW Part of the Baltic Shield: the Hf Isotope Evidence. *Journal of Petrology* **43**, 1725-1747.

Anderson, A.T., Swihart, G.H., Artioli, G. and Geiger, C.A. (1984) Segregation Vesicles, Gas Filter-Pressing, and Igneous Differentiation. *The Journal of Geology* **92**, 55-72.

Anderson, J.L. (1975) *Petrology and geochemistry of the Wolf River Batholith* [Ph.D.]:The University of Wisconsin-Madison, 297 p.

Anderson, J.L. and Bender, E.E. (1989) Nature and origin of Proterozoic A-type granitic magmatism in the southwestern United States of America. *Lithos* **23**, 19-52.

Annen, C., Blundy, J.D., Leuthold, J. and Sparks, R.S.J. (2015) Construction and evolution of igneous bodies: Towards an integrated perspective of crustal magmatism. *Lithos* **230**, 206-221.

Annen, C., Blundy, J.D. and Sparks, R.S.J. (2006) The Genesis of Intermediate and Silicic Magmas in Deep Crustal Hot Zones. *Journal of Petrology* **47**, 505-539.

Arculus, R.J. (2003) Use and Abuse of the Terms Calcalkaline and Calcalkalic. *Journal of Petrology* **44**, 929-935.

Artini, E. (1915) Due minerali di Baveno contenenti terre rare: weibyeïte e bazzite. *Atti della Reale Accademia dei Lincei, Rendiconti della Classe di Scienze Fisiche, Matematiche e Naturali* **24**, 313-319.

Asimow, P.D. and Ghiorso, M.S. (1998) Algorithmic modifications extending MELTS to calculate subsolidus phase relations. *American Mineralogist* **83**, 1127-1132.

Barbero, L. and Villaseca, C. (1992) The Layos Granite, Hercynian Complex of Toledo (Spain): an example of parautochthonous restite-rich granite in a granulitic area. *Earth and Environmental Science Transactions of the Royal Society of Edinburgh* **83**, 127-138.

Barnes, C.G., Werts, K., Memeti, V. and Ardill, K. (2020) Most granitoid rocks are cumulates: deductions from hornblende compositions and zircon saturation. *Journal of Petrology*.

Bayati, M., Esmaeily, D., Maghdour-Mashhour, R., Li, X.-H. and Stern, R.J. (2017) Geochemistry and petrogenesis of Kolah-Ghazi granitoids of Iran: Insights into the Jurassic Sanandaj-Sirjan magmatic arc. *Geochemistry* **77**, 281-302.

Beard, J.S. and Lofgren, G.E. (1989) Effect of Water on the Composition of Partial Melts of Greenstone and Amphibolite. *Science* **244**, 195.

Beard, J.S. and Lofgren, G.E. (1991) Dehydration Melting and Water-Saturated Melting of Basaltic and Andesitic Greenstones and Amphibolites at 1, 3, and 6.9 kb. *Journal of Petrology* **32**, 365-401.

Beattie, P. (1994) Systematics and energetics of trace-element partitioning between olivine and silicate melts: Implications for the nature of mineral/melt partitioning. *Chemical Geology* **117**, 57-71.

Bédard, J.H. (2005) Partitioning coefficients between olivine and silicate melts. *Lithos* **83**, 394-419.

Bédard, J.H. (2007) Trace element partitioning coefficients between silicate melts and orthopyroxene: Parameterizations of D variations. *Chemical Geology* **244**, 263-303.

Bédard, J.H. (2014) Parameterizations of calcic clinopyroxene—Melt trace element partition coefficients. *Geochemistry, Geophysics, Geosystems* **15**, 303-336.

Bergstøl, S. and Juve, G. (1988) Scandian ixiolite, pyrochlore and bazzite in granite pegmatite in terdal, Telemark, Norway. A contribution to the mineralogy and geochemistry of scandium and tin. *Mineralogy and Petrology* **38**, 229-243.

Bernhard, F., Walter, F., Ettinger, K., Taucher, J. and Mereiter, K. (1998) Pretulite, $ScPO_4$, a new scandium mineral from the Styrian and Lower Austrian lazulite occurrences, Austria, American Mineralogist, p. 625.

Bingen, B. and van Breemen, O. (1998) U-Pb monazite ages in amphibolite- to granulite-facies orthogneiss reflect hydrous mineral breakdown reactions: Sveconorwegian Province of SW Norway. *Contributions to Mineralogy and Petrology* **132**, 336-353.

Bjørlykke, H. (1935) The mineral paragenesis and classification of the granite pegmatites of Iveland, Setesdal, southern Norway.

Bjørlykke, H. (1937) The granite pegmatites of southern Norway. *American Mineralogist* **22**, 241-255.

Boesenberg, J.S. and Hewins, R.H. (2010) An experimental investigation into the metastable formation of phosphoran olivine and pyroxene. *Geochimica et Cosmochimica Acta* **74**, 1923-1941.

Bottinga, Y. and Weill, D.F. (1970) Densities of liquid silicate systems calculated from partial molar volumes of oxide components. *American Journal of Science* **269**, 169-182.

Bowman, A. and Foster, P. (1993) Density based exploration of bivariate data. *Statistics and Computing* **3**, 171-177.

Boyd, F.R. and England, J.L. (1960) Apparatus for phase-equilibrium measurements at pressures up to 50 kilobars and temperatures up to 1750°C. *Journal of Geophysical Research (1896-1977)* **65**, 741-748.

Bucholz, C.E., Stolper, E.M., Eiler, J.M. and Breaks, F.W. (2018) A Comparison of Oxygen Fugacities of Strongly Peraluminous Granites across the Archean–Proterozoic Boundary. *Journal of Petrology* **59**, 2123-2156.

Cámara, F., Marco, C., Kolitsch, U., Vignola, P., Hatert, F., Bittarello, E. and Bracco, R. (2018) *Bonacinaite, IMA 2018-056. CNMNC Newsletter No. 45, October 2018, page 1228*.

Candela, P.A. (1989a) Felsic magmas, volatiles, and metallogenesis. *Reviews in Economic Geology* **4**, 223-233.

Candela, P.A. (1989b) Magmatic ore-forming fluids: thermodynamic and mass-transfer calculations of metal concentrations. In ore deposition associated with magmas. *Reviews in Economic Geology* **4**, 203-221.

Candela, P.A. (1997) A review of shallow, ore-related granites: textures, volatiles, and ore Metals. *Journal of Petrology* **38**, 1619-1633.

Carmichael, I.S. (2002) The andesite aqueduct: perspectives on the evolution of intermediate magmatism in west-central (105–99°W) Mexico. *Contributions to Mineralogy and Petrology* **143**, 641-663.

Carmichael, I.S.E. (1991) The redox states of basic and silicic magmas: a reflection of their source regions? *Contributions to Mineralogy and Petrology* **106**, 129-141.

Černý, P. (1991) Rare-element Granitic Pegmatites. Part I: Anatomy and Internal Evolution of Pegmatitic Deposits. *Geoscience Canada* **18**.

Černý, P., Blevin, P.L., Cuney, M. and London, D. (2005) Granite-Related Ore Deposits, in: Hedenquist, J.W., Thompson, J.F.H., Goldfarb, R.J., Richards, J.P. (Eds.), One Hundredth Anniversary Volume. Society of Economic Geologists, pp. 337–370.

Černý, P. and Ercit, T.S. (2005) The Classification Of Granitic Pegmatites Revisited. *The Canadian Mineralogist* **43**, 2005-2026.

Chappell, B.W., Bryant, C.J. and Wyborn, D. (2012) Peraluminous I-type granites. *Lithos* **153**, 142-153.

Chappell, B.W. and Stephens, W.E. (2011) Origin of infracrustal (I-type) granite magmas. *Earth and Environmental Science Transactions of the Royal Society of Edinburgh* **79**, 71-86.

Chappell, B.W. and White, A.J.R. (1974) Two contrasting granite types. *Pacific Geology* **8**, 173-174.

Chappell, B.W. and White, A.J.R. (1992) I- and S-type granites in the Lachlan Fold Belt, in: Brown, P.E., Chappell, B.W. (Eds.), *The Second Hutton Symposium on the Origin of Granites and Related Rocks*. Geological Society of America.

Chappell, B.W. and White, A.J.R. (2001) Two contrasting granite types: 25 years later. *Australian Journal of Earth Sciences* **48**, 489-499.

Chassé, M., Griffin, W.L., Alard, O., O'Reilly, S.Y. and Calas, G. (2018) Insights into the mantle geochemistry of scandium from a meta-analysis of garnet data. *Lithos* **310-311**, 409-421.

Chassé, M., Griffin, W.L., O'Reilly, S.Y. and Calas, G. (2017) Scandium speciation in a world-class lateritic deposit. *Geochemical Perspectives Letters* **3**, 105-114.

Chou, I.M. (1986) Permeability of precious metals to hydrogen at 2kb total pressure and elevated temperatures. *American Journal of Science* **286**, 638-658.

Christie, D.M., Carmichael, I.S.E. and Langmuir, C.H. (1986) Oxidation states of mid-ocean ridge basalt glasses. *Earth and Planetary Science Letters* **79**, 397-411.

Clemens, J., Petford, N. and Mawer, C. (1997) Ascent mechanisms of granitic magmas: causes and consequences, in: Holness, M.B. (Ed.), *Deformation-Enhanced Fluid Transport in the Earth's Crust and Mantle*. Chapman and Hall, London, pp. 145-172.

Clemens, J.D., Holloway, J.R. and White, A.J.R. (1986) Origin of an A-type granite; experimental constraints. *American Mineralogist* **71**, 317-324.

Collins, W.J., Beams, S.D., White, A.J.R. and Chappell, B.W. (1982) Nature and origin of A-type granites with particular reference to southeastern Australia. *Contributions to Mineralogy and Petrology* **80**, 189-200.

Colson, R.O., McKay, G.A. and Taylor, L.A. (1988) Temperature and composition dependencies of trace element partitioning: Olivine/melt and low-Ca pyroxene/melt. *Geochimica et Cosmochimica Acta* **52**, 539-553.

Connelly, N.G., Damhus, T., Hartshorn, R.M. and Hutton, A.T. (2005) *Nomenclature of inorganic chemistry: IUPAC recommendations 2005*. The Royal Society of Chemistry.

Cooper, M.A., Hawthorne, F.C., Ball, N.A., Černý, P. and Kristiansen, R. (2006) Oftedalite, $(Sc,Ca,Mn^{2+})_2$ K $(Be,Al)_3Si_{12}O_{30}$, A New Member of the Milarite Group from the Heftetjern Pegmatite, Tørdal, Norway: Description and Crystal Structure. *The Canadian Mineralogist* **44**, 943-949.

Creaser, R.A., Price, R.C. and Wormald, R.J. (1991) A-type granites revisited: Assessment of a residual-source model. *Geology* **19**, 163-166.

Czamanske, G.K. and Wones, D.R. (1973) Oxidation during magmatic differentiation, Finnmarka complex, Oslo area, Norway: Part 2, the mafic silicates. *Journal of Petrology* **14**, 349-380.

Daigle, P.J. (2017) NI 43-101 Technical report on the Crater Lake Sc-Nb-REE Project Québec, Canada.

Dall'Agnol, R., Frost, C.D. and Rämö, O.T. (2012) IGCP Project 510 "A-type Granites and Related Rocks through Time": Project vita, results, and contribution to granite research. *Lithos* **151**, 1-16.

Deer, W.A., Howie, R.A. and Zussman, J. (1997) *Rock-forming Minerals: Double Chain Silicates*, 2nd Edition ed. Geological Society of London.

Deer, W.A., Howie, R.A. and Zussman, J. (2001) *Rock-forming Minerals: Framework Silicates: Feldspars*, 2nd Edition ed. Geological Society of London.

Deng, B., Li, G., Luo, J., Ye, Q., Liu, M., Peng, Z. and Jiang, T. (2017) Enrichment of Sc_2O_3 and TiO_2 from bauxite ore residues. *Journal of hazardous materials* **331**, 71-80.

Desborough, G.A. and Sharp, W.N. (1978) Tantalum, uranium, and scandium in heavy accessory oxides, Climax molybdenum mine, Climax, Colorado. *Economic Geology* **73**, 1749-1751.

Droop, G.T.R. (1987) A general equation for estimating Fe3+ concentrations in ferromagnesian silicates and oxides from microprobe analyses, using stoichiometric criteria. *Mineralogical magazine* **51**, 431-435.

Drüppel, K., Elsäßer, L., Brandt, S. and Gerdes, A. (2012) Sveconorwegian Mid-crustal Ultrahigh-temperature Metamorphism in Rogaland, Norway: U–Pb LA-ICP-MS Geochronology and Pseudosections of Sapphirine Granulites and Associated Paragneisses. *Journal of Petrology* **54**, 305-350.

Duyvesteyn, W.P.C. and Putnam, G.F. (2014) Scandium: A review of the element, its characteristics, and current and emerging commercial applications. EMC Metals Corporation, Sparks, Nevada, pp. 1-12.

Dymek, R.F. (1983) Titanium, aluminium and interlayer cation substitutions in biotite from high-grade gneisses, West Greenland. *American Mineralogist* **68**, 880-899.

Eby, G.N. (1990) The A-type granitoids: A review of their occurrence and chemical characteristics and speculations on their petrogenesis. *Lithos* **26**, 115-134.

Edelmann, F. (1926) Kolbeckit, ein neues sächsisches Mineral. *Jahrbuch für das Berg-und Hüttenwesen im Sachsen* **100**, 73-74.

Egorov, V.S., Kazakov, A.A., Kazantsev, V.V., Meshersky, Y.A. and G.E., O.R. (1993) Kumir scandium-rare-earth ore occurrence in Gornyi Altai. *Izvestiya Vysshikh Uchebnykh Zavedenii, Geologiya I Razvedka* **2**, 43-54.

Evans, T.M., C. O'Neill, H.S. and Tuff, J. (2008) The influence of melt composition on the partitioning of REEs, Y, Sc, Zr and Al between forsterite and melt in the system CMAS. *Geochimica et Cosmochimica Acta* **72**, 5708-5721.

Fairfield, P., Lonley, R., Widenbar, L., McEwing, S. and Kyle, J. (2018) Sunrise Nickel Cobal Project, New South Wales, Australia NI 43-101 Technical Report, SRK Consulting (Australia) Pty Ltd prepared for Clean TeQ Holdings Limited.

Fan, H.-R., Yang, K.-F., Hu, F.-F., Liu, S. and Wang, K.-Y. (2016) The giant Bayan Obo REE-Nb-Fe deposit, China: Controversy and ore genesis. *Geoscience Frontiers* **7**, 335-344.

Foord, E.E., Birmingham, S.D., Demartin, F., Pilati, T., Gramaccioli, C.M. and Lichte, F.E. (1993) Thortveitite and associated Sc-bearing minerals from Ravalli County, Montana. *Canadian Mineralogist* **31**, 337-346.

Frondel, C. (1970) Scandium-Rich Minerals From Rhyolite In Thomas Range, Utah. Mineralogical Society of America 1015 Eighteenth St, NW Suite 601, Washington, DC 20036, pp. 1058-1060.

Frost, C.D. and Frost, B.R. (2011) On ferroan (A-type) granitoids: their compositional variability and modes of origin. *Journal of Petrology* **52**, 39-53.
Gale, A., Dalton, C.A., Langmuir, C.H., Su, Y. and Schilling, J.-G. (2013) The mean composition of ocean ridge basalts. *Geochemistry, Geophysics, Geosystems* **14**, 489-518.
Gallahan, W.E. and Nielsen, R.L. (1992) The partitioning of Sc, Y, and the rare earth elements between high-Ca pyroxene and natural mafic to intermediate lavas at 1 atmosphere. *Geochimica et Cosmochimica Acta* **56**, 2387-2404.
Galuskina, I.O., Galuskin, E.V., Lazic, B., Armbruster, T., Dzierżanowski, P., Prusik, K. and Wrzalik, R. (2018) Eringaite, $Ca_3Sc_2(SiO_4)_3$, a new mineral of the garnet group. *Mineralogical Magazine* **74**, 365-373.
Ghiorso, M.S. and Gualda, G.A.R. (2015) An H2O–CO2 mixed fluid saturation model compatible with rhyolite-MELTS. *Contributions to Mineralogy and Petrology* **169**, 53.
Ghiorso, M.S., Hirschmann, M.M., Reiners, P.W. and Kress Iii, V.C. (2002) The pMELTS: A revision of MELTS for improved calculation of phase relations and major element partitioning related to partial melting of the mantle to 3 GPa. *Geochemistry, Geophysics, Geosystems* **3**, 1-35.
Ghiorso, M.S. and Sack, R.O. (1995) Chemical mass transfer in magmatic processes IV. A revised and internally consistent thermodynamic model for the interpolation and extrapolation of liquid-solid equilibria in magmatic systems at elevated temperatures and pressures. *Contributions to Mineralogy and Petrology* **119**, 197-212.
Gion, A.M., Piccoli, P.M. and Candela, P.A. (2018) Partitioning of indium between ferromagnesian minerals and a silicate melt. *Chemical Geology* **500**, 30-45.
Giordano, D., Russell, J.K. and Dingwell, D.B. (2008) Viscosity of magmatic liquids: A model. *Earth and Planetary Science Letters* **271**, 123-134.
Glazner, A.F., Bartley, J.M. and Coleman, D.S. (2019) A more informative way to name plutonic rocks. The Geological Society of America, GSA Today, pp. 4-10.
Goldsby, J., Jakupca, I., Farmer, S., Green, R., Demattia, B.T. and Loyselle, P. (2019) Evaluation Studies of an 800 W Solid Oxide-Based Fuel Cell Stack for Electrical Power in Aviation, 2018 Aviation Technology, Integration, and Operations Conference.
Goldschmidt, V.M. (1934) Drei Vorträge über Geochemie. *Geologiska Föreningen i Stockholm Förhandlingar* **56**, 385-427.
Goldschmidt, V.M. (1937) The principles of distribution of chemical elements in minerals and rocks. The seventh Hugo Müller Lecture, delivered before the Chemical Society on March 17th, 1937. *Journal of the Chemical Society (Resumed)*, 655-673.
Goldschmidt, V.M. (1954) *Geochemistry*. Oxford University Press.
Gramaccioli, C.M., Campostrini, I. and Orlandi, P. (2004) Scandium minerals in the miaroles of granite at Baveno, Italy. *European Journal of Mineralogy* **16**, 951-956.

Gramaccioli, C.M., Diella, V. and Demartin, F. (2000) The formation of scandium minerals as an example of the role of complexes in the geochemistry of rare earths and HFS elements. *European Journal of Mineralogy* **12**, 795-808.
Grant, K.J. and Wood, B.J. (2010) Experimental study of the incorporation of Li, Sc, Al and other trace elements into olivine. *Geochimica et Cosmochimica Acta* **74**, 2412-2428.
Green, T.H. and Pearson, N.J. (1986) Rare-earth element partitioning between sphene and coexisting silicate liquid at high pressure and temperature. *Chemical Geology* **55**, 105-119.
Gualda, G.A.R. and Ghiorso, M.S. (2015) MELTS_Excel: A Microsoft Excel-based MELTS interface for research and teaching of magma properties and evolution. *Geochemistry, Geophysics, Geosystems* **16**, 315-324.
Gualda, G.A.R., Ghiorso, M.S., Lemons, R.V. and Carley, T.L. (2012) Rhyolite-MELTS: a Modified Calibration of MELTS Optimized for Silica-rich, Fluid-bearing Magmatic Systems. *Journal of Petrology* **53**, 875-890.
Guastoni, A., Nestola, F., Ferraris, C. and Parodi, G. (2012) Xenotime-(Y) and Sn-rich thortveitite in miarolitic pegmatites from Baveno, Southern Alps, Italy. *Mineralogical Magazine* **76**, 761.
Gunow, A.J., Ludington, S. and Munoz, J.L. (1980) Fluorine in micas from the Henderson molybdenite deposit, Colorado. *Economic Geology* **75**, 1127-1137.
Gusev, A.I., Gusev, N.I. and Efimova, I.V. (2009) Magmatism and mineralisation of Kumir, Altai. *Rudy i metally* **6**, 21-28.
Gust, D.A. and Perfit, M.R. (1987) Phase relations of a high-Mg basalt from the Aleutian Island Arc: Implications for primary island arc basalts and high-Al basalts. *Contributions to Mineralogy and Petrology* **97**, 7-18.
Halkoaho, T., Ahven, M. and Rämö, O.T. (2013) A new type of magmatic Sc-Zr occurrencel located in the Kiviniemi area, Rautalampi, Central Finland, Mineral deposit research for a high-tech world. 12th Biennial SGA Meeting, pp. 12-15.
Halkoaho, T., Ahven, M., Rämö, O.T., Hokka, J. and Huhma, H. (2020) Petrography, geochemistry, and geochronology of the Sc-enriched Kiviniemi ferrodiorite intrusion, eastern Finland. *Mineralium Deposita*.
Hammarstrom, J.M. and Zen, E. (1986) Aluminum in hornblende: an empirical igneous geobarometer. *American Mineralogist* **71**, 1297-1313.
Hart, S.R. and Dunn, T. (1993) Experimental cpx/melt partitioning of 24 trace elements. *Contributions to Mineralogy and Petrology* **113**, 1-8.
Hauri, E.H., Wagner, T.P. and Grove, T.L. (1994) Experimental and natural partitioning of Th, U, Pb and other trace elements between garnet, clinopyroxene and basaltic melts. *Chemical Geology* **117**, 149-166.
Hawthorne, F.C., Oberti, R., Harlow, G.E., Maresch, W.V., Martin, R.F., Schumacher, J.C. and Welch, M.D. (2012) Nomenclature of the amphibole supergroup. *American Mineralogist* **97**, 2031-2048.
Helz, R.T. (1987) Differentiation behavior of Kilauea Iki lava lake, Kilauea Volcano, Hawaii: an overview of past and current work. *Magmatic Processes: Physicochemical Principles* **1**, 241-258.

Helz, R.T. and Wright, T.L. (1983) Drilling report and core logs for the 1981 drilling of Kilauea Iki lava lake, Kilauea volcano, Hawaii, with comparative notes on earlier (1967-1979) drilling experiences. Geological Survey, Reston, VA (USA).

Hill, E., Blundy, J.D. and Wood, B.J. (2011) Clinopyroxene–melt trace element partitioning and the development of a predictive model for HFSE and Sc. *Contributions to Mineralogy and Petrology* **161**, 423-438.

Himmelberg, G.R. and Loney, R.A. (1995) Characteristics and petrogenesis of alaskan-type ultramafic-mafic intrusions, Southeastern Alaska, Professional Paper 1564, - ed. United States Geological Survey.

Höche, T., Moisescu, C., Avramov, I., Rüssel, C. and Heerdegen, W.D. (2001) Microstructure of SiO2−Al2O3−CaO−P2O5−K2O−F- Glass Ceramics. 1. Needlelike versus Isometric Morphology of Apatite Crystals. *Chemistry of Materials* **13**, 1312-1319.

Hokka, J. and Halkoaho, T. (2015) 3D modelling and mineral resource estimation of the Kiviniemi Scandium deposit, Eastern Finland. Geologic Survey of Finland.

Holloway, J.R. and Burnham, C.W. (1972) Melting Relations of Basalt with Equilibrium Water Pressure Less Than Total Pressure1. *Journal of Petrology* **13**, 1-29.

Holtz, F. and Johannes, W. (1994) Maximum and minimum water contents of granitic melts: implications for chemical and physical properties of ascending magmas. *Lithos* **32**, 149-159.

Housh, T.B. and Luhr, J.F. (1991) Plagioclase-melt equilibria in hydrous systems. *American Mineralogist* **76**, 477-492.

Irvine, T.N. and Baragar, W.R.A. (1971) A Guide to the Chemical Classification of the Common Volcanic Rocks. *Canadian Journal of Earth Sciences* **8**, 523-548.

Irving, A. and Frey, F. (1976) Effect Of Composition On Partitioning Of Rare-Earth Elements, Hf, Sc And Co Between Garnet And Liquid-Experimental And Natural Evidence. *Transactions-American Geophysical Union* **57**, 339-339.

Jackson, S. (2008) LAMTRACE data reduction software for LA-ICP-MS. *Laser Ablation-ICP-Mass Spectrometry in the Earth Sciences: Current Practices and Outstanding Issues (Sylvester, P., Ed.), Mineralogical Association of Canada (MAC) Short Course Series* **40**, 305-307.

Jahns, R.H. (1982) Internal Evolution of pegmatite bodes, in: Černý, P. (Ed.), *Short Course in Granitic Pegmatites in Science and Industry*. Mineralogical Association of Canada, Winnipeg, pp. 293-327.

Jansen, J.B.H., Blok, R.J.P., Bos, A. and Scheelings, M. (1985) Geothermometry and Geobarometry in Rogaland and Preliminary Results from the Bamble Area, S Norway, in: Tobi, A.C., Touret, J.L.R. (Eds.), *The Deep Proterozoic Crust in the North Atlantic Provinces*. Springer Netherlands, Dordrecht, pp. 499-516.

Jenner, G.A., Foley, S.F., Jackson, S.E., Green, T.H., Fryer, B.J. and Longerich, H.P. (1994) Determination of partition coefficients for trace elements in high pressure-temperature experimental run products by laser ablation microprobe-

inductively coupled plasma-mass spectrometry (LAM-ICP-MS). *Geochimica et Cosmochimica Acta* **57**, 5099-5103.

Jochum, K.P., Stoll, B., Herwig, K., Willbold, M., Hofmann, A.W., Amini, M., Aarburg, S., Abouchami, W., Hellebrand, E., Mocek, B., Raczek, I., Stracke, A., Alard, O., Bouman, C., Becker, S., Dücking, M., Brätz, H., Klemd, R., de Bruin, D., Canil, D., Cornell, D., de Hoog, C.-J., Dalpé, C., Danyushevsky, L., Eisenhauer, A., Gao, Y., Snow, J.E., Groschopf, N., Günther, D., Latkoczy, C., Guillong, M., Hauri, E.H., Höfer, H.E., Lahaye, Y., Horz, K., Jacob, D.E., Kasemann, S.A., Kent, A.J.R., Ludwig, T., Zack, T., Mason, P.R.D., Meixner, A., Rosner, M., Misawa, K., Nash, B.P., Pfänder, J., Premo, W.R., Sun, W.D., Tiepolo, M., Vannucci, R., Vennemann, T., Wayne, D. and Woodhead, J.D. (2006) MPI-DING reference glasses for in situ microanalysis: New reference values for element concentrations and isotope ratios. *Geochemistry, Geophysics, Geosystems* **7**, 1-44.

Jochum, K.P., Willbold, M., Raczek, I., Stoll, B. and Herwig, K. (2005) Chemical Characterisation of the USGS Reference Glasses GSA-1G, GSC-1G, GSD-1G, GSE-1G, BCR-2G, BHVO-2G and BIR-1G Using EPMA, ID-TIMS, ID-ICP-MS and LA-ICP-MS. *Geostandards and Geoanalytical Research* **29**, 285-302.

Johan, Z., Ohnenstetter, M., Slansky, E., Barron, L.M. and Suppel, D. (1989) Platinum mineralization in the Alaskan-type intrusive complexes near Fifield, New South Wales, Australia part 1. platinum-group minerals in clinopyroxenites of the Kelvin Grove prospect, owendale intrusion. *Mineralogy and Petrology* **40**, 289-309.

Johannes, W. (1978) Melting of plagioclase in the system Ab−An−H_2O and Qz-Ab-An-H_2O at P_{H2O} =5 kbars, an equilibrium problem. *Contributions to Mineralogy and Petrology* **66**, 295-303.

Jolliff, B.L., Papike, J.J. and Shearer, C.K. (1992) Petrogenetic relationships between pegmatite and granite based on geochemistry of muscovite in pegmatite wall zones, Black Hills, South Dakota, USA. *Geochimica et Cosmochimica Acta* **56**, 1915-1939.

Joyce, A.S. (1970) *Geochemistry of the Murrumbidgee Batholith* [Ph.D.]:Australian National University, 219 p.

Kalashnikov, A.O., Yakovenchuk, V.N., Pakhomovsky, Y.A., Bazai, A.V., Sokharev, V.A., Konopleva, N.G., Mikhailova, J.A., Goryainov, P.M. and Ivanyuk, G.Y. (2016) Scandium of the Kovdor baddeleyite–apatite–magnetite deposit (Murmansk Region, Russia): Mineralogy, spatial distribution, and potential resource. *Ore Geology Reviews* **72**, 532-537.

Kempe, U. and Wolf, D. (2006) Anomalously high Sc contents in ore minerals from Sn–W deposits: Possible economic significance and genetic implications. *Ore Geology Reviews* **28**, 103-122.

Kogiso, T., Hirschmann, M.M. and Pertermann, M. (2004) High-pressure Partial Melting of Mafic Lithologies in the Mantle. *Journal of Petrology* **45**, 2407-2422.

Kolitsch, U., Kristiansen, R., Raade, G. and Tillmanns, E. (2010) Heftetjernite, a new scandium mineral from the Heftetjern pegmatite, Tørdal, Norway. *European Journal of Mineralogy* **22**, 309-316.

Krawczynski, M.J., Grove, T.L. and Behrens, H. (2012) Amphibole stability in primitive arc magmas: effects of temperature, H_2O content, and oxygen fugacity. *Contributions to Mineralogy and Petrology* **164**, 317-339.

Kress, V.C. and Carmichael, I.S.E. (1991) The compressibility of silicate liquids containing Fe_2O_3 and the effect of composition, temperature, oxygen fugacity and pressure on their redox states. *Contributions to Mineralogy and Petrology* **108**, 82-92.

Kuno, H. (1968) Differentiation of basalt magmas, in: Hess, H.H., Poldevaart, A.A. (Eds.), *Basalts: The Poldervaart treatise on rocks of basaltic composition*, pp. 623-688.

Lacroix, A. (1922) *Mineralogie de Madagascar, tome 1*.

Lange, R.A. (1994) The effect of H_2O, CO_2 and F on the density and viscosity of silicate melts. *Reviews in Mineralogy and Geochemistry* **30**, 331-369.

Lange, R.A. and Carmichael, I.S.E. (1987) Densities of Na_2O-K_2O-CaO-MgO-FeO-Fe_2O_3-Al_2O_3-TiO_2-SiO_2 liquids: New measurements and derived partial molar properties. *Geochimica et Cosmochimica Acta* **51**, 2931-2946.

Larsen, R.B., Polve, M. and Juve, G. (2000) Granite pegmatite quartz from Evje-Iveland: trace element chemistry and implications for the formation of high-purity quartz. *Norges Geologiske Undersokelse* **436**, 57-66.

Le Bas, M.J., Le Maitre, R.W., Streckeisen, A., Zanettin, B. and IUGS Subcommission on the Systematics of Igneous Rocks (1986) A chemical classification of volcanic rocks based on the total alkali-silica diagram. *Journal of Petrology* **27**, 745-750.

Lehmann, J. and Roux, J. (1986) Experimental and theoretical study of (Fe2+, Mg)(Al, Fe3+)2O4 spinels: Activity-composition relationships, miscibility gaps, vacancy contents. *Geochimica et Cosmochimica Acta* **50**, 1765-1783.

Lenczowski, B. (2002) New lightweight alloys for welded aircraft structure, Proceedings of the 23th International Congress of the Aeronautical Sciences-ICAS, pp. 4101.4101-4101.4104.

Liferovich, R.P., Yakovenchuk, V.N., Pakhomovsky, Y.A., Bogdanova, A.N. and Britvin, S.N. (1997) Juonniite, a new mineral of scandium from calcite-dolomite carbonatites of the Kovdor massif. *Zapiski Vserossijskogo Mineralogicheskogo Obshchestva* **126**, 56-63.

Loiselle, M.C. and Wones, D.R. (1979) Characteristics and origin of anorogenic granites. Geological Society of America, Abstracts with Programs, p. 468.

London, D. (1992) The application of experimental petrology to the genesis and crystallization of granitic pegmatites. *The Canadian Mineralogist* **30**, 499-540.

London, D. (2005) Granitic pegmatites: an assessment of current concepts and directions for the future. *Lithos* **80**, 281-303.

London, D. (2008) *Pegmatites*. Mineralogical Association of Canada.

London, D. (2018) Ore-forming processes within granitic pegmatites. *Ore Geology Reviews* **101**, 349-383.

London, D. and Kontak, D.J. (2012) Granitic Pegmatites: Scientific Wonders and Economic Bonanzas. *Elements* **8**, 257-261.
Longhi, J., Walker, D. and Hays, J.F. (1976) Fe and Mg in plagioclase, Lunar and Planetary Science Conference Proceedings, pp. 1281-1300.
Lynton, S.J., Candela, P.A. and Piccoli, P.M. (1993) An experimental study of the partitioning of copper between pyrrhotite and a high silica rhyolitic melt. *Economic Geology* **88**, 901-915.
Ma, C., Beckett, J.R. and Rossman, G.R. (2014a) Allendeite ($Sc_4Zr_3O_{12}$) and hexamolybdenum (Mo,Ru,Fe), two new minerals from an ultrarefractory inclusion from the Allende meteorite. *American Mineralogist* **99**, 654-666.
Ma, C., Krot, A.N., Nagashima, K. and Tschauner, O. (2014b) Warkite, IMA 2013-129. CNMNC Newsletter No. 20, June 2014: 552. *Mineralogical Magazine* **78**, 549-558.
Ma, C. and Rossman, G.R. (2009) Davisite, $CaScAlSiO_6$, a new pyroxene from the Allende meteorite. *American Mineralogist* **94**, 845-848.
Ma, C., Tschauner, O., Beckett, J.R., Rossman, G.R. and Liu, W. (2013) Kangite, $(Sc,Ti,Al,Zr,Mg,Ca,□)_2O3$, a new ultra-refractory scandia mineral from the Allende meteorite: Synchrotron micro-Laue diffraction and electron backscatter diffraction. *American Mineralogist* **98**, 870-878.
Madhusudhan Reddy, G., Mukhopadhyay, A.K. and Sambasiva Rao, A. (2005) Influence of scandium on weldability of 7010 aluminium alloy. *Science and Technology of Welding and Joining* **10**, 432-441.
Mahmood, A. (1983) Chemistry of biotites from a zoned granitic pluton in Morocco. *Mineralogical Magazine* **47**, 365-369.
Mahmood, A. and Bennani, A. (1984) S-type characteristics of the Hercynian granitoids of the Central Palaeozoic Massif, Morocco. *Geological Magazine* **121**, 301-309.
Manning, D.A.C. (1981) The effect of fluorine on liquidus phase relationships in the system Qz-Ab-Or with excess water at 1 kb. *Contributions to Mineralogy and Petrology* **76**, 206-215.
Marsh, B.D. (1996) Solidification fronts and magmatic evolution, Mineralogical Magazine, p. 5.
Marsh, B.D. (2019) in: Gion, A.M. (Ed.).
Mason, D.R. (1978) Compositional variations in ferromagnesian minerals from porphyry copper-generating and barren intrusions of the Western Highlands, Papua New Guinea. *Economic Geology* **73**, 878-890.
McDonough, W.F. and Sun, S.S. (1995) The composition of the Earth. *Chemical Geology* **120**, 223-253.
McKay, G.A. and Weill, D. (1977) KREEP petrogenesis revisited, Lunar and Planetary Science Conference Proceedings, pp. 2339-2355.
Mellini, M., Merlino, S. and Orlandi, P. (1982) Cascandite and jervisite, two new scandium silicates from Baveno, Italy. *American Mineralogist* **67**, 599-603.
Miyashiro, A. (1974) Volcanic rock series in island arcs and active continental margins. *American Journal of Science* **274**, 321-355.

Möller, A., O'Brien, P.J., Kennedy, A. and Kröner, A. (2002) Polyphase zircon in ultrahigh-temperature granulites (Rogaland, SW Norway): constraints for Pb diffusion in zircon. *Journal of Metamorphic Geology* **20**, 727-740.

Möller, A., O'Brien, P.J., Kennedy, A. and Kröner, A. (2003) Linking growth episodes of zircon and metamorphic textures to zircon chemistry: an example from the ultrahigh-temperature granulites of Rogaland (SW Norway). *Geological Society, London, Special Publications* **220**, 65.

Morganti, J. (1981) Ore deposit models—4. Sedimentary-type stratiform ore deposits: some models and a new classification. *Geoscience Canada* **8**, 65-75.

Müller, A., Flem, B., Snook, B., Bingen, B., Ihlen, P.M., Larsen, R.B. and Williamson, B.J. (2015) The Chemistry of Quartz in Granitic Pegmatites of Southern Norway: Petrogenetic and Economic Implications. *Economic Geology* **110**, 1737-1757.

Müller, A., Husdal, T., Sunde, Ø., Friis, H., Andersen, T., Johansen, T.S., Werner, R., Thoresen, Ø. and Olerud, S. (2017a) *Norwegian Pegmatites I: Tysfjord-Hamarøy, Evje-Iveland, Langesundsfjord*. Geological Society of Norway, Trondheim, Norway.

Müller, A., Romer, R.L. and Pedersen, R.-B. (2017b) The Sveconorwegian Pegmatite Province – Thousands of Pegmatites Without Parental Granites. *The Canadian Mineralogist* **55**, 283-315.

Müller, A., Spratt, J., Thomas, R., Williamson, B.J. and Seltmann, R. (2018) Alkali-F-Rich Albite Zones in Evolved NYF Pegmatites: The Product of Melt–melt Immiscibility. *The Canadian Mineralogist* **56**, 657-687.

Munoz, J.L. (1984) F-OH and Cl-OH exchange in micas with applications to hydrothermal ore deposits. *Reviews in Mineralogy and Geochemistry* **13**, 469-493.

Mutch, E.J.F., Blundy, J.D., Tattitch, B.C., Cooper, F.J. and Brooker, R.A. (2016) An experimental study of amphibole stability in low-pressure granitic magmas and a revised Al-in-hornblende geobarometer. *Contributions to Mineralogy and Petrology* **171**, 85.

Nandedkar, R.H. (2014) *Evolution of Hydrous Mantle-Derived Calc-Alkaline Liquids by Fractional Crystallization at 0.7 and 0.4 GPa – An Experimental Study* [PhD]:ETH Zurich, 204 p.

Nandedkar, R.H., Hürlimann, N., Ulmer, P. and Müntener, O. (2016) Amphibole–melt trace element partitioning of fractionating calc-alkaline magmas in the lower crust: an experimental study. *Contributions to Mineralogy and Petrology* **171**, 71.

Nandedkar, R.H., Ulmer, P. and Müntener, O. (2014) Fractional crystallization of primitive, hydrous arc magmas: an experimental study at 0.7 GPa. *Contributions to Mineralogy and Petrology* **167**, 1015.

Neiva, A.M.R. (1981) Geochemistry of hybrid granitoid rocks and of their biotites from central northern Portugal and their petrogenesis. *Lithos* **14**, 149-163.

Neumann, H. (1961) The scandium content of some Norwegian minerals and the formation of thortveitite, a reconnaissance survey. *Norsk Geologisk Tidsskrift* **41**, 197-210.

Nielsen, R.L., Gallahan, W.E. and Newberger, F. (1992) Experimentally determined mineral-melt partition coefficients for Sc, Y and REE for olivine, orthopyroxene, pigeonite, magnetite and ilmenite. *Contributions to Mineralogy and Petrology* **110**, 488-499.

Nielsen, T.F., Olsen, S.D. and Stensgaard, B.M. (2009) Developing a 3-D model for the Skaergaard intrusion in East Greenland: constraints on structure, mineralisation and petrogenetic models. *Geological Survey of Denmark and Greenland Bulletin* **17**, 61-64.

Norton, J.J. (1973) Lithium, cesium, and rubidium—the rare-alkali metals, in: Brobst, D.A., Pratt, W.P. (Eds.), Professional Paper, Washington, D.C., pp. 365-378.

Novák, M. (2007) Contamination in granitic pegmatites; examples from the Moldanubicum, Czech Republic, Granitic Pegmatites: the State of the Art International Symposium, University of Porto, Portugal, pp. 9-12.

Orlandi, P., Pasero, M. and Vezzalini, G. (1998) Scandiobabingtonite, a new mineral from the Baveno pegmatite, Piedmont, Italy. *American Mineralogist* **83**, 1330-1334.

Öz, D., Tomaschek, F., Lagos, M., Werner, R. and Geisler, T. (2018) Titanite U-Pb Geochronology of the Evje-Iveland Pegmatite Field, South-Norway, GeoBonn, Bonn, Germany.

Öz, D., Tomaschek, F., Werner, R. and Geisler, T. (2019) U-Th-total Pb geochronology of uraninite and its secondary phases (Evje-Iveland Pegmatite Field, Norway), GeoMünster, Münster, Germany.

Pan, Y. and Fleet, M.E. (2002) Compositions of the Apatite-Group Minerals: Substitution Mechanisms and Controlling Factors. *Reviews in Mineralogy and Geochemistry* **48**, 13-49.

Papale, P., Moretti, R. and Barbato, D. (2006) The compositional dependence of the saturation surface of H_2O + CO_2 fluids in silicate melts. *Chemical Geology* **229**, 78-95.

Patiño Douce, A.E. (1993) Titanium substitution in biotite: an empirical model with applications to thermometry, O_2 and H_2O barometries, and consequences for biotite stability. *Chemical Geology* **108**, 133-162.

Pedersen, M. (1993) *A geological study of the Flåt complex, Aust-Agder, Norway* [M.Sc. Thesis (in Danish)]:Copenhagen University, 128 p.

Pedersen, S. (1975) Intrusive rocks of the northern Iveland-Evje area, Aust-Agder. *Norges geologiske undersøkelse* **322**, 1-11.

Pedersen, S., Andersen, T., Konnerup-Madsen, J. and Griffin, W.L. (2009) Recurrent mesoproterozoic continental magmatism in South-Central Norway. *International Journal of Earth Sciences* **98**, 1151-1171.

Pereira, M.D. and Bea, F. (1994) Cordierite-producing reactions in the Pena Negra Complex, Avila Batholith, central Spain; the key role of cordierite in low-pressure anatexis. *The Canadian Mineralogist* **32**, 763-780.

Perfit, M.R. (1977) *The petrochemistry of igneous rocks from the Cayman Trench and the Captains Bay pluton, Unalaska Island: their relation to tectonic processes at plate margins*]:Columbia University, 237 p.

Petford, N. and Gallagher, K. (2001) Partial melting of mafic (amphibolitic) lower crust by periodic influx of basaltic magma. *Earth and Planetary Science Letters* **193**, 483-499.
Petrella, L., Williams-Jones, A.E., Goutier, J. and Walsh, J. (2014) The Nature and Origin of the Rare Earth Element Mineralization in the Misery Syenitic Intrusion, Northern Quebec, Canada. *Economic Geology* **109**, 1643-1666.
Pezzotta, F., Diella, V. and Guastoni, A. (2005) Scandium silicates from the Baveno and Cuasso al Monte NYF-granites, Southern Alps (Italy): Mineralogy and genetic inferences. *American Mineralogist* **90**, 1442-1452.
Piccoli, P.M. and Candela, P.A. (2002) Apatite in Igneous Systems. *Reviews in Mineralogy and Geochemistry* **48**, 255-292.
Popp, R.K., Gilbert, M.C. and Craig, J.R. (1977) Stability of Fe-Mg amphiboles with respect to oxygen fugacity. *American Mineralogist* **62**, 1-12.
Pursell, D.C. (2016) March Quarterly Report. Jervois Mining Ltd, Cheltenham, Australia.
Putirka, K. (2016) Amphibole thermometers and barometers for igneous systems and some implications for eruption mechanisms of felsic magmas at arc volcanoes. *American Mineralogist* **101**, 841-858.
Raade, G., Ferraris, G., Gula, A., Ivaldi, G. and Bernhard, F. (2002) Kristiansenite, a new calcium–scandium–tin sorosilicate from granite pegmatite in Tørdal, Telemark, Norway. *Mineralogy and Petrology* **75**, 89-99.
Rangott, M., Hutchin, S., Basile, D., Ricketts, N., Duckworth, G. and Rowles, T.D. (2016) Feasibility Study - Nyngan Scandium Project NI 43-101 Technical Report.
Rapp, R.P. (1995) Amphibole-out phase boundary in partially melted metabasalt, its control over liquid fraction and composition, and source permeability. *Journal of Geophysical Research: Solid Earth* **100**, 15601-15610.
Rapp, R.P. and Watson, E.B. (1995) Dehydration Melting of Metabasalt at 8–32 kbar: Implications for Continental Growth and Crust-Mantle Recycling. *Journal of Petrology* **36**, 891-931.
Rapp, R.P., Watson, E.B. and Miller, C.F. (1991) Partial melting of amphibolite/eclogite and the origin of Archean trondhjemites and tonalites. *Precambrian Research* **51**, 1-25.
Ray, G.L., Shimizu, N. and Hart, S.R. (1983) An ion microprobe study of the partitioning of trace elements between clinopyroxene and liquid in the system diopside-albite-anorthite. *Geochimica et Cosmochimica Acta* **47**, 2131-2140.
Riva, S., Yusenko, K.V., Lavery, N.P., Jarvis, D.J. and Brown, S.G.R. (2016) The scandium effect in multicomponent alloys. *International Materials Reviews* **61**, 203-228.
Robie, R.A. and Hemingway, B.S. (1995) Thermodynamic properties of minerals and related substances at 298.15 K and 1 bar (10^5 pascals) pressure and at higher temperatures, Bulletin 2131, - ed, United States Geological Survey, p. 461.
Roeder, P.L. and Emslie, R.F. (1970) Olivine-liquid equilibrium. *Contributions to Mineralogy and Petrology* **29**, 275-289.

Romer, R.L. and Smeds, S.-A. (1996) U-Pb columbite ages of pegmatites from Sveconorwegian terranes in southwestern Sweden. *Precambrian Research* **76**, 15-30.
Rosing-Schow, N., Müller, A. and Friis, H. (2018) A Comparison of the Mica Geochemistry of the Pegmatite Fields in Southern Norway. *The Canadian Mineralogist* **56**, 463-488.
Røyset, J. and Ryum, N. (2005) Scandium in aluminium alloys. *International Materials Reviews* **50**, 19-44.
Rudnick, R.L. and Gao, S. (2003) Composition of the continental crust, in: Holland, H.D., Turekian, K.K. (Eds.), *Treatise on Geochemistry*. Pergamon, Oxford, pp. 1-64.
Rushmer, T. (1991) Partial melting of two amphibolites: contrasting experimental results under fluid-absent conditions. *Contributions to Mineralogy and Petrology* **107**, 41-59.
Sakurai, K.-i., Nagashima, K. and Kato, A. (1962) Thortveitite from Kobe, Omiya, Kyoto, Japan. *Bulletin of the Chemical Society of Japan* **35**, 1776-1779.
Sawyer, E.W. (1991) Disequilibrium Melting and the Rate of Melt–Residuum Separation During Migmatization of Mafic Rocks from the Grenville Front, Quebec. *Journal of Petrology* **32**, 701-738.
Schärer, U., Wilmart, E. and Duchesne, J.-C. (1996) The short duration and anorogenic character of anorthosite magmatism: UPb dating of the Rogaland complex, Norway. *Earth and Planetary Science Letters* **139**, 335-350.
Scherer, E., Münker, C. and Mezger, K. (2001) Calibration of the Lutetium-Hafnium Clock. *Science* **293**, 683.
Schetelig, J. (1911) Über Thortveitit, ein neues Mineral. *Centralblatt für Mineralogie, Geologie und Paläontologie*, 721-726.
Shabani, A.A.T., Lalonde, A.E. and Whalen, J.B. (2003) Composition of biotite from granitic rocks of the Canadian Appalachian Orogen: A potential tectonomagmatic indicator? *The Canadian Mineralogist* **41**, 1381-1396.
Shannon, R.D.T. (1976) Revised Effective Ionic Radii and Systematic Studies of Interatomie Distances in Halides and Chaleogenides. *Acta crystallographica section A: crystal physics, diffraction, theoretical and general crystallography* **32**, 751-767.
Shea, T., Hammer, J.E., Hellebrand, E., Mourey, A.J., Costa, F., First, E.C., Lynn, K.J. and Melnik, O. (2019) Phosphorus and aluminum zoning in olivine: contrasting behavior of two nominally incompatible trace elements. *Contributions to Mineralogy and Petrology* **174**, 85.
Shimazaki, H., Yang, Z., Miyawaki, R. and Shigeoka, M. (2008) Scandium-Bearing Minerals in the Bayan Obo Nb-REE-Fe Deposit, Inner Mongolia, China. *Resource Geology* **58**, 80-86.
Simmons, W., Falster, A., Webber, K., Roda-Robles, E., Boudreaux, A.P., Grassi, L.R. and Freeman, G. (2016) Bulk Composition of Mt. Mica Pegmatite, Maine, USA:IMPLICATIONS For the Origin of an Lct Type Pegmatite By Anatexis. *The Canadian Mineralogist* **54**, 1053-1070.

Smith, J. and Brown, W. (1988) *Feldspar Minerals: Volume 1 Crystal Structures, Physical, Chemical, and Microtextural Properties* Springer-Verlag Berlin Heidelberg.
Smith, M.P. (2007) Metasomatic silicate chemistry at the Bayan Obo Fe–REE–Nb deposit, Inner Mongolia, China: Contrasting chemistry and evolution of fenitising and mineralising fluids. *Lithos* **93**, 126-148.
Smith, M.P. and Henderson, P. (2000) Preliminary Fluid Inclusion Constraints on Fluid Evolution in the Bayan Obo Fe-REE-Nb Deposit, Inner Mongolia, China. *Economic Geology* **95**, 1371-1388.
Smith, P.M. and Asimow, P.D. (2005) Adiabat_1ph: A new public front-end to the MELTS, pMELTS, and pHMELTS models. *Geochemistry, Geophysics, Geosystems* **6**.
Snook, B. (2014) *Towards exploration tools for high purity quartz: an example from the South Norwegian Evje-Iveland pegmatite belt* [PhD]:University of Exeter, 284 p.
Song, W., Xu, C., Smith, M.P., Chakhmouradian, A.R., Brenna, M., Kynický, J., Chen, W., Yang, Y., Deng, M. and Tang, H. (2018) Genesis of the world's largest rare earth element deposit, Bayan Obo, China: Protracted mineralization evolution over ~1 b.y. *Geology* **46**, 323-326.
Spirin, A., Ivanov, V., Nikonov, A., Lipilin, A., Paranin, S., Khrustov, V. and Spirina, A. (2012) Scandia-stabilized zirconia doped with yttria: Synthesis, properties, and ageing behavior. *Solid State Ionics* **225**, 448-452.
Stambouli, A.B. and Traversa, E. (2002) Solid oxide fuel cells (SOFCs): a review of an environmentally clean and efficient source of energy. *Renewable and Sustainable Energy Reviews* **6**, 433-455.
Steffenssen, G., Müller, A., Rosing-Schow, N. and Friis, H. (2019) The distribution and enrichment of scandium in garnets from the TØrdal pegmatites, south Norway, and its economic implications. *The Canadian Mineralogist* **57**, 799-801.
Stewart, D.B. (1978) Petrogenesis of lithium-rich pegmatites. *American Mineralogist* **63**, 970-980.
Stilling, A., Ćerný, P. and Vanstone, P.J. (2006) The Tanco Pegmatite at Bernic Lake, Manitoba. Xvi. Zonal and Bulk Compositions and Their Petrogenetic Significance. *The Canadian Mineralogist* **44**, 599-623.
Stockmarr, P. (1994) *A description of pegmatites at Åvesland and Evje, South Norway* [M.Sc. Thesis]:University of Copenhagen.
Sun, C. and Stimming, U. (2007) Recent anode advances in solid oxide fuel cells. *Journal of Power Sources* **171**, 247-260.
Suppel, D.W., Barron, L.M., Gould, K.W., Etheridge, L. and Tadros, N.Z. (1986) *Platinum in basic to ultrabasic intrusive complexes at Fifield: a preliminary report*.
Tarkhanov, A.V., Kulayev, A.R., Petrin, A.V. and Kozyr'kov, V.D. (1992) The Zheltorechensk vanadium-scandium deposit. *International Geology Review* **34**, 496-502.
Taylor, B.E. and Friedrichsen, H. (1983a) Light stable isotope systematics of granitic pegmatites from North America and Norway. *Chemical Geology* **41**, 127-167.

Taylor, B.E. and Friedrichsen, H. (1983b) Oxygen and hydrogen isotope disequilibria in the Landsverk I pegmatite, Evje, southern Norway: evidence for anomalous hydrothermal fluids. *Norsk Geologisk Tidsskrift* **63**, 199-209.

Taylor, J.R., Wall, V.J. and Pownceby, M.I. (1992) The calibration and application of accurate redox sensors. *American Mineralogist* **77**, 284-295.

Thomas, R., Webster, J.D. and Heinrich, W. (2000) Melt inclusions in pegmatite quartz: complete miscibility between silicate melts and hydrous fluids at low pressure. *Contributions to Mineralogy and Petrology* **139**, 394-401.

Tuthill, R.L. (1968) *The hydrothermal behavior of basalts in their melting range at 5 kilobars* [MSc]:Pennsylvania State University.

U.S. Geological Survey (2020) *Mineral commodity summaries 2020*. U.S. Geological Survey.

Vander Auwera, J., Bolle, O., Bingen, B., Liégeois, J.P., Bogaerts, M., Duchesne, J.C., De Waele, B. and Longhi, J. (2011) Sveconorwegian massif-type anorthosites and related granitoids result from post-collisional melting of a continental arc root. *Earth-Science Reviews* **107**, 375-397.

Villaseca, C. and Barbero, L. (1994) Chemical variability of Al-Ti-Fe-Mg minerals in peraluminous granitoid rocks from central Spain. *European Journal of Mineralogy* **6**, 691-710.

Wager, L.R. and Brown, G.M. (1968) *Layered Igneous Rocks*. Oliver and Boyd, Edinburgh.

Welsch, B., Hammer, J. and Hellebrand, E. (2014) Phosphorus zoning reveals dendritic architecture of olivine. *Geology* **42**, 867-870.

Werts, K., Barnes, C.G., Memeti, V., Ratschbacher, B., Williams, D. and Paterson, S.R. (2020) Hornblende as a tool for assessing mineral-melt equilibrium and recognition of crystal accumulation. *American Mineralogist* **105**, 77-91.

Westphal, M., Schumacher, J.C. and Boschert, S. (2003) High-Temperature Metamorphism and the Role of Magmatic Heat Sources at the Rogaland Anorthosite Complex in Southwestern Norway. *Journal of Petrology* **44**, 1145-1162.

Westrenen Wim, V., Blundy, J. and Wood, B. (1999) Crystal-chemical controls on trace element partitioning between garnet and anhydrous silicate melt, American Mineralogist, p. 838.

Whalen, J.B. (1993) Geology, petrography, and geochemistry of Appalachian granites in New Brunswick and Gaspésie, Quebec, Bulletin 436. Geologic Survey of Canada, p. 124.

Whalen, J.B. and Chappell, B.W. (1988) Opaque mineralogy and mafic mineral chemistry of I- and S-type granites of the Lachlan fold belt, Southeast Australia. *American Mineralogist* **73**, 281-296.

Whalen, J.B., Currie, K.L. and Chappell, B.W. (1987) A-type granites: geochemical characteristics, discrimination and petrogenesis. *Contributions to Mineralogy and Petrology* **95**, 407-419.

White, A.J.R., Clemens, J.D., Holloway, J.R., Silver, L.T., Chappell, B.W. and Wall, V.J. (1986) S-type granites and their probable absence in southwestern North America. *Geology* **14**, 115-118.

Williams-Jones, A.E. and Vasyukova, O.V. (2018) The Economic Geology of Scandium, the Runt of the Rare Earth Element Litter. *Economic Geology* **113**, 973-988.

Winter, J.D. (2010) *Principles of igneous and metamorphic petrology*, 2nd ed. Pearson Education.

Winther, K.T. and Newton, R.C. (1991) Experimental melting of hydrous low-K tholeiite: evidence onthe origin of Archaean cratons. *Bulletin of the Geological Society of Denmark* **39**, 213-228.

Wolf, M.B. and Wyllie, P.J. (1991) Dehydration-melting of solid amphibolite at 10 kbar: Textural development, liquid interconnectivity and applications to the segregation of magmas. *Mineralogy and Petrology* **44**, 151-179.

Wolf, M.B. and Wyllie, P.J. (1994) Dehydration-melting of amphibolite at 10 kbar: the effects of temperature and time. *Contributions to Mineralogy and Petrology* **115**, 369-383.

Wolf, M.B. and Wyllie, P.J. (1995) Liquid segregation parameters from amphibolite dehydration melting experiments. *Journal of Geophysical Research: Solid Earth* **100**, 15611-15621.

Wones, D.R. (1972) Stability of biotite-a reply. *American Mineralogist* **57**, 316-317.

Wones, D.R. and Eugster, H.P. (1965) Stability of biotite-experiment theory and application. *American Mineralogist* **50**, 1228-1272.

Wood, S.A. and Samson, I.M. (2006) The aqueous geochemistry of gallium, germanium, indium and scandium. *Ore Geology Reviews* **28**, 57-102.

Wright, T.L., Peck, D.L. and Shaw, H.R. Kilauea Lava Lakes: Natural Laboratories for Study of Cooling, Crystallization, and Differentiation of Basaltic Magma, *The Geophysics of the Pacific Ocean Basin and Its Margin*.

Wyllie, P.J. and Wolf, M.B. (1993) Amphibolite dehydration-melting: sorting out the solidus. *Geological Society, London, Special Publications* **76**, 405.

Yakovenchuk, V.N., Ivanyuk, G.Y., Pakhomovsky, Y.A., Panikorovskii, T.L., Britvin, S.N., Krivovichev, S.V., Shilovskikh, V.V. and Bocharov, V.N. (2018) Kampelite, $Ba_3Mg_{1.5}Sc_4(PO_4)_6(OH)_3{\cdot}4H_2O$, a new very complex Ba-Sc phosphate mineral from the Kovdor phoscorite-carbonatite complex (Kola Peninsula, Russia). *Mineralogy and Petrology* **112**, 111-121.

Yamamoto, O. (2000) Solid oxide fuel cells: fundamental aspects and prospects. *Electrochimica Acta* **45**, 2423-2435.

Yamamoto, O., Arati, Y., Takeda, Y., Imanishi, N., Mizutani, Y., Kawai, M. and Nakamura, Y. (1995) Electrical conductivity of stabilized zirconia with ytterbia and scandia. *Solid State Ionics* **79**, 137-142.

Yoder, H.S., Stewart, D.B. and Smith, J.R. (1957) Ternary feldspars. *Carnegie Institution of Washington Yearbook* **56**, 206-214.

Yoder, H.S. and Tilley, C.E. (1962) Origin of Basalt Magmas: An Experimental Study of Natural and Synthetic Rock Systems. *Journal of Petrology* **3**, 342-532.

Zen, E.A. (1986) Aluminum Enrichment in Silicate Melts by Fractional Crystallization: Some Mineralogic and Petrographic Constraints. *Journal of Petrology* **27**, 1095-1117.

Zhang, J., Humphreys, M.C.S., Cooper, G.F., Davidson, J.P. and Macpherson, C.G. (2017) Magma mush chemistry at subduction zones, revealed by new melt major element inversion from calcic amphiboles. *American Mineralogist* **102**, 1353-1367.